Mass Transport Deposits:
Implications for Reservoir Seals

Tuviere Omeru

Submitted in partial fulfilment of the requirements for the degree of Ph.D

Cardiff University

May 2014

DECLARATION

This work has not previously been accepted in substance for any degree and is not concurrently submitted in candidature for any degree.

Signed………….…………..(candidate)　　　Date………………………….

STATEMENT 1

This thesis is being submitted in partial fulfilment of the requirements for the degree of PhD.

Signed………….…………..(candidate)　　　Date………………………….

STATEMENT 2

This thesis is the result of my independent work/investigation, except where otherwise stated. Other sources are acknowledged by explicit references.

Signed………….…………..(candidate)　　　Date………………………….

STATEMENT 3

I hereby consent for my thesis, if accepted, to be available for photocopying and for inter-library loan, and for the title and summary to be made available to outside.

Signed………….…………..(candidate)　　　Date………………………….

STATEMENT 4: PREVIOUSLY APPROVED BAR ON ACCESS

I hereby consent for my thesis, if accepted, to be available for photocopying and for inter-library **loans after expiry of a bar on access previously approved by the Graduate Development Committee.**

Signed………….…………..(candidate)　　　　Date………………………….

Abstract

This thesis uses a combination of two-dimensional (2D) and three-dimensional (3D) seismic-reflection data to investigate the morphology and internal architecture of mass transport deposits (MTDs) from the west Nile delta, offshore Egypt and from the Deepwater Taranaki Basin, New Zealand. The overall aim of the project is to gain an improved understanding of the impact of MTDs on hydrocarbon seals. To this end a novel seismic based classification for MTDs that is directly mappable onto the problem of defining their potential as sealing sequences is proposed based on results of investigations from three core research chapters.

In the first core chapter, the phases and mechanisms of failure of three main MTDs (termed A, B and C) in the western Nile delta (Eastern Mediterranean) was investigated using 3D seismic data. Analysis of the geometries of the MTDs suggests that they were emplaced in at least two main phases: Progressive failure occurred initially with MTD A cutting through MTDs B and C. Retrogressive failure then occurred due to the natural unbalance of the supposed headwall of MTD A. Reconstruction of the pre-seabed topography suggests a minimum total volume (residual and depleted) of remobilisation of the order of 750 km^3, making this amongst the largest submarine landslide complexes documented to date. It is suggested that this giant slope failure might have posed a risk to the integrity of petroleum seals considering that the failure occurred in a gas rich province of the western Nile delta.

In the second core chapter, six large scale MTDs, stacked and locally amalgamated making up c. 50% of the stratigraphic succession were recognised and mapped using 2D seismic data. Key kinematic features suggest a north-westerly transport direction for all of the MTDs with the exception of MTD 6, having a south-westerly transport direction. There is seismic stratigraphic evidence in the form of both lateral and basal truncations suggesting that the MTDs were erosive during their emplacement. Estimation shows that c 70% of the final volume of MTD 6 was contributed from substrate cannibalization greater than the other five MTDs in the study area. This work suggests that the rheology of the substrate immediately beneath the seafloor might not be the only factor controlling the degree of substrate cannibalisation during MTD emplacement and that the nature of any triggering mechanism might also play an important role. This has a bearing on the MTD content (sandy or muddy dominated MTD) and would in turn influence the seal integrity of MTD.

The final core chapter presents insights into the dynamics of emplacement of MTD 6 using 3D seismic data. MTD 6 consists of five distinctive domains (labelled A – E). Domains A – C show evidence of deformation and remobilisation of c. 30% of a lower transparent interval while Domain D is characterised by a partial or complete loss of seismic character coupled with c. 30% reduction in thickness compared to adjacent domains. Based on the deformation styles, the transition across domain boundaries and the observed volume loss, a progressive stratal disaggregation is inextricably linked with gravity spreading as the mode of emplacement of MTD 6. This study highlights the power of 3D seismic data in unravelling the detailed processes involved during MTD emplacement and which may have significant implications as regards the translation and emplacement of other submarine slope failures in other continental margins.

Acknowledgements

Table of Contents

List of Figures

Chapter 1

Chapter 2

Chapter 3

Chapter 4

Chapter 5

List of Tables

Chapter 1

1.0 Introduction

1.1 Rationale

Mass-transport deposits (MTDs) is a seismic-stratigraphic term that was first introduced by (Weimer, 1989, 1990) to identify seismically chaotic deposits (i.e transparent and laterally discontinuous zones) generated by large scale sediment failures. The term encompasses all forms of gravity-induced slope failure processes including slides, slumps and debris flows (Jenner et al., 2007; Posamentier and Martinsen, 2011; Weimer and Shipp, 2004) with the exception of turbidites which are sediment flows deposited by turbidity currents (Shanmugam et al., 1994) (Fig. 1.1).

A geological seal is typically a rock of low permeability that serves as a physical barrier to fluid migration (Downey, 1994). Fine-grained siliciclastic (e.g., clay-rich shale) or an evaporite deposit (e.g., salt, anhydrite) are common seal rocks. In this study, only siliciclastic seals are considered. The low permeability character of seals, typically in the range of micro-Darcy (mD) permeabilities or less, is the product of small grain size (mm) and smaller pore-throat diameters (nanometers).

During the last decade, extensive interpretations of 3D seismic data have shown that MTDs are fundamental elements in the stratigraphic architecture of many continental margins. They constitute significant proportion of the stratigraphic succession. For example in Deepwater Brunei, MTDs comprise c. 50% of the depositional sequences (McGilvery and Cook, 2003). Offshore Nile they average 50% of the cumulative thickness of the post-Messinian and in some areas they constitute as much as 90% of the gross sedimentary thickness of the basin fill (Newton et al., 2004). (Posamentier and Walker, 2006) estimated that in the Miocene to Recent of the eastern Gulf of Mexico, MTDs constitute in excess of 50% of the entire section.
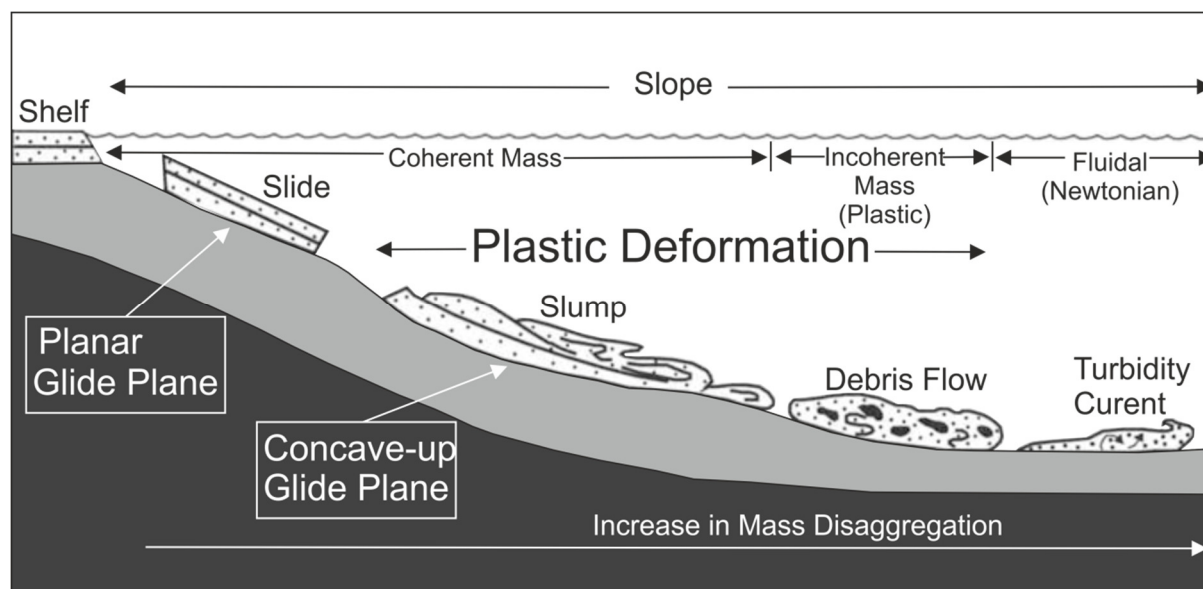
Figure 1.1. Schematic diagram showing four common types of gravity-driven processes that transport sediment into deep-water environments (from Shanmugam, 2006; Shanmugam et al., 1994).

In outcropping sections, such as in the Gull Island Formation of western Ireland, MTD make up more than 75% of slope strata (Martinsen et al., 2003). Consequently, these deposits have drawn much attention for both academia and industry. Much of this attention stems from their relevance in a social and economic sense.

 Key reason for this are:

1) They pose a direct threat to offshore infrastructure in terms of the performance of jetted conductors and suction anchor piles due to their over consolidated nature (i.e., higher undrained shear strengths) thus make it difficult to drill through (Jackson, 2012; Shipp et al., 2004; Weimer and Shipp, 2004).

2) Where the MTD involves large volumes they have the potential to generate catastrophic tsunami waves (e.g Giachetti et al., 2011; Hampton et al., 1996; Ward and Day, 2001)

3) Although deepwater turbidites remain a primary focus for the energy exploration industry, the realization that MTDs constitute a significant percentage of deepwater deposits by volume enhances industry's need to better understand the genesis and morphology of these deposits (Shipp et al., 2011).

Although these are valid concerns, the fact that MTDs constitute a primary component of heterogeneous siliciclastic seal sequences in many slope basins (Weimer and Slatt, 2004) remains largely neglected. Examples of where MTDs overlie fields can be found in Alaska's North Slope (Homza, 2004), northern deep Gulf of Mexico (Lapinski, 2003) deepwater northwest Borneo (Algar et al., 2011), and in CAPROCKs Case Study A (seal unit 3 and 4) and Case Study B datasets.

In all of these aforementioned examples there is plentiful evidence of significant hydrocarbon leakage observed on seismic data (because leakage of oil/gas from underlying reservoirs will mark and imprint the stratigraphic succession in the form of amplitude anomalies of varying expressions such as pipes, chimneys and wipe out zones), particularly in localized portions of

MTDs that, otherwise, would be expected to comprise low permeability, highly effective seal units. Therefore, the evaluation of seal quality in MTDs is crucial when the assessing leakage potential of a slope system containing different types of MTD, since MTDs can potentially exhibit local increases in permeability (possibly due to the cannibalization of seafloor sediments and/or remobilised channels within the MTDs) and, often, a large degree of structural deformation.

Despite the recognition of mass transport deposits (MTDs) as primary components of heterogeneous seal sequences in many petroliferous basins around the world, they are usually ignored in the search for petroleum. An important question posed to a seismic interpreter when dealing with MTDs embedded in sealing sequences is how effective these strata are as seal units for known hydrocarbon fields. Unfortunately this question has not received much attention. This is mainly due to the fact that more time is spent on characterising reservoir units which are the primary target, thus negating the possible impact of MTDs on the hydrocarbon seal integrity. Therefore, it is realized that by better understanding the inherent stratigraphic and structural properties of MTDs, it should be possible to better predict leakage. Thus, a study on the impact of MTDs on hydrocarbon seal was initiated to investigate this hypothesis, as part of the CAPROCKS consortium.

1.2 Aims of study

This research was conducted as part of a Joint Industry Project (JIP) (Newcastle, Cardiff, Leeds and Heriot Watt Universities, Anadarko, BHP Billiton, BG, BP, Chevron, ConocoPhillips, ENI, Petrobras, Statoil ASA and Total) whose main objective was to develop insights to the related processes of petroleum trapping and leakage. My contribution to this project is to use MTDs as a driver in understanding leakage phenomena through sealing lithologies by devising a robust seismic classification that is directly mappable into seal risk. As part of my contribution, I was tasked with compiling an atlas on MTD at outcrop (see

appendix) in order to assist the numerical modelling carried out at Heriot Watt University. The atlas was an agreed deliverable for the project in order to secure permission for data to be released and used in this project.

This overall aim of this PhD project is to develop strategies for geoscientists to evaluate seal risks of MTDs. To this end, a variety of factors were considered in order to derive some predictive parameter for seal quality of MTDs including (1) mode of failure (2) provenance or staging area of the mass-transport deposits (3) degree to which the mass-transport deposits have been disaggregated. An outline of the specific objectives for the thesis is presented in Section 1.3.

1.3 Overview

The aim of this chapter is to provide a brief overview of the current state of knowledge on mass transport deposits (MTDs) and thereby highlight the knowledge gap. More specifically the following aspects are considered in the preceding section 1) Classification of MTDs; 2) Occurrence and triggers of MTDs and; 3) Morphology of MTDs.

1.3.1 Classification and terminologies for MTDs

Mass transport also known as mass movement, mass wasting, or landsliding are general terms used for the failure, dislodgement, and downslope movement of sediment under the influence of gravity in both subaerial and submarine environments (Hampton et al., 1996; Posamentier and Walker, 2006; Varnes, 1978)

According to (De Blasio, 2011), in order to appreciate the differences between subaqueous and subaerial landslides, it is important to keep in mind that the different environment influences the mass transport products for a series of reasons in terms of :

1) Slope angle: the average slope angles are lower in the subaqueous environment. If we consider an object like a book resting on a plane inclined with angle $\emptyset$. Because we assume

the book to be static, according to the laws of dynamics the gravity force must be counterbalanced by the reaction force exerted by the plane. The gravity force "F"can be decomposed into the components normal and parallel to the plane: normal $F = Mg \cos \varnothing$ and parallel $F = Mg \sin \varnothing$. Thus the gravity pull, proportional to $\sin \varnothing$ in subaqueous environment is accordingly smaller.

2) Volume of sediments available: The volume of material available for landsliding is limited for a variety of reasons. First, because slopes are steeper than under the sea, the probability that thick amounts of loose sediments will build up thick units is scarce. In contrast, the gentler angles present in the sea makes sediments more stable. Second, on land the erosion globally prevails over sedimentation. Locally, powerful deposition may take place due, for example, to rivers or glaciers, but the associated deposits are relatively thin. In contrast, large amounts of sediments are deposited underwater, for example at the deltas of large rivers. The continuous sedimentation coupled to the small but nonzero slope angle may lead to enormous depositional systems of clastic sediments, often poorly consolidated and under pressure due to rapid sedimentation, like in the Ganges fan. At high latitudes, like around the Arctic ocean, glacial systems may substitute rivers in the process of producing huge deposits in shallow waters. The failure of these enormous masses may lead to the largest landslides known on Earth, in the range of thousands of km3.

3) Type of material involved: In the subaerial environment, volcaniclastic deposits, morains, loess, colluvium, and talus are relatively common clastic sediments. In the ocean, some of these types may be present but are not volumetrically significant. Clays and sands of various origin, transported by rivers offshore to long distances, are more common.

The rocks involved in submarine rock failures are usually basalts building up seamounts and ocean islands. Rock failures may also occur along the continental shore and involve a larger variety or rock types like crystalline or carbonate rocks. In contrast, there is no limitation to

the type of rock available for sliding in subaerial environment, even though the weakest rock types are obviously more likely to fail.

4) Presence of water as ambient fluid. Water alters in a substantial manner the behavior of a slide, not only at failure (the presence of pore water under pressure may reduce stability) but also during the flow. Water exerts a much greater drag force than air; in addition, the buoyancy decreases the effective gravity acting on the sliding material. However, water seems to enhance the flowing of landslides

However, subaerial and submarine mass gravity failures share almost the same features and related deposits have similar anatomy. Therefore the classification of subaerial landslides originally proposed by (Varnes, 1978) is relatively applicable to submarine slope failures. It is important to note that in this project, only gravity-driven processes in subaqueous environments are considered.

The classification of submarine MTDs has been the subject of debate since the earlier papers, such as (Dott Jr, 1963), describing submarine depositional processes. Some of the key issues leading to this debate include 1) the deformational processes occur at different scales and geological settings; 2) remobilised materials are transported by wide variety of mechanisms and therefore generate a huge spectrum of deposits and 3) many geological and geotechnical researchers studying these processes have been using terminologies influenced by their diverse backgrounds (Mulder and Alexander, 2001; Nardin, 1979; Shanmugam, 2000).

Submarine gravity-driven processes, partly based on (Dott Jr, 1963), (Dingle, 1977), (Nardin, 1979), (Hampton et al., 1996), (Mulder and Cochonat, 1996) are broadly classified into two types: (1) mass transport and (2) sediment flows (Table 1.1).

Mass transport is a general term used for the failure, dislodgement, and downslope movement of sediment under the influence of gravity in both subaerial and subaqueous environments. Mass-transport processes are composed mainly of slides and slumps. Whereas in sediment

flow, the interstitial fluid is driven by the grains moving downslope under the influence of gravity (Middleton and Hampton, 1973). Sediment flows is used for debris flows, and turbidity currents. Using rheology as the basis, deep-water sediment flows are divided into two broad groups, namely, (1) Newtonian flows and (2) Plastic flows. The Newtonian flows represent turbidity currents and plastic flows represent debris flows. This is analogous to the classification originally proposed by Dott (1963).

A slide is a coherent mass of sediment that moves along a planar glide plane and shows no internal deformation (Fig. 1.1). Slides represent translational movement.

A slump is a coherent mass of sediment that moves on a concave-up glide plane and undergoes rotational movements causing internal deformation (Fig. 1.1). In practice, distinguishing slides from slumps can be difficult. The term 'slump' is used for both a process and a deposit.

Debris flow is a sediment flow with plastic rheology and laminar state from which deposition occurs through freezing en masse (Fig. 1.1). Although most debris flows move as incoherent material, some plastic flows may be transitional in behavior between coherent mass movements and incoherent sediment flows.

Turbidity current is a sediment flow with Newtonian rheology and turbulent state in which sediment is supported by turbulence and from which deposition occurs through suspension settling (Fig. 1.1).

In addition to fluid rheology, flow state is used in distinguishing laminar debris flows from turbulent turbidity currents (Table 1.1). Reynolds (1883) demonstrated the difference between laminar and turbulent flows by injecting a thin stream of dye into the flow of water through a glass tube. At low rates of flow, the dye stream traveled in a straight path. This regular motion of fluid in parallel layers, without macroscopic mixing across the layers, is called a laminar flow. At higher flow rates, the dye stream broke up into chaotic eddies. Such

an irregular fluid motion, with macroscopic mixing across the layers, is called a turbulent flow. The change from laminar to turbulent flow occurs at a critical Reynolds number (the ratio between inertia and viscous forces) of about 2000.

$$\text{Reynolds number R} = \frac{\rho u D}{\mu}$$

Where ρ = Density*; u* = Velocity*; D* = Flow thickness and μ = Viscosity.

The classification summarised here (Table 1.1) based on those suggested by previous authors, attempts to utilize existing concepts and terminologies for interpreting common downslope processes.

Overall the scheme shows that the various processes exist as part of a continuum (Fig. 1.1), whereby one process may evolve into another with time, or depositional effects of one process type may trigger other processes (see Maltman, 1994; Posamentier and Martinsen, 2011; Shanmugam, 2006). A slide may be transformed into a slump. Upon addition of fluid during downslope movement, slumped material may transform into a debris flow. With increasing fluid content, plastic debris flows tend to become Newtonian turbidity currents (Fig. 1.1). However, not all turbidity currents evolve from debris flows. Some turbidity currents may evolve directly from sediment failures. Although turbidity currents may constitute a distal end member in basinal areas, they can occur in any part of the system (i.e., shelf edge, slope, and basin).

Although these existing classifications are useful from process and rheology perspectives, problems emerge when we try to apply them to both seismic data and to outcrop data (Shanmugam, 2006). Whilst it can be argued that some of these MTD types can be mapped in seismic, the primary problem is the fact that many are thinner than the vertical seismic resolution and therefore their interpretation using seismic data is ambiguous. For instance, an MTD with a "chaotic" seismic expression cannot be interpreted exclusively as a debris flow as it could also be a slide with coherent internally deformed material preserved.

Table 1.1: A classification of subaqueous gravity-driven process (after Shanmugam, 2006).

Major type	Nature of Moving material	Nature of movement	Sediment Concentration (volume %)	Fluid Rheology and flow state	Depositional process
Mass transport (also known as mass movement, mass wasting or landslide)	Coherent mass without internal deformation	Translational motion between stable ground and moving mass			Slide
	Coherent mass with internal deformation	Rotational motion between stable ground and moving mass	Not applicable	Not applicable	Slump
Sediment flow (in cases, mass transport)	Incoherent body (sediment water slurry)	Movement of sediment-water slurry *en masse*	High 25-95%	Plastic rheology and laminar state	Debris flow (mass flow)
Sediment flow	Incoherent body (water-supported particles in suspension)	Movement of Individual Particles Within the flow-	Low 1-23%	Newtonian rheology and turbulent state	Turbidity current

In addition, because multiple transport processes may have occurred within a single MTD, it is incorrect to characterise an entire deposit on seismic based on localised observation. However, MTD outcrops potentially allow the impact of small scale processes not seen on the seismic data to be constrained. A preliminary (and generally conceptual) attempt to compare seismic and outcrop structural data has been made by (Bull and Cartwright, 2010). (Moscardelli and Wood, 2008) proposed a classification scheme based on seismic data that goes beyond the traditional subdivision of MTDs into slides, slumps and debris flows but accounted for causal mechanisms and pre-failure conditions of MTDs (Fig. 1.2). This classification system defines two categories: attached MTCs and detached MTDs. Attached MTDs have also been subdivided into two subcategories: shelf attached and slope attached. However, the internal architecture of these MTDs was not sufficiently considered.

This lack of a seismic classification scheme for the internal architecture of MTDs is critical because it is thought that the leakage of hydrocarbon through a sealing sequence containing MTDs is partly controlled for a set of MTD seismic facies under a given geological conditions. By using observations from outcrops to aid seismic interpretation, it is possible to narrow the uncertainty range of the different MTD seismic facies and their seal prediction. The challenge therefore for a seismic interpreter is to map features using the seismic data, interpret the process implications thereof, and then predict the range of seal risk and quality at, and below, seismic resolution.

The description of the internal seismic architectures of MTDs in Chapters 3, 4 and 5 and other published seismic facies examples is intended to be the basis for proposing a new seismic classification scheme for MTDs in Chapter 6. The scheme is intended to allow a seismic interpreter to quickly assess the seal integrity impacts of MTDs.

TYPES OF ATTACHED MASS TRANSPORT COMPLEXES

(a) Slope Attached Mass Transport Complex
Upper Slope Collapse
Evacuated Strata
"Cookie Bite Features"
Slumps
Debris Flow

(b) Shelf Attached Mass Transport Complex
Shelf Edge Delta
Fluvio deltaic input
Slumps
Paleocanyon
Debris Flow
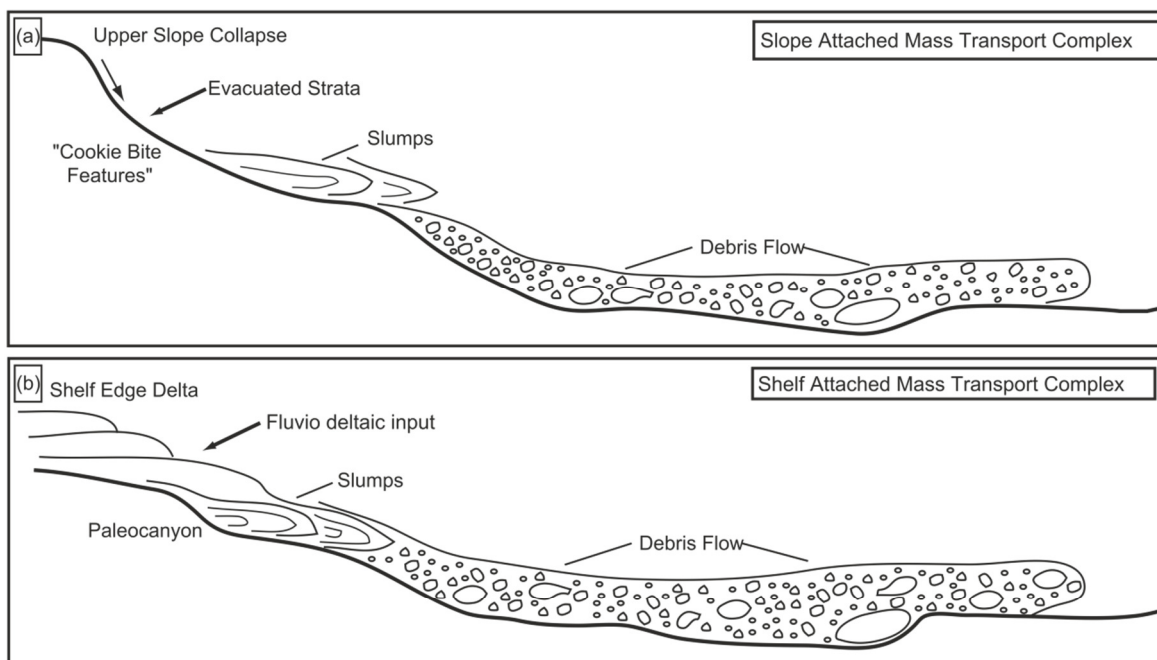
TYPES OF DETACHED MASS TRANSPORT COMPLEXES

(c) Slides
Debris Flow
Mud / Salt Volcano Ridge
Syndepositional Thrusts

(d) Mini-Basin
Slides
Salt
Debris Flow
Syndepositional Thrusts
Salt

(e) Levee Channel Complex
Channel
Levee
Levee
Debris Flow
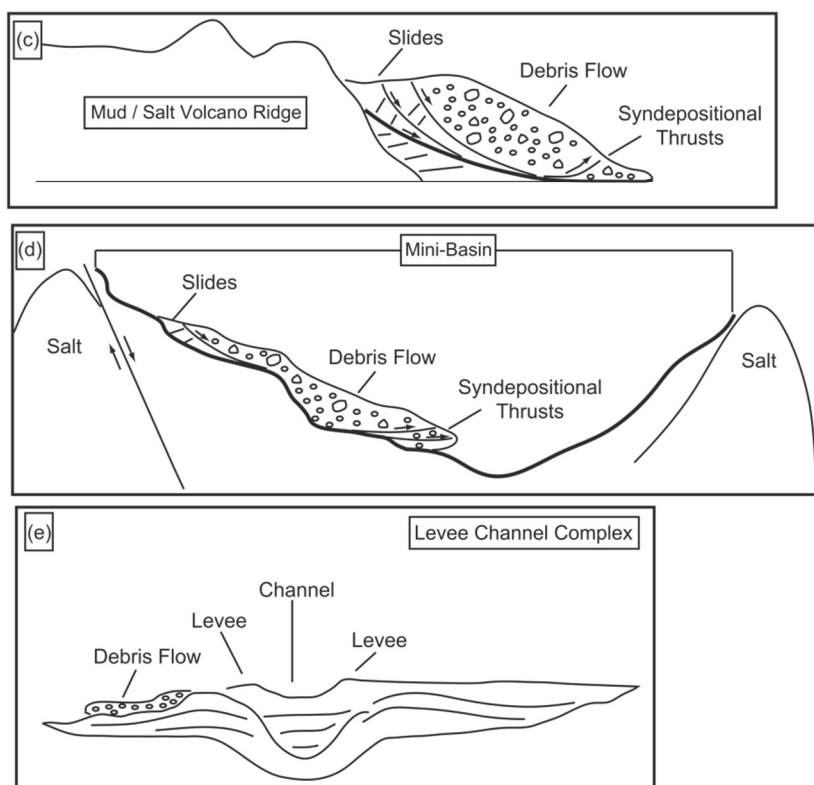
Figure 1.2. Schematic classification of MTDs based on causal mechanisms and pre-failure conditions (a) Slope-attached mass transport complex - sediments are derived from the catastrophic collapse of the upper slope area. (b) Shelf-attached mass transport complex sediments are provided by shelf-edge deltas and are dumped into the deep-marine basin. (c) Detached mass transport complex whose genesis is associated with the collapsing flank of a mud-volcano ridge. (d) Detached mass transport complex whose genesis is associated with oversteepening of one of the margins of a deep-water mini-basin. (e) Detached mass transport complex whose genesis is associated with a levee- channel complex MTDs, mass transport complexes (From Moscardelli and Wood, 2008).

1.3.2 Occurrence and slope failure initation

1.3.2.1 Occurrence

Evidence of small- and large-scale MTDs have been reported in almost every modern seafloor (and sub-seafloor), highlighting the important role of mass wasting processes in the evolution of modern ocean margins. Submarine MTDs have been reported from the Mediterranean (e.g. Frey-Martínez et al., 2006; Frey Martinez et al., 2005; Garziglia et al., 2008; Lastras et al., 2002; Loncke et al., 2009; Trincardi and Argnani, 1990) to the N Atlantic (e.g. Hühnerbach and Masson, 2004; Laberg and Vorren, 2000; Piper et al., 1988; Solheim et al., 2005a; Vanneste et al., 2006) to the W Atlantic (e.g. Embley, 1976; Gee et al., 1999), E Atlantic (e.g. O'leary, 1993; Popenoe et al., 1993) E Pacific (e.g. McAdoo et al., 2000). Despite the continuing investigation of MTDs worldwide, there are still no published studies on MTDs in the Deepwater Taranaki Basin (Tasman Sea). As petroleum exploration and production moves into greater water depths in the Taranaki Basin (Uruski, 2010), the research on MTDs (this project) in the area comes at a perfect time as they can act as seals to underlying petroleum reservoirs giving rise to alternative exploration targets in many parts of the world. A comprehensive study of the distribution and morphology of MTDs in the Deepwater Taranaki Basin is presented in Chapter 4.

1.3.2.2 Slope failure initiation

As sediments particles are being deposited they increasing interfere with each other, electrostatic bonds are initiated between them, thus imparting a physical cohesion to the sediments (Wetzel, 1990). Also, movement between adjacent grains begins to involve intergrain friction. For either or both reasons the sediments acquires some resistance to an applied shear stress. The maximum shear stress the sediment can sustain before failure is called its shear strength (Maltman, 1994).

Slope failure and downslope translation of all types of mass movement typically occurs when the shear strength or shear resistance of the sediments is exceeded by the applied shear stress (Hampton et al., 1996).

Terzaghi (1962) defined the shearing resistance of rock or sediment using the Mohr-Coulomb equation below:

$$\tau = C + \sigma n \tan \varnothing$$

where C is the cohesion of sediments, σn is the stress normal to the plane of failure and $\varnothing$ is angle of shearing resistance or internal friction which depends on the friction angle of individual grains and also on the packing geometry of the assemblage of grains along the failure surface (Iverson, 1997).

The role of pore fluids in slope failure is of crucial importance (Maltman, 1994). The fluid in sediments supports some portion of any applied load, giving rise to a pore or fluid pressure. In normally consolidating sediments, the portion of the burial load arising from the overlying column of pore fluid (plus sea water in the case of submarine MTDs) is called normal fluid pressure. The remaining component is that sustained by the sediment particles is called the effective stress σ', defined by the equation below:

$$\sigma' = \sigma - u$$

where σ is the total stress and u the fluid pressure. It is the effective stress rather than the total stress that controls deformation (this will be discussed later in this section). Therefore the Mohr-Coulomb equation can be modified with respect to effective stress:

$$\tau = C + (\sigma - u) \tan \varnothing$$

With increasing burial, the pore fluid has to be expelled in appropriate amounts if the pore volume is to reduce in equilibrium with additional load. The ability of sediments to dissipate pore fluid is a function of its permeability and this in turn depends on the configuration of the pores and particles in the sediments (Ahuja et al., 1989). If, after a given increment of

loading, and sediments lack sufficient permeability, the fluid, being virtually incompressible, has to sustain a disproportionate part of the load (Gretener, 1979). This pressure excess over the normal fluid pressure is termed overpressure. One of the profound implications that overpressure has on sediments is that it weakens the sediment. Since the fluid is sustaining an extra part of the stresses acting across the aggregate framework, the effective stress decreases, the intergrain friction is reduced and hence so is the sediment strength (Maltman, 1994). Therefore, as stated above it is the effective rather than the total stress that govern deformation.

Where the dissipation of pore fluid is greatly curbed, or increments of loading arise in addition to burial, say from the transmission of seismic waves, the pore fluid may have to sustain the entire stress acting on the sediment. In this situation the internal friction is effectively reduced to zero, and the aggregate, now lacking resistance to shear, behaves as a liquid (Maltman, 1994). The resulting phenomenon is term liquefaction.

The analyses of submarine slopes are commonly approached by an infinite slope analysis in which the failure plane is treated as planar and parallel to the free surface, and a small volume is taken to adequately represent the total sliding mass (De Blasio, 2011; Maltman, 1994). In the simplest view of stresses acting on a slope, if the sediment has an area A and a weight W (area x thickness x bulk density x gravitational acceleration), and slopes from the horizontal at an angle β , then the shear stress operating along the slope will be :

$$\tau = \frac{W \sin \theta}{A}$$

and the stress normal to the slope will be

$$\sigma n = \frac{W \cos \theta}{A}$$

Therefore, assuming that a potential detachment parallels the planar slope, the overlying load acts both to strengthen the sediment by increasing the stress normal to the failure plane and to promote failure along the plane by increasing the shear stress (De Blasio, 2011). Although

for slopes of low and moderate inclination the strength (increasing through the cosine of the slope angle) will grow more rapidly with increasing burial thickness than the shear stress (increasing through the sine of the slope angle), with steeper slopes (in which the sine values increase more rapidly than cosines) the opposite will be the case, Hence, sediments on slopes above a certain inclination will become increasingly unstable with progressive burial (Maltman, 1994). For many near-surface sediments, the contribution of cohesion to their strength is negligible. In this case, incorporating the later 2 equations into the basic Mohr coulomb equation gives:

$$\frac{W}{A} \sin \theta = \frac{W}{A} \cos \theta \tan \varnothing$$

At the failure condition of shear stress equalling strength, the load terms cancels out, so that

$$\tau = \varnothing$$

that is the slope cannot exist at an inclination (also known as the angle of repose) greater than friction angle of sediment.

Consequently, the potential for failure depends on the interplay between slope angles and sediment strength (Maltman, 1994). Baraza et al. (1990) suggested that in most geological situations, the slope angles and the mechanical properties are likely to be continuously evolving. Slope inclinations can change for a number of reasons including response to diapirism (Martin and Bouma, 1982), fault reactivation (Holler, 1985), salt movement (Almagor, 1984), and because of erosion at the slope foot (Schwab et al., 1988). The strength parameters of sediments will evolve through consolidation and diagenesis (Charles, 1982).

Hutchinson (1986) suggested based on Mohr coulomb principles that the masses termed slides are likely to form in low sensitivity clays or friction dominated clastic sediments. The author further suggested that the failed material would still be at its peak strength for localized, rotational slides but at the residual state for far travelled blocks. On the other hand, material forming slumps would exhibit lower strengths and commonly comprise higher

sensitivity. Flows showing plastic behaviour must have operated at a water content within the plastic range of the sediment, whereas those with fluid behaviour are probably of high sensitivity sediment which must have exceeded its liquid limit. Material with a relatively high plasticity index will tend to give thicker flows with a lesser run-out distance.

The reduction of effective stress and strength by overpressuring is a crucial factor in all settings of sediment deformation (Iverson, 1997; Maltman, 1994). The factors that have been established as contributing to the initiation of submarine MTDs can be broadly divided into two categories according to (Masson et al., 2010); 1) Triggers and 2) Preconditioning factors.

Triggers are defined as relatively short-period events that act to destabilize submarine slopes. They include earthquakes (Hampton et al., 1996), low tides, storm wave loading, tectonic movements (e.g. tilting due to margin subsidence or salt movement), changes in methane hydrate stability and sea-level change. Earthquakes are by far the most commonly involved trigger for most large historical submarine landslides (Masson et al., 2006).

In contrast, preconditioning factors include aspects of the gross structure and stratigraphy of the sediments and are thus related to properties of the sediments acquired during, or evolve from, the depositional process (Masson et al., 2010). These factors include presence of weak geological layers, overpressure due to rapid sediment accumulation, slope oversteepening, gas in sediment, glacial loading, volcanic activity and salt growth (Bünz et al., 2005; Canals et al., 2004; Hampton et al., 1996; Lastras et al., 2002; Locat and Lee, 2002; Masson et al., 2006; Masson et al., 2010; Sultan et al., 2004a; Tripsanas et al., 2004).

For the most part, the way in which these factors operate to trigger landslides, usually through rapid changes in sediment pore pressure, is understood, at least in principle.

However, much less is understood about the role of preconditioning factors (in comparison to triggers) in the initiation, size and frequency of giant landslides (Masson et al., 2010). MTDs are considered to result from a combined effect of several of these factors over time, although

the main trigger for failure could be preferentially linked to a specific one.

1.3.3 MTD Morphology

MTDs typically exhibit a tripartite morphology (Bull et al., 2009a; Lastras et al., 2002; Maltman, 1994; Posamentier, 2006; Posamentier and Martinsen, 2011); Extensional headwall domain, translational domain and compressional toe domain (Fig. 1.3). However there may be some overlap or the absence of one or two of the domains (Imbert et al., 2007). For instance, the extensional headwall domain is not always evident in MTDs related to active deformation of mobile strata (Gamboa et al., 2010; Richardson et al., 2011). In contrast, the headwall domain may be in physical continuity with the toe domain (Imbert et al., 2007).

1.3.3.1 Headwall Domain

The extensional headwall domain can also be referred to as the staging area, defined by (Posamentier and Martinsen, 2011) as that location where the MTD originate (Fig. 1.3). The authors pointed out that large MTDs (hundreds of km^3) commonly originate in the mid to upper slope while small MTDs (few m^3) are typically associated with channel–levee walls They suggested that the staging area of MTDs has a direct bearing on the lithologic character, an observation consistent with that of Moscardelli and Wood (2008) Figure 1.2.

Shelf-attached MTDs can have a mix of sand and mud, for example, whereas slope-attached MTDs will be more mud prone. Detached MTDs, such as those associated with salt domes or mud volcanoes, or those associated with oversteepened flanks of channel levees, are intrabasinal and commonly mud prone with locally derived material.

According to (Imbert et al., 2007) it is important to clearly distinguish the actual transported mass of an MTD from that which have merely undergone deformation with limited displacement when they were overloaded by the transported mass. In order to do this it is important to distinguish between two phenomenon: 1) Run-out: where the MTD travel long

distances by hydroplaning on the depositional surface and 2) Erosion or cannibalisation of the substrate characterised by basal surface ramps and flats geometries.

Experimental study has shown that submarine MTDs, and in particular debris flows exhibit extremely high mobility and hydroplaning has been suggested as a possible explanation especially when the artificial debris flow is rich in clay (Mohrig et al. 1998; Elverhøi et al. 2002). The process consists in the formation of a water corridor underneath the artificial mudflow (Mohrig et al. 1998). The water layer, typically some cm thick, causes the debris flow to travel with much reduced resistance at the bottom.

The erosion or cannibalisation of the substrate which is evident from the stratigraphic 'jumping' of the basal shear surface by way of ramps and intervening flat sections has been recognized from several studies (Trincardi and Argnani, 1990; Strachan, 2002a; Frey Martinez et al., 2005; Bull et al., 2009a). However, no studies have been undertaken to specifically analyse the position of ramps in a broader context, nor to quantify their dimensions and dip (Bull et al., 2009a).

Several factors have been suggested to as possible control the development of ramps. One factor could be related to the mechanical properties of the basal shear plane (e.g. lateral variations in friction). Another may relate to stresses generated as the failed material moves over the basal shear surface, or indeed, a combination of these two factors may be critical (Strachan, 2002a; Frey Martinez et al., 2005; Bull et al., 2009a).

Strachan (2002a) postulated that pre-existing weaknesses in the basal shear surface, such as faults or fracture may be exploited by localised erosion by the translating failed mass.

According to Bull at al. (2009a) the specific and selective nature of the localisation of the basal shear surface ramps strongly suggests that some degree of control is exerted by the horizons exploited by flat sections. Seismic based evidence for this concept was provided by Solheim et al. (2005), who noted that the jumps in basal surfaces from MTDs in the
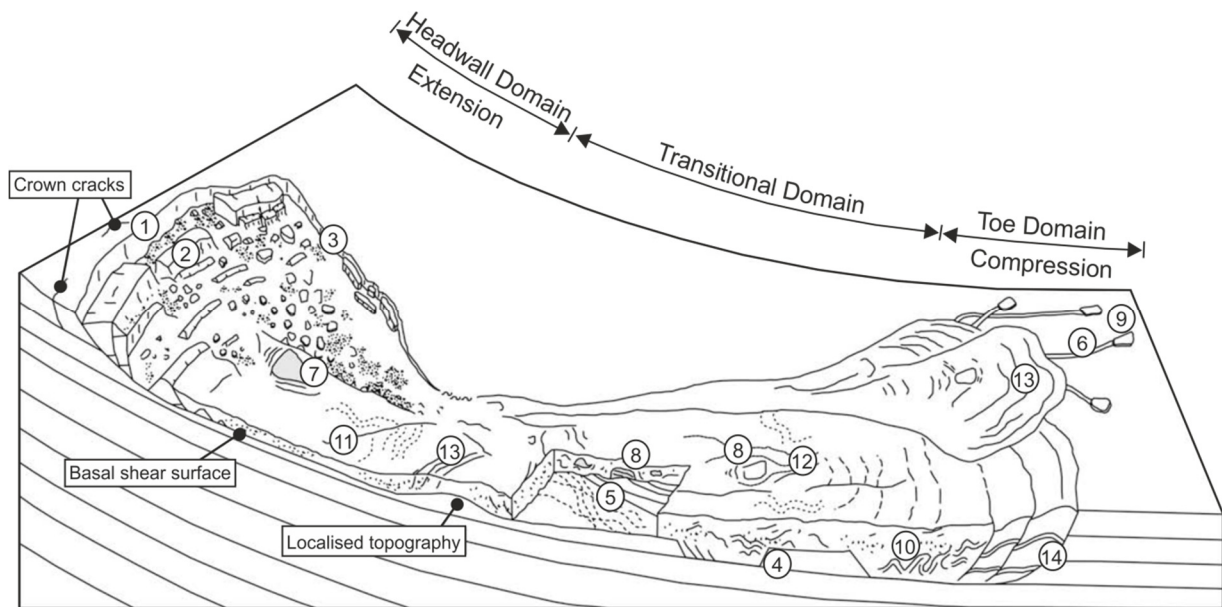
Figure 1.3. Schematic representation of a typical MTD tripartite morphology. Notice the associated features of the different domains. (1) Headwall scarp. (2) Extensional ridges and blocks. (3) Lateral margins. (4) Basal shear surface ramps and flats. (5) Basal shear surface grooves. (6) Basal shear surface striations. (7) Remnant blocks. (8) Translated blocks. (9) Outrunner blocks. (10) Folds. (11) Longitudinal shears/first order flow fabric. (12) Second order flow fabric. (13) Pressure ridges. (14) Fold and thrust systems. Modified after (Prior et al., 1984) and (Bull et al., 2009a).

Norwegian continental margin all did so in sedimentary units characterised by similar stratified seismic signatures.

The major operational consequence of run-out and /or cannibalisation of MTDs is the existence of a clear demarcation between sediment packages with very different lithological characteristics which will have implications for MTDs as hydrocarbon seals.

However, far little attention has been paid to evaluating the degree of substrate cannibalisation (sensu Gee et al., 2007) of an MTD versus the actual transported mass that runout. An attempt to evaluate these two emplacement mechanisms is presented in Chapter 4. Common features that are predominant in the headwall domains are headwall scarps, extensional ridges and blocks. Crown cracks are also common in non-failed slope strata resultant from extensional stresses in the vicinities of the main headwall scarp, and the presence of such features is prone to cause posterior retrogressive slope failures (Bull et al., 2009a; Pratson and Coakley, 1996).

1.3.3.2 Translational Domain

The transitional domain comprises the main translated body of the MTD (Bull et al., 2009a; Posamentier and Martinsen, 2011) (Fig. 1.3). The movement of the failed material across the basal surface can lead to intense deformation in which both extensional and compressive regimes may take place, due to differential moving of slide component and the margin-induced velocity gradient. At the outcrop scale, this may result in the superposition and coexistence of extensional and compressive structures affecting slide components (Farrell, 1984). However, there has been no seismic evidence to illustrate the overprinting of both extensional and compressional regimes in MTDs. This is probably due to the fact that it may not a common phenomenon or it has not just been observed because of the quality of some of the seismic data available to study MTDs. Other MTD features within this domain are the

lateral margins, the basal and upper surfaces (Bull et al., 2009a; Dunlap et al., 2010a; Frey-Martínez et al., 2006; Frey Martinez et al., 2005; Gamboa et al., 2012; Gee et al., 2005; Gee et al., 2006; Moscardelli et al., 2006; Posamentier, 2004) all of which provides useful kinematic indicators for interpreting the translation direction of MTDs (Bull et al., 2009a).

In a major study which set out to review seismic-scale kinematic indicators of MTDs, (Bull et al., 2009a) showed key geometrical and geological criteria for the recognition of all types of kinematic indicators in the tripartite classification scheme of MTDs (Fig. 1.4).

Irregular basal surfaces associated with erosive MTDs are often characterised by linear basal grooves (that run parallel to the main flow direction) and erosive "slots" or ramps (if a depression was created below the average level of the MTD base) (Bull et al., 2009a; Gee et al., 2005; Moscardelli et al., 2006; Posamentier and Kolla, 2003). Although much is currently known about the occurrence and morphology of these erosive features, the mechanism and under what circumstances does grooving of substrate occur has not been clearly established (Posamentier and Martinsen, 2011). The description of two sets of groves in relation to the internal deformation of a giant MTD in Deepwater Taranki Basin (Chapter 5) is intended to improve our current understanding of the mechanisms and circumstances under which groves form.

1.3.3.3 Toe Domain

Downslope of the transitional domain is the toe domain and it represents the terminus of the MTD (Fig. 1.3) (Bull et al., 2009a; Posamentier and Martinsen, 2011). The main deformational structures in the toe domain are thrust and fold systems at various scales that induce the formation of arcuate pressure ridges on the top surface of the MTD that develop perpendicularly to the transport direction (Bull et al., 2009a) These deformations are mainly caused by compressive stresses (Bull et al., 2009a; Flint et al., 2011; Frey-Martínez et al., 2006; Hampton et al., 1996; Posamentier, 2004).
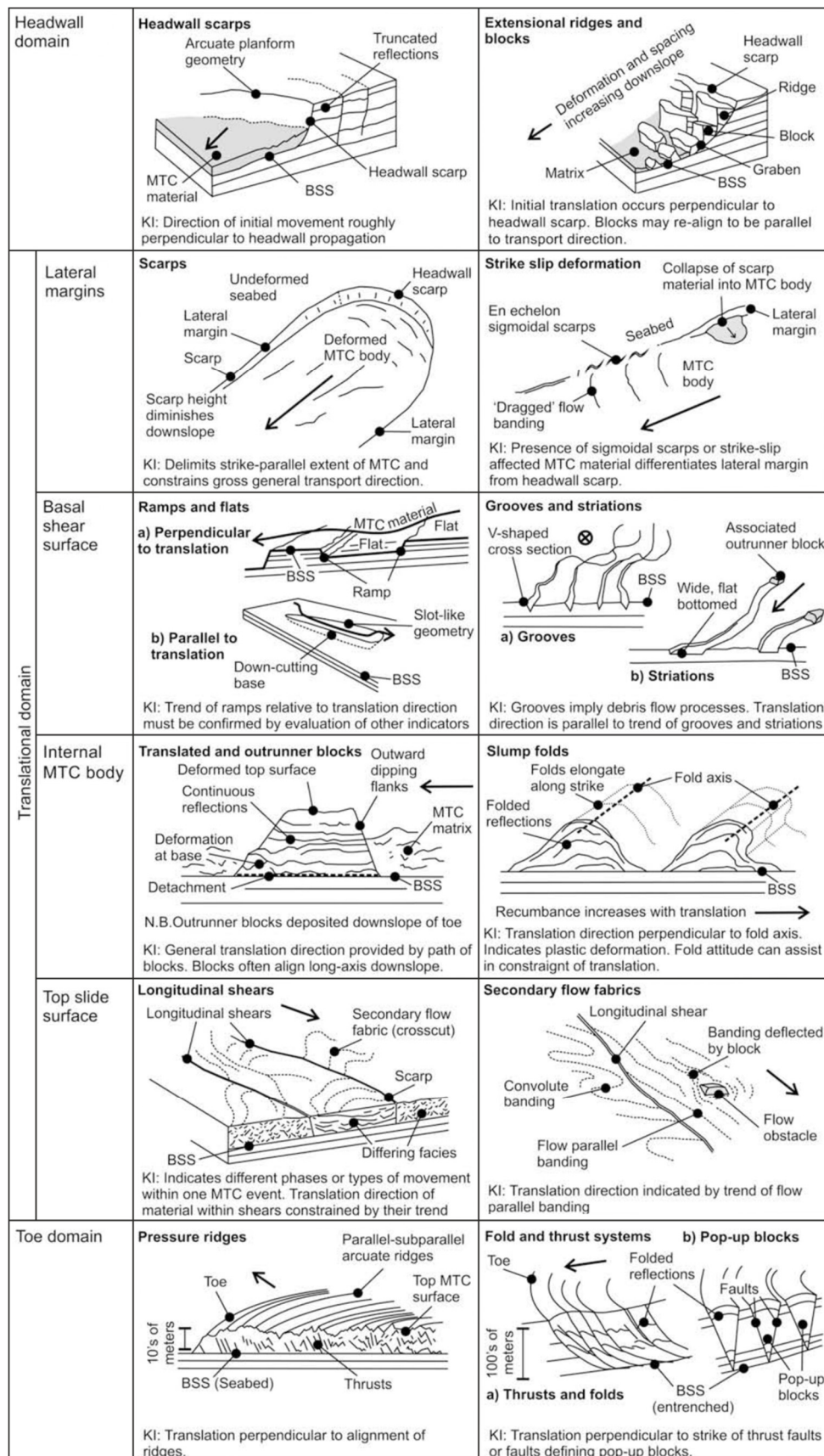
Figure 1.4. Summary diagram showing key geometrical and geological criteria for the recognition of all kinematic indicator types. BSS – basal shear surface. KI = kinematic information. Bold arrows indicate direction of translation (after Bull et al., 2009a).

(Frey-Martínez et al., 2006) classified the termination of remobilised material in the toe domain into 1) frontally confined characterised by buttressing of the remobilised strata against an abrupt frontal ramp without overrunning the undeformed downslope strata and 2) frontally emergent where the MTDs ramp up from the original basal shear surface, translating in unconfined manner over the seafloor with much larger downslope transport

The emplacement of MTDs strongly influences the physiography of the depositional context, in that the short time (*i.e.* geologically instantaneous) accumulation of huge amount of remobilised material causes a strong reduction of the basinal volumetric potential (*i.e.* accommodation space), generating punctual and localized minor depocenters around and/or above the MTC, due to its irregular surface perhaps.

The un-loading of the failure zone and the subsequent over-loading in the accumulation zone may also result in an isostatic rearrangement of the slope profile, with a relative upslope uplift and a downslope subsidence (Fig 1.5) (Dykstra, 2005) . Ingram et al. (2004) in a study of hydrocarbon accumulation in an active fold and thrust belt in Deepwater Northwest Borneo, suggested that tectonic uplift, erosion of the overburden and buoyancy of a large a large gas column can result in seal breach. Likewise, it is possible that isostatic rearrangement of the slope profile due to the loading and unloading of large MTDs may exert fundamental influences upon the seal integrity of any underlying reservoired hydrocarbon. The results presented in Chapter 3 seek to discuss this phenomenon in more detail.
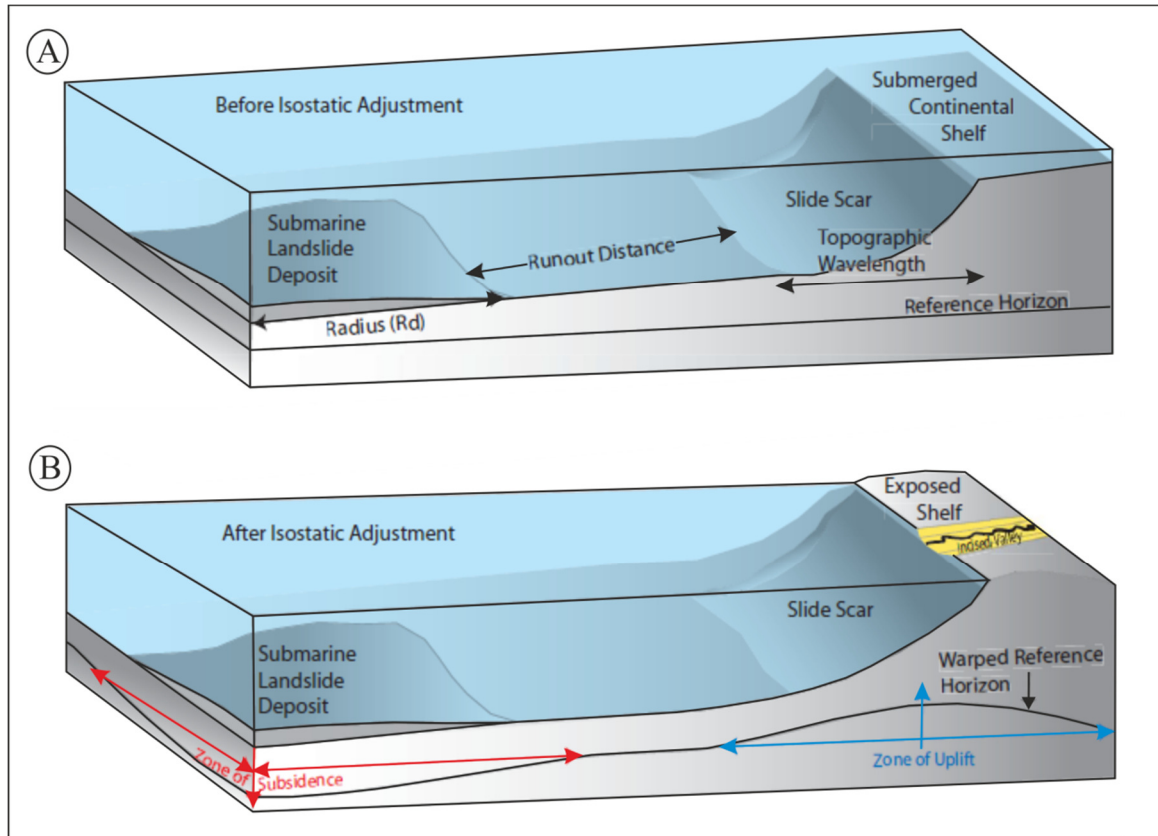
Figure 1.5. Cartoon exhibiting some of the factors and potential effects of the isostatic rebound after large-scale mass-transport events. A zone of subsidence forms under and surrounding the mass-transport deposit and a zone of uplift surrounds the slide-scar. If the uplift is great enough in amplitude it could potentially cause the shelf or shelf-edge to become emergent (Dykstra, 2005).

1.4 Aims of the Project

The major aim of this project is concerned with understanding the impact of MTDs on hydrocarbon seal integrity. The large number and scale of MTDs present in the study areas and the high quality of the seismic data available presents an opportunity to carry out a detailed description of external and internal architecture of the deposits. As such the specific objectives of this project are

1) Describe and document the range of seismic facies observed in MTDs using both 2D and 3D data.

> 1a) Identify and map MTDs in both the Deepwater Taranaki Basin, New Zealand and the west Nile delta, offshore Egypt dataset.
>
> 1b) To investigate the external morphology, internal structure and kinematic indicators within the MTDs in order to reconstruct the deformational history.
>
> 1c) To analyse and discuss the triggering mechanisms, sediment transport/erosion, kinematic information and remobilization processes of the MTDs

2) To analyse the detailed characteristics of MTD from outcrop analogues in order to understand sub-seismic deformational processes.

> 2a) To produce an atlas of MTD outcrops based on field and literature examples
>
> 2b) To transfer lessons learned from outcrop study of MTDs into seismic characterisation of MTDs.

3) Utilise the described internal deformational characteristics of MTDs in this project as well as from published literatures to devise a robust seismic classification scheme.

> 3a) For each seismic class, establish a definition, recognition criteria, mode of formation and consider the potential seal risk of the MTDs seismic facies

3b) A systematic methodology for the assessment of MTD seal integrity and risk is

proposed.

1.5 Thesis layout

The thesis is divided into seven chapters. The rationale behind the research project as well as

an overview of the research topics has been presented in **Chapter 1.**

This is followed by an overview of the dataset and the methodology used for this project, in

Chapter 2.

Chapters 3, 4 and 5 present the main results of this thesis. Each of these core chapters has

been written as manuscripts for publication, and they focus on various topics associated with

the implications of MTDs on hydrocarbon seals (Fig. 1.6). Each core chapter contain an

introduction, including the geological setting unique to the particular study areas, data and

methodology (which have been extracted and placed in Chapter 2), observations,

interpretations, discussion and conclusions.

Chapter 3 investigates the phases, mechanism and sequence of a multistage slope failure in

the West Nile Delta, Eastern Mediterranean (Fig.1.6). The loading and unloading phenomena

during MTD emplacement and its impact on seals is also discussed.

The first detailed investigation of the multiple, widespread MTD in Deepwater Taranaki

Basin, New Zealand with an aim to evaluate their distribution, characteristics and triggering

mechanism is presented in **Chapter 4** (Fig. 1.6).

An insight into the dynamics of a giant mass transport deposit from Deepwater Taranaki

Basin, New Zealand is presented in **Chapter 5** using high-resolution 3D seismic data (Fig.

1.6).

An over-arching summary and discussions / implications and areas for further research are

presented in **Chapter 6**. Conclusions drawn from this research project are presented in

Chapter 7.
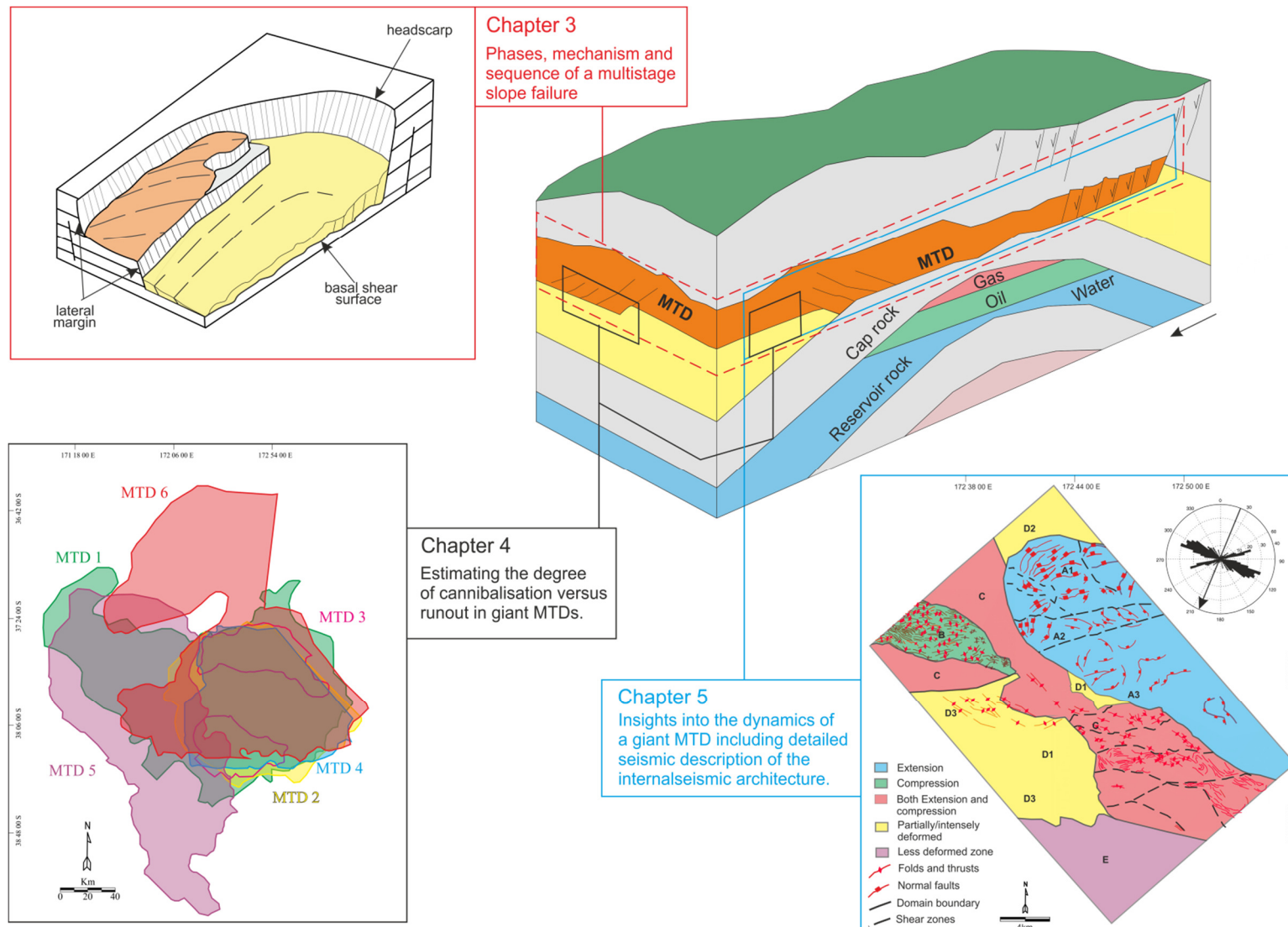
Figure 1.6. Synthesis of the main themes covered in the core chapters and how they fit into a conceptual model of MTD and hydrocarbon seal interaction.

Chapter 2

2.0 Data and Method

2.1 Introduction

The main results of this thesis presented in Chapters 3, 4, and 5 are based on the interpretation of both 2D and 3D seismic data. This chapter provides a brief overview of seismic data acquisition and processing, details of the specific datasets, interpretation and related methodologies for seismic studies of MTDs used in this thesis.

2.2 Seismic data acquisition and processing

Although 2D seismic data exerted a major influence on the development of basin analysis in the 1960s and 1970s (Sheriff and Geldart, 1995), the advent of 3D seismic technology with a significantly higher quality proved to be a major breakthrough in the interpretation of subsurface geology (Cartwright and Huuse, 2005). Seismic data acquisition of 2D seismic survey is conducted along lines to produce a vertical profile (Fig. 2.1) whereas 3D seismic survey is conducted over an area with a dense grid of lines to generate a 3D sub-surface volume (Fig. 2.1). The 3D seismic data provides detailed information of the subsurface to a resolution of only a few tens of metres, or even just a few metres as compared to the 2D survey particularly in areas of complex geological features (Bacon et al., 2007; Hart, 1999; Kearey et al., 2009; Posamentier et al., 2007).

2.2.1 3D Seismic data acquisition

During the acquisition of marine 3D seismic survey, acoustic wave generating device (usually an air-gun) produces body waves which subsequently travel down through the subsurface and are reflected back towards the surface by geological interfaces (Fig. 2.2) (Bacon et al., 2007). Hydrophones (deployed in a streamer towed behind a vessel at a depth of a few metres) detect the reflected signals and measure their amplitude and arrival two-way-travel times after the source is fired (Fig.2.2).
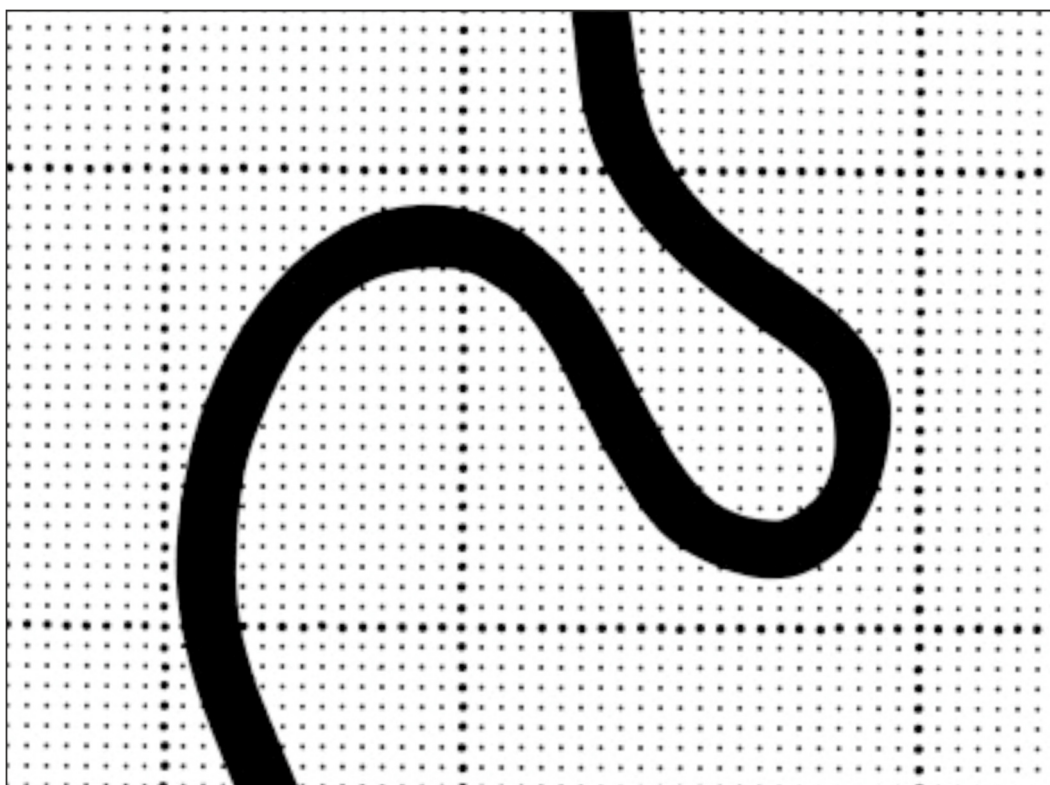
Figure 2.1. Areal coverage of a 3-D survey compared to the coverage of a grid of five 2-D lines, and the ability of each to delineate a meandering channel (Brown, 2011).
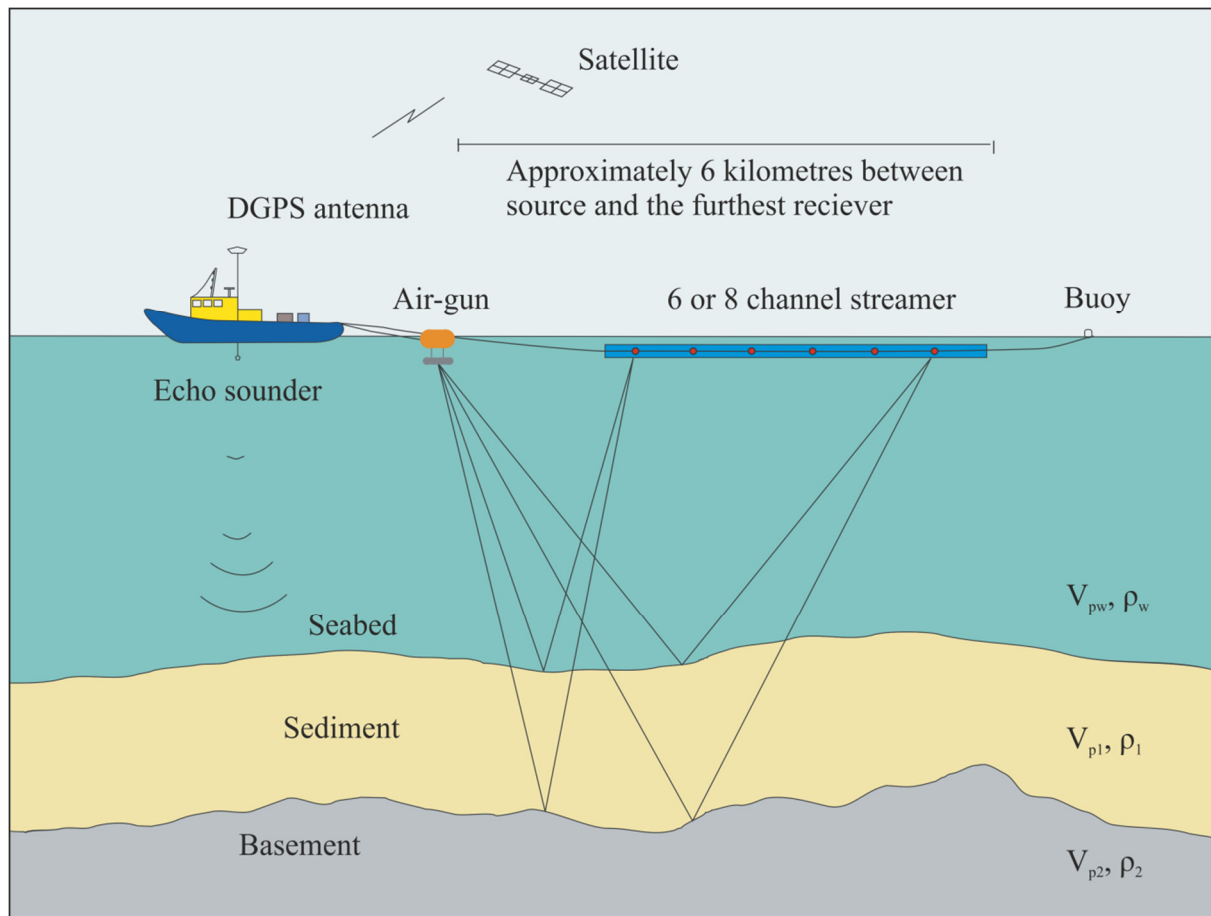
Figure 2.2. Schematic representation of the layout of 3D marine seismic survey. A towed acoustic source near the sea surface emits a sound wave that travels through the water. When the acoustic properties of the rock change, the P waves reflected to the surface are detected by hydrophones mounted in a long cable towed behind the boat. The hydrophone spacing partly controls the horizontal resolution of the seismic data (modified from Lee et al., 2004).

Marine seismic surveys are mainly concerned with P-wave reflections to detect the reflected energy because S-waves do not transmit through fluids as fluid has no capacity for shear (Bacon et al., 2007).

There has to be a change in acoustic impedance across a subsurface interface in order to generate reflection (Fig. 3.1). This acoustic impedance (Z) of a certain material is defined by

$$Z = Vp * \rho$$

Where ρ = density of the related material and Vp = velocity of seismic P-wave in the interval concerned (Bacon et al., 2007).

Increasing acoustic impedance is commonly displayed as a 'peak' on the seismic wavelet and considered as positive amplitude, while decreasing amplitude is considered as negative amplitude or 'trough'(Kearey et al., 2009; Sheriff and Geldart, 1995) (Fig.2.3). Wave displays are traditionally represented in distinct colours in what is termed the 'SEG (Society of Exploration Geophysicists) normal polarity' classification (Brown, 2011), being this the convention used in this thesis (Fig.2.3).

Due to the re-expansion of air bubble, the output signal with a main wavelet can be accompanied by a smaller secondary peak (Bacon et al., 2007). The smaller secondary peak can be removed, thus giving the input wavelet a more compact form. Therefore, a decision needs to be made at this point whether the output should be zero or minimum phase. The zero-phase wavelet is symmetrical about its peak while a minimum phase wavelet starts at zero and has as much energy near the start (Fig 2.2). Nowadays, the former type has gained the preference of seismic interpreters (Brown, 2011) as the centre of the wavelet is coincident with the geological interface causing the reflections.
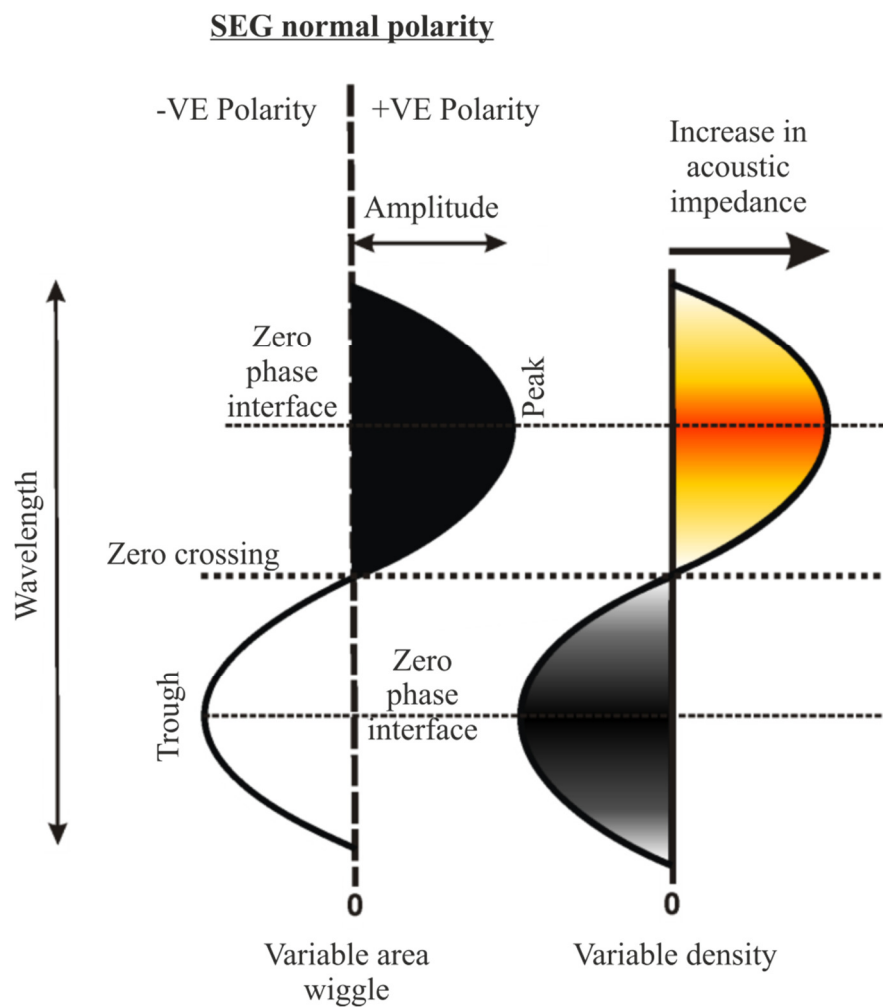
Figure 2.3. Schematic illustration of seismic data display in SEG convention. Variable area wiggle display (left) shows reflected energy is displayed as waveforms consisting of positive and negative amplitude values (peaks and troughs respectively). By removing the wiggle trace the seismic traces are shown as Variable density (right) display (modified from Hart, 1999).
.

2.2.2 Seismic data processing

The recorded reflected energy can be processed to produce an image of the subsurface geological structures. 3D data processing is similar to 2D data processing in most respects (Bacon et al., 2007). Three major steps in seismic data processing are 1) deconvolution 2) stacking and 3) migration (Fig. 2.4A)

Deconvolution is a process that sharpens the wavelet and removes any short period reverberations. It acts on the data along time axis and improves the temporal resolution by compressing the basic seismic wavelet.

Stacking is a process that involves adding of traces with different source-receiver offsets but a common midpoint together to improve signal to noise ratio. The traces are first corrected for the increased travel-time at the longer offsets due to the oblique travel path Normal Move Out (NMO), effects of subsurface dips Dip Move Out (DMO) and lateral velocity variation (Bacon et al., 2007). It compresses the data volume in the offset direction and yields the plane of stack section (Yilmaz and Doherty, 1987). The stacked trace, with much improved signal to noise ratio is then displayed as a seismic section.

Migration attempts to move dipping events to their true spatial locations at subsurface rather than their recorded location. It collapses diffraction patterns from points and edges and thus improves lateral resolution (Yilmaz and Doherty, 1987). The choice whether to migrate data before or after stacking is largely dependent on the velocity regime and the subsurface structural complexity (e.g dips) in the data (Bacon et al., 2007). Migrating a stacked section is called poststack migration, while migrating a prestacked section is called prestack migration. In addition, migration can be done in time or depth (with the final seismic section displayed in either time or depth) depending on the velocity variation and structural complexity (Fig. 2.4B). All the seismic data for this project are post stack time migrated (PSTM).
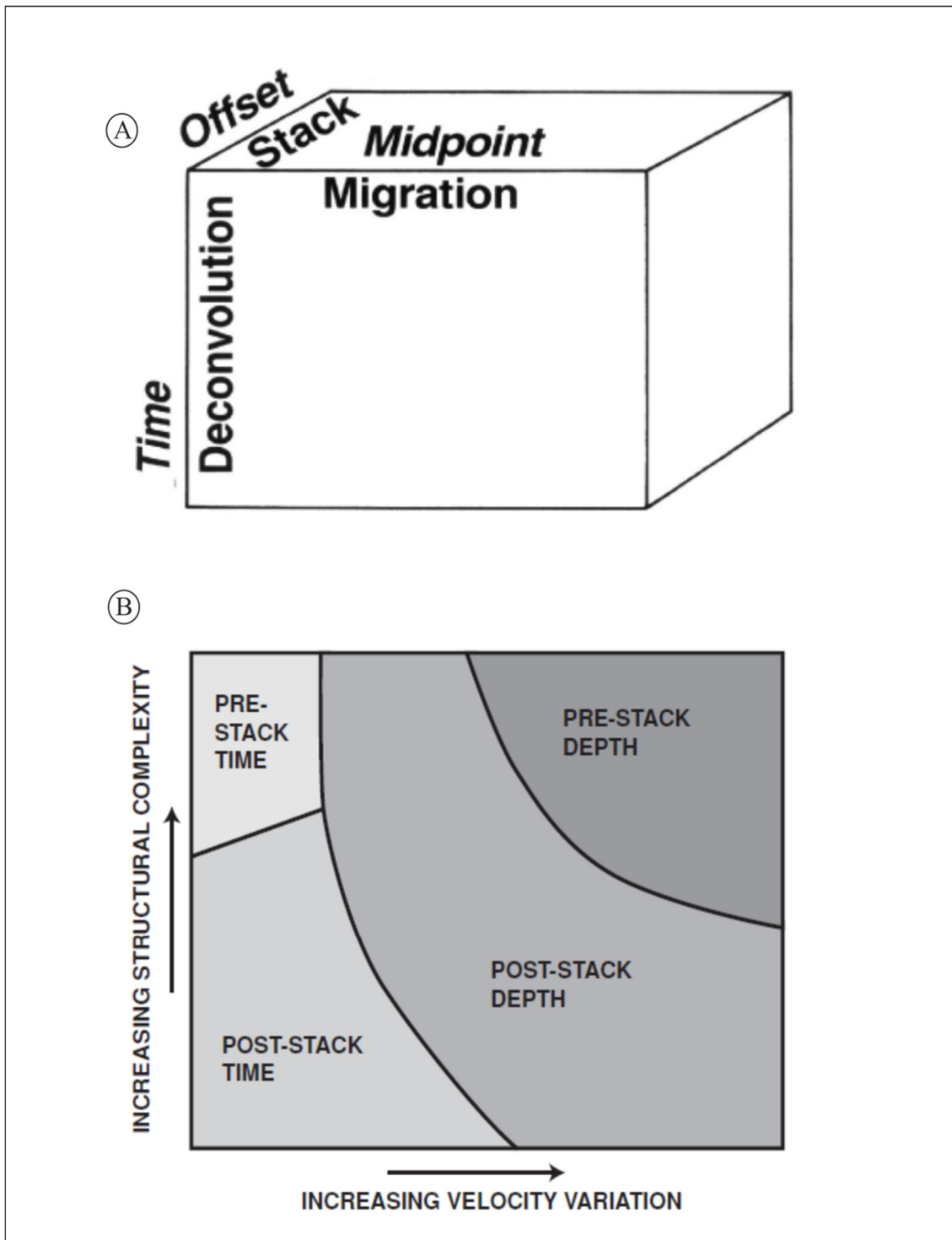
Figure 2.4 A) Seismic data volume represented in processing coordinate: midpoint-offset-time (from Yilmaz and Doherty, 1987) B) Appropriate methods of migration as a function of structures and velocity variation (from Brown, 2011).

2.2.3 Seismic resolution

The geologically significant features that can be recognised on seismic are affected by both the vertical and horizontal resolution of seismic data. Although, the seismic data for this project provides an excellent 2D and 3D seismic coverage of MTDs, it should be noted that the MTDs images on the seismic data are typically an order of magnitude larger than any observation at outcrop scale. The resolving power of the seismic data is always measured in terms of the seismic wavelength. The wavelength (λ) is defined as

$$\lambda = \frac{V}{F}$$

Where V = the wave velocity and F = dominant frequency

Seismic velocity increases with depth because the rocks are older and more compacted while the predominant frequency decreases with depth because the higher frequencies in the seismic signal are more quickly attenuated (Fig. 2.5A). Therefore the wavelength increases significantly with depth, making resolution poorer.

The vertical resolution is a measure of the ability to recognize individual, closely spaced reflections and is determined by the pulse length on the recorded seismic section (Kearey et al., 2009). The interaction of the wavelets from adjacent reflecting interfaces results in two limits of vertical resolution. The limit of separability/ maximum resolution possible is equal to one-quarter of a wavelength (or half a period) and is simply the bed thickness corresponding to the closest separation of two wavelets of a given bandwidth (Fig. 2.5B) (Brown, 2011). The tuning thickness is the bed thickness at which two events become indistinguishable in time. For thinner intervals than this, the amplitude is progressively attenuated until the limit of visibility is reached, when the reflection signal becomes obscured by the background noise (Fig. 2.5B) (Brown, 2011). The limit of visibility depends on the acoustic contrast of the geologic layer of interest relative to the embedding material, the
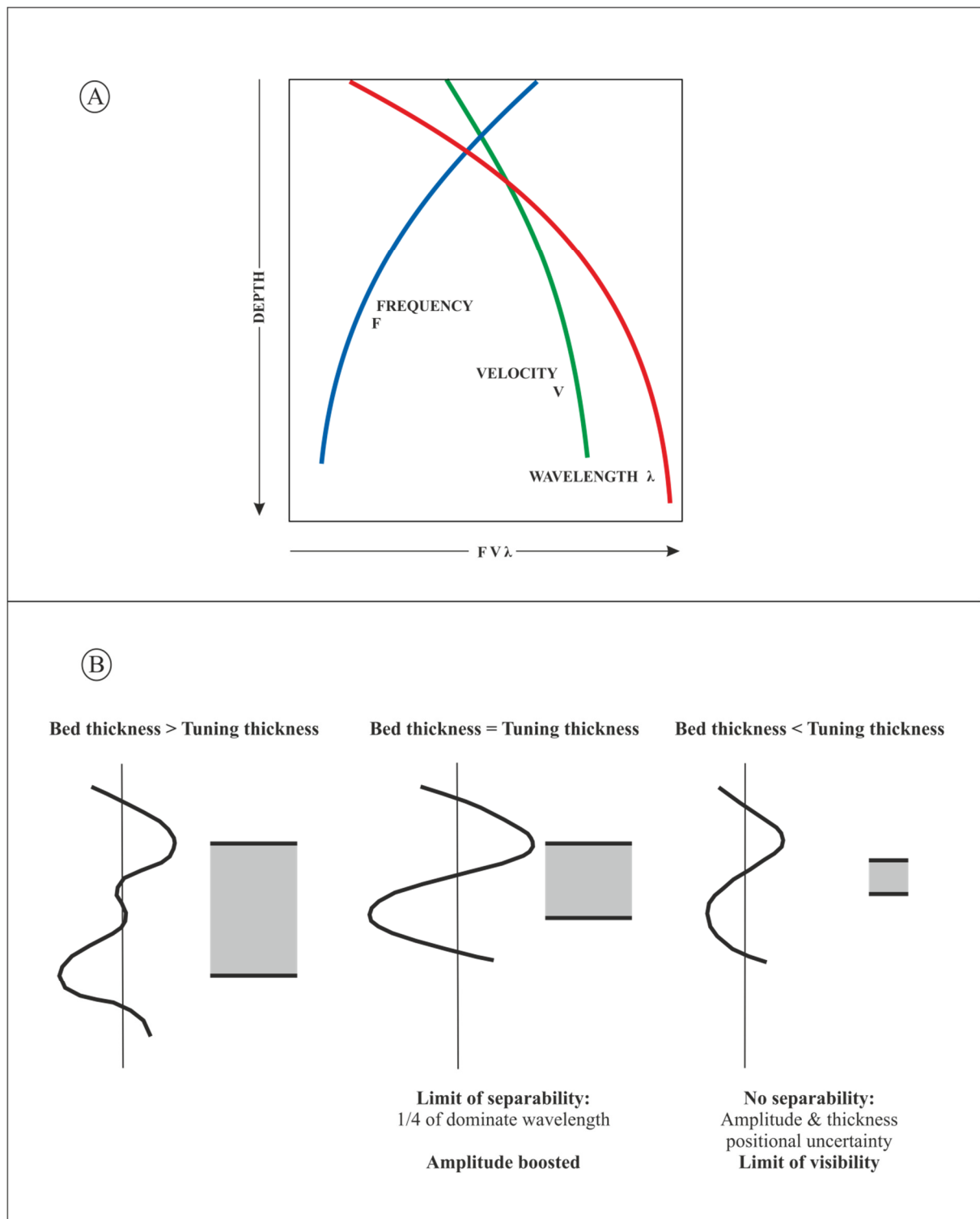
Figure 2.5 A) Wavelength, the seismic measuring rod, increases significantly with depth making resolution poorer. B) Resolution of the reflections from the top and bottom of a bed is dependent on the interaction of closely spaced wavelets (from Brown, 2011).

random and systematic noise in the data, and the phase of the data or the shape of the seismic wavelet (Brown, 2011).

The horizontal resolution refers to the minimal lateral proximity between two points that can still be recognized as individual points rather than one (Yilmaz and Doherty, 1987). It is a function of the spacing of the recording hydrophones and the width of the Fresnel zone. The spacing of the hydrophones determines the spacing of the depth estimate i.e. line spacing, from which the subsurface interface is reconstructed. For example, for a flat lying reflection (Fig. 2.6A), the horizontal sampling will be equivalent to half of the detector spacing which is equivalent to line spacing (or bin size) (Kearey et al., 2009)

The Fresnel zone is the part of the interface from which energy being returned to the detector within half a wavelength of the initial reflected arrival constructively interferes (Fig. 2.6B) (Kearey et al., 2009).The width of the Fresnel zone represents an absolute limit on the horizontal resolution of a reflection survey since reflectors separated by a distance smaller than this cannot be individually distinguished. (Kearey et al., 2009)

The width *w* of the Fresnel zone is defined by:

$$w = (2z\lambda)^{1/2} \text{ (for } z \gg \lambda)$$

where λ is the dominant wavelength of the source and *z is* the reflector depth

Seismic resolution (vertical and horizontal) generally decreases with depth because the high frequencies in the seismic signal are more quickly attenuated (lost by adsorption) (Brown, 2011).

Another important aspect that needs to be taken into consideration is the vertical exaggeration (VE) which refers to the distortion of seismic reflection of datasets. It is defined as the ratio of the vertical to horizontal scale n the depth domain (Stewart, 2011).

It should be noted that most of the seismic profiles presented in this thesis have been vertically exaggerated to enhance the interpretation of some the MTD features.
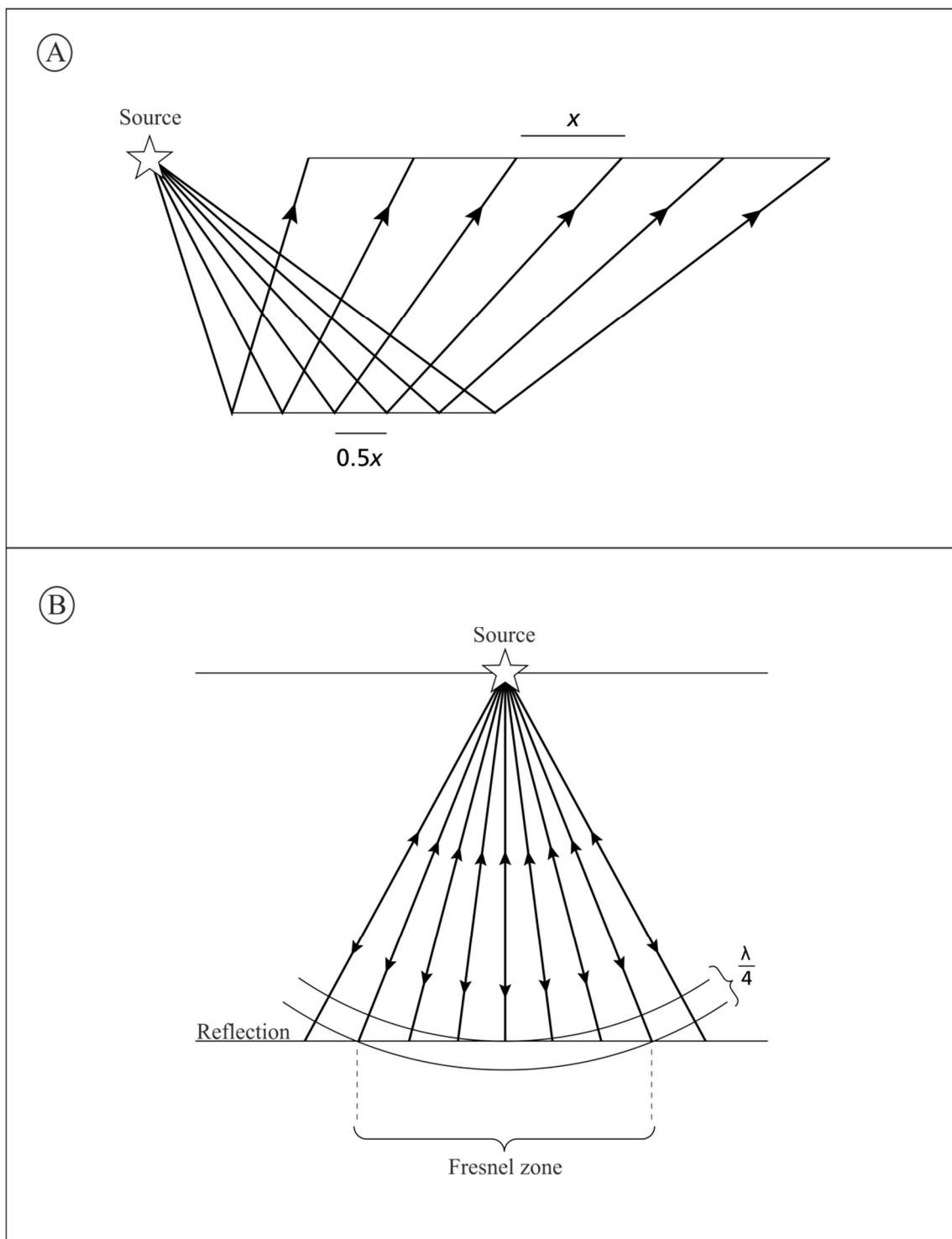
Figure 2.6. Schematic representation of the two main factors controlling horizontal resolution in seismic data. A) The horizontal sampling of a seismic reflection survey is half the detector spacing. B) Energy is returned to source from all points of a reflector. The part of the reflector from which energy is returned within half a wavelength of the initial reflected arrival is known as the Fresnel zone (from Kearey et al., 2009).

The vertical scale of both 2D and 3D seismic data are recorded in milliseconds (ms) two-way time (TWT) i.e. the time the P-wave takes to travel to the reflector and back again. The time can be converted to depth in metre if the seismic velocity at a particular depth interval is known. This is done by applying the following equation:

$$D = \frac{TWT}{2} * \frac{V}{1000}$$

Where D = Depth, TWT = Two-Way-Time in ms and V = Velocity in m/s.

Since well data were no available for this project, conversion of the seismic data from time to depth was impossible. Consequently all the heights and thickness measurements for the MTDs or related features in this project were presented in time (TWT).

2.3 Dataset

The main data used in this project consist of:

1) An industry 3D seismic survey from the West Nile Delta (Eastern Mediterranean)

(Fig. 2.7) acquired and processed in 1999 by BP and Partners. The 3D seismic data is a mosaic of smaller surveys of variable frequency and resolution. The data volume consist of

~ 6,400 km^2 of 3D seismic cube clipped at the Messinian (~ 4seconds) collected in ~ 100 – 2000 m water depth. The survey had an initial acquisition inline trace interval of 25m with crossline spacing of 25 m and a sampling interval of 4ms. The seismic data are near zero-phase and displayed with SEG normal polarity, i.e. an increase in acoustic impedance is represented by a positive amplitude excursion on the seismic trace. The dominant frequency of the dataset varies with depth, but it is approximately 45 Hz for the interval of interest, yielding a typical vertical resolution of 10 m based on an average seismic velocity of 1600 ms^{-1} as calculated from the checkshot survey of a calibration exploration borehole in the study area. There were no petrophysical data from exploration boreholes from the Pleistocene interval, hence the lithology or age calibration was not possible. Exploration targets are
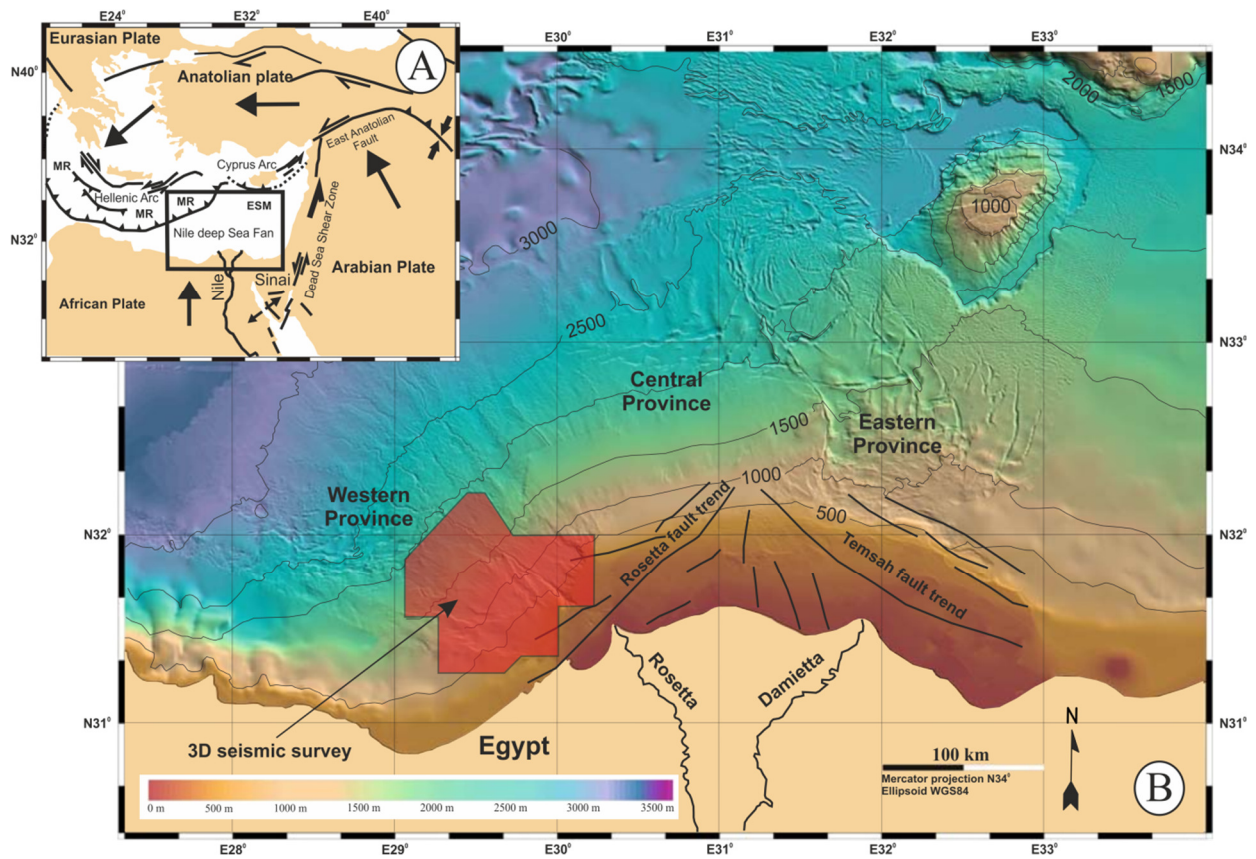
Figure 2.7 A) Geodynamic setting of the Eastern Mediterranean showing the study area indicated by the black box. B) Shaded bathymetry map of the Nile Deep Sea Fan (NDSF) showing the 3D seismic survey used in this project (indicated by the red polygon). Bathymetric contours are in metres.

mainly in the Pliocene succession in this area, which is where core and petrophysical data are concentrated.

2) A multibeam bathymetric map and 2D seismic data located within the Petroleum Exploration Permit 38451 ("PEP 38451") covering an area of c. 16,380 km^2 in the SE of the Deepwater Taranaki Basin, offshore New Zealand (Fig. 2.8B). The seismic survey was shot by TGS NOPEC Geophysical Company in 2001 and it consists of 34 lines comprising approximately 6700 full-fold km (Fig. 2.8B). The TGS-NOPEC data is now and has been incorporated with all all other seismic data available in the area. Data Acquisition was carried out by the vessel MV Polar Duke. A total of 73 line sequences were acquired comprising 6440.4 km of data.

The 2D survey has a coarse grid which varies from 12 x 12 km in the eastern part of the permit to 25 x 50 km and greater in the outer part.

Acquisition equipment included a Sleeve Airgun source (array of 3500 cu in. volume; firing pressure 2000 psi; firing interval +/- 10 ms) towed behind the ship at a 6m depth and a single digital streamer configured for 480 data traces. Sampling was at 2ms, recording for 3.0s.

Positioning was achieved using Differential GPS and onboard Quality Control was implemented using a ProMax QC system.

Line orientation was either in the Northwest-Southeast direction (and its reciprocal) or from Northeast-Southwest (and it's reciprocal), with the exception of one line which traversed the eastern half of the program block in a generally NS direction. Water depths varied greatly from as shallow as approximately 150 metres in the south to approx. 1900 metres in the North-west. Seismic profiles were processed using an adaptive deconvolution, bandpass filter was set at 3-6-90-120 Hz. The central frequency of the data is 65 Hz and spans from 0 to 110 Hz using a near surface sediment velocity of 1800 m/s, the vertical resolution of the data is in the order of ~ 6-7 m.
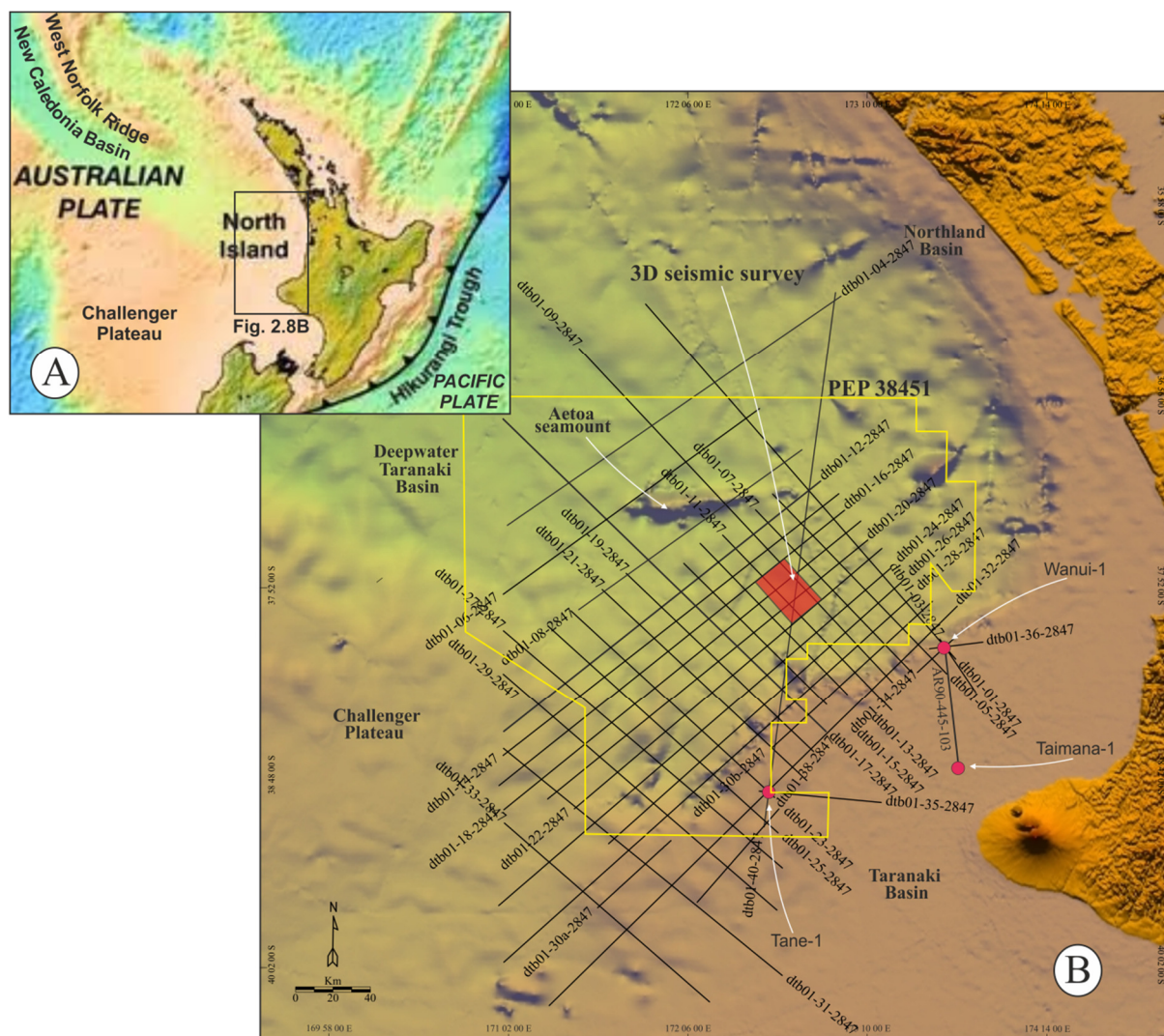
Figure 2.8 A) The Australian-Pacific plate boundary setting in the New Zealand region. The location of the study area is shown (black rectangle) (B) Mutibeam bathymetric map of the Deepwater Taranaki Basin showing the location of PEP 38451 (yellow polygon) and the coverage of the 2D seismic survey consisting of 34 lines (black straight lines) used in this study. In addition the location of the 3D seismic survey is shown (red box).

No wells have been drilled within offshore Deepwater Taranaki Basin and this precluded the calibration of the 2D seismic data. However, important information were extrapolated from drilled wells onshore (Fig. 2.8B) and published stratigraphy for nearby areas (Hansen and Kamp, 2006b).The 2D seismic data from the northwestern Taranaki Basin provided a regional understanding of the MTD stratigraphy and a context to the study of the 3D seismic volume (see detail in next paragraph).

3) The Romney 3D survey (Fig. 4.1 and 4.2) is also located within the Petroleum Exploration Permit 38451 ("PEP 38451") and images an area measuring 590 km ^{2} (Fig. 2.8B). The 3D seismic data was provided by Anadarko Petroleum Corporation as a 16-bit scale and clipped volume because it included multiple prospects and leads.

The data was processed to post-stack time-migration (PSTM), zero-phased, and Automatic Gain Control (AGC) was applied. The main frequency of the 3D seismic data is 50 Hz, yielding a vertical resolution of approximately 9 m which equals one quarter of the wavelength at the dominant frequency assuming a sediment velocity of 1800 m s^{-1}.

The final bin spacing of the seismic grid is 25 m x 25 m.

2.4 Methodology

The results presented in this thesis derived from mapping of 2D and 3D seismic data using

This section focuses on method generally applicable to the 2D and 3D results chapters.

Individual results chapters will provide further details of procedures used where necessary.

2.4.1 Recognition of MTDs on seismic reflection data

The following established key criteria (Bull et al., 2009a; Frey Martinez et al., 2005; Hampton et al., 1996; Posamentier and Walker, 2006) for the recognition of MTDs were used in this project. The seismic stratigraphic and morphological criteria for the recognition of mass-transport deposits is summarised in Figure 2.9. These criteria are highlighted below:

1) The seismic stratigraphic expression of MTDs is characterized by transparent to chaotic seismic reflections bounded by distinctive and laterally correlatable upper and lower bounding reflections (upper and basal surfaces respectively) with an often irregular geometry (Fig. 2.9A).

2) The basal surface is usually conspicuous in seismic data forming laterally continuous reflection that is concordant to the underlying stratigraphy (Fig. 2.9A). It is not uncommon to observe irregular topography of the basal surface due to the tendency of the MTD to erode deeply into the substrate during translation. The erosion is usually expressed in the form of long linear grooves or striations at the basal surface of the MTD (Fig. 2.9B). On the other hand the erosion process may result in significant "bulking up" of flow, as significant volumes of the basin-floor substrate are entrained into the translating mass (Fig. 2.9B).

3) The upper surface is usually represented by a laterally continuous or discontinuous and irregular reflection depending on the degree of internal deformation (Fig. 2.9C).

Ⓐ	Internal chaotic to transparent seismic refection character	SSW NNE 50 ms 1 km (Posamentier and Walker 2006)
Ⓑ	Substrate erosion in the form of basal grooving and/or deep erosional scour	N → Transport Direction Line A (Posamentier and Walker 2006) (Posamentier and Walker 2006)
Ⓒ	Irregular hummocks to featureless at the upper boundary	(Posamentier and Walker 2006)
Ⓓ	Presence blocks near the headwall	B NE Headwall scarp Block Graben Seabed SW 150 ms TWT 1 km Basal shear surface (Bull et al. 2009)
Ⓔ	Presence of thrust and fold structures near the toe or lateral margin	Decollément surface (Posamentier and Walker 2006)

Figure 2.9. Seismic stratigraphic and morphological recognition criteria for MTDs.

48

4) The limits of the upslope occurrence of MTD is marked by a headwall scarp, which occurs where the basal shear surface steepens and cuts through increasing shallower stratigraphy to intersect the surface (Fig. 2.9D). The headwall region is commonly characterized by extensional structures e.g. presence of rotated blocks, with clear detachment surfaces.

5) Compressional structures (e.g. thrust and fold structures) commonly occur downslope in the toe region (Fig. 2.9E).

2.4.2 Seismic attributes

Following the recognition of MTDs on either 2D and/or 3D seismic, they were mapped using Schlumberger Geoframe 4.2 seismic interpretation software. In order to describe the external morphology and internal character of the MTDs, an integrated 3D seismic interpretation approach (Bull et al., 2009a) was applied combining 3D visualisation, mapping and the construction of seismic attribute maps. Key reflections that defined both the upper and basal surfaces of the MTDs were picked manually on seismic profiles through the data using either fine or coarse grid mapping depending on the stratigraphy complexity of the MTD.

Seismic attributes are quantitative measure of seismic character that helps the seismic interpreter to better visualise or quantify relevant features on the seismic data (Chopra and Marfurt, 2005). In this project, seismic attribute maps provided information on the basal shear surface, internal geometry and palaeoflow directions of the MTDs.

Seismic attributes utilised in this research are described below:

Dip: or Dip Magnitude a time derived attribute that computes, for each trace, the best fit plane (3D) or line (2D) between its immediate neighbour traces on a horizon and outputs the magnitude of <u>dip (gradient)</u> of said plane or line measured in degrees.

Amplitude: Amplitude measures the distance between the peak and trough of the reflected wave, which is dependent on the energy of the incidence wave and the acoustic impedance contrast between the material above and below the interface that generated the reflection. Amplitude can be extracted along a mapped horizon and displayed as a horizon map. It can also be extracted form a specified time interval. Amplitude variation may be due to a number of factors, including porosity, fluid content, bed thickness and geometry (Hart, 1999). The presence of structures, sedimentological features, may therefore cause organised amplitude patterns such as linear or areal trends.

Root mean Square (RMS) Amplitude: Squares amplitude values over a specified window and then averages the results. The squaring of the amplitude values within the window means high amplitude is more noticeable in map view above the background contamination. The majority of the RMS amplitude maps generated in this project were windowed amplitude RMS amplitude maps within specified horizons, and were useful in identifying and characterising the internal structures of the MTDs.

Coherence: Coherence uses a set of mathematical calculations similar to correlation to compare adjacent waveforms (Brown, 2011). A coherency volume may be generated for a specified time interval and area and so it is often free from interpretational bias i.e. the utilization of mapped horizon is not a requirement (Brown, 2011). Like the 3D seismic volume, the coherency volume can be horizontally or stratigraphically sliced to enable the areal extent and later continuity of features to be examined. Coherence is excellent for mapping and identifying the 3D nature of faults.

2.4.3 MTD volume calculation

An estimate of the volumes for MTDs in the western Nile delta was calculated by using an average seismic velocity of 1600 m s^{-1} as calculated from the checkshot survey. While an

assumed seismic velocity of 1800 m s^{-1} was used in the volume calculation for MTDs in the Deepwater Taranaki Basin.

To date various methods have been developed to calculate the volume of remobilised MTD material (Canals et al., 2004). The volumes for the MTDs in this project were automatically calculated using Surfer 11 software. In order to do this, the mapped XYZ units of the upper and basal surfaces of each MTD were exported from Geoframe into Surfer 11 and then the necessary steps for volume calculation in Surfer was employed. Three different mathematical methods are used in Surfer to calculate the volume including: Trapezoidal rule; Simpson's rule and Simpson's 3/8 rule. It is worth noting that the calculated volumes using the three methods are consistent with volumes calculated manually with only minor discrepancy.

Chapter 3

At the time of thesis submission, Chapter 3 has been re-submitted for publication in Marine - Geology after revision and acceptance as Omeru, T., and Cartwright, J., *Multistage, progressive slope failure in the Pleistocene pro-deltaic slope of the West Nile Delta (Eastern Mediterranean).* The work presented in this chapter is that of the lead author. Editorial support was provided by the project supervisor, JAC in accordance with a normal thesis chapter.

3.0 Multistage progressive failure slope failure in the Pleistocene pro-deltaic of the West Nile Delta (Eastern Mediterranean)

3.1 Summary

The vast majority of submarine mass transport deposits (MTDs) have been attributed to retrogressive slope failure processes whereby an initial rupture zone migrates in a generally upslope direction towards the position of the ultimate headwall. Here we use 3D seismic data from the prodelta slope of the Western Nile delta to describe a series of volumetrically extensive MTDs (termed MTDs A, B and C) that are part of a linked sequence that failed progressively but with retrogressive modifications of the lateral and headwall margins. The MTDs have c. 500 - 1000 ms of relief on their marginal scarps with a minimum total volume of remobilised sediments of 750 km^3.

By comparing their motion histories, and by correlating their basal surfaces, we demonstrate that MTDs B and C are remnants of a single original body that was later cut by MTD A. This sequence is confirmed by cross-cutting relationships at the lateral boundaries between the three MTDs and the absence of any significant infill and burial of residual topography at the tops of MTDs B and C prior to the incision of MTD A. This implies that these two major submarine failures (MTD B/C, and then MTD A) were closely grouped in time. We suggest a mechanistic model whereby rapid load redistribution resulting from the initial failure led to localization of a deeper cutting failure, and the unloading in the headwall region then led to expansion of the deeper failure in an upslope direction until a new merged headwall was formed.

Correlation with MTDs identified downslope in previous studies suggests a date between 117–105 ka for this giant slope failure. This was a period of relative sea level fall in the Nile region which may have contributed to increased pore pressure. Slope failure on this scale was probably preconditioned by high sedimentation rates and under-compaction in a mud-rich succession, leading to local increases of pore pressure.

Reconstruction of the pre-seabed topography suggests a total volume (residual and depleted) of remobilisation of a minimum of the order of 750 km^3, making this amongst the largest submarine landslide complexes documented to date. It is suggested that this giant slope failure might have posed a risk to the integrity of petroleum seals considering that the failure occurred in a gas rich province of the western Nile delta.

3.2 Introduction

Submarine MTDs are common features in slope systems on continental margins and are capable of transporting sediments across the whole width of the continental rise to the abyssal plain (Canals et al., 2004; Hampton et al., 1996). It is commonly observed that MTDs cluster geographically through time (Masson et al., 2006; Masson et al., 2002), with failure-prone areas exhibiting pronounced vertical stacking to form MTD complexes.

The clustering of MTDs raises obvious questions about their actual mechanism of failure. Large MTDs are often described as being retrogressive (Bjerrum, 1955; Bryn et al., 2003; Homza, 2004; Kvalstad et al., 2001; Lucente and Pini, 2003; Prior et al., 1986; Sawyer et al., 2009) where the occurrence of an initial failure surface exposes an unstable headwall that subsequently fails upslope until a stable headwall is achieved. However, it has also been shown that subaerial MTDs can develop under conditions of progressive failure, where a series of failures sequentially cut further downdip, (Bernander, 2000; Bishop, 1967; Bjerrum, 1967; Dykstra, 2005; Stock et al., 2012). Perhaps the first clear evidence of progressive failure of a submarine landslide was presented by Frey Martinez et al. (2005) who showed 3D seismic mapping of a series of failure scars associated with the small volume Gaza Slide, in the Eastern Mediterranean, and where the final slide clearly incises into the earlier failure planes in a downslope position. It is unclear whether progressive failure is a viable mechanism for much larger scale submarine slope failures, where volumes of remobilised material may be several orders of magnitude larger than in those previously reported.

The study presented here is based on a high resolution 3D seismic interpretation of a region of a highly unstable slope on the flank of a major delta, and was motivated by the need to understand the interplay between the periodicity observed in repeated slope failures and the driving factors responsible for failure (see Masson et al., 2010 for review). The prodeltaic

slope region of the Western Nile Delta (Fig. 3.1) has been modified by submarine failures of various scales and frequencies. The close spatial association of the MTDs resulting from these failures raises fundamental questions of whether and to what extent they might be related and affords an opportunity to investigate the mode of failure. Previous studies in this area (Ducassou et al., 2009; Garziglia et al., 2008; Loncke et al., 2009; Rouillard et al., 2010) have documented a series of MTDs (Fig. 3.1B) establishing the basic morphological expression, age relationships, evolution and triggers. However, these authors did not have access to high resolution 3D seismic surveys and were therefore unable to explore the potential inter-relationships between these MTDs in three dimensions.

Although there are over ten individual MTDs developed within the Pleistocene succession in this area of the pro-deltaic slope, three in particular stand out as having originated from giant slope failures simply from their volume, and from the magnitude of their associated scarps (c. 500 – 1000 m). These three MTDs (named here MTDs A, B and C) are the focus of this study. These MTDs have been identified in previous studies but have not previously been mapped in detail. MTD A (this study) corresponds in part to previously identified slope failure deposits (SL 2 of Garziglia et al., 2008 and MTD 10 of Rouillard et al., 2010) (Fig. 3.1B) based on the fact that they occur on the same stratigraphic level. Similarly, MTDs B and C correspond to SL 4 and MTD 9 of Garziglia et al. (2008) and Rouillard et al. (2010) respectively (Fig. 3.1B). The main aims of this study are to:

(1) Describe the dimensions and the geomorphological characteristics of MTDs A, B and C.

(2) Determine the sequence of failure of these three MTDs by investigating the relationships between them, and to explore the question of whether they represent a single slope failure (and if so, what type) or separate events that exploited similar region of inherent slope instability and (3) Discuss the processes that preconditioned the slope for failure and potential triggering mechanisms.
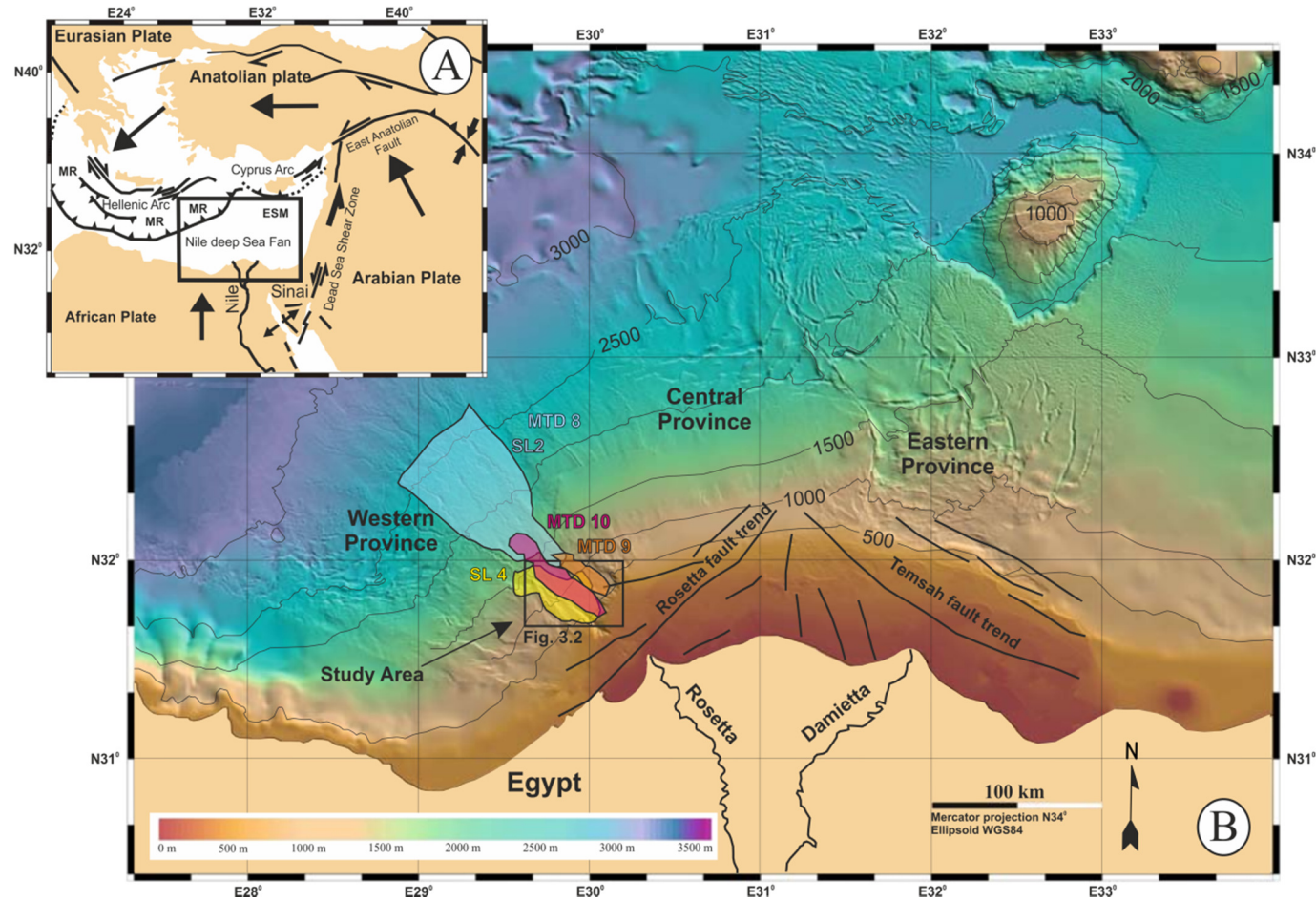
Figure 3.1 A) Geodynamic setting of the Eastern Mediterranean Basin. The study area is indicated by the black box. Grey arrows indicate relative plate motions. MR = Mediterranean Ridge; ESM = Eratosthenes seamount. B) Shaded bathymetry map of the Nile Deep Sea Fan showing the study area (indicated by the box) and the extent of previously mapped MTDs SL2 and SL4 (Gaziglia et al., 2008), MTD 8, 9 and 10 (Rouillard et al., 2010).

3.3 Geological setting

The study area is located on the western province of the Nile Deep Sea Fan (NDSF) (Fig. 3.1). The NDSF is a large (c. 100,000 km^2) sedimentary wedge which resulted from successive offshore growth of abundant terrigenous sediments delivered, since the Late Miocene, by the Nile River (Dolson et al., 2001; Mascle et al., 2006; Ross and Uchupi, 1977; Salem, 1976). The NDSF lies in a geodynamic setting that is characterised by a complex pattern of active, thick skinned, crustal tectonics resulting from interactions among various tectonic plates and microplates (Fig.3.1A) (Le Pichon et al., 1995; Mascle et al., 2000; McClusky et al., 2000; McKenzie, 1972; Westaway, 1994). Towards the north, the region was influenced by active subduction/collision (and associated southward growth of the Mediterranean Ridge) of Africa beneath Aegea-Anatolia along the eastern Hellenic and Cyprus arcs (McClusky et al., 2000). The motion of the Arabian plate with respect to Africa to the east and northeast led to active deformation along the Dead Sea/Levant and East Anatolian Fault Zones(Girdler, 1990). Some structures were also inherited from the very slow, almost aborted Suez Rift to the southeast (Courtillot et al., 1987). The Egyptian passive continental margin to the south is inferred to have been initiated by rifting from Jurassic to Early Cretaceous times (Dolson et al., 2001).

In the late Eocene and early Oligocene, as the Gulf of Suez began to open, northern Egypt was tectonically tilted northward toward the Mediterranean and large volumes of clastics entered the basin through deep canyons incised along the coastline high exposed Eocene and older carbonates (Dolson et al., 2005) (Fig. 3.3).

A major flooding event (Qantara transgression) was followed by large-scale regressions, which culminated in the Messinian drawdown or salinity crisis, when the entire shelf and slope system was subaerially exposed and deeply eroded (Dolson et al., 2005).
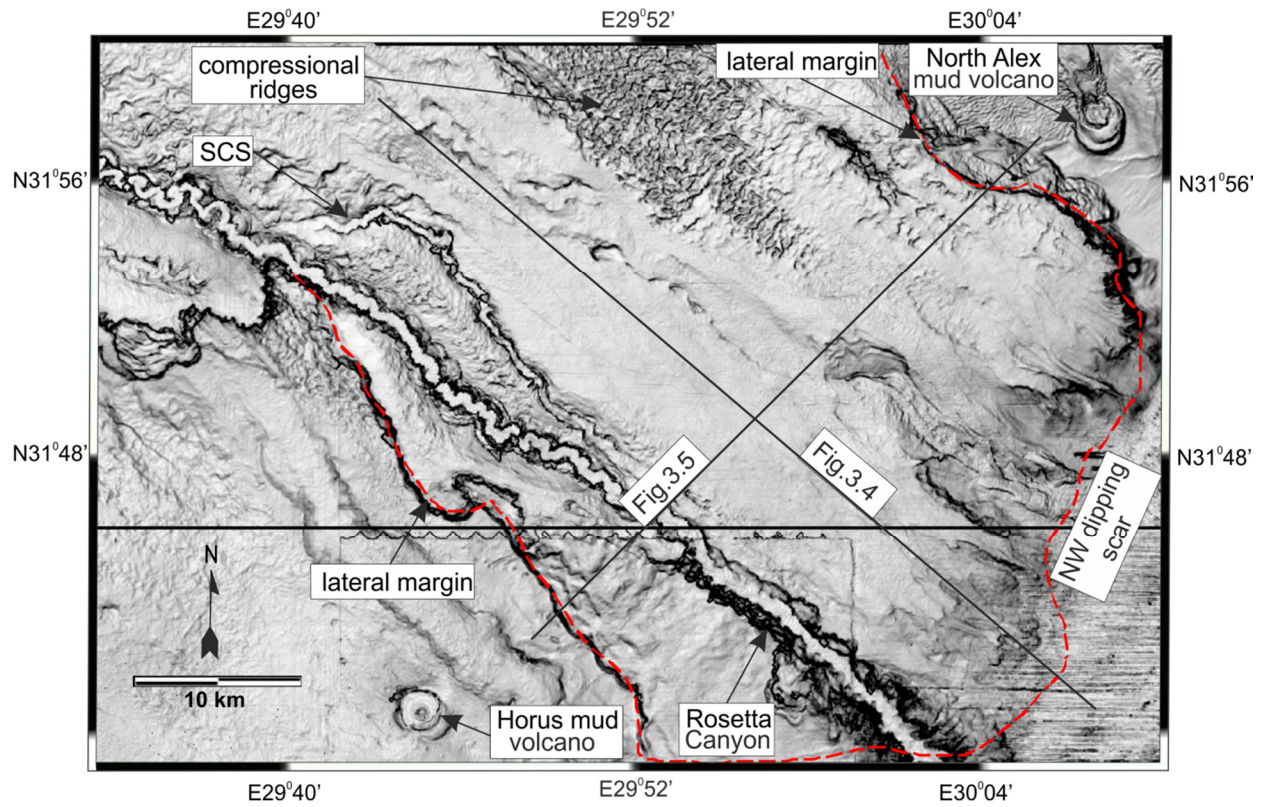
Figure 3.2. Time-dip attribute map of the seabed in the study area showing residual topography of the present day seafloor. Solid black lines indicate the location of seismic profiles. The red dashed line indicates the boundary of the underlying MTDs in this study. SCS = Slope Channel System.
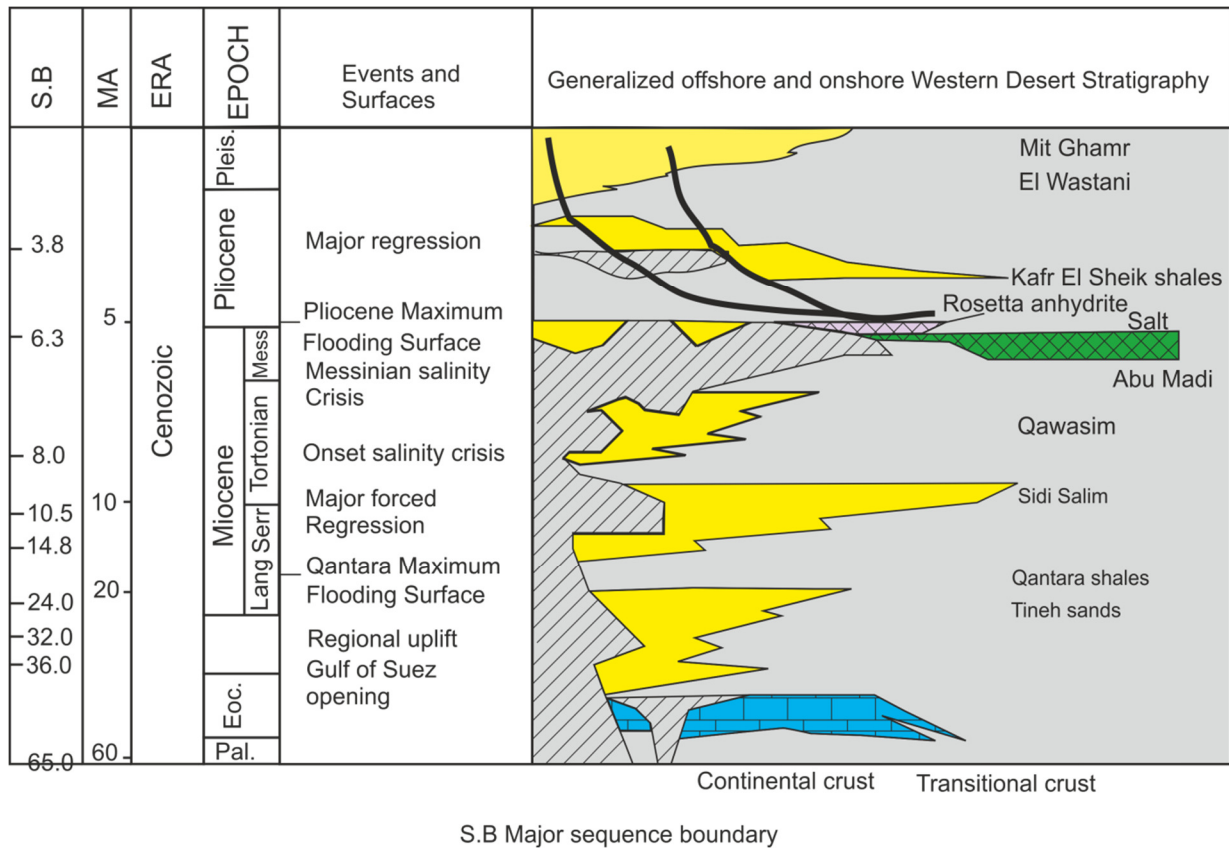
Figure 3.3. Onshore to offshore stratigraphy from the Western Desert to the deep water Nile delta (redrawn from Dolson et al., 2005.

Following the Messinian drawdown, transgressions resulted in deposition of the Abu Madi clastic system which was overlain by Lower Pliocene shales of the Kafr El Sheik Formation. Renewed Pliocene progradation began about 3.8 Ma and the current shelf edge marks the maximum seaward extension of the deltaic system. The recent terrigenous cone drapes a segment of a much older passive margin whose total sedimentary thickness (including the post-Miocene terrigenous cone) is believed to reach in excess of 9–10 km (Aal et al., 2000; Mascle et al., 2006).

The Nile delta is fed by two main branches of the Nile River (Fig. 3.1). The Rosetta branch feeds the western delta and slope and the Damietta branch feeds the eastern and central delta. A major submarine fan system dominates the slope to the north (Dolson et al., 2005). The steeper eastern slope region is dominated by rapid Plio-Pleistocene sedimentation in a growth fault province (Loncke et al., 2004). In contrast, the more gentle westward side of the Nile Delta which extends offshore (c. 80km) from the Rosetta branch across a wide continental shelf (Loncke et al., 2004) to the slope is dominated by extensive slope channel systems.

Structural controls on the stratigraphy of the study area are associated with two separate regimes: 1) regional basement-involved tectonics associated with the Rosetta Fault system inherited from the rifting period of the margin evolution (Aal et al., 2000) and 2) gravity driven tectonics linked to downslope Messinian salt spreading which strongly impacted continental slope morphology (Gaullier et al., 2000; Loncke et al., 2006). Two major fault trends characterise the Nile slope system: NW – SE Temsah trend and the NE – SW trending Rosetta fault (Aal et al., 2000).

Recent studies in the western province, (the study area) have shown that recently abandoned and active channel-levee systems, fluid seepage constructions and MTDs are the primary architectural elements controlling the slope evolution in the area (Dupré et al., 2007;

Garziglia et al., 2008; Loncke et al., 2009; Newton et al., 2004). Evidence of slope failure in the western slope area is evident from the residual topography of the present day seafloor in the form of an arcuate and irregular scar having a width of about 30 km (Fig. 3.2). (Garziglia et al., 2008) recognised and investigated seven successive MTDs (SL1-SL7) mainly in the uppermost 500 – 1500 m of the slope succession. The authors documented the morphological expression, internal configuration, basal surface geometry and age relationships of the MTDs. (Loncke et al., 2009) described the complexity of a pronounced scar at the head of the Rosetta Canyon and discussed its association with transparent acoustic deposits, and from this suggested ten episodes of sliding and/or slumping in three main periods intercalated with two periods of dominantly turbiditic deposition. (Ducassou et al., 2009), presented an overview of the evolution of the Nile Deep Sea Turbidite (NDST) system during the last 200 ky, over a series of glacial and interglacial cycles. The authors suggested that large slope failures played an important role in the overall evolution of the turbidite system. More recently, (Rouillard et al., 2010) identified and mapped 18 MTDs on the continental slope of the Rosetta turbidite system in a bid to tentatively reconstruct the depositional events for the last 200ky.

This study focuses on the Upper Pliocene/Pleistocene interval (El Wastini and Mit Ghamr formations) (Fig. 3.3), which in the study area comprises mainly claystones and thin, interbedded sandstones developed in channel-levee systems.

Representative regional seismic profiles (Figs. 3.4 and 3.5) located on the western slope illustrate the main structural and stratigraphic features of the study area. The MTDs represent approximately 25% of the gross stratigraphy of the interval of interest. The Pleistocene/ Holcene interval is condensed to the NW and SW (Figs. 3.4 and 3.5). A pronounced shelf-slope break occurs over deep structural fault blocks (Fig. 3.4). The Middle - Upper Pliocene
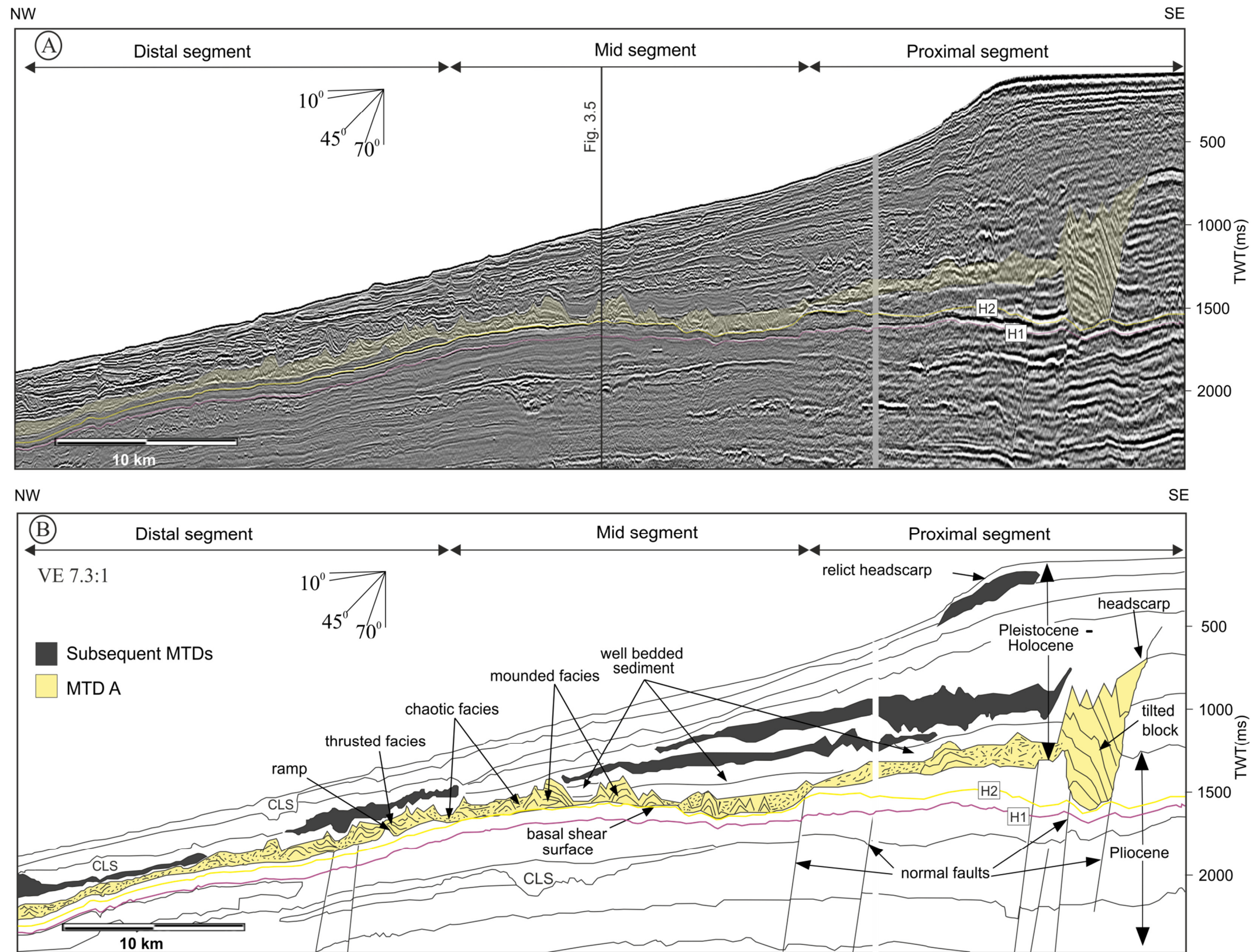
Figure 3.4 A) Representative dip oriented seismic profile through the central portion of the prominent scar observed on the sea floor (for location see fig. 3.2). B) Interpreted seismic profile showing MTD A and younger MTDs. In the proximal segment, MTD A headwall forms a steeply dipping interface forming the up-dip boundary between the continuous reflections of the upper slope and the breakaway fault bounded, tilted block. Compaction in the distal part of MTD A is inferred due to folding, reverse faulting and thrusting. Notice the irregular top and basal surfaces that bound MTD A. CLS = Channel levee system.
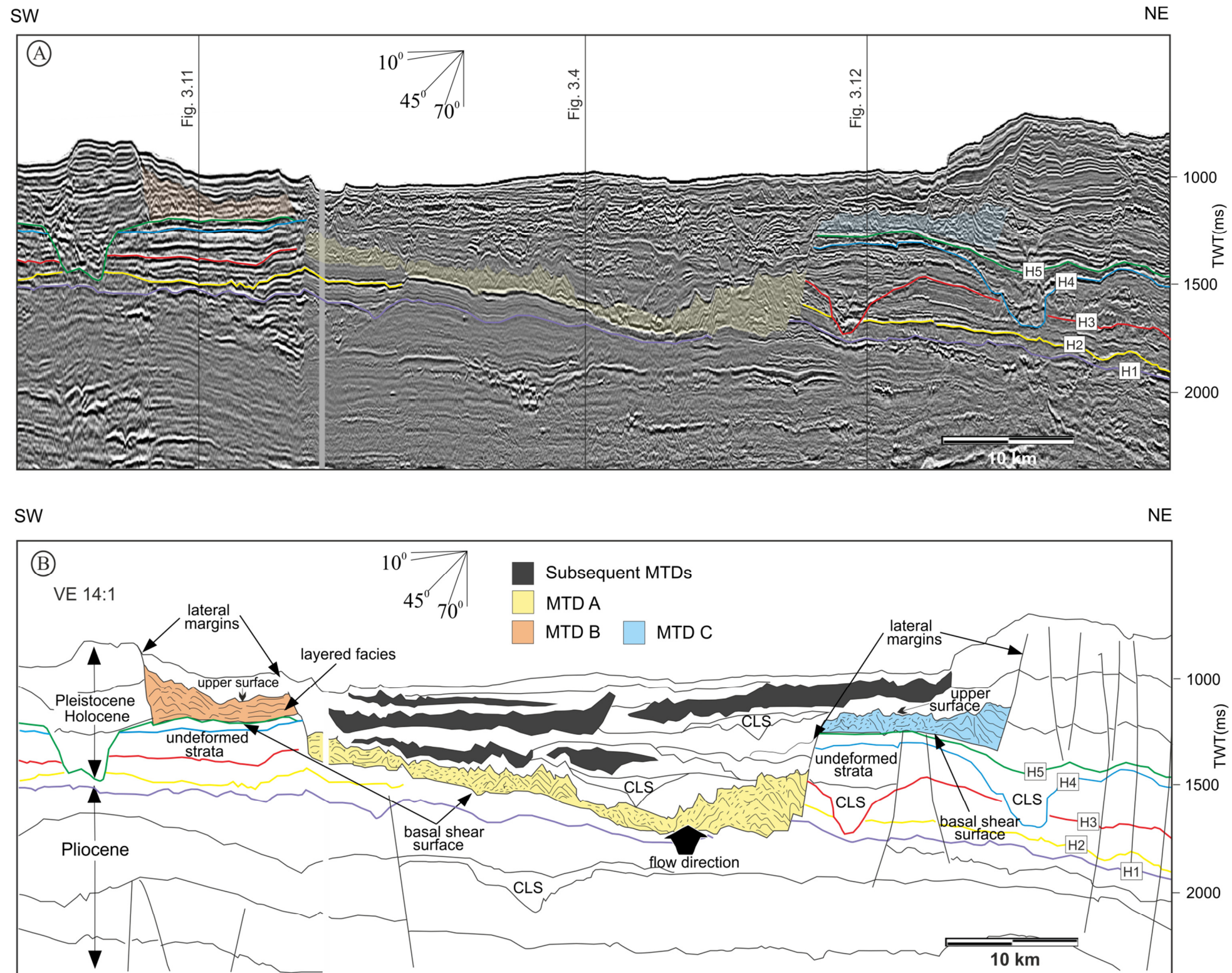
Figure 3.5 A) Representative strike oriented seismic profile across the mid-segment of MTDs A, B and C. Notice how the Pleistocene/ Holocene interval is condensed towards the SW. B) sketch of the interpreted seismic profile (see Fig. 3.2 for location). Notice how the lateral margins appear to climb from their detachment through in-situ stratigraphy, up across the chaotic deposits of the MTD B, which suggest that MTD A postdates MTD B. The upper surface of MTD A is irregular and terminates abruptly on the SW and NE lateral margins. CLS = Channel levee system.

stratigraphy is characterized by high amplitude reflections that are laterally continuous and which are interpreted as hemipelagic deposits. More variable amplitude and discontinuous seismic facies units interpreted as turbidites, and NW trending channel-levee systems. The Pleistocene interval comprises the three major MTDs which are the focus of this study (referred to as MTDs A, B and C in Fig. 3.5), along with a series of smaller mass transport deposits interbedded with hemipelagites and channel-levee deposits (Garziglia et al., 2008; Loncke et al., 2002) (Figs. 3 4 and 3.5).

The petroleum plays in the deep water fairway of the Nile slope region are dominated almost exclusively by stacked slope-channel systems (Figs. 3 4 and 3.5). To the west the dominant Pliocene play type consists of slope channels draped over large structural noses. Thick marine shales of the Kafr El Sheikh Formation provide the top seal to many post-Messinian hydrocarbon accumulations (combinations of biogenic and thermogenic gas) and are overpressured in much of the basin. Pliocene targets have readily direct hydrocarbon indicators (DHIs) which have enabled a sustained industry success rate of 90% (Dolson et al., 2005).

3.4 Observations and interpretation

3.4.1 General Physiography

In the study area, the present day shelf edge occurs at c. 100 m water depth and bounds an upper slope with a mean inclination of 3 - 5°. The position of the shelf edge is delimited by an arcuate scar, up to 500 m high, dipping steeply (10 - 20^{0}) in a northwesterly direction (Fig. 3.2). The seafloor morphology of the upper slope is irregular and shaped by the drape of near-surface hemipelagite sediments overlying combination of mass transport deposits and channel levees. The most prominent of the channel systems in the area is the NW-SE oriented Rosetta Canyon, which at the present day cuts through the scar (Fig. 3.2). The Rosetta Canyon is a

pronounced incisional feature close to the well-marked scar, but the canyon morphology reduces in relief in a downslope direction, and is gradually replaced by the morphology typical of a slope channel, with increasing sinuosity of the channel axis in a downslope direction. The scar is highly irregular, with local slope failures distributed along it at the seabed. Some 20-30 km downslope from this scarp is an area of pronounced linear ridges, interpreted as incompletely draped compressional ridges associated with a shallow buried mass transport deposit (Garziglia et al., 2008). Also prominent on the bathymetry map, just outside the lateral margins of the relict lateral margins of the scarp are the North Alex and Horus mud volcanoes (Fig. 3.2) (Loncke et al., 2004).

A representative seismic profile through the large downslope concave scar (which is the dominant feature) in the west Nile delta shows that the underlying headwall has been onlapped and back filled (Fig. 3.4). The Pliocene to Holocene slope is characterised by a succession of units that are recognisable as discrete bodies from their incoherent seismic character (Figs. 3.4 and 3.5). They are all crudely concordant to the gross stratification, but are bounded at their bases and tops by irregular surfaces, with often considerable erosional (base) or depositional relief (top) which allow them to be readily distinguished from undeformed and in-situ strata (Figs. 3.4 and 3.5).

These bodies are interpreted as MTDs by analogy with previous studies (e.g Frey Martinez et al., 2005, see methodology in Chapter 2). The fact that the underlying headwall has been onlapped and back filled suggests that the arcuate scar is a relict of a large erosional truncation buried under c. 500 m of overburden (Fig. 3.4) Five horizons numbered H1 to H5 have were identified and correlated over as much of the area as possible from the undeformed zone into the MTDs (Fig. 3.5).The geometry and architectural elements of the three main MTDs are described in detail in the following sections using a combination of seismic attribute maps and representative seismic profiles.
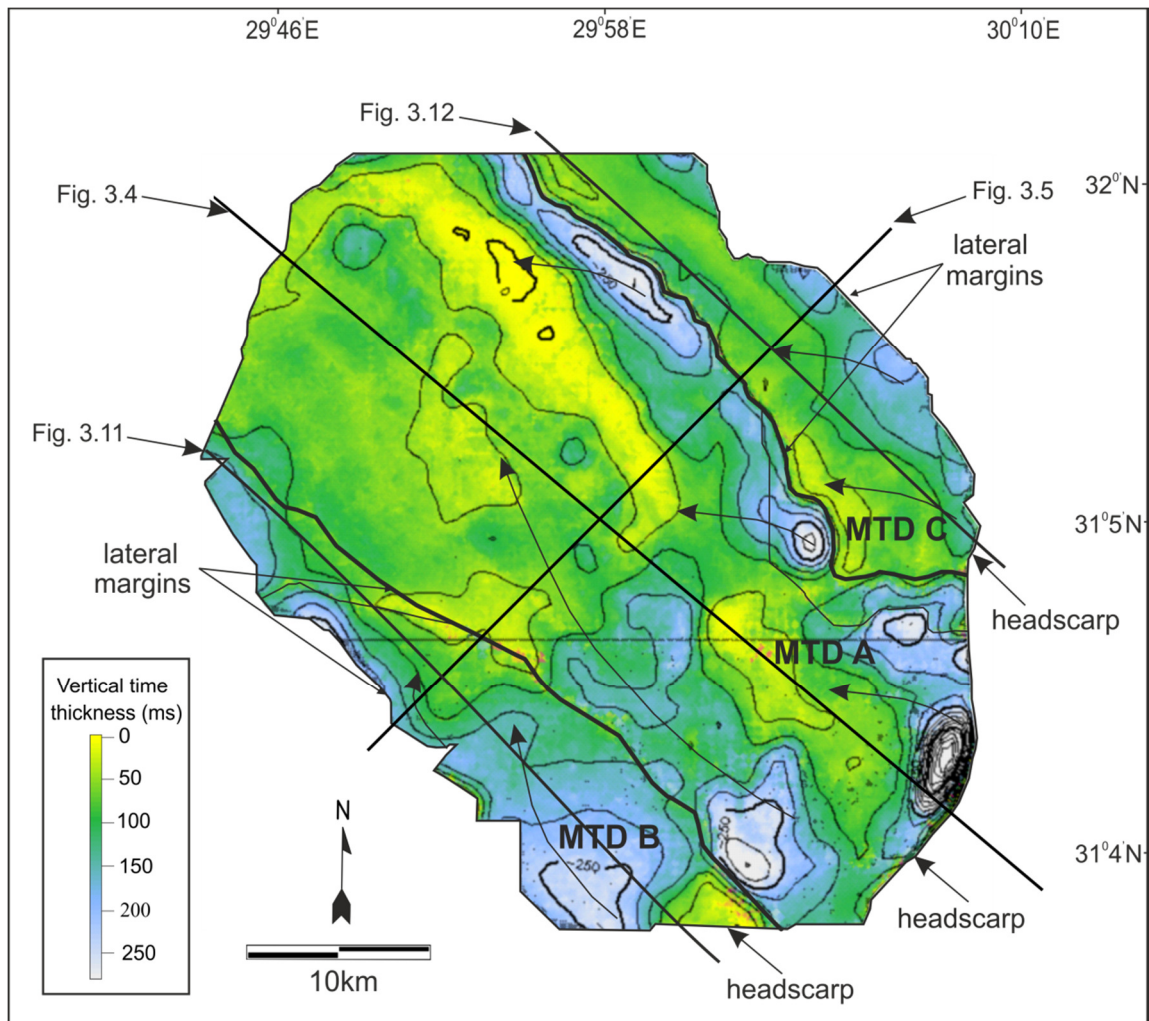
Figure 3.6. TWTT isochron map of the MTDs A, B and C which was used as a proxy to estimate the residual volume of deposits. Arrows indicates the thinning direction.
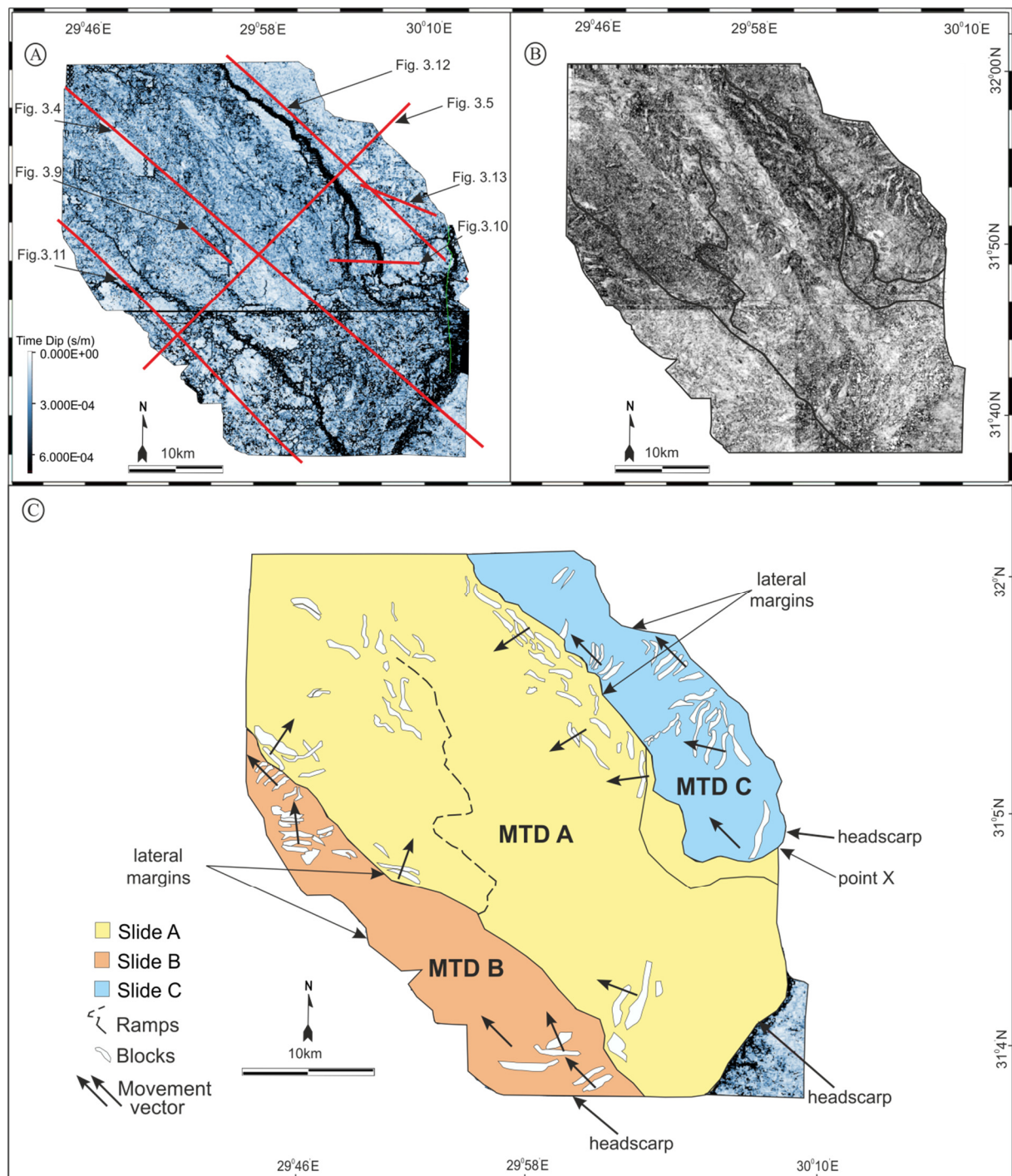
Figure 3. 7 A) Dip-structure map of the basal surfaces of MTDs A, B and C showing that they are elongated in a downslope direction B) Coherency slice taken 64 ms above the basal surfaces of MTDs A, B and C. High (white) coherency corresponds to blocks while low (dark) coherency represents chaotic sections. C) Interpretation map showing the various architectural elements of the MTDs.

3.4.2 MTD A

MTD A is recognised as the lowest deformed unit in the slope and marks the transition between the Upper Pliocene and the Lower Pleistocene (Figs. 3.4 and 3.5). The main MTD A body is elliptical in map view (Figs. 3.6 and 3.7), elongated in a NW-SE direction. MTD A is divided into three segments (proximal segment is nearest to the head region; medial segment occupies the central area of the deposit and the distal segment is situated farthest away from the headwall) based on its internal and external structural and topographic relationships (Fig. 3.4). MTD A varies significantly in its two-way travel time (TWT) thickness. In the proximal segment, MTD A reaches up to 300 ms thick and thins progressively towards the distal segment (Figs. 3.4 and 3.6). MTD A also thins from its lateral margins towards the centre (Figs. 3.5 and 3.6).

The buried NE - SW oriented headwall of MTD A (Fig. 3.7), visible in the proximal segment of the slope, defines the upslope margin of MTD A (Fig. 3.4). The seismic resolution is generally poor in this headwall region due to shoaling of the seabed and influence of seabed multiples along with scattering of incident reflection energy from the highly irregular scarp topography. Nevertheless, it is possible to interpret the headwall intermittently along its strike, and its relief is observed to be consistently of the order of 1000 ms with a northwesterly inclination of c. 20°.

The headwall is delineated by extensional faults which bound a huge 5 km long , 3 km wide and 800 ms high rotated block resulting in a conspicuous depression (up to 300 ms) of the basal shear surface in that area (Fig. 3.4 and 3.7). Upslope of the headwall, seismic reflections comprising the laterally equivalent units of MTD A are continuous and undisturbed.
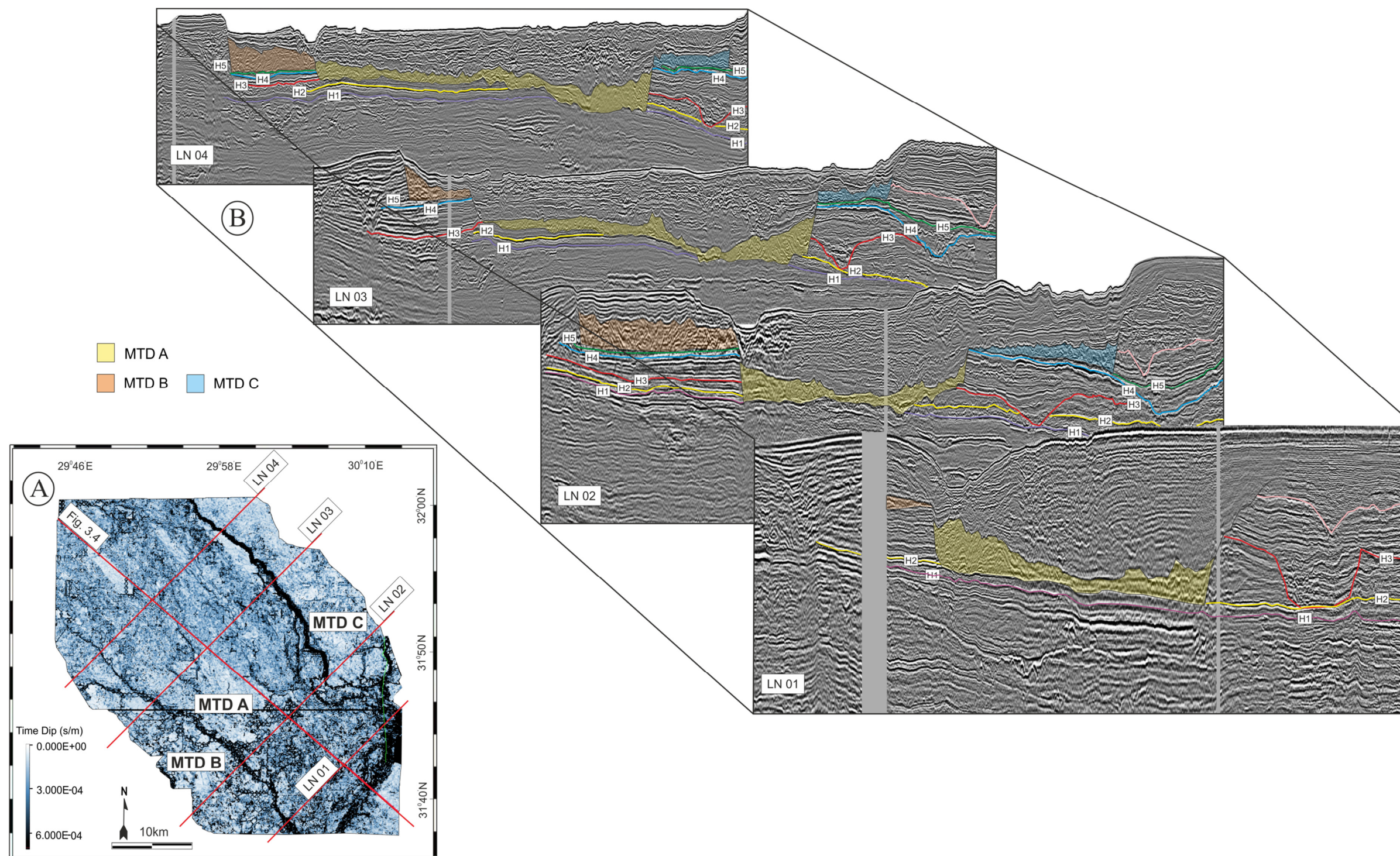
Figure 3.8 A) Dip-structure map of the basal surfaces of MTDs A, B and C showing the locations of the seismic profiles in figure 3.8B. B) Fence diagram showing variable thickness as well, heights of the lateral margins, geometry of the basal surfaces of MTDs A, B and C. MTDs B and C are interpreted to be one and same failure.

The lateral margins of MTD A are seen as sharp boundaries separating the highly chaotic seismic facies of the deposit and the undeformed strata outside of the MTD (i.e. along slope to the NE and SW) (Fig. 3.5). The maximum height of the SW lateral margins is 500 ms measured in either an upslope or downslope position (Fig. 3.8B). The SW lateral margin gradually decreases in magnitude downslope while the NE lateral margin appears to increase in magnitude downslope. The inclination of the lateral margins ranges from 7° to 10°. A striking observation is that, both the NE and SW lateral margins appear to climb from their base through in-situ stratigraphy, up across the chaotic deposits of the MTD B and MTD C (Figs. 3.5 and 3.8).

In map view (Figs. 3.6 and 3.7), the lateral margins of MTD A have a prominent SE - NW orientation and appear to be separated from the headwall. The SW lateral margin extends for c. 40 km in a downslope direction from the inferred junction with the headscarp. The NE lateral margin extends for a distance of c. 30 km and is interpreted to form a junction with the headwall of MTD C close to the northern limit of MTD A headwall (point X on Fig. 3.7C).

The upper surface of MTD A is represented by a weak amplitude positive reflection that varies in topography from the proximal to distal segments (Figs. 3.4 and 3.5). In the proximal and mid-segments (Fig. 3.4), the upper surface is highly irregular and discontinuous while in the distal segment the upper surface becomes more regular and continuous further downslope. It terminates abruptly at the lateral margins (Figs. 3.5 and 3.8), and is overlain either by well stratified post failure drapes of hemipelagic sediments (mid segment, Fig. 3.4), younger slide deposits or channel levee systems (Fig. 3.5).

The basal surface of MTD A is a low amplitude reflection with negative polarity (high impedance to low impedance) (Figs.3.4and 3.5). It is irregular and truncates underlying continuous seismic reflections with regions that are concordant and discordant to underlying stratigraphy, occasionally with a ramp and flat geometry. The basal surface cuts up c.150 ms

(c. 120 m) of stratigraphy at a major ramp structure with a thrust fault that dips c. 4° east separating undeformed strata downslope and deformed strata within MTD A (Figs. 3.4 and 3.9). This ramp is clearly seen on a dip-attribute map and a coherence slice taken 64 ms above the basal surface (Fig. 3.7A and B respectively) as an irregular N-S striking boundary separating two regions of contrasting textures. The basal surface then flattens down-slope to become concordant in the westernmost part of the distal segment (Fig. 3.4).

The internal seismic character of MTD A is dominated by low to high reflective, chaotic, layered, folded and thrusted seismic facies based on their configuration and reflection termination, which has aided its interpretation as a mass transport deposit (Bull et al., 2009a; Moscardelli et al., 2006). Chaotic (disintegrated reflections) and folded (mounded reflections) seismic facies are observed throughout the middle segment of MTD A (Fig. 3.4). At the boundary between the distal and mid segment, thrust faults are observed where the basal surface ramps up stratigraphy. The thrusted "facies" appear as imbricate thrust packages with moderate amplitude and low continuity (Fig. 3.9).

A large number of elongate (typically 1 km wide, 5-7 km long), relatively intact blocks of failed material are mapped in certain areas of MTD A. The distribution of these blocks is best seen using a flattened coherence map (Figs. 3.7B) which shows the long axis of orientations and the general planform morphology of the blocks particularly adjacent to the NE lateral margin of MTD A. The blocks have a dominant NW - SE long-axis orientation. The blocks have a maximum height of 250 m and measure between to 250 and ca. 500 m across. The original stratigraphy is well preserved within some of these blocks and it is possible to unambiguously correlate packages of reflections from within the blocks, across bounding listric faults, to the adjacent sections of undeformed strata (Fig. 3.10).
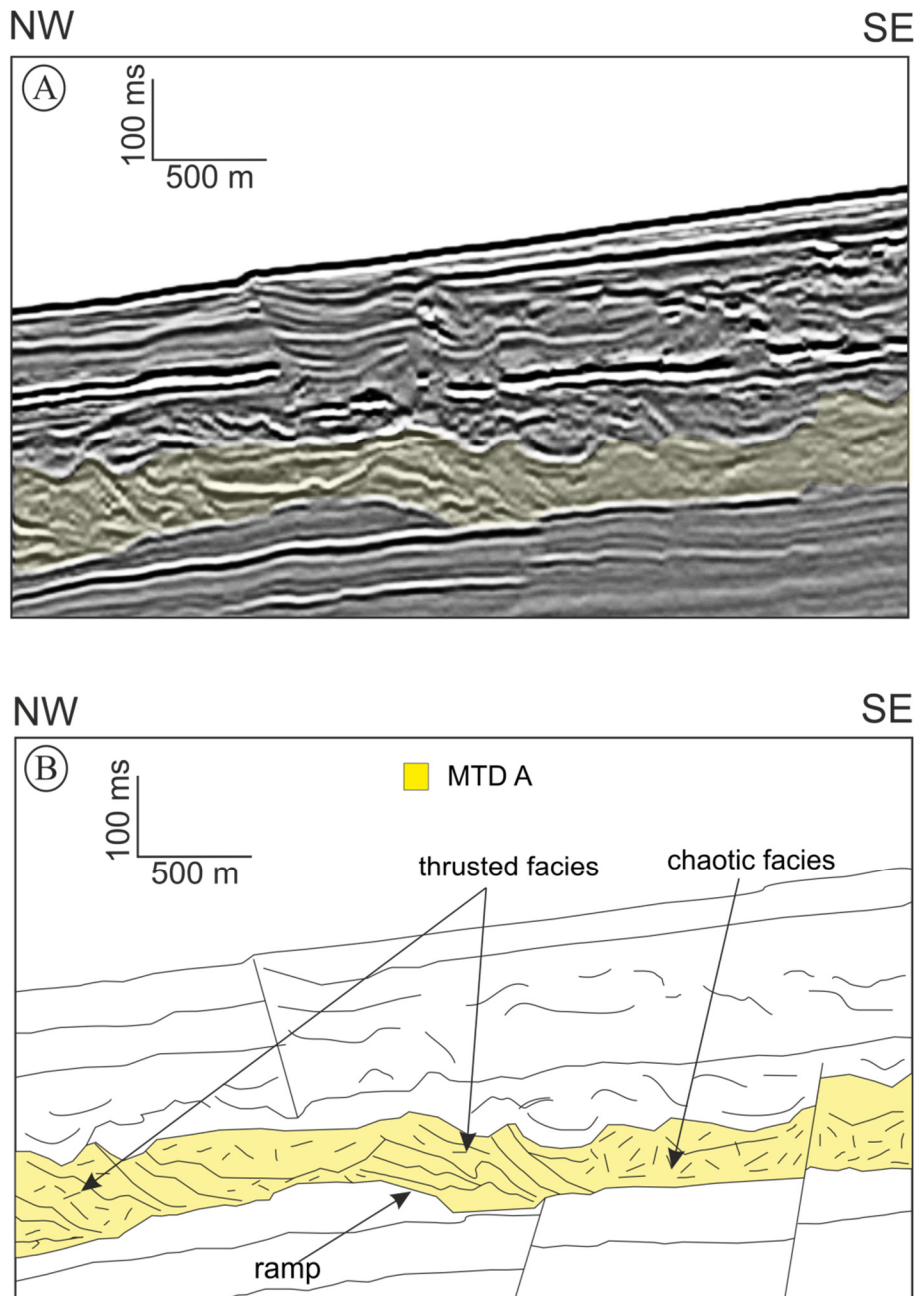
Figure 3.9 A) Representative dip oriented seismic profile through the ramp at the boundary between the mid segment and the distal segment (see Fig. 3.7A for line location).B) Interpreted seismic profile shows the basal surface cuts up c. 150 m of stratigraphy with associated thrust faults that dip c. 40 east separating undeformed strata downslope and deformed strata of MTD A.
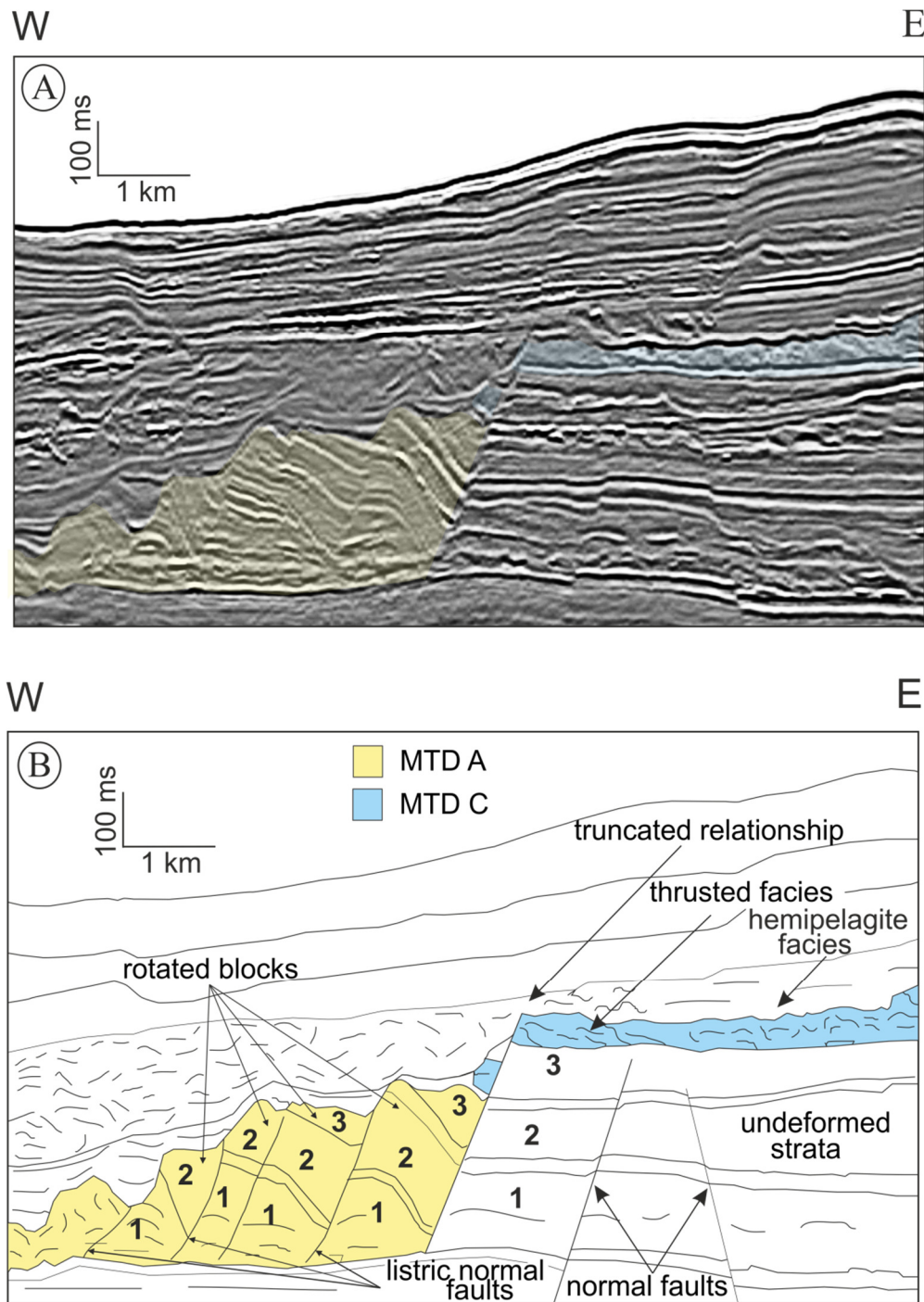
Figure 3.10 A) Representative seismic profile (see Fig. 3.7A for line location) the NE lateral margin of MTD A. B) Interpreted seismic profile showing the relationship between MTD A stratigraphy and the undeformed strata along the northeastern margin. Notice how the normal fault that defines the lateral margin of MTD A truncates MTD C Listric faults bound rotated MTD blocks that show less internal deformation.

Interpretation

The heave associated with the breakaway fault at the headwall involves approximately 4 km of lateral movement away from the footwall (Fig. 3. 4). It is inferred, therefore, that MTD A has moved a minimum distance of 4 km downslope in its proximal part.

Lateral margins and long axis orientations of blocks are invaluable kinematic indicators and allow the transport direction of MTDs to be constrained (Bull et al 2009). In this study, the NW – SE oriented lateral margins suggest that the cross transport direction of MTD A is the NW (c.f. Bull et al 2009), consistent with this being the maximum dip direction of the slope. However, locally, the presence of blocks within MTD A with a NW –SE long axis orientation in contrast suggests a SW transport at least locally within the general confines of the gross NW directed failure. This local SW transport is consistent with the interpretation that these blocks formed by retrogressive extensional widening of the original failure surface along the lateral margins, by analogy with a similar process inferred for the lateral margins of the Storegga Slide (Kvalstad et al., 2005). The observation that these faulted blocks contain downfaulted remnants of MTD C, implies that MTD C predates MTD A. Importantly, the observation that both the NE and SW lateral margins of MTD A transect from the basal surface through in-situ stratigraphy, and cross-cut the chaotic deposits of MTD B and MTD C (Figs. 5, 8 and 10) is taken to suggest that MTD A postdates MTDs B and C. The upper terminus of these two lateral margins to MTD A is precisely at the top surface of MTDs B and C (Figs. 3.5, 3.8 and 3.10), implying that there was no major time gap between the emplacement of the three MTDs.

The rugose character of the upper surface of MTD A is interpreted to result from the cannibalisation from above of later smaller slope failures (Fig. 3.5) as well as being shaped by the internal deformation within MTD A. Therefore, the observed thickness of MTD A does not equate to its original thickness immediately after failure and translation. This
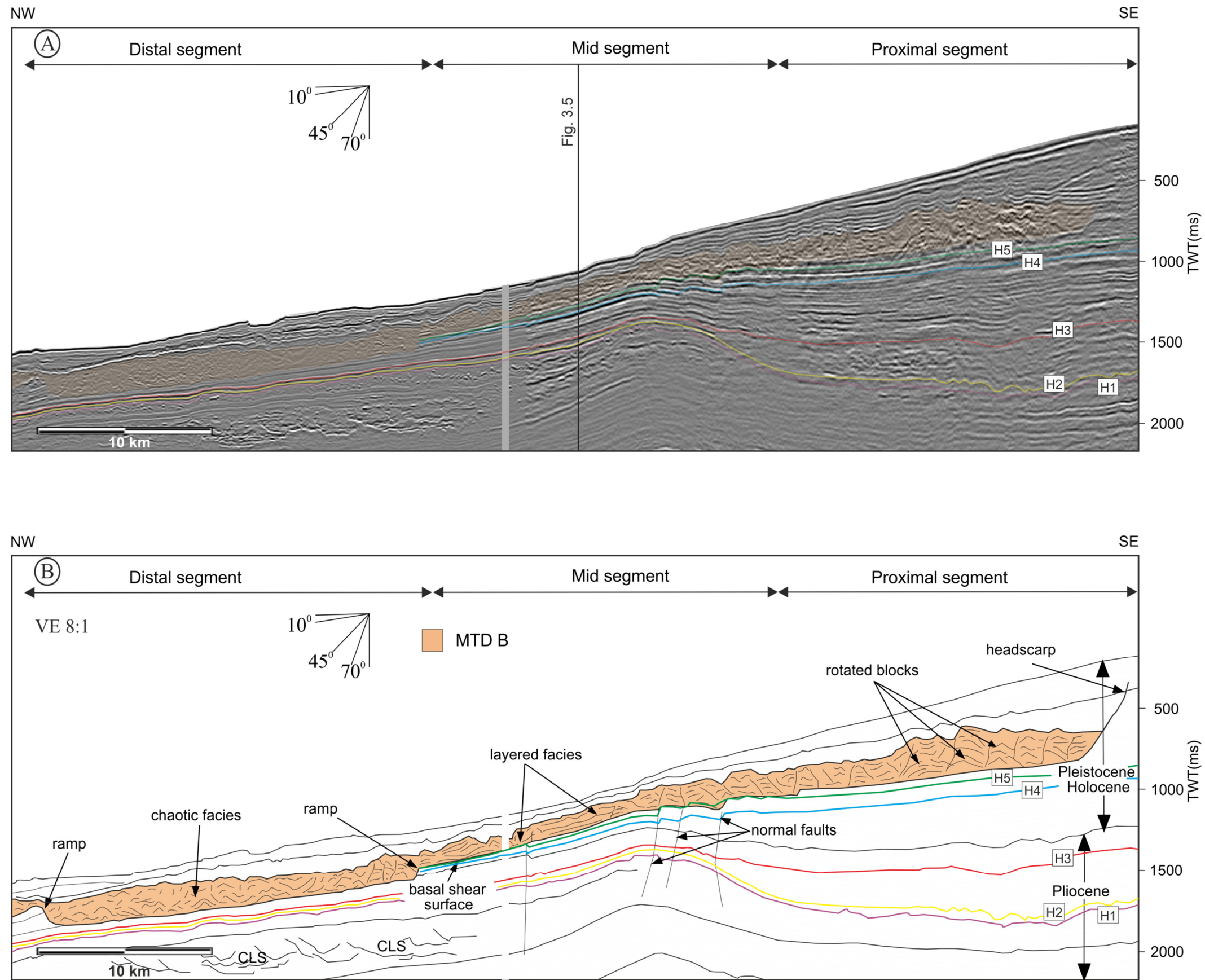
Figure 3.11 A) Representative dip oriented seismic profile through MTD B (for location see fig. 3.7A). B) Interpreted seismic profile showing the geometry of MTD B. In the proximal segment, blocks are bounded by extensional normal faults and are enclosed in chaotic matrix. The mid-segment is dominated by rotated blocks enclosed chaotic facies Thrusted facies dominate the distal segment. CLS = Channel levee system.

cannibalisation is most clearly seen at the lateral margins in the faulted stratigraphy, where the uppermost pre-failure units are progressively more attenuated across each faulted block (Fig. 10).

3.4.3 MTD B

MTD B is located to the south-western margin of MTD A (Figs.3.5, 3.6 and 3.7), and it is elongated in the north-westerly down-dip direction similar to MTD A. However, MTD B lies at a significantly higher stratigraphic level compared to MTD A (Fig. 3.5). MTD B varies in thickness significantly along slope (Fig. 3.11). It is c. 300 ms thick in both the proximal and distal segments but less than 150 ms thick in the mid segment.

The headwall of MTD B is located in the proximal segment of the upper slope (Fig. 3.11). It is represented by a steep dipping scarp c. 12° that reaches a maximum height of 250 ms. In map view, the headwall of MTD B is c. 10 km wide (Fig. 3.7) and oriented in an E - W direction.

The SW lateral margin of MTD B is sharply defined by a steep scarp (c. 7°) that delimits the chaotic and deformed seismic facies of the deposit from the undeformed adjacent strata (Fig. 3.5). The height of the SW lateral margins varies significantly downslope. It is c. 100 ms in the proximal segment and increases progressively downslope to 300 ms high (maximum) in the distal segments (Fig. 3.8). The NE lateral margin coincides with the SW lateral margin of MTD A. The lateral margins of MTD B have a SE - NW orientation in map view (Fig. 3.7), with the SW margin being irregular relatively to the NW margin.

The upper surface of MTD B is a laterally correlatable, high amplitude, positive reflection with a generally slightly irregular relief different from MTD A (Fig. 3.11). The relief on the upper surface of MTD B is noticeable in the proximal and mid segments where it reaches up to 20 ms. The upper surface of MTD B terminates abruptly against the SW lateral margin (at

c. 100 ms below the upper tip of the margin) (Figs. 3.5 and 3.8). The upper surface of MTD B is overlain by hemipelagite facies (Figs. 3.5 and 3.11).

The basal surface is marked by a discontinuous low amplitude reflection with negative polarity (high impedance to low impedance) (Fig. 3.11). In the proximal and mid segments of MTD B, the basal surface is relatively smooth, continuous, regular and concordant. Although, some minor offsets and basal surface ramps can be observed in the mid and distal segments respectively (Fig .3.11). The height of the ramps range between 100 - 150 ms. The strata beneath the basal surface are regular and layered.

The internal seismic character of MTD B in the proximal segment is dominated by low to moderate amplitude blocks bounded by extensional normal faults enclosed in a chaotic matrix (Fig. 3.11). Layered seismic facies marked by high amplitude parallel and continuous reflections characterize the mid segment (Fig. 3.11). Whereas chaotic, highly disintegrated, low amplitude facies are widely distributed in the distal segment of MTD B. However, some NE NE - SW elongated coherent ridge-like features are observed in the distal segment. These features are best seen on the flattened coherency map (Fig. 3.7B) where they are typically 2 - 3 m long and c. 250 m wide. They are less obvious on the representative seismic profile (Fig. 3. 11).

Interpretation

The NW – SE orientation of the lateral margins of (c.f. Bull et al., 2009) suggests a NW transport direction for MTD B. The elongated NE – SW coherent ridge-like features that dominate the distal segment of MTD B are interpreted as blocks (c.f. Bull et al 2009). The long axis orientation of blocks suggests a dominant NW transport direction for MTD B which is consistent with that suggested by the lateral margin.
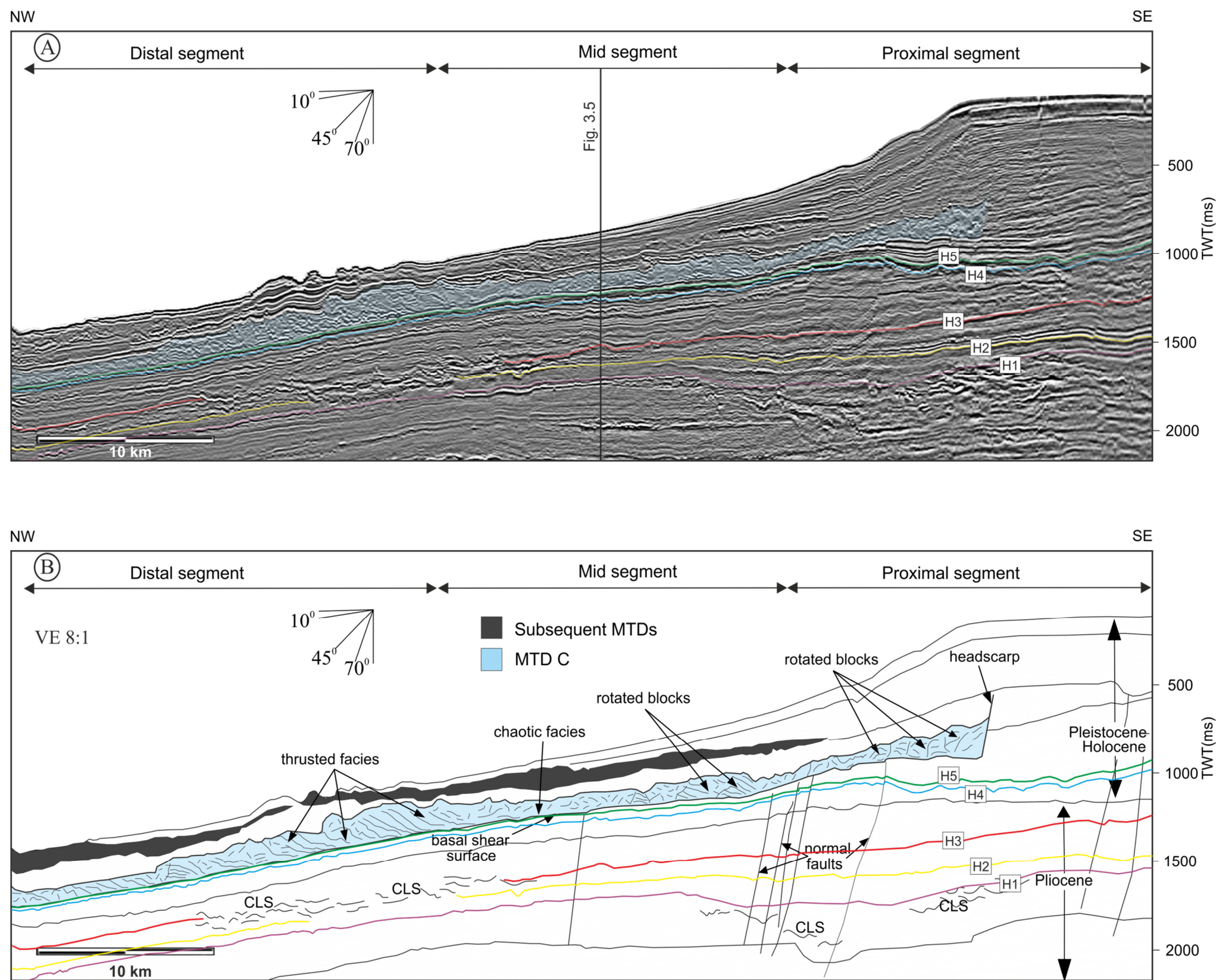
Figure 3.12 A) Dip oriented seismic profile through MTD C (for location see fig. 3.7A). B) Sketch of the interpreted slide unit discussed in the text. In the proximal segment, MTD B is by dominated blocks bounded by extensional normal faults enclosed in chaotic matrix. Chaotic facies are widely distributed in the mid segment. While thrusted facies dominate the distal segment. Notice how the basal surface is concordant with underlying straigraphy. CLS = Channel levee system.

The fact that the slightly irregular relief of the upper surface of MTD B mimics to some degree the style of internal deformation of the deposits coupled with the overlying hemipelagic sediments (Figs. 3.5 and 3.11), suggests that MTD B has not undergone cannibalisation to the same degree as that described above for MTD A.

3.4.4 MTD C

MTD C is located on the north-eastern side adjacent to MTD A (Figs.3.5, 3.6 and 3.7), and it is elongated in the north-westerly down-dip direction similar to MTDs A and B. MTD C lies at a higher stratigraphic level compared to MTD A (c. 1500 ms below the present day seabed in Fig. 3.5). It varies in thickness significantly along slope (Fig. 3.12). It is c. 300 ms thick in both the proximal and distal segments but less than 150 ms thick in the mid segment.

Although a significant portion of MTD C appears to be missing in the proximal segment (Figs. 3.7 and 3.8), the headwall of MTD C is still slightly preserved close to the northern limit of MTD A headwall (point X on Fig. 7C). The preserved headwall is oriented in a N – S direction (Fig. 3.7), and it is defined on a representative dip seismic profile (Fig. 3.12), by a steep scarp (c. 12$^°$) that demarcates the chaotic and deformed seismic facies of MTD C from the undeformed strata outside of the deposit along slope to the southeast. The preserved headscarp reaches a maximum height of 300 ms.

The NE lateral margin of MTD C is sharply defined by a c. 500 ms high (maximum), southwestwardly dipping steep scarp (c. 7$^°$) that delimits the chaotic and deformed seismic facies from the undeformed strata. The SW lateral margin coincides with the NE lateral margin of MTD A (Figs. 3.5, 3.8 and 3.10). Both these lateral margins of MTD C are oriented SE – NW (Fig. 3.7).

The upper surface of MTD C is marked by a laterally correlatable, high amplitude, positive reflection (Fig. 3.12). with a generally irregular relief similar to that of MTD B. The relief is

pronounced (up to 100 ms) in the distal segment of MTD C where the upper surface mimics the style of internal deformation of the slide deposits (Fig. 3.12). It terminates abruptly against the NE lateral margin at c. 300 ms below the upper tip of the margin (Fig. 3.5). The upper surface of MTD C is overlain by hemipelagite facies (Fig. 3.12).

The basal surface of MTD C is marked by a discontinuous low amplitude reflection with negative polarity (high impedance to low impedance) (Fig. 3.12). It is generally continuous and concordant with the underlying stratigraphy. Beneath the relatively continuous, regular and concordant basal shear surface of MTD C the strata are more regular and layered.

MTD C is dominated by elongated ridge-like features (similar to those seen in MTDs A and B and therefore interpreted as blocks) in the proximal and mid- segments (Fig. 3.7B). These blocks have a dominantly NE – SW orientation and are bounded by extensional normal faults (Fig. 3.12). These fault bounded blocks are well seen in Figure 3.13 where they are enclosed in a chaotic matrix and display stratigraphic continuity with the underlying strata. The preservation of internal stratigraphy allows clear correlation with the undeformed slope succession across the scarp (Fig. 3.13). The fault blocks are typically between 500 -1000 m wide and 2 - 5 km long. Thrusted facies which appear as imbricate thrust packages with moderate amplitude and low continuity dominate the distal segment of MTD C (Fig. 3.12). The thrust faults vary in height from 100 to 200 ms (average 150 ms), and their tip to tip distances are 100 - 150 m. The thrust planes dip between 15 - 25°.

Interpretation

The elongated, dominantly NE – SW oriented blocks coupled with the NW – SE orientation of the lateral margins of suggests a NW transport direction for MTD C (c.f. Bull et al., 2009) similar to MTD B. The observation that it is generally overlain by hemipelagite facies excludes the possibility of any significant cannibalisation of MTD C by younger failures and
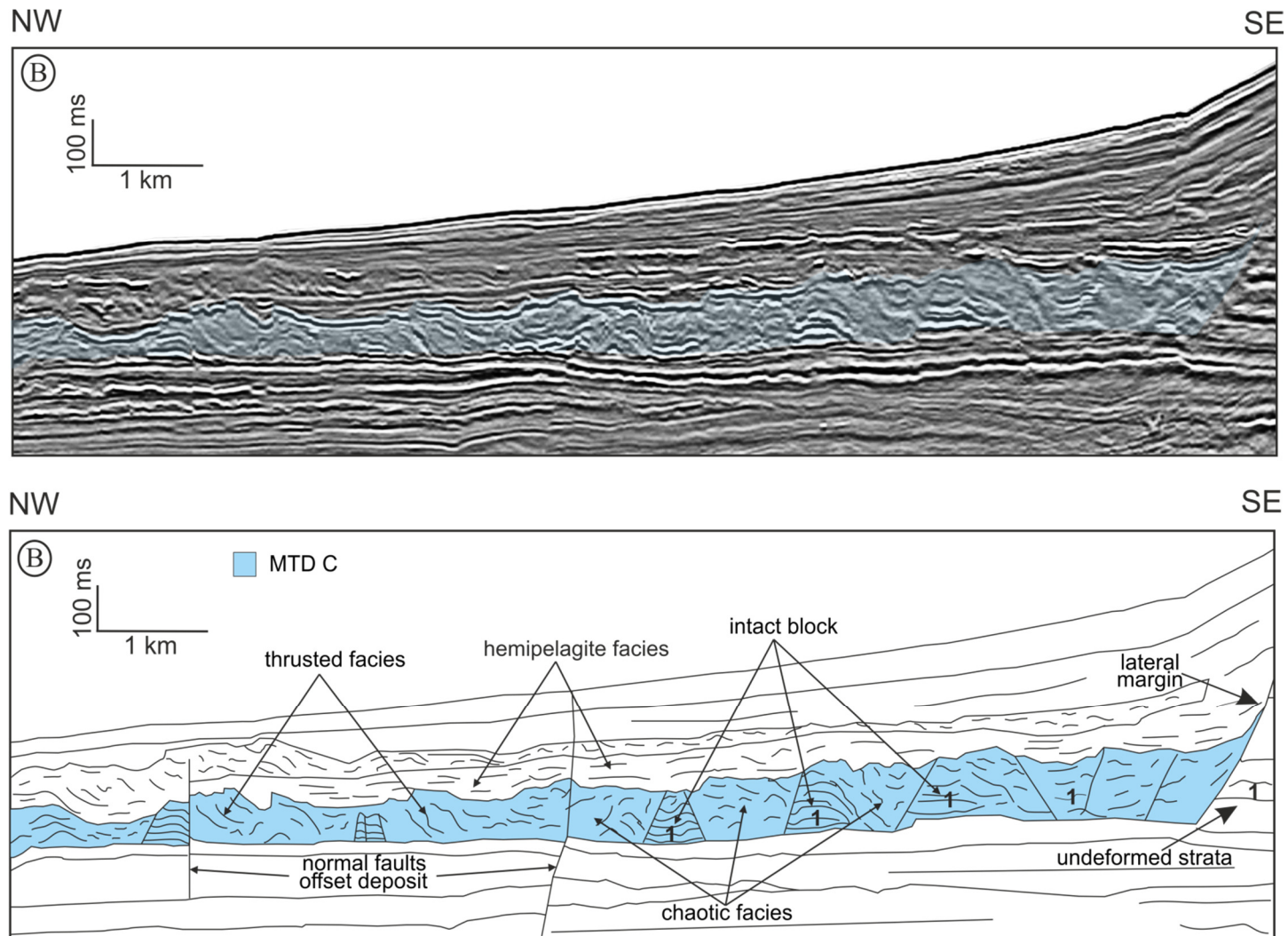
Figure 3.13 A) Representative seismic profile through MTD C (see Fig. 3.7A for line location). B) Interpretation seismic profile showing the intact blocks bounded by chaotic matrix of MTD C. Notice the vertical stratigraphic continuity with underlying non-MTD strata.

hence the irregular relief of the upper surface is interpreted to be as a result of the internal deformation of the deposits (Figs. 3.5 and 3.12).

3.4.5 Relationship between MTDs A, B and C

As mentioned previously, five horizons numbered H1 to H5 have been identified and correlated over much of the area as possible from the undeformed zone into the MTDs (Figs. 3.5, 3.11 and 3.12). The cross-sectional area occupied by MTD A corresponds to the local disappearance of most of the interval comprised between horizons H2 and H5. This observation is consistent downslope and it is evident in the fence diagram shown in Figure 3.8. Although the Pleistocene/ Holocene slope interval is condensed to the NW and SW it is possible to unambiguously correlate these key horizons across the gap created by the emplacement of MTD A. The correlation of these horizons show that the basal detachments of MTDs B and C lie on precisely the same stratigraphic level (H5 in Figs. 3.5 and 3. 8). Furthermore, it is evident that the listric and/ or normal faults that define both the NE and SW lateral margins of MTD A truncate MTDs B and C but do not propagate above the deposits (Figs 3.5 and 3.8). Rather, the faults tip out at the upper surfaces of MTDs B and C.

Based on extrapolation of pre-MTD stratigraphy across the gap between MTDs B and C, it is interpreted that they represent one and the same MTD. Analysis of the truncated relationship of the internal lateral margins of MTDs B and C is very potent in revealing the relative chronology of the MTCs, and in this case it is apparent that MTDs B and C (Figs. 3.5 and 3.10 respectively) occurred first, and they was truncated and cannibalised in its central region along with underlying undeformed slope sediments and incorporated into MTD A.

Given the enormous height of the headwall of MTD A (c. 1000 ms) relative to the moderate thickness of the deposit in the proximal segment (Fig. 3.4), it is evident that a large degree of depletion of the proximal segment has occurred (sensu. Frey-Martínez et al., 2006).

Since MTDs A, B and C are well defined by basal and upper surfaces as well as lateral

margins, a 'time thickness' map was generated which was used as an input for a calculation of the residual volume (Fig. 3.6). The residual volume is the volume of sediment accumulated in the downslope depositional section while the depleted volume corresponds to the volume of sediment missing in the headwall region (Fig. 3.14). It is important to note that the values on the isochron map are considered to be a minimum value of the original thickness because of reductions in thickness caused by post-depositional compaction and cannibalisation. Using a P-wave velocity of 1600 ms^{-1} for the MTD interval a total residual volume of c. 270 km^3 (subdivided into 170 km^3 for the MTD A unit; c. 50 km^2 for the MTD B unit; and c. 50 km^2 for the MTD C) was estimated. Despite the limitation of this method (including sometimes the poorly imaged basal surface as well as the assumed P wave velocity), it is still the most widely applied (Canals et al., 2004). A depleted volume of 480 km^3 was calculated by reconstructing the pre-slide seabed topography by projection across the headwall and lateral margins (Figs. 3.4 and 3.5). This projection assumed that there were no previous failure surfaces in this area to produce an irregular seafloor, which is consistent with the seismic stratigraphy of the study area since no large MTDs are seen in the preserved stratigraphy in the footwalls to any of the margins of MTD A. The total volume of sediment remobilized (V_T) is broadly estimated to be 750 km^3. However, it is important to note that the calculated residual volume is most likely an underestimate because the down-dip limits of the MTDs lie outside the limits of the 3D seismic survey used in this study, and we cannot be confident of the full extent of the remobilized units in a downslope direction.

A remarkable observation is that the depleted volume calculated here (c. 480 km^3) is similar to that calculated for MTD SL2 (c. 500 km^3) (Garziglia et al., 2008) immediately downslope (outside of our dataset) (Fig. 3.1). This striking similarity leads to the suggestion that a significant proportion of the more distal SL2 material was derived as fully remobilised material from the emplacement of MTD A in a more proximal position.
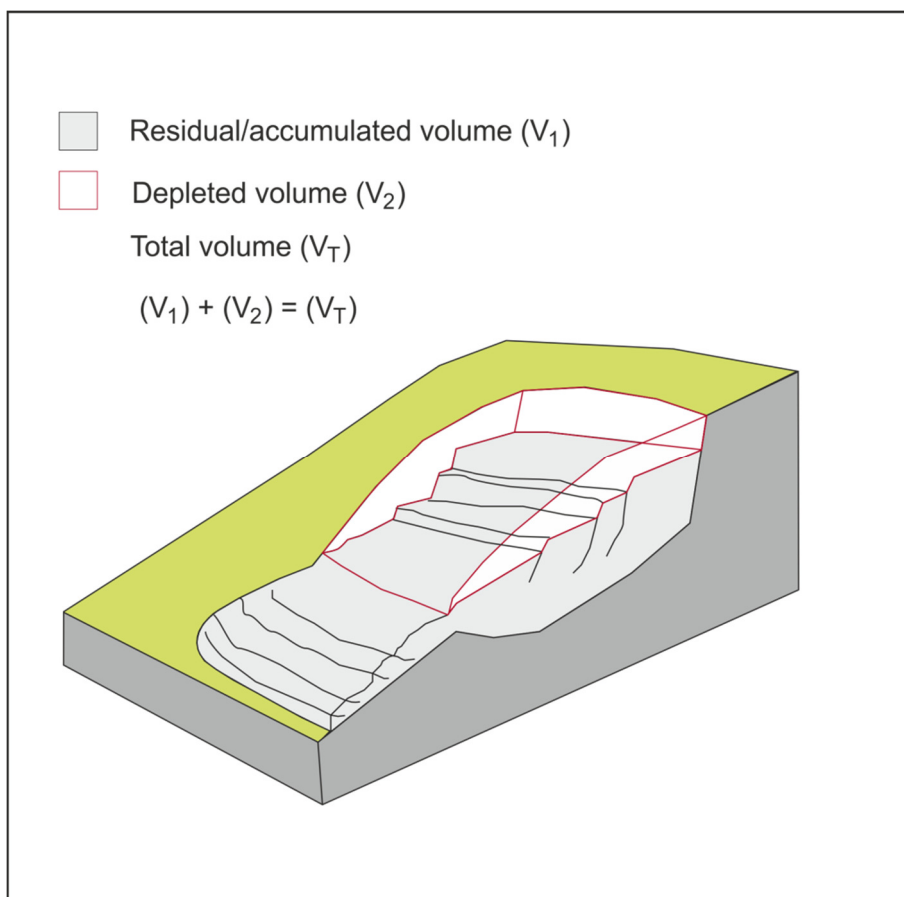
Figure 3.14. Cartoon showing the different volumes referred to in the text.

3.5. Discussion

One of the most important observations relating to the three MTDs described above is the scale of the two main levels of detachment within the Pleistocene (basal surfaces of MTD A and that of combined B/ C) and the large stratigraphic separation between them (c. 500 ms in the mid segment; Fig. 3.5). The detailed 3D seismic analysis provides strong evidence that these three MTDs are closely linked in time and space suggesting a fundamental connection in their sequence of propagation and failure. But how can two major slope failures be connected, if they are developed on such widely separated stratigraphic levels of detachment?

In this section, the following points are developed as the main themes of this discussion:

1) The mode of failure for MTDs A, B and C.

2) The source environment, preconditioning factors and triggers for failure in the study area.

3) A comparison of architecture, formation and triggering of MTDs A, B and C with other known submarine failures.

4) The implication of the studied MTDs on hydrocarbon seals.

3.5.1 Mode o**f Failure**

In the present study, the presence or absence of headwall, parallelism and truncated relationship of the lateral margins, and more importantly the long axis orientation of blocks within the MTDs are the best evidence to elucidate the kinematics of failure. Based solely on the analysis of map relationships, three contrasting hypotheses for the mode of failure for MTDs A, B and C could be considered as plausible alternatives: 1) the MTDs are separate events widely separated in time; 2) MTDs are part of a linked sequence that failed retrogressively and 3) MTDs are part of a linked sequence that failed progressively (i.e. downslope with time).

The stratigraphy and cross-cutting relationships along the various lateral margins provide the best means for discriminating between these possible alternative failure sequences. Based on these relationships, it was argued above that MTDs B and C are one and the same event. The fact that they occur on the same stratigraphic level and that the stratigraphy beneath both deposits is correlatable is a powerful argument for directly linking MTDs B and C into an origin from a single larger combined failure event. Furthermore, the cross cutting relationship at the lateral margins of MTD A implies that MTD A postdates this combined MTD B/C (Fig. 3.5). The fact that the marginal faults defining the retrogressively widened lateral margins of MTD A do not propagate above MTDs B and C then additionally argues that these events were not separated by a significant time gap, or we would observe a drape at the top of MTDs B and C truncated by the lateral margin faults of MTD A. It is concluded therefore, that the first hypothesis, that there were two failure events separated by a significant time gap is very unlikely.

An alternative explanation is that the MTDs were part of a linked sequence that failed entirely retrogressively where later failure events propagated upslope from the locus of the first failure (e.g. Kvalstad et al., 2005; Lucente and Pini, 2003). If this was the true, then it would be expected that the long axis orientation of the blocks within MTD A and MTDs B and C would be consistent across the lateral margins and equate to a retrogressive transport direction. However, the kinematic indicators of transport direction for MTDs B and C are broadly downslope i.e. NW oriented, whereas the kinematic indicators of the local faulted blocks defining the margins of MTD A are crudely orthogonal to the lateral margins. These latter transport directions are indeed consistent with a retrogressive failure mode, whereas the former are not (Fig. 3.7C). It is difficult to reconcile these conflicting kinematic indicators with a single, retrogressive failure progression from MTD A to MTDs B/C. In addition, it is also hard to reconcile the c. 500 ms near vertical separation from the basal detachment level

of MTD A to that of MTD B with a retrogressive failure mechanism. Why would such a large vertical jump occur in retrogressive failure? Interestingly in this respect, we note that the fact that MTD B is not present south of the junction of the respective headwalls (point X on Fig. 7) suggests that MTD A must have cut back in a retrogressive manner through MTD B into the undeformed sediments comprising the footwall region.

In order to link all these key observations, we instead suggest that the most satisfactory explanation is provided by the third hypothesis, namely that the three MTDs are part of a linked sequence that failed progressively (i.e. downslope with time), but with retrogressive modifications of the lateral and headwall margins.

A number of previous studies have suggested conceptual models for the development of progressive failures and these fall into broadly two groups: (1) those that are driven by rapid loading of the headwall region (e.g Minisini et al., 2007; Schnellmann et al., 2005; Watt et al., 2012b); and (2) those that are driven by combined unloading and overloading due to redistribution of remobilised material associated with an initial failure (Dykstra, 2005).The first type of model does not seem applicable in the study area, since there is no evidence for any excessive loading of the headwall region immediately prior to failure. The second type of progressive failure seems much more likely as an explanation of the failures leading to MTDs A, B and C, as discussed below.

In this second model, progressive failures are viewed as commencing with failure and sliding of strata on the upper portion of a slope (Dykstra, 2005; Petley et al., 2005) (Fig. 3.15A). The partial or complete removal of this failed mass reduces the stress on the slope immediately in the region downdip of the headwall such that pressure gradients develop towards the ramp in the toe region of the MTD (Fig. 3.15A). The transfer of remobilised material downslope, results in a complementary overloading of the downslope region, further enhancing pressure gradients through differential (and high strain rate) loading. This pressure gradient will
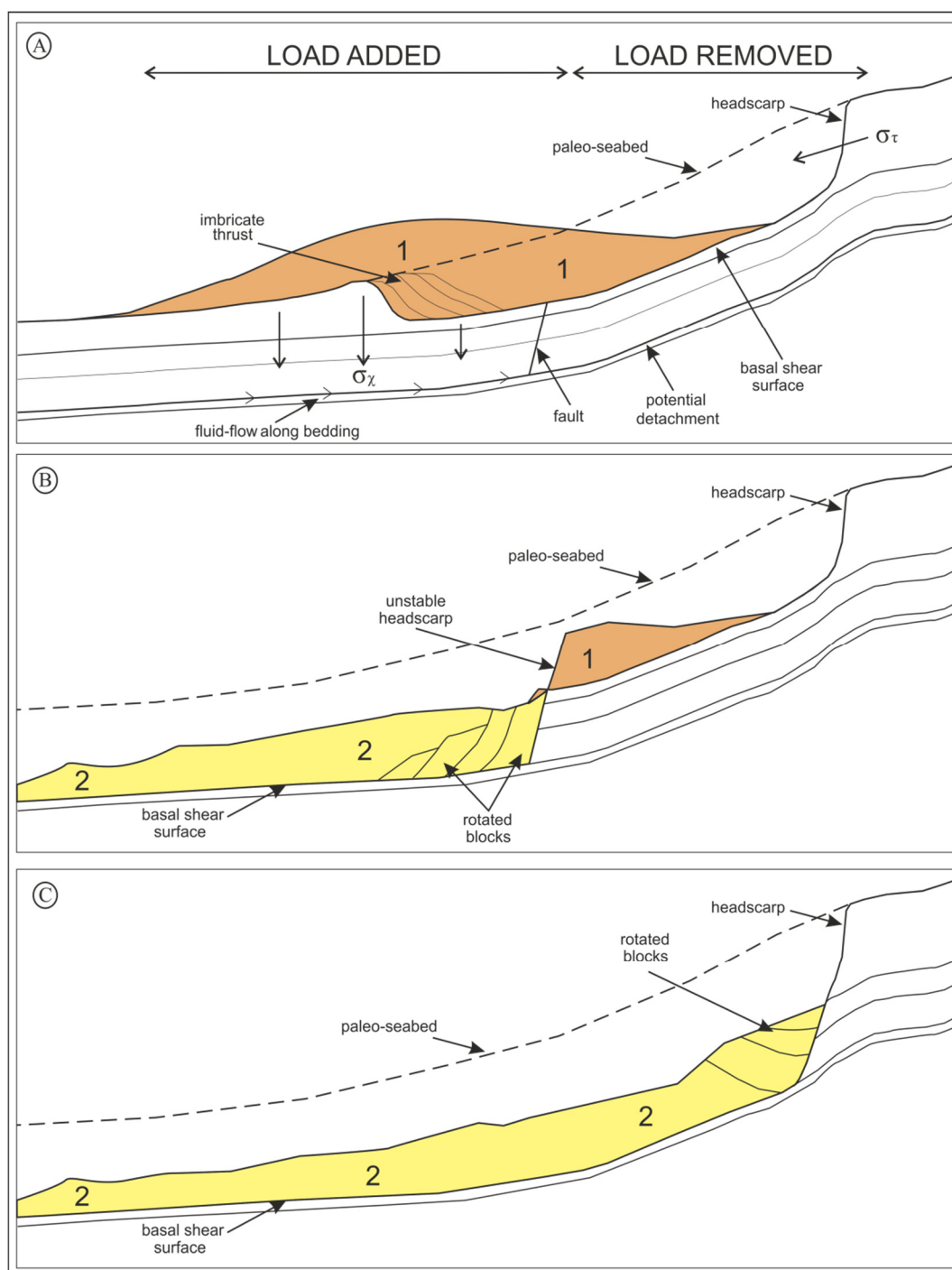
Figure 3.15. Schematic illustration of stages involved in the progressive and retrogressive failure mechanism. A) Removal of sediment from the headwall causes a decrease in lithostatic stress in the orientations shown by the tension arrow ($\sigma\tau$), while the transfer of remobilised material downslope, results in a complementary overloading of the downslope region, ($\sigma\chi$). The changes will create a pressure gradient from the area under the MTD to the headwall region, which will encourage fluid flow along bedding in an up-dip direction and increase the likelihood of progressive failures. B) Progressive failure gives rise to an unstable headwall, which eventually results in a series of failures that sequentially follow the initial slide downslope. C) Retrogressive failure stops when the failures reach some critical updip point that becomes the final headwall, in this case the pre-existing headwall of MTD B. brown: event 1; yellow: event 2.

encourage fluid-flow along bedding in an up-dip direction and increase the likelihood of progressive failures nucleating somewhere in the region where high pore pressure exploits any susceptible weaknesses in the sedimentary layering (Figs. 3.15B and C) (Dykstra, 2005).

This conceptual framework can be applied to the study area, where the initial failure would have been updip, and led to the accumulation of the combined MTD B/C. It is suggested that a progressive failure was induced by the combination of unloading of the c. 500m high headwall region, substantial remobilisation and depletion of a large area of the combined failure surface, and overloading by the rapid deposition of remobilised material in the region of the downslope ramp. After the occurrence of this progressive failure (leading to the initiation of MTD A), a headwall for MTD A would have been created (Fig. 3.15B), thus opening up a region of further unloading and free surface beneath and laterally downflank of the headwall. A combination of height and greater inclination of the headwall coupled with a decrease of the lateral confining pressure would have created a highly unstable headwall which then triggered upslope migration of the headwall retrogressively until a stable position was reached close to the break of slope at the head of the continental slope (Fig. 3.15C) (Dykstra, 2005). Support for the suggested retrogressive modification of the headwall of MTD A can be found in the fact that only a single detachment is present along the axis of MTD A with a headwall that is c. 1000 ms in height (Fig. 3.4) which corresponds to the merger of two headwalls with individual heights of c. 500 ms. It is also supported by the striking parallelism between the lateral margins of MTDs A, B and C (Fig. 3.7). The map relationships of the distinctive features of the MTDs in the study area therefore argue for the likelihood of a causal, rather than a simply coincidental spatial relationship.

In summary, a five stage evolutionary model is proposed (Fig. 3.16):

1) A period of continental slope and basin sedimentation across the western Nile delta which preceded the emplacement of MTD B/C (Fig. 3.16A). The clay intercalations within the Mit Ghamr Formation probably acted as seals, restricting upward movement of compaction fluids and building up pore pressure thereby preconditioning the slope for failure (c.f. Mulder and Cochonat, 1996).

2) Failure resulted in the initial emplacement of MTD B/C on the upper portion of the slope along the headwall scarp and along the sub-horizontal layer in the NW direction. The slide block broke up into segments, with the long axis perpendicular to the direction of motion (Fig. 3.16B).

3) The emplacement of MTD B/C in the toe domain was complimentary to the depletion of sediments in the head domain such that a pressure gradient was instigated between the area under the deposit and that under the slide-scar resulting in fluid flow up-dip along bedding which subsequently led to failure down-dip (Fig. 3.16C).

4) Progressive failure resulted in the emplacement of MTD A with different long-axis orientations of blocks compared to MTD B/C suggesting a different transport direction (Fig. 3.16D).

5) The height and steepness of inclination of the headwall of MTD A resulted in the decrease of the lateral confining stress which subsequently resulted in an unstable condition. Consequently MTD A cut back in a retrogressive manner giving rise to the morphology observed today (Fig. 3.16E).
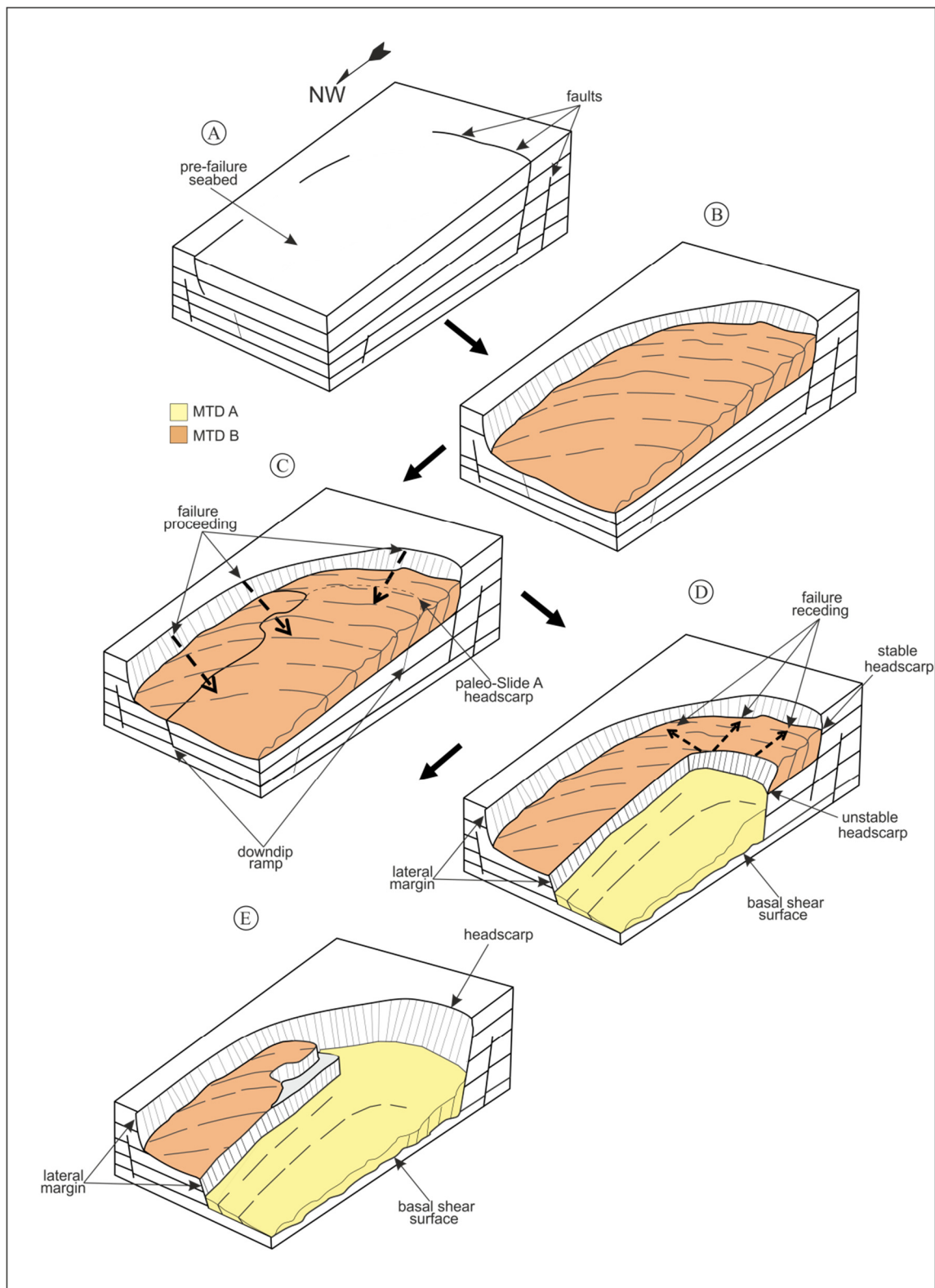
Figure 3.16. Sketches illustrating the proposed complex evolution of MTDs A and C. A) Reconstructed pre-failure setup. B) Initial failure and deposition of MTD C. C) The remobilisation and deposition of material, sets up a pressure gradient between the area under the MTD and that under the headwall which will encourage fluid flow along bedding in an up-dip direction and increase the likelihood of progressive failures D) Emplacement of MTD A with long axis orientation of blocks different from MTD C. The headwall becomes unstable due to height and steep inclination plus reduced lateral confining stress E) MTD A cuts back in a retrogressive manner with complete evacuated of MTD B material in the head region.

3.5.2 Source environment, preconditioning factors and triggers

The MTDs in this study formed in the shelf-break/upper- slope region of the Nile delta and it is characterised by a regionally extensive headwall (c. 35 km long as in the case of MTD A, see Fig. 3.7C) and thus, they are classified as slope-attached MTD (sensu. Moscardelli and Wood, 2008). Seismic reflections associated with the collapsed materials that are contained in the up-dip MTD A tend to be discontinuous and chaotic. (Ducassou et al., 2009) suggested that the triggering of gravity processes over the whole Nile margin is preconditioned by both sea level fluctuations and changes in volumes of sediment supply related to climate change on land.

The time period between 120 to103 ky marked the onset of falling of sea level, and correlates with the Saharian Pluvial period on the Nile sources. This induced a substantial increase of sediment supply on the margin and a rapid progradation of the shelf edge via the construction of thick prograding outer shelf deltas near the head of the Rosetta Canyon (Rouillard et al., 2010).

Between 117 and 105 ky, the failures identified as MTDs 9 and 10 by Rouillard et al. (2010) (Fig. 3.1) were triggered on the upper slope and SL 2 of Garziglia et al. (2008) was triggered on the mid slope . The same age is therefore proposed for the combined series of failures leading to the formation of MTDs A, B and C (this study) based on the stratigraphic correlation noted earlier in the chapter.

In such a high sedimentation rate depositional system, the likeliest preconditioning factors leading to slope failure are high pore pressure generation (Masson et al., 2010) but the presence of mechanically weak layers due to initial depositional conditions cannot be excluded (Bryn et al., 2005b; Loseth et al., 2011). Rapid sedimentation will result in overpressure because the rate of sedimentation outstrips the ability of the sediments to dissipate the pore water adequately, thus decreasing the effective stress, the intergrain friction

and the sediment strength (see Section 1.3.2.2). The presence of free gas at shallow depth has also been suggested as a preconditioning factor for slope instability in the Rosetta area of western Nile delta (Garziglia et al., 2008), and this is reasonable since the western Nile delta is known as a gas rich province (Dolson et al., 2005).

Triggering mechanisms are invariably elusive for most submarine slope failures, and those found in the study area (MTDs A, B, C) are no exception. Some of the commonly cited mechanisms can, however be excluded. For example, dissociation of gas hydrates is widely invoked as a causal mechanism for other slope failures around the world (Sultan et al., 2004b). However the failures leading to MTDs A, B and C occurred in water depths that were too shallow for stable gas hydrate formation, given the warm sea-bottom temperatures in the region (Praeg, 2006). The absence of bottom simulating reflections indicative of gas hydrates in our dataset emphasises this point. Praeg (2006) estimated that methane hydrates may only occur in the Nile Deep Sea Turbidite System (NDST) below depths of 1000 – 1250 m, whereas our study area was located in a water depth range of <750 m during the Late Pleistocene, judging by clinoform relief.

In the absence of any direct evidence for a trigger mechanism, the most likely explanation in a region of pronounced active tectonics and seismicity is that a major earthquake caused the destabilization of a broad area of the upper slope and subsequent failure. It is notable, that a series of major basement faults underlie the study area (Aal et al., 2000) and some of these have been demonstrably active during the Late Pleistocene (Georgiopoulou and Cartwright, 2013), raising the probability for an earthquake triggering mechanism in the study area.

3.5.3 Comparison with other major submarine landslides

One of the most striking observations from this study is the combined excavation of the pre-existing slope sediments in the order of c. 1000 ms (Figs. 3.4 and 3.5) which makes it one of

the deepest excavations by slope failure of its type in the world. Only the Hinlopen and Canary Slides with headwall heights of c. 1400 m and c. 1100 m respectively (Vanneste et al., 2006) are comparable. However, the total residual volume of MTDs A, B and C (approximately 270 km^3) is much lower compared to other submarine landslides.

Several studies of slope failure on continental margins using 3D seismic data such as the Storegga slide (Bryn et al., 2005a), Hinlopen slide (Vanneste et al., 2006), and in the southern Cretan Sea (Strozyk et al., 2009) have shown that they develop retrogressively. In this study we have made a case that a major submarine slide formed progressively. The progressive failure mechanism has been invoked in eastern Canadian and Scandinavian sensitive clays based on experimental (Locat et al., 2011) and numerical (Eberhardt et al., 2004) analysis, but not previously for a submarine failures of these proportions. This study therefore extends the scale of previously reported progressive landslides by 1 - 2 orders of magnitude in volume and in scarp height, and demonstrates that this mode of failure may be more prevalent than the current literature would suggest.

3.5.4 Implications for petroleum systems

The absence of lithologic calibration in the study area does not allow the evaluation of the porosity and permeability of the MTDs to constitute a potential reservoir. However, based on the generally chaotic and transparent seismic character (suggesting they are mud rich) of the MTDs they do not seem to constitute good reservoirs in this area.

The concept of MTDs shaping hydrocarbon traps has been previously discussed by (Moscardelli et al., 2006) and (Beaubouef and Abreu, 2010). These authors observed that the type of lithologies directly overlying erosion surfaces of MTDs represents a key factor in impeding fluid migration through the stratigraphic succession. In this study the MTDs appear to be excellent top seals given that they are generally characterized by chaotic and mud rich facies (as suggested from the transparent seismic facies).

Another concept that has been less explored is rapid unloading due to slope failure (as in this study where a combined excavation of the pre-existing slope sediments amounts to c. 1000 m high headwall) can have severe impact on petroleum system. MTDs A, B and C overlie Pliocene gas reservoirs imaged on seismic data as numerous channel complexes oriented NW - SE (Dolson et al., 2005). It is important to know the timing of these failure events and the hydrocarbon charge into reservoirs for accurate predictions to be made on seal integrity and field distribution

Seal failure could occur via a hydraulic fracturing mechanism due to rapid unroofing of a thick failure deposit. Leakage would occur through macroscopic extension fractures (Corcoran and Doré, 2002). Such permeable extensional fracture networks are likely to form in response to elevated pore fluid pressures in excess of the in situ minimum stress. These changes in the effective stress conditions of topseal can be induced by changes in tectonic load (rapid unloading). This rapid unloading without the re-equilibration of elevated pore pressures (Hermanrud et al., 2013) could potentially result in pervasive hydraulic fractures in top seals which could subsequently lead to catastrophic loss of pre-existing hydrocarbon fill. It is suggested that rapid release of the overburden confinement would have led to transient high overpressure particularly in the gas reservoirs thus resulting in hydraulic leakage (see Ingram et al., 2004).

3.6. Conclusions

3D Seismic data have provided an opportunity to examine a major submarine slope failure in the western Nile delta. Stratigraphical and morphological analyses reveal that:

1. The very large and deeply cutting slope failure is a composite of two separate but spatially and temporally connected MTDs; one nestled within another, and with their own distinct lateral margins.

2. The large failure affected an area of c. 1400 km^2, and a total volume of c. 750 km^3 was remobilised.

3. The MTDs are thought to have experienced at least two main phases of emplacement during the mid to late Pleistocene involving: 1) progressive failure occurred initially with MTD A cutting through B and C then; 2) retrogressive failure occurred due to the natural unbalance of the supposed headwall of MTD A.

4. Preconditioning of the slope prior to the failure events most likely relates to differential and high sedimentation rates induced during the Sahara Pluvial period in the western Nile delta and local increases of pore pressure. Another preconditioning factor prior to triggering of the failures may be the presence of gas in shallow sediments.

5. The combined excavation of the pre-existing slope sediments amounts to c.1000 m which makes it one of the deepest incising of its type in the world might have probably been a risk to petroleum systems considering the failure occurred in a gas rich province of the western Nile delta.

Chapter 4

4.0 Evaluating the degree of Cannibalization versus Run-out in multiple widespread Mass Transport Deposits: A case study from the Deepwater Taranaki Basin, New Zealand.

4.1 Summary

Two-dimensional (2D) seismic-reflection data has shed light on the character of a series of mass transport deposits (MTDs) emplaced in the Plio-Pleistocene Giant Foreset Formation of Deepwater Taranaki Basin, New Zealand. Six large scale mass transport deposits, stacked and locally amalgamated, are recognised, making up c. 50% of the succession. Key kinematic features suggest a north-westerly transport direction for all of the MTDs with the exception of MTD 6 which has a south-westerly transport direction.

There is seismic stratigraphic evidence in the form of both lateral and basal truncations suggesting that the MTDs were erosive during their emplacement. The volume of cannibalization versus run-out material for each MTD was estimated by interpolation of MTD geometry between cross- sections. Our estimation shows that > 60% or less of the final volume of the MTDs was contributed from substrate cannibalization with the exception of MTD 6 with estimated cannibalised volume of 70%.

Slope failure is believed to have been facilitated by rapid sedimentation on the shelf margin from Late Miocene to recent times, coupled with concomitant rapid oversteepening of the slope, indicated by the development of headwall scarps along the bounding surfaces of progradational foresets. In contrast, the different translation direction of MTD 6 suggests it might be related to the structural tilting associated with the northern graben.

This work suggests that the rheology of the substrate immediately beneath the seafloor might not be the only factor controlling the degree of substrate cannibalisation during MTD emplacement and that the nature of any triggering mechanism might also play an important role. This has a bearing on the MTD content (sandy or muddy dominated MTD) and would in turn influence the seal integrity of the MTD.

4.2 Introduction

It is well established that submarine MTDs are common features on continental margins and that they are major contributors to the transfer of sediments from continental shelf to the deep ocean (Canals et al., 2004; Masson et al., 2006; Piper et al., 1999). Many of the large MTDs that were emplaced in the Neogene have thicknesses exceeding 100m and volumes in excess of 100 km^3 (Table 1). In order to fully understand the source materials for MTDs, it is important to emphasize the difference between two existing emplacement mechanisms for MTDs: 1) Run-out: where the MTD travel long distances by hydroplaning (see Section 1.3.3.1) on a deposition surface characterised by the progressive transition between the MTD and the sub-adjacent undeformed strata (e.g Le Friant et al., 2003; Mohrig et al., 1998); 2) Erosion or cannibalisation of the substrate shown by the truncation of the underlying undeformed strata by the MTD basal surface eg (Gee et al., 2006) and /or the abrupt transition of the lateral margins (Deplus et al., 2001; Le Friant et al., 2003).

Seismic studies have shown that in most cases MTDs are derived not only from far-travelled materials that collapsed from high on the slope (run-out), but also from different parts of the shallow substrate to the sea-bed (erosion/cannibalisation) (Bull et al., 2009a; Moscardelli and Wood, 2008). These seismic studies are important because they show how material of different sources can combine, increasing the volume of the final deposit. Furthermore, since ancient analogues of MTDs are directly associated with regional seals of some of the world's largest oil and gas reserves e.g. (Homza, 2004; Lapinski, 2003; Talling et al., 2007), the possible incorporation of large volumes of material remobilised from the substrate has a direct bearing on the sand-mud ratio (Moscardelli and Wood, 2008; Posamentier and Martinsen, 2011), resulting in a variety of facies with implications for hydrocarbon seal integrity. There is therefore a need to track and quantify the material from the different source

areas for a fuller understanding of emplacement processes of MTDs and more importantly to evaluate the implications such varied source material has on seal integrity.

The description and quantification of substrate erosion versus run-out is rarely undertaken for major submarine landslides (Prior et al., 1986) however, there have been recent attempts e.g the giant Brunei Slide (Gee et al., 2007) the Matakaoa Debris Flow (Joanne et al., 2013) and the Aga MTD (Clark and Cartwright, in prep). Indeed, evaluations based on reconstructing the geometry of the pre-failure slope template, based on adjacent extrapolated thickness data from nearby undisturbed slopes, will be biased because the true geometry of the failed mass is unknown and it is likely that under or over estimation of the eroded material will occur. Likewise by comparing the thickness of truncated units at the base of debrites with the debrite thickness or evaluation that is based on datasets covering only a small portion of the MTD will significantly underestimate the eroded volume. Within this perspective, a more holistic approach which involves assessing not only the basal surface erosion but the geometries of both the headwall and the lateral margins when preserved would be more realistic in evaluating the role of substrate erosion and/or run-out during MTD emplacement.

The Deepwater Taranaki Basin (Fig. 4.1) which is an emerging and highly prospective petroleum basin (Uruski, 2008), offers an opportunity to holistically study the distribution and morphological characteristics of giant MTDs as well as the quantification of substrate erosion versus run-out. This is made possible by the interpretation of high resolution bathymetric and 2D seismic reflection data covering in most cases the entire portion of some of the MTDs.

This chapter presents a holistic investigation of giant MTDs within the Plio-Pleistocene succession in the Deepwater Taranaki Basin using a 2D seismic survey. The main aims of this chapter are: 1) describe the morphology, geometry, and lateral extents of each MTD; 2) describe their stratigraphic relationships and source areas; 3) develop a simple stratigraphic

approach to quantify the degree of substrate cannibalization for each MTDs; 4) provide age estimates for the deposits; 5) briefly discuss the implications of substrate cannibalization on seal integrity in the Deepwater Taranaki Basin, which is receiving increased interest as a site of potential future exploration. In particular, the results from this chapter provide a basis for the detailed 3D investigation of the youngest MTD in Chapter 5.

4.3 Geological Setting

This study focuses on the Deepwater Taranaki Basin, an extension to the northwest of the Taranaki Basin. The Taranaki Basin covers an area of about 330 km^2 and it is located along the west coast of the North Island and extends onshore in the Taranaki Peninsula and northernmost South Island (Fig. 4.1B). The basin and its deepwater extension developed within the apex of the New Caledonia Basin (Fig. 4.1A).

Structurally the basin is subdivided into the Eastern Mobile Belt and the Western Stable Platform (King and Thrasher, 1996) (Fig. 4.2). The Eastern Mobile Belt has a composite architecture and evolution, and has been variably overthrust, folded, extended, uplifted, and eroded (Armstrong et al., 1998; Kamp et al., 2004; King and Thrasher, 1996). Conversely, the Western Stable Platform is relatively stable and has been influenced by crustal flexure (Holt and Stern, 1994) but has not been internally disrupted by faulting (King and Thrasher, 1996).

The Taranaki Basin formed during the Late Cretaceous, and initially underwent extension associated with the spreading of the Tasman Sea. The pre-break up rifting in the Late Cretaceous affected the present-day Taranaki Shelf as a result of differential spreading directions in the Tasman and Southern Oceans, causing minor rotation of south-eastern New Zealand relative to northwest New Zealand. This rifting episode is documented in several sedimentary basins, but generally not in the Deepwater Taranaki Basin, where the Taranaki Delta was deposited between about 100 Ma and 75 Ma within the failed rift of the New
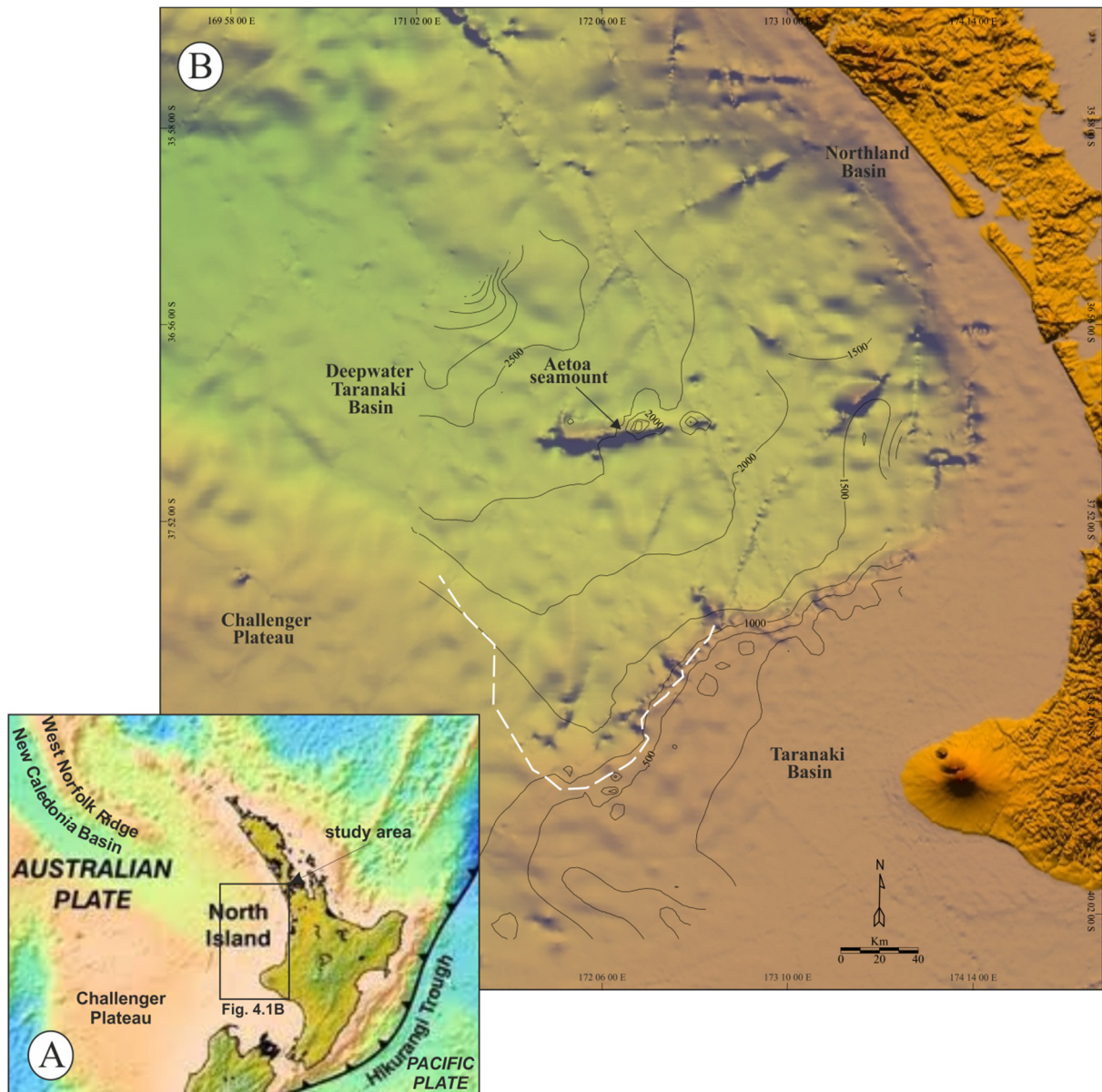
Figure 4.1 A) The Australian-Pacific plate boundary setting in the New Zealand region (B) Bathymetric map showing the morphology of the northwest New Zealand region and the Deepwater Taranaki Basin. Contours are in metres below sea level and are drawn every 500 metres. The southern embayment is outlined by white dash line.

Caledonia Basin (Fig. 4.3B). The initiation of Tasman Sea spreading is thought to have occurred around 80 Ma (Sutherland et al., 2001).

In the Deepwater Taranaki Basin, the break-up unconformity is recorded by transgression across the top of the Taranaki Delta by the North Cape Formation about 75 Ma. Spreading continued in the Tasman Sea until about the end of the Palaeocene (~55 Ma) (Fig. 4.3C). Meanwhile, the New Zealand region had begun to subside as a response to post-break-up cooling of the New Zealand mini-continent as it moved away from the spreading ridges in the Tasman Sea and Southern Ocean. One effect of the subsidence was to gradually reduce source areas and hence sediment supply into the Taranaki region.

During the Eocene, at c. 40 Ma, the Emerald Basin began opening as a result of differential stresses imposed by cessation of seafloor spreading in the Tasman Sea while the Southern Ocean continued to develop. The anti-clockwise rotation imposed upon the southern part of the New Zealand mini-continent resulted in extension in the Solander Basin (Turnbull and Uruski, 1993) while northwest New Zealand underwent gentle compression (Uruski et al., 2002). Large, open folds were formed in the western part of the permit ("PEP 38451" see Chapter 2) area and minor faulting affected much of the Deepwater Taranaki Basin at this time. This was accompanied by continued thermal subsidence of the mini-continent and a reduced sediment supply.

From the middle to late Oligocene the eastern margin of the basin started to subside more rapidly, and this has been attributed to lithospheric loading associated with the initial phase of development of the Australia-Pacific plate boundary zone through the New Zealand platform. During the Miocene the basin registered the influence of the evolving plate boundary in its structures and sediment types much more clearly. This involved earliest Miocene basement over-thrusting on the Taranaki Fault, and late-early Miocene formation of the Tarata Thrust Zone (Fig. 4.2 and 4.3D). By the middle Miocene the direct effects of compression
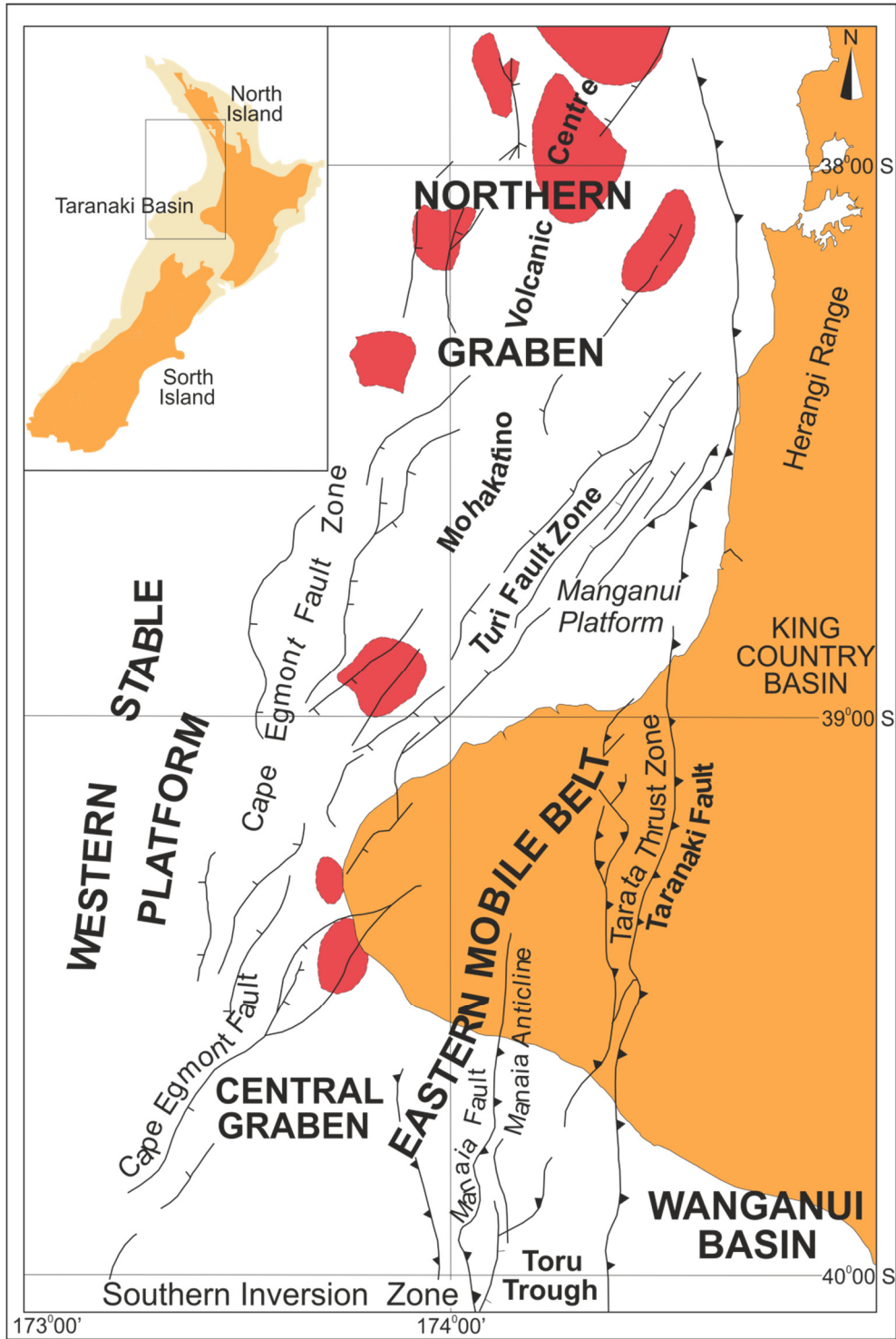
Figure 4.2. Structural domains and principal tectonic and volcanic features of Taranaki Basin (Modified from King and Thrasher, 1996).
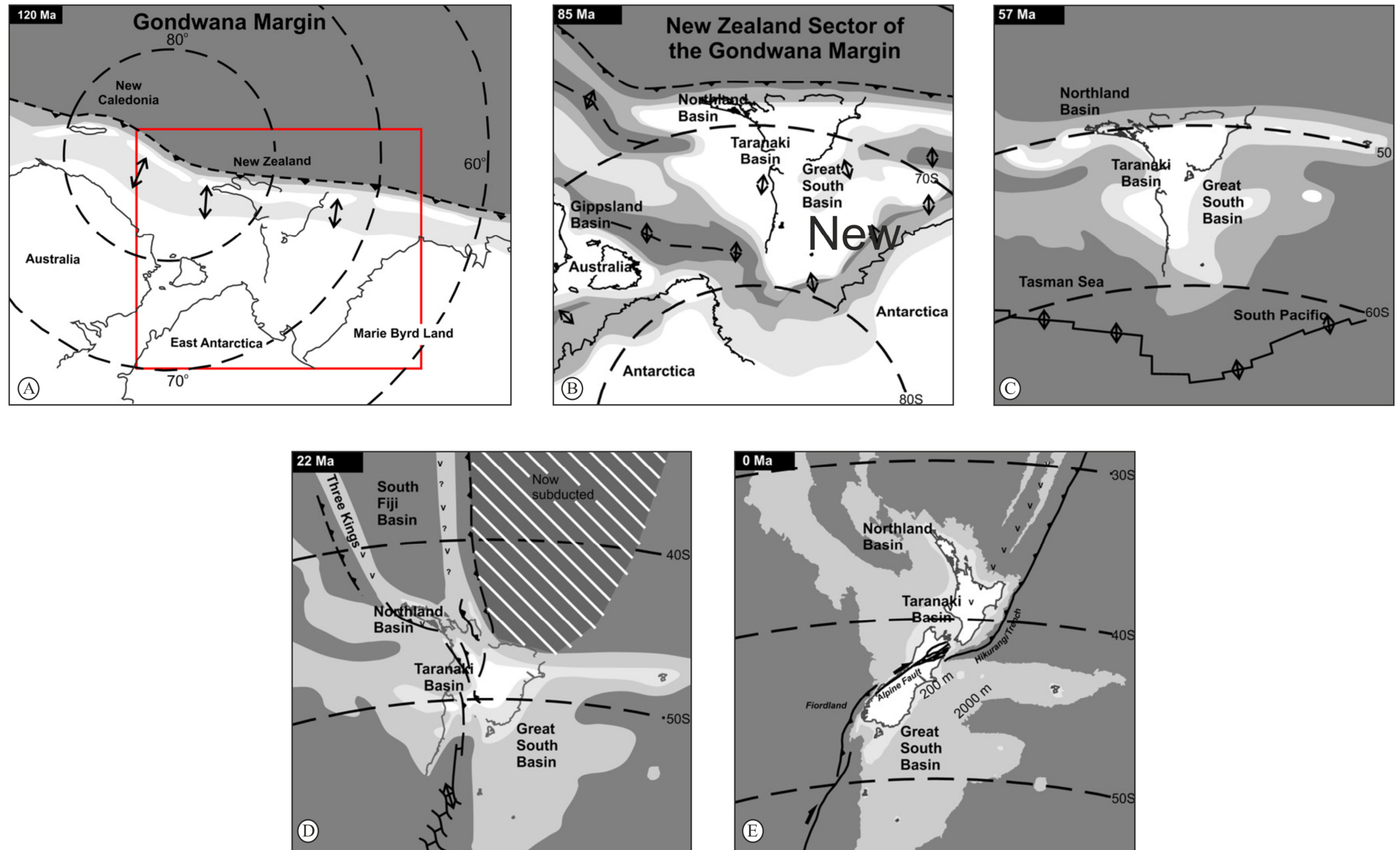
Figure 4.3. Plate tectonic evolution of New Zealand (after Sutherland et al., 2001; Uruski, 2010). (A) New Zealand was part of the Gondwana margin since at least the Permian. A) By 120 Ma rifting was widespread. The box shows the subsequent maps of the New Zealand portion of the Gondwana margin. B) Sea-floor spreading was underway in the Tasman Sea and Southern Ocean and rifting continued across the region. (C) Sea-floor spreading was about to cease in the Tasman Sea c. 57 Ma. The New Zealand mini-continent had been subsiding for at least 10 My. Its land area shrank and sediment supply diminished as the transgression progressed. The Emerald Basin to the south of South Island opened during the Eocene, creating rifting in the south and minor compression in the north. (D) New Zealand landmass was being uplifted and provided an abundant source of clastic material into most sedimentary basins. (E) Present-day New Zealand.
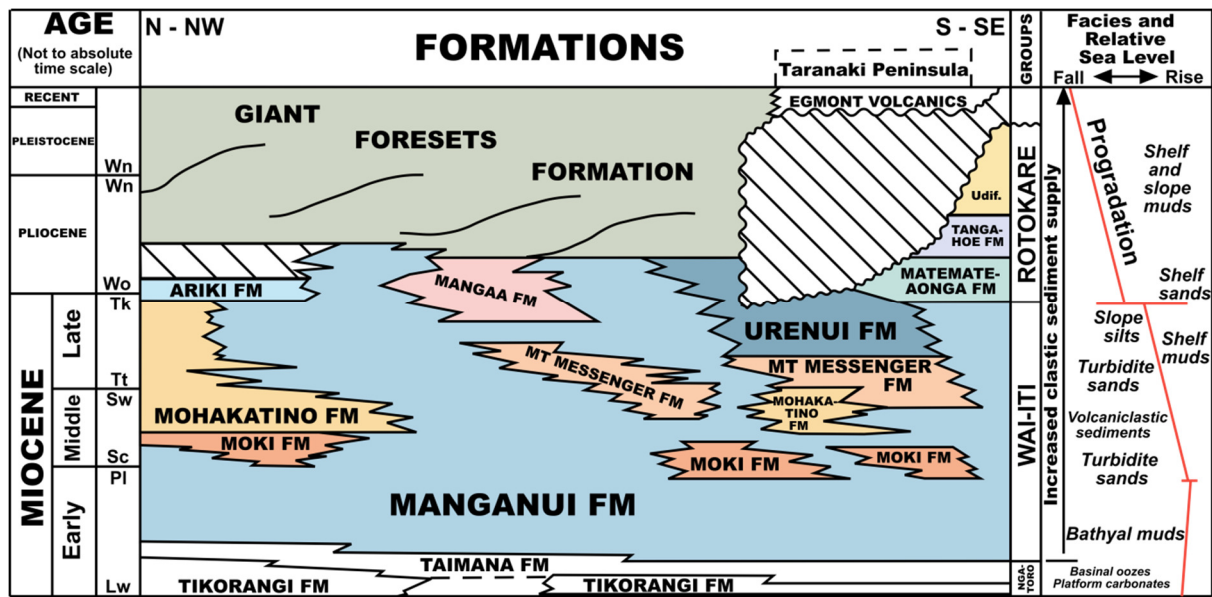
Figure 4.4. Miocene to Recent stratigraphy for the Taranaki Basin. This figure illustrate the general age and propagational nature of the Giant Foreset Formation (Modified from King and Thrasher,1996).

within the northern part of the basin and along its eastern margin had ceased. This coincided with the onset of submarine arc volcanism within northern part of the basin (Mohakatino Volcanic Centre; Fig. 4.2). The volcanic arc paralleled the trend of the contemporaneous subduction zone. Eruptions continued until about 7-8 Ma (King and Thrasher, 1996). The volcanic massifs remained as topographic highs influencing sediment distribution patterns until the Late Pliocene.

During the Pliocene, the volcanic arc migrated south-eastwards onshore into the Taupo Volcanic Zone, where it has been active since the Late Pliocene or Early Pleistocene (Fig. 4.3E). Following the migration of volcanism onshore, the northern parts of the Taranaki Basin became extensional, with formation of the Northern and Central Grabens. These depocentres were rapidly in filled by progradation of the Giant Foresets Formation.

The Giant Foresets Formation comprises a shelf to slope to basin floor succession of fine muds, through to silts and sands (ARCO Pet. Ltd. (NZ) Inc.1992; Shell BP Todd 1981; Hematite Petroleum 1970). The top-sets often contain shelly or pebbly intervals, and the succession is sporadically volcaniclastic. Correlative units of the Giant Foresets Formation onshore include the Tangahoe Mudstone and Whenuakura Subgroup and younger Nukumaruan and Castlecliffian strata in Wanganui Basin (Fig. 4.4) (Hansen and Kamp, 2002). The Giant Foresets Formation is underlain by the Manganui, Mangaa, or Ariki formations and in places by Miocene volcanic massifs (Fig. 4.4).

4.3 Specific data and methodology

4.3.1 Data

This study is based on multibeam bathymetric map and 34 Pre-Stack Time Migrated (PSTM) 2D seismic lines. The data lies mostly to the northwest of the Taranaki shelf edge (Fig. 4.5), across the slope and into the head of the New Caledonia Basin, a major present-day
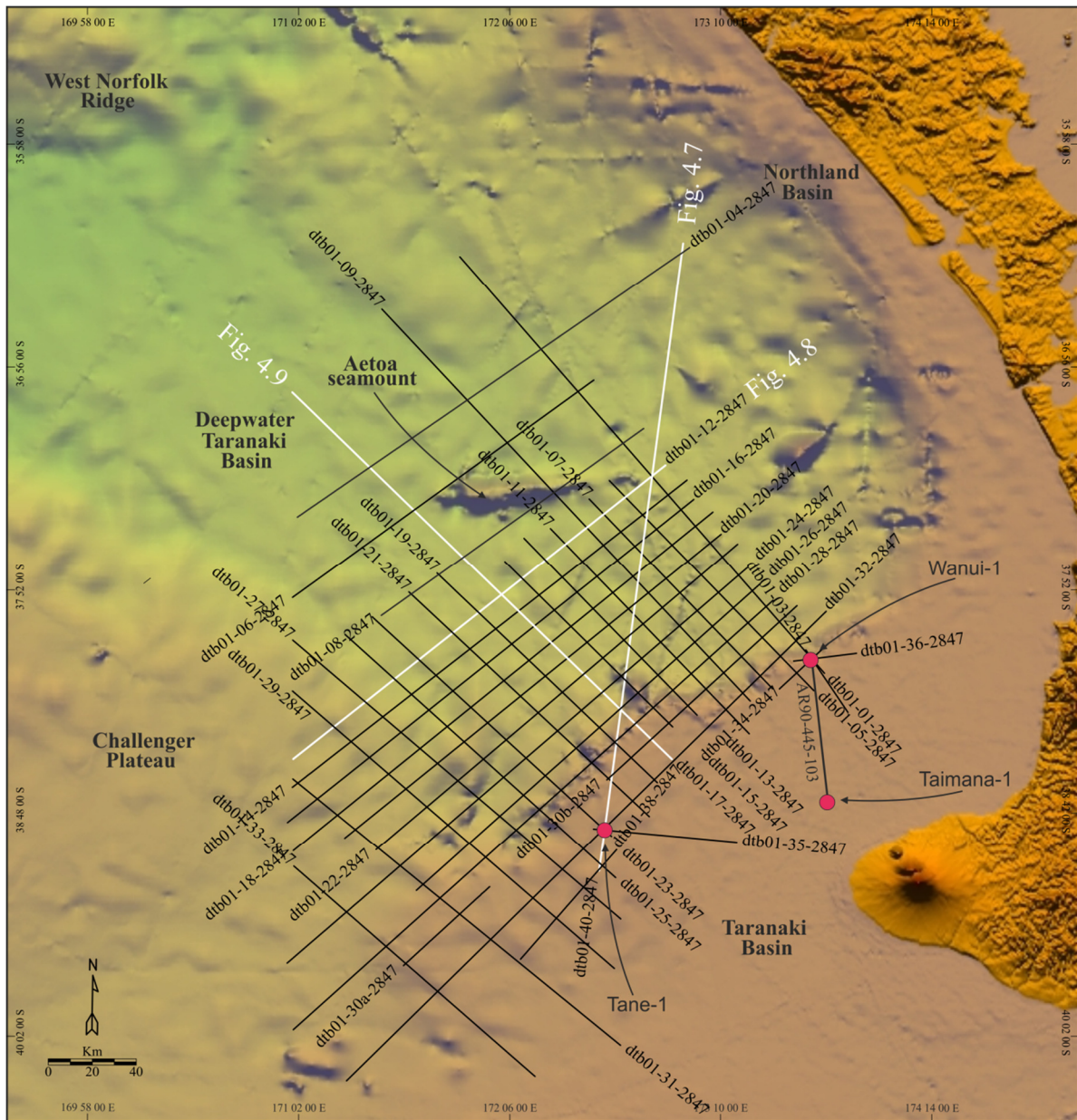
Figure 4.5. Bathymetric map of the northwest New Zealand region showing the 2D seismic profile coverage (indicated by thin black lines) used in this chapter. Seismic sections shown in Figures 4.7, 4.8 and 4.9 are indicated by white lines. Locations of wells are shown with red circles. Named wells are key ties to the TGS-NOPEC Astrolabe data set.

bathymetric trough approximately 4000 km long (see Chapter 2 for details about the dataset). The MTDs were interpreted using Schlumberger Geoframe 4.2 seismic interpretation software.

4.3.2 Methodology

Mapping and volume calculations were conducted using methods outlined in Chapter 2. However, in order to quantify the cannibalized volumes, the geometries of the MTD margins were assessed for abrupt truncations (steps) or pinch-out (run-out) relationships (Fig. 4.6A). A comparison of the truncated lateral margin geometry with the overall MTD thickness i.e step height versus total MTD thickness (run-out) provided a ratio of eroded/deposited material along strike as shown in Figure 4.6A. The eroded/deposited material for each MTD was estimated by interpolation between seismic profiles and by comparing the eroded /cannibalised area with the pinch-out/run-out area (Fig. 4.6B). The ratio was used as a proxy to crudely estimate the volume of the MTD material that was contributed by cannibalisation and/or run-out. Although the seismic profiles were not regularly spaced, this degree of 2D sampling reveals the variability of the geometries of the MTDs.

4.4 Observation and Interpretation

4.4.1 Seafloor Morphology

The seafloor is characterised by a conspicuous 360 km long and 200 km wide bowl-shaped depression which covers an area of c. 56,570 km^2 (Fig 4.1B). The depression is bounded by the Taranaki shelf edge to the south, east and northeast, and by the smooth-topped Challenger Plateau to the southeast, and then extends across the slope into the head of the New Caledonia Basin. Water depths range from c. 300 m at the shelf edge to just over 2500 m towards the north- eastern limits of the study area. The seafloor is interrupted at the centre of
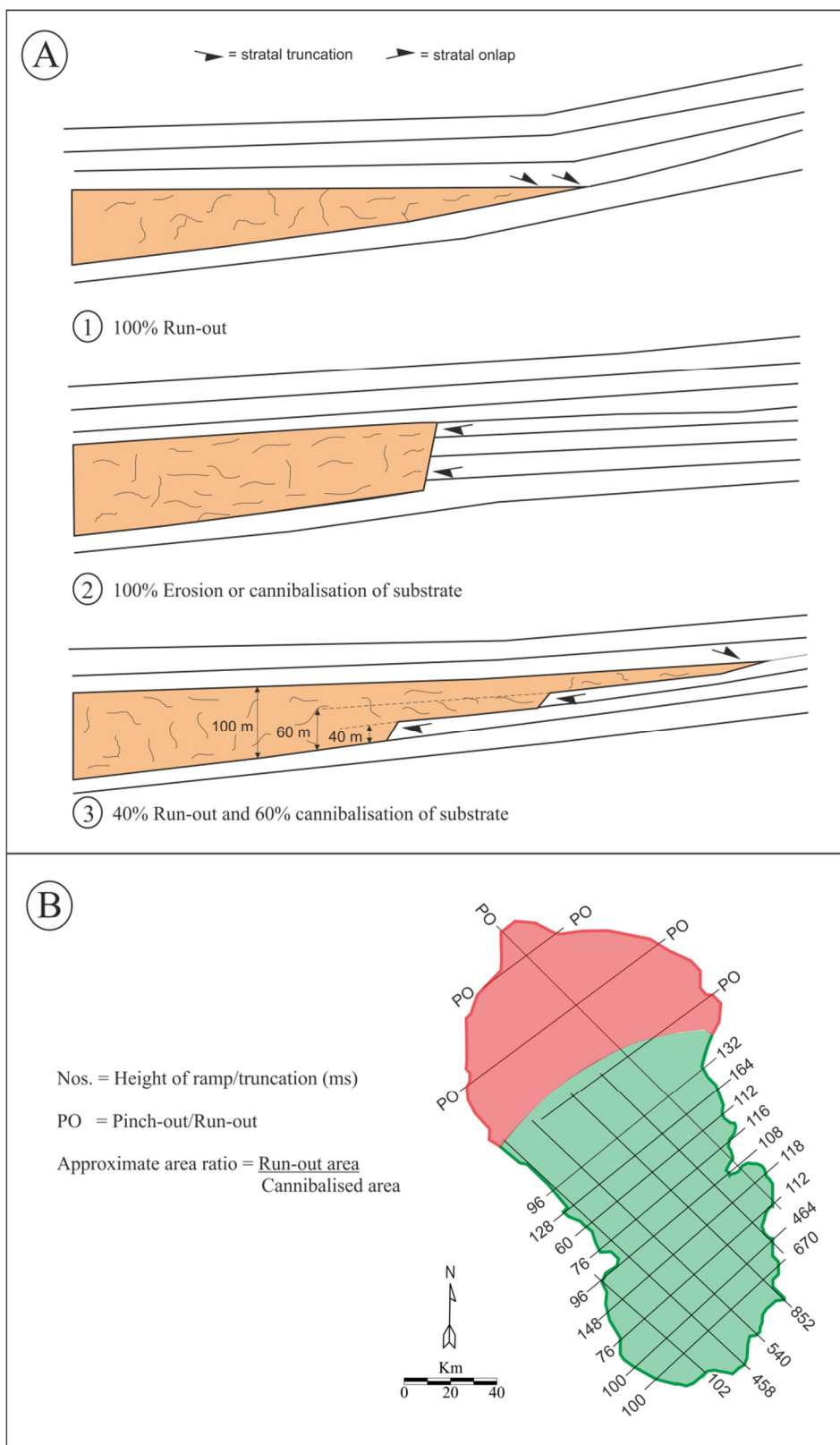
Figure 4.6 A) 1) Pinch-out relationship of lateral margin suggests 100% run-out of deposit 2) Lateral truncation suggests 100% erosion or cannibalization of the substrate 3) Depending on the step height versus the overall thickness of the MTD, a % ratio of cannibalized and deposited volume is assigned. B) The MTD material contributed via cannibalization or run-out was estimated by interpolating between the seismic profiles.

the bowl shaped depression by the presence of the elongated ENE oriented irregular-topped Aetoa Seamount (Fig. 4.1B). The isolated seamount is Miocene-aged (25 to 5 Ma) and rises up to 900 m from a depth of 2150 m (Brodie, 1965). The basin floor appears to be generally smooth, although recently deposited sediment can be observed as hummocky mounds (Fig. 4.1B).

Representative seismic profiles across the study area show that the conspicuous depression observed on the seafloor is a relict topography inherited from a series of large-scale, stacked and locally amalgamated slope failures (Figs. 4.7, 4.8 and 4.9). The Taranaki shelf edge is distinctively steeper (3° – 10°) compared to the 2° to 5° slopes of the Challenger Plateau, southeast of the study area. The Taranaki shelf edge and continental slope is heavily incised by submarine canyons. This is seen clearly on seismic profiles as a series of V-shaped depressions that are associated with faults (Figs. 4.7 and 4.9).

4.4.2 Landslide stratigraphy

The Pliocene to Holocene slope succession in the Deepwater Taranaki Basin is characterised by units that are recognisable as discrete bodies from their transparent and/or chaotic seismic character (Figs. 4.7, 4.8, 4.9). These bodies are all crudely concordant to the gross stratification, but are bounded at their bases and tops by irregular surfaces with often considerable erosion (base) or deposition (top). These characteristics allow them to be readily distinguished from undeformed adjacent strata which display continuous and coherent seismic character. They are also characterised by generally chaotic to discontinuous internal stratification and are therefore interpreted as MTDs by their strong similarity with previously described MTDs (see Chapter 2.4). They constitute about 50% of the Pliocene – Holocene slope stratigraphy in this area of the basin.
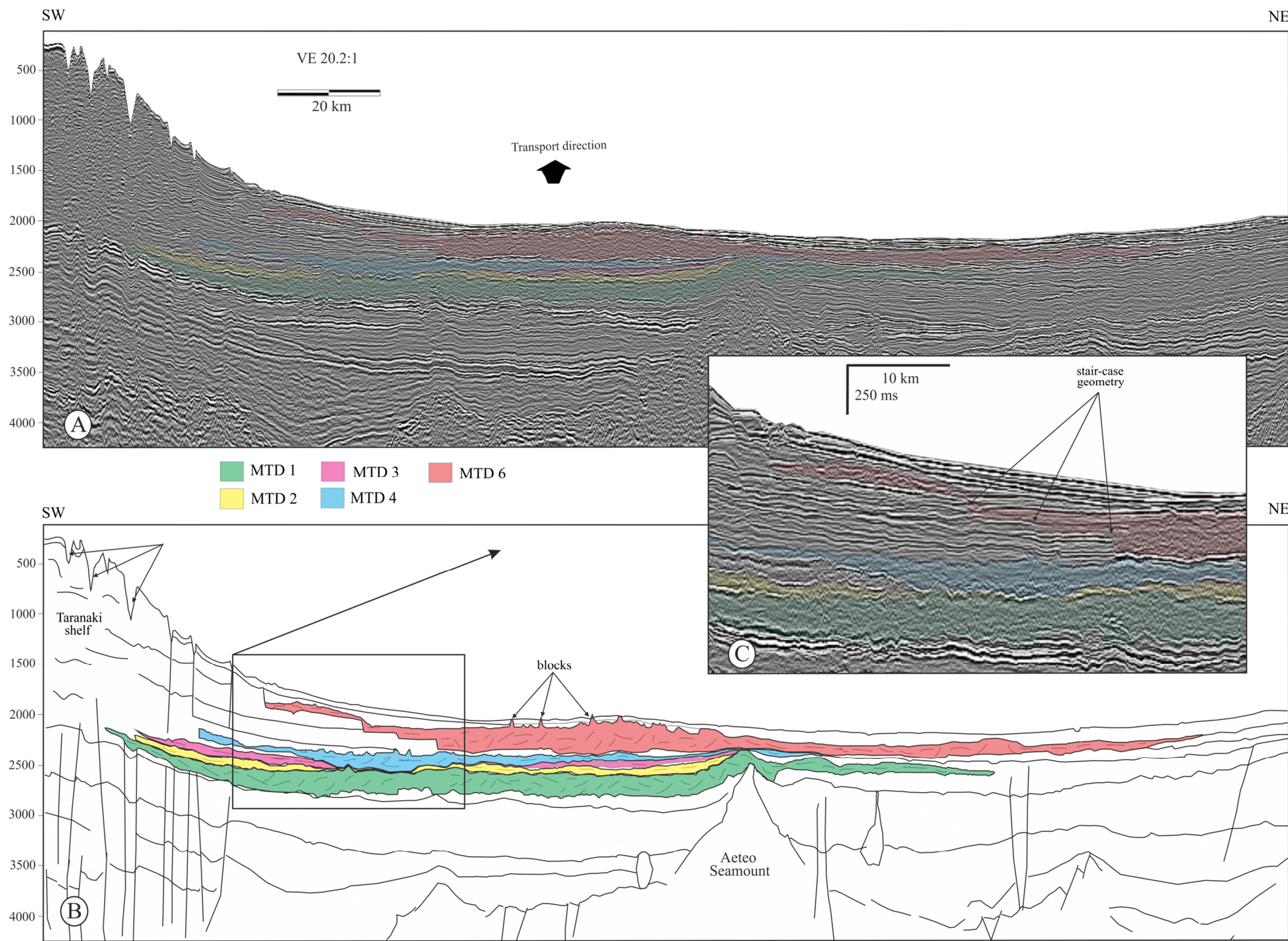
Figure 4.7 A) Un-interpreted 2D seismic profile dtb01-40 (See Fig. 4.5 for location) (B) Interpreted seismic profile showing the distribution of the MTDs 1-4 and 6 discussed in text (C) Zoomed in section of MTD 6 lateral margin showing staircase geometry.

SW

NE

(A)

VE 15.6:1

20 km

TWT(ms)
1500
2000
2500
3000
3500
4000

SW

NE

seabed scarp aligned with MTD 5 margin

pinch-out

ramp

10 km
250 ms

MTD 1	MTD 4
MTD 2	MTD 5
MTD 3	MTD 6

(C)

SW

(B)

Top Miocene

Top Eocene

Top Cretaceous

Top Rakopi FM.

TWT(ms)
1500
2000
2500
3000
3500
4000

Challeger Plateau

ramp

blocks

MTD 1 truncates the eastern flank of the seamount

Aeteo Seamount
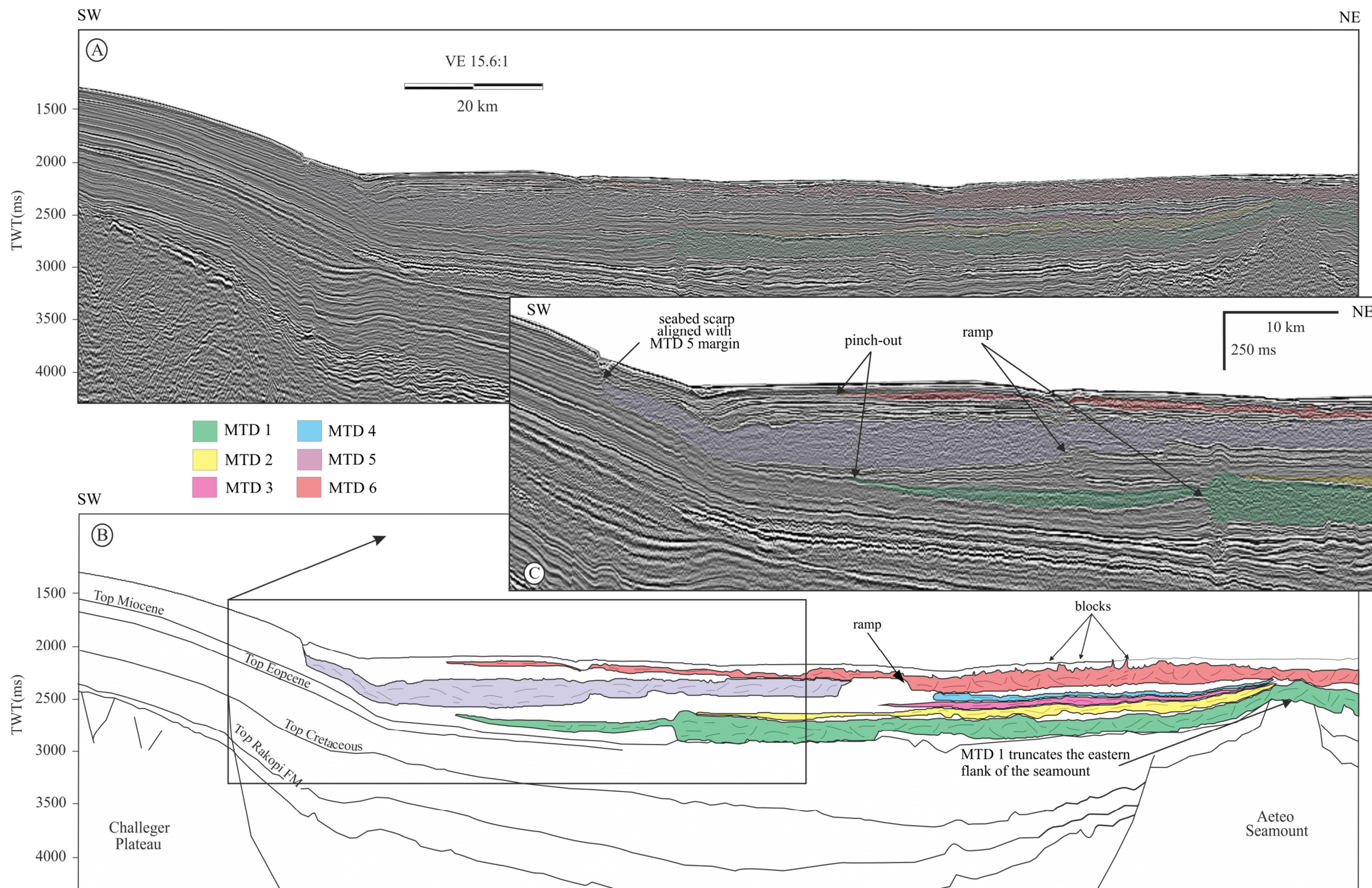
Figure 4.8 A) Interpreted 2D seismic profile dtb01-12 (See Fig. 4.5 for location) (B) Interpreted seismic profile showing the distribution of the MTDs 1-6 discussed in text.(C) Notice the conspicuous thinning of MTDs 1 in the zoomed in section due to the ramping up of their basal surface.
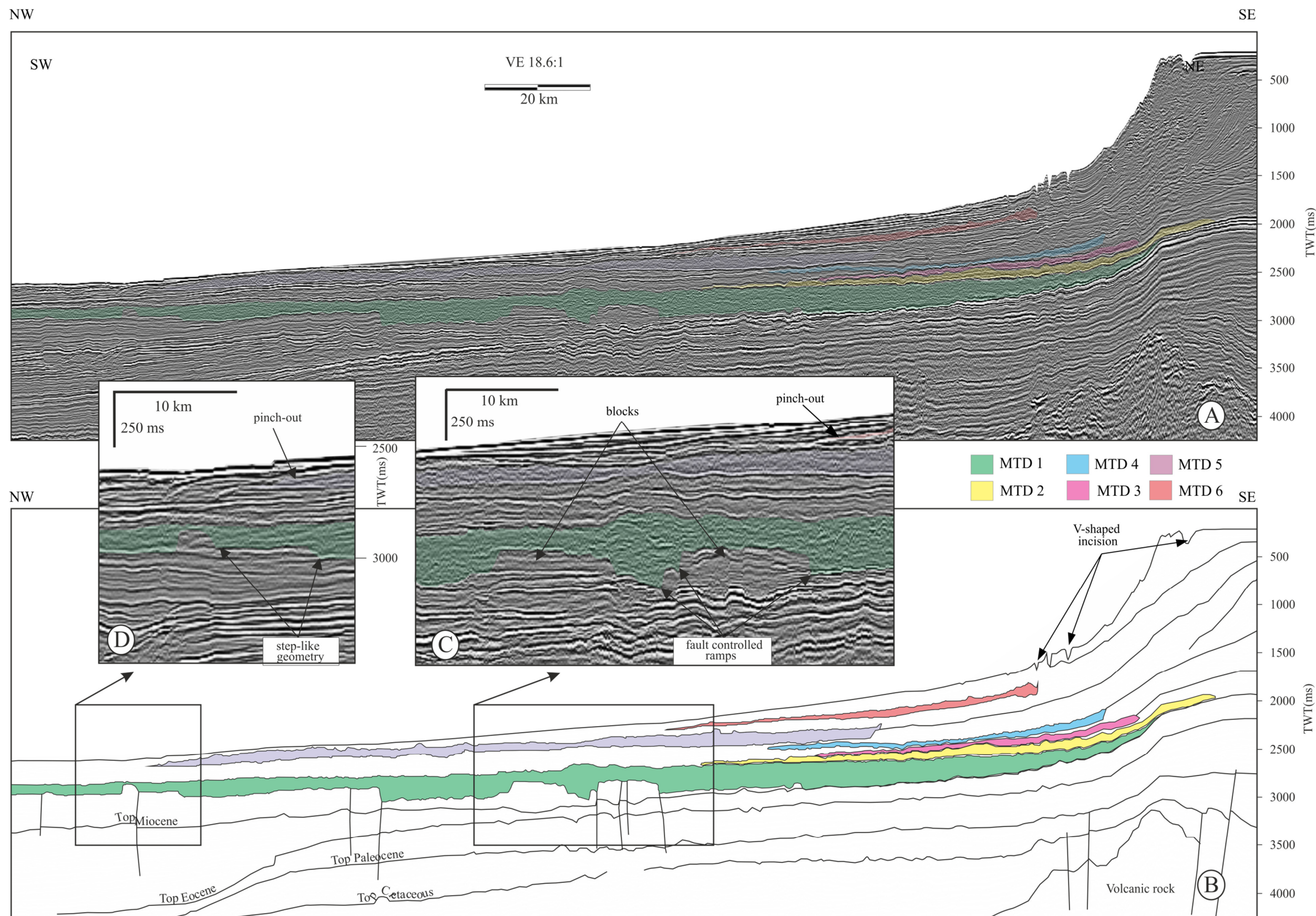
Figure 4.9 A) Uninterpreted 2D seismic reflection profile dtb01-21(See Fig. 4.5 for location) (B) Interpreted reflection seismic profile showing the distribution of the MTDs 1-6 discussed in text (C) Zoomed in section showing intact blocks (D) Another zoomed in section showing staircase geometry of MTD 1.

Six distinctive and widespread MTDs referred to as MTD 1 - 6 (with MTD 1 being the oldest at the lowest stratigraphic position and MTD 6 the youngest) are recognised within the Pliocene – Holocene interval (Figs. 4.7, 4.8, 4.9 and Table 1). The 2-D seismic data has allowed the accurate mapping of the upper, lower and lateral limits of each of these MTDs as well as understanding their spatial distribution in time. The geometry, architectural elements and complex kinematic history of MTD 1 – 6 are examined in detail in the following sections using a combination of isochron maps and representative seismic profiles.

4.4.2.1 MTD 1

MTD 1 is the oldest of the MTDs imaged in the study area and for most of its area it lies at the transition between the Upper Miocene and Lower Pliocene (Figs. 4.7, 4.8 and 4.9). The deposit has a pear-shaped body in map view, elongate in a WNW-ESE direction, narrowing downslope (Fig. 4.10) and covers a minimum area of ca. 20,887 km^2 with an estimated residual volume (see Chapter 3 for definition) of 4,064 km^3. No evidence of a headwall to MTD 1 has been interpreted on seismic reflection profiles, probably due to the limited areal coverage of the dataset.

The two-way travel time (TWT) thickness of MTD 1 varies considerably from the proximal eastern region where it reaches a maximum of ca. 390 ms and gradually thins and tapers to pinch-out towards to the distal western and south westerly limits (Fig. 4.10). In addition, a conspicuous reduction in thickness of MTD 1 occurs towards the south west formed by the ramping up of the basal surface of the deposit until it tapers to pinch-out (Figs. 4.8 and 4.10). Towards the north, the deposit thins to c. 50 ms above the Aeteo Seamount before it tapers to pinch-out (Fig. 4.7). However, it truncates the eastern flank of the Aeteo Seamount with almost uniform thickness of c. 250 ms (Fig. 4.8).

The spatial variation in thickness within MTD 1 (Fig. 4.10) can be related to the variations in

Table 4.1: Morphological characteristics of the MTDs identified in this study.

Deposit	Translation direction	Area (km²)		Mean Thickness (ms twt)	Volume (km³)	Estimated Cannibalization (%)
		Minimum	Maximum			
MTD 1	E – WNW	20,887	?	~390	4,064	60
MTD 2	E – WNW	11,548	?	~320	1,325	40
MTD 3	E – WNW	4,276	?	~200	377	?
MTD 4	E – WNW	10,128	?	~240	961	40
MTD 5	S – NW	-	18,364	~450	2,643	60
MTD 6	NE – SW	22,397	?	~300	3,733	70
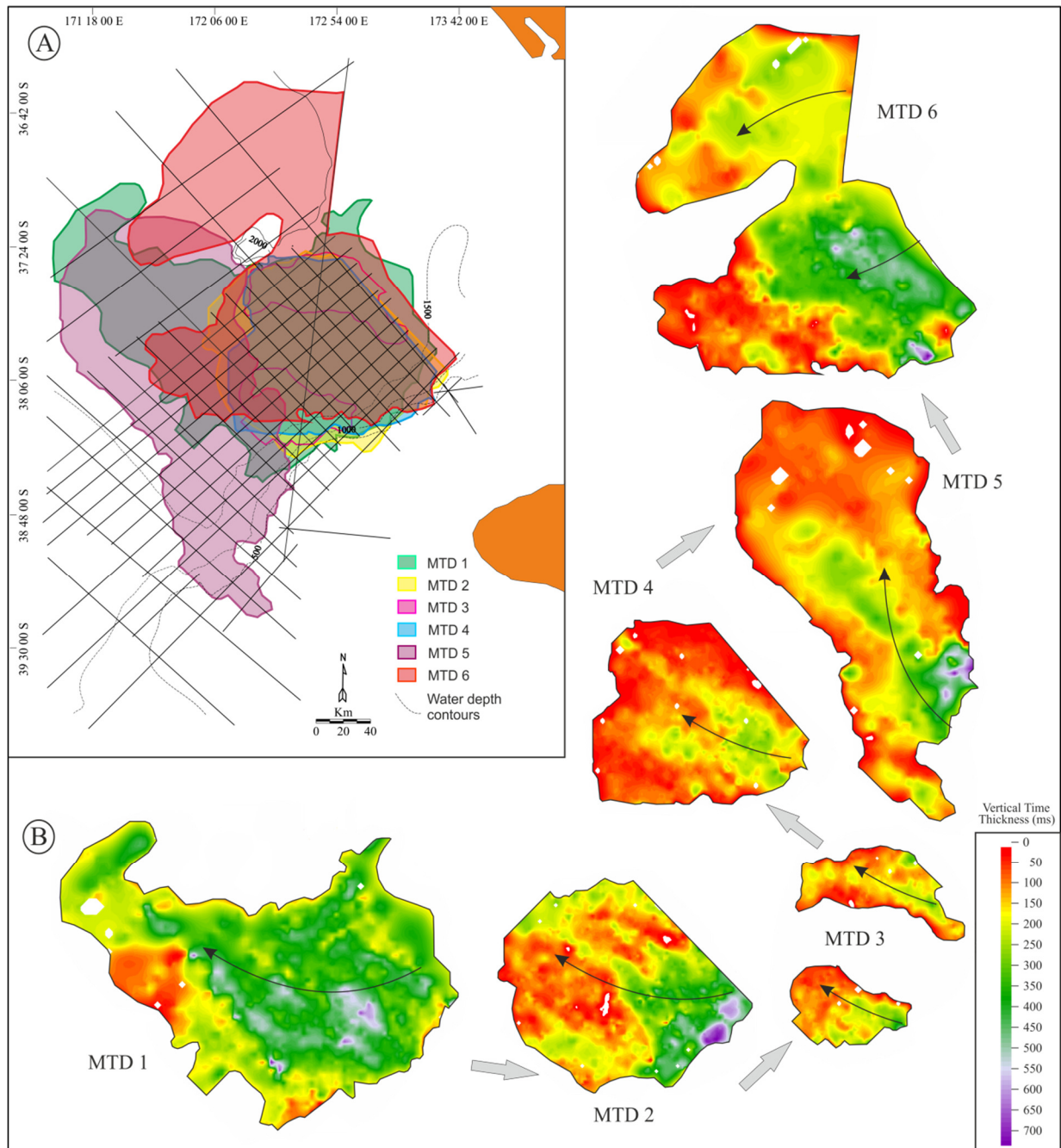
Figure 4.10 A) Outline map of the large MTDs discussed in the text. Black straight lines show coverage of 2D seismic data. (B) Isopach maps for all individual MTDs discussed in the text showing inferred transport direction. The grey arrows show the deposit age sequence, from the oldest unit to the youngest.

the geometry of the basal surface and to the relief of the Aeteo Seamount (Figs. 4.7, 4.8 and 4.9), which suggests that both these have influenced the distribution of the deposit.

The basal surface of MTD 1 is defined by a low amplitude reflection with negative polarity (high impedance overlying low impedance - see Chapter 2). Seismic profiles show that the basal surface of MTD 1 directly overlies the Top Miocene reflection for approximately 25% of the area it spans, especially in the eastern proximal areas (Fig. 4.9B). It separates the transparent and chaotic facies of MTD 1 from the underlying high amplitude continuous reflections that characterise the Late Miocene units in the east and the moderate continuous amplitude reflection of the Early Pliocene units towards the west. At the transition between the eastern and western parts of MTD 1 there is evidence of truncation of underlying undeformed strata (Fig. 4.9).

In the eastern parts of MTD 1, the basal surface is fairly continuous and concordant with the Top Miocene reflection but with some minor undulating topography (Fig. 4.9). However, towards the west it is steps up and follows along higher stratigraphic levels, exhibiting a staircase geometry.

Towards the central areas of MTD 1, the basal surface cuts up and down stratigraphy to leave as residual features two "islands" of undisturbed strata. These are interpreted as remnant blocks (cf. Bull et al., 2009a) which have vertical concordance with underlying strata with no visible detachment surface (Fig. 4.9C). The largest remnant block measures 200 ms high and c. 10 km long.

The concordance of the remnant blocks with the underlying strata suggests that they have not experienced failure (Frey Martinez et al., 2005; Garziglia et al., 2008). It represents an obstacle to the advance of failed material, since it affects the local thickness distribution of MTD 1. More recently, (Gafeira et al., 2010) presented an interesting model to explain the preservation of large remnant blocks within a failed deposit. According to the model, "the

propagation of two adjacent cauliflower shaped headwall leads to the preservation of an isolated portion of ridge which would originally have separated them". Given that the remnant block lies in the eastern proximal areas of the MTD 1, it is possible that the same process of formation resulted in its preservation.

Further to the west, the basal surface lies at a higher stratigraphic level as it cuts up stratigraphy developing a step-like geometry (Figs. 4.9D). Individual ramps measure up to 100 ms in height and have inclinations ranging from 20°- 35°. Two sets of ramps are observed in MTD 1; those associated with faults and those that are not fault controlled (Fig. 4.9C).

Furthermore, the basal surface appears to be crudely concordant with the underlying stratigraphy in the western region (Fig. 4.11C). Nevertheless, there is clear evidence of erosion of the basal surface and the erosive feature is interpreted as slot (c.f. Bull et al., 2009a) (4.11C). The slot has a long axis oriented in the downslope direction and measures c. 10 km in width with a relatively steep (c. 35°) angled ramp.

The down cutting or up stepping of basal surfaces interpreted as ramps are commonly observed in mass transport deposits (Frey-Martínez et al., 2006; Moscardelli et al., 2006; Solheim et al., 2005b; Strachan, 2002; Vanneste et al., 2006) and their origins have been related to the mechanical properties of the basal surface and/or stresses created by the translating mass transport deposit over the basal surface (Bull et al., 2009a). The fact that there is no observable correlation between the throws of the faults and the ramp offset of the basal surface suggests that the ramps were not created by the fault. However, it is interpreted that these faults acted as pre-existing vertical zones of weakness that the translating failed mass exploited (Bull et al., 2009a; Strachan, 2002), which eventually led to the development of ramps. It is suggested that those ramps not related to faults are related to localised variation of the stress conditions for propagation of the failure surface or to changes in the mechanical properties of the basal surface (Frey Martinez et al., 2005).
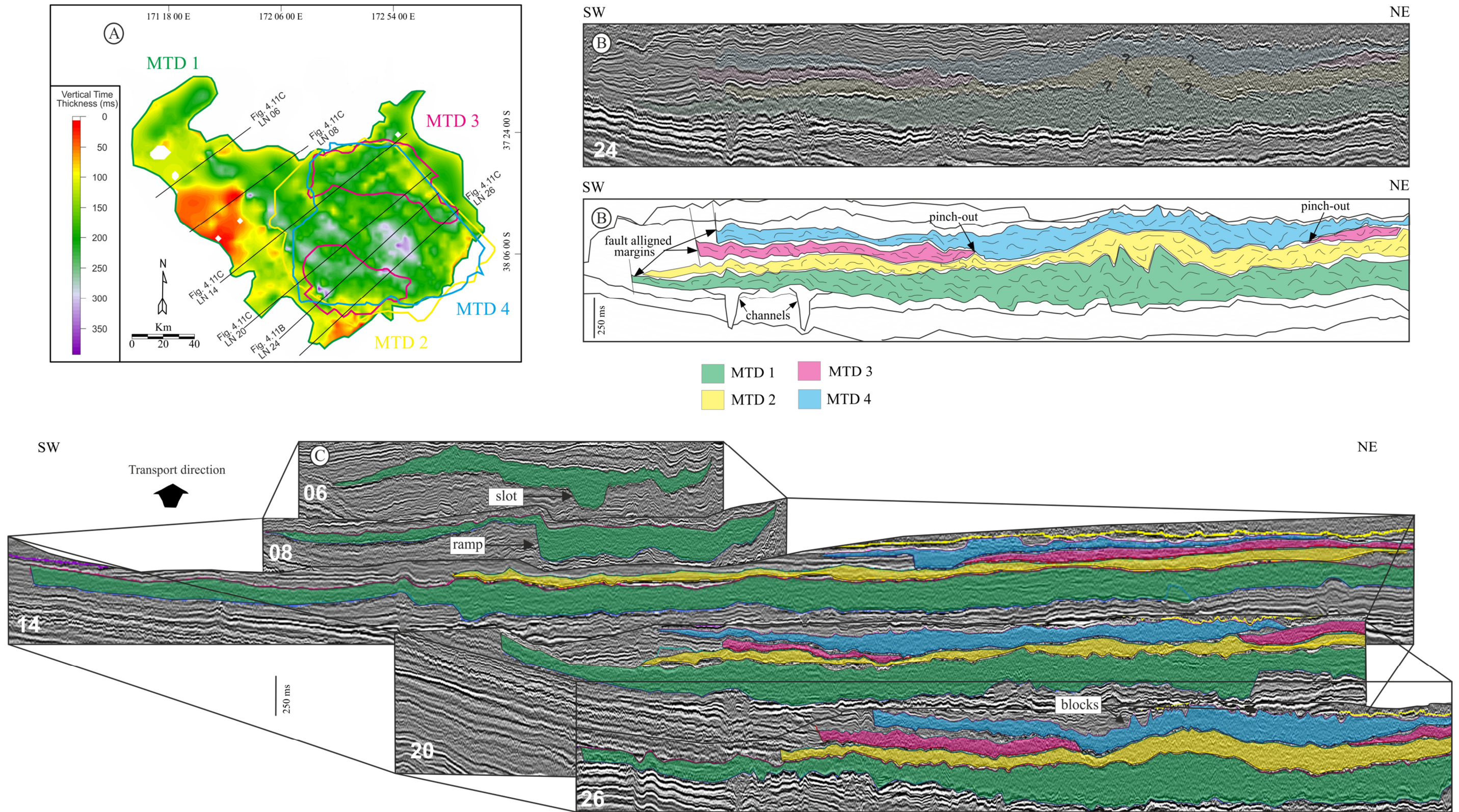
Figure 4.11 A) Isopach map for the MTD 1, and superimposed outlines of MTDs 2, 3 and 4. Black straight lines show the 2D seismic profiles discussed in text. (B) Seismic profile showing the relationship between MTD 1-4 in the proximal region. Notice the amalgamation of the four MTDs in this region (C) Fence diagram showing the downslope variation of the lateral margins of MTDs 1-4.

.

A high amplitude reflection marks the upper surface of MTD 1, and separates it from the overlying MTD 2. In general, it is crudely concordant to the basal surface. However, in the eastern part of the deposit it becomes increasingly irregular, discontinuous and eventually disappears, making it difficult to differentiate MTD 1 from the overlying chaotic seismic facies of MTD 2 (Fig. 4.11B).

The lateral margins of MTD 1 are recognised on strike oriented seismic profiles as abrupt scarps in the eastern proximal area of the deposit (Fig. 4.11C), separating the chaotic seismic facies of MTD 1 from the adjacent undeformed strata. The height of the lateral margin is at least 50 ms (with inclinations ranging between 25°- 40°) in the proximal part of the deposit. In contrast, downslope towards the western distal parts, the lateral margin is represented by pinch-out relationships (Figs. 4.7, 4.8 and 4.11C). In map view, the lateral margins of MTD 1 have a general E - NW orientation (Fig. 4.11A). The northern and eastern lateral margins of MTD 1 extend for over 160 km in the downslope direction and converge in distal areas.

The orientation of the lateral margins of MTDs is invaluable as kinematic indicators (Bull et al., 2009a) and suggests north-westerly transport direction for MTD 1.

MTD 1 is dominated by chaotic and transparent seismic facies (Figs. 4.7, 4.8, 4.9 and 4.11) with some minor evidence of isolated blocks which have coherent internal seismic reflections.

MTD 1 is directly overlain by MTD 2 on the eastern region (Fig. 4.9) but towards the western region, MTD 1 is separated from MTD 5 by up to 200 m thick well stratified unit (Fig. 4.8).

4.4.2.2 MTD 2

MTD 2 directly overlies MTD 1 and it is locally absent in the western region (Figs. 4.9 and 4.11C). The main slide body is sub-circular in shape where mapped (truncated at the edge of the data in the northeast) and covers a minimum area of c. 11,548 km^2 with an estimated

minimum volume of 1,325 km^3. MTD 2 shows marked thickness variation having a maximum observed thickness of 320 ms in the eastern proximal region decreasing downslope to c. 25 ms in the central region until it tapers to pinch-out in the south-westerly direction (Fig. 4.10B).

The basal surface of MTD 2 is defined by a low amplitude reflection with negative polarity similar to MTD 1 (Figs. 4.7, 4.8, 4.9 and 4.11). It is quite irregular and generally concordant with the underlying upper surface of MTD 1 especially in the proximal north-eastern region (Fig. 4.11C). In contrast, towards the west, MTD 2 is observed to be separated from MTD 1 sometimes by very thin units of continuous seismic reflections (Fig. 4.8B).

The upper surface of MTD 2 is defined by a high amplitude reflection similar to that of MTD 1 and it separates MTD 2 from the overlying MTD 3. It is generally continuous and irregular upslope and becomes quite regular downslope (Fig. 4.11C).

Only the south-western lateral margin of MTD 2 is observed due to the limits of the available dataset and it is seen as an abrupt scarp in the upslope region similar to MTD 1. A maximum height of c. 40 ms is measured for the southern lateral margin in an upslope position. However, further downslope, the same lateral margin is represented by a pinch-out relationship (Fig. 4.11C).

The WNW-ESE orientation of the lateral margins (Bull et al., 2009a) coupled with the gradual reduction in the thickness of the deposit towards the north-west (Fig. 4.10A) suggests a WNW transport direction for MTD 2 similar to MTD 1.

4.4.2.3 MTD 3

MTD 3 is the smallest of all the MTDs in the study area. It overlies MTD 2 and it is overlain by MTD 4 (Fig. 4.11B and C). MTD 3 comprises two sub-units (northern and southern) separated in the middle by the amalgamation of the overlying MTD 4 and the underling MTD

2 (Fig. 4.11B and C). In plan view, MTD 3 covers a total area of c. 4,276 km^2 with an estimated total volume of 377 km^3 (Fig. 4.10B). Each of the sub-units of MTD 3 is crudely elliptical in planform with the northern sub-unit covering 2,403 km^2 with an estimated volume of 187 km^3 and the southern sub-unit extending over 1,873 km^2 with an estimated volume of 190 km^3 (Fig. 4.10B).

The basal surface of both sub-units that constitute MTD 3 is marked by a low amplitude reflection with negative polarity similar to MTD 1 and 2 (Figs. 4.7, 4.8, 4.9 and 4.11B and C). Upslope, the basal surface is quite irregular and generally concordant with the underlying upper surface of MTD 2 (Fig. 4.11C).

The upper surface of MTD 3 is defined by a high amplitude reflection and it separates MTD 3 from the overlying MTD 4. It is generally continuous and irregular upslope and becomes quite regular downslope (Fig. 4.11C).

An important observation from the mapping of the lateral margins of both sub-units is that their external lateral margins are seen as abrupt scarps (except towards the distal western limits) similar to those described for MTD 1 and 2 (Fig. 4.11C). However, the internal lateral margins of both sub-units are represented by pinch-out or truncation relationships (Figs. 4.7 and 4.11C) which probably suggest that the central part of the deposit have been eroded. In map view, the lateral margins of both sub-units of MTD 3 have an east-west orientation (Fig. 4.10B). This observation coupled with the gradual reduction in MTD 3 thickness towards the northwest suggest a WNW transport direction for MTD 3 (c.f Bull et al., 2009a) similar to MTDs 1 and 2.

4.4.2.4 MTD 4

MTD 4 directly overlies MTD 3 wherever it is present but directly overlies MTD 2 for c. 50% of its area (Fig. 4.11C). The shape of MTD 4 is comparable to that of MTD 2 (Fig.

4.10B) and it spans a minimum area of c.10, 128 km^2 with an estimated volume of 961 km^3. MTD 4 shows marked thickness variations having a maximum thickness of 320 ms in the eastern proximal region decreasing downslope to c. 25 ms in the central region until it tapers to pinch-out in the south-westerly direction (Fig. 4.10B and 4.11C).

As with the previously described MTDs, the basal surface of MTD 4 is marked by a low amplitude reflection with negative polarity similar MTDs 1, 2 and 3 (Figs. 4.7, 4.8 and 4.9). Upslope, the basal surface is quite irregular and generally concordant with the underlying upper surface of MTD 3 and MTD 2 wherever present (Fig. 4.11C).

The upper surface of MTD 4 is defined by a high amplitude reflection which is generally continuous. In the upslope proximal region, the upper surface of MTD 4 is highly irregular characterised by pronounced positive features that are c. 50 ms high (Fig. 4.11B and 4.11C). These protuberances are interpreted to be possibly due to the existence of intact blocks within the chaotic matrix of MTD 4.

Similar to MTD 2, only the southern lateral margin is preserved and the east-west orientation of the lateral margin (c.f. Bull et al., 2009a) coupled with the decreasing thickness of the deposit towards the north west (Fig. 4.10B) suggests a WNW transport direction for MTD 4.

4.4.2.5 MTD 5

MTD 5 is located south of the Aetoa Seamount and extends for c. 220 km from the shelf edge in a north westerly direction (Fig. 4.10A). It has fan shape geometry in plan view, elongated in a NW-SE direction (Fig. 4.10B), and covers an area of c. 18,364 km^2 with an estimated volume of 2,643 km^3. The deposit displays considerable lateral thickness variation as with the other previously described MTDs, ranging from 400 ms to 700 ms in the proximal south-eastern headwall region (Figs. 4.12A and C). The thickness gradually decreases downslope in the north westerly direction until it tapers to pinch-out in the distal margins of the deposit.
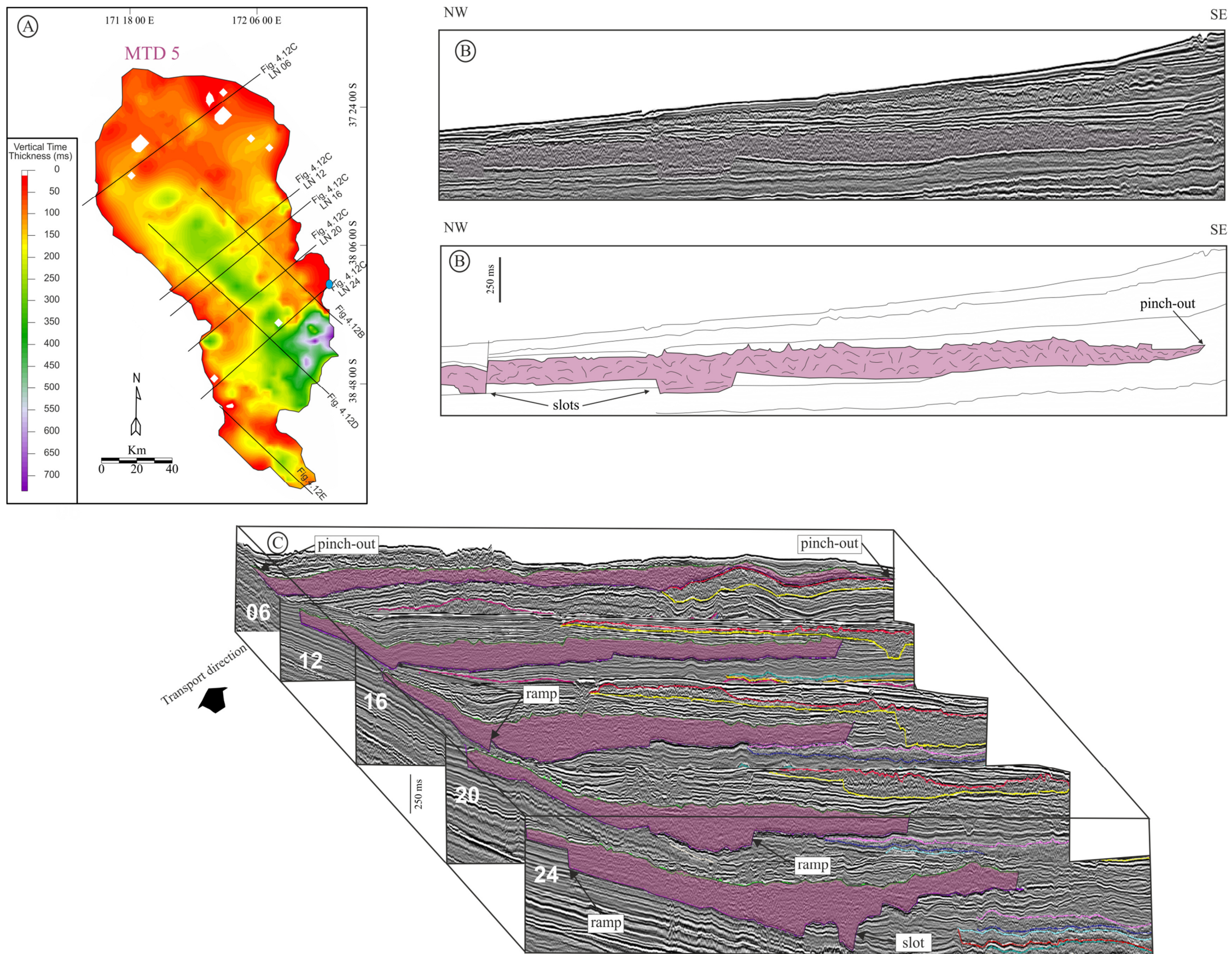
Figure 4.12 A) Isopach map for the MTD 5. Black straight lines show the 2D seismic profiles discussed in text. (B) Seismic line showing the both fault controlled slot and non -fault controlled slot (C) Fence diagram showing the highly erosive basal surface and variable thickness of MTD 5. Also notice the variable geometry of the lateral margins.

Unlike the previously described MTDs in the study area, the buried headwall of MTD 5 is imaged in the 2D seismic data and it is preserved in the proximal south eastern region underneath the shelf edge (Fig 4.12D). Although the use of 2D seismic data precluded a more detailed analysis of the headwall (because of the poor imaging and wide spacing of lines), it is believed to be a north-south trending irregular boundary reaching c. 40 km in length (Fig. 4.12A) with a relief of c. 400 ms, having a westerly inclination ranging from $40°$ to $55°$ (Fig. 4.12D).

Sitting directly above the headwall and downlapping onto the upper surface of MTD 5 are a set of prograding clinoforms (the Giant Foresets Formation, Fig. 4.4). This juxtaposition indicates high sediment input into the basin and could therefore be used to suggest that MTD 5 originated from the over steepening of the slope (see Discussion). Immediately south of the of the headwall, there is evidence for a relatively smaller scar which extends for c. 10 km (Figs. 4.12A and 4.12E) with a more gentle inclination ($30°$ to $40°$) than the main headwall.

The smaller scar is interpreted to originate from the instability caused by the failure of the main headwall. Given the maximum headwall height of c. 400 ms observed in the headwall region of MTD 5 and the relative thickness of the deposit (Fig. 4.12D), it is certainly conceivable that a significant amount of depletion took place in the headwall domain of MTD 5.

The basal surface of MTD 5 is defined by a generally continuous, low amplitude reflection that truncates the underlying undeformed strata (Fig. 4.12). Towards the western limits of the deposit, the basal surface is smooth and follows stratigraphy (Fig. 4.12C). However, it ramps up or down stratigraphy downslope, cutting staircase geometries. The basal surface of MTD 5 progressively truncates underlying stratigraphy in the middle where the maximum thickness is observed (Fig. 4.12C). The most dramatic evidence of erosion of the basal surface is observed in the southern proximal area of MTD 5, the basal surface exhibits a c. 1 km wide, and at least 100 ms deep U-shaped depression with a steep angled ramp (c. $35°$)(Fig. 4.12C).

NW   SE

NW   SE
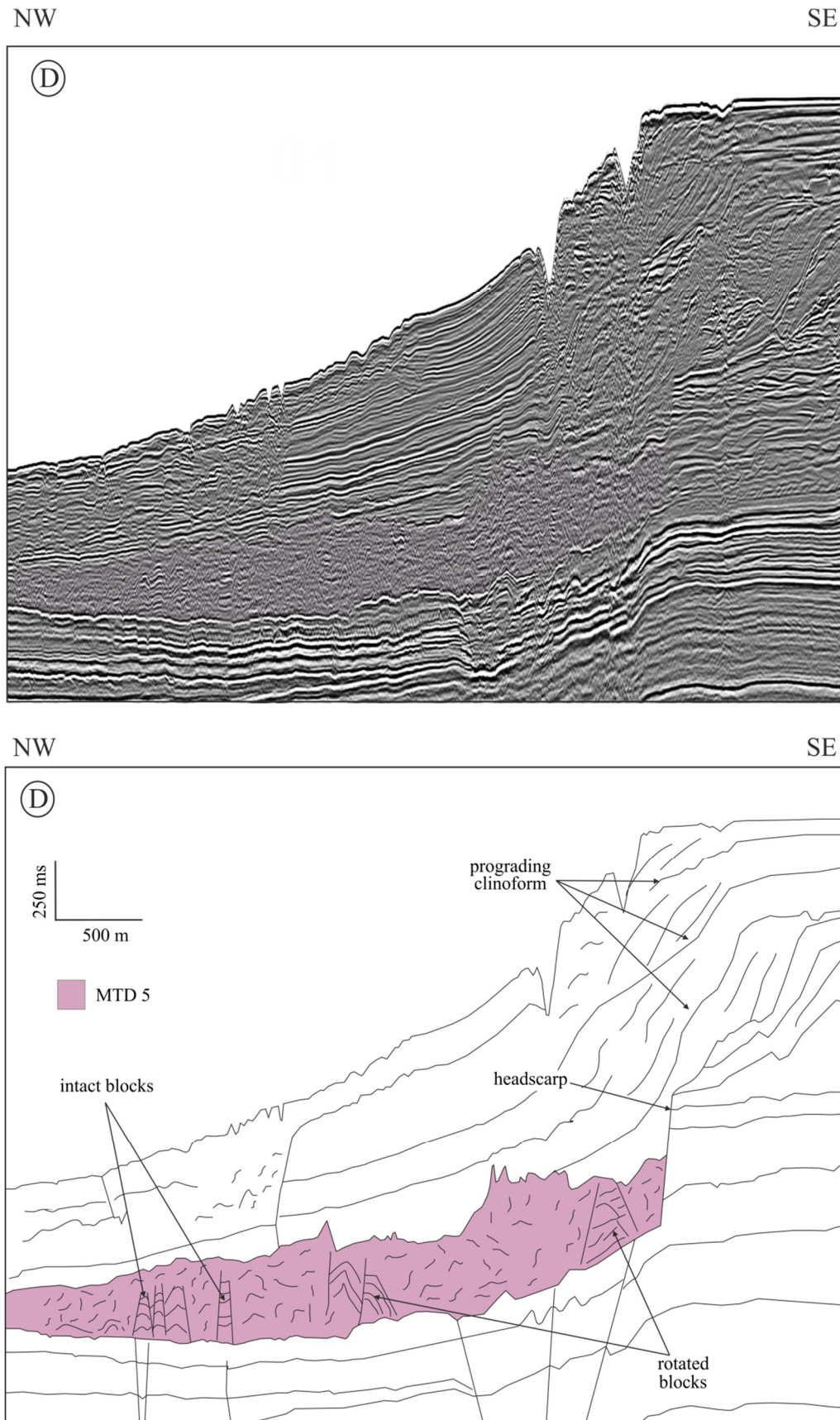
Figure 4.12 D) Uninterpreted and interpreted seismic profile (see Fig. 4.12A for location) showing MTD 5 headwall beneath prograding clinoform.

This U-shaped depression is interpreted as a slot (cf. Bull et al., 2009a) and appears to be isolated. Unfortunately it cannot be traced downslope because of the wide grid spacing of the 2D lines. Further downslope, the basal surface cuts down stratigraphy and forms two wide bottom depressions (Fig. 4.12B). The ramps that link the basal surface at these depressions are at least 250 ms high. The north-westerly ramp is associated with underlying faults but interestingly, the negligible vertical throws of the faults do not in any way conform to the vertical offsets of the basal surface (Fig. 4.12B). This observation is consistent with similar observations made of MTD 1. In the distal region of MTD 5, the basal surface is concordant with underlying strata with pinch-out relationships observed at both the western and eastern lateral margins (Fig. 4.12C).

The upper surface of MTD 5 is marked by a high amplitude, positive reflection that is generally continuous and sometimes concordant with the basal surface (Fig. 4.12). The upper surface has a smooth topography for the greater part of MTD 5 (Figs. 10b and 10c), but some irregular features were observed especially in the headwall region. This irregular geometry is interpreted to be related to the internal morphology of MTD 5 (Figs. 4.12D and 4.12E).

The internal seismic character of MTD 5 is dominated by transparent and chaotic facies (Fig. 4.12) similar to the MTDs described in the previous sections, although there are high amplitude coherent seismic reflections, bounded by normal faults close to the headwall region (Fig. 4.12D). These high amplitude coherent reflections are interpreted as intact blocks.

The western and eastern lateral margins for the largest portion of the perimeter of MTD 5 are represented by an abrupt ramp that cuts up stratigraphy from the basal surface (Fig. 4.12C). They separate the chaotic seismic facies of MTD 5 from the adjacent undeformed strata. The maximum height of both lateral margins is c. 150 ms measured in the proximal southern
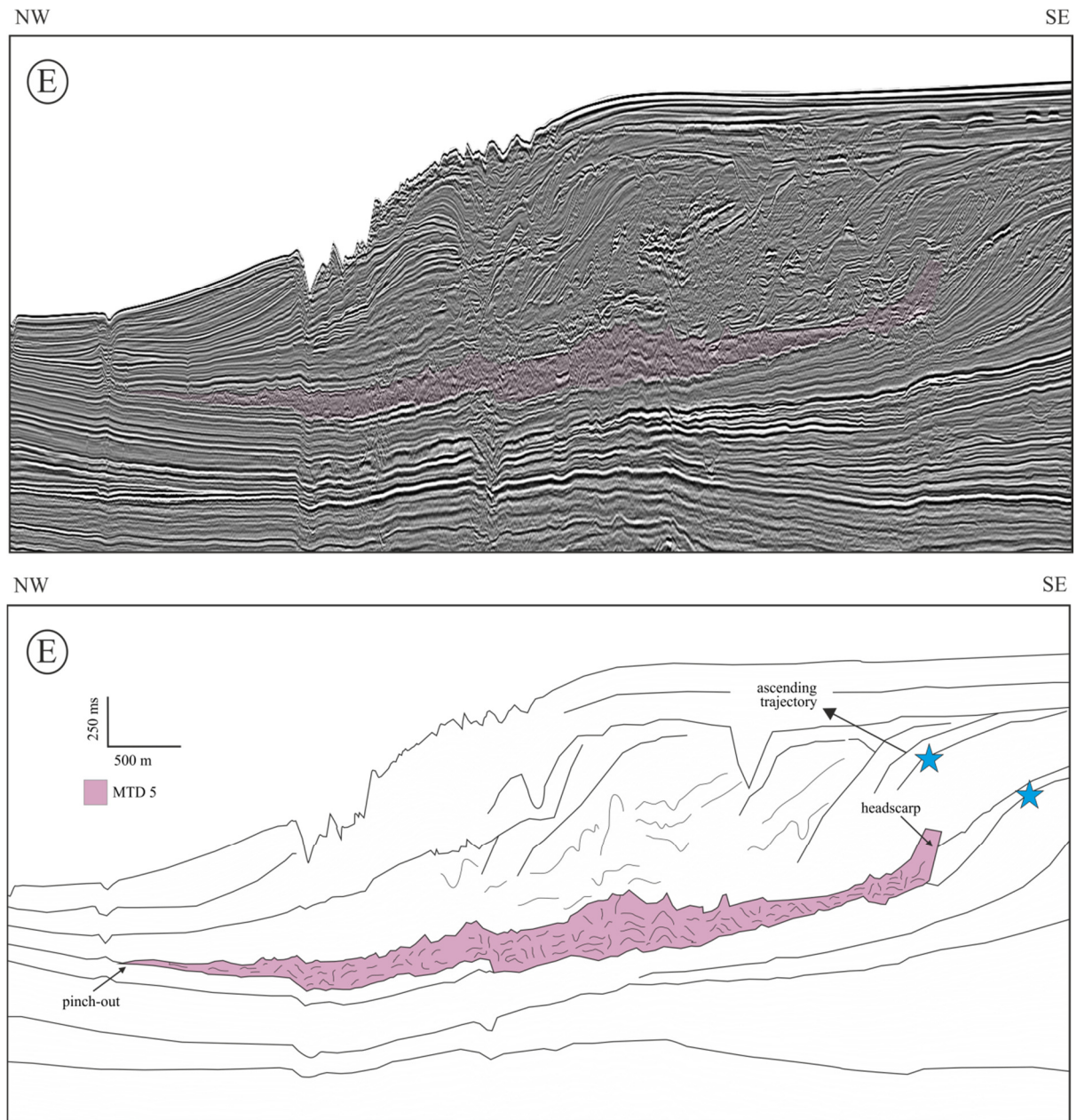
Figure 4.12 E) Uninterpreted and interpreted seismic profile (see Fig. 4.12A for location) showing Secondary headwall interpreted to be the consequence of the main headwall in Fig. 4.12D. The blue stars mark the position of the rollover points of the clinothemes embedding the MTD 5.

region. However, downslope in distal area of MTD 5, both the western and eastern lateral margins taper to a pinch-out (Fig. 4.12C line 06). The western lateral margin of MTD 5 extends up to the seabed, especially in the proximal southern region forming a depression on the present day seabed (Fig. 4.8B), whilst becoming increasingly buried in distal regions. In map view, both lateral margins have segments with a NNW-SSE and a NW - SE orientation which suggests NW transport direction for MTD 5 (cf. Bull et al., 2009a).

The down-cutting or up-stepping of the basal surface coupled with laterally migrating style of erosion observed at the margins imply that MTD 5 cannibalised and eroded the pre-existing sedimentary sequence during its failure and emplacement.

4.4.2.6 MTD 6

MTD 6 is the youngest and largest of the mass transport deposits in the study area (Figs. 4.7, 4.8 and 4.9). It forms a two lobed deposit separated by the Aetoa Seamount (Fig. 410A). MTD 6 covers an area of 22,397 km^2 with an estimated volume of 3,733 km^3 (Fig. 4.13A). The southern lobe being the larger of the two lobes covers an area of 12,400 km^2 and has a frontal length of c. 180 km. The northern lobe covers an area of 9,997 km^2 with a frontal length of c. 160 km (Fig. 4.13A). As with the other MTDs described in this study MTD 6 has considerable variation in thickness. As with MTDs 1 - 4, the headwall of MTD 6 is not visible on the available dataset (Fig. 4.13).

The basal surface of MTD 6 is marked by a low amplitude negative reflection similar to the other basal surfaces described in previous sections. In the northern lobe, the basal surface is continuous and truncates the underlying undeformed strata (Fig. 4.13B), which suggests that the MTD was erosive in this region. In contrast, in the southern lobe the basal surface is mostly irregular and appears to be generally concordant with the underlying undeformed strata (Fig. 4.13C). However, it is characterized by V-shaped incisions which are
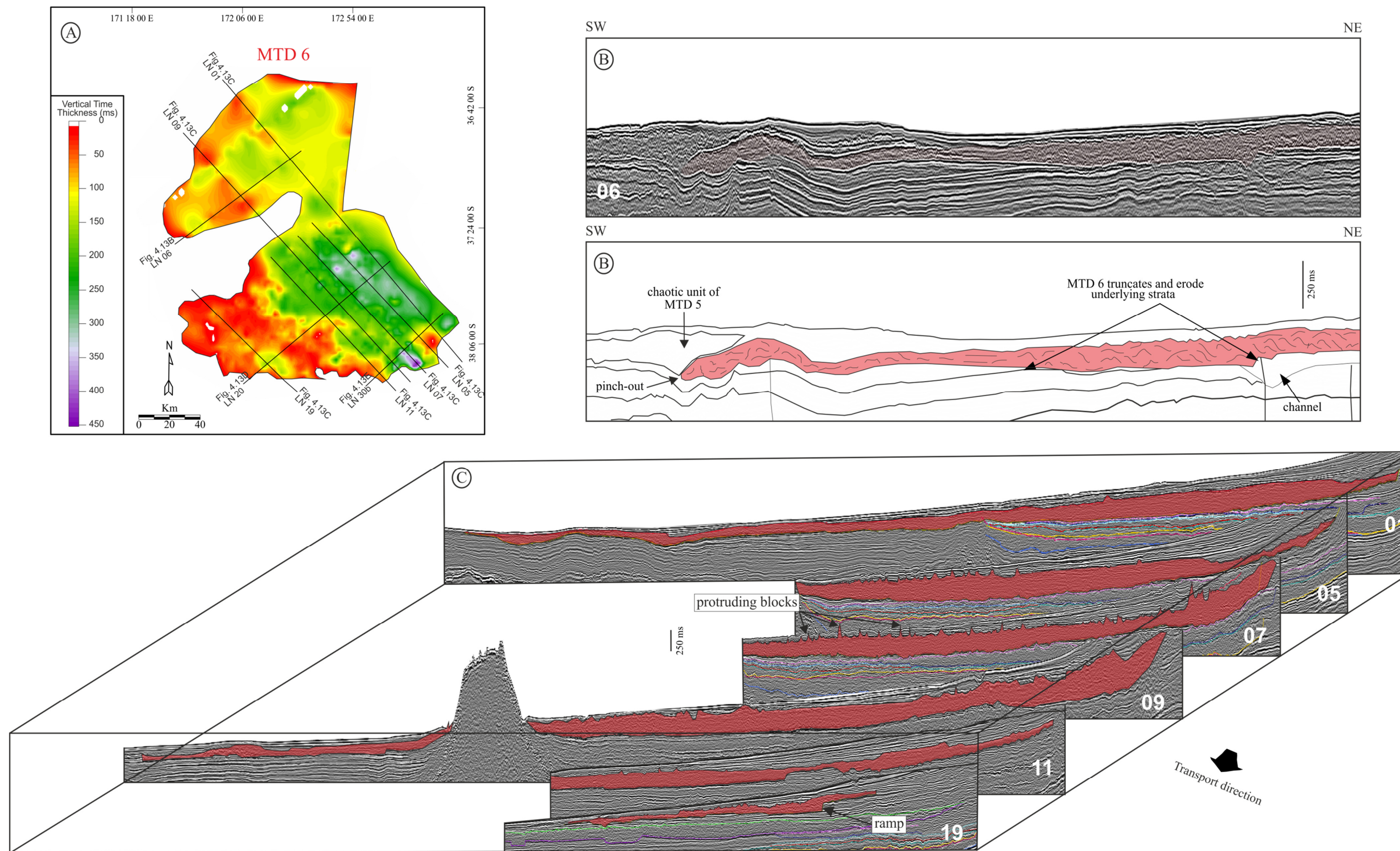
Figure 4.13 A) Isopach map for the MTD 6. Black straight lines show the 2D seismic profiles discussed in text (B) Seismic line showing the erosional basal surface of the northern lobe of MTD 6. (C) Fence diagram showing variable geometry of MTD 6 lateral margin. Notice how the basal surface is generally concordant with the underlying stratigraphy in the southern lobe.

preserved (Figs. 4.13D and E) ranging in depth from c. 20 – 50 ms and can be as wide as 500 m wide. These incisions are interpreted as grooves (cf. Bull et al., 2009a; Gee et al., 2006); their presence indicates the transportation of rigid blocks within the deposit.

Towards the margins of the southern lobe of MTD 6, the basal surface cuts along different stratigraphic levels creating staircase geometries (Figs. 4.7C, 4.13D and E). Towards the south-western margin, the basal surface ramps up c. 100 ms of stratigraphy (Fig. 4.13D). More interestingly, three staircase geometries are observed towards the limits of MTD 6 (Fig. 4.13D) with heights ranging from 60 – 150 ms and a northeasterly inclination ranging from $30°$ to $40°$. The central of these ramps, is associated with a fault.

The upper surface of MTD 6 is represented by a high amplitude reflection similar to the other MTDs described in this study. The topography of the upper surface varies significantly. In the northern lobe, the upper surface has a generally smooth topography (Fig. 4.13B) and it is generally overlain by undeformed strata (Fig. 4.13C) (except in distal areas where it is overlain by the chaotic unit of MTD 5 (Fig. 4.13B). In contrast to the northern lobe, in the proximal region of the southern lobe, the upper surface is highly irregular and characterized by elongated ridge-like positive features similar to the topography observed in MTD 4. (Figs. 4.11C, 4.13D and E). These feature reach up to 250 ms in height and up to 200 m wide. They are sometimes observed to extend all the way through to impinge on the present day seabed especially in the central region of the southern lobe (Fig. 4.13C, line 07). They tend to be associated with underlying grooves observed on the basal surface and appear to have retained a high degree of internal coherency of reflections similar to that seen in MTD 5 (Fig. 4.12D). The positive structures observed in the upper surface of MTD 6 have previously been interpreted as mud volcanoes resulting from dewatering of deposit during emplacement (Uruski, 2008).
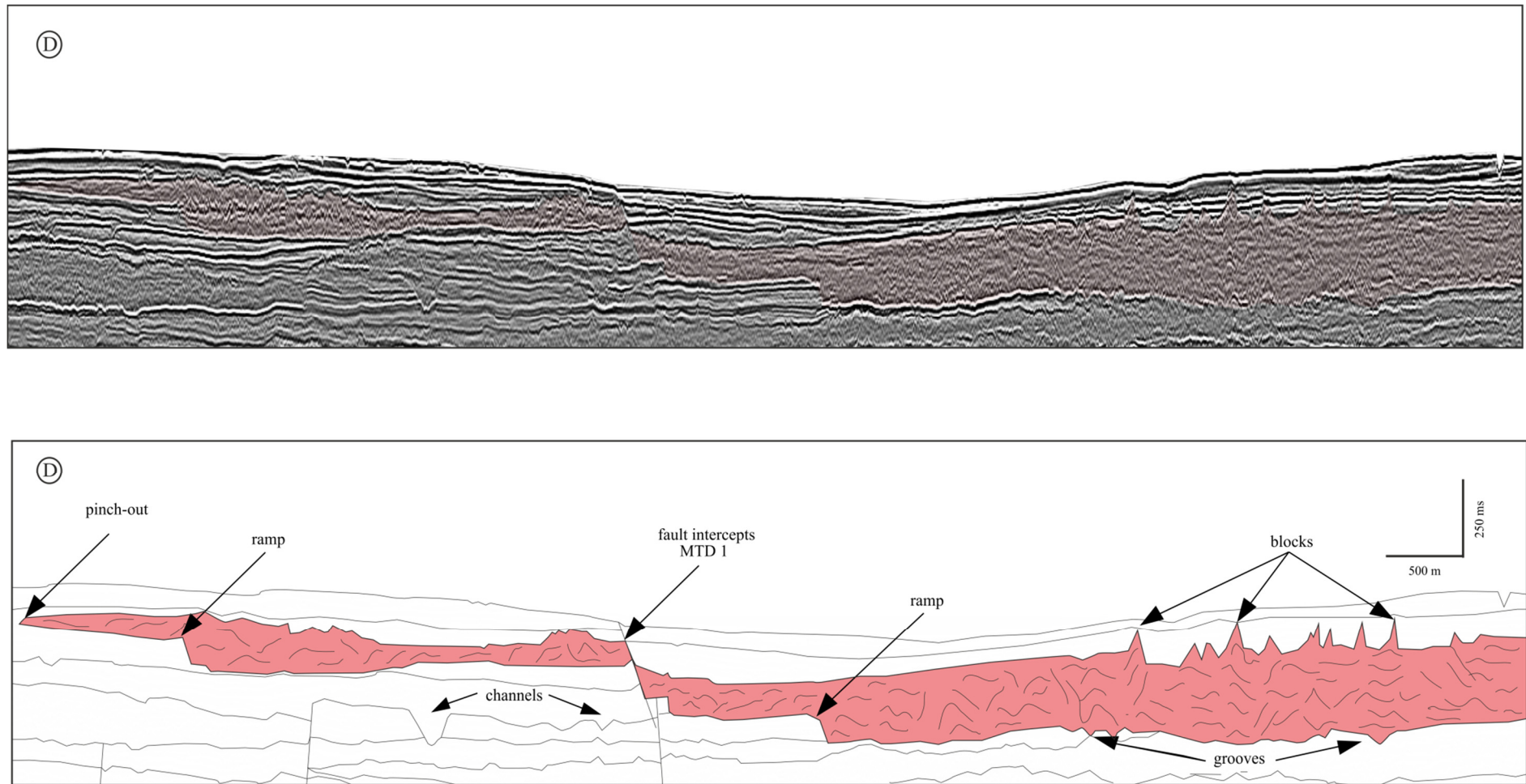
Figure 4.13 D) Uninterpreted and interpreted distal region of MTD 6 (southern lobe, see Fig. 4.13 A for location). Notice the stair case geometry of the basal surface. Also notice the alignment of the grooves beneath the diapiric features interpreted as blocks.
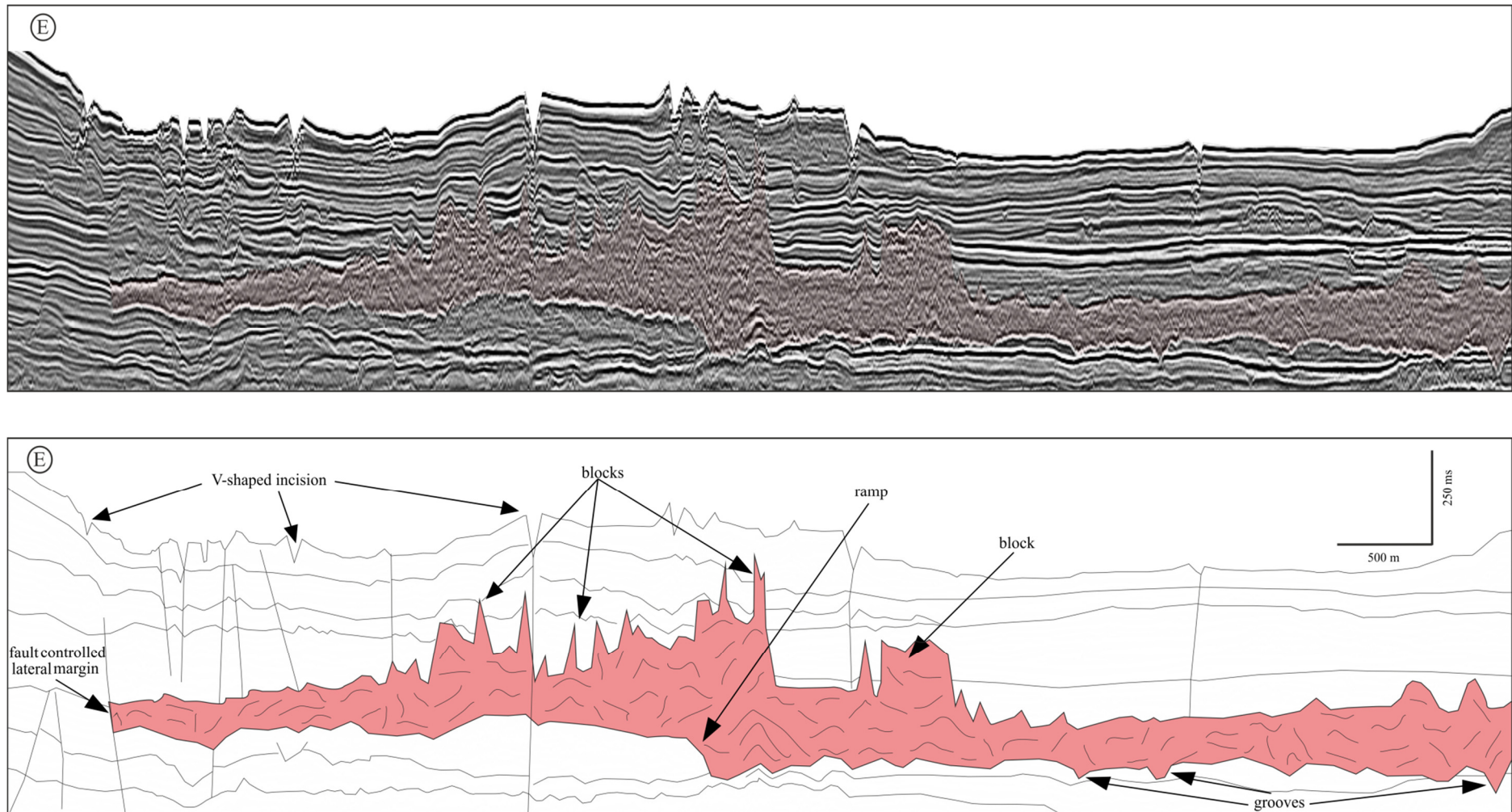
Figure 4.13 E) Uninterpreted and interpreted lateral margin of MTD 6 (southern lobe, see Fig. 4.13A for location). Notice the erosive basal surface, blocks as well as the fault controlled lateral margin.

In contrast, these structures are interpreted here as blocks within MTD 6 due to the fact that most of them are associated with underlying groves, suggesting that they are probably blocks scouring the basal surface during emplacement (Figs. 4.13C, D and F).

Protruding blocks of similar morphology like the ones observed in this study have been reported in previous studies (Bull et al., 2009a; Crutchley et al., 2012).

Although some internal coherency of reflectors is apparent within the main body of MTD 6, transparent and chaotic seismic facies dominate the entire MTD 6. In addition, some high amplitude coherent reflections are occasionally observed within the transparent and chaotic unit similar to those observed within MTD 5.

The NE-SW oriented southern lateral margin of MTD 6 is generally represented by an abrupt scarp that cuts up stratigraphy from the basal surface (Fig. 4.13C). The height of the scarp ranges from 30 ms to c. 300 ms. However, the NE-SW oriented northern lateral margin of MTD 6 taper to pinch-out for most of its length (Fig. 4.13A and C). The orientation of both lateral margins coupled with the reduction in thickness of MTD 6 towards the southwest suggests a SW transport direction for MTD 6 (cf. Bull et al., 2009a), different from the transport directions interpreted for the other MTDs in the study area.

4.4.3 Relationship between MTDs 1, 2, 3 and 4

The first four MTDs (1- 4) appear to overlap spatially over a large part of the study area (except for MTD 1 which extends further to the west) (Fig. 4.10A). They are separated in the main by a single continuous to discontinuous high amplitude reflection (Figs. 4.11B and 4.14B). It is difficult to define a precise boundary for the MTDs especially in the proximal eastern region where they are amalgamated. Since there is no clear correlation of their basal surfaces to respective headwalls (possibly because the headwalls lie outside the area of data coverage) it is legitimate to ask the fundamental question regarding their relationship namely:

Are these four MTDs discrete failures or were they emplaced as a single composite cogenetic deposit?

The fact that they have different lateral margins (Fig. 4.11C) implies that they are discrete MTDs. However, the fact that they are only separated by a single reflection suggests that they are closely related in time. It is also possible that the MTDs were each translated synchronously, and separately eroding their boundaries during emplacement. Similar high amplitude reflections within MTDs have been recognised in previous studies. Recently, (Watt et al., 2012b) suggested that high amplitude reflection between two discrete units does not necessarily represents a time gap between units, and that that the material above and below may have moved synchronously. Conversely, a boundary between successive MTDs of more than one reflection may suggest a distinct time gap between subunits of a period sufficient for resolvable thickness unit to be deposited on top of the first MTD.

4.4.4 Relationship between MTDs and the Aoteo Seamount

The spatial distribution and variation in thickness of the MTDs around the Aoteo Seamount suggests that the topography of the Seamount directly influenced the emplacement of the MTDs in the study area. The irregular-shaped Aotea Seamount is located west of the North Island, approximately 160 km downslope from the enormous N-S trending scarp present on seabed (Fig. 4.1). The isolated ENE trending seamount rises to 900 m from a depth of 2150 m and extends along its length for c, 50 km as previously mentioned. The location of the Aetoa Seamount in a region where basaltic volcanism is prevalent (Brodie, 1965) together with the shape and seismic facies suggests that it is volcanic (Figs. 4.14 and 4.15)

The MTDs identified in this study cluster around the Aetoa Seamount in plan view (Fig. 4.14A). On a representative dip oriented seismic profile (Fig. 4.14B), MTD 6 is observed on
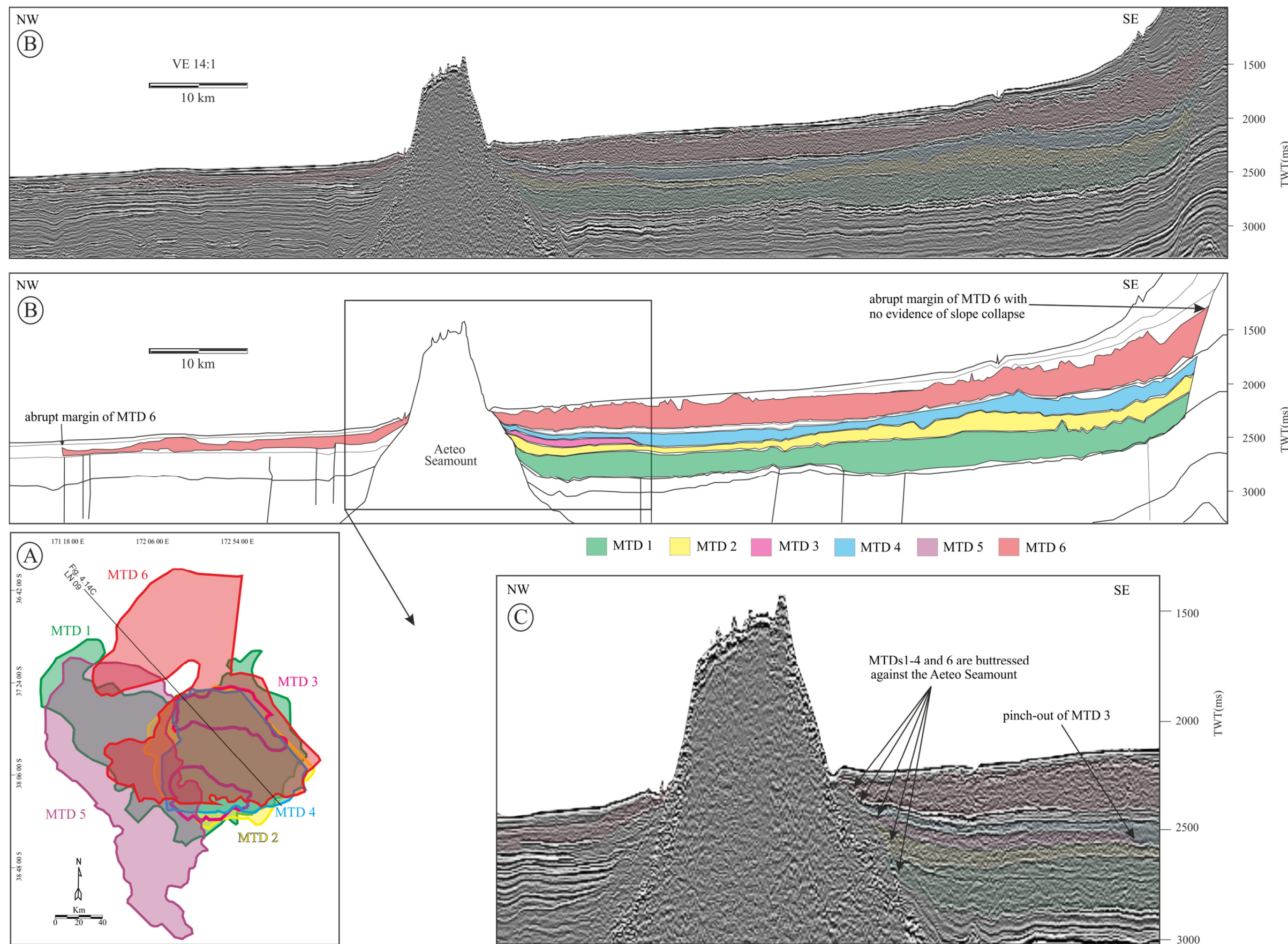
Figure 4.14 A) Map showing the relationship of the MTDs with the Aeteo Seamount B) A representative dip oriented seismic profile through the middle of the seamount C) Zoomed in portion of the flanks of the seamount shows that MTD 2, 3 and 4 onlap against the flanks of the seamount.
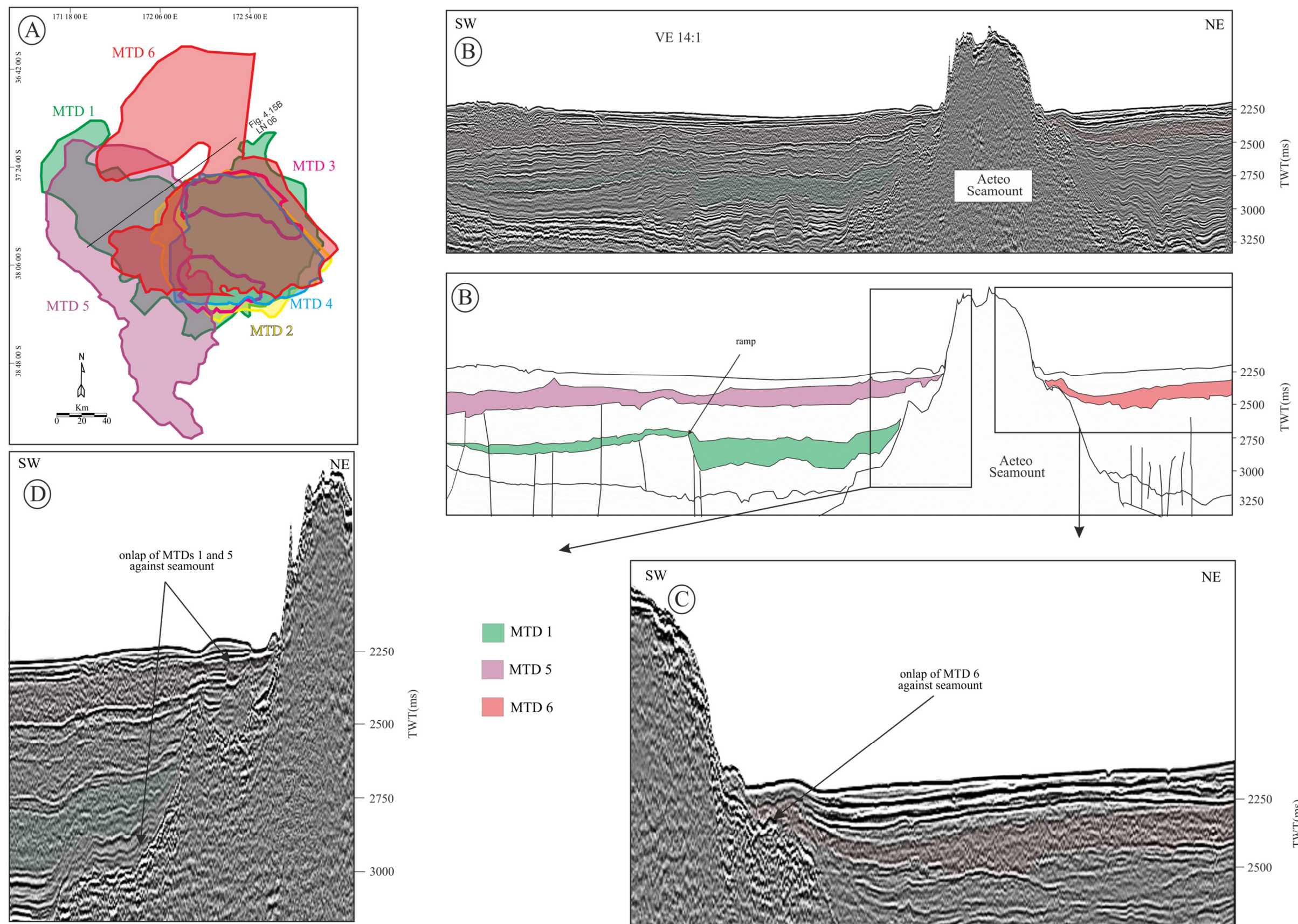
Figure 4.15 A) Map showing the relationship of the MTDs with the Aeteo Seamount B) A representative strike oriented seismic profile through the middle of the seamount C) Zoomed in portion of the flanks of the seamount shows that MTD 6 onlap against the flanks of the seamount D) Another zoomed in portion of the flank showing onlap of MTDs 1 and 5.

either sides of the seamount pinching out on its flanks. In contrast, MTDs 1-4 are only observed south of the seamount with pinch-out geometries on its southern flank. The Aetoa Seamount does not necessarily act as an obstacle to the emplacement of MTD 5 since it is not located entirely on its path. Although, MTD 5 tapers to pinch-out on the south-eastern flank of the seamount (Fig. 4.15). More interestingly, MTD 6 is buttressed against the Aeteo Seamount.

These relationships suggest that the Aeteo Seamount formed a rigid massif which restricted the advancement of the MTDs. More importantly, the symmetry of the deflection of MTD 6 around the northern and southern flanks of the seamount is a powerful kinematic indicator because it suggests a NE-SW transport direction consistent with the interpretation derived from the orientation of the lateral margins of MTD 6. Similar patterns have been reported in previous studies where an obstacle such as a mud volcano alters the flow path of an MTD (Richardson et al., 2011). Deflection such as this argues that the main emplacement mechanism in the distal area was run-out which is evidenced in the distal limits of MTD 6 in both the northern and southern lobes (Figs. 4.13B and D). In contrast, MTD 6 abuts a normal fault scarp in the south-eastern part of the lobe (Fig. 4.13E), suggesting that the fault was active and formed a seafloor scarp when MTD 6 was emplaced.

4. 5 Discussion

The mapping of the six giant MTDs in the Taranaki Basin revealed that they are discrete and widespread with significant volumes. In addition, they occur at different stratigraphic levels within the Plio-Pleistocene succession and show evidence of significant substrate erosion, which raises obvious questions about their source material, age, triggers and significance to hydrocarbon seal integrity. Each of these questions is dealt with in detail in the following sections.

4.5.1 Source materials for the MTDs: balancing substrate cannibalisation against run-out.

In the case of the six MTDs in the study area, it is proposed that their origin is not only related to the deposition (run-out) of collapsed slope material but also erosion and incorporation of the substrate (cannibalisation) (Figs. 4.11, 4.12 and 4.13). The lack of 2D seismic data coverage across the northern and eastern areas of the shelf edge does not allow us to make an unambiguous connection between MTDs 1 – 4 and their respective headwalls. However, the spatial organisation of the MTDs compared with the physiography of the shelf edge coupled with the E - W orientation of their lateral margins (Fig. 4.16A) and the gradual reduction in thickness of the four MTDs to the west (Fig. 4.10B) suggest that the headwalls of MTDs 1 – 4 must lie to the east. It is conceivable that MTDs 1 - 4 were originally sourced from the lower eastern shelf edge (Fig. 4.16A).

In order to constrain the source material and quantify how much of the MTD volume is contributed via substrate cannibalisation and/or runout, an interpolation between seismic profiles was used to estimate the ratio of eroded /cannibalised area with the pinch-out/ run-out margin length (see Fig. 4.6B for method). This ratio was used as a proxy to estimate the amount of MTD material that was contributed by cannibalisation and/or run-out.

In the case of MTD 1, the fence diagram in Figure 4.11C shows strong evidence of erosion at the southern lateral margin (represented by abrupt truncation in lines 14, 20 and 26) and run-out further downslope (represented by pinch-out in lines 06 and 08). This relationship is clearly depicted in Figure 4.17A, although some pinch-out geometries are observed towards the eastern proximal limits of the deposit. Based on the ratio of cannibalised/run-out area and the thickness it is suggested that more than c. 60% of the MTD 1 volume was contributed via cannibalisation of the substrate and thus gives a ratio of 2,450/4,064 km^3.
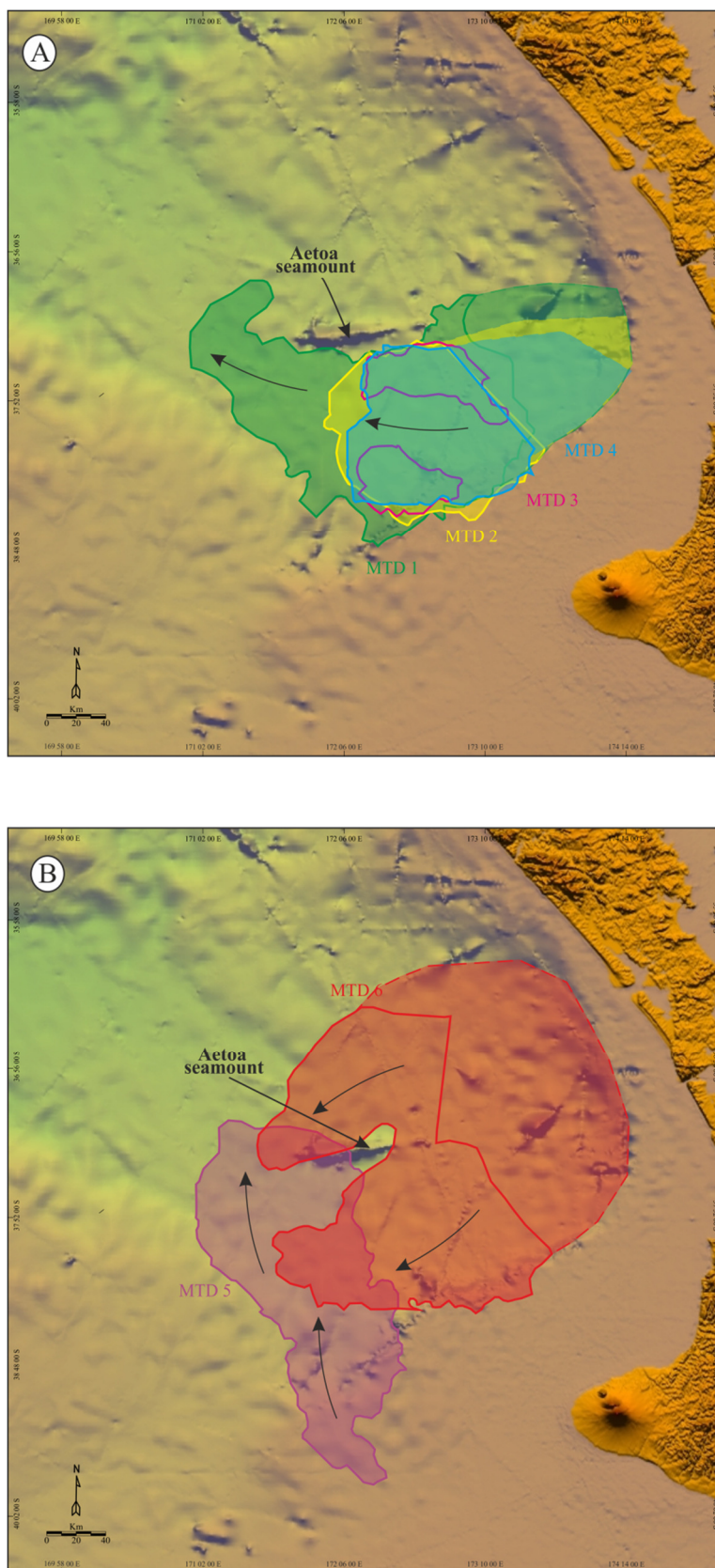
Figure 4.16. Maps showing the spatial relationships between the (A) MTDs 1-4 and the central region of the conspicuous scar on the present day seabed (B) MTD 5 and the southern embayment as well as MTD 6 with the north-eastwen edge of the scar.
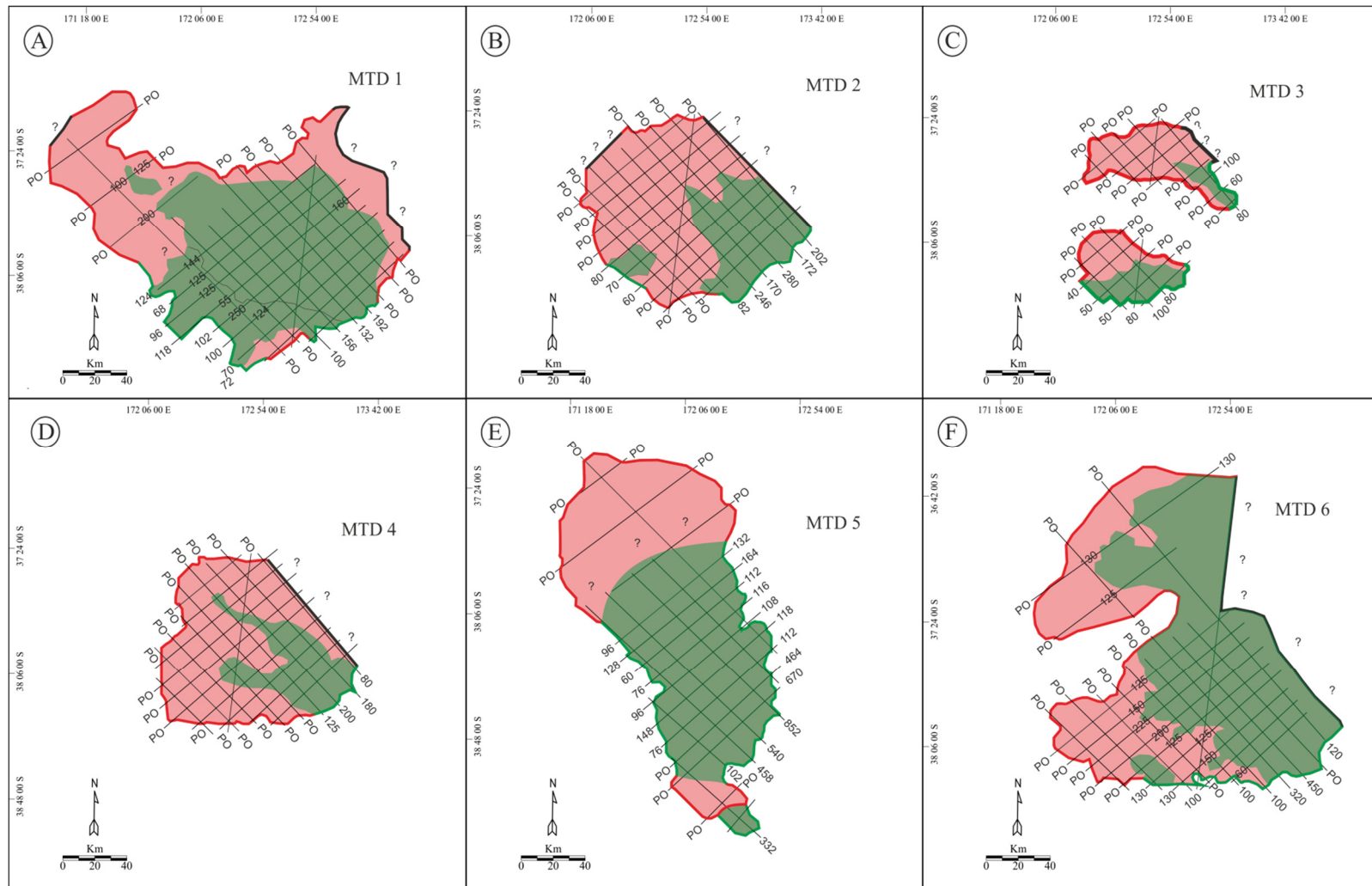
Figure 4.17. Illustration of how MTD material contributed via cannibalization or run-out was estimated. MTD 6 has a higher ratio of cannibalised/ remobillised material compared to MTDs 1 - 5. Green area represents interpreted cannibalised area while red area represents the interpreted pinch-out area. Black lines represents seismic profiles. Ramp heights are shown in numbers (ms TWT) while pinch-out geometry is illustrated with "PO".

On the contrary, there is less evidence of substrate erosion for MTD 2 because the lateral margins are defined by pinch-out configuration rather than ramp for most of its length (Fig. 4.11C lines 14, 20 and 4.17B). However, the irregular topography of the basal surface and the difficulty in differentiating the deposit from the underlying MTD 1 in places (Fig. 4.11B) suggest that part of MTD 1 may have been eroded during the emplacement of MTD 2. It is therefore suggested that c. 40% of the deposit was added by cannibalisation (Fig.4.17B, giving a ratio of cannibalised/remobilised material of 530/1,352 km^3.

It is difficult to estimate the ratio of cannibalised/remobilised material of MTD 3 due to the limited volume preserved (Fig. 4.11C lines 26, 20, 16 and 4.17C). From the morphology and geometry of MTD 3, it is interpreted that substantial parts of the deposit have been eroded/cannibalise by the emplacement of MTD 4. Therefore any estimation of the cannibalised/remobilised material for MTD 3 would not be representative.

Again, there is less evidence of substrate cannibalisation for MTD 4 (similar to MTDs 2) because the lateral margins are defined by pinch-out configuration rather than ramp for most of its length (Figs. 4.11C lines 14, 20 and 4.17D). Therefore it is suggested that c. 40 % of the deposit was added by cannibalisation (Fig. 4.17D), giving a ratio of cannibalised/remobilised material of 384/961 km^3.

Of the six MTDs described in this study, only MTD 5 has a well-defined headwall imaged on the seismic data (Fig. 4.12D). This preservation of original relief allows the source area of the failure to be constrained. As argued earlier, the SE - NW orientation of the lateral margins, and the presence of an associated headwall, which is located in the south beneath the shelf edge (Fig. 4.16B) together suggest a source area from the south. This evidence, together with the fact that the limits of the headwall of MTD 5 accords well with the scar on the seabed (Fig. 4.16B), suggests that the failure of the MTD 5 is related to the scar that forms an embayment (encircled by white dotted lines in Fig. 4.1) observed on the present day seabed

towards the south. A significant part of the volume of MTD 5 was added by substrate erosion and cannibalisation. Although, the basal surface appear to be concordant with the underlying sediment (especially in the south-western region of the MTD 5), there is evidence of abrupt truncations observed at both lateral margin (Fig. 4.12C lines 16, 20, 24 and 4.17E) as well as series of basal truncations (Figs. 4.12B and C, lines 20 and 24) of underlying sediments. Further downslope, the lateral margins pinches out suggesting MTD ran-out towards its distal limits (Fig. 4.12C, line 06 and 4.17E). These observations suggests that perhaps more than c. 60% of the MTD 5 volume similar to MTD 1 was contributed via cannibalisation of the substrate (Fig. 4.17E), thus giving a ratio of cannibalised/remobilised material of 1,585/2,643 km^3.

The NE - SW orientation of the lateral margins of MTD 6 suggests that it was sourced from the north-eastern edge of the scarp observed on the present day seabed (Fig. 4.16B). This implies that the translation direction of MTD 6 is significantly different from the translation direction of the other MTDs in this study and orthogonal to the N - W downslope direction. Since the available dataset does not extend to the presumed headwall it is difficult to ascertain this discrepancy. However, it is unlikely that MTD 6 translated in the northwest downslope direction because a critical examination of the southern lateral margin (Figs. 4.7C and 4.13C) shows that it is not associated with collapsed clinoforms. The margin is rather defined either by either pinch-outs or lateral truncations. Furthermore, the fact that MTD 6 is deflected around the flanks of the SW – NE oriented Aetoa Seamount (Fig. 4.14A and B) and appears to climb by ramping up against the flanks in the central region (Fig. 4.15C) suggest a source area from the northeast. This evidence coupled with the gradual reduction in thickness towards the southwest observed in the two lobes until they taper to pinch-out in distal areas (Fig. 4.10B), clearly provide further evidence for a southwest direction of propagation.

The extent of the slope failure region of MTD 6 is presumably related to the large remnant topographic feature observed on the present day seabed, and which results from incomplete healing of the topography left by this submarine failure and the fact that it is the youngest of the series of large slope failures in this area. Although MTD 6 appears to be characterised by a continuous basal surface, there is pronounced evidence for basal truncation of the underlying sediments. This is clearly seen from the basal grooves underneath protruding blocks (Fig. 4.13C), frontal and lateral truncations in the southern lobe (Fig. 4.17F), and basal truncation in the northern lobe (Fig. 4.13B). Based on these observations it is suggested that MTD 6 has undergone more cannibalisation compared to the other MTDs in this study. It is crudely estimated that MTD 6 has undergone c. 70 % of substrate cannibalisation (Fig. 4.13C, lines 01, 05, 07, 09, 11, 19 and 4.17F), thus giving a ratio of cannibalised/remobilised material of 2,403/3,733 km^3.

Subtrate Cannibalisation: Summary

Based on the estimated values for cannibalised/run-out material reported for the six MTDs in the study area, it is evident that a significant proportion of all six MTDs have had their remobilised volumes added by substrate cannibalisation during the emplacement of the MTDs. Elsewhere, a significant proportion of the final submarine MTD volume have been reported to be added by substrate incorporation. For instance, (Prior et al., 1986) reported that 50% of the 0.06 km^3 Kitimat MTD at fjord-front delta in British Columbia was incorporated through basal erosion. Also, a similar proportion (at least 40% of 1050 km^3) of incorporated substrate material was reported for the Matakoa debris flow, offshore East Cape New Zealand (Joanne et al., 2013). (Gee et al., 2007) estimated that 80% of the total volume of the giant Brunei Slide was incorporated by substrate cannibalisation.

It is worth noting that the estimated eroded and/or run-out volumetric proportion of the MTDs in this study has not taken into account the effect of subsequent compaction of the

sediments after failure. This is because of the lack of petrophysical data as no well has been drilled in the study area. Therefore, the estimated volumes are bulk volumes corresponding to the amount of displaced material observed today.

Furthermore, a high confidence level is placed on the estimated cannibalised/remobilised volume of MTD 5 because the headwall and lateral margins are well constrained on the available dataset. For the other MTDs, the estimated eroded and/or deposited volumetric proportions represent the minimum volumes due to the uncertainty in the full areal extent of each MTD stemming from the incomplete seismic coverage and resulting uncertainty in the observation of headwall.

When the fence diagrams (Figs 4.11C, 4.12C, 4.13C and 4.17) and the cannibalised area of the six MTDs (Fig. 4.17) are compared, it is evident that the MTDs are laterally erosive in proximal areas and tend to run-out in distal areas. In addition there is no clear preference for basal truncation in the MTDs. These observations suggest that the erosive power of the MTDs is more acute in proximal areas than distal areas. Prior studies show that the degree of basal erosion is often determined by the rheology of basin-floor sediments (Joanne et al., 2013). Sandy material is more prone to erosion than silty and clayey material (Charlton, 2007) since sand grains have low cohesive electro-chemical forces. The silt fraction may thus play a role in the degree of cannibalisation.

More interestingly, MTD 6 (having a south westerly translation direction different from the other MTDs in this study) is the least cannibalised. This suggests that there could be a relationship between cannibalisation and MTD direction and trigger (see section 4.5.3).

4.5.2 Age control

The limited penetration and lack of core data in the study area prevents direct dating of the MTDs. However, we propose a relative age for the various MTDs studied based on their

depth, overlying sediment thickness observed on seismic data, and sedimentation rates calculated from previous studies from Wanui-1 located adjacent to the grid of available seismic data (Fig. 4.5).

(Hayward, 1984) proposed sedimentation rates as high as 10 cm/100 yrs in the Giant Foreset facies during the Mid-Pliocene (Waipipian) and Early Pleistocene (Nukumaruan) deduced from micropaleontological studies (Fig. 4.18A). However, during the intervening Mangapanean Stage, sedimentation rates were low, generally only 2 - 3 cm/100 yrs. The high sedimentation rates reported by (Hayward, 1984) are consistent with (Hansen and Kamp, 2006a) who observed slumping on their seismic record in two distinct periods Late Pliocene (Waipipian to Mangapanian), and Early Pleistocene (upper Nukumaruan to Castlecliffian) (Fig. 4.18B).

Based on these observations and by jump correlating key seismic horizons in Figure 4.18B into the present study area, it is proposed that MTD 1 - 4 were deposited during the Waipanian to Mangaoanian, therefore an age between c. 3.6 Ma (base Wapaipanian) to 3 Ma for MTDs 1 – 4 is assigned. While for MTD 6, an age of c. 1.8 Ma which corresponds to the age of the Upper Nukumaruan is suggested. MTD 5 appears to be separated from MTD 1 by an average of ca. 200 m of undeformed strata (Fig. 4.9). However, there is strong evidence to suggest that the basal surface of MTD 5 eroded and incorporated the underlying strata during its emplacement (Fig. 4.12C). Consequently, the first continuous reflection below the chaotic seismic facies of MTD 5 would not represent the time of emplacement, and the age of the MTD 2 would be overestimated. However, I suggest an age of c. 2 Ma for MTD 5.
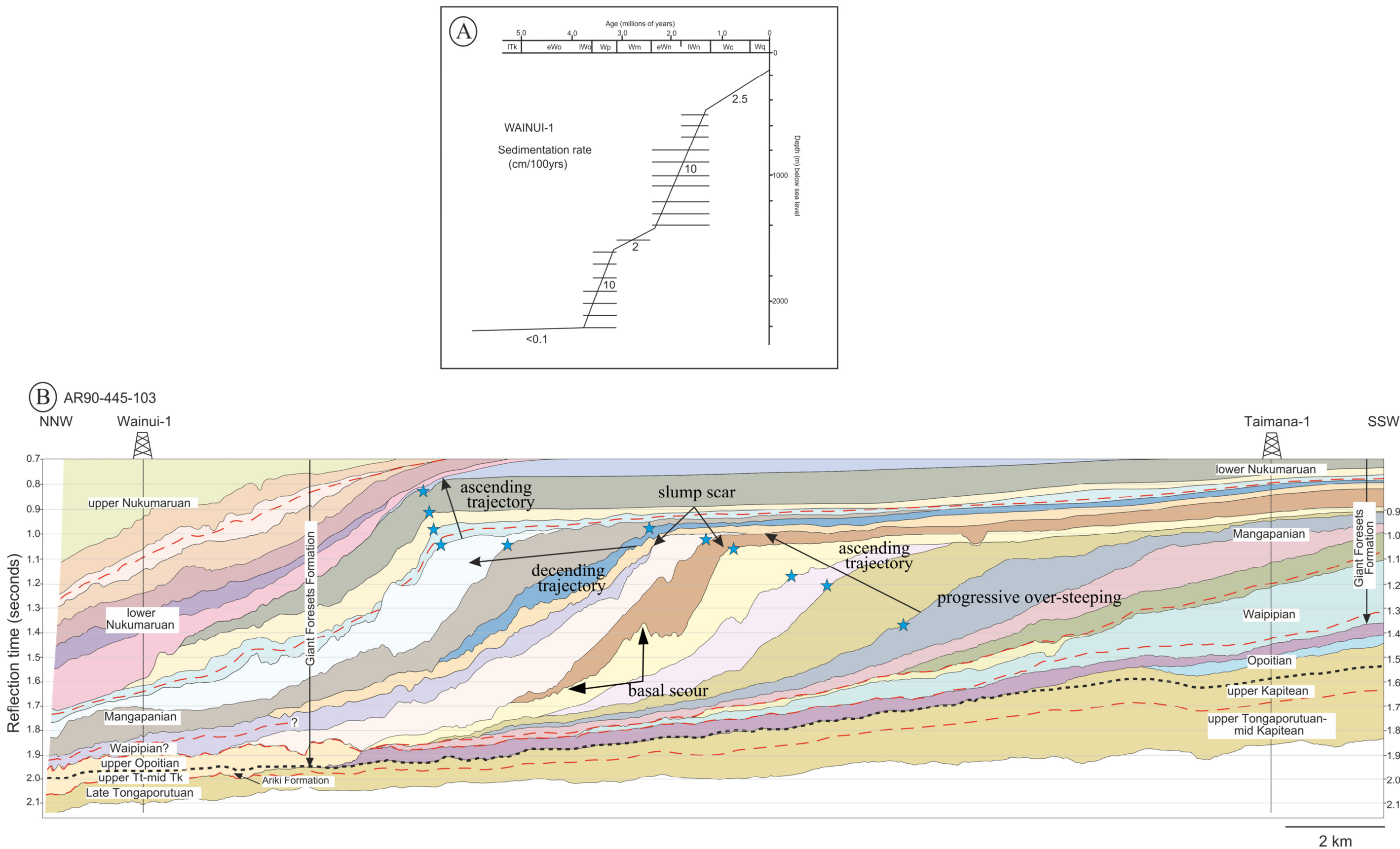
Figure 4.18 A) Sedimentation rate based on biostratigraphic data from Wanui-1well, Taranaki Basin (Data from Hayward ,1984). (B) Schematic interpretation of seismic line AR90-445-103 (see Fig. 4.5 for location) with approximate positions of biostratigraphic correlation (modified from Hansen and Kamp, 2006).The blue stars mark the position of the rollover points of the clinothemes embedding the MTDs.

4.5.3 Potential trigger for MTDs

Slope failure is believed to have been facilitated by rapid sedimentation related to the rapid progradation of the modern continental margin towards the northwest during the Pliocene and Pleistocene. Rapid sedimentation will result in overpressure because the rate of sedimentation outstrips the ability of the sediments to dissipate the pore water adequately, thus decreasing the effective stress, the intergrain friction and the sediment strength (see Section 1.3.2.2).

Relative sea level trend can be estimated by examining the long-term trends of rollover trajectory (i.e., the pathway taken by the shelf-edge during margin development) of the clinothemes in seismic line AR90-445-103 (Fig. 4.18B) (sensu Dalla Valle et al., 2013; Helland-Hansen and Hampson, 2009). It was observed that from the Opoitian to Nukumaruan an ascending trajectory indicating sea level rise associated with progressive oversteepening of slope resulted in mass wasting. This is indicated by the development of headwall scarps along the bounding surfaces of progradational foresets. Above the Nukumaruan, water depth deepened again to outer shelf showing that sea level oscillated during this period.

Similarly, in the case of MTD 5 enclosed within a clinotheme (Fig.4.12E), a high-angle ascending rollover trajectory, with high aggradation is observed. This evidence indicates that MTD 5 was preconditioned for failure during relative sea level rise characterized by high sedimentation rates along the entire slope margin. It is assumed that the same mechanism of failure triggered MTDs 1 - 4 in the Deepwater Taranaki Basin. This assumption is based on the fact that MTDs 1 - 4 have a WNW basin-ward translation direction (Fig. 4.10B) almost similar to the NW translation direction of MTD 5.

However, it is very unlikely that same mechanism triggered MTD 6 given that during the late Nukumaruan to recent, the propagation front of the Giant Foresets Formation moved rapidly towards the north and west through to the present position of the shelf-slope break (Fig. 4.19) (Hansen and Kamp, 2006b; Soenandar, 1992). This is orthogonal to the interpreted
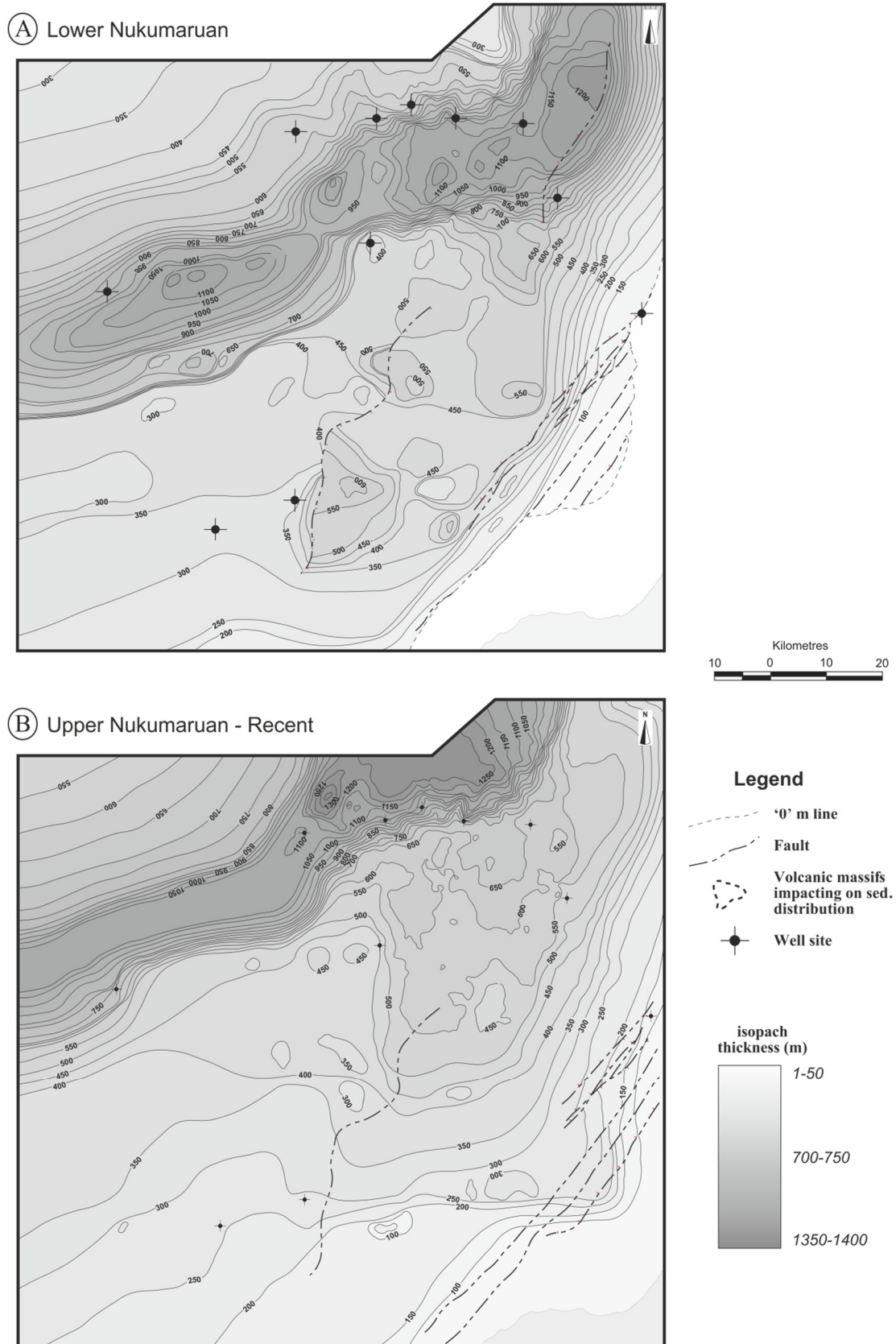
Figure 4.19. Isopach maps for northern Taranaki Basin for A) lower Nukumaruan and B) upper Nukumaruan–Recent intervals. Contours have been drawn at 50 m thickness intervals. '0' m line is the point at which section is no longer present due to post-depositional erosion (from Hansen and Kamp, 2006a).

translation direction of MTD 6, and suggests that another factor might be responsible for triggering MTD 6, such as an earthquake. This idea is especially plausible, considering that the area east of the projected headwall of MTD 6 was tectonically active after the deposition of the Giant Foresets Formation (Fig.4.2) (Soenandar, 1992).

Cyclic loading through the oscillatory transmission of seismic waves (Seed and Idriss, 1982) or in subaqueous sediments buried (in typical water conditions) no more than about 200 m, from the passing of travelling pressure waves at the sea surface (Seed and Rahman, 1978) will result in incremental accumulation of overpressure (because each fluid pressure response is incompletely dissipated before the next pulse) thus decreasing the effective stress, the intergrain friction and the sediment strength (see Section 1.3.2.2) The overpressure may rise to equal the burial pressure, hence reducing the effective stress to zero and in the absence of significant cohesion, the sediment now lacks shear strength and temporarily exists as a fluid (Maltman, 1994).

4.5.4 Comparism with other Slope failures

The calculated volumes for the six MTDs in this study rank them among the largest submarine slope failures at passive margins known to date (Table 2). MTD 6, in particular has a volume, five or six times higher than the passive margin megaslides off NW Africa, such as the Sahara Slide with a volume of 1100 km^3 (Masson et al., 1993) which is far less than the smallest MTD in the study area (MTD 3 with a volume of 377 km^3). However, the volume for MTD 6 is comparable with the Storegga Slide off Norway with a volume of about 3000 km^3 (Canals et al., 2004).

Given that Landslide volume is a key parameter in generating tsunamis as well as landslide dynamics (initial acceleration and maximum velocity), and the water depth (Løvholt et al., 2005; Masson et al., 2006; Tinti et al., 2006) and the fact that the gigantic Storegga Slide

Table 4.2: Comparison of the geological settings, volumes, areas, emplacement processes and speculated mechanisms of the MTDs in this study with other known MTDs.

Landslide	Geological Setting	Volume (km³)	Area (km²)	Emplacement Processes	Speculated Triggering Mechanism
MTD 1 (this study)	Passive margin, high Terrigenous input.	4,064	20,887	Dominant process appears to be substratum erosion.	High sedimentation rate with concomitant slope over-steeping
MTD 6 (this study)	Passive margin, high Terrigenous input.	3,733	22,397	Dominant process appears To be progressive deformation	Earthquake activity likely
Storegga **(Canals et al., 2004)**	Passive margin, sediment input to upper slope by ice sheets during cold periods.	3,000	44,000	Wide range of processes from avalanche and block sliding to debris flow and mud flow.	Earthquake activity associated with post glacial isostatic rebound. Presence of gas and gas hydrate
MTD 5 (this study)	Passive margin, high Terrigenous input.	2,643	18,364	Dominant process appears to be substratum erosion.	High sedimentation rate with concomitant slope over-steeping
MTD 2 (this study)	Passive margin, high Terrigenous input.	1,325	11,548	Dominant process appears to be substratum erosion.	High sedimentation rate with concomitant slope over-steeping
Sahara **(Masson et al., 1993)**	Passive margin, minimal Terrgineous input. Highly Productive surface water	1,100	30,000	Dominant process appears to be debris flow, plus rafted tabular blocks with a basal shearing layer.	Unknown
MTD 4 (this study)	Passive margin, high Terrigenous input.	961	10,128	Dominant process appears to be substratum erosion	High sedimentation rate with concomitant slope over-steeping
MTD 3 (this study)	Passive margin, high Terrigenous input.	377	4,276	Dominant process appears to be substratum erosion.	High sedimentation rate with concomitant slope over-steeping
BIG'95 **(Canals et al., 2004)**	Passive margin. Failure occurred adjacent to the 900 km long Ebro River.	26	2,000	Large km scale tabular landslide blocks and debris flow matrix.	Earthquake activity likely

triggered a tsunami locally exceeding 20 m in height (Bondevik et al., 2003), the large volume of the giant MTDs in the Deepwater Taranaki Basin immediately raises the question of whether they triggered major tsunamis?

4.5.5 Significance of MTDs to Hydrocarbon exploration

Since the Deepwater Taranaki Basin is an extension to the northwest of New Zealand only currently producing sedimentary basin, the Taranaki Basin, it has been investigated for its petroleum potential using available seismic data tied to shallow onshore wells (Uruski, 2008). Although the Giant Foresets Formation has never been the target of active hydrocarbon exploration in the Taranaki Basin, comparison with the mud-dominated Mississippi Fan, Gulfof Mexico, suggests that possible reservoir facies may be contained within channel sands, unchannelised channel lobes and potentially sand-prone levees immediately adjacent to initial channels (Hansen and Kamp, 2006b).

Given that the geometry and extent of the MTDs in the Deepwater Taranaki Basin have been constrained (this study), it is conceivable that the MTDs can act as seals to the Miocene channels as observed on our dataset since their onshore equivalents have been investigated to be mud dominated (Hansen and Kamp, 2006a). However, it is important to consider the role erosion and incorporation of substrate material may have played in compromising seal integrity. A key factor noted earlier that determines the degree of basal erosion is the rheology of basin-floor sediments (Joanne et al., 2013). Sandy material is more prone to erosion than silty and clayey material (Charlton, 2007) since sand grains have low cohesive electro-chemical forces. Therefore, it is conceivable for MTDs that largely comprise cannibalised material from the substrate (such as the MTDs in this study), that there may be a significant percentage of coarse sand to silt which could possibly compromise the seal integrity of such MTDs. Nonetheless, a vital first step in understanding the influence of MTDs on the seal integrity is in recognising highly cannibalised MTDs and distinguishing
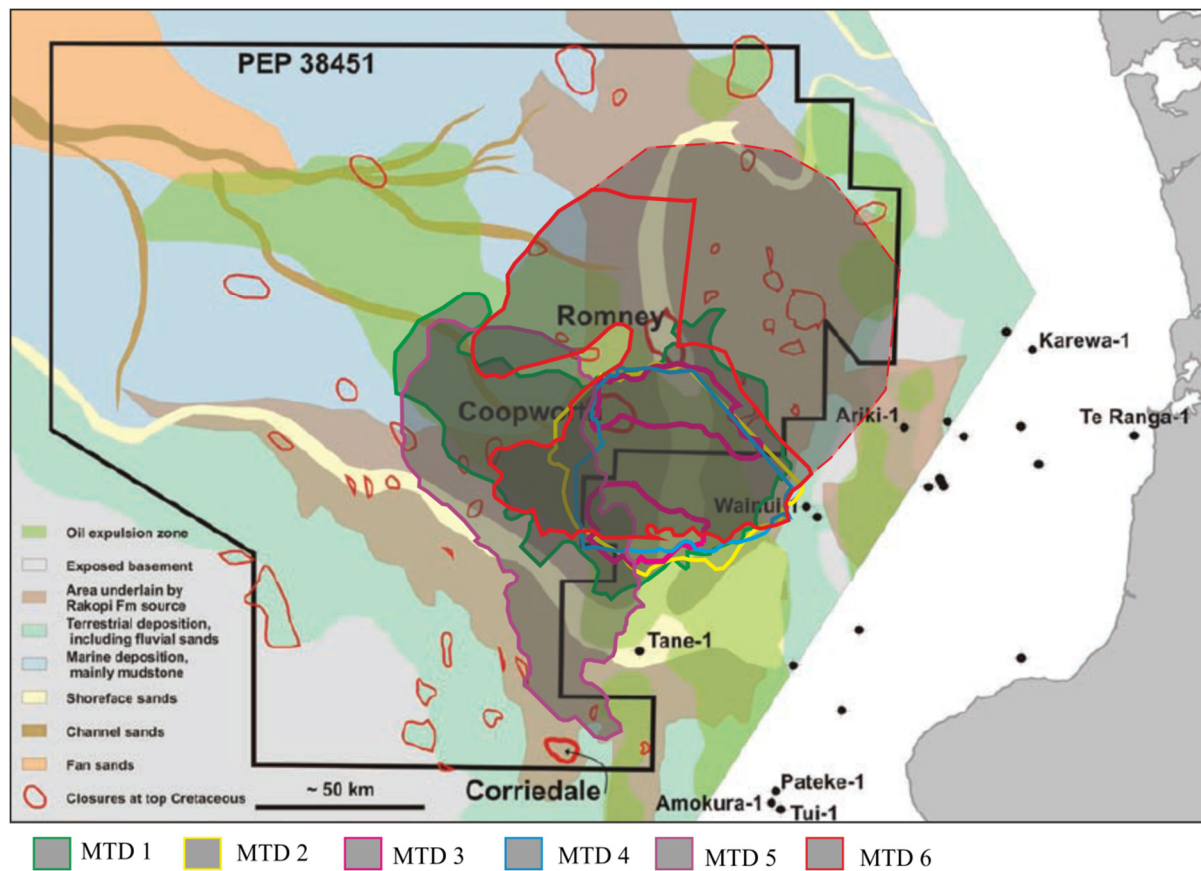
Figure 4.20. Play fairway map showing Palaeogeography at top Cretaceous time (65 Ma) (modified from Uruski, 2008). Notice how the Coopworth prospect is overlain by MTDs 1-4 and 6. While the Romney prospect is overlain by MTD 6.

them from purely depositional MTDs that have large run-out distances. It is also worth noting that the underlying units that exhibit most signs of having been cannibalised contain large deepwater submarine channel levee systems, and these have evidently been incorporated into the MTDs (see appendix, Fig 4.33).

Furthermore, based on the extrapolation of known geology (including source rock, reservoir and seal reports) from onshore New Zealand as well as wells and seismic below the shelf into deepwater, three firm prospects (Romney, Coopworth and Corredale) were defined (Fig. 4.20). One of the interesting aspects that arise from this study is that the MTDs described inthe chapter overlie these Late Cretaceous prospects and more specifically the Late Miocene channels (Figs. 4.20). It is suggested that if these prospects are to be drilled the effect of the MTDs on the design and installation of offshore facilities should be taken into consideration due to the increased consolidation of the MTD material (Shipp et al., 2004). If penetrating through these MTDs is unavoidable then an appropriate drilling plan should be put in place.

4.6 Conclusions

A high-resolution bathymetric and two-dimensional (2D) seismic reflection data from the Deepwater Taranaki basin (North New Zealand) has allowed a detailed morphological analysis of six giant mass transport deposits within the Plio-Pleistocene Giant Foreset Formation. The following conclusion can be made:

1) MTDs 1-5 have a north-westerly transport direction and MTD 6 has a south-westerly transport direction.

2) All six MTDs were emplaced between 3.6 Ma and 1.8 Ma and have volumes ranging between 377 km^3 and 4,064 km^3, thus they are among the largest submarine MTDs known from passive continental margins.

3) An estimation of 70% of the final volume of MTD 6 was contributed from substrate cannibalization, greater than any of the other MTDs in the study area.

4) The failure of MTD 1-5 is believed to have been facilitated by rapid sedimentation on the shelf margin from Late Miocene to recent times coupled with concomitant rapid overstepping of slope indicated by the development of headwall scarps along the bounding surfaces of progradational foresets. MTD 6 is believed to have been triggered by tectonic activity (e.g faulting) given that it was emplaced in a translation direction different from the other MTDs in the study area.

5) The acute substrate cannibalisation of MTD 6 and the different translation direction compared to the other MTDs in the study area suggests a relationship between MTD trigger and cannibalization of the substrate.

Chapter 5

5.0 Insights into the dynamics of a giant mass transport deposit from high-resolution 3D seismic data, Deepwater Taranaki Basin, New Zealand.

5.1 Summary

Analyses of a high resolution three-dimensional (3D) marine seismic dataset acquired in the Deepwater Taranaki Basin, New Zealand provides insights into the dynamics of emplacement of the latest submarine mass transport deposit (termed MTD 6) within the Giant Foresets Formation.

MTD 6 consists of distinctive domains (labelled A – E) that detach on a common basal surface except for the Domain E that detaches on a higher stratigraphic level. Each domain of MTD 6 is characterised by different internal deformation fabrics, and a translation direction that is not consistent with the orientation of the two sets of underlying grooves observed on the basal surface. Domains A – C show evidence of deformation and remobilisation of c. 30% of a lower transparent interval while Domain D is characterised by a partial or complete loss of seismic character coupled with c. 30% reduction in thickness compared to adjacent domains. Due to the deformation style, the transition across domain boundaries and the observed volume loss a progressive stratal disaggregation is inextricably linked with gravity spreading as the mode of emplacement of MTD 6. Ranking of the kinematic indicators based on their reliability suggest a dominant SW translation direction for MTD 6.

This study highlights the power of 3D seismic data in unravelling the detailed processes involved during MTD emplacement and which may have significant implications as regards the translation and emplacement of other submarine slope failures in other continental margins.

5.2 Introduction

The recognition and description of six large MTDs within the Plio-Pleistocene interval in the Deepwater Taranaki Basin using 2D seismic data sheds light on the character and translation directions of the MTDs (see Chapter 4). Key kinematic information derived from the identification of primary constraining features such as lateral margins, indicated a SW transport direction for MTD 6 different from the gross general transport direction to the NW for MTDs 1-5 (Fig. 5.1).

The regional interpretation (in chapter 4) is limited by the spatial and vertical resolution of the 2D seismic data and restricts the degree to which MTD morphology and internal structures can be imaged in detail. In addition, given that the headwall of MTD 6 was not imaged on the available 2D seismic data, key questions about the translation direction remain. Primary of this is, how would MTD 6 have a SW transport direction within the Giant Foreset Formation whose depositional pattern clearly relates to the rapid progradation of the modern continental margin towards the northwest (Hansen and Kamp, 2006a; Soenandar, 1992)

In the last decade, 3D seismic technology has advanced our understanding of emplacement processes of MTDs at a level of detail that is necessary to test models of how material moves and evolves during the emplacement process (Bull et al., 2009a; Crutchley et al., 2012; Frey-Martínez et al., 2006; Posamentier and Martinsen, 2011).

In this chapter, a high resolution 3D seismic data set provides insights into the emplacement process of MTD 6 to a level of detail beyond that which could be achieved using 2D seismic data (Chapter 4). The aim of this chapter therefore, is to:

1) Determine the actual transport direction of MTD 6 through the mapping of the basal
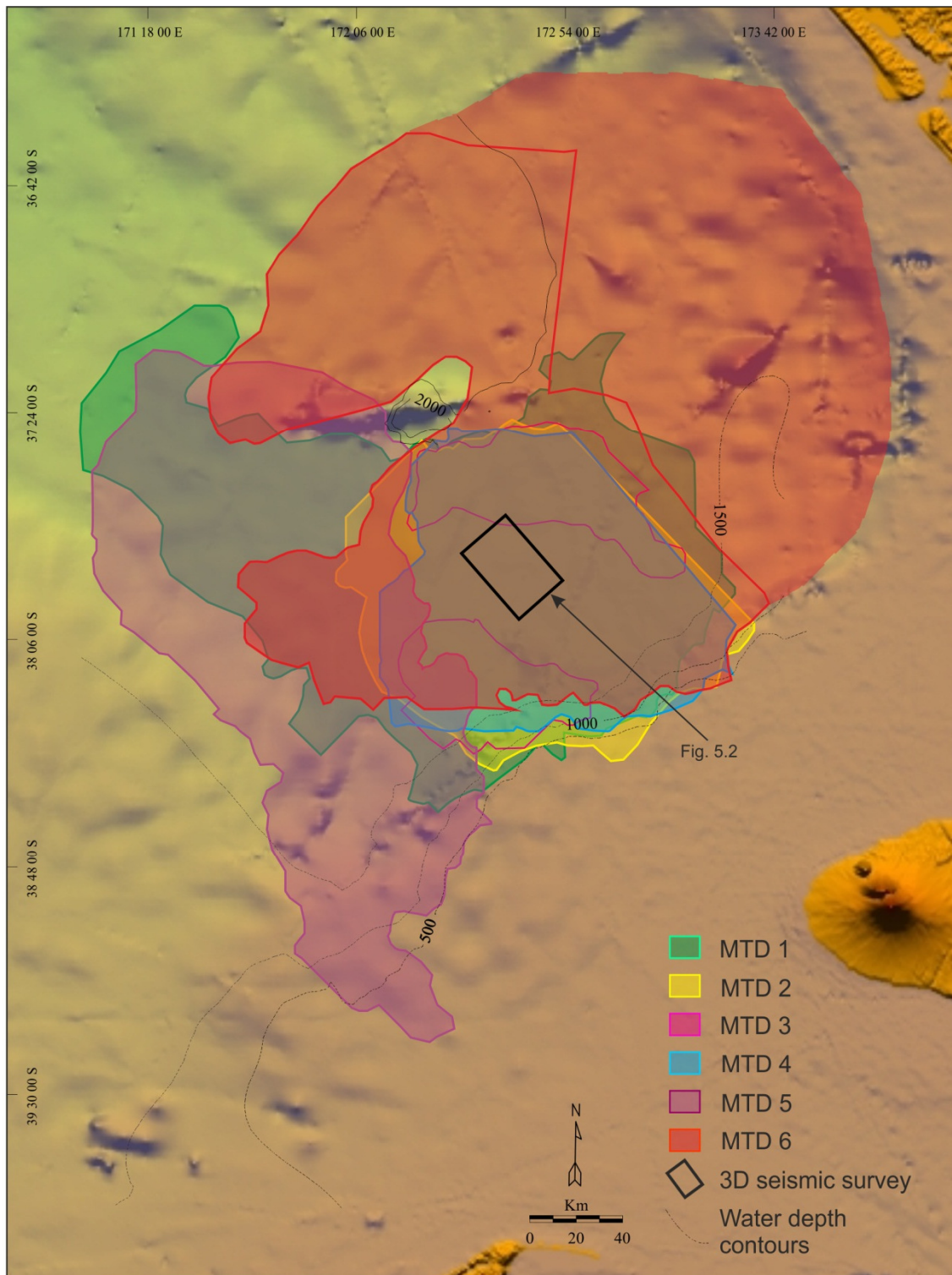
Figure 5.1. Mutibeam bathymetry map of the Deepwater Taranaki Basin showing the outline of MTDs 1- 6 interpreted from the 2D seismic data in Chapter 4. The interpreted southwest transport direction of MTD 6 is different form the gross transport direction of MTDs 1 - 5 discussed in the present study. The location of the 3D survey used in the present study is shown. Seabed contours are drawn at 500 m intervals.

160

surface and also to determine whether the direction of transport can be constrained from the internal architecture.

2) To examine the nature of the internal seismic architecture of MTD 6, and attempt to find out the process of deformation.

This second objective is important as it might reveal clues as regards the mode of emplacement. Although the examples presented in this chapter are specific to the study area, the ideas presented may be applicable to other MTDs worldwide.

5.3 Specific study area and dataset

This study focuses on MTD 6; the youngest and largest of the MTDs in the Plio-Pleistocene Giant Forset Formation of the Deepwater Taranaki Basin (Fig. 5.1); MTD 6 is located approximately 80 km north from the Taranaki Peninsula in a water depth ranging from 500 to 1150 m, with slope gradients between 2° and 0.5^o. MTD 6 is a two-lobed deposit, and covers an area of 22,397 km^2 with an estimated residual volume of 3,733 km^3. It is separated by the Aetoa Seamount and thus interpreted to have a SW translation direction (see Chapter 4).

The primary data for this study is the Romney 3D survey (Fig. 5.1 and 5.2) located on the southern lobe of MTD 6 and which images an area measuring 590 km ^{2}. Further information regarding the seismic data can be found in Chapter 2.2.

5.3 Observations and interpretations

5.3.1 General Characteristics

The seafloor exhibits a highly disrupted, rugose character (Fig. 5.2). It is generally characterised by some dip-parallel linear and concentric features in the southern region of the study area, although a series of subtle NE – SW lines are observed that are artefact of acquisition (ship track acquisition) (Fig. 5.2). In the northern region, the seafloor appears to
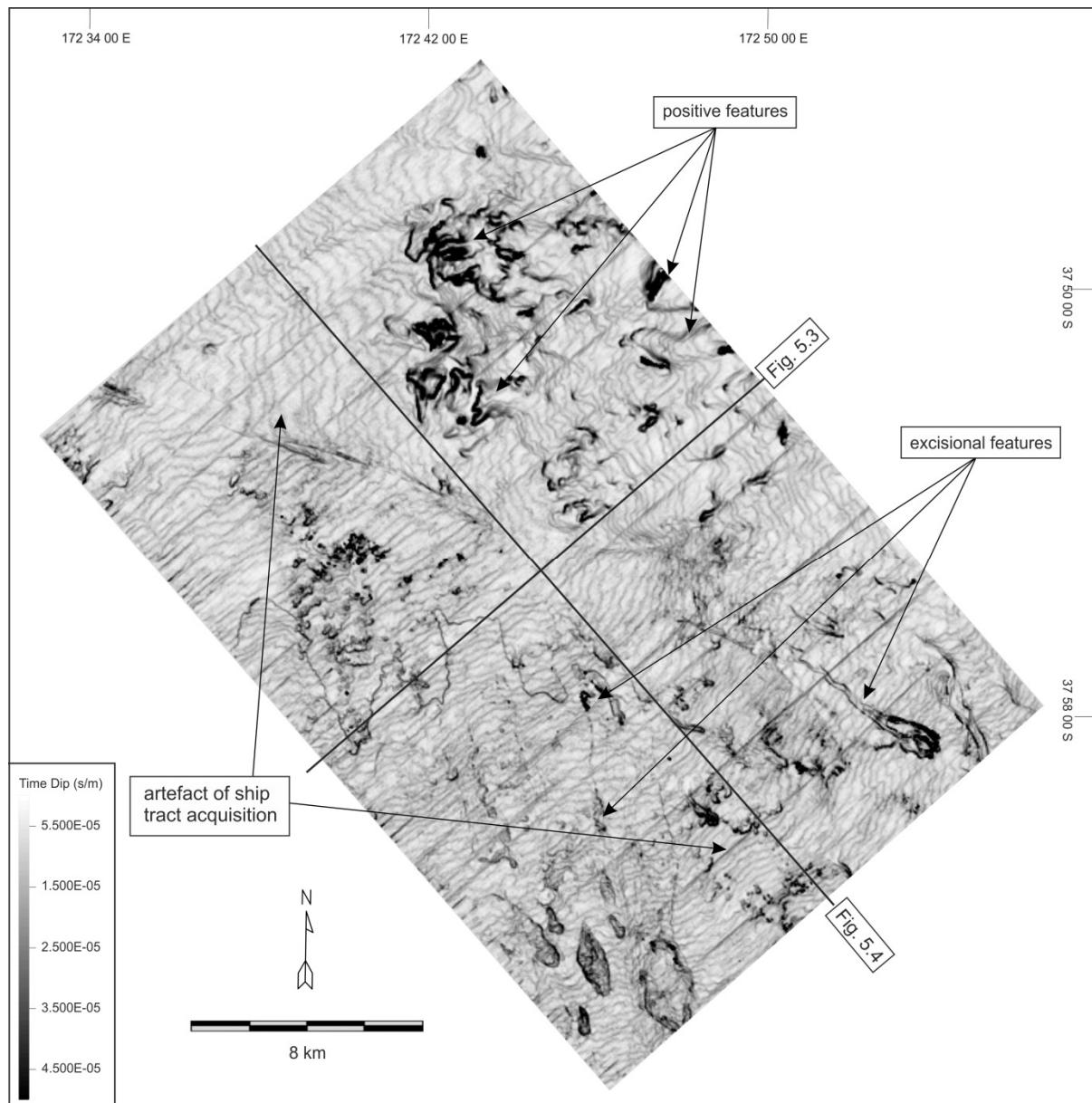
Figure 5.2. Time-dip attribute map extracted from the present day seabed in the Romney 3D area showing the rough seafloor morphology in the north of the survey, interpreted as protruding blocks. Also notice the dip-parallel lineaments upslope of the survey interpreted as excisional features. The locations of seismic profiles shown in Figures 5.3 and 5.4 are shown.
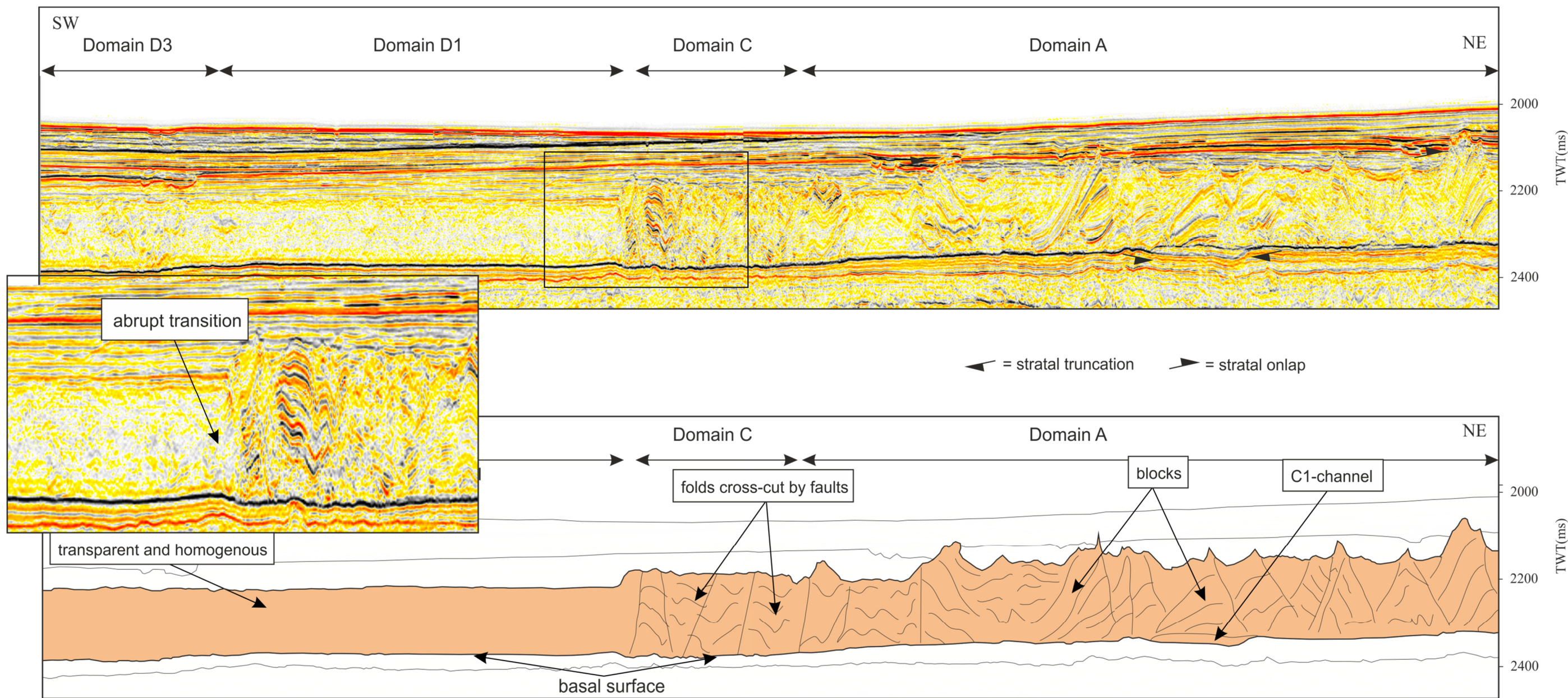
Figure 5.3. Composite seismic strike profile taken through the study area (see Fig. 5.2 for location) showing the position and the high degree of continuity of the basal detachment horizon. Also notice the abrupt transition between Domains A and B defined by a marked change in the internal deformational pattern of the MTD 6.
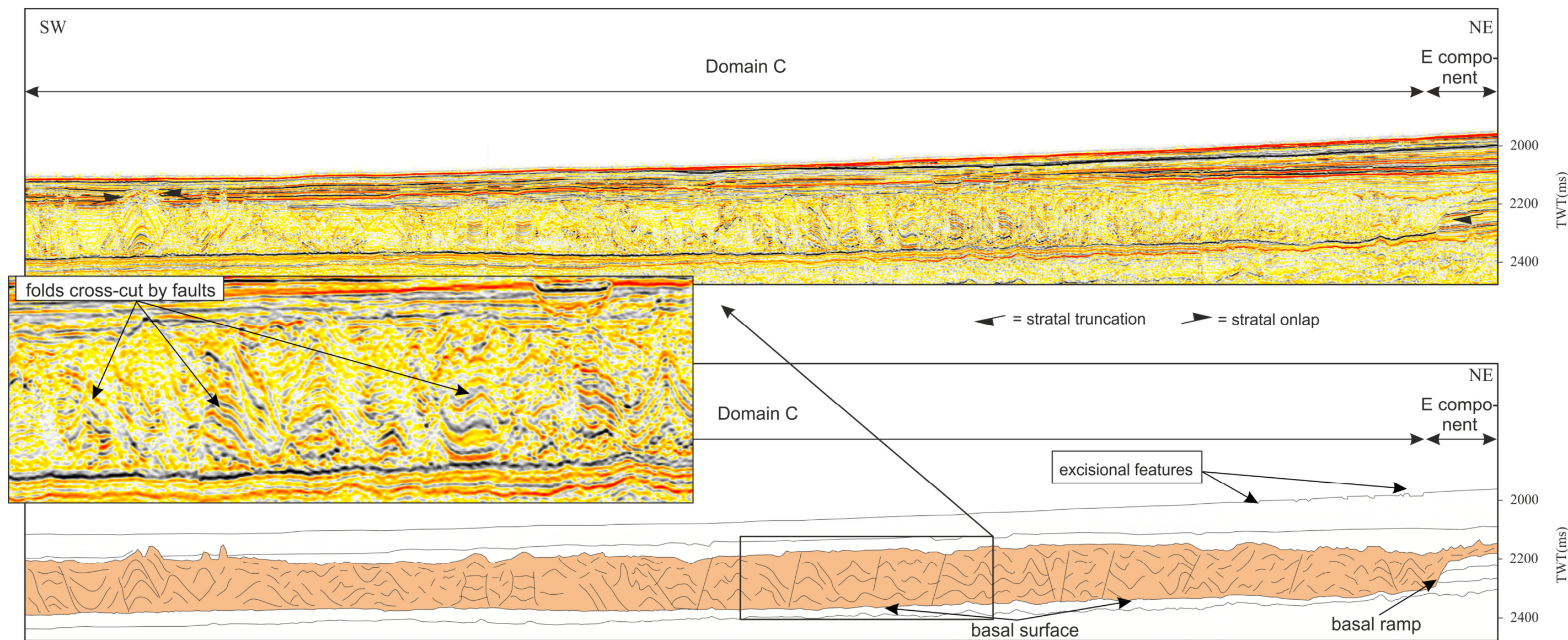
Figure 5.4. Composite seismic dip-profile taken through the study area (see Fig. 5.2 for location) showing the position and the high degree of continuity of the basal detachment horizon. Also notice the internal deformational pattern of the MTD.

be rough and characterised by high dip values. Detailed study reveals that the rough seafloor is due to the presence of rotated blocks (described in more detail in Section 5.3.3).

Two representative regional seismic profiles show that the dip-parallel linear and concentric features observed on the seafloor corresponds to subtle excisional features (Figs 5.3 and 5.4). MTD 6 is buried at an average depth of 150 m below the seabed (based on assumed seismic velocity of 1800 ms^{-1} for the shallow succession) by high amplitude continuous seismic reflections. It is generally characterized internally by transparent, low to moderate amplitude reflections showing varied seismic characters (see Section 5.4 for detailed description of the internal seismic character of MTD 6). The dominant lithology of slumped facies in the Giant Forset Formation is a chaotic mix of mudstone, siltstone, fine sandstone and shell hash (Hansen and Kamp, 2006b). MTD 6 is bounded by a continuous lower and irregular upper reflections termed the basal and upper surfaces respectively.

5.3.2 Basal Surface

MTD 6 detaches on a common horizon across most of the study area and is clearly identified from seismic profiles as a high amplitude negative reflection (Figs. 5.3 and 5.4). Due to the consistent strength of the reflection it was possible to track the basal surface of MTD 6 with a high degree of accuracy through the 3D seismic cube.

The basal surface in the study area is generally continuous and sub-parallel to the underlying undeformed strata, dipping locally between 0.5$^{°}$ and 2$^{°}$ to the west (Figs. 5.3, 5.4 and 5.5). However, the basal surface of MTD 6 appears to dip regionally in the southern lobe towards the NW before it flattens out towards the NW limits of the 3D seismic survey (Fig. 5.6). The basal surface is characterised by four significant features including ramp, groves, scours and mounds (Fig. 5.7). These features will be described in detail in the following sections.
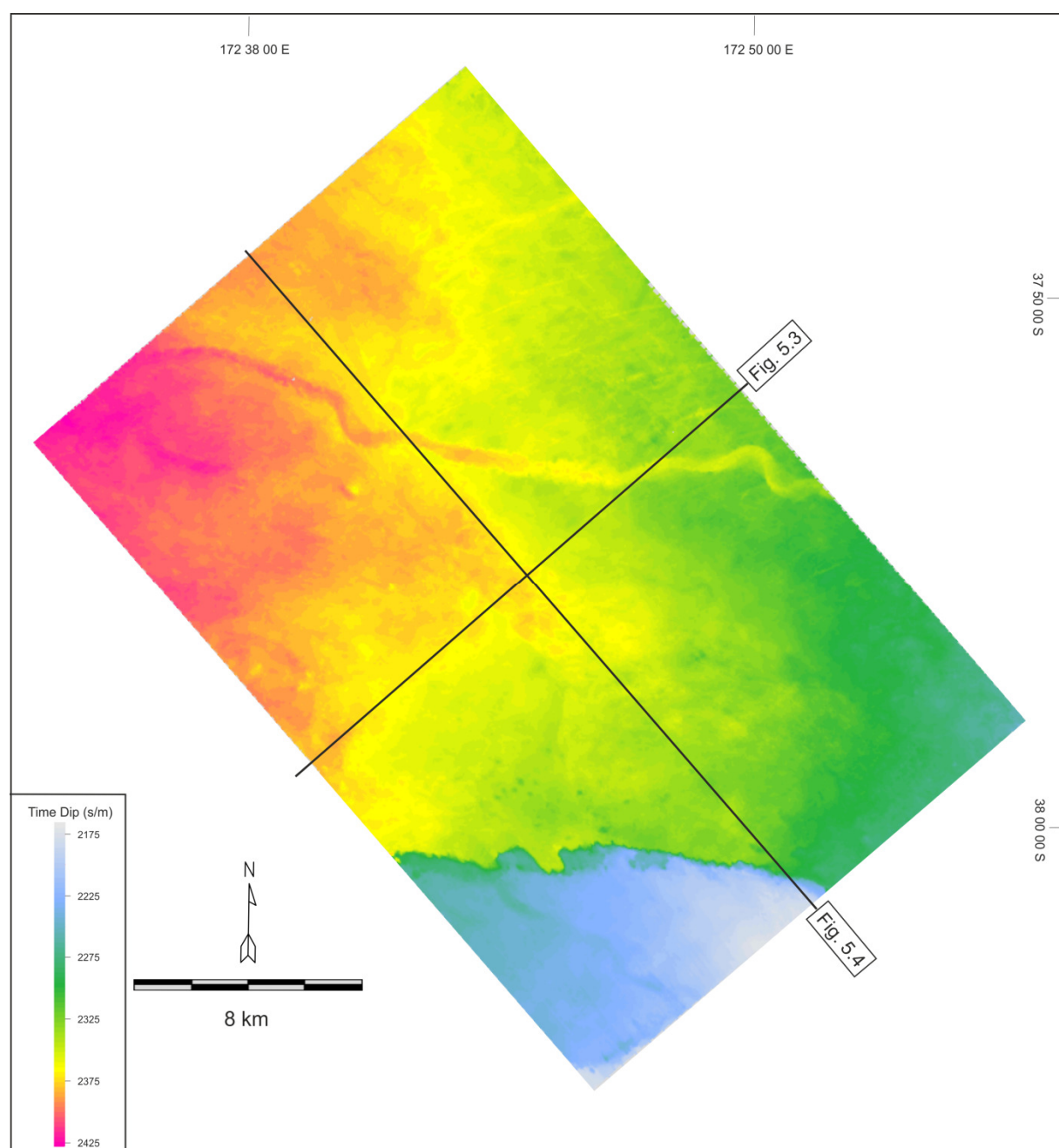
Figure 5.5. Time-structure map of the basal surface of MTD 6. Notice how the basal surface dips gently towards the NW and the sharp E-W slope change in the south of the study area. The sharp change of slope is irregular and characterized by sharp bends especially at its western limits. The locations of seismic profiles shown in Figures 5.3 and 5.4 are shown.
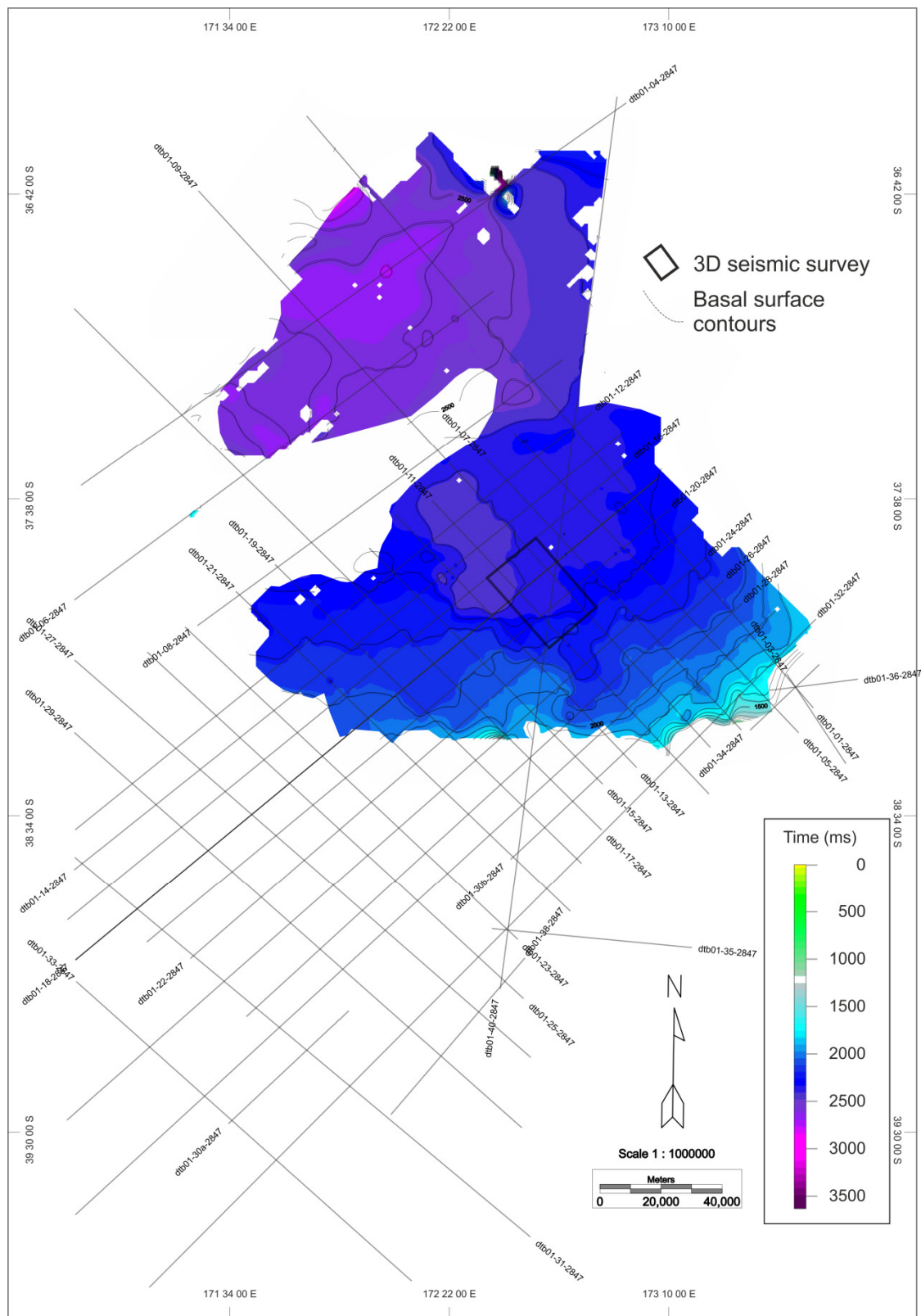
Figure 5.6. Time-structure map of the basal surface of the entire MTD 6 based on the interpretation of 2D seismic profiles lines shown in the figure. Notice how the basal surface in the southern lobe dips steeply in the south eastern region of the southern lobe and then gently towards the centre region before flattening out in the north-western edge of the 3D seismic survey. Contours are every 500 ms.
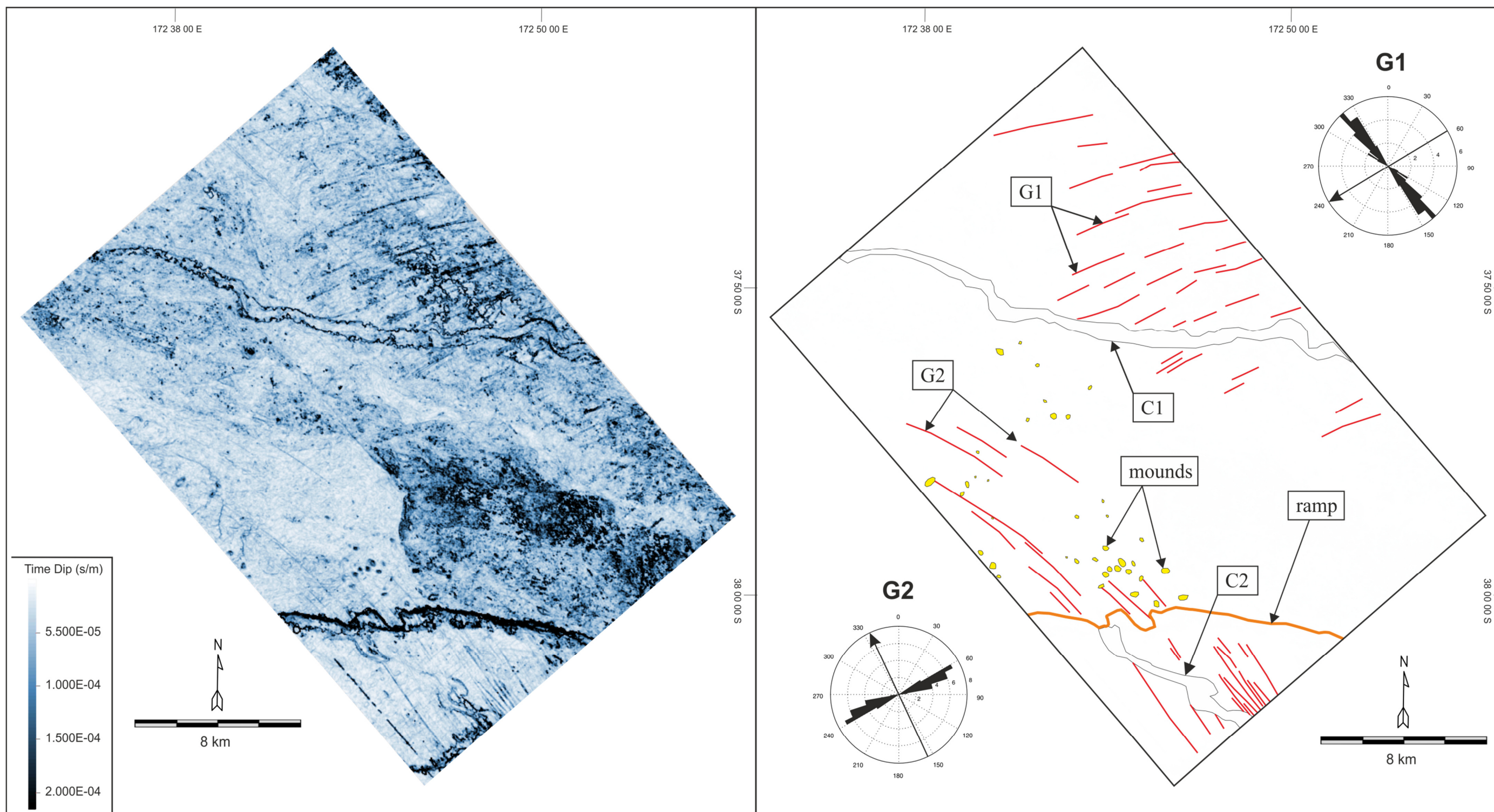
Figure 5.7 A) Uninterpreted time-dip map of the basal surface of MTD 6.B) Interpreted time-dip map of the basal surface of MTD 6 showing the main geomophological elements that characterise the basal surface. Notice the 2 sets of lineations labelled G1 and G2. The rose plots show that the G1 and G2 lineations have markly different orientation. Also notice the two paleo-channels (labelled C1 and C2) with different orientation. The coloured dots represent subsurface mounded features which are randomly distributed. The irregular E - W oriented ramp is also highlighted.
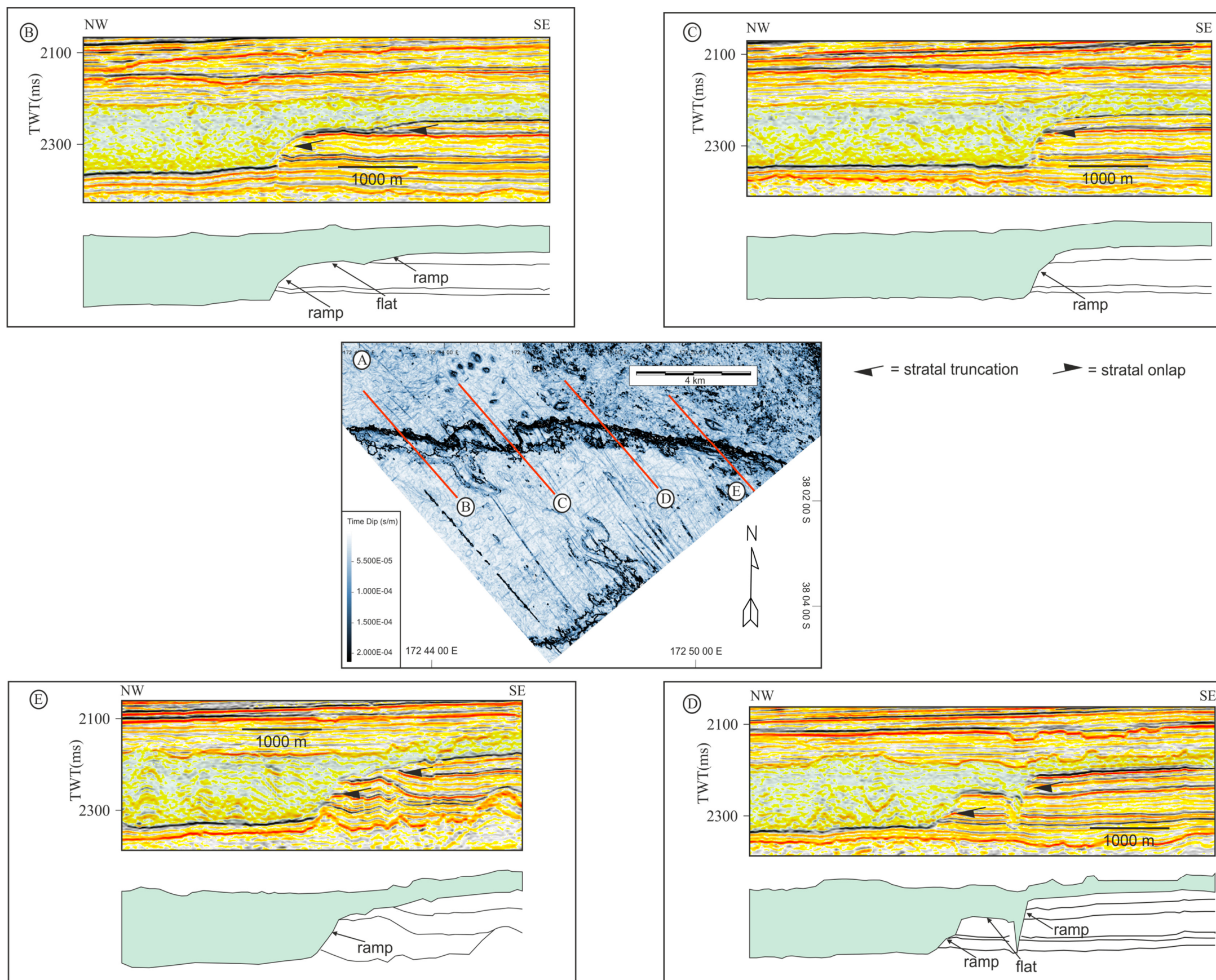
Figure 5.8. Geometry and orientation of the ramp identified at the base of MTD 6. A) Time-dip map of the basal suface showing the E-W orientaion of the ramp.B-E) Cross sections illustrating the geometry of the ramp from west to east.

5.3.2.1 Ramp

The westward dipping basal surface of MTD 6 is interrupted by an E - W oriented sharp change in dip in the south of the study area (Fig. 5.7). The sharp change in dip corresponds to a sharp change in slope on the basal surface (Fig. 5.5). Representative seismic profiles across the sharp change in dip observed on the base of MTD 6 (Fig. 5.8A) reveal that it is the expression of a stratigraphic step in the basal surface (Fig. 5. 8B - E) interpreted as a ramp in accordance to previous studies (Bull et al., 2009a; Frey-Martínez et al., 2006). The ramp dips between 10^0 and 15^0 predominantly in the NW direction.

Towards the west, the basal surface can be seen to cut up c. 60 ms of stratigraphy and then runs along a bedding parallel segment for c. 1 km before cutting up another c. 30 ms of stratigraphy (Fig. 5.8 B). Whereas towards the center of the ramp, this ramp-flat-ramp relationship is not observed; rather a single ramp with vertical drop of c. 100 ms is observed (Fig 5.8 C). Further east, the ramp-flat-ramp geometry is observed again (Fig. 5.8 D). Interestingly, the second ramp is defined by a fault that cuts through the intermediate basal surface and extends to the original stratigraphic level of the original basal surface (Fig. 5.8 D). The ramp becomes relatively linear on the easternmost profile, dipping 35° over a vertical extent of c. 60 ms and 20° higher up (Fig. 5.8 E).

In plan view, the ramp is characterized by irregular geometry and varies quite dramatically from the west to the east. Towards the western limits of the ramp, two 'U' shaped features (labeled U1 and U2 in Figures 5.9 A and B) are observed. One of the 'U' shaped features (U2) is more pronounced and is delimited by steep ramps, which cut discordantly down section to within 50 ms of the original basal surface (Fig. 5. 9C). The intervening flat section is c. 1000 m wide.

There are linear features that are oriented in a N - S direction on either sides of the 'U'
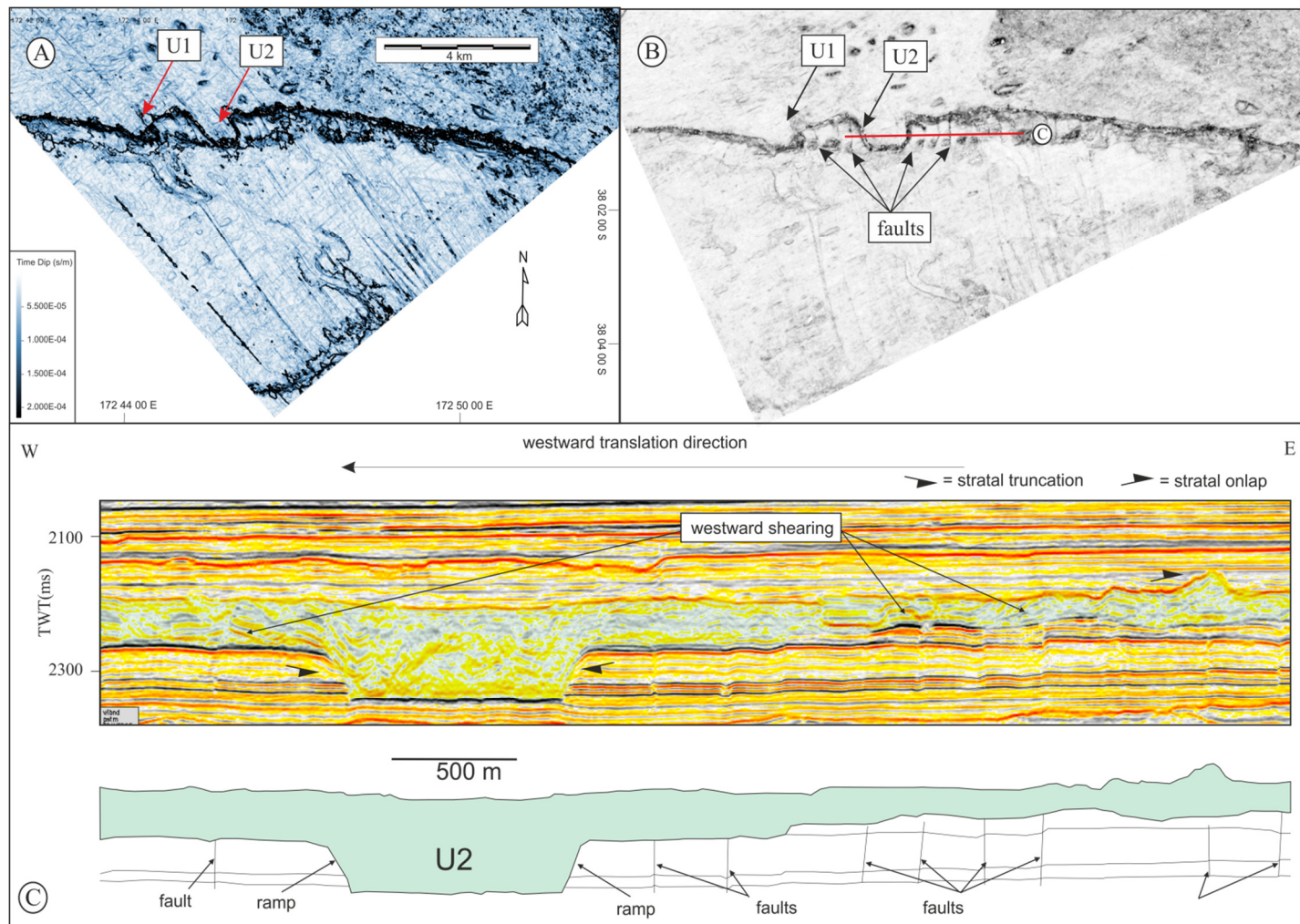
Figure 5.9 A) Enlargement of the time-structure map of the basal surface of MTD 6 showing the E - W trending ramp and two "U" shaped salients (labelled U1 and U2) that indent the ramp. B) Structurally flattened coherency map of the basal surface showing the morphology of the ramp in more detail C) Seismic profile parallel to the ramp across the U2 salient (see fig. 5.9A for location) showing N-S trending faults on either sides of the U2. A westward translation direction is interpreted for MTD 6 based on the westwards shearing of blocks and associated faults.

shaped feature. This is seen clearly on a coherency slice flattened on the basal surface of MTD 6 (Fig. 5.9B). These linear features correspond in seismic profile to faults that detach at the same stratigraphic level with the U2 feature (Fig. 5.9C). The faults tip-out beneath the ramped basal surface in the southern part of the study area.

Ramp and flat relationships are quite common in other major slides, where the switching between two or more preferred stratigraphic levels for the flat segment of the basal shear surface possibly reflects the availability of more than a single surface of low shear strength (Bull et al., 2009a). Although the basal surface of MTD 6 appears to be continuous and gently dipping, it is interpreted to be locally erosive during the translation of MTD 6. This interpretation has been made on the basis of: 1) the presence of an E - W trending ramp in the southern part of the 3D seismic cube (Figs. 5.8 and 5.9) which is considered to be linked with the presence of pre-existing weaknesses in the form of faults. Ramps are excellent kinematic indicators and have mostly been reported to trend perpendicular to the main transport direction (Gawthorpe and Clemmey, 1985; Hjelstuen et al., 2007; Trincardi and Argnani, 1990). However, (Bull et al., 2009a) suggested that ramps may also occur trending parallel to the transport direction and that where they do, they are interpreted as "slots", which are narrow closely spaced ramps that cut down stratigraphy. In this present study, the later kinematic interpretation of (Bull et al., 2009a) seems to be more appropriate, however, the E – W oriented ramp is interpreted as a lateral ramp rather than a slot due to the presence of the N - S oriented faults on either side of the U2 shaped feature (interpreted as a salient) (Fig. 5.9). Furthermore, the blocks which are delineated by the N-S oriented faults appear to be sheared towards the west (Fig. 5.9C) and thus suggest a westward transport direction. It is conceivable that further translation of MTD 6, could have resulted in the erosion of any underlying pre-existing faults especially to the west of the U2 salient.

5.3.2.2 Grooves

Two sets of parallel elongate linear features (labeled G1 and G2 in Fig. 5.7) are observed to incise the basal surface of MTD 6. These well-developed lineations (G1 and G2) are oriented in markly differing directions. The G1 lineations are oriented in the NE – SW direction and are especially well developed in the northern part of the study area where they are up to 6 km long and 100 – 200 m wide (Fig. 5.7B). Seismic profiles perpendicular to the G1 lineations (Figs. 5.10B - E) reveal that they a least 50 m wide and are incised to a depth of c. 5 - 10 m and are aligned with the lower edges of the blocks within MTD 6. The G1 lineations appear to be shorter towards the south-eastern part of the study area than those observed in the northern part, limited to 2 km in length and 100 – 200 m wide (Fig. 5.7B). However, they exhibit the same widths and depths as those in the northern part of the study area and sometimes align with the lower edges of blocks (Figs. 5.11B and C).

In the south of the study area, the G2 lineations, oriented in the SE – NW direction can be observed on either side of the E – W oriented ramp but are not continuous across the ramp (Fig. 5.7B). The G2 lineations south of the ramp are in general (< than 100 m wide), shorter and more closely spaced than those north of the ramp (Fig. 5.12B and C).

The G2 lineations north of the ramp measure up to c. 8 km in length (Fig. 5.7B) and are barely recognizable on seismic profile (Fig. 5.13B). Linear features are absent in the south eastern and north western parts of the basal surface (Fig. 5.7B).

Long lineations on the basal surfaces of MTDs, which are 'v'shaped in cross sections have previously been identified elsewhere using 3D seismic data and have been interpreted as grooves (Posamentier and Kolla, 2003) or furrows (Gee et al., 2005). They are thought to be the result of erosional action of coherent blocks with the translated material (Bull et al., 2009a; Gee et al., 2005; Posamentier and Kolla, 2003). These authors also suggested that they
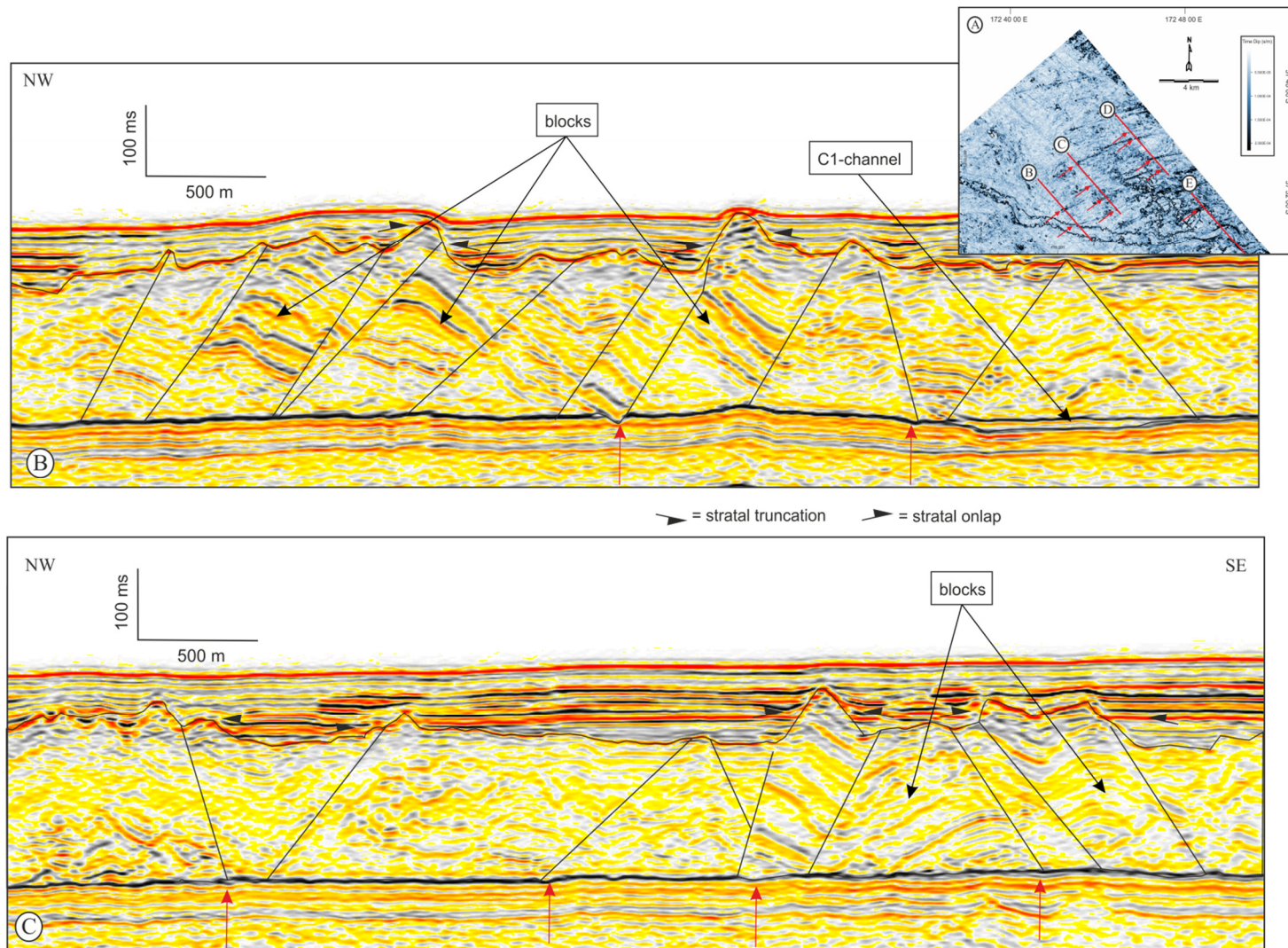
Figure 5.10 A) Enlarged dip-structure map of the basal surface of MTD 6 showing the G1 lineations in the northern part of the study area and location of seismic profiles shown in B, C, D and E. Seismic profiles (B) and (C) through the G1 lineations (indicated by red arrows) shown in Fig. 5.10A Seismic profiles (D) and (E) through the G1 lineations (indicated by red arrows) shown in Fig. 5.10A.
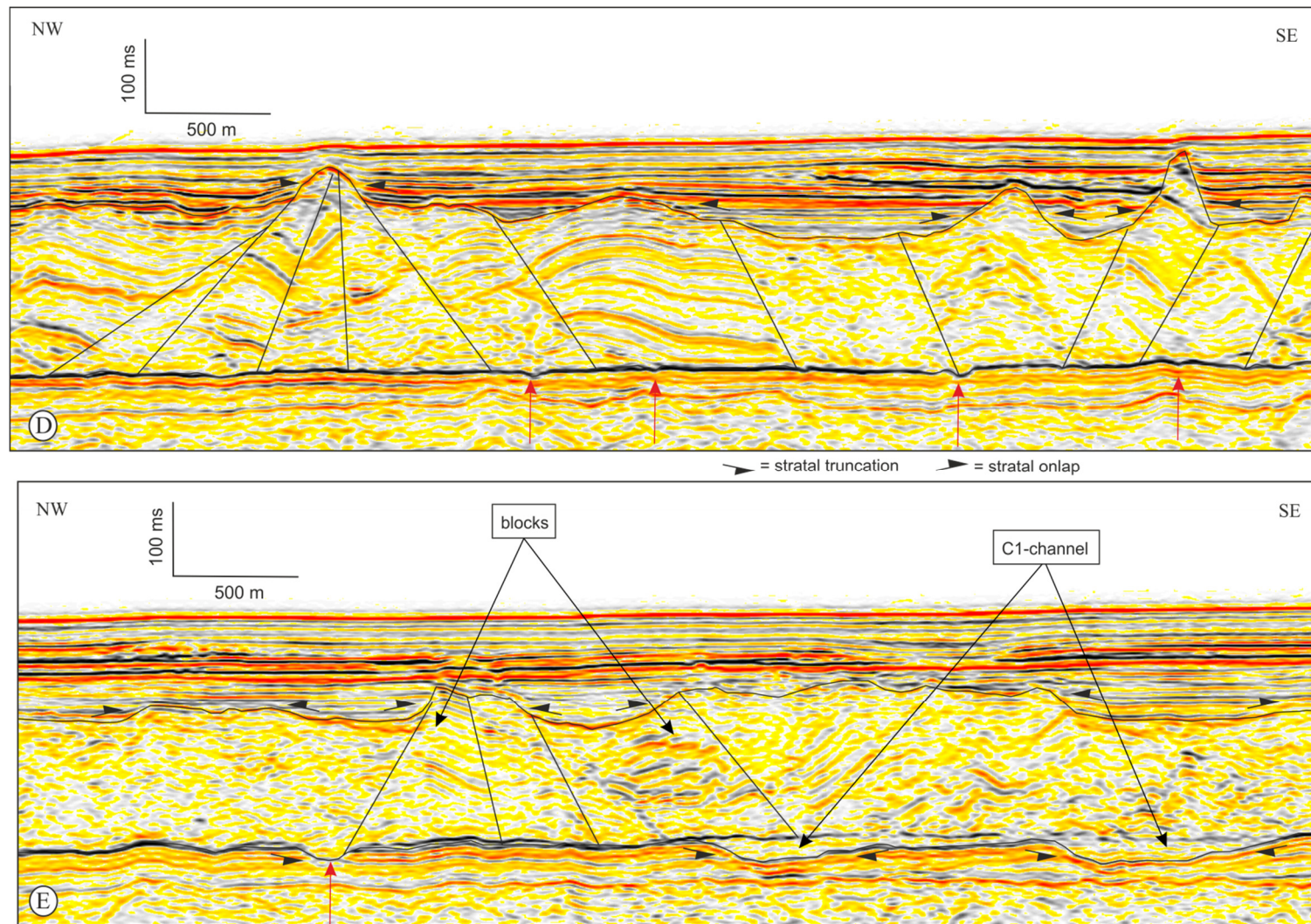
Figure 5.10 (Contd). Seismic profiles (D) and (E) through the G1 lineations (indicated by red arrows) shown in Fig. 5.10A.
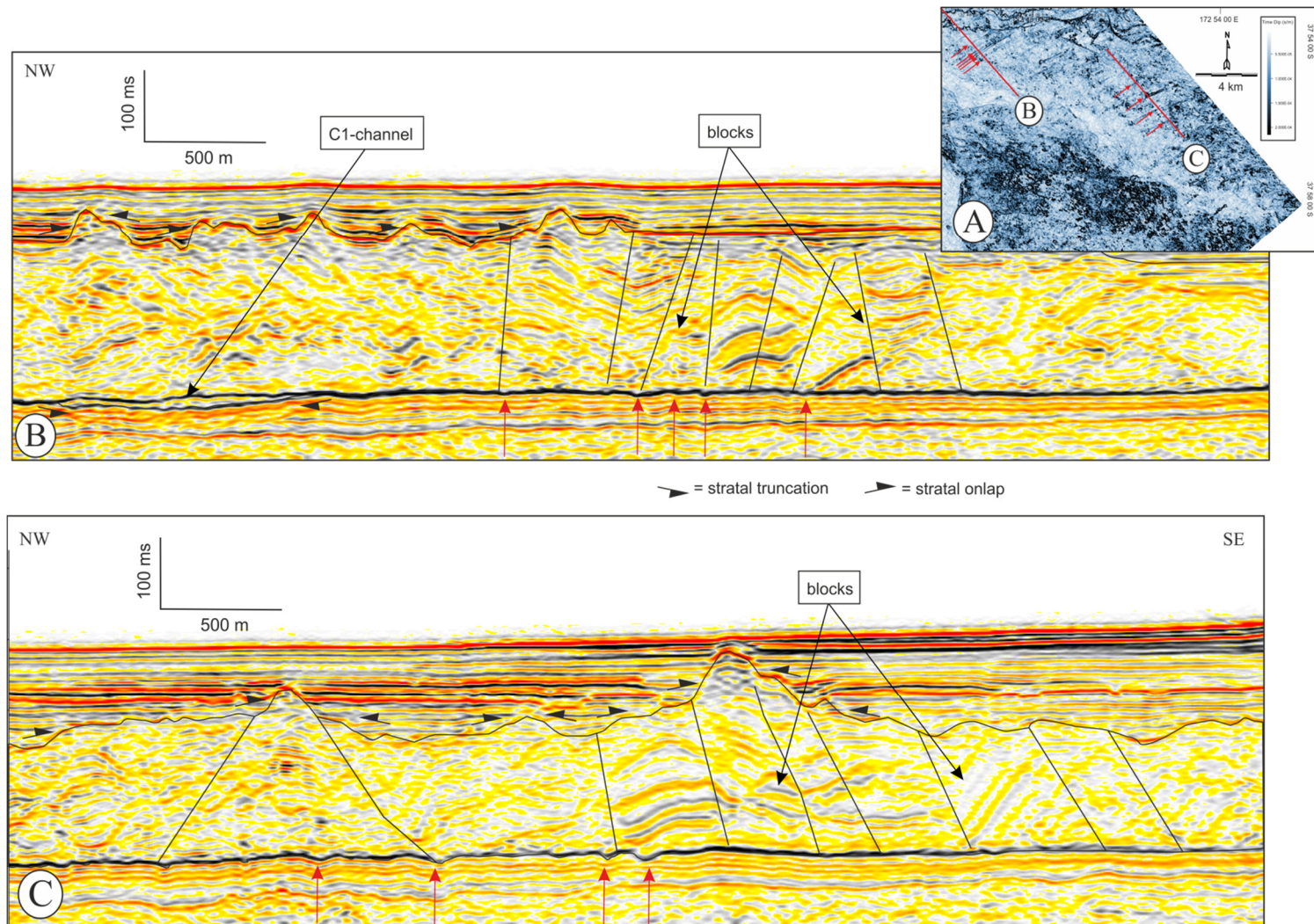
Figure 5.11 A) Enlarged dip-structure map of the basal surface of MTD 6 showing the lineations in the south-eastern part of the study area and location of seismic profiles shown in B and C. Seismic profiles (B) and (C) through well-developed G1 lineations (indicated by red arrows) shown in Fig. 5.11A.

are useful kinematic indicators since they reveal information relating to the transport direction of the mass transport deposit downslope. Therefore the G1 lineations (NE - SW) would suggest a WSW translation direction for MTD 6 (Fig. 5.7B), which is consistent with the downslope direction (Fig. 5.5). In contrast, the G2 lineations (SE – NW) strike northwest and could therefore be taken to imply a NW translation direction for MTD 6. This conflict in kinematic indicators will be addressed later in the discussion (Section 5.5).

5.3.2.3 Paleo-channels

The basal surface of MTD 6 is incised by two erosional features (Fig. 5.7B) that are interpreted as deepwater channels by virtue of the fact that they display a meandering nature (Pickering et al., 1995).

The C1 channel (north of the study area) is c. 30 km long and is oriented in a WNW direction (Fig. 5.7B), with widths ranging from 500 - 1.2 km, and not less than 10 m in depth (Fig. 5.10B and E)

The C2 channel (south of the study area) is c. 8 km long and it is oriented in a NW direction (Fig. 5.7B), having a variation in width ranging from 1 km to less than 500 m, and not less than 10 m in depth (5.12B and C). The C2 channel is more sinuous than the northern scour and terminates abruptly at the E – W trending basal ramp (Fig. 5.7B).

A high amplitude, continuous, flat lying reflection runs across the top of the C1 channel (Figs. 5.10B and 5.10E). However this observation is not consistent with that of the C2 channel, having a chaotic channel fill configuration (Fig. 5.12B and C).

Several channel systems occur within the Plesitocene (Upper Nukumaruan to Castlecliffan) interval of Giant Foreset Formation, and are invariably incised into the shelf sediment (Hansen and Kamp, 2006b). The meandering nature of the C1 and C2 channels in this study are indicative of the low gradient associated with the slope (Pickering et al., 1995). The high
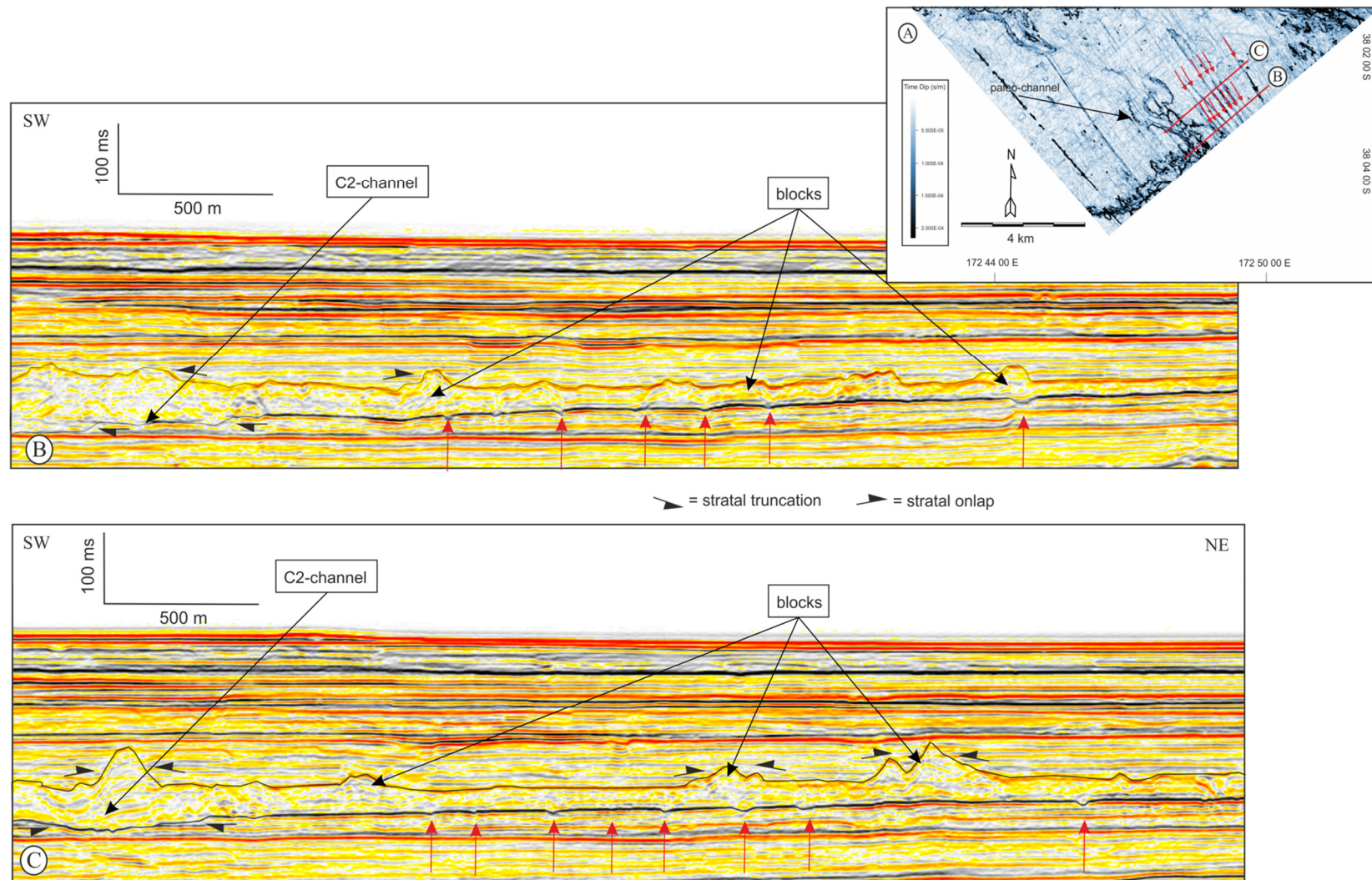
Figure 5.12 A) Enlargement of the dip-structure map of the basal surface showing the G2 lineations south of the E -W oriented basal ramp of MTD 6. Seismic profiles (B) and (C) through the G2 lineations indicated by red arrows. Notice the paleo-channel without an intervening high amplitude reflection across.
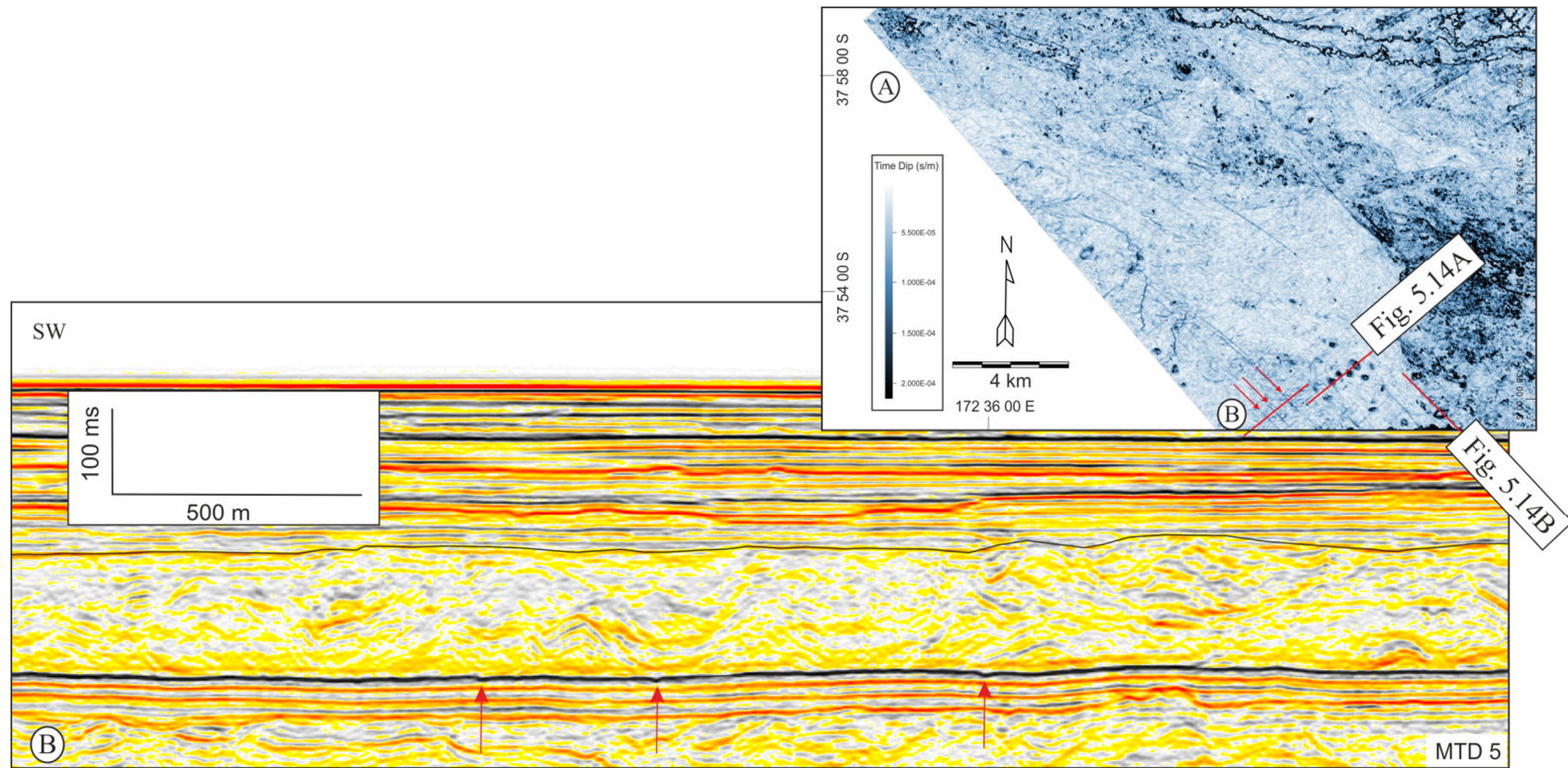
Figure 5.13 A) Enlargement of the dip-structure map of the basal surface showing the G2 lineations north of the E -W oriented basal ramp of MTD 6 and seismic profile location through the mounds. (B) Seismic profiles through the G2 lineations indicated by red arrows. Notice the subtle G2 lineations.

amplitude continuous reflection across the C1 channel suggests it predates the MTD 6 failure event (Figs. 5.10B, E and 5.11B). The absence of a continuous high amplitude reflection across the C2 channel implies that MTD 6 incorporated the C2 channel material and thus suggests that MTD 6 had the capacity to erode previously deposited channelized material even with the low gradient of the slope in that region (Figs. 5.12B and C). Furthermore, the abrupt termination of the C2 channel at the E – W trending basal ramp (fig. 5.7B) suggests the latter was cut by the basal ramp and therefore predates the ramp.

5.3.2.4 Subsurface mounds

Thirty two localized sub-circular shaped features can be identified on the basal surface of MTD 6, mainly located north of the E –W oriented ramp (Fig. 5.7B). They are irregularly distributed and do not have discernible spatial relationships with each other. However, they are much more densely developed closer to the ramp than further away from the ramp. These circular features have variable diameters ranging from 0.5 to 0.8 km.

Representative seismic profiles across these sub-circular features show that they correspond to transparent coherent convex up features (Figs. 5.14A and B), developed within the underlying seismically transparent and chaotic MTD (termed MTD 5). More specifically, the internal architecture of these features are sometimes characterised by either stacked convex up reflections (Fig. 14A) or inclined reflections bounded by planar normal faults (Fig. 14B) The majority of these features sometimes cut through a relatively thin and undeformed intervening high amplitude unit between MTD 5 and the overlying MTD 6 with strong evidence of passive onlap on their flanks (Fig. 5.14C).

These features are interpreted as folds and or faulted blocks within the underlying MTD 5 based on their preserved geometries. The fact that there is strong evidence for passive onlap on these structures with high angle of repose suggests one of two possibilities 1) MTD 6 did
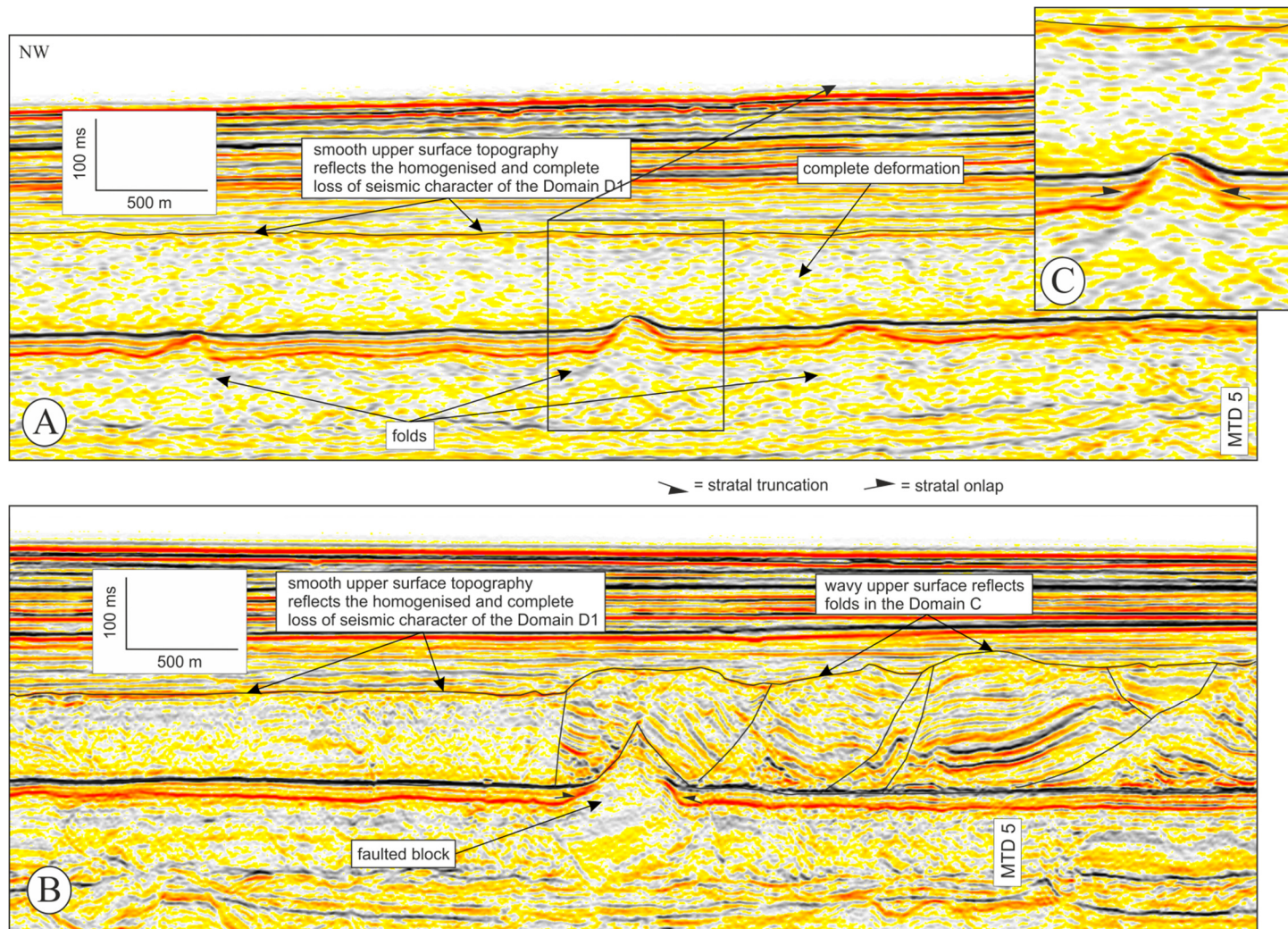
Figure 5.14. Seismic profiles A and B through the mounded structures shown in figure 5.13A show that they correspond folds and faulted blocks respectively within the underlying MTD 5. Notice how the structures cut through the intervening high amplitude reflections c) Enlarge seismic profile showing one of the folds and the presence of passive onlap on the flanks with no erosion at the top.

not have the capacity to erode or bevel out the structure during its translation and emplacement or 2) MTD 6 was probably formed in-situ. These two contrasting hypotheses will be discussed later in Section 5.5.

5.3.3 Upper Surface

The upper surface of MTD 6 is represented by a high amplitude reflection (Figs. 5.3 and 5.4). The topography of the upper surface varies laterally within the study area from generally smooth, through undulating to highly irregular topography (Figs. 5.3, 5.4 and 5.15). There isa close correspondence between the topography of the upper surface and the nature of the internal deformation of MTD. Where the internal seismic character is homogenous and highly deformed the upper surface tends to have a smooth topography (Fig. 5.3). In contrast, where the internal seismic architecture is incoherent and discontinuous then the upper surface is characterized by a highly irregular topography (Figs. 5.3 and 5.4). In the northeastern part of the 3D seismic survey (Fig. 5.15), the upper surface is characterized by elongated ridge-like positive features while towards the northwest, it is characterized by an alternating bands of moderate to high time values. In the south-western region the upper surface appears to be smooth with relatively constant time values.

The fact that there is a close correspondence between the topography of the upper surface and the nature of the internal deformation suggests that the topography of the upper surface is controlled by the internal deformation within MTD 6 (sensu. Bull et al., 2009a). A detailed description of the upper surface topography, in relation to the internal architecture is given in the following section (section 5.3.4). In general, the undulose upper surface of MTD 6, especially in areas of complex deformation (e.g blocks and folds) is interpreted as depositional relief expressed at the seabed which was subsequently onlapped by undeformed strata (Figs. 5.3 and 5.4).
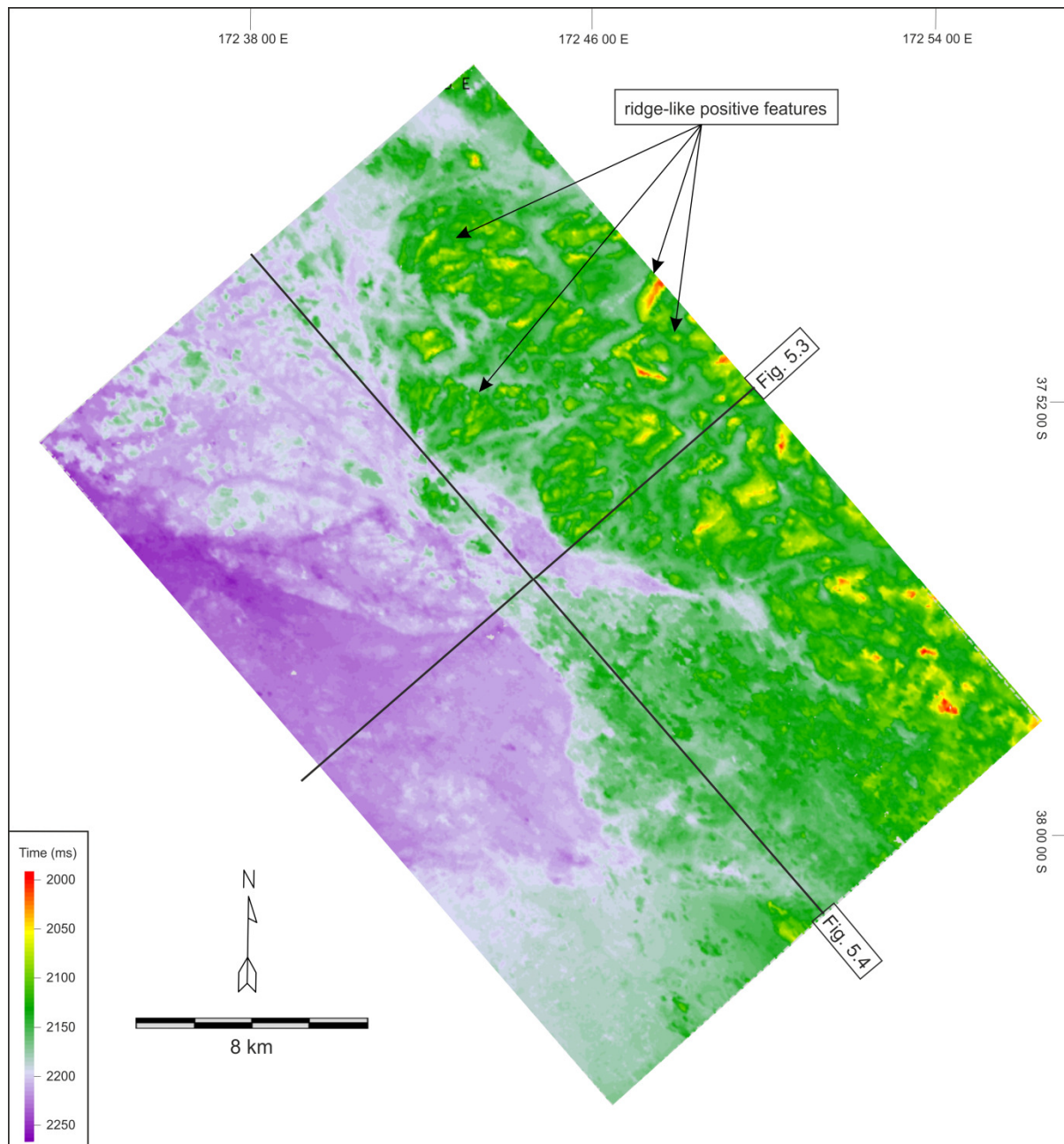
Figure 5.15. Time map of the upper surface of MTD 6 showing the irregularity of the upper surface especially pronounced towards the north eastern part of the study areas evidence from the alternating bands of high and moderate time values. In contrast, towards the south the topography of the upper surface is smooth characterised by local constant time values in places. The locations of seismic profiles shown in Figures 5.3 and 5.4 are shown.

5.3.4 Internal structure

MTD 6 has a varied internal architecture both laterally and vertically throughout the full thickness (Figs. 5.3 and 5.4). Consequently, a series of windowed Root Mean Square (RMS) amplitude maps were generated to investigate the internal structure of MTD 6 (Fig 5.16) (cf. Gafeira et al., 2010; sensu McGilvery and Cook, 2003), in combination with seismic profile interpretation. Five distinctive domains have been identified based on systematic amplitude analysis on a representative RMS amplitude map (Fig. 5.17) and these are now described in detail in the following sections.

5.3.4.1 Domain A

Domain A is defined by high to moderate amplitude patterns that typically form elongated arcuate to parallel features, as well as isolated square to circular features that generally exhibit internal stratification (Figs. 5.18A and 19A) A representative seismic profile through Domain A reveals that the amplitude features are characterised by coherent, inclined segments that are separated by extensional planar normal faults that tip out at the base of MTD 6 (Fig. 5.19A).

These coherent moderate to high amplitude features are interpreted as fault bounded blocks by analogy to previous studies (Bull et al., 2009a; Frey Martinez et al., 2005; Micallef et al., 2007).

Three Sub-Domains (A1, A2, and A3) are identified within Domain A based on the morphology and the long axis orientation of the extensionally fault bounded blocks (Fig. 5.18). The main boundaries separating the three sub-domains are sharp and are oriented in a WSW direction.

The blocks in Sub-Domain A1 are mostly arcuate and occur in a repetitive parallel to sub-parallel pattern and vary in length between 1 - 4 km (Fig. 5.18A). Although the arcuate and
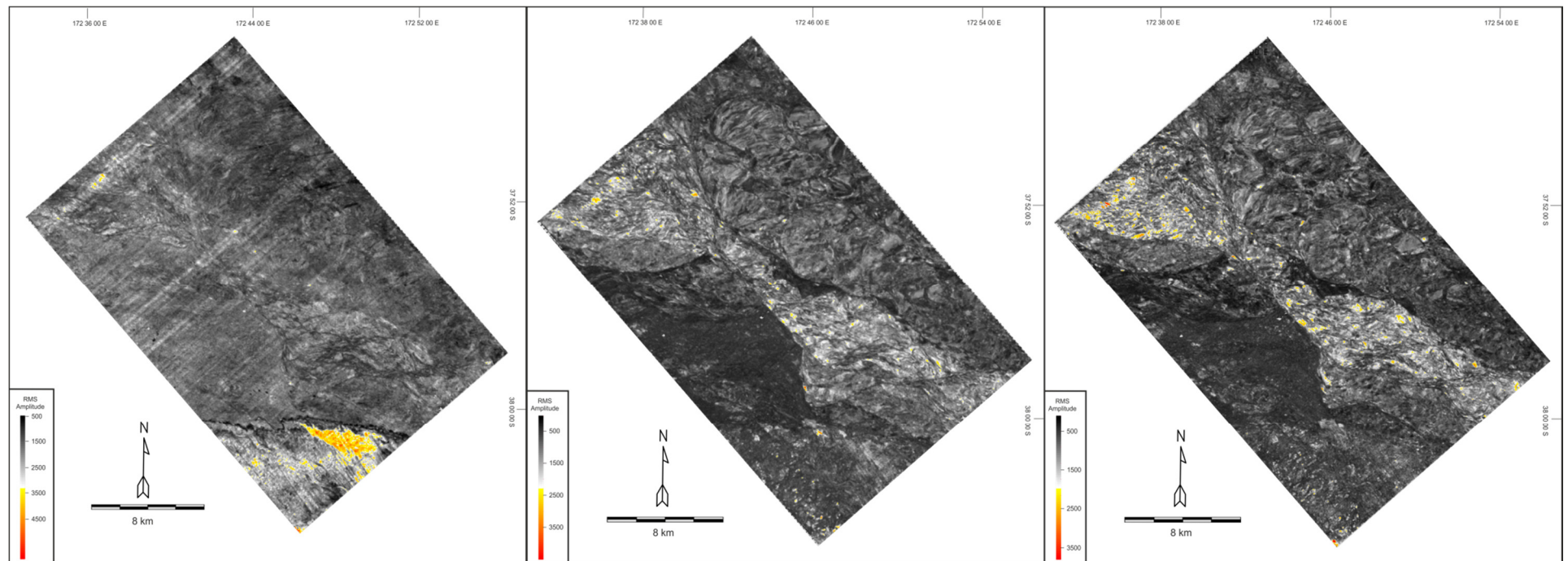
Figure 5.16. Series of Root mean square (RMS) amplitude maps generated for MTD 6 from the basal to upper surfaces A) 0-25% B) 25-50% C) 50-75% above the basal surface of MTD 6. Notice how the amplitude changes systematically from the base to the top.
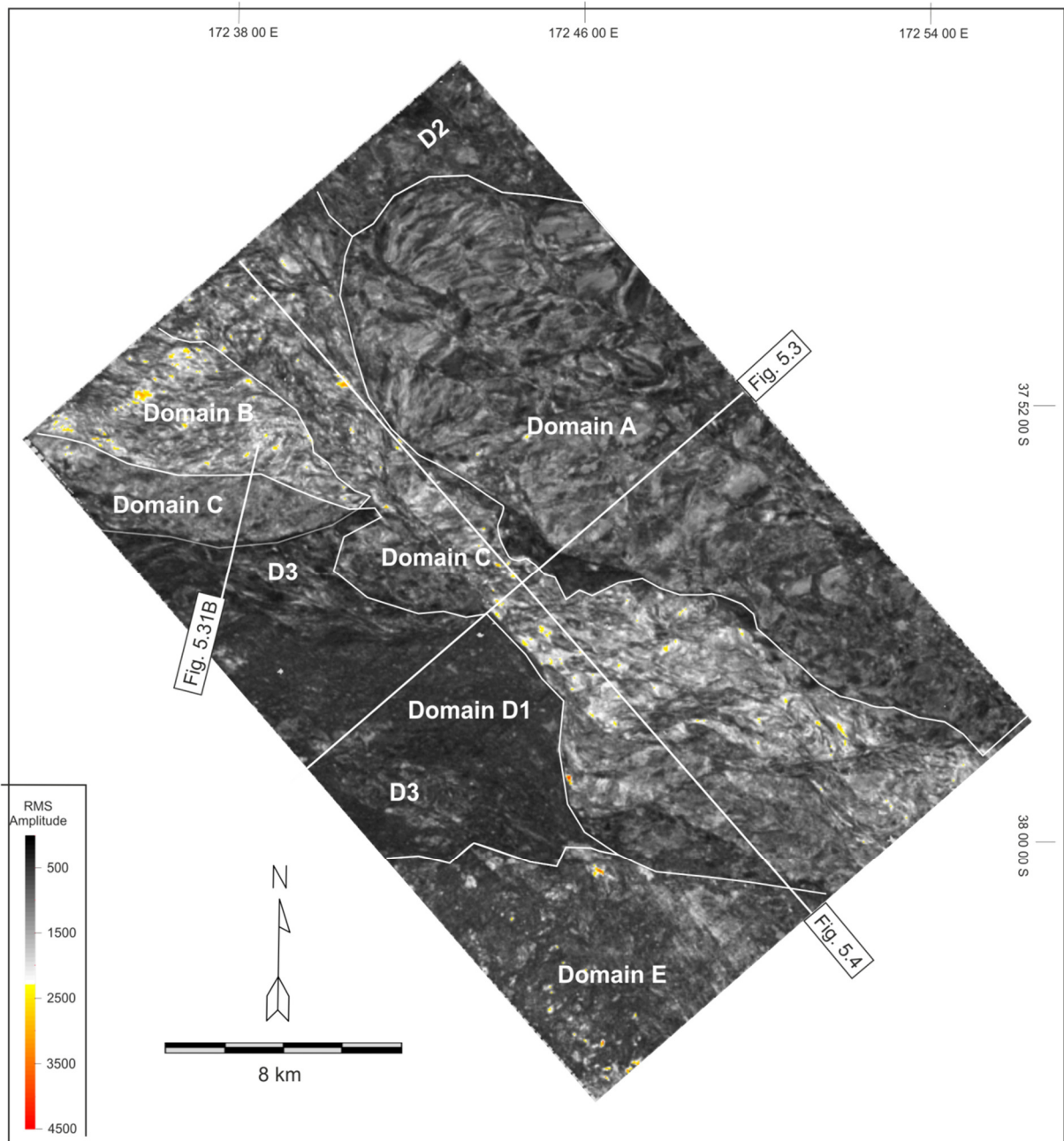
Figure 5.17. Representative windowed (25%-50%) RMS amplitude map of MTD 6 showing five distinctive domains (A-E) based on the amplitude reflectivity and pattern.
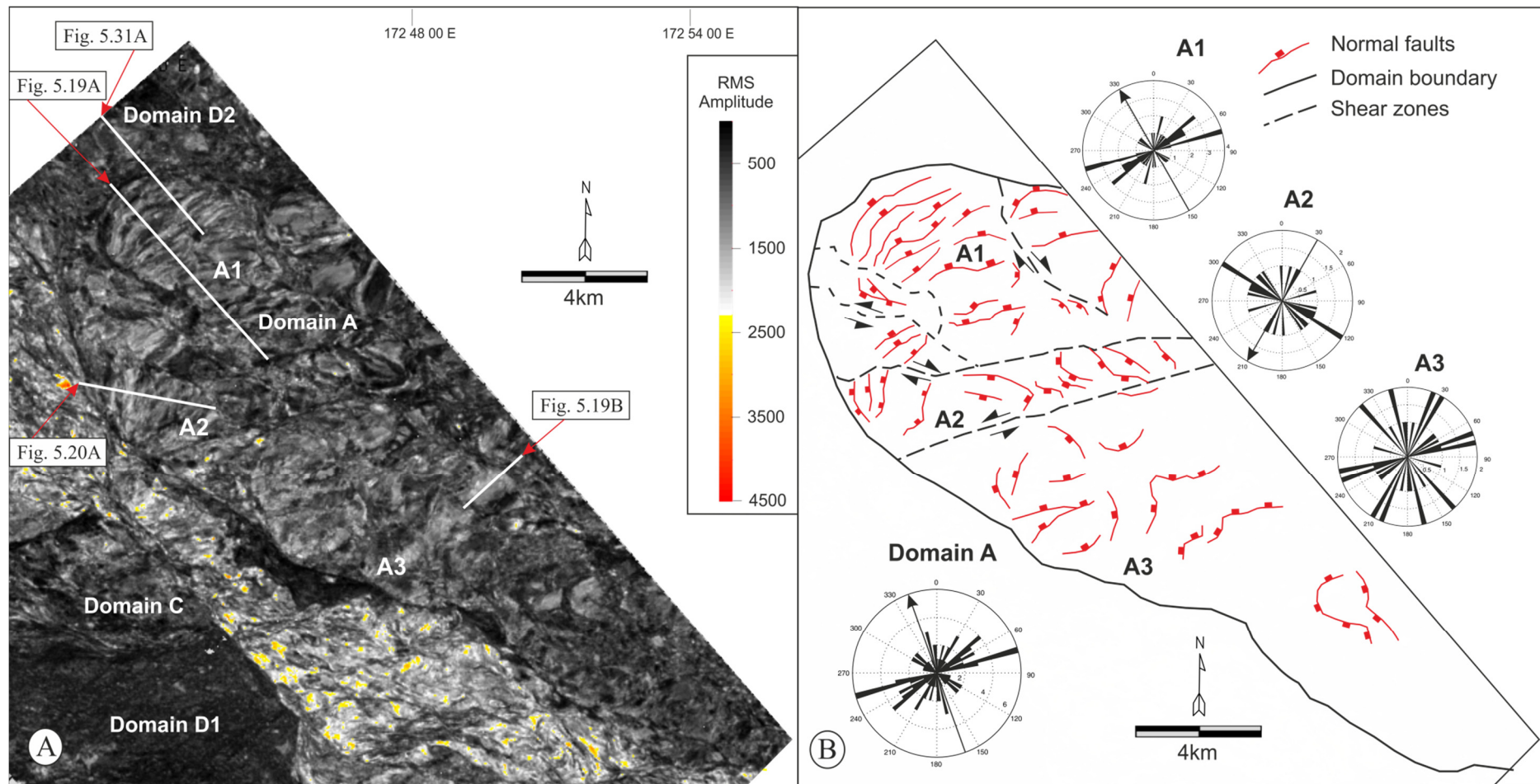
Figure 5.18. Enlarged uninterpreted windowed RMS amplitude map of MTD 6 (see Figure 5.17 for location) showing Domain A (A) and interpreted deformational pattern (B). Note the varied long axis of orientation of blocks between Sub-Domains A1, A2 and A3. The rose plots on the right of Fig. 5.18B shows the dominant orientation of faults in each sub domain, while a composite rose diagram is shown in the bottom left. The arrows indicate the interpreted local transport directions.

repetitive patterns of the blocks are quite well developed, in some places they are not laterally continuous especially towards the ENE and WSW areas of the sub-domain (Fig. 5.18A). The predominant strike of the fault bounded blocks is ENE-WSW (Fig. 5.18B), although a minor variation occurs towards the western part of Sub-Domain A1 where the orientation of the blocks changes to NW – SE.

Detailed strain analysis of faults bounding blocks in the Sub-Domain A1 was based on line balancing of the representative seismic dip profile across sub-domain where there were no significant dips out of the plane of section (Fig. 5.19C). The faults bounding the blocks have varying dip angles between 15° and 25°. A net extension of c. 210 m was calculated based on the difference between the measured value of extension (distance from A - B in Figure 19C) and the restored length of the marker horizon (blue horizon).

The fault bounded blocks in Sub-Domain A2 are generally shorter than the blocks in Sub-Domain A1, averaging c. 2 km in length with the predominant strike of the faults being NW-SE (Fig. 5.18B). A representative seismic profile through Sub-Domain A2 reveals that they are characterised by moderate to high amplitude fault bounded blocks similar to those in Sub-Domain A1 (Fig. 5.20A). However, strain analysis of fault bounding blocks in the Sub-Domain A1 could not be carried out because the blocks appear to dip significantly out of plane throughout the domain (Figs. 5.18B and 5.20A).

In Sub-Domain A3, towards the south-eastern part of the study area, the block morphology becomes less distinct (Fig. 5.18B), with blocks being more discontinuous and incoherent, and thus lack consistency in long axis orientation.

A critical observation is that the stratigraphy preserved in the blocks in Domain A are generally divisible into distinct upper and lower packages; an upper package characterised by high amplitude, continuous and inclined reflections, and a lower package that consists of transparent and chaotic seismic reflections which is c. 100 m thick (Fig. 5.19A). This can be
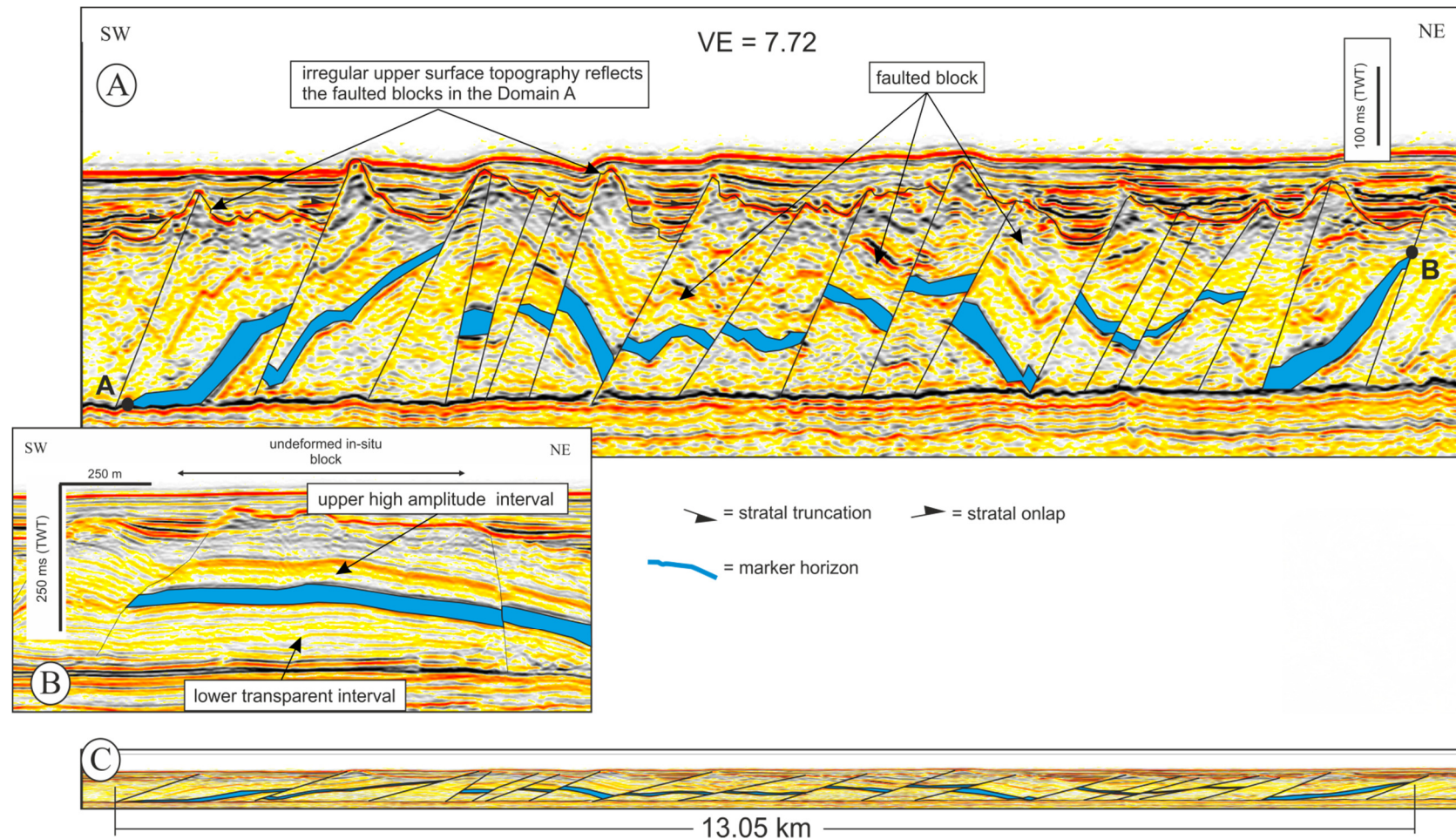
Figure 5.19 A) Representative seismic dip profile through Sub-Domain A1 (see Fig. 5.18 for location) showing the interpretation of planar fault bounded blocks. The faults tip-out at the base of MTD 6. Notice the normal and reverse relationship of the marker horizon (blue horizon) across the faults and the deformational pattern. B) Strike oriented seismic profile through the block in Sub-Domain A3 showing the original stratigraphic template of the interval. C) The same seismic profile in A without vertical exaggeration. The maximum extension, implied by the separation along the detachment (distance from A to B) is 13.05 km, while the restored length measured from the marker horizon is 12.84.
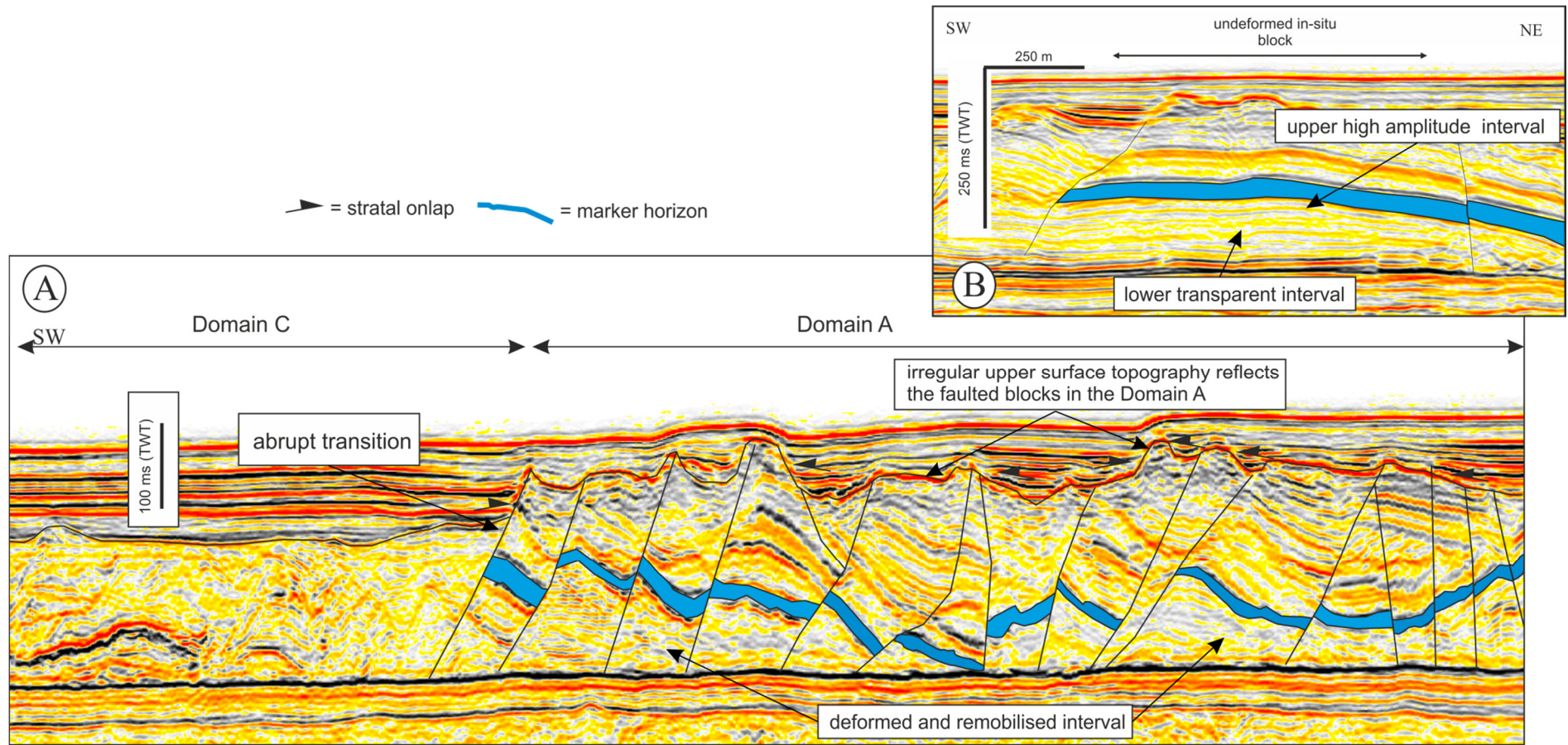
Figure 5.20 A) Seismic profile across Sub-Domain A2 (see Fig. 5.18A for location) showing the deformation and remobilisation of the lower transparent unit. B) The original stratigraphic configuration of the undeformed interval (see Fig.5.18 A for location).

seen clearly in an undeformed block in Sub-Domain A3 (Fig. 5.19B) where the block displays stratigraphic continuity with the underlying strata with no evidence of shear deformation on the base. Due to the distinctive character of the block, it is interpreted to represent the original stratigraphic template of the interval and thus is used as a marker for detailed stratigraphic correlation within Domain A.

A critical observation based on reflection correlation in Domain A (Figs. 5.19A and 5.20A), is that it is possible to identify and correlate a marker horizon (blue horizon) from one block to another dipping at varying angles. The marker horizon is offset across each extensional planar fault in a variety of senses (see below). The transparent and continuous lower interval present in the undeformed block (Fig. 5.19A) is observed to be chaotic and partly preserved or to be missing where the marker horizon dips at varying angles or is juxtaposed against the basal surface in the Domain A (Figs 5.19A and 5.20A).

Domain A is the most extensive of all the domains covering approximately 181 km^2 in the north eastern unconfined part of the study area (Fig. 5.17). The MTD 6 has an average thickness of c. 250 ms in Domain A region (Fig. 5.19A) making it the thickest domain in the study area. This is seen clearly on the isochron map of MTD 6 (Fig. 5.21) by comparing the thickness of Domain A with other adjacent domains.

It is challenging to estimate the volumetric proportion of the missing lower transparent interval in Domain A because of the varied deformation pattern of the blocks and the uncertainties stemming from the tracking of the marker horizon (blue) throughout the domain. However, from a comparison of the deformed transparent unit within Domain A (Figs. 5.19A and 5.20A) with the c. 100 ms thick undeformed transparent unit in the original stratigraphic configuration of the interval (Figs. 5.19B and 5.19B) it is estimated that c. 30% of the lower transparent and chaotic interval in Domain A is missing.

Most of the blocks in Domain A, separated by planar normal faults are interpreted to have formed due to extension and rotation of the pre-failed slope sediments (Figs. 5.19A and 5.20A). The portion of the lower transparent interval missing is interpreted to have been deformed and remobilised during failure.

This deformation presumably postdated or occurred synchronously with the localisation of planar normal faults because the bed dips (evident from the dips of the marker horizon) appear to be modified by the subsequent deformation (Fig. 5.19A). Furthermore, the small net extension of 210 m calculated in Sub-Domain A1 is thought to be as a result of the reverse relationship of the marker horizon across the planar faults which can be explained by volume loss from the lower interval (Fig. 5.19A).

A striking pattern of high isopach values in Domain A (Fig. 5.21) is interpreted to result from the rotated and protruding characteristics of the blocks thus giving it a characteristic irregular upper surface throughout much of the region (Figs.5.19A and 5.20A).

The long axis orientation of extensionally bounded fault blocks is invaluable as a kinematic indicator in the study of MTDs (Bull et al., 2009a). Based on the observation of the strike of their bounding faults, a NW transport direction is interpreted for Sub-Domain A1 (Fig. 5.18B) while a SW transport direction is interpreted for Sub-Domain A2. The lack of preservation and consistency in long axis orientation in Sub-Domain A3 suggest that the degree of deformation was probably higher than those of Sub-Domains A1 and A2 (Fig. 5.18B). The boundaries separating Domain A into three sub-zones (Fig. 5.18B) are interpreted as shear zones (sensu. Gafeira Gonçalves, 2010). They are common features of MTDs and they are mainly observed at the base of the deposit, along lateral margins or within the deposit between areas of remoulded material moving at different speeds, at different times, with different flow behaviour or with different material characteristics (Gafeira et al., 2010). Recent analogue modelling of debris avalanches has shown that strike-
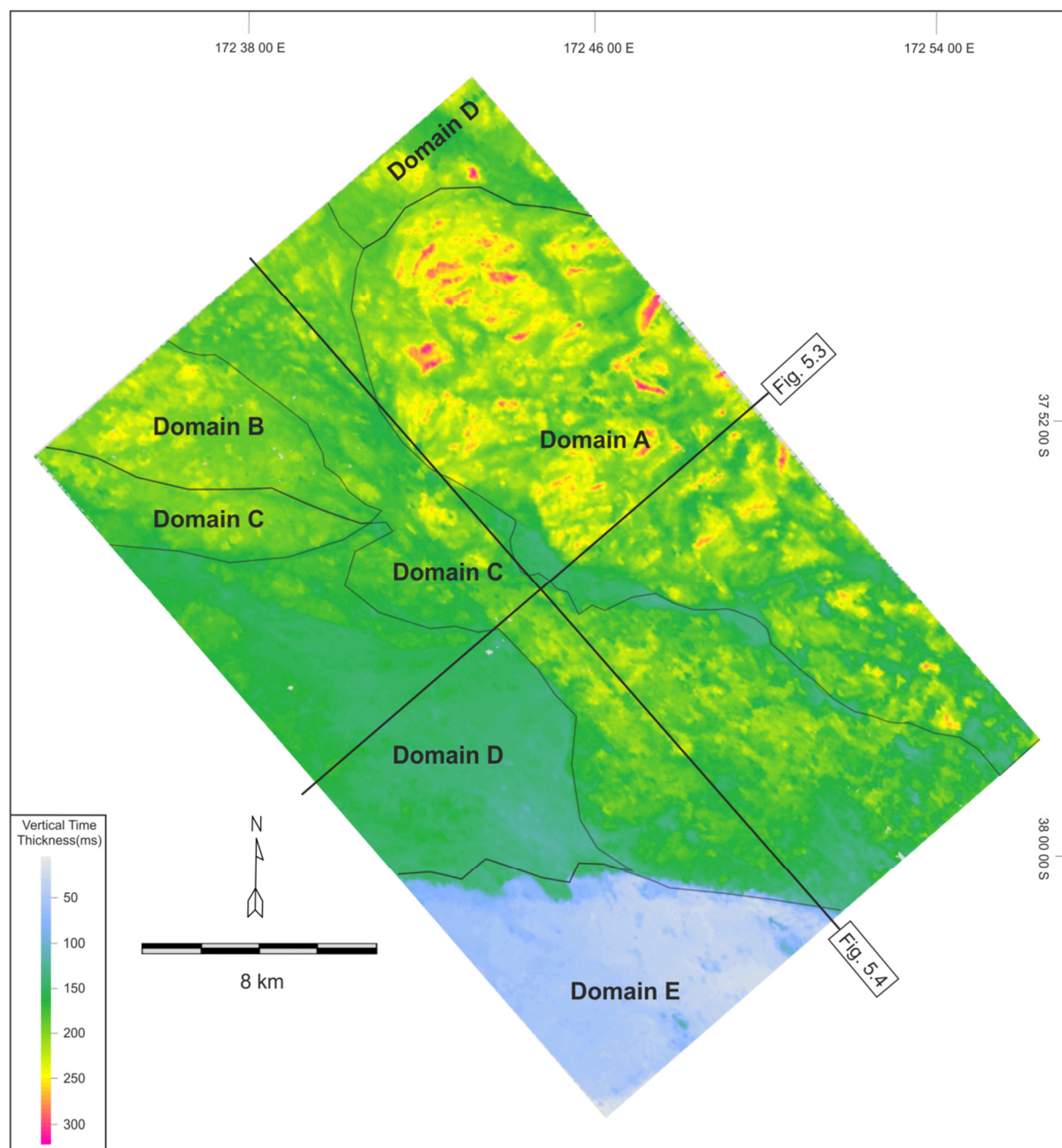
Figure 5.21. Isochron map of MTD 6. The thickest MTD 6 material is observed to occur in the north and north-eastern corner of the study area whilst the thinnest deposits are observed in the southern corner. The locations of seismic profiles shown in Figures 5.3 and 5.4 are shown.

slip faults develop within the failing mass in order to accommodate strain generated by spatially variable emplacement velocities (Crosta et al., 2012; Longchamp et al., 2012). However, the same interpretation cannot hold true for the main shear zones separating Sub-Domains A1, A2 and A3 since the strike of the fault bounded blocks within the sub-domains are oriented in markly different directions. Therefore, it is very unlikely that they were generated by spatially variable emplacement velocities. This would imply that either the flow behaviour and/or the material characteristics are the main controlling factors for the development of these shear zones. It is suggested that the shear zones within Sub-Domain A1, which are mainly oriented in a NW direction (Fig 5.18B) is a manifestation of the spatially variable emplacement velocities across the sub-domains (Crutchley et al., 2012).

5.3.4.2 Domain B

Domain B is defined by a series of elongated ridges and troughs with alternating high to moderate amplitudes respectively that are either straight or arcuate and are mostly parallel to each other (Fig. 5.22). These ridges and troughs are seen on a representative seismic profile to consist of imbricated sequences of upright folds. The folds consist of multiple alternate bands of high and low amplitude reflections (Fig. 5.23). Thrusts structures are observed towards the north-western part of this domain, with most of the thrust faults detaching on the basal surface (Fig. 5.23B).

Domain B is located on the western corner of the study area (Fig. 5.17) and covers a relatively small portion of the survey area (c. 41 km^2). Although the morphological signature of Domain B appear to be similar to that of Domain A, the series of ridges and troughs in the Domain B are thinner and longer (Fig. 5.22A) than those in Sub-Domains A1 and A2 (Fig. 5.18A). Individual ridges measure up to 1.75 km in length and are irregularly spaced. The
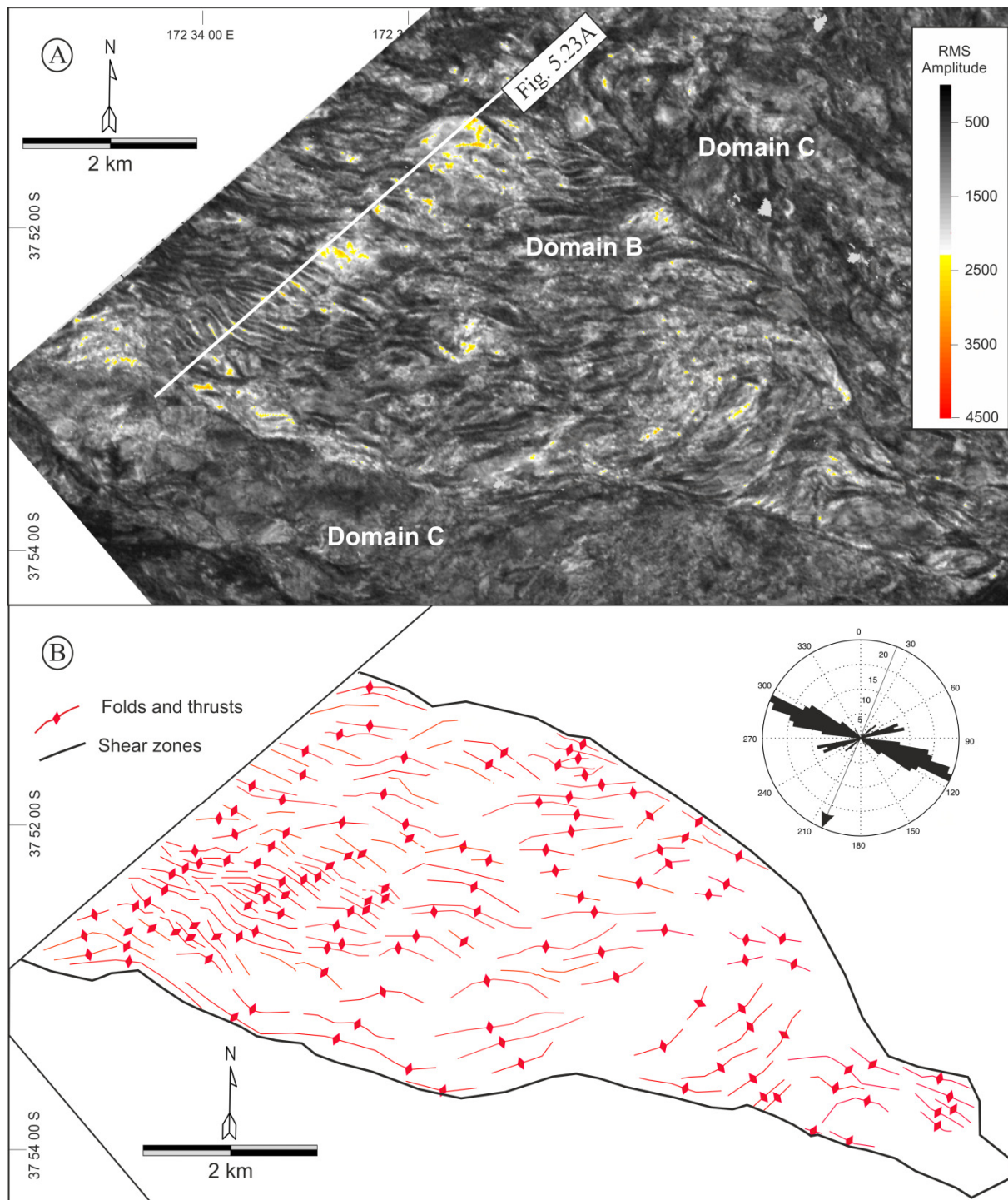
Figure 5.22 A) Enlarged uninterpreted windowed RMS amplitude map of Domain B (see Fig. 5.17 for location) showing enlongated ridges and troughs. The location of the seismic profile shown in Figure 5.23A is shown. (B) Interpreted Domain B showing ridges closely spaced towards the west of the domain relative to the northern and eastern parts of the domain. The rose plot shows that the predominant strike direction of the ridges is WNW – ESE.
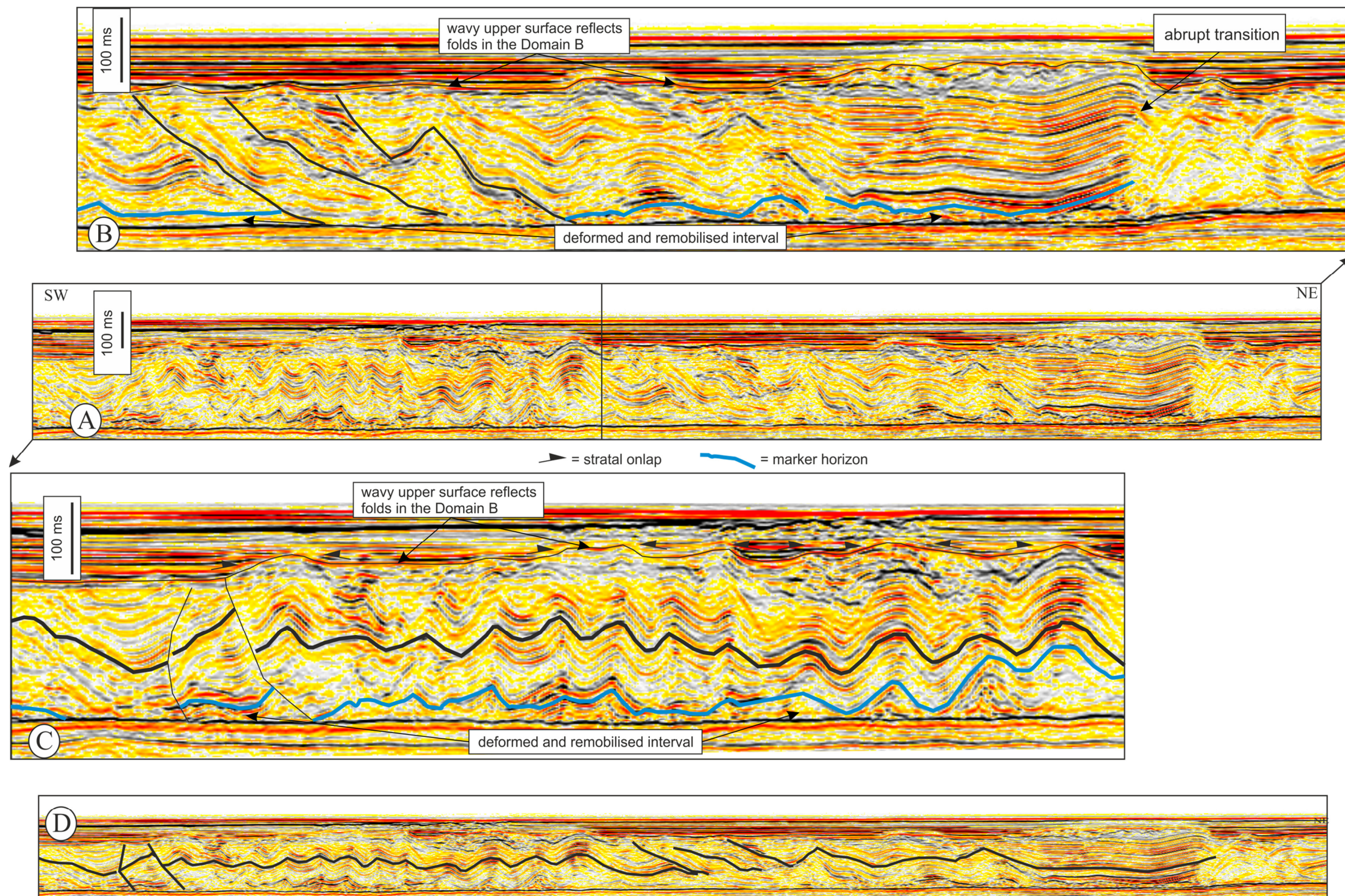
Figure 5.23 A) Seismic dip profile through Domain B (see fig. 5.20 for location) with vertical exaggeration showing a suite of upright folds and imbricated thrusts. This profile was used to estimate the amount of stratal shortening represented in Domain B. (B) Enlargement of the seismic profile in A showing imbricated thrusts structures detaching on the basal surface of the deposit (C) Enlargement of the seismic profile in A showing imbricated thrusts structures. Notice how the lower marker horizon sometimes terminate against the basal surface D) same seismic profile in A (with no vertical exaggeration) used to estimate the amount of stratal shortening represented in Domain B. The deformed distance between the first fault (on the left of D) and the end of the black horizon in (D) is 3.69 km; its restored equivalent distance is 4.8 km, so the net contraction is 1.11 km.

ridges are closely spaced towards the west of the domain relative to the northern and eastern parts. They predominantly strike in the WNW – ESE (Fig. 5.22B).

Thrust faults within Domain B of MTD 6 vary in height from 75 to 125m (average 85 m), basal tip to upper tip distances are 100–150m. The thrust planes dip between 15–25° and the maximum thrust displacement ranges from 20 to 30 m (Fig. 5.23B). Detailed strain analysis of folds and thrusts in Domain B was based on line balancing similar to that carried out for Domain A. An estimated amount of shortening of c. 1.11 km is accommodated by the folds and thrust structures (Fig 5.23D).

A critical observation based the representative seismic profile across the fold axis strikes in Domain B is that a higher marker horizon (black) can be tracked across the folds (Figs. 5.23B and C), while a lower marker horizon (blue) sometimes abuts and terminates against the basal surface. It is conceivable that part of the deformed unit beneath the lower marker horizon (blue horizon) is missing and this observation is consistent with that seen in Domain A (Fig. 5.19).

The thickness of MTD 6 in Domain B varies between 200 ms to 250 ms (Figs. 5.21 and 5.23), and this observation is largely due to the undulating upper surface within the domain.

The suite of upright folds and imbricated thrust faults observed in Domain B are interpreted to form under compressional stress that derives from the internal buttressing or slowing down of the translating MTD probably due to a decrease in the gradient of the basal surface (Bull et al., 2009a; Frey-Martínez et al., 2006). The evidence for this is supported by the fact that Domain B lies in a relatively flat region within the MTD 6 (Fig. 5.6). In addition, contractional ridges have been reproduced in regions where failure decelerates on a more gently dipping basal surface in analog models (Major, 1997; Moriwaki et al., 2004). Furthermore, upright symmetrical folds such as those observed in Domain B suggest that the MTD 6 has not translated long distances (Farrell and Eaton, 1987). In fact, the blocks just

behind the upright folds are observed to collide and override them resulting in the thrust blocks in Figure 5. 23B.

Folds and thrust structures are valuable kinematic indicators of the MTD translation direction because they are thought to be oriented transversely to the dominant transport direction (Bull et al., 2009a). Consequently, the NW - SE oriented arcuate ridges that correspond to the folds and thrust system in Domain B (Fig. 5.22B) indicates a dominant SW transport direction. It is very unlikely that a local NW transport direction could be interpreted for the Domain B because of the position of the thrust structures behind the upright asymmetrical folds and the convex downslope arcuate shape of the elongated ridges. Therefore, these features jointly imply that the failure propagated in the SW direction parallel to bedding but ceased with the development of upright folds. However the increased propagation of the failed material behind the folds was accommodated by slip on the thrust faults which developed over and behind the upright folds (Fig.5.23B).

5.3.4.3 Domain C

Domain C is defined by high to moderate amplitude, isolated square to circular features and elongated ridges that are straight or arcuate and sometimes parallel, similar to those seen in Domain B (Fig. 5.24A). They strike in a dominant WNW – ESE direction. A close examination of Domain C on representative seismic profiles reveals its complex internal structure (Fig. 5.25). The WNW – ESE elongated or arcuate ridges correspond to folds that are discontinuous and are cross-cut by planar normal faults which results in a complex set of alternating compressional and extensional structures (Fig. 5.25). The faults are sometimes observed to extend to the basal surface or terminate on a lower marker horizon (blue). The marker horizon (blue) is sometimes in contact with the basal surface or even terminates against it. This observation is consistent with the basal geometry interpreted in Domains A
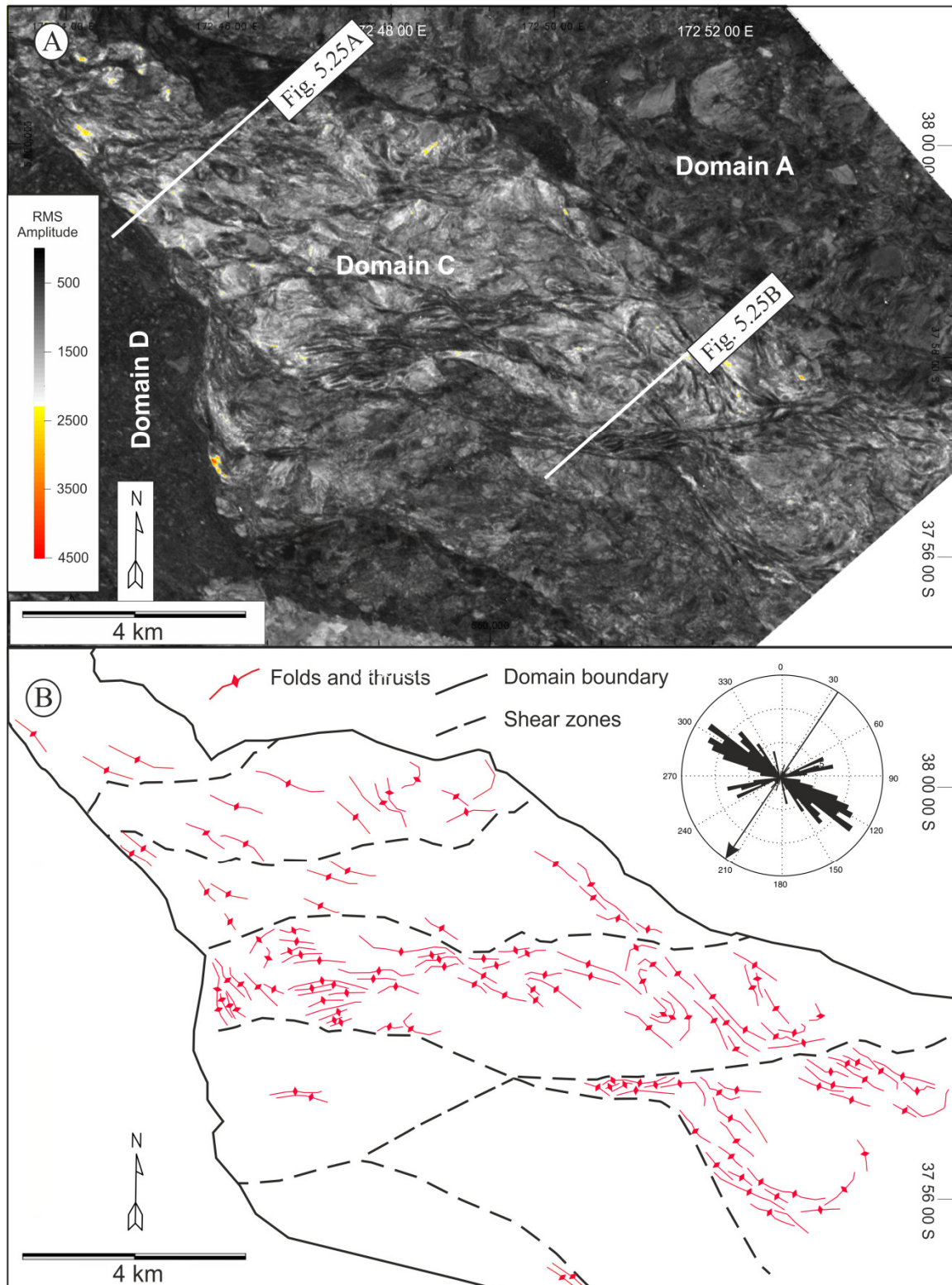
Figure 5.24 A) Enlarged uninterpreted windowed RMS amplitude map 25-50% window within Domain C (see Fig. 5.17 for location) showing complex deformation of alternating contractional and extensional zone. The locations of seismic profiles shown in Figures 5.25A and B are shown. (B) Interpreted Domain B showing elongated ridges that are either straight or arcuate as well as high amplitude random blocks Rose plot show a predominant WNW – ESE direction for the folds.
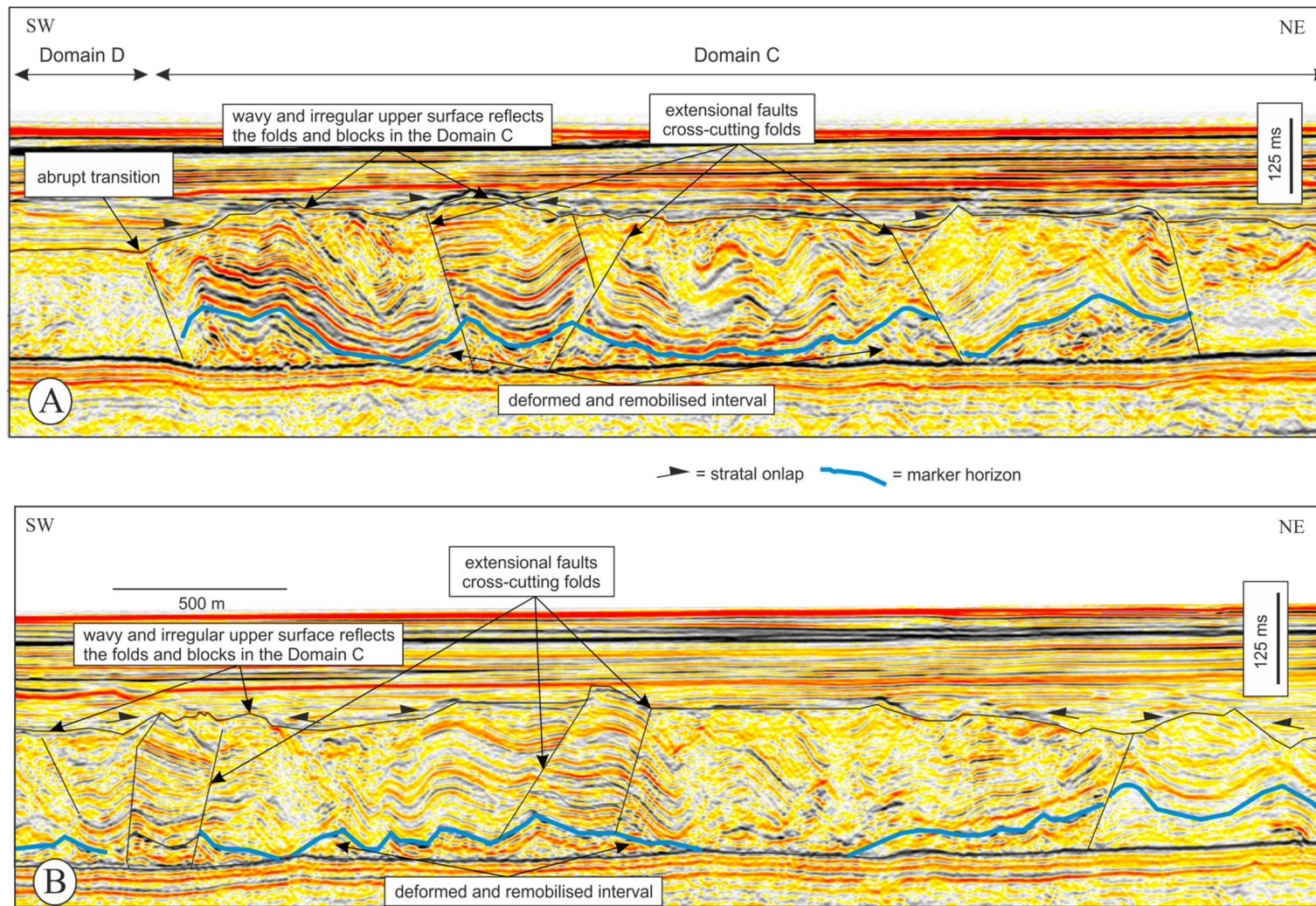
Figure 5.25. Seismic dip profiles through the central region (A) and the south-eastern region (B) of Domain C showing folds that are crosscut by faults. Notice the variation of the marker horizon (blue) bounding the deformed and remobilised unit in both seismic profiles and how it is sometimes juxtaposed against the basal surface. Also notice the abrupt boundary separating Domains C and D in (A).

and B (Figs. 5.19 and 5.23 respectively). Domain C is relatively extensive and covers approximately 176 km^2 of the study area. It spans the entire length of the study area, although it bifurcates in the central region, with one branch extending towards the northwest and the other towards the west (Fig. 5.17). Furthermore, it fans out from the central region towards the south-eastern limits of the study area.

A set of lineations that are generally oriented in an E- W direction are recognised in Domain C (Fig. 5.24). These lineations are mainly observed in the south-eastern part of the study area and appear to be semi-parallel to each other in most cases, although, they cross-cut each other in the southern limits of the surface. They increase in length from c. 2 km the central region to c. 10 km towards the south-eastern limits of the study area.

The suite of upright folds in Domain C has expressions of in-plane compressional structural style that are similar in many aspects to those observed in Domain B. However, the relationships of the folds and normal planar faults structures in Domain C (Fig. 5.25) suggest a strain overprinting deformational style (cf. Farrell, 1984). The cross-cutting of the folds by planar normal faults and the fact that the faults sometimes terminate on the lower marker horizon (blue) suggest that contractional strain was overprinted by later extensional strain. Strain overprinting is common in outcrop examples of mass transport deposit but seldom described in seismic examples (see Apendix of Atlas of MTDs).

(Farrell, 1984) proposed a model for strain overprinting which can be explained by the propagation of a special dislocation termed an anti-dislocation (Fig. 5.26). The anti-dislocation will propagate either to the rear or front and re-deform the mass transport deposit as it regains cohesion with the substrate. Farrell (1984) suggested that when an MTD comes to rest at the base of slope, the anti-dislocation will migrate up the basal surface with associated contractional waves being the final strain overprint (Fig. 5.26A). On the contrary,
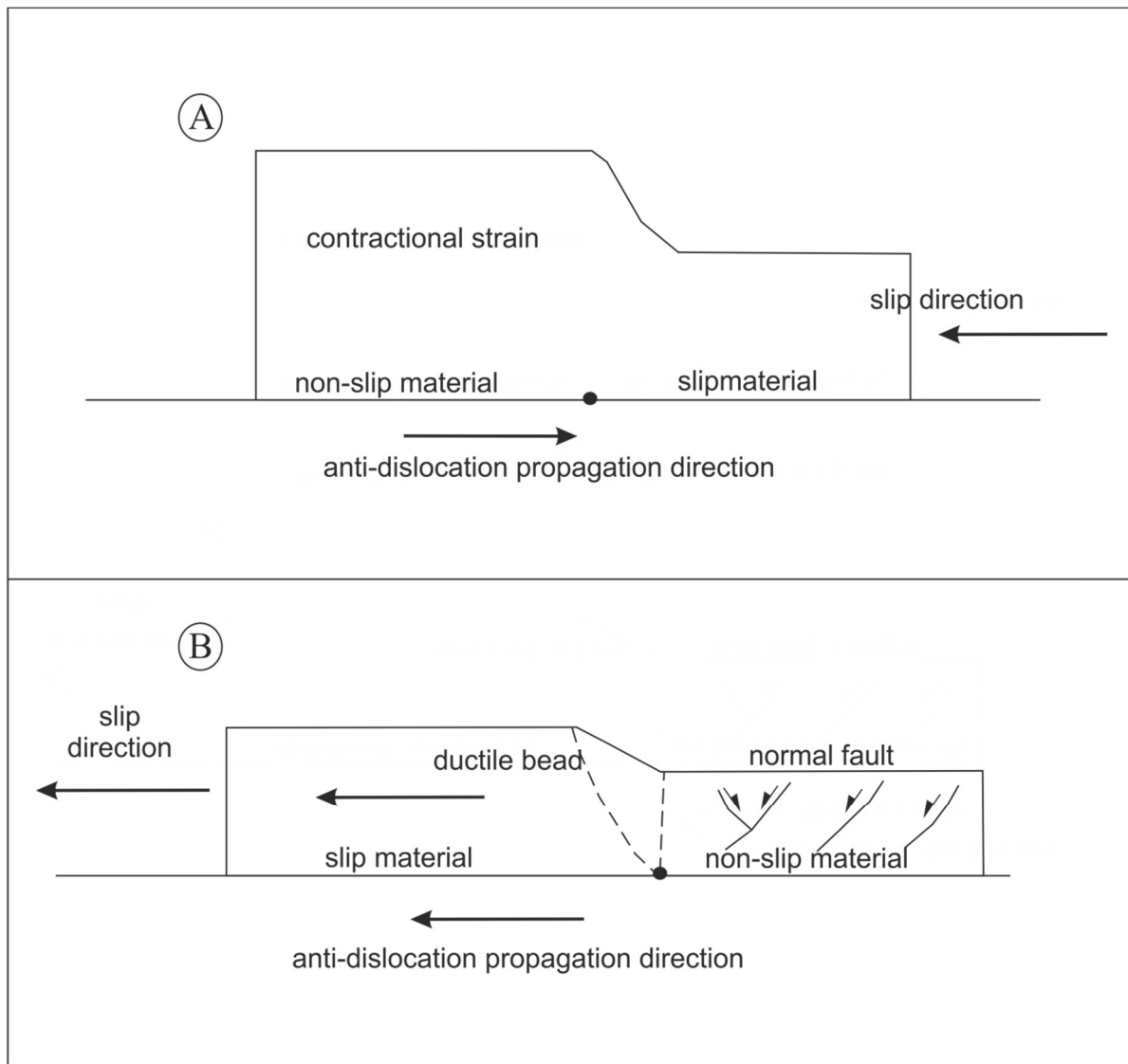
Figure 5.26 Diagram illustrating the strain overprinting in slumps (modified from Farrell, 1984). A) If slumps halt first at their downslope margin, the anti-dislocation associated with contractional strain wave will propagate upslope through the slump, overprinting any earlier formed structures by contractional structures. B) In contrast, if the slumps halt first at their upslope margin (for instance due to initial pore-water escape there), the anti-dislocation associated with an extensional strain wave will propagate downslope through the slumps, causing extensional structures to overprint earlier formed structures.

if the MTD occurs in a region of elevated pore pressure, fluids will escape preferentially from fractures/faults in the rear of the MTD, since the initial failure event has left the rear portion of the MTD cut by normal faults (Farrell, 1984). This will increase the shear strength at the rear of the MTD, causing the upslope propagation to arrest. An anti-dislocation will migrate from the rear to the front of the MTD as it is moving, with extensional waves being the final strain overprint (Farrell, 1984) (Fig. 5.26B). The sequence of events suggested for the later model can be applied to the structural interpretation of Domain C. It is conceivable that the extensional strain that characterised Domain C migrated downslope and overprinted the already developed contractional structures of Domain C once Domain A came to rest because of increased friction on the basal surface.

As previously mentioned, the folds axes and fault strikes are invaluable kinematic indicators of the MTD translation direction because they are thought to be oriented transversely to the dominant transport direction (Bull et al., 2009a). Consequently, the dominant NW - SE oriented folds axes in Domain C (Fig. 5.24B) indicates a SW transport direction similar to those in Domain B. Although, there is evidence of minor variation in the transport direction to the NW as indicated by some of the structures in this complex domain (Fig. 5.24B). The interpreted dominant SW transport direction in Domain C is consistent with the set of E – W oriented lineations interpreted as shear zones (Fig. 5.24B). They appear to share the same E - W orientation to those separating the sub-domains of Domain A. However the shear zones in Domain C are thought to be manifestation of the spatially variable emplacement velocity/speed across the Domain C (sensu. Crutchley et al., 2012).

5.3.4.4 Domain D

Domain D is defined generally by a low amplitude facies with some occasional isolated high amplitude features in plan view (Fig. 5.27). Representative seismic profiles show that it is

characterised by acoustically transparent, homogenised facies with the preservation sometimes of ghost stratigraphy of remnant structures (Fig. 5.28). Domain D covers a total area of c. 128 km^2 and is divided into three sub domains (Sub-Domains D1, D2 and D3) (Fig. 5.17) on the basis of the presence or lack of remnant structures and if there are, the type of strain associated with the remnant structures within the domain.

Domain D1 is characterised by very low amplitude facies and lacks any sort of remnant structures in map view (Fig. 5.27). It is transparent, completely homogenised with a characteristic smooth upper surface (Figs. 5.3, 5.14A and 5.28A). Domain D2 is defined by moderate amplitude features in map view (Fig. 5.18A) which corresponds to partial remnants of extensional blocks. It has an undulating upper surface (Fig. 5.31A). Domain D3 is characterised by moderate amplitude features in map view (Fig. 5.27) which correspond to partial remnants of contractional folds with a sometimes undulating upper surface similar to Domain D2 (Figs. 5.28B and 5.31B).

A critical observation is that MTD 6 reduces in thickness in Domain D, to typically between 100 – 150 ms, much thinner compared to adjacent domains (excluding the Domain E, south of the E – W trending ramp) (Figs. 5.3 and 5.21).

An interesting observation is that a high concentration of the mounded structures beneath MTD 6 (Figs. 5.7B) is restricted to the Domain D region. This can be clearly observed by comparing the interpreted dip map of the basal surface and windowed amplitude map of the deposit (Figs. 5.7B and Fig 5.17 respectively).

The homogeneous acoustic character of Domain D (especially Domain D1) is thought to result from complete or partial deformation and subsequent remobilisation of previously deformed structures within MTD 6 (especially in the adjacent Domains A and C). This interpretation is based on the preservation of ghost stratigraphy of either extensional or contractional structures that characterise the aforementioned domains. Furthermore, the
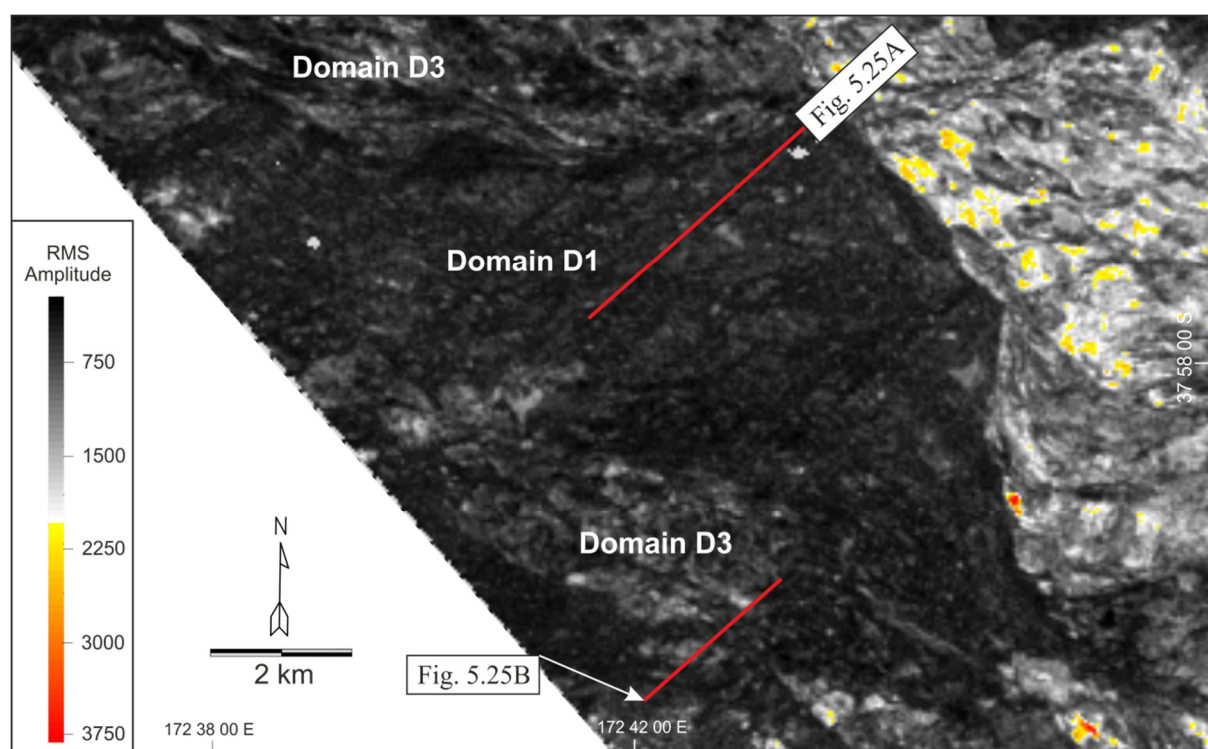
Figure 5.27. Enlarged uninterpreted RMS amplitude map (25-50% window) within Domain D of MTD 6 (see Fig. 5.17 for location) showing both the low amplitude facies that characterised Sub-Domain D1 and the moderate amplitude ridge-like features that characterise Sub-Domain D3. These features are interpreted as remnants of contractional structures (folds). The locations of seismic profiles in Figures 5.28A and B are shown.
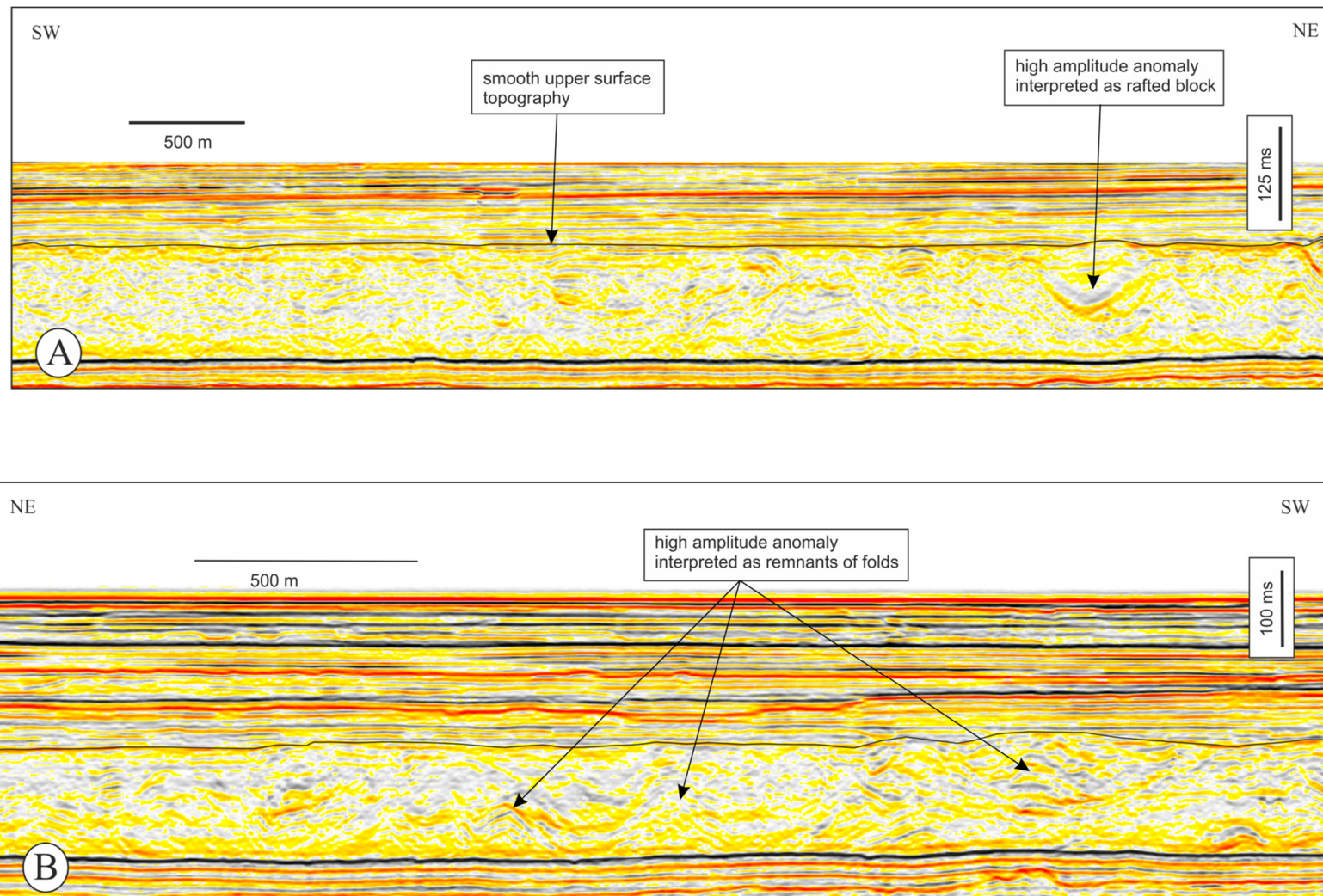
Figure 5.28 A) Seismic profile through Domain D1 of MTD 6 showing a transparent and highly deformed deposit. Notice the smooth and continuous upper surface B) Seismic profile through Domain D3 showing transparent and remnants of contractional structures (folds) within the deposit (see Fig. 5.27 for the location of the seismic profiles).

interpretation is supported by the fact that MTD 6 is characterised by a reduction in thickness in Domain D compared to the other domains (Figs. 5.3 and 5.21). An exception is Domain E, but this can be explained because it mobilises younger sediments on a higher stratigraphic level (Fig. 5.8). The almost complete loss of seismic character is perhaps similar to phenomena seen at smaller scale that has been recognised in cores collected from MTDs (e.g (e.g Tripsanas et al., 2008), as well as MTD outcrops (e.g Ogata et al., 2012) and in other seismic studies of MTDs (e.g Huvenne et al., 2002; Jackson, 2012). Given the key observations, the Domain D1 is therefore interpreted here as a seismic expression of a matrix: the ultimate product of a mass transport related soft sediment deformation recording the complete stratal disruption of poorly lithified stratigraphic successions (Ogata et al., 2012). Although there is no well control to calibrate the lithology and physical properties of MTD 6, the transparent seismic character (Fig. 5.13C and D) suggests a dominantly fine-grained parent lithotype.

5.3.4.5 Domain E

Domain E is generally defined by a high to moderate amplitude mottled pattern, although some isolated high amplitude features can also be identified in map view (Fig. 5.29). It is located south of the E – W trending ramp and covers c. 51 km^2 of the study area (Fig. 5.17). The seismic expression of Domain E is characterised by a transparent, laterally continuous to discontinuous and relatively coherent reflection package (Fig. 5.30). Locally, however, the isolated high amplitude features observed in map view are interpreted as laterally restricted blocks (sensu. Jackson, 2012) and this can be clearly seen in Figure 5.29.

The upper surface of MTD 6 within Domain E is sometimes characterised by an undulating topography with relief of up to 60 ms, especially in areas where the blocks are well developed (Fig. 5.12). In contrast, the upper surface is smooth where blocks are predominantly absent (Fig. 5.30).
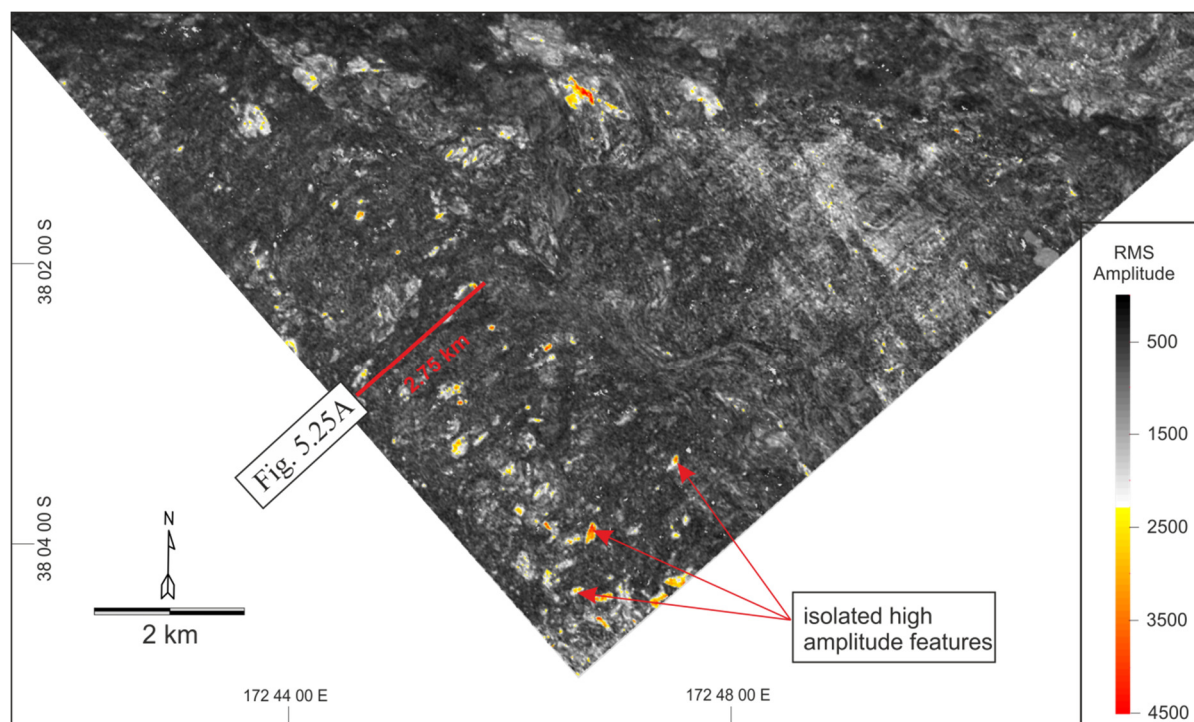
Figure 5.29. Enlarged RMS amplitude map (25-50% window) within Domain E of MTD 6 (see Fig. 5.17 for location) showing a low amplitude mottled pattern. The isolated high amplitude features are interpreted as intact discontinuous blocks. The location of the seismic profile in Figure 5.28A is shown.
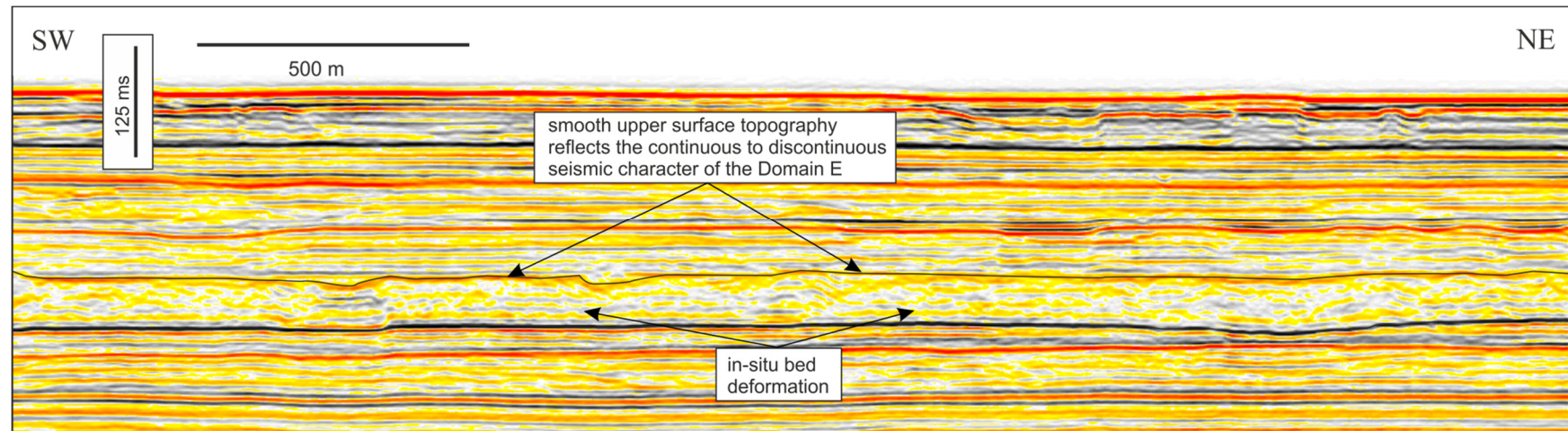
Figure 5.30 A) Seismic dip profiles through Domain E showing continuous to discontinuous amplitude reflection which implies that Domain E has undergone less deformation.

The basal surface of MTD 6 within the Domain E is characterised by subtle relief i.e. grooves where blocks are developed (Fig. 5.12). The relatively continuous and coherent seismic reflections within Domain E (Figs. 5.12B-C and 5.30) suggests that it has not been highly deformed. In fact, the layered stratigraphy of the blocks within Domain E (Figs. 5.12B-C) suggests that the blocks were probably formed in-situ and have not been transported any significant distance.

Domain E lies at a higher stratigraphic level compared to the other domains of MTD 6 which detach on a common basal surface. Consequently, it is thought to result from the mobilisation of younger sediments on a higher stratigraphic level from the main MTD 6 failure as previously mentioned (Fig. 5.9B – E). This would imply that Domain E would have represented an earlier failure which predated the emplacement of the other domains of MTD 6. This interpretation is supported by the abrupt termination of the NW oriented paleo channel observed on the basal surface of MTD 6 in Domain E region (Figure 5.7) and the westward shearing of blocks on the adjacent to the E –W oriented ramp that delimits Domain E (Fig. 5.9).

5.3.4.6 Domain boundaries

The boundaries between the identified domains within the study area appear to vary from one domain to the next. Sub-Domains A1 and D2 in the northern part of the study area is separated by an arcuate NW dipping boundary across which no thickness variation is observed (Figs. 5.18A and 5.31A). However, Sub-Domain D2 becomes increasingly transparent with some isolated high amplitude coherent reflections and has been interpreted in this study as remnants of extensionally faulted blocks preserved within the highly deformed Domain D. This evidence implies that the boundary between Sub-Domains A and D2 is transitional (Fig. 5.31A).
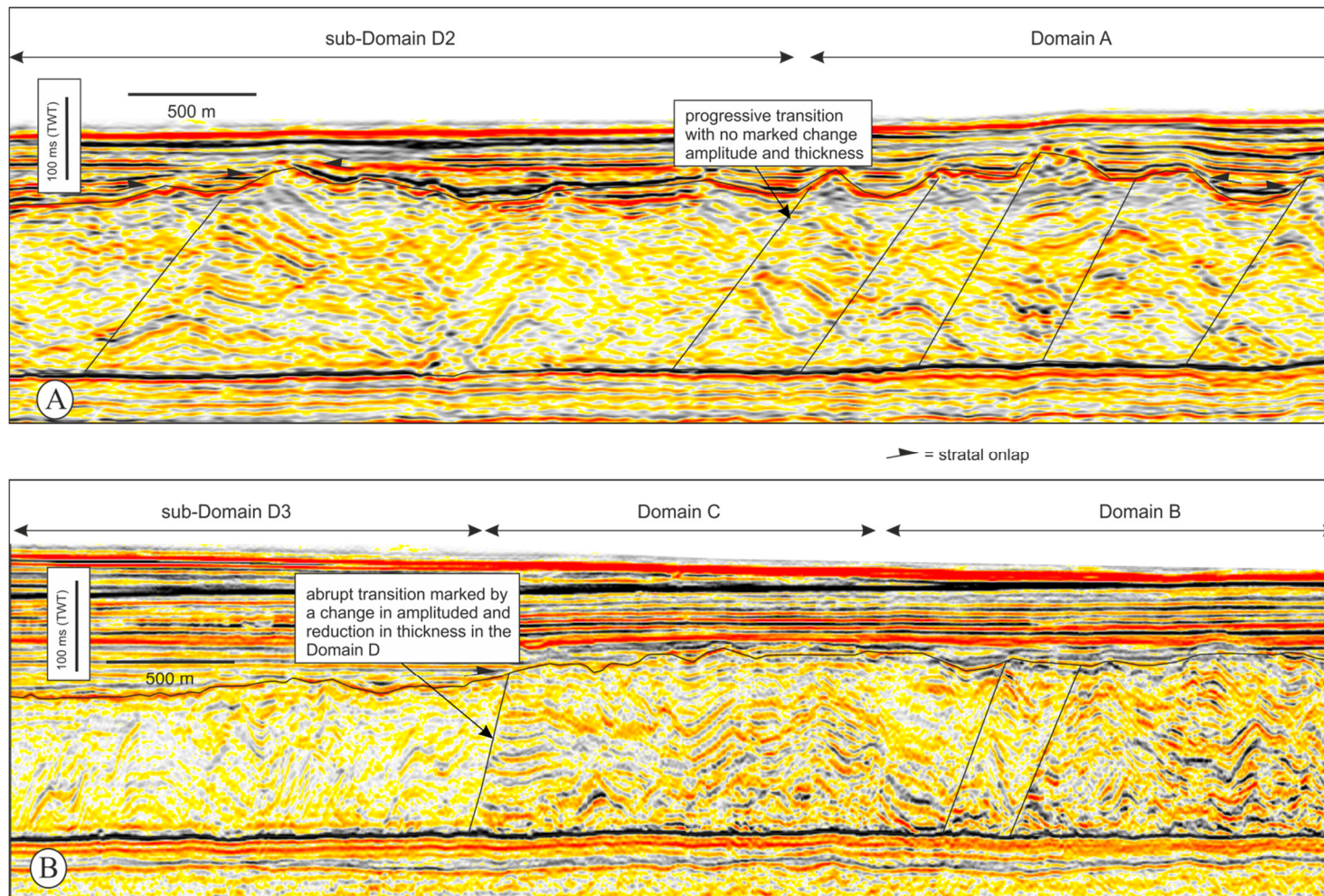
Figure 5.31. Representative seismic profiles across A) the boundary between Sub-Domain A1 and Sub-Domain D2 (see Fig. 5.18A for location) showing a progressive transition with no marked changes in thickness or amplitude. B) the boundary between Domain C and Sub-Domain D3 (see Fig. 5.17 for location) showing an abrupt transition with marked changes in amplitude and reduction in thickness in Sub-Domain D3.

In contrast, Sub-Domain A2 is separated from Domain C in the central region by a SW- in dipping fault across which there is a clear change in internal architecture and a 25 ms reduction in thickness in Domain D (Fig. 5.20A). This evidence implies an abrupt transition between Sub-Domain A2 and Domain C.

There is no variation in amplitude and/or thickness of MTD 6 across the WNW boundary separating Domains B and C except for the deformational styles in these domains (Figs. 5.17 and 5.31B). These observations suggest a progressive transition between both domains.

However, the WNW boundary separating Domain C and Sub-Domain D3 is characterised by a change to low amplitude and with a slight reduction in thickness of c. 20 ms in Sub-Domain D3 (Fig. 5.31B). Similarly the generally NW oriented boundary separating Domains C from Sub-Domain D1 in the central region appears to be abrupt with a significant change in sediment remobilization style (Fig. 5.3). Sub-Domain D1 becomes transparent and there is also a marked reduction in thickness (c. 40 ms) compared to Domain C. These observations suggest an abrupt transition into Domain D from adjacent domains and would thus imply a deformational process that is significantly different from the adjacent domains.

Domain D is separated from Domain E by a boundary that is defined by an E-W oriented ramp in contrast to other boundaries in the study area. The boundary is generally marked by a reduction in MTD 6 thickness and deformation style in Domain E as previously mentioned (Fig. 5.8). MTD 6 is characterised by chaotic low amplitude seismic facies (in some cases representing preserved remnant structures) and tends to be c. 70 ms thick in Domain D. However, MTD 6 reduces in thickness to c. 30 ms and becomes less chaotic across the boundary with continuous to discontinuous low amplitude reflection packages in Domain E.

5.4 Discussion

The geomorphologic and stratigraphic interpretation of MTD 6 using 3D seismic data and techniques has shown that the internal architecture consist of five distinctive domains (labelled A – E) occurring over a gently dipping basal surface except for Domain E which occurs on a higher stratigraphic level. These domains are characterized by contrasting deformational styles and thus different kinematic indicators. Domain A is dominated by barely deformed extensionally faulted blocks moving differentially (Figs. 5.18 and 5.19). Domain B is dominated by contractional folds and thrust structures with a dominant SW translation direction (Figs. 5.22 and 5.23). Strain overprinting where early formed folds are truncated by late faults characterise Domain C with a dominant SW transport direction (Figs 5.24 and 5.25). Domain D is characterised by intense deformation and partial deformation of previously extensional and contractional structures coupled with c. 30% reduction in thickness compared to adjacent domains (except Domain E) (Figs. 5.27 and 5.28). Furthermore, the basal surface of MTD 6 is characterized by the presence of two sets of grooves (G1 and G2 which are oriented in SW and NW directions respectively), and the E – W oriented ramp (Fig 5.7).

All of these observations raise obvious questions: 1) What do the contrasting kinematic indicators tell us about the transport direction of the entire MTD 6? 2) What process of deformation explains the close proximity of the distinctive domains? 3) What controls the deformation and remobilization of part of the lower transparent interval in Domains A, B and C and in addition to the partial and/or complete deformation of Domain D.

In this section, an attempt is made to answer these questions. Particular emphasis is placed on 1) Ranking the kinematic indicators in order of their reliability to determine the actual transport direction of MTD 6, and 2) Comparing the deformational styles across domain boundaries in order to unravel the deformational processes.

5.4.1 Kinematic indicators

From Chapter 4, the identification of primary constraining features of MTD 6 (including lateral margins, deflection around the Aeteo Seamount and the thickness reduction towards distal areas), suggested a SW transport direction within the Giant Foreset Formation whose depositional patterns clearly relates to the rapid progradation of the modern continental margin towards the NW (Hansen and Kamp, 2006a; Soenandar, 1992).

In this chapter, the high resolution 3D seismic survey revealed the presence of series of SW – NE oriented G1 lineations (interpreted as grooves) directly underlying the extensionally faulted blocks of Domain A (Fig. 5.7). Grooves have been suggested as very useful kinematic indicators since they reveal information relating to the transport direction of the mass transport deposit downslope (Bull et al., 2009a; Gee et al., 2005; Posamentier and Martinsen, 2011). Therefore the 3D seismic data is ideally suited for investigating the relationship between the blocks in the Domain A and the well preserved underlying grooves. However, in this present study, the orientation of the underlying G1 lineations is parallel to the extensional fault strikes bounding the blocks. Thus the translation direction of the MTD cannot be simply inferred as suggested by previous authors (Bull et al., 2009a; Gee et al., 2005; Posamentier and Martinsen, 2011). To investigate this question further, the RMS amplitude map (Fig. 5.17) showing the detailed orientation of the blocks within MTD 6 was draped over the time-structure map of the basal surface showing the orientation of the G1 and G2 lineations (Fig. 5.7). This combined image reveal that some of the lineations observed on the time dip map of the basal surface are shear/fault planes separating individual blocks that once extended to the basal surface (Fig 5.32).

A seismic profile parallel to the transport direction of the blocks in Sub-Domain A1 suggests that these blocks are rotated elements of the original pre-failure stratigraphy that have been displaced from the SE – NW along a series of normal faults (Fig. 5.19).
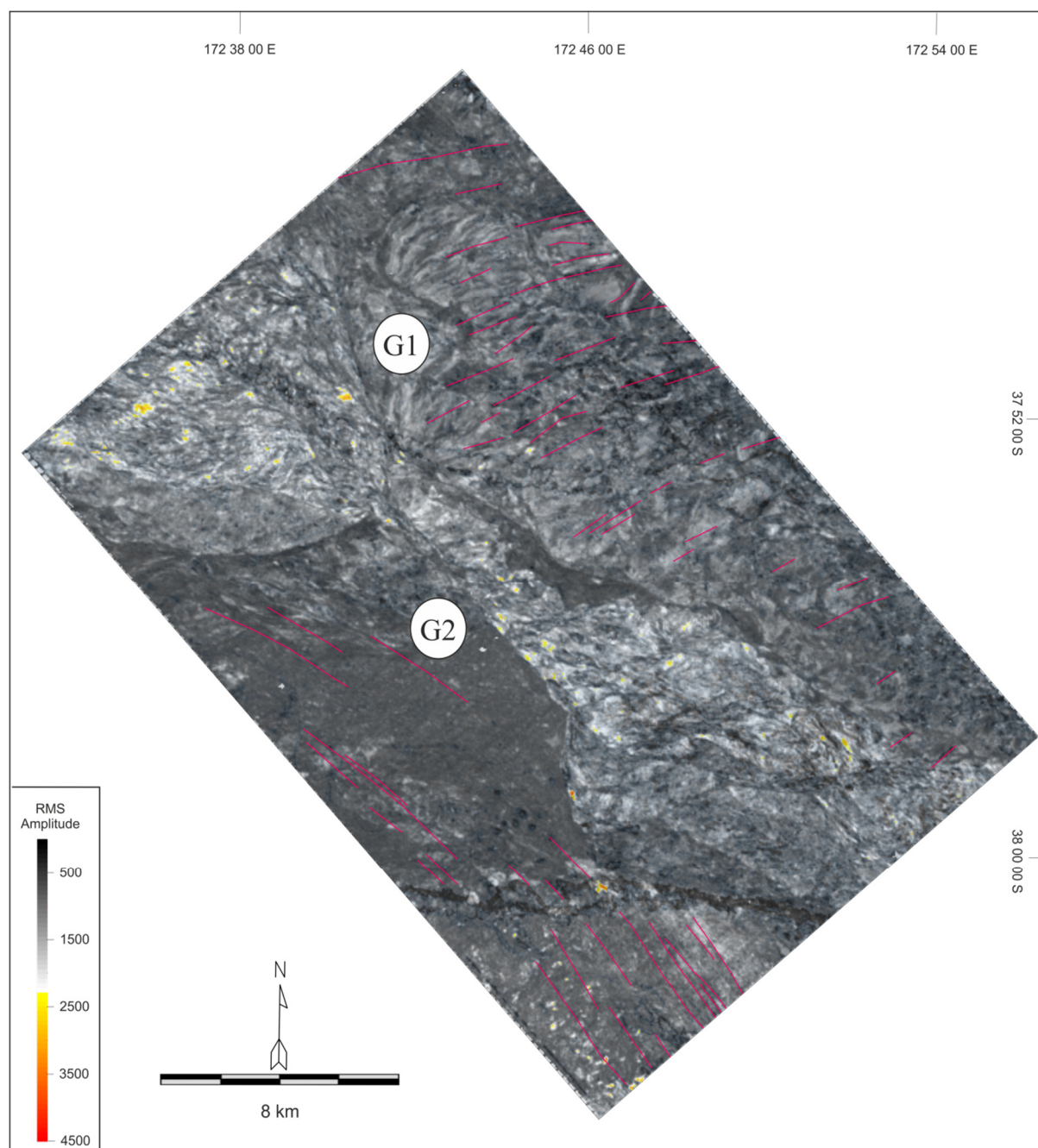
Figure 5.32. RMS amplitude map in Figure 5.16A draped over the time dip map in figure 5.7B Note that the high RMS amplitudes are displayed in white and orange (interpreted as MTD blocks or folds), and low amplitudes are dark grey (interpreted as matrix) in order to obtain a better visualisation of the morphological features involved. The orientations of the two sets of grooves on the basal surface of MTD 6 are labelled G1 and G2.

A similar pattern has been observed in Sub-Domain A2, however, with a NE – SW transport direction (Fig. 5.20A).

The detailed image of blocks and in corresponding seismic profiles clearly reveals that they represent a series of extensional 'domino' blocks especially within Sub-Domains A1 and A2. The presence of the SW – NE trending G2 lineations (Fig. 5.7B) on the basal surface both north and south of the E – W trending ramp further complicates the kinematic analysis. Although the G2 lineations south of the ramp appear to be aligned with seismically coherent blocks similar to the G1 lineations (Fig. 5.23). The existence of the lineations north of the E – W trending ramp is somewhat enigmatic because they occur underneath Domain D which is highly deformed and structureless and therefore interpreted to have undergone comprehensive disaggregation and mobilisation. In fact, the moderate deformation of the blocks is difficult to equate with any significant transport distance, but precise translation distances cannot be quantified. It is therefore suggested here that the G1 and G2 basal grooves beneath MTD 6 are not reliable kinematic indicators in determining the translation direction of the deposit.

Shear zones are useful kinematic indicators for MTDs as they provide key evidence to understand mass movement processes (Gafeira et al., 2010). However, they may 1) represent local shear, that may not be representative of the general trend 2) be inactive boundaries transferred along the mass movement or. 3) represent apparent differences in the transport velocity due to differences of when the flow occurred i.e. the interface of two sections of the MTD that ceased their motion at different times during translation will resemble the interface between flows that were moving simultaneously but at different speeds Thus the use of shear zones as kinematic indicators should be approached with caution (Gafeira et al., 2010).

Shear zones were recognised within Domains A and C which were highlighted by 1) the iso-

orientation of elongated elements as in the case of Domain A (Fig. 5.18) or 2) the presence of elongated lineations within an internal brittle zone which developed within a ductile zone as in the case of Domain C (Fig. 5.24). Although these shear zones can be traced through several kilometres and are predominantly oriented in both the E- W directions it is difficult to establish the sense of shear especially in Domain C, since no offset of the structures was recognised (Fig. 5.24). However, the rotation of some of the fold axes (c. 45°) in the southern-half of the area under study (Fig. 5.24), relative to the northern half, suggests that some movement occurred along these shear zones. Since the actual sense of shear is difficult to interprete for the major shear zones in Domains A and C, it is suggested here that they are not reliable kinematic indicators in this study.

Alternatively, structural analysis of both planar (fault strikes e.g. Bull et al., 2009a) and linear features (i.e. fold axis trends e.g Strachan and Alsop, 2006) in Domains A, B and C revealed different transport directions (Figs. 5.18B, 5.22B and 5.24B). However, these structures predominantly strike in a WNW – ESE orientation. This is well seen in Figure 5.33 with all of the kinematic indicators from these domains summarised. This evidence implies a gross general transport direction for MTD 6 to the SW, consistent with that suggested in Chapter 4. However, local contrasting transport direction to the NW is also evident.

Furthermore, as previously mentioned, the E – W oriented ramp is a reliable kinematic indicator for interpreting the translation direction for MTD 6. Although it cross-cuts the NW – SE oriented paleo-channel (C2) which would have aided its interpretation as a frontal ramp orthogonal to the transport direction (sensu. Bull et al., 2009a). The presence of the N- S trending faults on either side of salient (labelled U2) (Fig. 5.9) associated with the ramp suggests otherwise. The blocks delineated by the N-S trending faults appear to be sheared towards the west (Fig. 5.9C) and thus suggest a westward transport direction for the MTD, at least for Domain D adjacent to the ramp.
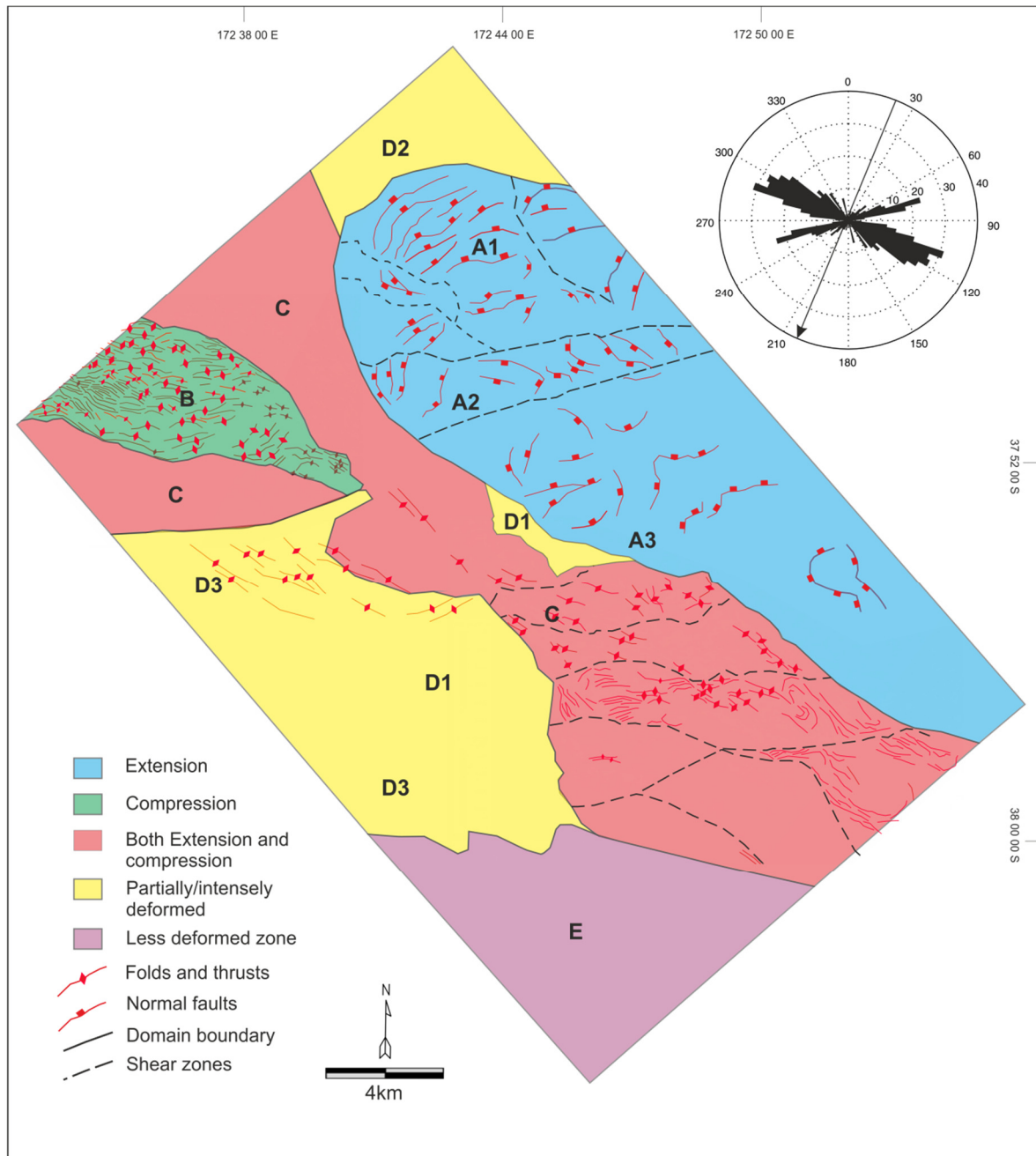
Figure 5.33. Interpretative map of MTD 6 within the 3D seismic survey showing the different internal structures that characterise the five distinctive domains. The rose diagram calculated from all the structures in the domains shows a SW dominant transport direction of MTD 6. The shear zones are mainly oriented in the WSW -W direction.

A brittle behaviour is assumed at this ramp and the N- S trending faults observed on the ramp are thought to have developed progressively during the emplacement of MTD 6 to the SW. This interpretation is consistent with that suggested by the folds and thrust structures developed in Domains B and C. Therefore, the interpreted true transport direction for the MTD 6 based on all of the kinematic indicators discussed above is suggested to be SW (Fig.5.33).

5.4.2 Deformation Processes

The fact that Domains (A - D) of MTD 6 share a common basal surface implies that they occurred simultaneously. The undulating geometry and sometimes juxtaposition of the marker horizon (blue) against the basal surface in the Domains A, B and C is consistent with the degree of thinning caused by the partial removal of the underlying transparent interval. The detailed morphology and internal structure outlined above is strikingly different from the idealised models of slope failure from continental margins.

Consequently, any plausible interpretation to explain the process of deformation of MTD 6 within the study area should account for the critical c. 30% volume loss via the deformation and remobilisation of the lower transparent unit coupled with the abrupt boundary transition, intense deformation and the relative reduction in thickness observed in Domain D. Two hypotheses that could explain the observed deformation within MTD are discussed below.

5.4.2.1. In-situ Liquefaction (subsurface evacuation model)

Submarine slope failure involving the mobilization of a lower transparent unit above which a rigid, coherent unit was translated and broken up has been described from the Norwegian continental margin (Bull *et al*., 2009) (Fig. 5.34A). The authors observed a complete depletion of a substantial volume of the lower part of the original slope template coupled with the distinct lack of shear on the basal surface They argued that such subsurface evacuation.
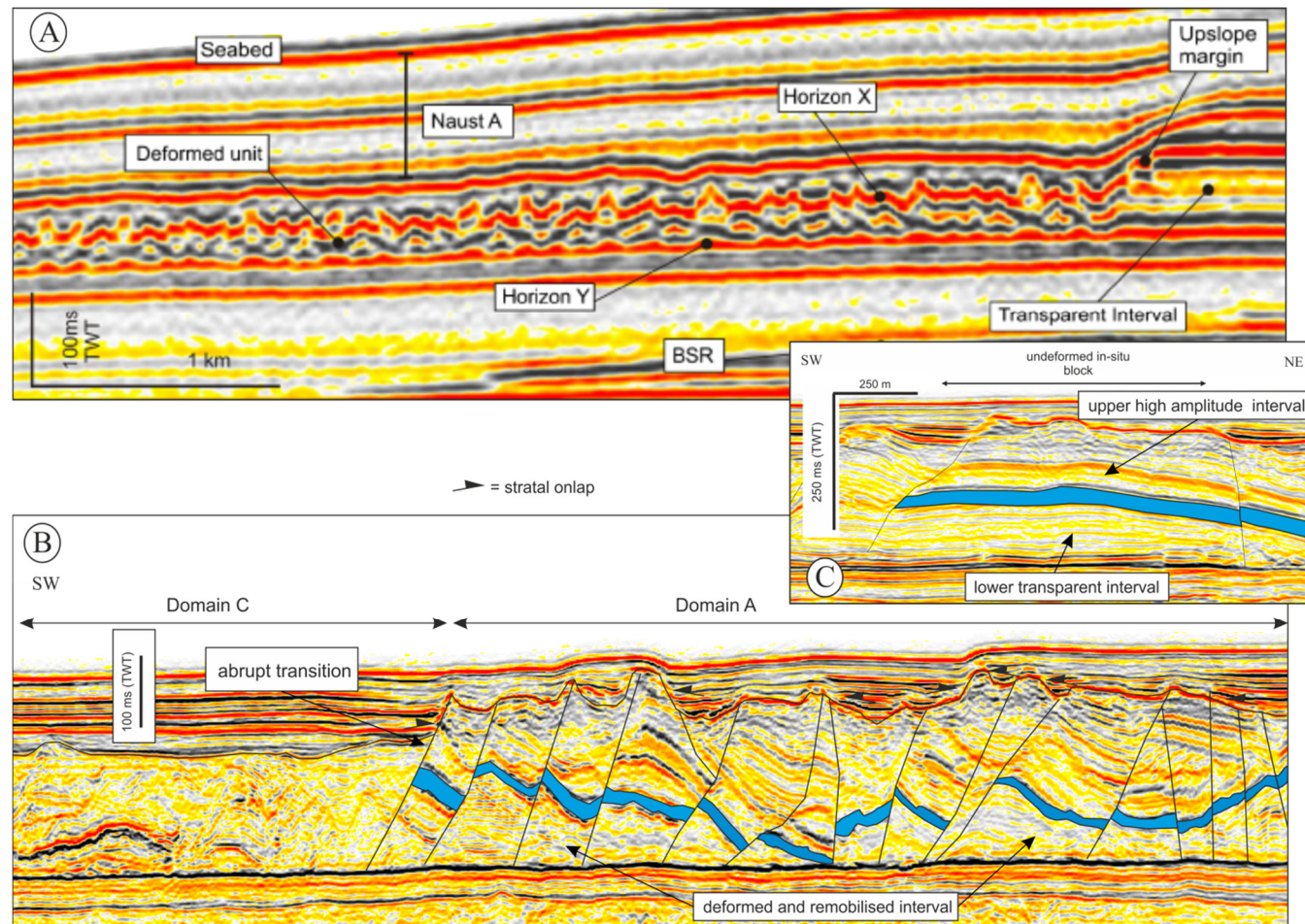
Figure 5.34. Comparison of a similar slope failure process found in the Norwegian Continental Margin with that observed in the present study A) Seismic dip profile showing thickness change across the upslope margin and how Horizon X is readily correlated from the upslope deformed region updip in the undeformed slope sediment suggesting the remobilisation of a lower unit (from Bull et. al., 2009) B) Seismic profile across the sub-Domain A2 (see Fig. 5.18A for location) showing the deformation and remobilisation of the lower transparent interval similar to the Norwegian case study in A. C)The original stratigraphic configuration of the undeformed interval (see Fig.5.18 A for location).

mechanism was facilitated by the liquefaction and subsequent remobilisation of material beneath a relatively competent overburden. They interpreted the transparent interval to constitute part of the widespread sheet-like contourite which is known to have a high clay and water content and thus readily develop overpressure and sensitivity due to their fine-grained lithology and rapid accumulation.

This model appears to be consistent with the geometry of the internal structure observed in Domains A, B and C of MTD 6 in that there is evidence for the deformation and remobilisation of the thick transparent lower interval in Domains A, B and C (Figs. 5.19, 5.23 and 5.25 respectively). In fact, a comparison of the model with observations from Sub-Domain A2 shows that the deformation and remobilisation of the lower transparent interval allowed for extreme block rotations. There are no wells to ascertain the true lithologies of the sediments in the study area, and hence no way to test the sensitivity of clay behaviour. Nonetheless, a correlation with three exploration wells outside of the area (see Figure 4.4 in Chapter 4) suggests that some of these failed sediments predominantly comprise of unconsolidated mud rich facies.

Furthermore, the model cannot explain the occurrence of the grooves (labelled G1 and G2 in Fig. 5.8) observed on the basal shear surface which has been interpreted in this study to have resulted from the sinking of overlying extensionally faulted blocks. Furthermore, the abrupt transition from the alternating compressional and extensional structures in Domain C, to the transparent and loss of seismic character of Domain D, coupled with the thickness reduction (Fig. 5.3) is not consistent with the subsurface evacuation model. In addition, if the subsurface evacuation model described the deformation process for MTD 6, the downslope distal limits of MTD 6 should be thicker than the proximal areas because of the mobilisation and addition of the evacuated material from the lower transparent interval. However, the fact that the limits of MTD 6 have already be been constrained (see Chapter 4) and the isochron

map shows progressive downslope thinning suggest that the evacuated material which is expected to behave in a highly mobile manner (Bull et al., 2009b) did not travel a significant distance downslope. This observation argues against the liquefaction/subsurface evacuation model, since it does not clearly fit into in the formation of MTD 6.

5.4.2.2. Progressive stratal disaggregation

An alternative mechanism that could explain the differential internal deformation of MTD 6 as shown in the various domains is progressive stratal disaggregation (Festa et al., 2012; Lucente and Pini, 2003; Ogata et al., 2012). This kind of deformation has been recognised in outcrop examples of mass transport deposits and it commonly involves poorly-lithified or loose material, and results in the formation of a broad spectrum of structures ranging from folded and boudinaged successions (e.g. slump deposits) to block-in-matrix bodies (e.g. debris flow deposits). These products are characterized by the occurrence of a strongly mixed, liquidized matrix (i.e. hyper-concentrated suspension sensu Mutti, 1992) enveloping disrupted layers and blocks. Those layers or blocks may show different degrees of lithification, and represent the final product of progressive downslope, soft sediment deformation (e.g. Maltman, 1994; Ogata, 2010). The latter deformation is enabled by the relative movement of unlithified masses with progressive flow transformation, stratal disaggregation or both, of the partially-to largely lithified sediments (Pini et al., 2012).

A careful examination of the internal fabric of the domains with their boundary relationships reveals that the larger scale processes that occurred during the emplacement of MTD 6 would have been progressive stratal disaggregation. The common occurrence of the deformed and remobilised material beneath the structures in Domains A, B and C may represent early stages of remobilisation. Whilst the transparent, partial and or complete loss of seismic character observed in Domain D, coupled with the thickness reduction, may represent the

"frozen-in" later stages of intense deformation and remobilisation. It is suggested here that the deformation and remobilisation of part of the lower transparent interval (as observed in Domains A, B and C) or complete loss of seismic character (as observed in Domain D) would probably have involved a substantial degree of liquefaction. (Maltman, 1994) defined liquefaction as the total loss of strength which results when the pore fluids reach lithostatic values. Furthermore, the near-random distribution of blocks in Sub-Domain A3 and lack of longitudinal ridges point towards a block in matrix fabric suggesting that any form of pattern that would have been preserved must have been destroyed by the progressive stratal disaggregation within the domain.

However, the abrupt transition from the alternating compressional and extensional structures in Domain C, to transparent and complete loss of seismic character in Domain D coupled with the thickness reduction (Fig. 5.3) cannot be justified solely by progressive deformation during the emplacement of MTD 6.

According to (Festa et al., 2012), the nature of the transition between the different types of mass-transport chaotic bodies is controlled by the different velocities of movement, the geometry and morphology of the depositional setting, the mode of failure propagation (progressive vs. retrogressive collapse), and the composition and degree of lithification of sediments (related to the stratigraphic level of the rupture surface). In this study, the relatively small amount of extensional strain in Domain A and contractional strain in Domain B suggest that it is unlikely for MTD 6 to have translated a significant distance to allow for the intense deformation observed in Domain D. Therefore, it is suggested here that the velocity of movement of Domain D will not have accounted for the abrupt transition between Domains C and D. Likewise, the geometry and the morphology of the depositional setting or the mode of failure of MTD 6 cannot account for the abrupt transition because the domains detach on a common horizon suggesting they probably occurred simultaneously. Alternatively the

composition and degree of lithification of the sediments which is thought to be related to the stratigraphic level of the rupture surface, appears to be the most plausible explanation for such an abrupt transition.

The deformation style of MTD 6 corresponds very closely to that described by (Micallef et al., 2007), and (Lucente and Pini, 2003) where they have argued that the deformation is the result of gravity spreading. (Micallef et al., 2007) suggested that spreading can involve both extensional and contractional deformation which results in closely spaced series of coherent blocks or groups of highly convex downslope facing ridges and troughs. A close examination of the isochron map of MTD 6 and corresponding seismic profiles suggests that there has been some degree of thinning most especially within Domain D (Figs. 5.3 and 5.5). Moreover, there is evidence for thinning within Domains B, C and D, given that the continuous marker horizon (blue) is sometimes juxtaposed in an angular relationship with the basal surface (Fig. 5.18B). This juxtaposition implies that there has been remobilisation of a lowermost unit. In addition, lateral extension as well as compression is evident within Domains A and B respectively.

Spreading where the entire section collapsed under its own weight after losing its basal support can explain the different translation directions observed in the Domain A (sensu Lucente and Pini, 2003) (Fig. 5.18B). The varied deformation that is exhibited in all of the domains suggests that MTD 6 did not translate downslope as a coherent slab and thus argues against the gravity gliding model (Schultz-Ela, 2001). Rather, it has undergone significant differential internal deformation which was probably active during various stages during its emplacement.

Furthermore, a comparison of gravity driven processes in salt tectonics and submarine MTDs is drawn based on the fact that they can both be explained by the gravity gliding and spreading models. (Brun and Fort, 2011) proposed that the contrasted migration patterns of

extension and contraction and related structural inversion provided a good diagnostic of dominant gliding versus pure spreading. They suggested that in dominant gliding there is up-dip migration of contraction towards extensional up-dip domain which results in inversion of previously extensional structures. Whilst in pure spreading both extension and contraction migrates downslope with extensional domain reaching that were previously contractional thus resulting in the extensional inversion of previously contractional structures (Brun and Fort, 2011). Their model is consistent with the anti-dislocation model proposed for slump development by (Farrell, 1984) which is illustrated in figure 5.19C. In the present study, there is strong evidence that the extensional strain that characterised the Domain A upslope, migrated downslope and overprinted the previously developed contractional structures of Domain C (Fig. 5.25), which again suggests a gravity spreading model. Based on these observations, the gravity spreading model is the most defensible and therefore proposed here as the dominant mechanism of emplacement of MTD 6.

5.4.3 Slope failure trigger mechanism

From Chapter 4, it was argued that MTDs 1-5 within the Giant Foresets Formation in the Deepwater Taranki Basin were preconditioned for failure by high rate of sedimentation into the basin coupled with concomitant over-steepening of slope (see Section 1.3.2.2). This argument was based on the fact that the timing of the MTDs correlated well with a time of high sedimentation rates into the basin. More specifically the headwall of MTD 5 was developed along the bounding surfaces of progradational foresets (see Figure 4.10). However, MTD 6 appears to be anomalous. Although the headwall was identified in the 2D dataset, there is no correlation of bounding surfaces of progradational foresets and there is no evidence of depletion (sensu Frey Martinez et al., 2005). This evidence coupled with the dominant SW translation direction is in stark contrast to the earlier MTDs suggesting that the

processes that accounted for the earlier failures (MTDs 1-5) are strikingly different from those that resulted in the emplacement of MTD 6.

Two critical pieces of evidence that might help in unravelling the cause of failure are 1) the relatively shallow level of the basal surface of MTD 6 defined by a high amplitude laterally continuous negative reflection and 2) the presence of shear on the basal surface. Both lines of evidence suggest that the failure was caused by the presence of a mechanically weak layer linked to the development of overpressure build-up resulting in hydroplastic deformation of the failed interval as opposed to true liquefaction that is characterised by lack of evidence for shear along the base surface (Bull et al., 2009b). A similar mechanism has been proposed for other failures e.g the Afen Slide (Wilson et al., 2004) and the Rebelde Slide (Ashabranner et al., 2010)

Maltman (1994) suggested that cyclic loading due to the oscillatory transmission of seismic waves could result in submarine slope failures due to induced elevated pore fluid pressures, which often fail to be completely dissipated before the next pore fluid excursion. The author further suggested that the rapidity of such loading will reduce the effective stress to zero, and liquefaction can occur.

Whilst it may be argued that significant overpressures are not likely to have developed at such shallow burial depths at a time when these sediments would only be weakly lithified, it is important to note that the potential for liquefaction decreases with increasing overburden pressure, such that the maximum reported depth of liquefaction effects is 10 m and most liquefaction develops in sediment buried less than 5 m (Obermeier, 1996).

The failure of MTD 6 and subsequently liquefaction may have been triggered by faulting and volcanism related to the subduction of the Pacific Plate along the Hikurangi margin. However, most of the faulting and volcanism that was active between 4 and 8 Ma, migrated southwards from the northern part of the basin, but slowed and ceased at c. 2 Ma (Giba et al.,

2010). Since about 2 Ma, active normal faulting has been mainly focused in the region of the Taranaki Peninsula (Giba et al., 2010). Likewise the only active volcano at present is the southernmost onshore volcano, Mt Taranaki (Downey et al., 1994). Although the timing of MTD 6 (c. 1.8 Ma) is relatively recent, compared to the active timing of these events that may have been associated with seismicity and ground motion, it is suggested here that they may have primed and caused the failure of MTD 6. Therefore, a triggering mechanism due to ground motion caused by the passage of earthquake related seismic wave is favoured as the likely cause for MTD 6.

5.5 Conclusions

1. A high resolution 3D seismic dataset acquired in the Deepwater Taranaki Basin, New Zealand provides insights into the dynamics of emplacement of the latest submarine MTD (termed MTD 6) within the Giant Foresets Formation.

2. MTD 6 consists of 5 distinctive domains (labeled A – E) characterised by different internal deformation fabrics, and translation directions that are not consistent with the orientation of the two sets of underlying grooves observed on the basal surface.

3. Domain A is dominated by barely deformed extensionally faulted blocks moving differentially. Doman B is dominated by contractional folds and thrust structures with a dominant SW translation direction. Domain C is characterised by strain overprinting where early formed folds are truncated by late faults with a dominant SW transport direction. Domain D is characterised by intense deformation and partial deformation of previously extensional and contractional structures coupled with c. 30% reduction in thickness compared to adjacent domains. Domain E is characterised by continuous to discontinuous reflections with evidence of in-situ blocks.

4. The two sets of underlying grooves (G1 and G2 are oriented in SW and NW directions respectively) seem to align with the edges of extensionally faulted blocks or in-situ blocks. They are interpreted to result from the sinking of the blocks.

5. Ranking of all of the kinematic indicators in the study area based on their reliability suggests an overall SW transport direction for MTD 6.

6. Analyses of the deformational structures within the domains and their boundaries suggest a progressive stratal disaggregation would be a plausible deformation process with the lack of seismic character and lose of strength in Domain D being the ultimate product.

1) **Chapter 6**

Chapter 6

6.0 Summary and Discussion

6.1 Introduction

The preceding chapters in this PhD project have presented detailed analysis of the architecture of submarine MTDs using bathymetry, commercial two-dimensional (2D) and three-dimensional (3D) seismic reflection data from Deepwater Taranaki Basin New Zealand and the west Nile delta, offshore Egypt.

In this chapter, the key scientific results from the preceding core result chapters (Chapters, 3, 4 and 5) are summarised in order to address the main questions that pertain to the impact of submarine MTDs as hydrocarbon seals. These core result chapters were initially structured into three semi-independent units in an attempt to investigate specific questions emanating from this project. Figure 1.6 illustrates how these core results chapters fit in a unified geological model.

The main aim of this chapter is to propose a seismic based MTD classification for seal prediction. In addition, lessons learned from outcrop studies of MTDs will be briefly highlighted. However, for detailed outcrop observations of MTDs the reader is referred to the atlas of MTDs in the appendix. The general limitations for the project are highlighted and the some ideas for future research are presented.

6.2 Summary of results

6.2.1 Results from Multistage progressive failure slope failure in the Pleistocene pro-deltaic of the West Nile Delta (Eastern Mediterranean) (Chapter 3).

Chapter 3 presented a 3D Multistage progressive failure slope failure emplaced during the Plio-Pleistocene in the western Nile delta fed by the Rosetta branch of the Nile delta (Eastern Mediterranean) which allowed for holistic study of the phases and mechanism of failure.

The main aims of Chapter 3 were to (1) Describe the dimensions and the geomorphological characteristics of MTDs A, B and C. (2) Determine the sequence of failure of these three MTDs by investigating the relationships between them, and to explore the question of whether they represent a single slope failure (and if so, what type) or separate events that exploited similar region of inherent slope instability and (3) Discuss the processes that preconditioned the slope for failure and potential triggering mechanisms and (4) Understand the implications of the occurrence of these MTDs in a prolific gas-rich province such as the Nile delta.

By comparing their motion histories, and by correlating their basal surfaces, we demonstrate that MTDs B and C are remnants of a single original body that was later cut by MTD A. This sequence is confirmed by cross-cutting relationships at the lateral boundaries between the three MTDs and the absence of any significant infill and burial of residual topography at the tops of MTDs B and C prior to the incision of MTD A. This implies that these two major submarine failures (MTD B/C, and then MTD A) were closely grouped in time. We suggest a mechanistic model whereby rapid load redistribution resulting from the initial failure led to localization of a deeper cutting failure, and the unloading in the headwall region then led to expansion of the deeper failure in an upslope direction until a new merged headwall was formed.

Correlation with MTDs identified downslope in previous studies suggests a date between 117–105 ka for this giant slope failure. This was a period of relative sea level fall in the Nile region which may have contributed to increased pore pressure. Slope failure on this scale was probably preconditioned by high sedimentation rates and under-compaction in a mud-rich succession, leading to local increases of pore pressure.

Ultimately the research presented in in Chapter 3 showed that the reconstruction of the pre-seabed topography suggest a total volume (residual and depleted) of remobilisation of a

minimum of the order of 750 km^3, making this amongst the largest submarine landslide complexes documented to date. Furthermore, given that this extraordinary event occurred in an area of active gas accumulation in shallow-level slope channel reservoirs, we suggest that rapid unloading of such a large magnitude (750 km^3) of overburden would have had significant consequences for any reservoired hydrocarbons, including leakage by topseal failure and remigration to up dip traps. Similar impacts might be expected for many other slope systems on continental margins, where reservoired hydrocarbons might be prone to leakage or remigration as a result of large slope failures.

6.2.2 Results from the Evaluation of the degree of Cannibalization versus Run-out in multiple widespread Mass Transport Deposits: A case study from the Deepwater Taranaki Basin, New Zealand.

Chapter 4 provided the first detailed investigation of mass wasting processes within the Plio-Pleistocene Giant Foreset Formation in the continental slope of Deepwater Taranaki Basin, New Zealand using a high-resolution bathymetric and two-dimensional (2D) seismic reflection data.

The aims of Chapter 4 were to (1) describe the morphology, geometry, and lateral extents of each MTD; (2) describe their stratigraphic relationships and source areas; (3) develop a simple stratigraphic approach to quantify the degree of substrate cannibalization for each MTDs; (4) provide age estimates for the deposits; (5) briefly discuss the implications of substrate cannibalization on seal integrity.

Detailed seismic morphological and stratigraphical analysis of the Pliocene to Holocene slope succession showed that the Deepwater Taranaki Basin is characterised by six distinctive giant MTDs referred to as MTD 1 - 6 (with MTD 1 being the oldest at the lowest stratigraphic position and MTD 6 the youngest). The MTDs are stacked and locally amalgamated making up c. 50% of the stratigraphic succession were recognised and mapped. Key kinematic

features suggest a north-westerly transport direction for all of the MTDs with the exception of

MTD 6 having a south-westerly transport direction. There is seismic stratigraphic evidence in

the form of both lateral and basal truncations suggesting that the MTDs were erosive during

their emplacement. The volume of cannibalization versus run-out material for each MTD was

estimated by the interpolation of MTD geometry between cross- sections. Our estimation

shows that c 70% of the final volume of MTD 6 was contributed from substrate

cannibalization greater than the other five MTDs in the study area. This work suggests that

the rheology of the substrate immediately beneath the seafloor might not be the only factor

controlling the degree of substrate cannibalisation during MTD emplacement and that the

nature of any triggering mechanism might also play an important role. This has a bearing on

the MTD content (sandy or muddy dominated MTD) and would in turn influence the seal

integrity of MTD.

6.2.3 Results from Insights into the dynamics of a giant mass transport deposit from high-resolution 3D seismic data, Deepwater Taranaki Basin, New Zealand.

Chapter 5 presents insights into the dynamics of emplacement of the latest submarine mass

transport deposit (termed MTD 6 in Chapter 4) within the Giant Foresets Formation in the

Deepwater Taranaki Basin, New Zealand using a high resolution three-dimensional (3D)

seismic dataset.

This aim of this chapter was to investigate the morphology and detailed internal structures of

MTD 6 beyond that which could be constrained previously from 2D seismic data (Chapter 4)

in order to gain insights into the emplacement process.

MTD 6 consists of distinctive domains (labelled A – E) that detach on a common basal

surface except for the Domain E that detaches on a higher stratigraphic level. Each domain of

MTD 6 is characterised by different internal deformation fabrics, and a translation direction

that is not consistent with the orientation of the two sets of underlying grooves observed on the basal surface. Domains A – C show evidence of deformation and remobilisation of c. 30% of a lower transparent interval while Domain D is characterised by a partial or complete loss of seismic character coupled with c. 30% reduction in thickness compared to adjacent domains. Based on the deformation styles, the transition across domain boundaries and the observed volume loss, a progressive stratal disaggregation is inextricably linked with gravity spreading as the mode of emplacement of MTD 6. Ranking of the kinematic indicators based on their reliability suggest a dominant SW translation direction for MTD 6. This study highlights the power of 3D seismic data in unravelling the detailed processes involved during MTD emplacement and which may have significant implications as regards the translation and emplacement of other submarine slope failures in other continental margins.

6.3 Implication of research

The overarching objective of the CAPROCKS project is to produce methodologies with which to quantify seal risk. Since MTDs have been the focus of this research, two main themes will be discussed based on the results from the three core research chapters in order to understand the potential mechanisms and pathways by which petroleum would migrates through these deposits. 1) MTDs seismic facies classification based on seal prediction and 2) the implication of each proposed seismic facies class on seal integrity.

6.3.1 MTDs seismic facies classification based on seal prediction

It has been pointed out that the role of the MTDs in analogous hydrocarbon traps has been less explored (Beaubouef and Abreu, 2010). Although 3D seismic characterisation of MTDs has been carried out extensively from a number of case studies in a range of basins, no comprehensive scheme has been presented to classify their internal architecture in a manner

that is directly mappable onto the problem of defining their potential as sealing sequences (see Chapter 1).

Much of the work done on classifying the internal architecture of MTDs has been undertaken in the context of flow processes (Nemec, 1990; Shanmugam, 2006). Thus, subdivisions of MTD classification into slides, slumps and debris flows are common based on their increasing degree of internal deformation, associated with translation distance.

(Tripsanas et al., 2008) presented a facies scheme based on the systematic description of submarine MTDs by the detailed sedimentological analyses of cores from the continental margins of the north-west Gulf of Mexico and south-eastern Canada. Although the classification scheme described above is very useful in understanding the mode of transport during MTDs emplacement it is limited for the purpose of assigning risk levels to seals because it is based largely on the core-scale properties of MTDs which is not sufficient enough to characterised the entire MTD.

In order to assign risk levels to MTDs which are now being increasingly recognised as ubiquitous components of hydrocarbon seals, a three dimensional (3-D) architecture of the MTD must be defined including a description of heterogeneities on any observable scale, not merely those accessible from core or well data (Cartwright et al., 2007).

Seismic data, however, have a resolution of at least several meters and do not provide direct information on the lithology which is critical in assigning a risk to seismic facies classes. In the absence of seismic calibration, prediction on MTD lithology heterogeneities can be based on exposed outcrops of MTDs provide good analogues to assess for such heterogeneities. In this project however, some scenarios were considered (high N/G, moderate N/G and low N/G) in order to make predictions about seal integrity of MTDs (this will be discussed in Section 6.3.3).

In this present section, a seismic facies classification for MTDs is presented based on an extensive review of the internal 3D seismic architecture of MTDs from this project (Chapters 3 and 5) and other published literature. In order to ground truth the classification scheme with lithology information and evaluate the leakage or seal potential a comprehensive atlas of mass transport deposit outcrops (see Appendix) has been compiled. The approach is to define and classify seismic facies of MTDs by outlining groups of reflections with distinct parameters (e.g. size amplitude seismic reflection continuity, and texture) and identifying possible conduits (both stratigraphic and structural conduits) within each class.

The proposed seismic facies classification scheme for MTDs is a qualitative object based scheme compared to traditional sedimentary-based facies classification (Tripsanas et al., 2008), whereas the latter is based on the lithology information in each class, seismic facies analysis is based on dominant geological features within chaotic reflections called objects. The seismic facies classification for MTDs provides a seismic interpreter with a rapid analysis of the deposit whose aim is to come up with a risk map that can better inform exploration decision making.

6.3.2 Analysis of MTD Seismic Facies

MTD seismic facies analysis is different from seismic sequence analysis where reflection characteristics are thought to correspond to unique geological and depositional history of a sequence (Mitchum Jr et al., 1977). Rather, it recognises the fact that MTDs are deformed sediments, remobilised to different degree (seismically resolvable) by variable transport process or mechanisms from their original depositional configuration. It is important to note that due to the resolution of seismic data (see Chapter 2) and for the purpose of developing a seismic based classification, only MTDs which have thicknesses equal to or greater than 100 m are considered in the proposed classification. The classification workflow consists of three steps:

1) The basal shear and top surfaces (upper and lower limits) should be accurately mapped to assess the MTD geometry and to generate a thickness map;

2) If the MTD is greater than 100 m in thickness then it is best to divide the deposit iso-proportionally in windows and calculate the Root Mean Square (RMS) amplitude for each window to unravel the MTD morphology by looking at patterns and colour distribution (Brown, 1999). Otherwise it can be calculated for the whole MTD if thickness is equal to 100 m. Other seismic attributes that would help the interpreter unravel the internal architecture of an MTD are coherences slices. Although slicing through the MTD would be the quickest way to rapidly access the internal morphology, it does not uniquely define the seismic facies as the internal architecture of an MTD would probably vary laterally and vertically over a short distance (see Chapter 5).

3) Pattern recognition techniques are employed to interpret the RMS amplitude map. Traces which are close together in term of seismic attribute will stand in the same group of seismic facies (Fournier et al., 2002). It is essential for an interpreter to iterate between section and plan views during the interpretation of the MTD interval, which is a critical step in the seismic interpretation (Posamentier et al., 2007).

After an extensive review of published seismic examples of MTDs and using the aforementioned workflow for the seismic data available for this project, three main types of deformation are recognised within MTDs consisting of (1) layered, (2) blocky, and (3) amorphous, based on five criteria including a) external geometry, b) internal reflection configuration, and inferred stress regime, c) reflection continuity, d) amplitude strength and RMS amplitude and/or coherency pattern (Table 6.1). It is observed that in many petroliferous basins, at least two of the three types of facies are developed in MTDs , and in some, the three types can be found distributed within a single MTD.

In the section below, we review each of the three main facies type in detail, providing examples of seismic expression, and discussion on the possible leakage pathways for each of the type under a variety of geological circumstances (e.g. increasing N/G).

6.3.2.1 Layered Facies

The layered facies is defined by parallel to sub parallel bedded reflections which are generally semi-continuous to continuous and concordant to underlying and overlying reflection packages over their entire length or at least for a considerable length of displacement (Fig. 6.1 and Table 6.1). The layered facies is usually characterised by high to low and sometimes transparent amplitude reflectivity. Minor folding and/or faulting can be observed sometimes within the facies (Fig. 6.1D and E). Examples of layered facies in MTDs have been documented from the Ebro Continental Margin, offshore northeastern Spain (Frey Martinez et al., 2011; Fig. 6.1A and B); from the western Porcupine Basin, offshore SW Ireland (Huvenne et al., 2002; Fig. 6.1C), from around Montserrat, in the Lesser Antilles volcanic arc (Watt et al., 2012a; Fig. 6.1F; Watt et al., 2012b; Figs. 6.1D and E), and from Upper Oligocene Frio Formation, south Texas Gulf Coast (Ogiesoba and Hammes, 2012; Figs. 6.1G, H and I).

The relatively semi-continuous to continuous and concordant seismic expression of the layered facies almost similar to undeformed strata leads to consideration of the recognition of such MTDs in seismic data. (Ogiesoba and Hammes, 2012) suggested that the lack of recognition of the layered facies is further compounded by the less degree of deformation. The authors also suggested that when MTDs get buried to depths > 2 km some of the diagnostic features are obliterated because the sediments become compacted to such a degree that they end up paralleling the bedding plane. The difficulty in recognizing the layered MTD facies could be due to poor data quality as with the other MTD facies types described here.

Table 6.1: Overview of key observations of MTD seismic facies classes

	Facies	Mechanism	Cross sectional seismic expression (internal configuration; continuity; external geometry; amplitude strength)	Plan-view appearance (RMS amplitude or coherence or time slice patterns; amplitude strength)	Spatial distribution within MTDs	Seismic examples
Increasing degree of deformation	Layered		Wavy, parallel to subparallel; continuous to discontinuous sheet; flat basal and upper surfaces; transparent, moderate to high	low to moderate amplitude blocky pattern or featureless light colored on coh. slice	Occur anywhere within MTDs from up-dip extensional domain to down-dip contractional domain	Figure 6.1
	Blocky	Extensional	Discrete units of stratal reflections separated by normal or listric faults; generally flat basal surfaces and irregular upper surfaces; moderate to high	Moderate to high amplitude; Thick elongated ridges	Usually found in the up-dip extensional domain (headwall) but can also be observed in the translational or toe domains	Figure 6.2
		Contractional	Discrete units of imbricated thrusts or folded reflections; generally flat basal surfaces and irregular upper surfaces; moderate to high	Thin elongate ridges with fold hinges corresponding to long axis; moderate to high amplitude	Usually found in the down-dip contractional domain (toe) or in the translational or toe domains	Figure 6.3
		Hybrid	Imbricated thrusted or folded reflections cross-cut by faults or vice versa; generally flat basal surfaces and irregular upper surfaces; moderate to high	Complex planform geometry; moderate to high	Usually found in the translational domain	Figure 6.4
	Amorphous	Incomplete Deformation	Localised packages of coherent reflections (blocks) within chaotic matrix; flat basal and upper surfaces; low to transparent	Isolated irregular shaped high amplitude geometric feature within dark and mottled texture	Found anywhere within an MTD but usually in the translational domain	Figure 6.5
		Complete Deformation	Total loss of seismic character; low to transparent	Dark amplitude or low coherency	Usually found anywhere within an MTD	Figure 6.6
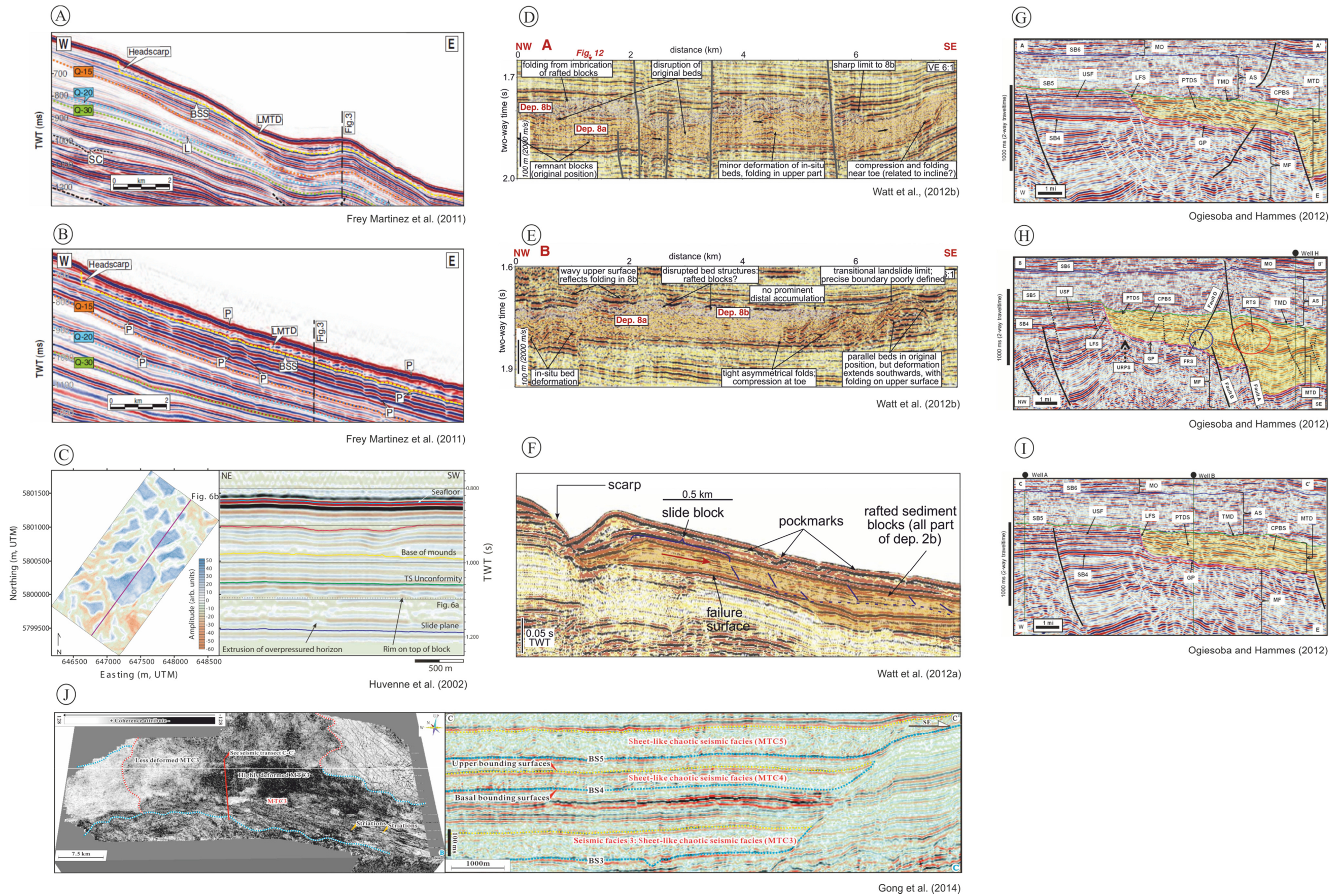
Figure 6.1. Seismic examples of layered facies in MTDs. A) and B) from the Ebro Continental Margin (offshore northeastern Spain); C) from the western Porcupine Basin, offshore SW Ireland; D), E) and F) from around Montserrat, in the Lesser Antilles volcanic arc G), H) and I) from upper Oligocene Frio Formation, south Texas Gulf Coast.

However, with careful mapping, using seismic attributes such as RMS amplitude (Fig. 6.1C; Huvenne et al., 2002) or coherency slices (Fig.. 6.1J; Gong et al., 2014), and recognizing the basal surface, the layered facies may be identified. They sometimes display a blocky pattern on RMS amplitude maps why on coherency slices, they display a featureless light coloured patterns. The less deformed seismic expression of the layered facies suggest that the MTD has not been translated any significant distance. The example presented in Figure 6.1C has been interpreted as a buried slab slide which resulted from the sudden collapse of a relatively thin but spatially extensive package of consolidated sediments upon liquefaction of an overpressured weak layer (Huvenne et al., 2002). The term `slab slide' does not mean that the detached mass was displaced as one entity. During downslope transport (or maybe even before) the materials may be folded, fractured or rumpled into a block or rubble slide. The layered facies represents an early stage of slope failure.

6.3.2.2 Blocky Facies

The blocky facies is defined seismically as a discrete and coherent unit (meter- to hundreds of meter-sized possibly up to km-scale) of moderate to high amplitude reflections that are associated with a strong structural fabric (including fault bounded blocks, folds and thrusts) in their interior (Table 6.1).

In contrast to the layered facies class (described in the penultimate section), in which original bedding planes were preserved with no significant deformation during emplacement of the MTD, and thus causing MTD packages to be similar to adjacent undeformed unit, the blocky facies discussed here are at a higher degree of deformation and as such are easily recognisable. The blocky facies have been subdivided into three families: extensional blocky, compressional blocky and hybrid blocky (overprint of both extension and compression) (Table 6.1) depending on the type of strain that is produced during propagation.

The rationale behind this subdivision is not only on the type of strain that is produced during propagation of the MTD but also on the fact that the factors that control leakage through these classes might be different.

6.3.2.2.1 Extensional blocky facies

The extensional blocky facies is defined by moderate to high amplitude, discontinuous and coherent reflections that are bounded by downslope dipping shear planes which are interpreted usually as normal to listric faults (Fig. 6.2 and Table 6.1). They usually have an irregular upper surface and a generally flat basal surface with evidence of striations/grooves.

On RMS amplitude maps they are characterised by linear ridge and trough morphology (Fig.6.2C and E). Dip oriented seismic profiles across the linear ridges display the diagnostic rotated extensional blocks of the facies better than strike-oriented seismic profiles that sometimes show only chaotic internal reflection geometries.

The extensional blocky facies usually occur in the upslope region in close vicinity to the headwall scarp (Bull et al., 2009a).

This facies class is interpreted to have undergone extension in a sub-horizontal direction because the shear planes dips at the angle expected for Mohr-coulomb failure (Kvalstad et al., 2005). The surfaces of the blocks are usually steeper than the basal surface on which they are displaced which indicates that they have tiled downslope. The close spatial relationship and the less deformed geometry of the blocks suggest that downslope translation was limited.

A typical example of the extensional blocky facies from the upper part of the Storegga Slide is shown in Figure 6.2C (Kvalstad et al., 2005). A pattern of nearly intact triangular ridges and graben structures is revealed on the dip oriented seismic profile. Based on morphology and seismic data, the slide mechanism was interpreted to be retrogressive sliding over a sensitive base layer, where the slide activity generates progressive softening of the sensitive
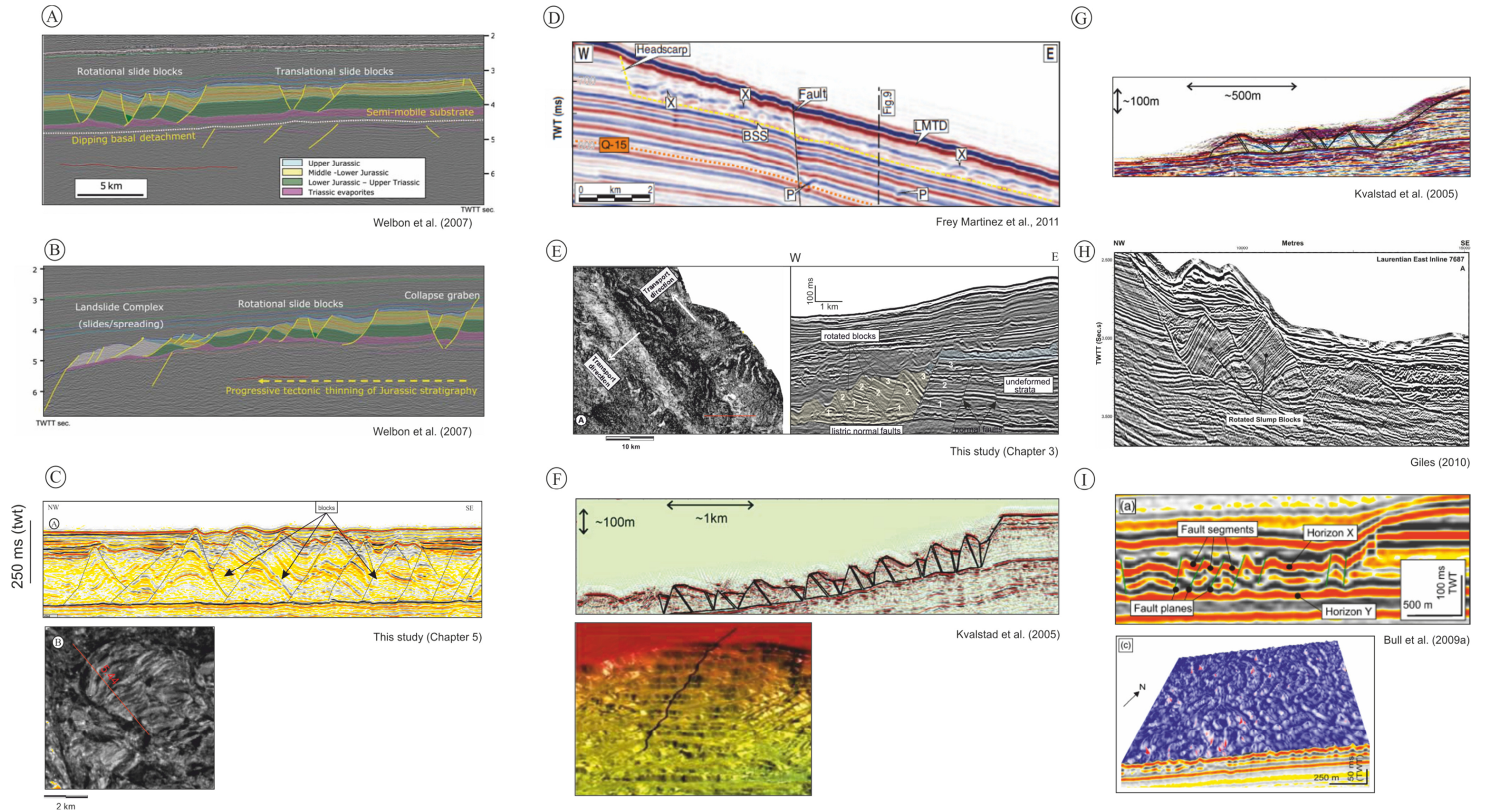
Figure 6.2. Seismic examples of Extensional Blocky Facies in MTDs. A) and B) from the eastern part of Halten Terrace in Norway; C) from this study (Chapter 5) ; D), from the Ebro Continental Margin (offshore northeastern Spain); E) from western Nile Delta (this study, Chapter 3) F) and G) from the upper headwall in the Ormen Lange area; H) southwestern Newfoundland Margin, Eastern Canada; I) from northern flank of the giant Storegga Slide on the Norwegian continental margin.

base layer as the slide retrogressively spreads upslope and also laterally (Kvalstad et al., 2005).

Similar examples of the extensional blocky facies have been described from the eastern part of Halten Terrace in Norway (Welbon et al., 2007, Figs. 6.2A and B); from the Ebro Continental Margin, offshore northeastern Spain (Frey Martinez et al., 2011; Fig.6.2D), from the western Nile Delta (this study, Chapter 3; Fig. 6.2E), from Deepwater Taranaki Basin (this study, Chapter 5; Fig. 6.2 C) from the southwestern Newfoundland Margin, Eastern Canada (Giles, 2010; Fig. 6.2G), from the upper headwall in the Ormen Lange area (Kvalstad et al., 2005; Fig. 6.2H), and from northern flank of the giant Storegga Slide on the Norwegian continental margin (Bull et al., 2009b; Fig. 6.2I). Although the extensional blocky facies is rare in outcrops, it is represented as rotated blocks bounded by extensional faults (see appendix, Fig. 2.46).

6.3.2.2.2 Contractional blocky facies

The contractional blocky facies is defined by a moderate to highly discrete set of reflections that have been folded and/or thrusted above a basal shear surface (Fig. 6.3, Table 6.1)

On seismic profiles, folds occur as series of upright symmetrical fold structures (Fig. 6.3F) or asymmetric recumbent folds. Asymmetric folds, however, are rarely observed on seismic data probably because they are poorly imaged on seismic data but they are usually observed in field analogues. A comparison of seismic example of asymmetric recumbent folds with outcrop analogues is presented in the appendix (Figs. 2.11, 2.12 and 2.13). The transport direction of the MTD has been suggested to be the main factor controlling the recumbent fold vergence (Farrell, 1984).

Thrusts structures tend to occur as imbricated coherent set of reflections that propagate from the basal surface towards the upper surface separated by fault planes that generally dip towards the headwall (Fig. 6.3D and E). However fault planes may dip towards the transport

direction thus representing back-thrust related to larger synthetic thrusts (Martinsen and Bakken, 1990).

On RMS amplitude maps, the contractional blocky facies (folds and thrust structures) are observed as series of arcuate ridges and troughs which commonly trend in a convex downslope pattern, aligned similarly to a frontal margin (Fig. 6.3D and F).

Similar seismic examples of contractional blocky facies in MTDs have been described from the Levant Basin (Frey-Martínez et al., 2006; Fig. 6.3A), from the Qiongdongnan Basin (Gong et al., 2014; Fig. 6.3H and I; WU et al., 2011; Fig. 6.3B); C), from the uppermost Pleistocene, offshore Trinidad (Brami, 2000; Fig.6.3D), from the Niger Delta Basin, F) from the Deepwater Taranaki Basin (this study, Chapter 5), and from the Ebro Continental Margin (Frey Martinez et al., 2011; Fig. 6.3G).

The plan view of contractional blocky facies is similar in appearance to the extensional blocky facies (Figs. 6.2E and F), but the ridges of the contractional blocky facies are thinner Contractional blocky facies are usually found in the toe region of MTDs but they can also occur in up-dip regions. They have been interpreted to result from the cessation of movement of the failed mass downslope usually associated with a rapid change in gradient of the basal surface which generates compressional strain within MTDs (Farrell, 1984; Martinsen and Bakken, 1990).

Another remarkable style of thrust structures observed in MTDs from the 'compression zone' on the southern Storegga Slide margin (Bull et al., 2009a) is presented in Figure 6.3C. In this example the symmetric thrust developed a series of pop-up blocks, which nucleated at the basal surface and propagated upwards. In plan-view a pattern of sub-parallel NNE-trending lineations which correspond to the detachments of the frontal ramp and successive faults is revealed on a slice through a coherency volume (Fig. 6.3C).
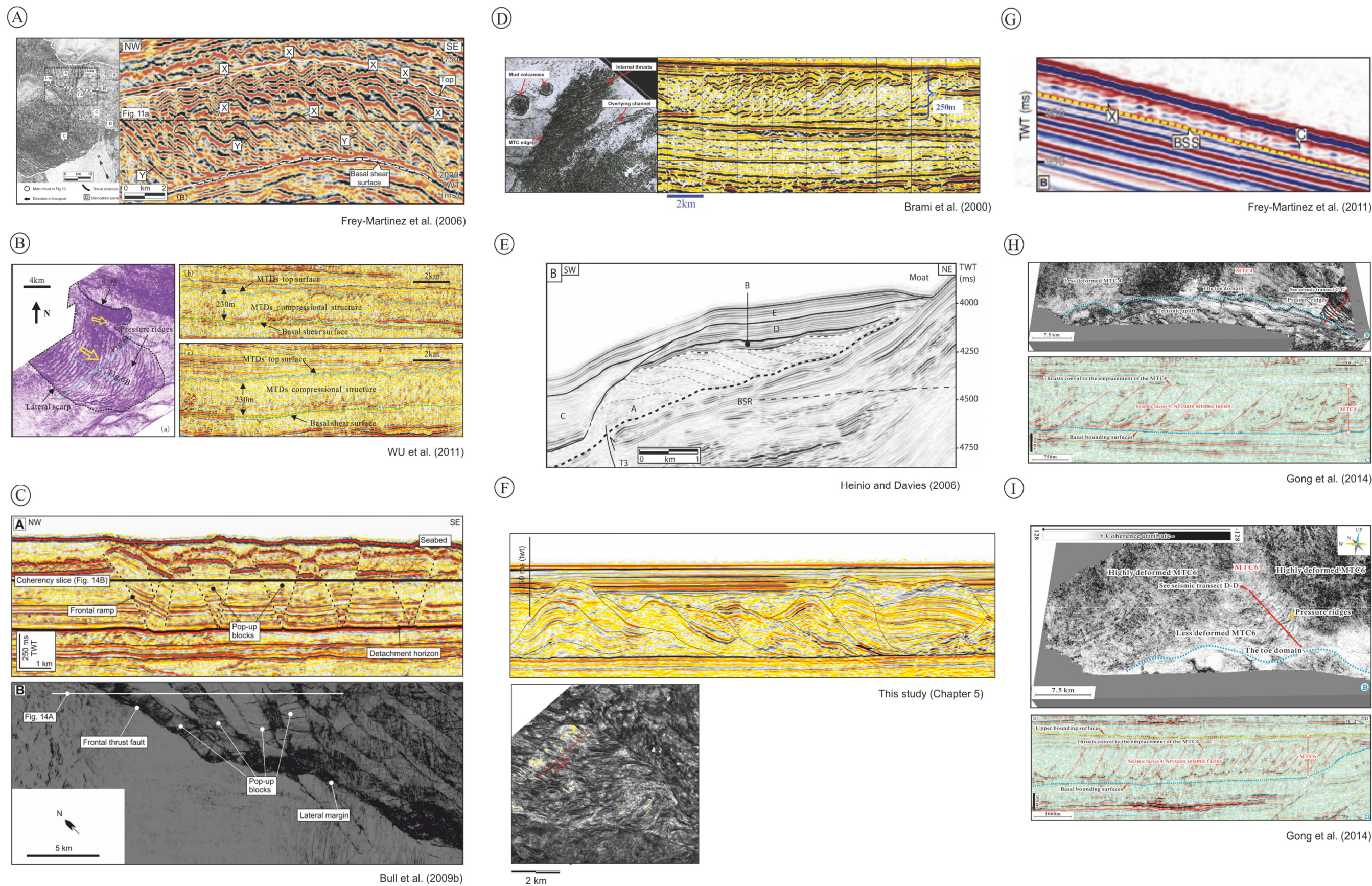
Figure 6.3. Seismic examples of contractional blocky facies in MTDs. A) from the Levant Basin; B) from the Qiongdongnan Basin; C) compression zone' on the southern Storegga Slide margin; D) from the uppermost Pleistocene, offshore Trinidad; E) from the west Niger Delta Basin, F) from this study (Chapter 5); G) from the Ebro Continental Margin (offshore northeastern Spain); H) and I) from the Qiongdongnan Basin along the northwestern South China Sea margin.

6.3.2.2.3 Hybrid blocky facies

The hybrid blocky facies is defined by high to moderate amplitude that imbricated thrusted and/or folded coherent reflections that have been cross-cut by faults (Fig. 6.4 Table 6.1). In plan view the hybrid blocky facies have a complex plan view geometry consisting of isolated square to circular features and elongated ridges that are straight or arcuate and sometimes parallel. The hybrid blocky facies is generally characterised by irregular top and flat basal surfaces (Fig. 6.4A and B).

Although the extensional and contractional blocky seismic facies appear to be common features in the headwall and toe regions of MTDs, the hybrid blocky facies (presented in Chapter 5, Section 5.3.4.3) is a more unusual style of deformation within MTDs, and to the authors knowledge have not been reported in any other seismic based study of MTDs.

The hybrid blocky facies have been interpreted to result from strain overprinting, where contractional strain have been overprinted by later extensional strain (Farrel, 1984).

Based on the mechanism of formation and observations from this study, the hybrid blocky facies is usually found in the translational domain of MTDs.
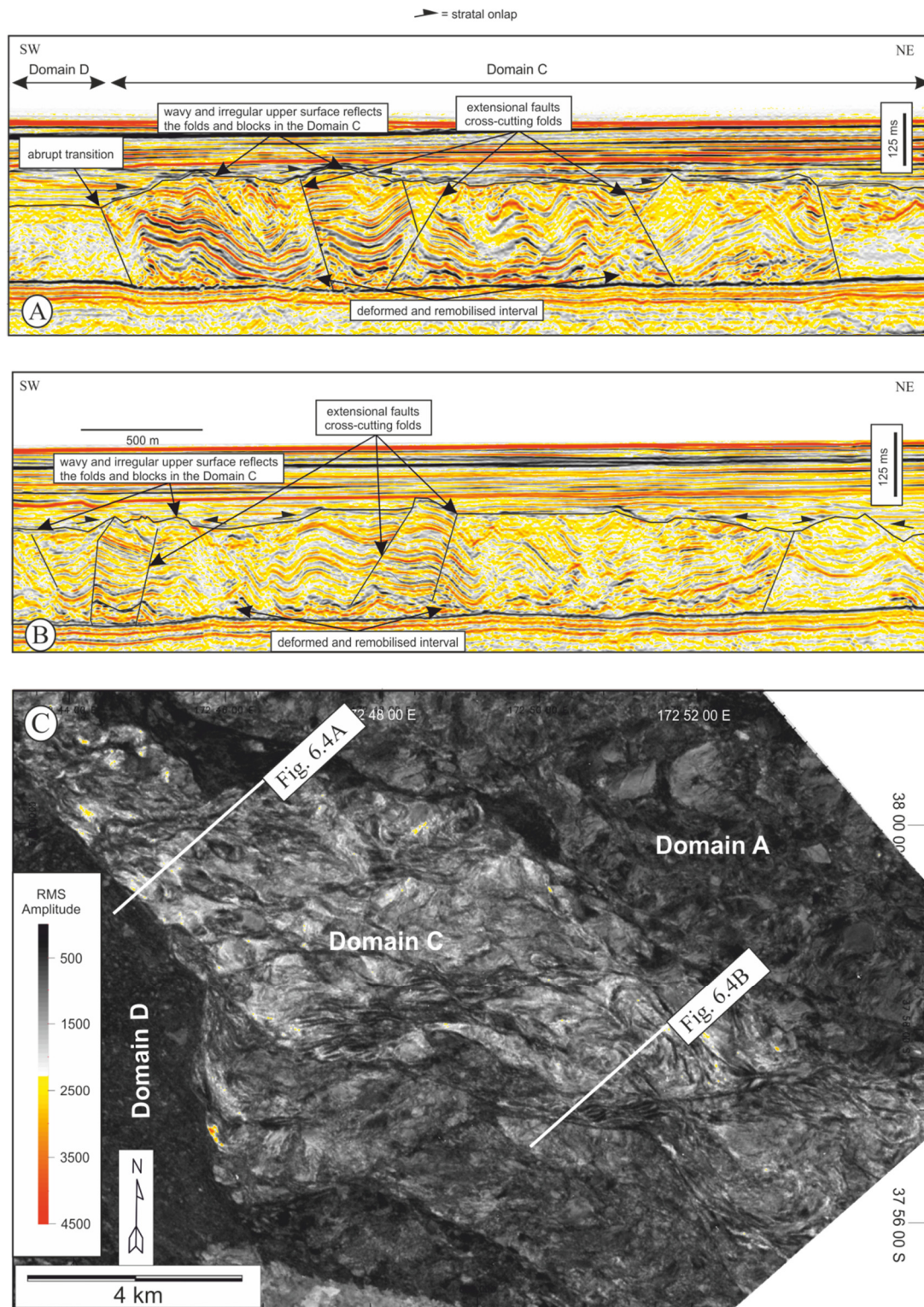
Figure 6.4. Seismic examples of hybridl blocky facies in MTDs from the Deepwater Taranaki Basin, New Zealand (this study, Chapter 5).

6.3.2.3 Amorphous Facies

The amorphous facies is mainly characterised by a chaotic, low amplitude seismic facies which envelopes, injects and in other cases, sustains discrete MTD elements (ranging from km-scale to m-scale). The amorphous facies have been subdivided into two families: incomplete and complete deformation depending on the preservation of isolated coherent units with the chaotic seismic facies (Figs. 6.5, 6.6 and Table 6.1). As in the case of the blocky facies, the rationale behind this subdivision is based on the fact that the factors that control leakage through these classes might be different.

6.3.2.3.1 Incomplete deformation

The incompletely deformed amorphous seismic facies is defined by localised irregular-shaped high-amplitude coherent reflections usually surrounded by low amplitude, chaotic seismic facies (Fig. 6.5; Table 6.1). These coherent reflections are clearly seen as isolated high amplitude feature in RMS amplitude maps or a feature with high coherency or coherency slices respectively (Fig. 6.5B and C respectively). This facies class can be found in any of the domains within an MTD.

The incomplete amorphous seismic facies generally exhibit irregular top and flat basal surfaces and have been described from the Levant Basin (Bull et al., 2009a; Fig. 6.5A), from Safi haute mer area, offshore Morocco (Dunlap et al., 2010b; Fig. 6.5B), from the Espirito Santo Basin, offshore Brazil (Alves and Cartwright, 2010; Fig. 6.5D; Jackson, 2011; Fig. 6.5F), from Brunei Deepwater margin (McGilvery and Cook, 2003; Fig. 6.5E), from the Ebro Continental Margin, offshore northeastern Spain (Giles, 2010; Fig. 6.5G), from the lower Paleocene strata, offshore Morocco (Lee et al., 2004; Fig. 6.5H) and from the Deepwater Taranaki Basin (see Chapter 5).
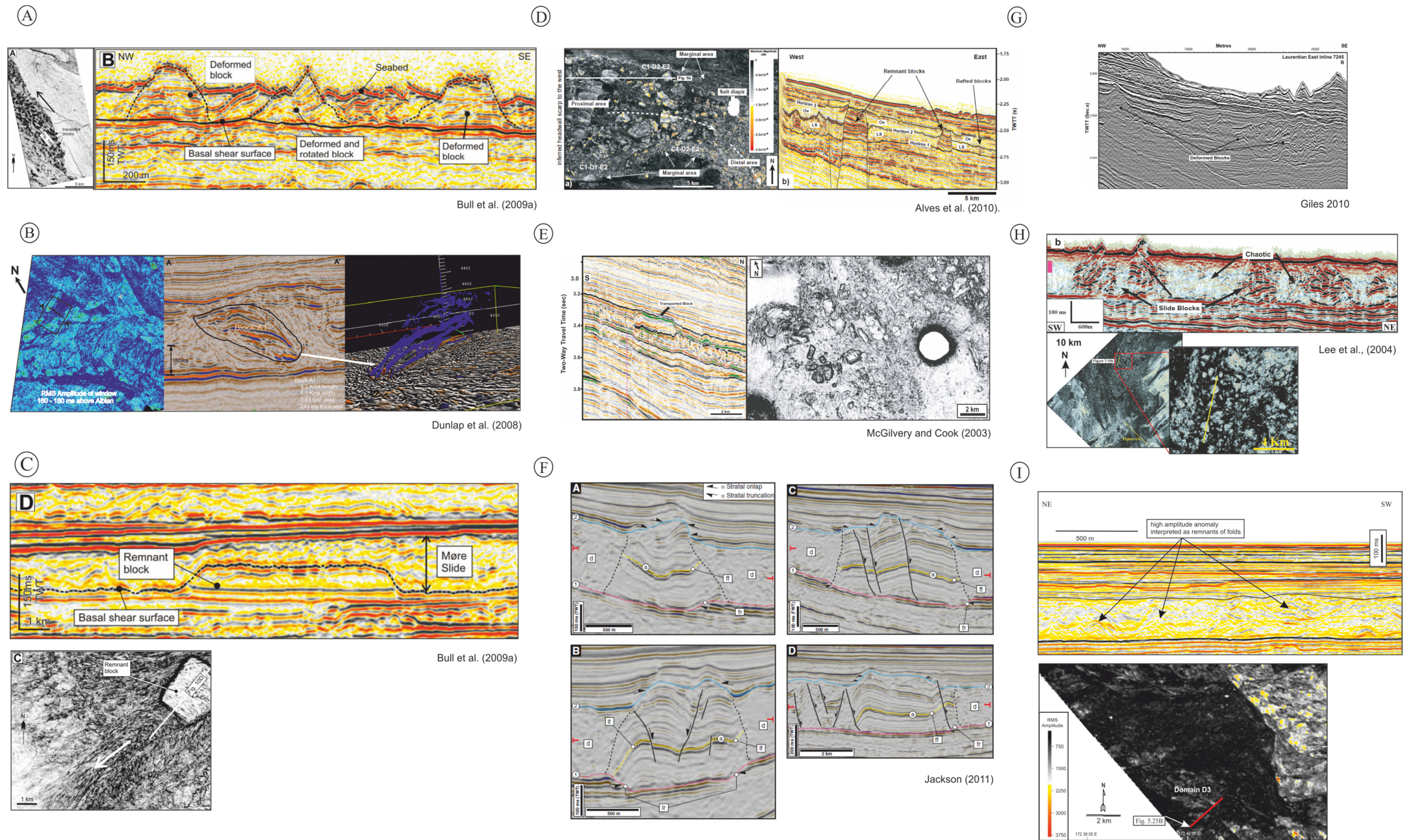
Figure 6.5. Seismic examples of incomplete deformated amorphous facies in MTDs. A) from the Levant Basin; B) from Safi haute mer area offshore morocco; C) compression zone' on the southern Storegga Slide margin; D) from the Espirito Santo Basin, offshore Brazil; E) from Brunei deepwater margin; F) from Santos Basin, offshore Brazil G), from the Ebro Continental Margin (offshore northeastern Spain); H) from the Lower Paleocene strata, offshore Morocco; I) from the Deepwater Taranaki Basin (this study, Chapter 5)

The high-amplitude coherent reflections may represent individual MTD "remnant block" if left in situ (Fig. 6.5C), or "rafted block" if substantially translated downslope and tilted as they were eroded away at their base during slope failure (Fig. 6.5B) (Masson et al., 1993). Some of the blocks contain normal faults which display displacements of up to 30 m, or are gently folded (Fig. 6.5F). The boundary between the blocks and the surrounding chaotic reflections is usually sharp and may dip up to 80° (Figs. 6.5A, F and H). The high-amplitude coherent reflections may also represent remnants of folded and/or thrusted structures (Fig. 6.5I).

The low amplitude, chaotic seismic facies is analogous to matrix material in outcrop (see appendix, Fig. 10.7). The appearance of the matrix is usually that of sandy/pebbly mudstone and can be either concentrated in the basal portion or along block boundaries. (Ogata, 2010) suggested that the matrix material originates from the progressive stratal disruption of poor to unlithified sediments (see Chapter 5) linked to the liquefaction process in the failure plane.

6.3.2.3.2 Complete deformation

The completely deformed amorphous facies is defined by low reflectivity, transparent to semi-transparent and highly chaotic seismic expression that lack coherent components (Fig. 6.6 and Table 6.1). They are usually characterised by flat and/or concordant upper and basal surfaces. On a root mean square (RMS) amplitude maps extracted in a gated windows within MTDs from the Taranaki Basin and offshore Morocco, the amplitude the may vary from moderate to low values (or mottled appearance) (Figs. 6.6E and F respectively). Their transparent to semi-tranparent acoustic signature is typical of unstructured, nonstratified sediments, suggesting strong reworking. This completely deformed amorphous facies have been interpreted as debrites (sensu Jackson, 2012; Piper et al., 1999).
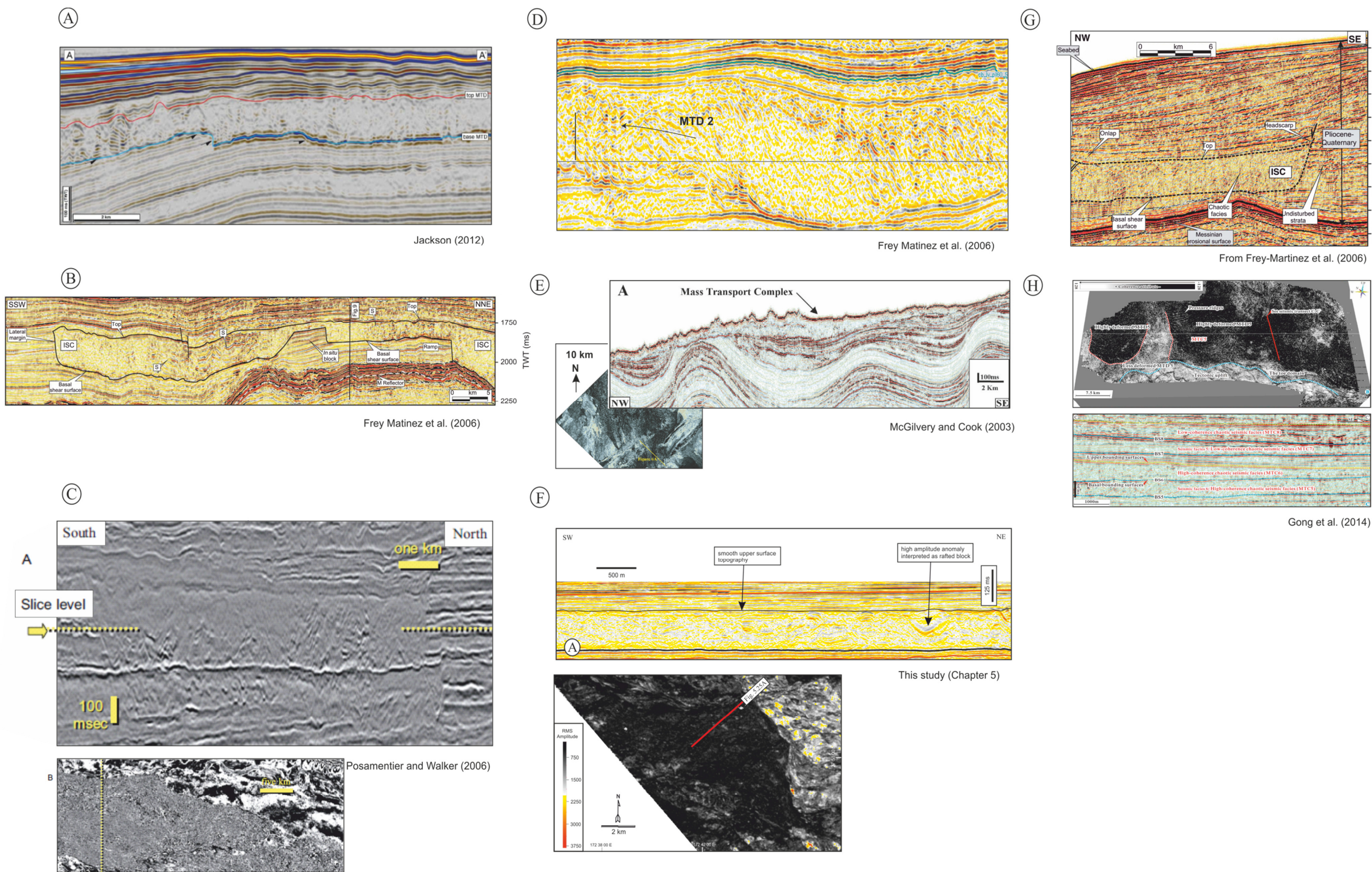
Figure 6.6. Seismic examples of completely deformed amorphous facies in MTDs. A) from the Espirito Santo Basin, offshore Brazil; B), D) and G) from the Levant Basin; C) from the eastern Gulf of Mexico; E) from the Lower Paleocene strata, offshore Morocco; F) from the Deepwater Taranaki Basin (this study, Chapter 5); H) from the Qiongdongnan Basin along the northwestern South China Sea margin.

As earlier noted, the low amplitude, chaotic seismic facies is analogous to matrix material in outcrop. However, in this case, it involves the complete disaggregation of poor to un-lithified sediments (Ogata, 2010) (see appendix, Fig. 10.7).

It is observed that this facies class is common and can be localised within an MTD or widespread, thus dominating an entire MTD.

6.3.3. Probable seal risk of seismic facies classes

The seismic facies classes of MTDs would have significantly different implications for hydrocarbon potential. It has been suggested the type of lithologies directly overlying these erosion surfaces, and hence, the transmissibility of the sealing surfaces, represents a key factor in impeding fluid migration through the stratigraphic succession (Moscardelli et al., 2006). Using these datasets, and lessons learned from outcrop analogues of the different seismic classes of MTDs (trend for N/G), an idealized representation of the classes described in this chapter, and the implication each class has on hydrocarbon seal integrity can be predicted qualitatively (Fig. 6.7). In doing this, how connectivity would be impacted within each proposed seismic class by varying the original post-depositional template from low to high N/G is considered. It should be noted that quantitative evaluation of the seal risk for each class is being undertaken as part of CAPROCKS by Couples and Ma at Heriot Watt University, but the results are not available at the time of submission.

Starting with the layered facies, with a N/G between 0.05 - 0.2, it is expected that it will represent a low risk seal (Fig. 6.7) because the semi continuous and continuous beds within the MTD will impede the leakage of hydrocarbons. A typical example of an MTD from the Espírito Santo Basin, southeast Brazil, interpreted here to fall into the layered facies
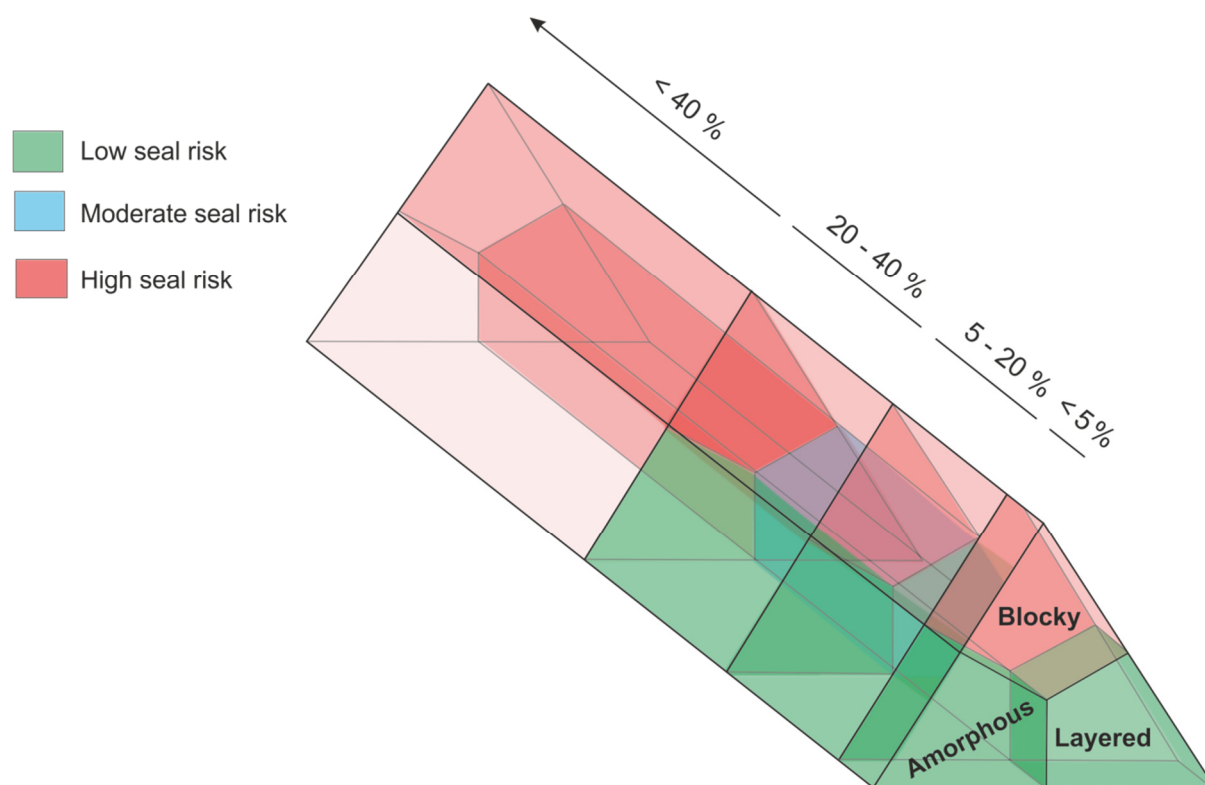
Figure 6.7. A method to predict seal integrity of MTDs based on the proposed classification (this study) and by varying the original post-depositional template from low to high N/G. Using an idealized N/G input data based on outcrop studies, predictions of the seal integrity can be made for the end member processes (See text for details).

classification is presented in Figure. 6.8A (Gamboa et al., 2012) . In this example, a local

amplitude increase which has been interpreted to be fluid-related (because they are typical of

bright spots and occur in stratigraphic intervals with proven presence of hydrocarbons) is

trapped underneath the impermeable MTD (Fig.6.8A). This indicates that the layered MTD

facies with a low N/G may act as a barrier to fluid leakage.

However, it is expected that with a progressive increase in N/G from 0.2 – 0.4, and eventually

above 0.4 (Fig. 6.7), a layered MTD facies will represent moderate and high seal risk

respectively. This idea is plausible because outcrop observations suggest that it is possible to

have a sandy dominated MTD (see appendix, Fig. 10.11), where possible hydrocarbon

migration/leakage might occur via permeable beds (diffusion). Although, such diffusive fluid

migration processes might occur over a long geological timescale.

In the blocky MTD seismic facies (both extensional and contractional) the seal risk will

depend significantly on the preservation of the original stratigraphy of the coherent blocky

component, height of blocky component and the presence of internal or fault bounded blocks

as compared to the variability in N/G. It is expected that the presence of fault bounded blocks

in the extensional blocky facies will potentially induces sharp variations in the internal

permeability of the MTD.

Numerous authors have suggested faults as being a potential leakage route through sealing

sequences (e.g. Bolås and Hermanrud, 2003; Cartwright et al., 2007). More specifically,

previous studies provide evidence for leakage through faults present in MTDs. (Gamboa et

al., 2012) documented a series of vertical migration paths related to fault bounded blocks

within an MTD in the Espírito Santo Basin (Fig. 6.8B and C). They suggested that fluids

sourced from Late Cretaceous strata migrated through fault bounded blocks in the MTD with

evidence of brightening in or above the fault-bounded blocks.
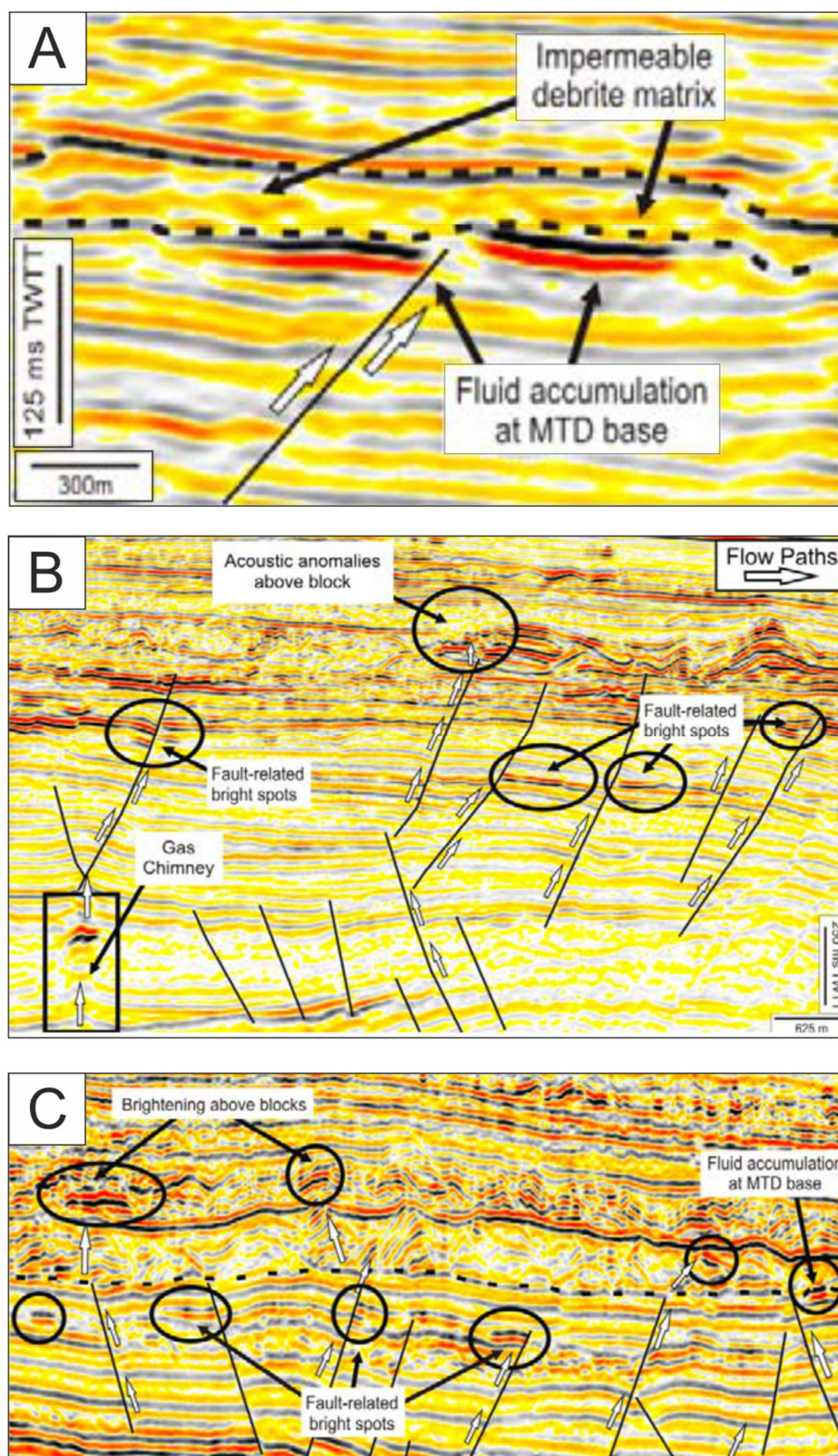
Figure 6.8. Seismic profiles form the Espírito Santo Basin showing high amplitude anomalies interpreted to be fluid related (from Gamboa et al., 2011). A) High amplitude anomalies trapped beneath an the basal surface of an MTD interpreted here as layered facies MTD due to the continuous to discontinuous reflection within it; B) and C) Faults in MTD are associated with fluid migration, sourced from Late Cretaceous strata. Brightening in or above fault-bounded blocks, or the block-matrix contact suggest permeability enhancement features within the MTD. When blocks are absent, fluids are trapped underneath the low permeability debrites.

256

In the offshore Eel River Basin, pockmarks have been observed at the headwall scarp of a submarine slide (Foland et al., 1999). Similarly, (Yang et al., 2013) proposed that the spatial relationship of high amplitude anomalies (HAAs) and buried MTDs in the continental margin, offshore Mauritania show strong evidence for upward gas migration along margins or local faults associated with underlying MTDs. The authors suggested that upward fluid migration controlled by MTDs may have played a significant role in the formation of HAAs.

In reality, most of the normal faults that define the extensional blocky class will be closed as evidenced from seismic because confining stress would generally keep the low angle fault surfaces closely shut tight. For hydrocarbons to migrate upwards along these faults, they would need to possess a significantly higher permeability of the fault zone materials or the planes would need to be dilated, at least partially , and this latter state can only occur as a result of significant overpressure such that the fault or fracture will be open for a time until the pressure has dropped (Bjørkum et al., 1998). Therefore, only dilation under high pore fluid pressure (probably from the underlying reservoir) would render the faults as conduits, and this should be regarded as a mechanical seal failure involving reactivation.

Evidence of normal faults acting as conduits for fluid migration has been observed in outcrops (see appendix, Fig.10.13). In this example, mineralization along a fault plane (veins) is visible which corroborates with seismic observation.

The seal risk associated with the folded structures in the contractional blocky facies class will depend on the presence of numerous sub-seismic faults on the crest of folds which could possibly connect permeable sandy beds of the fold limb. However this leakage mechanism requires that the sub-seismic faults do not form clay smear or cataclastic seals against the leaky strata (Ingram and Urai, 1999).

Evidence for leakage through crestal faults is visible in outcrops south of Whangaparaoa Head in the Whangapararoa Peninsula (Spörli and Rowland, 2007; see appendix, Fig. 10.14).

The authors suggested that carbonate concretions aligned parallel to the axis of a recumbent fold indicated persistent migration of formation fluids.

The seal risk associated with imbricate thrusts structures in the contractional blocky facies class will be the headwall dipping thrust faults that might act as migration conduits for hydrocarbons.

(Morita et al., 2011) suggested that dewatering structures which are strongly dependent on the development of imbricate structures within MTDs in the continental slope off Shimokita Peninsula, NE Japan, acted to drain excess fluid that accumulated upon the slip planes (Fig. 6.9). The authors proposed that the damped and dimmed reflections in the dewatering structures and in the MTD indicated that the distribution of natural gas is strongly related to fluid circulation in and around the MTD (Fig. 6.9).

As with the extensional blocky facies class, these thrust faults are expected to be closed because confining stress but would probably dilate under high pore fluid pressure, thus acting as a conduit for leakage.

The hybrid blocky facies class is expected to be of higher risk with regards to seals since the seal risk is expected to be a combination of the seal risk associated with both the extensional blocky and contractional blocky facies.

An increased N/G (< 40%) in the blocky facies (Fig.6.7) is expected to further render the MTD as high seal risk because possible migration conduit might occur via permeable beds without any faulting. For instance, high amplitude reflections that propagate from the base towards the upper surface in imbricate thrusts structures (e.g. Figs. 6.3A, D and F) might represent thin sandy beds with relatively high permeabilities and relatively low capillary entry pressures that may compromise the seal integrity (Wehr et al., 2000).
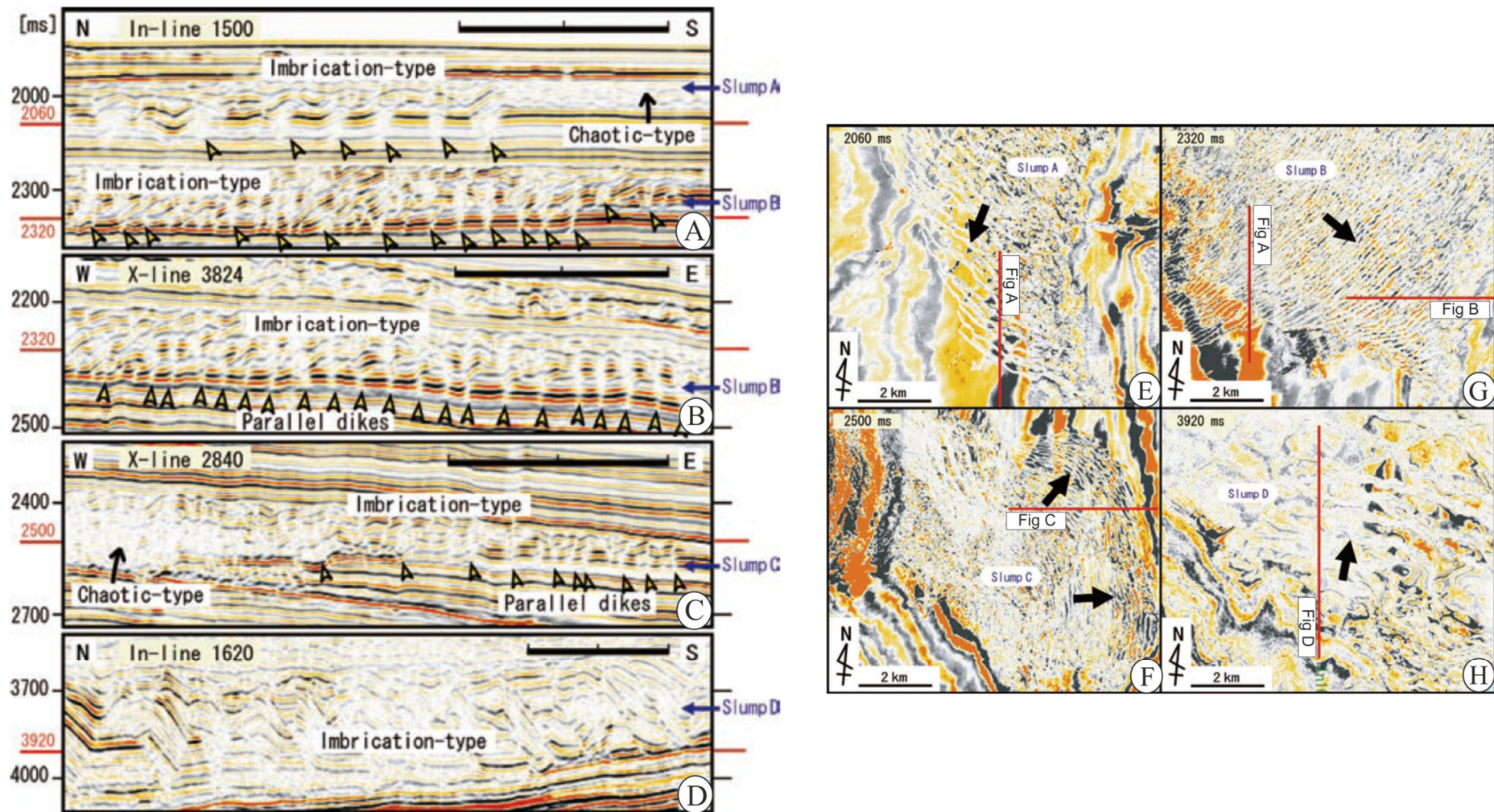
Figure 6.9. Seismic profiles (A - D)from the continental slope off Shimokita Peninsula, NE Japan (from Morita et al., 2011) showing imbricate structures within MTDs and related dewatering structures in 3d seismic sections. The occurrence of parallel dikes, which represent dewaterinig structures (open arrow heads), is strongly dependent on the nature of imbrication. Each scale bar is 2km. Red horizontal bars and time depths (ms) corresponds to the time slice images shown in Figs. 6.9E – H. Notice Parallel dikes (apparent in the images as linear features) strike perpendicular to the transport direction (arrows).

Given a low N/G (0.5), the amorphous facies is generally expected to represent low seal risk (Fig. 6.7). However, the remnant or rafted blocks in the incompletely deformed amorphous facies class (Fig. 6.5) can constitute viable fluid pathways on otherwise low-permeability units. For instance, in Figure 6.5F, there is evidence for internally faulted remnant blocks and as such these faults can act as conduits for fluid migration/leakage.

With increasing N/G (0.5 – 0.4)and depending on the connectivity of the sandy beds (i.e. isolated sandy beds) within the amorphous facies, it is still expected to represent low seal risk (Fig. 6.7) with regards to seal not considered as uniform beds of sand. However, with > 0.4 N/G, the amorphous facies is expected to represent a high risk seal. Taking into account the fact that with a high N/G, it is very likelytthat sandy units with relatively high permeabilities will form a connected network.

Summary

The seismic characterisation of the internal architecture of MTDs in this project has revealed that they are characterised by varied internal structures and this has led to the robust seismic classification scheme that has accounted for these variabilities and thus can be applicable worldwide (Table 6.1).

Previous studies have revealed (within the Blocky MTD facies) high amplitude anomalies lining up not only with faults bounded blocks (Gamboa et al., 2011), but also with imbricate thrust structures (Morita et al., 2011) . Other features associated with gas seepage (e.g., pockmarks) have also been reported above MTDs, along the margins (Yang et al., 2013).

Consequently, the faults in the blocky facies are suggested as potential hydrocarbon-migration pathways within an MTD. If a blocky MTD seismic facies dominants an MTD at the top of a potential hydrocarbon trap, and if high amplitude anomalies (HAAs) or other features indicating fluid migration are present along the fault bounded blocks, the prospect can be regarded as a high risk with respect to seal integrity.

It has also been shown that MTDs represented by chaotic seismic reflections and characterised by the absence of any coherent blocky element (layered and/or amorphous MTD facies), trap fluid related amplitude high anomalies beneath their basal surfaces and are thus believed to be low risk with regards to seal integrity.

However, it is observed that given the depositional environment of most MTDs, a weak relationship exists between the classified seismic facies and the lithology of MTDs because the lithologic content mainly depends on the material source (Prather et al., 1998). However, if enough impedance contrast is visualised, the MTD may be considered as sand prone (Meckel III, 2011), and as such the seal risk will depend on the connectivity of the coarser (higher permeability) beds. Therefore, once it has been established that the MTD is sand prone using other possible diagnostic criteria (e.g. wireline logs), the primary risks associated with the chaotic facies may be fluid migration pathways provided by connections between sandy units via the thinly bedded sand. However, leakage through such connected sand beds is believed to represent relatively slow flux rates (pers. Comm. Jingsheng Ma).

As such, the mapping of these various MTD classes in seismic data, and the detection of features that can indicate fluid-migration pathways (e.g. high amplitude anomalies, damp and dimmed reflections), have significance in MTD seal integrity analysis and in the process of risking hydrocarbon prospects. It is proposed in this project that the geometry of the internal seismic character of an MTD and the N/G play an important role in determining the sealing capacity i.e. whether the MTD leaks or not.

6.4 Project limitations

Thorough investigations of MTDs with regards to understanding their internal architecture, morphology evolution and failure mechanisms using a combination of both 2D and 3D seismic datasets from two case studies have been carried out in this project. Although the thorough investigation has improved our overall understanding of MTDs, some grey areas which were imposed by certain project limitations still exist. These include: 1) lack of other data types e.g. well data and 2) limited seismic data coverage.

Firstly, is the lack of well data, which is probably the most significant limitation in this project. The availability of well data would have allowed the establishment of MTD lithology and the absolute ages of the various MTDs in the both case studies. For instance, in Chapter 3, the ages of MTDs A, B and C were loosely constrained using published data. Similarly in Chapter 4, the age and timing of MTDs 1 - 6 were loosely constrained by identifying underlying sedimentary packages, and sedimentation rates from published literatures. The establishment of the absolute ages of the MTDs in this project coupled with the timing of their emplacement may help in unravelling their cause of failure and future occurrence.

Secondly, the limited seismic data coverage which was evident in the core result chapters, particularly in Chapter 4. Although the 2D seismic lines covered to vast area and to a large extent most of the studied MTDs, the fact that the coverage did not extend to the northern part of the Taranaki shelf edge precluded the interpretation the headwall regions and thus the exact geographical extent and the volumes of some of the giant MTDs, which would have been very useful. Similarly, 3D seismic data which have proven to be one of the most powerful tools for the geological investigation of both ancient and recent MTDs was limited in volume in this project, covering small subarea (see Chapter 5). Whilst the analysis of the small 3D volume in Chapter 5 have proven to be successful, the availability of a larger 3D

volume, covering most part of the study area would have allowed a complete interpretation of the internal fabric, emplacement mechanism and evolution of the MTDs, thus improving our understanding.

6.5 Recommendation for further work

Although there is much direct geological and geophysical evidence for migration of fluids through MTDs, there is little information on the rate at which these flows occur. As such, going further in our general understanding of the impact of MTDs on hydrocarbon seal integrity requires a numerical modelling approach dealing with hydrocarbon leakage through the various proposed classes in this project. Such models should provide more details not only on the possible relationship between modelled migration routes and the location of certain major leakage features for each MTD seismic class, but also on the quantification of the hydrocarbon volumes leaked via MTDs through geologic time.

Another aspect that needs to be modelled is the "geologically instantaneous" loading and unloading of MTDs during (see, for instance, Chapter 3). This will greatly improve our knowledge of the result of loading and unloading is MTDs since it is difficult to assess without taking into account the rates at which each process acts.

The classification scheme proposed in this project needs to be recalibrated to geology for two reasons; first, seismic facies are not directly linked with geological facies since seismic resolution is limited with respect to the size of geological heterogeneities; and second, probabilities cannot be interpreted as proportions of geological facies. Consequently further detailed studies of these proposed seismic facies types will lead to a better understanding of the sealing capacity of MTDs and associated risk.

<u>Chapter 7</u>

7.0 Summary and Conclusions

7.1 Summary

2D and 3D seismic characterisation of Mass transport deposits (MTDs) from the west Nile delta, offshore Egypt and from the Deepwater Taranaki Basin, New Zealand have provided a wealth of information relating to diverse aspects including internal architecture, morphology, kinematic indicators and deformational history. Although this study has focussed primarily on MTDs from these geographical regions, it is expected that the results will find broad applicability to MTDs in other settings and locations worldwide.

The general conclusions drawn from this study and the summarised conclusions from the core result chapters are presented in this chapter.

7.2 General conclusions

1) MTDs constitute a primary component of heterogeneous siliciclastic seal sequences in many slope basins.

2) The interpretation and analysis of seismic reflection data provides detailed information on the external and internal structures of MTDs which is critical to evaluate their failure and triggering mechanisms.

3) A comprehensive and robust scheme seismic based classification of MTDs that is directly mappable onto the problem of defining their potential as sealing sequences has been proposed MTDs are classified as (1) layered, (2) blocky, and (3) amorphous depending on their a) external geometry, b) internal reflection configuration, inferred stress regime, c) reflection continuity, d) amplitude strength and RMS amplitude and/or coherency pattern. The classification scheme can be applied by an interpreter within a short time frame.

4) Integrated field-based approach to the study of MTDs is extremely useful to solve many of the interpretative problems.

7.3 Conclusions from Chapter 3

- 3D Seismic data have provided an opportunity to examine a major submarine slope failure in the western Nile delta.

- The Giant failure is a composite of two separate but spatially and time related MTDs; one nestled within another, and with their own distinct lateral margins.

- The giant failure affected an area of c. 1400 km^2, and a total volume of c. 750 km^3 was remobilised.

- The MTDs are thought to have experienced at least two main phases of emplacement during the mid to late Pleistocene involving: 1) progressive failure occurred initially with MTD A cutting through B and C then; 2) retrogressive failure occurred due to the natural unbalance of the supposed headwall of MTD A.

- Preconditioning of the slope prior to the failure events most likely relates to differential and high sedimentation rates induced during the Sahara Pluvial period in the western Nile delta and local increases of pore pressure. Another preconditioning factor prior to triggering of the failures may be the presence of gas in shallow sediments.

- The combined excavation of the pre-existing slope sediments amounts to c.1000 m which makes it one of the deepest incising of its type in the world might have probably been a risk to petroleum systems considering the failure occurred in a gas rich province of the western Nile delta.

7.4 Conclusions from Chapter 4

- A high-resolution bathymetric and two-dimensional (2D) seismic reflection data from the Deepwater Taranaki basin (North New Zealand) has allowed a detailed

morphological analysis of six giant mass transport deposits within the Plio-Pleistocene Giant Foreset Formation. The following conclusion can be made:

- MTDs 1-5 have a north-westerly transport direction and MTD 6 has a south-westerly transport direction.

- 2) All six MTDs were emplaced between 3.6 Ma and 1.8 Ma and have volumes ranging between 377 km^3 and 4,064 km^3, thus they are among the largest submarine MTDs known from passive continental margins.

- 3) An estimation of 70% of the final volume of MTD 6 was contributed from substrate cannibalization, greater than any of the other MTDs in the study area.

- 4) The failure of MTDs 1-5 is believed to have been facilitated by rapid sedimentation on the shelf margin from Late Miocene to recent times coupled with concomitant rapid overstepping of slope indicated by the development of headwall scarps along the bounding surfaces of progradational foresets. MTD 6 is believed to have been triggered by tectonic activity (e.g. faulting) given that it was emplaced in a translation direction different from the other MTDs in the study area.

- 5) The acute substrate cannibalisation of MTD 6 and the different translation direction compared to the other MTDs in the study area suggests a relationship between MTD trigger and cannibalization of the substrate.

7.5 Conclusions from Chapter 5

- A high resolution 3D seismic dataset acquired in the Deepwater Taranaki Basin, New Zealand provides insights into the dynamics of emplacement of the latest submarine MTD (termed MTD 6) within the Giant Foresets Formation.

- MTD 6 consists of 5 distinctive domains (labeled A – E) characterised by different internal deformation fabrics, and translation directions that are not consistent with the orientation of the two sets of underlying grooves observed on the basal surface.

- Domain A is dominated by barely deformed extensionally faulted blocks moving differentially. Doman B is dominated by contractional folds and thrust structures with a dominant SW translation direction. Domain C is characterised by strain overprinting where early formed folds are truncated by late faults with a dominant SW transport direction. Domain D is characterised by intense deformation and partial deformation of previously extensional and contractional structures coupled with c. 30% reduction in thickness compared to adjacent domains. Domain E is characterised by continuous to discontinuous reflections with evidence of in-situ blocks.

- The two sets of underlying grooves (G1 and G2 are oriented in SW and NW directions respectively) seem to align with the edges of extensionally faulted blocks or in-situ blocks. They are interpreted to result from the sinking of the blocks.

- Ranking of all of the kinematic indicators in the study area based on their reliability suggests an overall SW transport direction for MTD 6.

- Analyses of the deformational structures within the domains and their boundaries suggest a progressive stratal disaggregation would be a plausible deformation process with the lack of seismic character and lose of strength in Domain D being the ultimate product.

References

Aal, A. A., El Barkooky, A., Gerrits, M., Meyer, H., Schwander, M., and Zaki, H., 2000, Tectonic evolution of the Eastern Mediterranean Basin and its significance for hydrocarbon prospectivity in the ultradeepwater of the Nile Delta: The Leading Edge, v. 19, no. 10, p. 1086-1102.

Ahuja, L., Cassel, D., Bruce, R., and Barnes, B., 1989, Evaluation of spatial distribution of hydraulic conductivity using effective porosity data: Soil Science, v. 148, no. 6, p. 404-411.

Algar, S., Milton, C., Upshall, H., Roestenburg, J., and Crevello, P., 2011, Mass-transport deposits of the Deepwater Northwestern Borneo Margin-Characterization from seimic reflection, borehole and core data with implications for hydrocarbon exploration and exploitation. In:Shipp, R. C., Weimer P., Posamentier, H. W. (eds) Mass-transport deposits in deepwater settings. SEPM (Society for Sedimentary Geology) Special Publications, vol. 96, pp. 351-366.

Almagor, G., 1984, Salt-controlled slumping on the Mediterranean slope of central Israel: Marine geophysical researches, v. 6, no. 3, p. 227-243.

Alves, T. M., and Cartwright, J. A., 2010, The effect of mass-transport deposits on the younger slope morphology, offshore Brazil: Marine and Petroleum Geology, v. 27, no. 9, p. 2027-2036.

Armstrong, P. A., Allis, R. G., Funnell, R. H., and Chapman, D. S., 1998, Late Neogene exhumation patterns in Taranaki Basin (New Zealand): Evidence from offset porosity-depth trends: Journal of Geophysical Research: Solid Earth (1978–2012), v. 103, no. B12, p. 30269-30282.

Ashabranner, L., Tripsanas, E., and Shipp, R., 2010, Multi-direction flow in a mass-transport deposit, Santos Basin, offshore Brazil, Submarine mass movements and their consequences, Springer, p. 247-255.

Bacon, M., Simm, R., and Redshaw, T., 2007, 3-D seismic interpretation, Cambridge University Press.

Baraza, J., Lee, H. J., Kayen, R. E., and Hampton, M. A., 1990, Geotechnical characteristics and slope stability on the Ebro margin, western Mediterranean: Marine Geology, v. 95, no. 3, p. 379-393.

Beaubouef, R., and Abreu, V., 2010, MTCs of the Brazos-Trinity slope system; thoughts on the sequence stratigraphy of MTCs and their possible roles in shaping hydrocarbon traps, Submarine Mass Movements and Their Consequences, Springer, p. 475-490.

Bernander, S., 2000, Progressive landslides in long natural slopes: potential extension and configuration of finished slides in strain-softening soils.

Bishop, A., Progressive failure-with special reference to the mechanism causing it, *in* Proceedings Proc. Geotech. Conf., Oslo1967, Volume 2, p. 142-150.

Bjerrum, L., 1955, Stability of natural slopes in quick clay: Geotechnique, v. 5, no. 1, p. 101-119.

Bjerrum, L., 1967, Progressive failure in slopes of overconsolidated plastic clay and clay shales: Journal of Soil Mechanics & Foundations Div.

Bjørkum, P. A., Walderhaug, O., and Nadeau, P. H., 1998, Physical constraints on hydrocarbon leakage and trapping revisited: Petroleum Geoscience, v. 4, no. 3, p. 237-239.

Bolås, H. M. N., and Hermanrud, C., 2003, Hydrocarbon leakage processes and trap retention capacities offshore Norway: Petroleum Geoscience, v. 9, no. 4, p. 321-332.

Bondevik, S., Mangerud, J., Dawson, S., Dawson, A., and Lohne, Ø., 2003, Record-breaking height for 8000-year-old tsunami in the North Atlantic: Eos, Transactions American Geophysical Union, v. 84, no. 31, p. 289-293.

Brami, T. R., 2000, Late Pleistocene deep-water stratigraphy and depositional processes, offshore Trinidad and Tobago.

Brodie, J., 1965, Aotea Seamount, eastern Tasman Sea: New Zealand journal of geology and geophysics, v. 8, no. 3, p. 510-517.

Brown, A., 2011, Interpretation of three-dimensional seismic data, SEG Investigations in Geophysics 9 and AAPG Memoir 42.

Brun, J.-P., and Fort, X., 2011, Salt tectonics at passive margins: geology versus models: Marine and Petroleum Geology, v. 28, no. 6, p. 1123-1145.

Bryn, P., Berg, K., Forsberg, C. F., Solheim, A., and Kvalstad, T. J., 2005a, Explaining the Storegga slide: Marine and Petroleum Geology, v. 22, no. 1, p. 11-19.

Bryn, P., Berg, K., Stoker, M., Haflidason, H., and Solheim, A., 2005b, Contourites and their relevance for mass wasting along the Mid-Norwegian Margin: Marine and Petroleum Geology, v. 22, no. 1, p. 85-96.

Bryn, P., Solheim, A., Berg, K., Lien, R., Forsberg, C., Haflidason, H., Ottesen, D., and Rise, L., 2003, The Storegga Slide complex; repeated large scale sliding in response to climatic cyclicity, Submarine mass movements and their consequences, Springer, p. 215-222.

Bull, S., and Cartwright, J., 2010, Small-scale insights into seismic-scale slumps: a comparison of slump features from the Waitemata Basin, New Zealand, and the Møre Basin, Off-shore Norway, Submarine Mass Movements and Their Consequences, Springer, p. 257-266.

Bull, S., Cartwright, J., and Huuse, M., 2009a, A review of kinematic indicators from mass-transport complexes using 3D seismic data: Marine and Petroleum Geology, v. 26, no. 7, p. 1132-1151.

-, 2009b, A subsurface evacuation model for submarine slope failure: Basin Research, v. 21, no. 4, p. 433-443.

Bünz, S., Mienert, J., Bryn, P., and Berg, K., 2005, Fluid flow impact on slope failure from 3D seismic data: a case study in the Storegga Slide: Basin Research, v. 17, no. 1, p. 109-122.

Canals, M., Lastras, G., Urgeles, R., Casamor, J., Mienert, J., Cattaneo, A., De Batist, M., Haflidason, H., Imbo, Y., and Laberg, J., 2004, Slope failure dynamics and impacts from seafloor and shallow sub-seafloor geophysical data: case studies from the COSTA project: Marine Geology, v. 213, no. 1, p. 9-72.

Cartwright, J., and Huuse, M., 2005, 3D seismic technology: the geological 'Hubble': Basin Research, v. 17, no. 1, p. 1-20.

Cartwright, J., Huuse, M., and Aplin, A., 2007, Seal bypass systems: AAPG bulletin, v. 91, no. 8, p. 1141-1166.

Charles, J., 1982, Appraisal of the influence of a curved failure envelope on slope stability: Geotechnique, v. 32, p. 389-392.

Charlton, R., 2007, Fundamentals of fluvial geomorphology, Routledge.

Chopra, S., and Marfurt, K. J., 2005, Seismic attributes—A historical perspective: Geophysics, v. 70, no. 5, p. 3SO-28SO.

Corcoran, D., and Doré, A., 2002, Top seal assessment in exhumed basin settings—Some insights from Atlantic margin and borderland basins: Norwegian Petroleum Society Special Publications, v. 11, p. 89-107.

Courtillot, V., Armijo, R., and Tapponnier, P., 1987, The Sinai triple junction revisited: Tectonophysics, v. 141, no. 1, p. 181-190.

Crosta, G., De Blasio, F., De Caro, M., Volpi, G., and Frattini, P., Granular flows on erodible layers: type and evolution of flow and deposit structures, *in* Proceedings EGU General Assembly Conference Abstracts2012, Volume 14, p. 11572.

Crutchley, G. J., Karstens, J., Berndt, C., Talling, P., Watt, S., Vardy, M., Hühnerbach, V., Urlaub, M., Sarkar, S., and Klaeschen, D., 2012, Insights into the emplacement dynamics of volcanic landslides from high-resolution 3D seismic data acquired offshore Montserrat, Lesser Antilles: Marine Geology.

Dalla Valle, G., Gamberi, F., Rocchini, P., Minisini, D., Errera, A., Baglioni, L., and Trincardi, F., 2013, 3D seismic geomorphology of mass transport complexes in a foredeep basin: Examples from the Pleistocene of the Central Adriatic Basin (Mediterranean Sea): Sedimentary Geology, v. 294, p. 127-141.

De Blasio, F. V., 2011, Introduction to the physics of landslides: lecture notes on the dynamics of mass wasting, Springer.

Deplus, C., Le Friant, A., Boudon, G., Komorowski, J.-C., Villemant, B., Harford, C., Ségoufin, J., and Cheminée, J.-L., 2001, Submarine evidence for large-scale debris avalanches in the Lesser Antilles Arc: Earth and Planetary Science Letters, v. 192, no. 2, p. 145-157.

Dingle, R., 1977, The anatomy of a large submarine slump on a sheared continental margin (SE Africa): Journal of the Geological Society, v. 134, no. 3, p. 293-310.

Dolson, J., Boucher, P., Siok, J., and Heppard, P., Key challenges to realizing full potential in an emerging giant gas province: Nile Delta/Mediterranean offshore, deep water, Egypt, *in* Proceedings Geological Society, London, Petroleum Geology Conference series2005, Volume 6, Geological Society of London, p. 607-624.

Dolson, J., Shann, M., Matbouly, S., Hammouda, H., and Rashed, R., 2001, Egypt in the twenty-first century: petroleum potential in offshore trends: GEOARABIA-MANAMA-, v. 6, p. 211-230.

Dott Jr, R., 1963, Dynamics of subaqueous gravity depositional processes: AAPG Bulletin, v. 47, no. 1, p. 104-128.

Downey, M. W., 1994, Hydrocarbon Seal Rocks: Chapter 8: Part II. Essential Elements.

Downey, W., Kellett, R., Smith, I., Price, R., and Stewart, R., 1994, New palaeomagnetic evidence for the recent eruptive activity of Mt. Taranaki, New Zealand: Journal of volcanology and geothermal research, v. 60, no. 1, p. 15-27.

Ducassou, E., Migeon, S., Mulder, T., Murat, A., Capotondi, L., Bernasconi, S. M., and Mascle, J., 2009, Evolution of the Nile deep-sea turbidite system during the Late Quaternary: influence of climate change on fan sedimentation: Sedimentology, v. 56, no. 7, p. 2061-2090.

Dunlap, D. B., Wood, L. J., Weisenberger, C., and Jabour, H., 2010a, Seismic geomorphology of offshore Morocco's east margin, Safi Haute Mer area: AAPG bulletin, v. 94, no. 5, p. 615-642.

-, 2010b, Seismic geomorphology of offshore Moroccos east margin, Safi Haute Mer area: AAPG bulletin, v. 94, no. 5, p. 615-642.

Dupré, S., Woodside, J., Foucher, J.-P., de Lange, G., Mascle, J., Boetius, A., Mastalerz, V., Stadnitskaia, A., Ondréas, H., Huguen, C., Harmégnies, F., Gontharet, S., Loncke, L., Deville, E., Niemann, H., Omoregie, E., Olu-Le Roy, K., Fiala-Medioni, A., Dählmann, A., Caprais, J.-C., Prinzhofer, A., Sibuet, M., Pierre, C., and Damsté, J. S., 2007, Seafloor geological studies above active gas chimneys off Egypt (Central Nile Deep Sea Fan): Deep Sea Research Part I: Oceanographic Research Papers, v. 54, no. 7, p. 1146-1172.

Dykstra, M., 2005, Dynamics of sediment mass-transport from the shelf to the deep sea: Unpublished Ph. D. Dissertation, University of California, Santa Barbara.

Eberhardt, E., Stead, D., and Coggan, J., 2004, Numerical analysis of initiation and progressive failure in natural rock slopes—the 1991 Randa rockslide: International Journal of Rock Mechanics and Mining Sciences, v. 41, no. 1, p. 69-87.

Embley, R. W., 1976, New evidence for occurrence of debris flow deposits in the deep sea: Geology, v. 4, no. 6, p. 371-374.

Farrell, S., 1984, A dislocation model applied to slump structures, Ainsa Basin, South Central Pyrenees: Journal of Structural Geology, v. 6, no. 6, p. 727-736.

Farrell, S., and Eaton, S., 1987, Slump strain in the Tertiary of Cyprus and the Spanish Pyrenees. Definition of palaeoslopes and models of soft-sediment deformation: Geological Society, London, Special Publications, v. 29, no. 1, p. 181-196.

Festa, A., Dilek, Y., Pini, G., Codegone, G., and Ogata, K., 2012, Mechanisms and processes of stratal disruption and mixing in the development of mélanges and broken formations: redefining and classifying mélanges: Tectonophysics, v. 568, p. 7-24.

Flint, S., Hodgson, D., Sprague, A., Brunt, R., Van der Merwe, W., Figueiredo, J., Prélat, A., Box, D., Di Celma, C., and Kavanagh, J., 2011, Depositional architecture and sequence stratigraphy of the Karoo basin floor to shelf edge succession, Laingsburg depocentre, South Africa: Marine and Petroleum Geology, v. 28, no. 3, p. 658-674.

Foland, S., Maher, N., and Yun, J., 1999, Pockmarks along the Californian Continental Margin: implications for fluid flow: AAPG Bull, v. 83, p. 681-706.

Fournier, F., Déquirez, P.-Y., Macrides, C. G., and Rademakers, M., 2002, Quantitative lithostratigraphic interpretation of seismic data for characterization of the Unayzah Formation in central Saudi Arabia: Geophysics, v. 67, no. 5, p. 1372-1381.

Frey-Martínez, J., Cartwright, J., and James, D., 2006, Frontally confined versus frontally emergent submarine landslides: a 3D seismic characterisation: Marine and Petroleum Geology, v. 23, no. 5, p. 585-604.

Frey Martinez, J., Cartwright, J., and Hall, B., 2005, 3D seismic interpretation of slump complexes: examples from the continental margin of Israel: Basin Research, v. 17, no. 1, p. 83-108.

Gafeira Gonçalves, J., 2010, Submarine mass movement processes on the North Sea Fan as interpreted from the 3D seismic data: University of Edinburgh.

Gafeira, J., Long, D., Scrutton, R., and Evans, D., 2010, 3D seismic evidence of internal structure within Tampen Slide deposits on the North Sea Fan: are chaotic deposits that chaotic?: Journal of the Geological Society, v. 167, no. 3, p. 605-616.

Gamboa, D., Alves, T., and Cartwright, J., 2011, Distribution and characterization of failed (mega) blocks along salt ridges, southeast Brazil: Implications for vertical fluid flow on continental margins: Journal of Geophysical Research: Solid Earth (1978–2012), v. 116, no. B8.

-, 2012, Seismic-Scale Rafted and Remnant Blocks over Salt Ridges in the Espírito Santo Basin, Brazil, Submarine Mass Movements and Their Consequences, Springer, p. 629-638.

Gamboa, D., Alves, T., Cartwright, J., and Terrinha, P., 2010, MTD distribution on a 'passive'continental margin: The Espírito Santo Basin (SE Brazil) during the Palaeogene: Marine and Petroleum Geology, v. 27, no. 7, p. 1311-1324.

Garziglia, S., Migeon, S., Ducassou, E., Loncke, L., and Mascle, J., 2008, Mass-transport deposits on the Rosetta province (NW Nile deep-sea turbidite system, Egyptian margin): characteristics, distribution, and potential causal processes: Marine Geology, v. 250, no. 3, p. 180-198.

Gaullier, V., Mart, Y., Bellaiche, G., Mascle, J., Vendeville, B. C., and Zitter, T., 2000, Salt tectonics in and around the Nile deep-sea fan: insights from the PRISMED II cruise: Geological Society, London, Special Publications, v. 174, no. 1, p. 111-129.

Gawthorpe, R., and Clemmey, H., 1985, Geometry of submarine slides in the Bowland Basin (Dinantian) and their relation to debris flows: Journal of the Geological Society, v. 142, no. 3, p. 555-565.

Gee, M., Gawthorpe, R., and Friedmann, J., 2005, Giant striations at the base of a submarine landslide: Marine Geology, v. 214, no. 1, p. 287-294.

Gee, M., Gawthorpe, R., and Friedmann, S., 2006, Triggering and evolution of a giant submarine landslide, offshore Angola, revealed by 3D seismic stratigraphy and geomorphology: Journal of Sedimentary Research, v. 76, no. 1, p. 9-19.

Gee, M., Masson, D., Watts, A., and Allen, P., 1999, The Saharan debris£ ow: an insight into the mechanics of long runout submarine debris£ ows: Sedimentology, v. 46, p. 317-335.

Gee, M., Uy, H., Warren, J., Morley, C., and Lambiase, J., 2007, The Brunei slide: a giant submarine landslide on the North West Borneo Margin revealed by 3D seismic data: Marine Geology, v. 246, no. 1, p. 9-23.

Georgiopoulou, A., and Cartwright, J. A., 2013, A critical test of the concept of submarine equilibrium profile: Marine and Petroleum Geology, v. 41, p. 35-47.

Giachetti, T., Paris, R., Kelfoun, K., and Pérez-Torrado, F. J., 2011, Numerical modelling of the tsunami triggered by the Güìmar debris avalanche, Tenerife (Canary Islands): Comparison with field-based data: Marine Geology, v. 284, no. 1, p. 189-202.

Giba, M., Nicol, A., and Walsh, J., 2010, Evolution of faulting and volcanism in a back-arc basin and its implications for subduction processes: Tectonics, v. 29, no. 4.

Giles, M. K., Mass transport processes on the southwestern Newfoundland margin, eastern Canada: Mechanisms for deep water sediment transport, *in* Proceedings Masters Abstracts International2010, Volume 49.

Girdler, R., 1990, The Dead Sea transform fault system: Tectonophysics, v. 180, no. 1, p. 1-13.

Gong, C., Wang, Y., Hodgson, D. M., Zhu, W., Li, W., Xu, Q., and Li, D., 2014, Origin and anatomy of two different types of mass-transport complexes: A 3D seismic case study from the northern South China Sea margin: Marine and Petroleum Geology.

Gretener, P. E., 1979, Pore pressure: fundamentals, general ramifications and implications for structural geology (revised edition).

Hampton, M. A., Lee, H. J., and Locat, J., 1996, Submarine landslides: Reviews of geophysics, v. 34, no. 1, p. 33-59.

Hansen, R. J., and Kamp, P. J., 2002, Evolution of the Giant Foresets Formation, northern Taranaki Basin, New Zealand.

-, 2006a, An integrated biostratigraphy and seismic stratigraphy for the late Neogene continental margin succession in northern Taranaki Basin, New Zealand: New Zealand Journal of Geology and Geophysics, v. 49, no. 1, p. 39-56.

-, Sequence stratigraphy and architectural elements of the Giant Foresets Formation, northern Taranaki Basin, New Zealand, *in* Proceedings Proceedings of New Zealand Petroleum Conference2006b, p. 6-10.

Hart, B. S., 1999, Definition of subsurface stratigraphy, structure and rock properties from 3-D seismic data: Earth-Science Reviews, v. 47, no. 3, p. 189-218.

Hayward, B. W., 1984, Foraminiferal biostratigraphy of Wainui-1 offshore well, west Taranaki, New Zealand Geological Survey, Department of Scientific and Industrial Research.

Helland-Hansen, W., and Hampson, G., 2009, Trajectory analysis: concepts and applications: Basin Research, v. 21, no. 5, p. 454-483.

Hermanrud, C., Venstad, J. M., Cartwright, J., Rennan, L., Hermanrud, K., and Bolås, H. M. N., 2013, Consequences of Water Level Drops for Soft Sediment Deformation and Vertical Fluid Leakage: Mathematical Geosciences, v. 45, no. 1, p. 1-30.

Hjelstuen, B. O., Eldholm, O., and Faleide, J. I., 2007, Recurrent Pleistocene mega-failures on the SW Barents Sea margin: Earth and Planetary Science Letters, v. 258, no. 3, p. 605-618.

Holler, P., 1985, Fracture activity: A possible triggering mechanism for slope instabilities in the Eastern Atlantic?: Geo-marine letters, v. 5, no. 4, p. 211-216.

Holt, W., and Stern, T., 1994, Subduction, platform subsidence, and foreland thrust loading: The late Tertiary development of Taranaki Basin, New Zealand: Tectonics, v. 13, no. 5, p. 1068-1092.

Homza, T. X., 2004, A structural interpretation of the Fish Creek slide (Lower Cretaceous), northern Alaska: AAPG bulletin, v. 88, no. 3, p. 265-278.

Hühnerbach, V., and Masson, D., 2004, Landslides in the North Atlantic and its adjacent seas: an analysis of their morphology, setting and behaviour: Marine Geology, v. 213, no. 1, p. 343-362.

Hutchinson, J., 1986, A sliding-consolidation model for flow slides: Canadian Geotechnical Journal, v. 23, no. 2, p. 115-126.

Huvenne, V. A., Croker, P. F., and Henriet, J. P., 2002, A refreshing 3D view of an ancient sediment collapse and slope failure: Terra Nova, v. 14, no. 1, p. 33-40.

Imbert, P., Cretu, M., Oppeneau, T., Camy-Peyret, J., Morice, M., and Vittori, J., The Architecture of Large Mass-Transport Complexes–Long Runout Deposits vs. Deformed Substrate, *in* Proceedings 69th EAGE Conference & Exhibition2007.

Ingram, G., Chisholm, T., Grant, C., Hedlund, C., Stuart-Smith, P., and Teasdale, J., 2004, Deepwater North West Borneo: hydrocarbon accumulation in an active fold and thrust belt: Marine and Petroleum Geology, v. 21, no. 7, p. 879-887.

Ingram, G. M., and Urai, J. L., 1999, Top-seal leakage through faults and fractures: the role of mudrock properties: Geological Society, London, Special Publications, v. 158, no. 1, p. 125-135.

Iverson, R. M., 1997, The physics of debris flows: Reviews of geophysics, v. 35, no. 3, p. 245-296.

Jackson, C. A.-L., 2012, The initiation of submarine slope failure and the emplacement of mass transport complexes in salt-related minibasins: A three-dimensional seismic-reflection case study from the Santos Basin, offshore Brazil: Geological Society of America Bulletin, v. 124, no. 5-6, p. 746-761.

Jackson, C. A., 2011, Three-dimensional seismic analysis of megaclast deformation within a mass transport deposit; implications for debris flow kinematics: Geology, v. 39, no. 3, p. 203-206.

Jenner, K. A., Piper, D. J., Campbell, D. C., and Mosher, D. C., 2007, Lithofacies and origin of late Quaternary mass transport deposits in submarine canyons, central Scotian Slope, Canada: Sedimentology, v. 54, no. 1, p. 19-38.

Joanne, C., Lamarche, G., and Collot, J. Y., 2013, Dynamics of giant mass transport in deep submarine environments: the Matakaoa Debris Flow, New Zealand: Basin Research.

Kamp, P. J., Vonk, A. J., Bland, K. J., Hansen, R. J., Hendy, A. J., McIntyre, A. P., Ngatai, M., Cartwright, S. J., Hayton, S., and Nelson, C. S., 2004, Neogene stratigraphic architecture and tectonic evolution of Wanganui, King Country, and eastern Taranaki Basins, New Zealand: New Zealand Journal of Geology and Geophysics, v. 47, no. 4, p. 625-644.

Kearey, P., Brooks, M., and Hill, I., 2009, An introduction to geophysical exploration, John Wiley & Sons.

King, P. R., and Thrasher, G. P., 1996, Cretaceous Cenozoic geology and petroleum systems of the Taranaki Basin, New Zealand, Institute of Geological & Nuclear Sciences.

Kvalstad, T., Nadim, F., and arbitz, C., Deepwater geohazards: Geotechnical concerns and solutions, *in* Proceedings Offshore Technology Conference2001.

Kvalstad, T. J., Andresen, L., Forsberg, C. F., Berg, K., Bryn, P., and Wangen, M., 2005, The Storegga slide: evaluation of triggering sources and slide mechanics: Marine and Petroleum Geology, v. 22, no. 1, p. 245-256.

Laberg, J., and Vorren, T., 2000, The Trænadjupet Slide, offshore Norway—morphology, evacuation and triggering mechanisms: Marine Geology, v. 171, no. 1, p. 95-114.

Lapinski, T., 2003, 3-D stratigraphic and structural evolution of the Thunder Horse mini-basin: Mississippi Canyon, northern deep Gulf of Mexico: unpublished MS thesis, University of Colorado.

Lastras, G., Canals, M., Hughes-Clarke, J., Moreno, A., De Batist, M., Masson, D., and Cochonat, P., 2002, Seafloor imagery from the BIG'95 debris flow, western Mediterranean: Geology, v. 30, no. 10, p. 871-874.

Le Friant, A., Boudon, G., Deplus, C., and Villemant, B., 2003, Large-scale flank collapse events during the activity of Montagne Pelée, Martinique, Lesser Antilles: Journal of Geophysical Research: Solid Earth (1978–2012), v. 108, no. B1.

Le Pichon, X., Chamot-Rooke, N., Lallemant, S., Noomen, R., and Veis, G., 1995, Geodetic determination of the kinematics of central Greece with respect to Europe: Implications for eastern Mediterranean tectonics: Journal of Geophysical Research: Solid Earth (1978–2012), v. 100, no. B7, p. 12675-12690.

Lee, H.-Y., Park, K.-P., Koo, N.-H., Yoo, D.-G., Kang, D.-H., Kim, Y.-G., Hwang, K.-D., and Kim, J.-C., 2004, High-resolution shallow marine seismic surveys off Busan and Pohang, Korea, using a small-scale multichannel system: Journal of applied geophysics, v. 56, no. 1, p. 1-15.

Locat, A., Leroueil, S., Bernander, S., Demers, D., Jostad, H. P., and Ouehb, L., 2011, Progressive failures in eastern Canadian and Scandinavian sensitive clays: Canadian Geotechnical Journal, v. 48, no. 11, p. 1696-1712.

Locat, J., and Lee, H. J., 2002, Submarine landslides: advances and challenges: Canadian Geotechnical Journal, v. 39, no. 1, p. 193-212.

Loncke, L., Gaullier, V., Bellaiche, G., and Mascle, J., 2002, Recent depositional patterns of the Nile deep-sea fan from echo-character mapping: AAPG bulletin, v. 86, no. 7.

Loncke, L., Gaullier, V., Droz, L., Ducassou, E., Migeon, S., and Mascle, J., 2009, Multi-scale slope instabilities along the Nile deep-sea fan, Egyptian margin: A general overview: Marine and Petroleum Geology, v. 26, no. 5, p. 633-646.

Loncke, L., Gaullier, V., Mascle, J., Vendeville, B., and Camera, L., 2006, The Nile deep-sea fan: an example of interacting sedimentation, salt tectonics, and inherited subsalt paleotopographic features: Marine and Petroleum Geology, v. 23, no. 3, p. 297-315.

Loncke, L., Mascle, J., and Parties, F. S., 2004, Mud volcanoes, gas chimneys, pockmarks and mounds in the Nile deep-sea fan (Eastern Mediterranean): geophysical evidences: Marine and Petroleum Geology, v. 21, no. 6, p. 669-689.

Longchamp, C., Charrière, M., and Jaboyedoff, M., Analogue modelling of rock avalanches and structural analysis of the deposits, *in* Proceedings EGU General Assembly Conference Abstracts2012, Volume 14, p. 9320.

Loseth, H., Wensaas, L., and Gading, M., 2011, Deformation structures in organic-rich shales: AAPG bulletin, v. 95, no. 5, p. 729-747.

Løvholt, F., Harbitz, C. B., and Haugen, K. B., 2005, A parametric study of tsunamis generated by submarine slides in the Ormen Lange/Storegga area off western Norway: Marine and Petroleum Geology, v. 22, no. 1, p. 219-231.

Lucente, C. C., and Pini, G. A., 2003, Anatomy and emplacement mechanism of a large submarine slide within a Miocene foredeep in the northern Apennines, Italy: A field perspective: American Journal of Science, v. 303, no. 7, p. 565-602.

Major, J. J., 1997, Depositional processes in large-scale debris-flow experiments: The Journal of Geology, v. 105, no. 3, p. 345-366.

Maltman, A., 1994, geological deformation of sediments, Chapman & Hall.

Martin, R. G., and Bouma, A. H., 1982, Active diapirism and slope steepening, northern Gulf of Mexico continental slope: Marine Georesources & Geotechnology, v. 5, no. 1, p. 63-91.

Martinsen, O. J., and Bakken, B., 1990, Extensional and compressional zones in slumps and slides in the Namurian of County Clare, Ireland: Journal of the Geological Society, v. 147, no. 1, p. 153-164.

Martinsen, O. J., Lien, T., Walker, R. G., and Collinson, J. D., 2003, Facies and sequential organisation of a mudstone-dominated slope and basin floor succession: the Gull Island Formation, Shannon Basin, Western Ireland: Marine and Petroleum Geology, v. 20, no. 6, p. 789-807.

Mascle, J., Benkhelil, J., Bellaiche, G., Zitter, T., Woodside, J., and Loncke, L., 2000, Marine geologic evidence for a Levantine-Sinai plate, a new piece of the Mediterranean puzzle: Geology, v. 28, no. 9, p. 779-782.

Mascle, J., Sardou, O., Loncke, L., Migeon, S., Caméra, L., and Gaullier, V., 2006, Morphostructure of the Egyptian continental margin: insights from swath bathymetry surveys: Marine Geophysical Researches, v. 27, no. 1, p. 49-59.

Masson, D., Harbitz, C., Wynn, R., Pedersen, G., and Løvholt, F., 2006, Submarine landslides: processes, triggers and hazard prediction: Philosophical Transactions of the Royal Society A: Mathematical, Physical and Engineering Sciences, v. 364, no. 1845, p. 2009-2039.

Masson, D., Huggett, Q., and Brunsden, D., 1993, The surface texture of the Saharan Debris Flow deposit and some speculations on submarine debris flow processes: Sedimentology, v. 40, no. 3, p. 583-598.

Masson, D., Watts, A., Gee, M., Urgeles, R., Mitchell, N., Le Bas, T., and Canals, M., 2002, Slope failures on the flanks of the western Canary Islands: Earth-Science Reviews, v. 57, no. 1, p. 1-35.

Masson, D., Wynn, R., and Talling, P., 2010, Large landslides on passive continental margins: processes, hypotheses and outstanding questions, Submarine mass movements and their consequences, Springer, p. 153-165.

McAdoo, B., Pratson, L., and Orange, D., 2000, Submarine landslide geomorphology, US continental slope: Marine Geology, v. 169, no. 1, p. 103-136.

McClusky, S., Balassanian, S., Barka, A., Demir, C., Ergintav, S., Georgiev, I., Gurkan, O., Hamburger, M., Hurst, K., and Kahle, H., 2000, Global Positioning System constraints on plate kinematics and dynamics in the eastern Mediterranean and Caucasus: Journal of Geophysical Research: Solid Earth (1978–2012), v. 105, no. B3, p. 5695-5719.

McGilvery, T., and Cook, D. L., The influence of local gradients on accommodation space and linked depositional elements across a stepped slope profile, offshore Brunei, *in* Proceedings Gulf

Coast Section SEPM Foundation 23rd Annual Bob F. Perkins Research Conference Proceeding2003, SEPM, p. 23-55.

McKenzie, D., 1972, Active tectonics of the Mediterranean region: Geophysical Journal of the Royal Astronomical Society, v. 30, no. 2, p. 109-185.

Meckel III, L. D., 2011, Reservoir characteristics and Classification of Sand-Prone Submarine Mass Transport deposits. In:Shipp, R. C., Weimer P., Posamentier, H. W. (eds) Mass-transport deposits in deepwater settings. SEPM (Society for Sedimentary Geology) Special Publications, vol. 96, pp. 423–452.

Micallef, A., Masson, D. G., Berndt, C., and Stow, D. A., 2007, Morphology and mechanics of submarine spreading: A case study from the Storegga Slide: Journal of Geophysical Research: Earth Surface (2003–2012), v. 112, no. F3.

Middleton, G., and Hampton, M., 1973, Subaqueous sediment transport and deposition by sediment gravity flows, Stanley DJ, Swift DJP, Marine Sediment Transport and Environmental Management, 1976, 197-218, Wiley, New York.

Minisini, D., Trincardi, F., Asioli, A., Canu, M., and Foglini, F., 2007, Morphologic variability of exposed mass-transport deposits on the eastern slope of Gela Basin (Sicily channel): Basin Research, v. 19, no. 2, p. 217-240.

Mitchum Jr, R., Vail, P., and Sangree, J., 1977, Seismic stratigraphy and global changes of sea level: Part 6. Stratigraphic interpretation of seismic reflection patterns in depositional sequences: Section 2. Application of seismic reflection configuration to stratigraphic interpretation.

Mohrig, D., Ellis, C., Parker, G., Whipple, K. X., and Hondzo, M., 1998, Hydroplaning of subaqueous debris flows: Geological Society of America Bulletin, v. 110, no. 3, p. 387-394.

Morita, S., Nakajima, T., and Hanamura, Y., 2011, Submarine slump sediments and related dewatering structures: observations of 3D seismic data obtained for the continental slope off Shimokita Peninsula, NE Japan: J Geol Soc Japan, v. 117, p. 95-98.

Moriwaki, H., Inokuchi, T., Hattanji, T., Sassa, K., Ochiai, H., and Wang, G., 2004, Failure processes in a full-scale landslide experiment using a rainfall simulator: Landslides, v. 1, no. 4, p. 277-288.

Moscardelli, L., and Wood, L., 2008, New classification system for mass transport complexes in offshore Trinidad: Basin Research, v. 20, no. 1, p. 73-98.

Moscardelli, L., Wood, L., and Mann, P., 2006, Mass-transport complexes and associated processes in the offshore area of Trinidad and Venezuela: AAPG bulletin, v. 90, no. 7, p. 1059-1088.

Mulder, T., and Alexander, J., 2001, The physical character of subaqueous sedimentary density flows and their deposits: Sedimentology, v. 48, no. 2, p. 269-299.

Mulder, T., and Cochonat, P., 1996, Classification of offshore mass movements: Journal of Sedimentary Research, v. 66, no. 1, p. 43-57.

Mutti, E., 1992, Turbidite sandstones, Agip, Istituto di geologia, Università di Parma.

Nardin, T. R., 1979, A Review of Mass Movement Processes Sediment and Acoustic Characteristics, and Contrasts in Slope and Base-of-Slope Systems Versus Canyon-Fan-Basin Floor Systems.

Nemec, W., 1990, Aspects of sediment movement on steep delta slopes: Coarse-grained deltas, p. 29-73.

Newton, C., Shipp, R., Mosher, D., and Wach, G., Importance of mass transport complexes in the Quaternary development of the Nile Fan, Egypt, *in* Proceedings Offshore Technology Conference2004.

O'leary, D., 1993, Submarine mass movement, a formative process of passive continental margins: the Munson-Nygren landslide complex and the southeast New England landslide complex: Submarine Landslides: Selected Studies in the US Exclusive Economic Zone, v. 2002, p. 23-39.

Obermeier, S. F., 1996, Use of liquefaction-induced features for paleoseismic analysis—an overview of how seismic liquefaction features can be distinguished from other features and how their regional distribution and properties of source sediment can be used to infer the location and strength of Holocene paleo-earthquakes: Engineering Geology, v. 44, no. 1, p. 1-76.

Ogata, K., 2010, Mass transport complexes in structurally-controlled basins: the Epiligurian Specchio Unit (Northern Apennines, Italy): Unpublished PhD thesis, University of Parma, v. 476.

Ogata, K., Mutti, E., Pini, G. A., and Tinterri, R., 2012, Mass transport-related stratal disruption within sedimentary mélanges: Examples from the northern Apennines (Italy) and south-central Pyrenees (Spain): Tectonophysics, v. 568, p. 185-199.

Ogiesoba, O., and Hammes, U., 2012, Seismic interpretation of mass-transport deposits within the upper Oligocene Frio Formation, south Texas Gulf Coast: AAPG bulletin, v. 96, no. 5, p. 845-868.

Petley, D. N., Higuchi, T., Petley, D. J., Bulmer, M. H., and Carey, J., 2005, Development of progressive landslide failure in cohesive materials: Geology, v. 33, no. 3, p. 201-204.

Pickering, K. T., Hiscott, R. N., and Kenyon, N. H., 1995, Atlas of Deep Water Environments: Architectural Style in Turbidite Systems, Chapman & Hall.

Pini, G. A., Ogata, K., Camerlenghi, A., Festa, A., Lucente, C. C., and Codegone, G., 2012, Sedimentary mélanges and fossil mass-transport complexes: a key for better understanding submarine mass movements?, Submarine Mass Movements and Their Consequences, Springer, p. 585-594.

Piper, D. J., Cochonat, P., and Morrison, M. L., 1999, The sequence of events around the epicentre of the 1929 Grand Banks earthquake: initiation of debris flows and turbidity current inferred from sidescan sonar: Sedimentology, v. 46, no. 1, p. 79-97.

Piper, D. J., Shor, A. N., and Clarke, J. E. H., 1988, The 1929 "Grand Banks" earthquake, slump, and turbidity current: Geological Society of America Special Papers, v. 229, p. 77-92.

Popenoe, P., Schmuck, E., and Dillon, W., 1993, The Cape Fear landslide: slope failure associated with salt diapirism and gas hydrate decomposition: Submarine landslides: Selected studies in the US Exclusive Economic Zone: US Geological Survey Bulletin, v. 2002, p. 40-53.

Posamentier, H., Stratigraphy and geomorphology of deep-water mass transport complexes based on 3D seismic data, *in* Proceedings Offshore Technology Conference2004.

Posamentier, H., 2006, Deep-water turbidites and submarine fans: Facies models revisited, p. 397-520.

Posamentier, H., and Martinsen, O., 2011, The character and genesis of submarine mass-transport deposits: insight from outcrop and 3D seismic data: Mass-Transport Deposits in Deepwater Settings, p. 7-38.

Posamentier, H., and Walker, R., 2006, SEPM SP84–Facies Models Revisited, SEPM.

Posamentier, H. W., Davies, R. J., Cartwright, J. A., and Wood, L., 2007, Seismic geomorphology-an overview: SPECIAL PUBLICATION-GEOLOGICAL SOCIETY OF LONDON, v. 277, p. 1.

Posamentier, H. W., and Kolla, V., 2003, Seismic geomorphology and stratigraphy of depositional elements in deep-water settings: Journal of Sedimentary Research, v. 73, no. 3, p. 367-388.

Praeg, D., Gas hydrate stability in the Mediterranean Sea since the last glacial maximum: results from the HYDRAMED project, *in* Proceedings Geophysical Research Abstracts2006, Volume 8, p. 05917.

Prather, B. E., Booth, J. R., Steffens, G. S., and Craig, P. A., 1998, Classification, lithologic calibration, and stratigraphic succession of seismic facies of intraslope basins, deep-water Gulf of Mexico: AAPG bulletin, v. 82, p. 701-728.

Pratson, L. F., and Coakley, B. J., 1996, A model for the headward erosion of submarine canyons induced by downslope-eroding sediment flows: Geological Society of America Bulletin, v. 108, no. 2, p. 225-234.

Prior, D. B., Bornhold, B. D., and Johns, M., 1984, Depositional characteristics of a submarine debris flow: The Journal of Geology, p. 707-727.

Prior, D. B., Doyle, E. H., and Neurauter, T., 1986, The Currituck Slide, mid-Atlantic continental slope—revisited: Marine Geology, v. 73, no. 1, p. 25-45.

Reynolds, O., 1883, An experimental investigation of the circumstances which determine whether the motion of water shall be direct or sinuous, and of the law of resistance in parallel channels: Proceedings of the royal society of London, v. 35, no. 224-226, p. 84-99.

Richardson, S. E., Davies, R. J., Allen, M. B., and Grant, S. F., 2011, Structure and evolution of mass transport deposits in the South Caspian Basin, Azerbaijan: Basin Research, v. 23, no. 6, p. 702-719.

Ross, D. A., and Uchupi, E., 1977, Structure and sedimentary history of southeastern Mediterranean Sea-Nile Cone area: AAPG Bulletin, v. 61, no. 6, p. 872-902.

Rouillard, P., du Fornel, E., Migeon, S., Dauphin, L., and Mascle, J., Shelf-to-basin floor seismic expression of the Rosetta system (Western Nile Delta, Egypt): a modern analogue of deep-water reservoirs, *in* Proceedings North Africa Technical Conference and Exhibition2010.

Salem, R., 1976, Evolution of Eocene-Miocene sedimentation patterns in parts of northern Egypt: AAPG Bulletin, v. 60, no. 1, p. 34-64.

Sawyer, D. E., Flemings, P. B., Dugan, B., and Germaine, J. T., 2009, Retrogressive failures recorded in mass transport deposits in the Ursa Basin, Northern Gulf of Mexico: Journal of Geophysical Research: Solid Earth (1978–2012), v. 114, no. B10.

Schnellmann, M., Anselmetti, F. S., Giardini, D., and McKENZIE, J. A., 2005, Mass movement-induced fold-and-thrust belt structures in unconsolidated sediments in Lake Lucerne (Switzerland): Sedimentology, v. 52, no. 2, p. 271-289.

Schultz-Ela, D., 2001, Excursus on gravity gliding and gravity spreading: Journal of Structural Geology, v. 23, no. 5, p. 725-731.

Schwab, W., Lee, H., Kayen, R., Quinterno, P., and Tate, G., 1988, Erosion and slope instability on Horizon Guyot, Mid-Pacific mountains: Geo-marine letters, v. 8, no. 1, p. 1-10.

Seed, H. B., and Idriss, I., 1982, Ground motions and soil liquefaction during earthquakes, Earthquake Engineering Research Institute Oakland, CA.

Seed, H. B., and Rahman, M., 1978, Wave-induced pore pressure in relation to ocean floor stability of cohesionless soils: Marine Georesources & Geotechnology, v. 3, no. 2, p. 123-150.

Shanmugam, G., 2000, 50 years of the turbidite paradigm (1950s—1990s): deep-water processes and facies models—a critical perspective: Marine and Petroleum Geology, v. 17, no. 2, p. 285-342.

-, 2006, Deep-Water Processes and Facies Models: Implications for Sandstone Petroleum Reservoirs: Implications for Sandstone Petroleum Reservoirs, Elsevier.

Shanmugam, G., Lehtonen, L. R., Straume, T., Syvertsen, S. E., Hodgkinson, R. J., and Skibeli, M., 1994, Slump and debris-flow dominated upper slope facies in the Cretaceous of the Norwegian and northern North seas (61-67 N): implications for sand distribution: AAPG bulletin, v. 78, no. 6, p. 910-937.

Sheriff, R. E., and Geldart, L., 1995, Exploration seismology: Cambridge: Cambridge University Pressp.

Shipp, R., Nott, J., and Newlin, J., Physical characteristics and impact of mass transport complexes on deepwater jetted conductors and suction anchor piles, *in* Proceedings Offshore Technology Conference2004.

Shipp, R. C., Weimer, P., and Posamentier, H. W., 2011, Mass-transport deposits in deepwater settings, SEPM Soc for Sed Geology.

Soenandar, H., Seismic stratigraphy of the Giant Foresets Formation, offshore north Taranaki–Western Platform, *in* Proceedings 1991 New Zealand Petroleum Conference Proceedings, Ministry of Commerce1992, p. 207-233.

Solheim, A., Berg, K., Forsberg, C., and Bryn, P., 2005a, The Storegga Slide complex: repetitive large scale sliding with similar cause and development: Marine and Petroleum Geology, v. 22, no. 1, p. 97-107.

Solheim, A., Bryn, P., Sejrup, H., Mienert, J., and Berg, K., 2005b, Ormen Lange—an integrated study for the safe development of a deep-water gas field within the Storegga Slide Complex, NE Atlantic continental margin; executive summary: Marine and Petroleum Geology, v. 22, no. 1, p. 1-9.

Spörli, K., and Rowland, J., 2007, Superposed deformation in turbidites and syn-sedimentary slides of the tectonically active Miocene Waitemata Basin, northern New Zealand: Basin Research, v. 19, no. 2, p. 199-216.

Stewart, S., 2011, Vertical exaggeration of reflection seismic data in geoscience publications 2006–2010: Marine and Petroleum Geology, v. 28, no. 5, p. 959-965.

Stock, G. M., Martel, S. J., Collins, B. D., and Harp, E. L., 2012, Progressive failure of sheeted rock slopes: the 2009–2010 Rhombus Wall rock falls in Yosemite Valley, California, USA: Earth Surface Processes and Landforms, v. 37, no. 5, p. 546-561.

Strachan, L., and Alsop, G., 2006, Slump folds as estimators of palaeoslope: a case study from the Fisherstreet Slump of County Clare, Ireland: Basin Research, v. 18, no. 4, p. 451-470.

Strachan, L. J., 2002, Slump-initiated and controlled syndepositional sandstone remobilization: an example from the Namurian of County Clare, Ireland: Sedimentology, v. 49, no. 1, p. 25-41.

Strozyk, F., Huhn, K., Strasser, M., Krastel, S., Kock, I., and Kopf, A., 2009, New evidence for massive gravitational mass-transport deposits in the southern Cretan Sea, eastern Mediterranean: Marine Geology, v. 263, no. 1, p. 97-107.

Sultan, N., Cochonat, P., Canals, M., Cattaneo, A., Dennielou, B., Haflidason, H., Laberg, J., Long, D., Mienert, J., and Trincardi, F., 2004a, Triggering mechanisms of slope instability processes and sediment failures on continental margins: a geotechnical approach: Marine Geology, v. 213, no. 1, p. 291-321.

Sultan, N., Cochonat, P., Foucher, J.-P., and Mienert, J., 2004b, Effect of gas hydrates melting on seafloor slope instability: Marine Geology, v. 213, no. 1, p. 379-401.

Sutherland, R., King, P., and Wood, R., Tectonic evolution of Cretaceous rift basins in south-eastern Australia and New Zealand: implications for exploration risk assessment, *in* Proceedings Proceedings of the PESA Eastern Australasian Basins Symposium2001, Volume 25, p. 28.

Talling, P., Wynn, R., Masson, D., Frenz, M., Cronin, B., Schiebel, R., Akhmetzhanov, A., Dallmeier-Tiessen, S., Benetti, S., and Weaver, P., 2007, Onset of submarine debris flow deposition far from original giant landslide: Nature, v. 450, no. 7169, p. 541-544.

Terzaghi, K., 1962, Stability of steep slopes on hard unweathered rock: Geotechnique, v. 12, no. 4, p. 251-270.

Tinti, S., Pagnoni, G., and Zaniboni, F., 2006, The landslides and tsunamis of the 30th of December 2002 in Stromboli analysed through numerical simulations: Bulletin of Volcanology, v. 68, no. 5, p. 462-479.

Trincardi, F., and Argnani, A., 1990, Gela submarine slide: A major basin-wide event in the Plio-Quaternary foredeep of Sicily: Geo-marine letters, v. 10, no. 1, p. 13-21.

Tripsanas, E. K., Bryant, W. R., and Phaneuf, B. A., 2004, Slope-instability processes caused by salt movements in a complex deep-water environment, Bryant Canyon area, northwest Gulf of Mexico: AAPG bulletin, v. 88, no. 6, p. 801-823.

Tripsanas, E. K., Piper, D. J., Jenner, K. A., and Bryant, W. R., 2008, Submarine mass-transport facies: new perspectives on flow processes from cores on the eastern North American margin: Sedimentology, v. 55, no. 1, p. 97-136.

Turnbull, I. M., and Uruski, C., 1993, Cretaceous and Cenozoic sedimentary basins of Western Southland, South Island, New Zealand: Monogr./Inst. of geol. and nuclear sciences.

Uruski, C., Exploring deepwater Taranaki Basin, *in* Proceedings 2008 New Zealand Petroleum Conference Proceedings2008.

Uruski, C., Stagpoole, V., Isaac, M., King, P., and Maslen, G., 2002, Seismic Interpretation Report-Astrolabe Survey, Taranaki Basin, New Zealand: Institute of Geological & Nuclear Sciences confidential client report, v. 70.

Uruski, C. I., 2010, New Zealand's deepwater frontier: Marine and Petroleum Geology, v. 27, no. 9, p. 2005-2026.

Vanneste, M., Mienert, J., and Bünz, S., 2006, The Hinlopen Slide: A giant, submarine slope failure on the northern Svalbard margin, Arctic Ocean: Earth and Planetary Science Letters, v. 245, no. 1, p. 373-388.

Varnes, D. J., 1978, Slope movement types and processes: Transportation Research Board Special Report, no. 176.

Ward, S. N., and Day, S., 2001, Cumbre Vieja volcano—potential collapse and tsunami at La Palma, Canary Islands: Geophysical Research Letters, v. 28, no. 17, p. 3397-3400.

Watt, S., Talling, P., Vardy, M., Heller, V., Hühnerbach, V., Urlaub, M., Sarkar, S., Masson, D., Henstock, T., and Minshull, T., 2012a, Combinations of volcanic-flank and seafloor-sediment failure offshore Montserrat, and their implications for tsunami generation: Earth and Planetary Science Letters, v. 319, p. 228-240.

Watt, S., Talling, P., Vardy, M., Masson, D., Henstock, T., Hühnerbach, V., Minshull, T., Urlaub, M., Lebas, E., and Le Friant, A., 2012b, Widespread and progressive seafloor-sediment failure following volcanic debris avalanche emplacement: landslide dynamics and timing offshore Montserrat, Lesser Antilles: Marine Geology, v. 323, p. 69-94.

Wehr, F., Fairchild, L., Hudec, M., Shafto, R., Shea, W., and White, J., 2000, AAPG Memoir 73, Chapter 10: Fault Seal: Contrasts Between the Exploration and Production Problem.

Weimer, P., 1989, Sequence stratigraphy of the Mississippi Fan (Plio-Pleistocene), Gulf of Mexico: Geo-Marine Letters, v. 9, no. 4, p. 185-272.

-, 1990, Sequence Stratigraphy, Facies Geometries, and Depositional History of the Mississippi Fan, Gulf of Mexico (1): AAPG bulletin, v. 74, no. 4, p. 425-453.

Weimer, P., and Shipp, C., Mass transport complex: musing on past uses and suggestions for future directions, *in* Proceedings Offshore Technology Conference2004.

Weimer, P., and Slatt, R. M., 2004, 7. Deepwater Reservoir Elements: Mass-transport Complexes and Slides, Petroleum Systems of Deepwater Settings, Society of Exploration Geophysicists and European Association of Geoscientists and Engineers, p. 7-1-7-32.

Welbon, A., Brockbank, P., Brunsden, D., and Olsen, T., 2007, Characterizing and producing from reservoirs in landslides: challenges and opportunities: Geological Society, London, Special Publications, v. 292, no. 1, p. 49-74.

Westaway, R., 1994, Present-day kinematics of the Middle East and eastern Mediterranean: Journal of Geophysical Research: Solid Earth (1978–2012), v. 99, no. B6, p. 12071-12090.

Wetzel, A., 1990, Interrelationships between porosity and other geotechnical properties of slowly deposited, fine-grained marine surface sediments: Marine Geology, v. 92, no. 1, p. 105-113.

Wilson, C. K., Long, D., and Bulat, J., 2004, The morphology, setting and processes of the Afen Slide: Marine geology, v. 213, no. 1, p. 149-167.

WU, S. G., QIN, Z. L., WANG, D. W., PENG, X. C., WANG, Z. J., and YAO, G. S., 2011, Analysis on Seismic Characteristics and Triggering Mechanisms of Mass Transport Deposits on the Northern Slope of the South China Sea: Chinese Journal of Geophysics, v. 54, no. 6, p. 1056-1068.

Yang, J., Davies, R. J., and Huuse, M., 2013, Gas migration below gas hydrates controlled by mass transport complexes, offshore Mauritania: Marine and Petroleum Geology, v. 48, p. 366-378.

Yilmaz, Ö., and Doherty, S. M., 1987, Seismic data processing, Society of Exploration Geophysicists Tulsa.

Appendices

Atlas of Mass Transport Deposit Outcrops

Tuviere Omeru, Joseph A. Cartwright

Table of Contents

Chapter 1: An Introduction to the Atlas of Mass Transport Deposits Outcrop

Executive Summary

The Atlas of Mass Transport Deposits (MTD) Outcrops is a collection of qualitative descriptions of MTD outcrops from around the world (field areas in 5 countries) (Figure 1.1). These outcrops also span most of the Phanerozoic (Table 1.1).

The Atlas is intended to give a good background 'overview' of each of the major field areas where the best described MTDs are found. We summarise the geological setting of each example as well as the detailed description of selected outcrops from these localities. There are many publications on individual outcrop of submarine mass transport deposits, but these have not been synthesised in this atlas fomat before.

The goal of this atlas is to build on this previous work by fully describing the various architectures seen in these outcrop deposits with regards to their hydrocarbon seal implications. This Atlas provides the first collection of qualitative architectural description on outcrops of MTDs that may be used for forward modelling to predict reservoir seal risk.
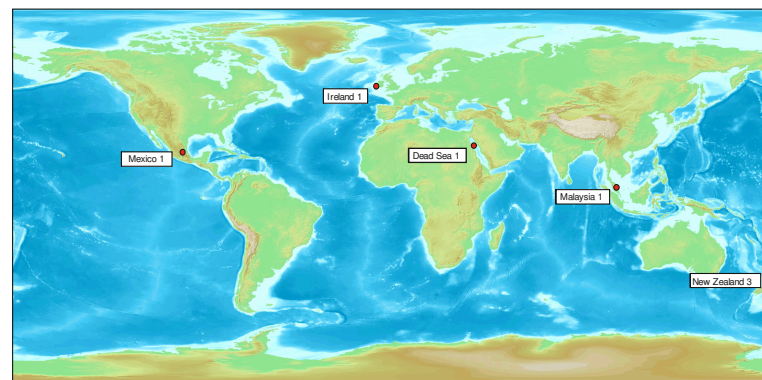
Figure 1.1. Map showing the location of outcrops of mass transport deposits described in this Atlas. Although, New Zealand has the most outcrop summaries (3 chapters), there are a variety of geographic locations (5 countries and five continents) and age ranges.

Table 1.1. Characteristics of the main outcrops of mass transport deposits in this atlas.

Outcrop (location)	Formation	Age	References
Waitemata Basin, northern New Zealand.	East Coast Bay Formation	Early Miocene	Sporli and Rowland (2008)
Little Manly Beach, Waitemata Basin, New Zealand.	East Coast Bay Formation	Early Miocene	Strachan (2008)
North Taranaki Basin, New Zealand.	Mount Messenger and Urenui Formations	Late Miocene	Greg et al. (2006) King et al. (2011)
Central Peninsular Malaysia	Semantan Formation,	Mid - Late Triassic	Madon (2010)
Dead Sea Basin	Lisan Formation	Late Pleistocene	Alsop and Marco (2011 2012, 2013)
Tampico-Misanta Basin, Northeastern Mexico	Chicontepec Formation	Late Paleocene-Eocene	Cossey (2011)
Shannon Basin, western Ireland	Gull Island Formation	Late Carboniferous (Namurian)	Martinsen and Lien (2007) Lien et al. (2007)

Rational:

Mass transport deposits (MTDs) are common in deep-marine sequences, often in close association with turbidity current deposits (turbidites). These deposits usually are thought to be largely mud rich deposits, and are widely developed as a primary component of heterogeneous seal sequences in many slope basins (Fig. 2.1). Examples of where MTDs occur in the sealing sequences for major hydrocarbon accumulations can be found in Alaska's North Slope (Homza, 2003), northern deep Gulf of Mexico (Lapinski, 2003), deepwater northwest Borneo (Algar et. al. 2011), as well as in Case Study A and B of CAPROCKS. The authors of these studies noted above have suggested that the presence MTDs in seals can severely impact seal integrity and facilitate leakage. In the same vein, some mass transport deposits exhibit properties with some degree of reservoir quality (e.g., Jennette et al., 2000; Algar et al., 2011; Meckel et al., 2011), indicating that not all mass flows are composed of monotonous mud! The message here is simple: the final character of the MTD (seal versus reservoir) depends on the starting material: mud in mud out, but mixed facies in, could lead to poor seal and/or reservoir out!
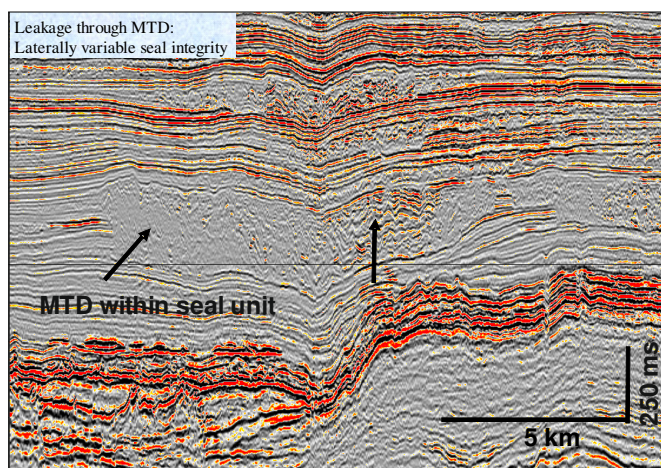
Figure 1.1. A classical example where an MTD leaks as well as seal from the Levant Case study, Eastern Mediterranean.

In spite of the common occurrence and distinctive geometry of mass transport deposits, their internal structures are not well known. Consequently there is a need for better understanding of processes and the internal structure of MTDs for deepwater petroleum exploration and more importantly understanding the risk they pose to seal integrity.

Power of 3D interpretation

Over the last decade, 3D seismic data acquired in deep-water settings for hydrocarbon exploration purposes, has proven to be a powerful tool in the identification, description of the external and internal complexities of MTDs (Cartwright and Huuse, 2005; Frey Martinez et al. 2005; Moscardelli et al., 2006; Bull et al., 2009). 3D seismic interpretation has revolutionised our understanding of MTDs and their gross architecture and basin scale distribution. However, seismic studies provide only partial information about the internal architecture of MTDs, mainly because of the resolution limit of the geophysical method, the ambiguity of interpretation (e.g. Gardner et al., 1999; Lee et al., 2004) and the common presence of transparent zones (Coleman and Garrison, 1977). Sophisticated attribute based methods (e.g. Frey Martinez et al. 2006) have compensated to some extent those resolution limitations, but the detailed structural and lithological picture obtained from even high resolution seismic studies is still limited and that is where outcrop analogues play a vital role.

Critically, outcrops provide detailed information on the lithology at the mm-scale, the internal architecture (connectivity, internal deformation styles and fabrics and impacts of deformation on physical properties, external geometries (nature of detachments at base, nature of the top surface of an MTD, rheology (evidence of brittle/ductile/liquefied behaviours) and possible fluid flow pathways of MTDs links to pockmarks, sand volcanoes at top of MTDs). Outcrop data thus allow important considerations on post-depositional processes and connectivity. Therefore, outcrop study is thus a fundamental tool for understanding the impact of MTDs on reservoir seal integrity in the context of hydrocarbon leakage.

However, some grey areas still exist. For example, detailed information about in-situ properties for MTDs cannot be obtained from outcrop observations. Also due to the overall scarcity of extensive well preserved outcrop exposures of MTDs (Ineson, 1985; Macdonald et al., 1993), it is quite difficult to place an outcrop in a specific spatial context- where would the particular outcrop 'sample' fit into the broader domainal context within an MTD? (these domains are typically defined as (1)updip extensional , (2) downdip contractional and (3) translational domains. (e.g. Farrel, 1984; Gawthorpe and Clemmey, 1985; Pickering, 1987; Martinsen, 1989; Tarquin Teale and Young,1987; Martinsen and Bakken, 1990; Leigh and Hartley, 1992).

The evident limitations of outcrop studies in general is the overall scarcity (or poorly recognised) of extensive, widely distributed and clearly correlatable exposures of well-preserved large-scale (i.e. equivalent in scale to those commonly seen on seismic data for many slope systems) mass transport deposits (Ineson, 1985; Macdonald et al., 1993).

Consequently, it is ideal to combine outcrop studies with seismic studies to make informed decisions about the internal structures and of MTDs and their potential seal risk.

Objectives:

The aim of this atlas is to document a range of outcrop examples of mass transport deposits detailing the internal architecture of these deposits in order to assess seal quality (i.e. connectivity of MTD strata, distribution of lithotypes, deformational style, and rheology). This approach is used to assess the leakage potential of mass transport deposits.

Mass Transport Depost (MTDs): an overview

Mass transport deposits (MTDs) includes all kinds of gravity induced or down-slope deposits (slides, slumps and debris flow), with the exception of turbidites. The resulting deposit occur at various scales: ranging from a few meters in thickness and a few hundred square meters in area, to hundreds of meters in thickness and thousands of square kilometers in area.

There are three principal domains recognised in a landslide: a) an up-dip extensional domain where faulting, crown scarps and local seafloor collapse are recorded; b) a translational domain, in which failed sediment is transported downslope above a glide plane; c) a down-dip contractional domain, in which failed sediment accumulates and are usually associated with folds and thrust structures. Figure 1.2 shows the main domains of an MTD.
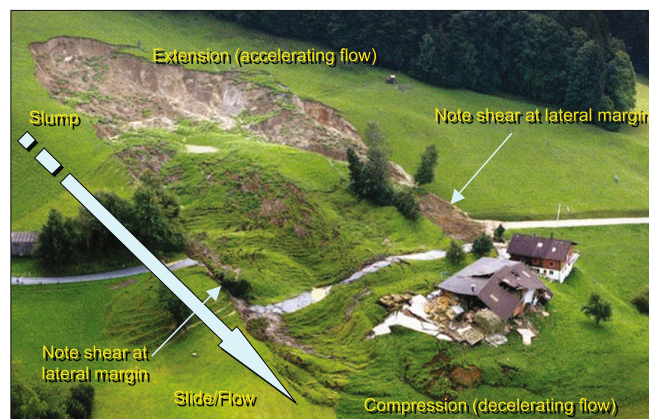
Figure 1.2. Modern subaerial mass transport feature in the Austrian Alps. Note the extensional normal faults in the upslope area and the compressional thrust faults in the downslope area. Extension proximally implies accelerating flow, and compression distally implies decelerating flow at the time the event occurred. Note also shearing that characterizes lateral margins of the MTD. Note farm house for scale (from Posamentier and Martinsen 2011).

The failure and downslope movement of MTDs depends on whether shear strength or shearing resistance of sediments is exceeded by the applied shear stress. However the type and the magnitude of mass transport is also influenced by other factors including the type of sediment, sedimentation rate, slope angle, heterogeneity of sediments (whether bedded or homogeneous), permeability, and to what extent pore waters in sediments are drained (Posamentier and Martisen, 2011). Consequently, the MTD type can vary temporally and spatially.

Slides involve mass movement of sediments with little or no internal deformation; the slide overlies a distinct shear surface (sensu Stow, 1986; Martinsen, 1994) Slumps are characterized by significant internal distortion of bedding, above a basal shear surface (e.g., Stow, 1986; Martinsen,1989; Martinsen and Bakken, 1990). Nevertheless, primary bedding should be recognizable. Debris flows are cohesive to non-cohesive laminar flows that transport unsorted and disaggregated debris that can travel across extremely low-gradient slopes. There is a continuous transition between slides, slumps, and plastic flows, and many mass transport deposits may show characteristics of all three modes of transport (e.g., Bakken, 1987; see also below). Therefore, careful analysis is required to understand the temporal and spatial behaviour of the processes producing the mass-transport deposit and to categorize them satisfactorily.

References

Alsop, G.I., Marco, S. 2011. Soft-sediment deformation within seismogenic slumps of the Dead Sea Basin. Journal of Structural Geology 33, 433-457.

Alsop, G.I., Marco, S. 2012. A large-scale radial pattern of seismogenic slumping towards the Dead Sea Basin, Journal of the Geological Society v.169; p99-110..

Alsop, G.I, Marco, S., 2013. Seismogenic slump folds formed by gravity-driven tectonics down a negligible subaqueous slope, Tectonophysics doi: 10.1016/j.tecto.2013.04.004

Algar S., . Milton C., Upshall H., Roestenburg J., Crevello P., 2011. Mass Transport Deposits of the Deepwater Northwestern Borneo Margin- Characterization from Seismic Reflection, Borehole and Core Data with Implications for Hydrocarbon Exploration and Exploitation. Mass Transport Deposits in Deepwater Settings. Society for Sedimentary Geology (SEPM) Special Publication No. 96, p. 351–366.

Bakken, B., 1987, Sedimentology and syndepositional deformation of the Ross Slide, Western Irish Namurian Basin, Ireland: Unpublished Cand. Scient. Thesis, Geological Institute, Dep. A, University of Bergen, Bergen, Norway, 182 p.

Bull, S., Cartwright, J. Huuse, M., 2009. A review of kinematic indicators from mass-transport complexes using 3D seismic data. Marine and Petroleum Geology, 26, 1132-1151.

Cartwright, J.A. and Huuse, M. 2005. 3D Seismic: The geological 'Hubble.' Basin Research. 17, 1-20

Coleman, J.M., Garrison, L.E., 1977. Geological aspects of marine slope stability, northwesternGulf of Mexico. Marine Geotechnology 2, 9–44

Cossey Stephen P.J., 2011, Mass transport deposits in the Upper Paleocene Chicontepec Formation, Mexico, in: Shipp C. R., Weimer P., Posamentier H. W., (eds) Mass-Transport Deposits in Deepwater Settings. Society for Sedimentary Geology (SEPM) Special Publication No. 96, p. 269–277

Frey Martinez, J., Cartwright, J. & Hall, B. 2005. 3D seismic interpretation of slump complexes: examples from the continental margin of Israel. Basin Res., 17-83.

Frey-Martinez, J., Cartwright, J., James, D, 2006. Frontally confined versus frontally emergent submarine landslides: a 3D seismic characterisation: Marine and Petroleum Geology, v. 23, p. 585–604.
Farrell, S.G., 1984, A dislocation model applied to slump structures:Journal of Structural Geology, v. 6, p. 727–736.Gardner et al., 1999

Gawthorpe, R.L., Clemmey, H., 1985. Geometry of submarine slides in the Bowland Basin (Dinantian) and their relation to debris flows:Geological Society of London, Journal, v. 142, p. 555–565.

Homza, 2003 Ineson, J.R., 1985. Submarine glide blocks from Lower Cretaceous of the Antarctic Peninsula. Sedimentology, 32, 659-722.

Jennette, D.C., Garfield, T.R., Mohrig, D.C. & Cayley, G.T. 2000. The interaction of shelf accommodation, sediment supply and sea level in controlling the facies, architecture and sequence stacking patterns of the Tay and Forties/Sele basin-floor fans, Central North Sea. In: Weimer, P., Slatt, R.M., Coleman, J. et al. (eds) Deep-Water Reservoirs of the World. Proceedings of the GCSSEPM Foundation 20th Annual Research Conference. The Write Enterprise, Houston, Texas, 402–421

King P. R., Ilg B. R., Arnot M., Browne G. H., Strachan L. J., Crundwell M., Helle k. 2011. Outcrop and Seismic Examples of Mass Transport deposits from Late Miocene Deep-water Succession, Taranaki Basin New Zealand. Mass-Transport Deposits in Deepwater Settings SEPM (Society for Sedimentary Geology) Special Publication No. 96, p. 311–348..

Lapinski, T. G., 2003. 3-D stratigraphic and structural evolution of the Thunder Horse minibasin, Mississippi Canyon, northern deep Gulf of Mexico: Unpublished M.S. thesis, University of Colorado, 165 p.

Lee, H.J., Normark, W.R., Fisher, M.A., Greene, H.G., Edwards, B.D., Locat, J., 2004. Timing and extent of submarine landslides in Southern California—Offshore Technology Conference, Houston. paper n°16744.

Leigh, S., Hartley, J.A. 1992. Mega debris flow deposits from the Oligo-Miocene Pinodos foreland basin, western mainland Greece: implications for transport mechanism in ancient deep marine basins. Sedimentology, 39: 1003-1012.

Lien T., Martisen O. J., Walker R., 2007. An Overview of the Ross Formation, Shannon Nasin, Western Ireland, in Nilsen, T.H., Shew, R.D., Steffens, G.S., and Studlick, J.R.J. eds., Atlas of Deep-Water Outcrops: American Association of Petroleum Geologists, Studies in Geology 56, Ch. 49, p. 192–195.

Macdonald, D.I.M., Moncrieff, A.C.M., Butterworth, P.J., 1993. Giant slide deposits from Mesozoic fore-arc basin, Alexander Island, Antarctica. Geology 21, 1047–1050

Madon Mazlan , 2010. Submarine mass-transport deposits in the Semantan Formation (Middle-Upper Triassic), central Peninsular MalaysiaBulletin of the Geological Society of Malaysia 56,15 – 26.
-
Martisen, O.J., 1994, Mass movements, in Maltman, A., ed., The Geological Deformation of Facies: Oxford, U.K., Blackwell, p. 399–444.

Martinsen, O.J., 1989. Styles of soft-sediment deformation on a Namurian delta slope, Western Irish Namurian Basin, Ireland, in Whateley, M.K.G., and Pickering, K.T., eds., Deltas; Sites and Traps for Fossil Fuels: Geological Society of London, Special Publication 41, p. 167–177.

Martinsen O.J., Bakken, B., 1990. Extensional and compressional zones in slumps and slides in the Namurian of County Clare, Eire: Geological Society of London, Journal, v. 147, p. 153–164.

Martinsen O. J., Lien T., 2007. Contrasting styles of slope deposition in the Gull Island Formation, Ireland, in Nilsen, T.H., Shew, R.D., Steffens, G.S., and Studlick, J.R.J. eds., Atlas of Deep-Water Outcrops: American Association of Petroleum Geologists, Studies in Geology 56, Ch. 53, p. 210–214.

Moscardelli, L. Wood, L., Mann, P., 2006. Mass-transport complexes and associated processes in the offshore area of Trinidad and Venezuela: American Association of Petroleum Geologists, Bulletin, v. 90, p.1059–1088.

Posamentier H. W., Martinsen O. J., 2011. The Character and Genesis of Submarine Mass Transport Deposits: Insights from Outcrop and 3D Seismic Data. Mass-Transport Deposits in Deepwater Settings. Society for Sedimentary Geology (SEPM) Special Publication No. 96, p. 7–38.

Pickering, K.T., 1979. Possible retrogressive flow slide deposits from the Kongsfjord Formation: a Precambrian submarine fan, Finnmark, N. Norway. Sedimentology 26, 295-306.

Sporli K. B., Rowland J. V., 2007. Superposed deformation in turbidites and syn-sedimentary slides of the tectonically active Miocene Waitemata Basin, northern New Zealand. Basin Research 19, 199–216.

Stow, D.A.V., 1986, Deep Clastic Seas, in Reading, H.G., ed., SedimentaryEnvironments and Sediments: London, Chapman & Hall, p. 127–165.

Strachan, L.J., 2008. Flow transformations in slumps: a case study from the Waitemata Basin New Zealand. Sedimentology, 55,1311-1332.

Tarquin Teale, C. & Young, J.R., 1987. Isolated olistoliths from the Longobucco Basin, Calabria, Southern Italy. - in J.K. Leggett & G.G. Zuffa, eds.; Marine Clastic Sedimentology, 75-88.
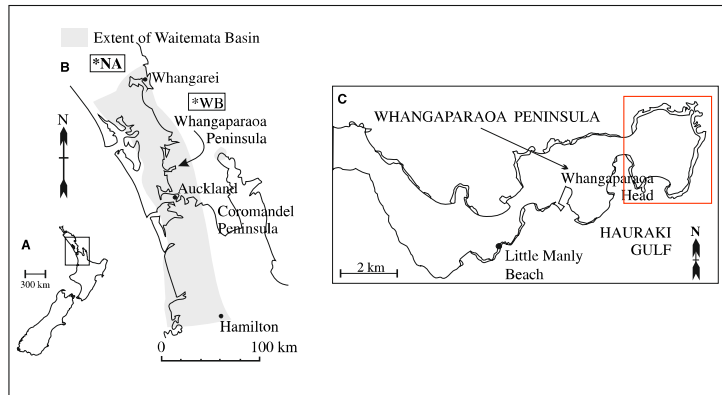
Figure 2.1. A) Map of New Zealand, the box indicates the area covered in B. B) Map showing the extent of Waitemata Basin shaded. NA, approxinmate position of the Northern Allochthon WB, approximate position of the Waipapa Basement. C) Outline map of the Whangaparoa Peninsula showing the Whangaparoa head (red box) where most of the photogaphs were taken (redrawn from Strachan, 2008).

Geological Setting:

The New Zealand micro-continent (Fig. 2.1) experienced a radical change in tectonics in the Miocene, (Sporli, 1989a; King, 2000). A new convergent plate-tectonic regime established itself, after a prolonged period of mainly extensional deformation from ca. 84 Ma to ca. 54 Ma associated with the break-away of the micro-continent from Gondwana (Gaina et al., 1998). This eventually led to the formation of the presently active Alpine Fault/HikurangiTrough plate boundary , which today traverses the length of New Zealand. An early manifestation of this imposition of convergent tectonics on a previously passive margin was the Late Oligocene emplacement of the Northland Allochthon from the NE in northern New Zealand(Ballance & Sporli, 1979; Hayward et al., 1989; Rait, 2000). After the Miocene, the plate boundary migrated toits present position along the SE-coast of the North Island, rotating by 90° into a NE trend and the region of the Waite-mata Basin was relegated to a less-active backarc setting.

.

Basal sediments of the Waitemata Basin indicate initial very shallow water conditions (Ricketts et al., 1989; Hayward, 2004) followed by a sudden drop to bathyal depths, possibly due to down-dragging of the hanging-wall plate in the subduction zone. This would be compatible with forced subduction, a regime commonly associated with the formation of a new convergent plate boundary (Gurnis et al., 2004; Stern, 2004). After King (2000), the new plate boundary propagated southward into northern NewZealand in the time period from 27 to 23 Ma.This migration must have influenced the tectonic situation of the Waitemata Basin, contributing to the complexity of its deformation.

Figure 2.2. Overview of the main cliff sections of the peninsular. Cliff height is 150m. Note the complex arrangement of panels of heterolithic facies, suggesting more than one detachment surface is present. This may be typical of the contractional style of many seismically imaged MTDs.

Thrusts and folds

Figure 2.4.

Figure 2.3. Structural styles vary in this contractional domain, over lateral distances of 1km or less. Here we see upright folds only 1km away from the previous image. Note that the layering is alternations of sandstone and mudstone, with a N/G of about 50%. Look at the scale of the fold: how thick do you think this MTD is? We can estimate the thickness here by drawing the hidden parts of the lower limbs of the fold. The cliff is 120m high!!! Would this unit seal?

Figure 2.4. Contrasts in N/G occur laterally on scales of 10s of metres. This image was taken 100m to the right of the previous image centre, and shows the heterolithic unit juxtaposed against a low N/G unit, of highly sheared mudstone (arrowed). Cliff height 120m. This emphases that MTDs with similar structural style could be good or bad seals across quite short distances, depending on the lithology.

Figure 2.5. This image was is same as the previous image, but taken under different light. It highlights the two dominant structural styles in the contractional domain in this area. They are thrust faults (arrowed) and upright to recumbent folds.

Figure 2.5.

Figure 2.6. Danger!! It is always good to remind yourself at outcrop that leakage is three-dimensional….and few outcrops give the same perspective as a 3D cube, albeit with the extra resolution that outcrop geology affords (see Section 1). Plumbing through connected recumbently folded units will involve along strike plunging and fold juxtaposition. Arrows here signify a hypothetical leakage route.

Figure 2.7. Can folds be leaky? Here we see a another 3D exposure of recumbent fold with consistent bed thickness. However, through the hinge of the fold there is no ductile deformation rather we see carbonate concretions aligned parallel to the fold axis on the left side of the fold possibly indicating persistent leakage of formation fluids.

Figure 2.8. Detailed view of the complex deformation typically seen it the cores of many of the recumbent folds. Note the many small thrust faults that serve to accommodate the complex strain variation between low and high N/G units (bed thickness variations).

Figure 2.9. Another example of Large scale recumbent folding in the peninsular. Cliff height is c. 30m.

Figure 2.10. Close-up view of of the recumbent fold head.
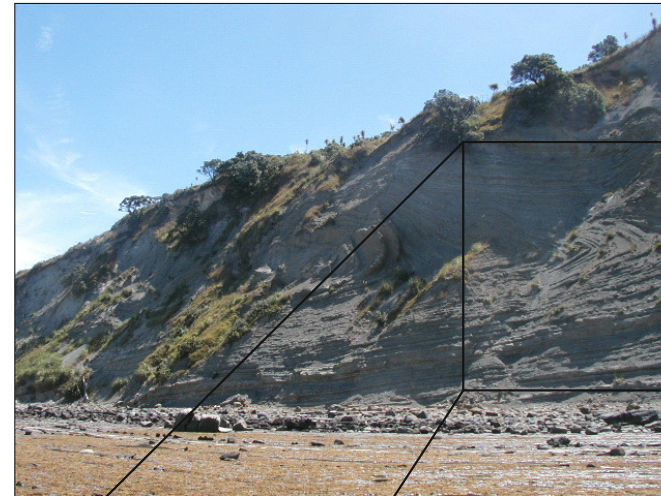
Figure 2.9
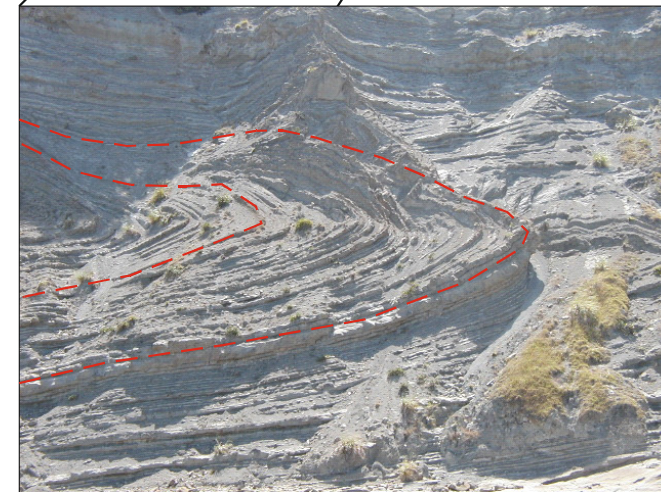
Figure 2.10

Figure 2.11.

Figure 2.12.

Figure 2.13.

250 m
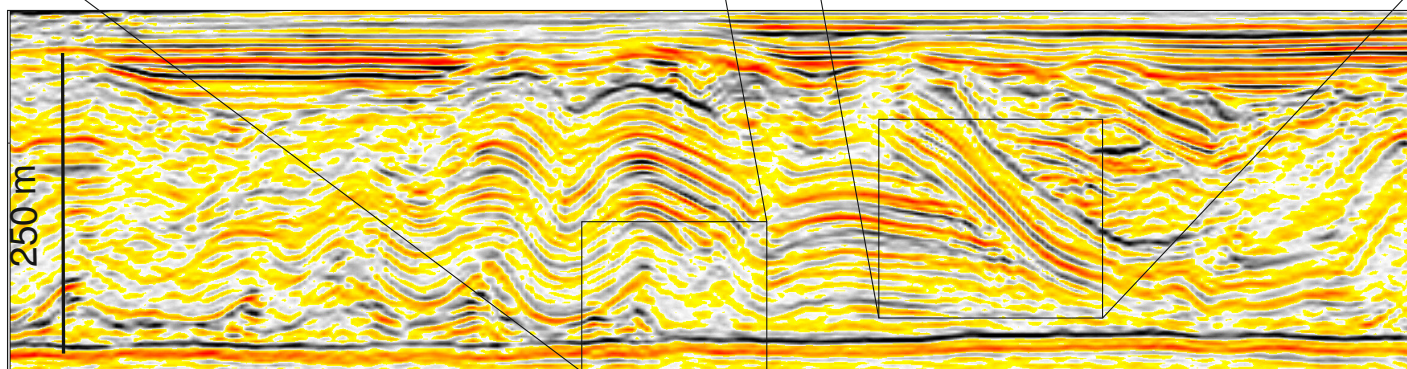
Exercise:

Figure 2.11. Can you identify any thrusts or is the structure simply a fold complex?

Figure 2.12. Is this a thrust or a normal fault? Is this a dip section or possibly a strike section? Cliff height 30m.

Figure 2.13. Are both structures visible in seismic?

Figure 2.14. Seal capacity is critically dependent on lithofacies: this example shows a highly heterolithic unit caught up in a large recumbent fold, with many small intralimb thrusts (e.g. dotted line). This would be a very poor seal, because there are so many potential conduits from base to top of the MTD. Note also the two blocks of sandstone caught up in the sheared limb (arrowed). Cliff height 40m.

Figure 2.15. Another example of the recumbent fold-thrust association that dominates the contractional style in this MTD complex. In this case the fold has been beheaded by the thrust. Many examples of seismic scale contractional domains may consist of this type of structural style. Cliff height 30m.

Figure 2.16. Here is a an illuminated side view of the previous figure showing detailed lithology and beds of the recumbent fold-thrust association.

Figure 2.17. Recumbent folds are present at all scales from centi-metres to 100s of metres (wavelength).This next set of images shows the range of recumbent folds, and smaller scale structures associated with them e.g faults.
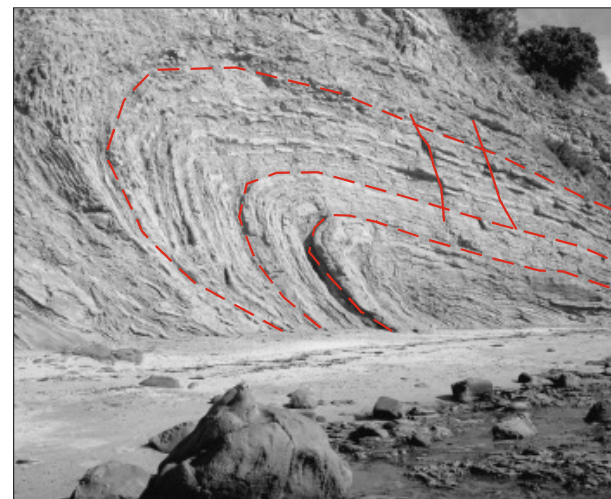
Figure 2.18. Here we see another example of a recumbent fold with a faulted right limb. These example would probably not be imaged by conventional 3D seismic, with a cliff height of 30m, and in a thin bedded facies. However, it is proposed that many of the seismically imaged contractional domains with closely spaced thrusts would also have this type of structure embedded.
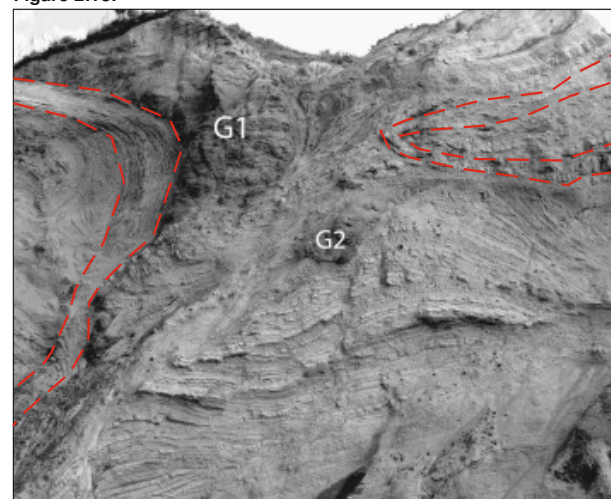
Figure 2.19. Here we see an example of a complex contractional zone. The hinge area of a recumbent fold is present at the top left while a smaller grit body (G2) below to the right forms a sigmodal shear sense indicator.

Figure 2.18.

Figure 2.19.

Strain overprinting in MTDs

Figure 2.20. In some areas of the major MTD there is a close association between recumbent folding/thrusting and minor extension. Here we see a panel 20m across, with a thrust out recumbent fold , and over the upper limb is a generally flat lying, thin bedded (levee or distal turbidite) facies. Note the large number of small extensional faults (decimetre throws) dipping generally left to right (e.g. dotted line). Would these compromise the seal, at least locally, and offer migration paths upwards through anotherwise flat lying and probably locally sealing unit?
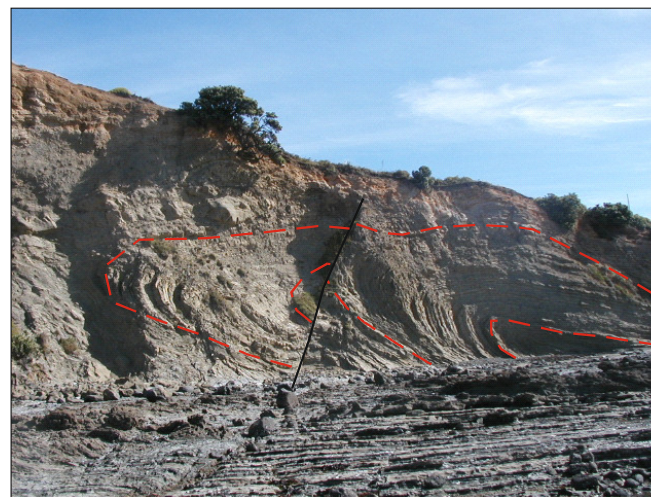
Figure 2.21. Another 30-50m amplitude recumbent fold, with a later extensional fault cutting across the nose. Note that the steep, lower limbs would not be imaged, giving the impression on seismic data that this unit was simply thrusted, or perhaps, the seismic expression would simply be of a gently undulating geometry. Seismically, MTDs that appear as low deformational units, may in fact be like this, and highly deformed. This thin bedded but high N/G facies would render the MTD a very poor seal. Cliff height 50m.

Figure 2.23

Figure 2.22. Here we see an example of a Z shaped recumbent folded structure which highlights the complex nature of contractional zones.

Figure 2.23. Close-up of the hinge area of the upper recumbent fold in Fig. 22, showing in detail small sub seismic faults which could possibly link up leaky strata forming a tortuous, yet effective, leak pathway over geological timescale.

Figure 2.24. Close-up of fig. 22, showing in detail the evident, strong thickening of the hinge zone, characterizing thin-bedded folded elements. Notice the fracture filled veins which suggest that the hinge areas in folded structures are potential conduits zones.

Figure 2.24

Figure 2.26. Close up view of Fig. 25 showing extensional faults in detail. These faults might as migration pathways for fluids.
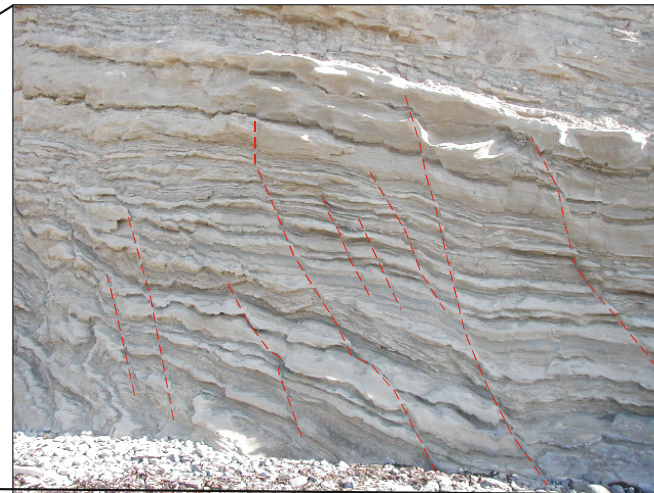
Figure 2.25. Small scale extension associated with recumbent folding is ubiquitous in the peninsular as a consequence of limb extension whilst the sediments are highly unconsolidated. However, there is sufficient integrity such that bedding continuity is maintained. You can imagine that doubling or tripling the strain may well lead to total disaggregation into a much more highly sheared mix of sandstone and claystone (high N/G), and could even end up looking like a debrite.

Faults and fracture within MTDs

Figure 2.27. Minor extension fault dipping left to right with decimetre throws. Would these compromise the seal, at least locally, and offer migration paths upwards through an otherwise flat lying and probably decimetre throws locally sealing unit?
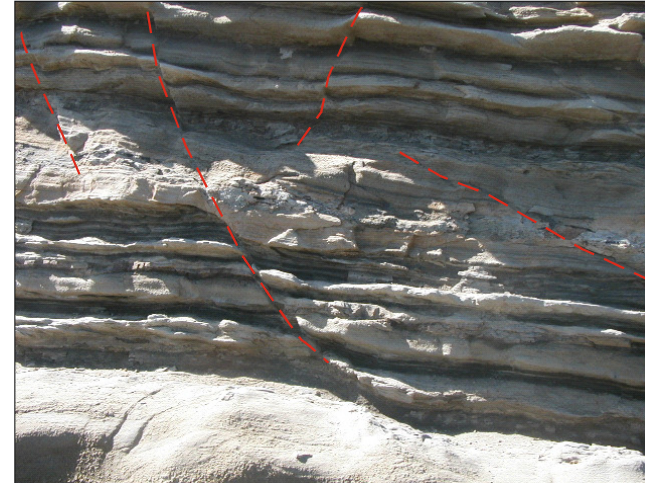
Figure 2.28. Minor extension dipping left to right with decimetre throws. Would these compromise the seal, at least locally, and offer migration paths upwards through an otherwise flat lying unit.

Figure 2.29. Another dose up view of extensional faults. These faults might as migration pathways for fluids.
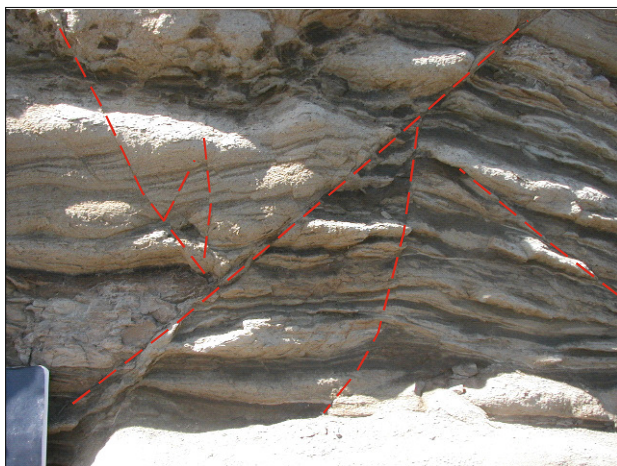
Figure 2.30. Minor extension dipping right to left with preserved veins. This provides evidence that these seemingly tight faults can be migration paths through an otherwise flat sealing unit.

Figure 2.32. Dense array of fracture network in a fine grained unit.

Figure 2.31. An extension fault dipping right to left to with decimetre throws. However there is no evidence of fluid migration through the fault.

Figure 2.33. Here we see another dense array of fracture network in a fine grained unit.

Figure 2.34. Extensional fault dipping right to left with preserved veins. This provides evidence that these seemingly tight faults can be migration paths through an otherwise flat sealing unit.

Figure 2.35. Example of sand-injectite through a more coherent turbidite sequence. Human being for scale for scale.

Figure 2.36. Another example of sand-injectite but this time through fine grained matrix component.

Basal shear surface
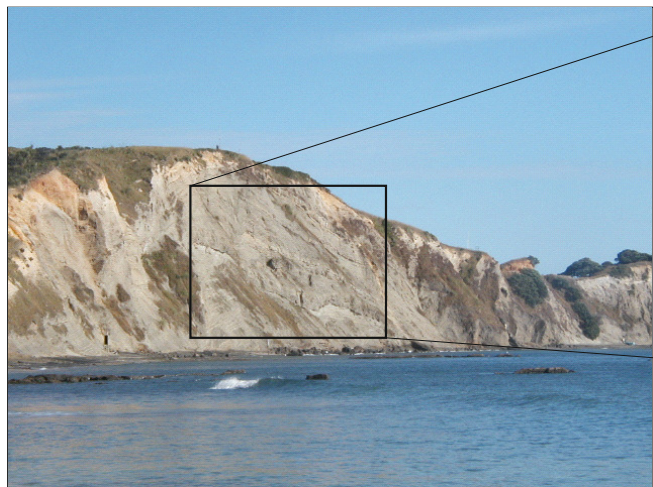
Figure 2.38.

Figure 2.37. In contrast to the previous example, this basal surface is highly irregular (as most commonly seen on seismic examples), with a sharp base defining a groove or slot like shape(see inset zoom). Cliff height is 140m.

Figure 2.38. In contrast to the previous example, this basal surface is highly irregular (as most commonly seen on seismic examples), with a sharp base defining a groove or slot like shape (see inset zoom). Cliff height is 140m.

Figure 2.39. Seismic profile show an unequivocal example of an iregular basal surface shown in Fig. 2.38.
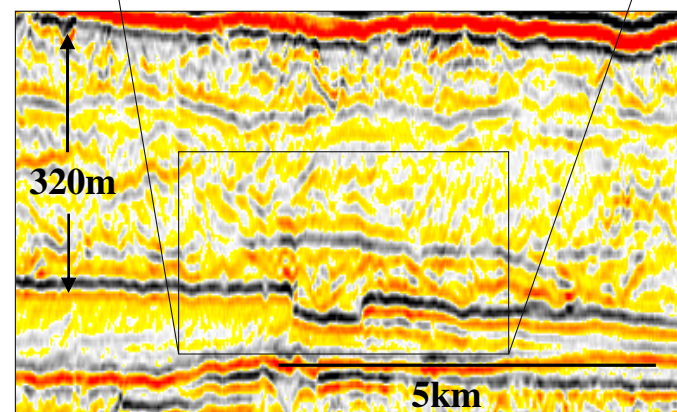
Figure 2.39.

Figure 2.40. An example of a concordant basal surface, but where recumbent folds sit directly onto this surface. Cliff height is 10m.
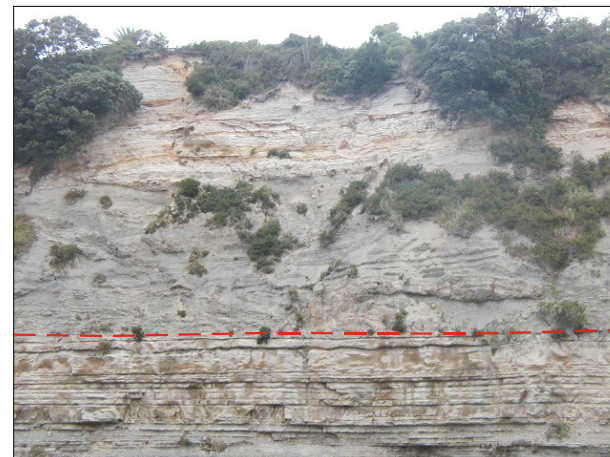
Figure 2.41. Superb example of a concordant basal surface, with a low N/G MTD about 15m thick (just about seismically resolvable for Case Study A or B type of data).

100m
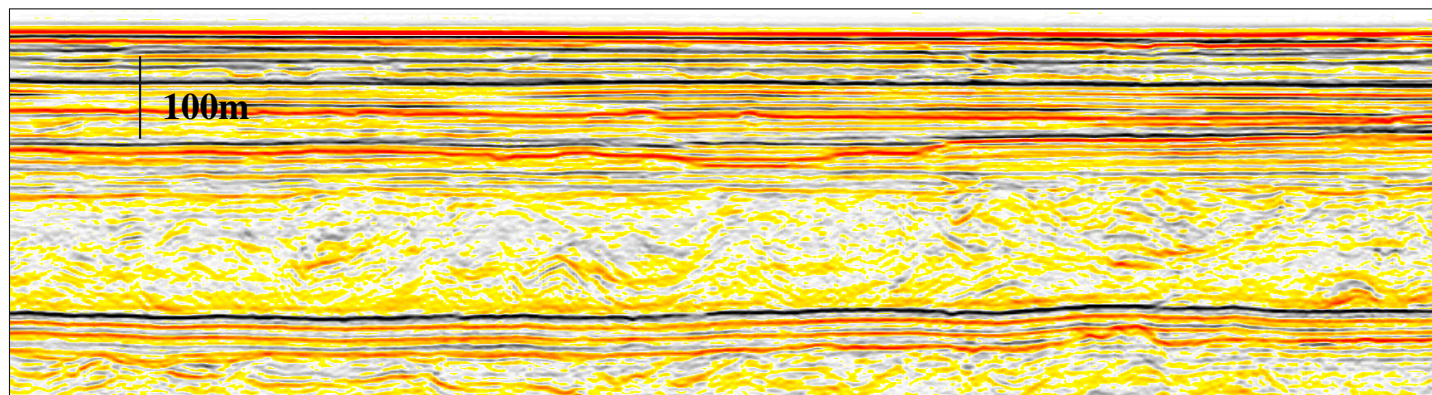
Figure 2.42. Seismic profile showing a transparent MTD (mud-rich), with a concordant basal surface.

Figure 2.43. Here we see non concordant basal surface but a scouring of the basal surface by a huge block.
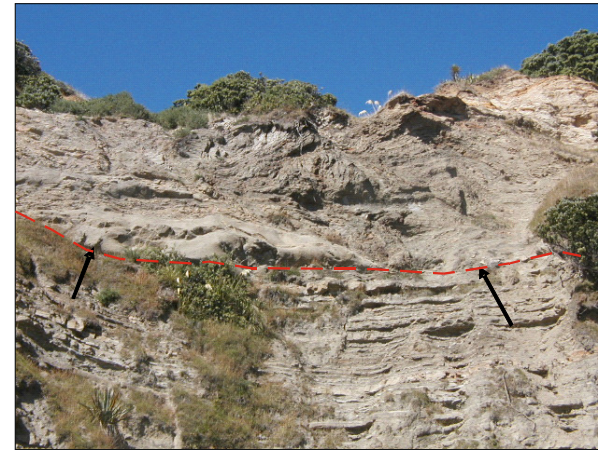
Figure 2.44. Detachments occur on a range of scales, either as bases to individual MTDs, or as local structural detachments (low angle flats' to intra-MTD thrusts). Here we see the base of an MTD with a concordant geometry (arrowed). Cliff height 50m.

Rotated extentional blocks
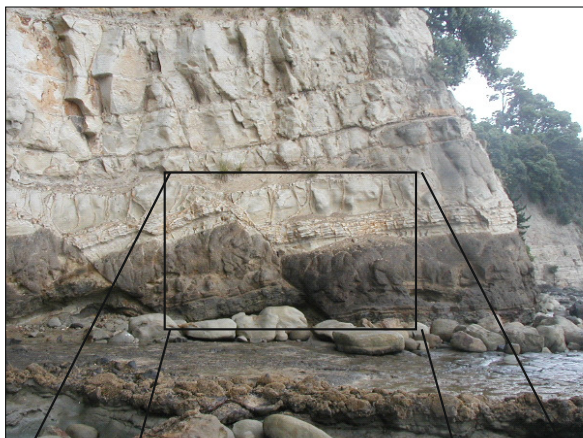
Figure 2.45.

Figure 2.47. Seismic profile showing rotated blocks bounded by extensional normal faults.

Figure 2.45. Here we see extensional faults bounding huge rotated blocks, typical of headwall regions of MTDs.

Figure 2.46. Close up of rotated blocks seen in Fig. 2.45.

Isolated blocks

Figure 2.48. Examples of floating blocks can be seen in a number of localities in the peninsular. Here, an elliptical shaped megaclast or block of sandstone appears stranded within a low N/G interval. But closer inspection should reveal that this clast might in fact be a detached recumbent fold, with two noses giving the appearance of an ellipsoid. Block is 10m wide.
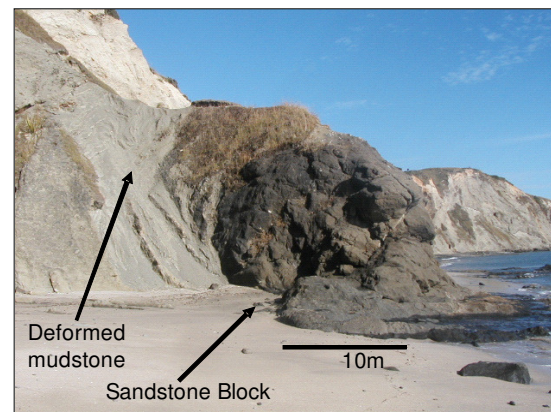
Figure 2.50. Here is another example of a relatively rigid block of volcanoclastic sandstone entrained in a deformed mudstone matrix.
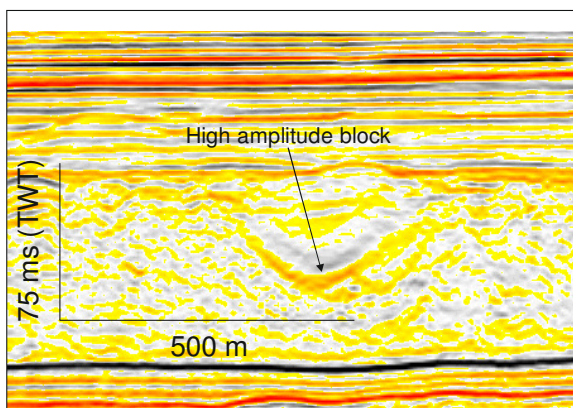
Figure 2.49. An example of an isolated block in-matrix texture in seismic profile.

Liquefaction/fluidization
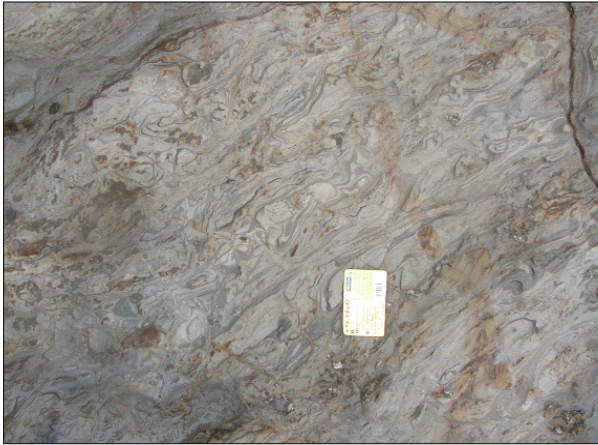
Figure 2.51. Fluidization within MTD.

Figure 2.53. Representative seismic profile showing a highly deformed and transparent MTD interpreted to have undergone liquefaction.

Figure 2.52. Small clast being transported in fluidized matrix.

Summary

1) The Mass transport deposit outcrops of the Miocene Waitemata Basin in northern New Zealand are mainly characterized by seismic scale (> 10 m thick) contractional folds and thrust structures with recumbent folds being the most common.

2) Other structures present are rotated blocks bounded by extensional faults as well as isolated faults.

3) Evidence for overprinting of contractional structures by extensional faults are evident.

4) Where the basal detachments are present, they are usually sharp with more or less translational upper surfaces. Rare grooves caused by the translating blocks are sometimes present.

References

Ballance, P. F. & Sporli ,K. B. (1979) Northland Allochthon. J.R. Soc. NZ., 9, 259-275.

Gaina, C.,Muller, D.R. & Roger, J.Y., et al (1998) The tectonichistory of the Tasman Sea: a puzzle with 13 pieces. J. Geophys. Res. Solid Earth, 103(B6), 12413-12433.

Gurnis, M., Hall, C. & Lavier, L. (2004) Evolving force balance during incipient subduction. Geochem. Geophys. Geosyst. - G3, 5, 7.

Hayward, B.W. (2004) Foraminifera-based estimates of paleobathymetry using Modern Analogue Technique, and the subsidence history of the early Miocene Waitemata Basin. New Zealand. NZJ. Geol. Geophys., 47, 749-767.

Hayward, B.W., Brook, F.J. & Isaac, M.J. (1989) Cretaceous to middle tertiary stratigraphy, paleogeography and tectonic historyof Northland, New Zealand. In: Geology of Northland- Accretion, Allochthons and Arcs at the Edge of the New Zealand Micro Continent (Ed. by K.B . Sporli & D. Kear), R. Soc. NZ Bull., 26, 47-62.

King, P.B. (2000) Tectonic reconstructions of New Zealand: 40 Ma to the Present. NZJ.Geol. Geophys., 43, 611-638.

Rait, G.J. (2000) Thrust transport directions in the Northland Allochthon,New Zealand.NZJ. Geol.Geophys., 43, 271-288.

Ricketts, B.D., Ballance, P.F., Hayward, B.W. & Mayer, W. (1989) Basal Waitemata Group lithofacies: rapid subsidence in an early Miocene interarc basin, New Zealand. Sedimentology, 36, 559-580.

Sporli, K.B.& Kadar, A. (1989) Structurally superposed sheets of Cretaceous-Tertiary sedi- ments at Pahi,North Kaipara Harbour, New Zealand. In: Geology of NorthlandAccretion, Allochthons and Arcs at the Edge of the New Zealand Micro-Continent (Ed. by K.B. Sporli & D.Kear), R. Soc.NZ. Bull., 26, 115-125.

Sporli K. B., Rowland J. V. (2007). Superposed deformation in turbidites and syn-sedimentary slides of the tectonically active Miocene Waitemata Basin, northern New Zealand. Basin Research 19, 199–216.

Stern, R.J. (2004) Subduction initiation spontaneous and induced. Earth Planet. Sci. Lett., 226, 275-292.
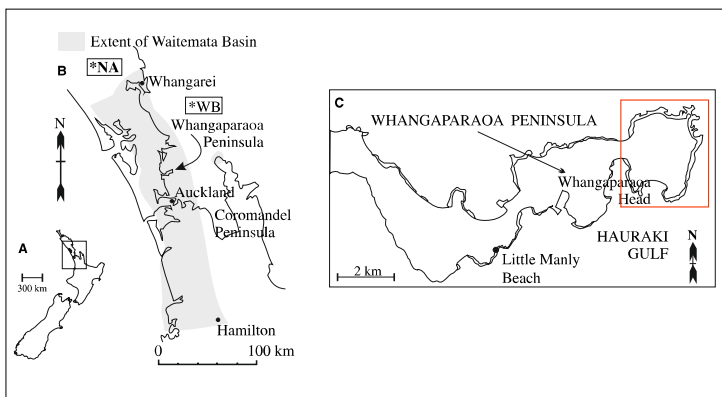
Figure 3.1. A) Outline map of New Zealand, the box indicates the area covered in B. B) Map showing the extent of Waitemata Basin shaded. NA, approxinmate position of the Northern Allochthon WB, approximate position of the Waipapa Basement. C) Outline map of the Whangaparoa Peninsula showing the Whangaparoa head (red box) where most of the photogaphs were taken (Redrawn from Strachan, 2008).

Geological Setting:

The Little Manly Slump occurs in the Miocene infill of the Waitemata Basin (Fig. 3.1a), whose initiation is thought to be linked to the development of a new convergent plate- tectonic regime represented in the present day by the Alpine Fault/Hakurangi Trough plate boundary (Ballance et al.1982).

The study area is located c. 40 km north of Auckland on the Whangaparaoa Peninsula (Fig. 3.1c), where the slump is exposed for c. 600 m at Little Manly Beach, in 8–15 m high cliffs made accessible by wave-cut platforms (Fig. 3.2).

The basin fill reflects initial shallow marine conditions followed by rapid deepening, with the basin receiving mostly turbiditic clastic sediments (Ricketts et al. 1989). The Little Manly Slump is interpreted to have developed in an outer fan setting, translating downslope to the SW (Strachan 2002). The slump incorporates three main lithologies: medium- and coarse-grained turbidite sandstones, and a fine-grained mudstone interpreted as back-ground hemipelagic sedimentation (Strachan 2002).
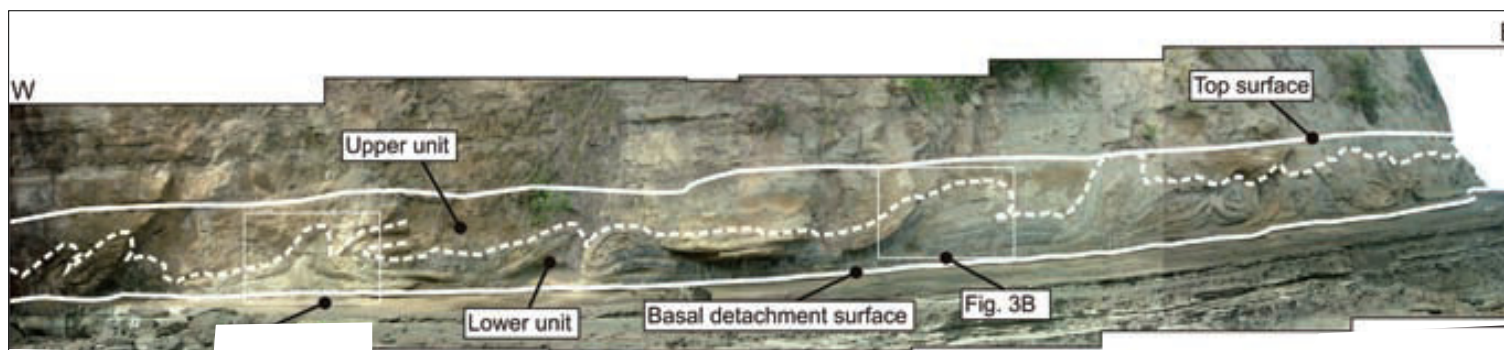
Figure 3.2. The MTD is segregated into two structurally and sedimentologically distinct units. Also note the sequence of folds defined by coherently deformed coarse sandstone beds (Bull and Cartwright, 2010).

Small scale folds and thrust

Figure 3.4.

Figure 3.5. Close-up of previous fig.3.3 showing the complex nature of the fold structure.

Figure 3.3. Recumbent fold defined by coarse sandstone beds. Between fold limbs, the medium-coarse grained lithology and fine-grained mud exhibit competency contrasts and intense ductile deformation.

Figure 3.4. Close-up of previous Fig.3.3 showing the complex nature of the fold structure.

Figure 3.6. Folds occur at a number of scales, ranging from decimetre to sub-centimetre. Here we see an example of well preserved folds and a slump scale thrust characterized by a curved, ramping geometry.

Figure 3.7. Fold formed by coarse sandstone bed. The 'core' of the fold is occupied by a plug of medium-coarse grained material around which a thin, fine- grained mudstone has deformed in an intense, highly ductile manner.

Figure 3.8. Here we see a fined grained highly deformed ductile unit.
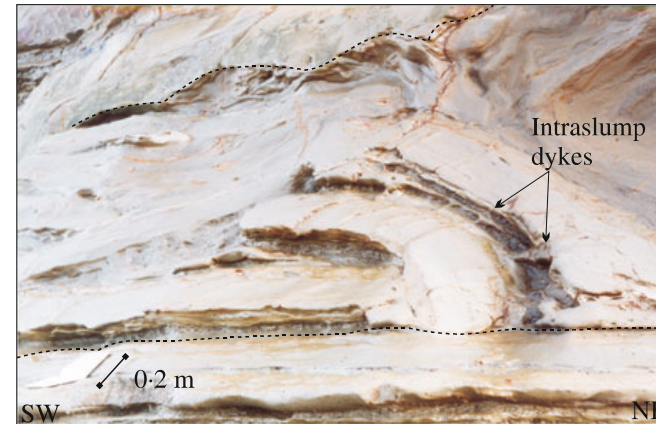
Figure 3.9. Intraslump coarse-grained sandstone dykes.
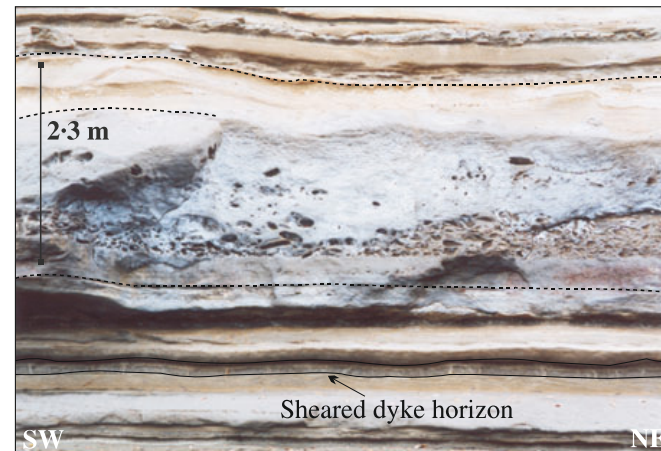
Figure 3.10. Example of clast dominated texture composed of fine-grained calacareous sands and muds which display a crude imbrication.
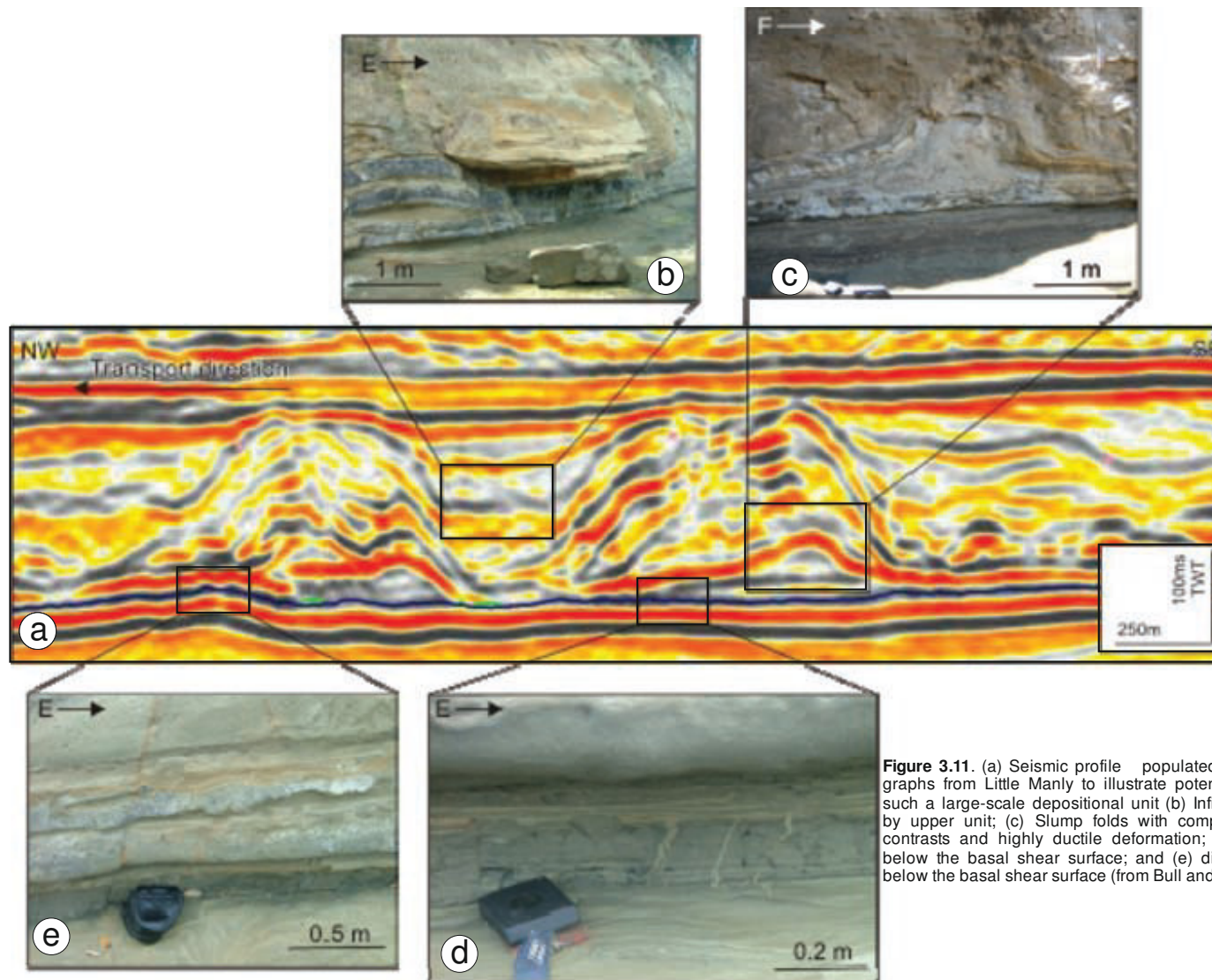
Figure 3.11. (a) Seismic profile populated with field photographs from Little Manly to illustrate potential complexity of such a large-scale depositional unit (b) Infilling of lower unit by upper unit; (c) Slump folds with complex competency contrasts and highly ductile deformation; (d) Clastic dykes below the basal shear surface; and (e) disruption of beds below the basal shear surface (from Bull and Cartwright 2010)

Figure 3.12. Small-scale slump involving only two beds within otherwise flat-bedded succession.

0·08 m

Intrabed-scale faulting
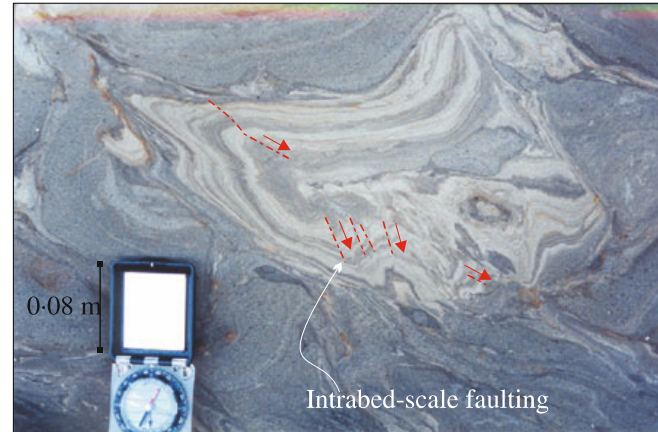
Figure 3.14. Plan view showing small-scale intrabed faults.

2·08 m

H

Sheared dyke horizon

SW   NE

Sandstone dyke

Intrabed fault

W   2·52 m   E

Boudinaged fold limbs

0·22 m

SW   NE
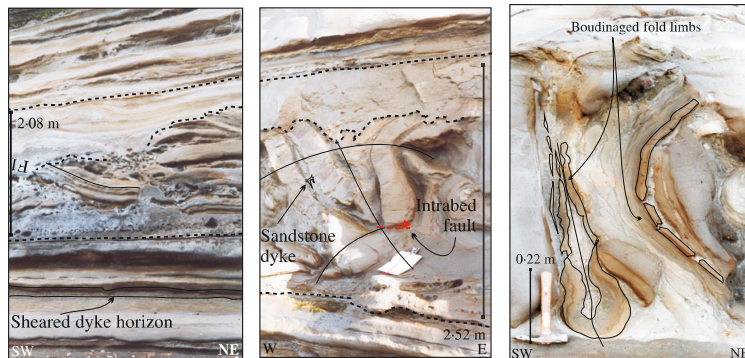
Figure 3.13.a) Fragmented fold limbs and clasts within the Little Manly Slump. **b)** Note the fragmented fold hinge and intraslump dyke. **c)** Examples of boudinage associated with phase 2 folding.

Summary

1) The Little Manly Slump outcrop (bed-scale only few meters thick) has a lower unit that exhibits a variety of ductile compressional and brittle extensional structures, including folds of various styles and sizes and intra-slump to slump-scale normal and thrust faults.

2) The lower unit have a high degree of lateral variation in the style and intensity of deformation.

3) The basal and upper surfaces of the Little Manly Slump are sharp with the upper surface overlain conformably by further sand-rich units.

4) Ptygmatically folded dykes are present beneath the sandstone bed which predominantly underlies the basal shear surface of the slump, as well as within the slumped unit.

References

Ballance P. F, Pettinga J. R, Webb C.,1982. A model of the Cenozoic evolution of northern NewZealand and adjacent areas of the southwest Pacific. Tectonophys 87: 37–48

Bull S., Cartwright J., 2010. Small-Scale Insights into Seismic-Scale Slumps: A Comparison of Slump Features from the Waitemata Basin, New Zealand, and the Møre Basin, Off-Shore Norway. D.C. Mosher et al. (eds.), Submarine Mass Movements and Their Consequences, Advances in Natural and Technological Hazards Research, Vol 28, 257.

Ricketts, B. D., Ballance, P. F., Hayward, B. W. & Mayer, W., 1989. Basal Waitemata Group lithofacies: rapid subsidence in an early Miocene interarc basin, New Zealand. Sedimentology, 36, 559-580.

Strachan, L.J., 2002. Slump-initiated and controlled syndepositional sandstone remobilization an example from the Namurian of County Clare, Ireland. Sedimentology, 49,25–41.

Strachan, L.J., 2008. Flow transformations in slumps: a case study from the Waitemata Basin New Zealand. Sedimentology, 55,1311-1332.

Chapter 4: Mass Transport Deposit of the Taranaki Basin, northern New Zealand.
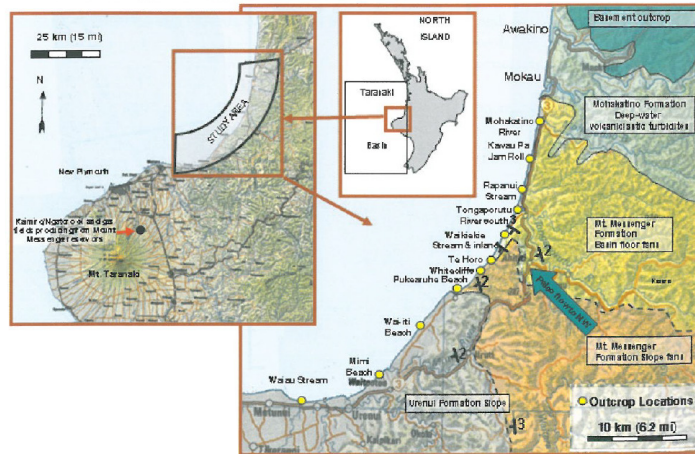
Figure 4.1. The coastal outcrop transect is located on the western side of New Zealand's North Island, northeast of the city of New Plymouth. A 40 km long section is documented here . Deep water Miocene rocks are also exposed along the shore-line for a further 30km north of the study area (from King et al., 2007b).

Geological Setting:

The north Taranaki coastline, located northeast of New Plymouth (Fig. 4.1), affords world-class exposures of deep-water siliciclastic strata in a Late Miocene (Tortonian), seaward-stepping, basin-floor to slope depositional system (Mount Messenger and Urenui Fms) (King et al., 2011).

Uplift and tilting of the Late Miocene strata within the past few million years has produced gentle stratal dips to the southwest, such that a 2- km-thick Mohakatino–Urenui succession is exposed in sea cliffs along a total outcrop length of about 65 km. The oldest, deepest water (basin floor) deposits are located in the north of the study area, and the youngest, shallowest-water (uppermost slope) deposits are located in the south.

MTDs in the north Taranaki outcrop section range widely in scale (seismic, sub-seismic, meter), depositional setting (mid fan to slope), stratigraphic relationship with surrounding strata, degree of deformation and types of beds involved. They are also exposed in geographically widespread localities, in northern, central, and southern parts of the section.
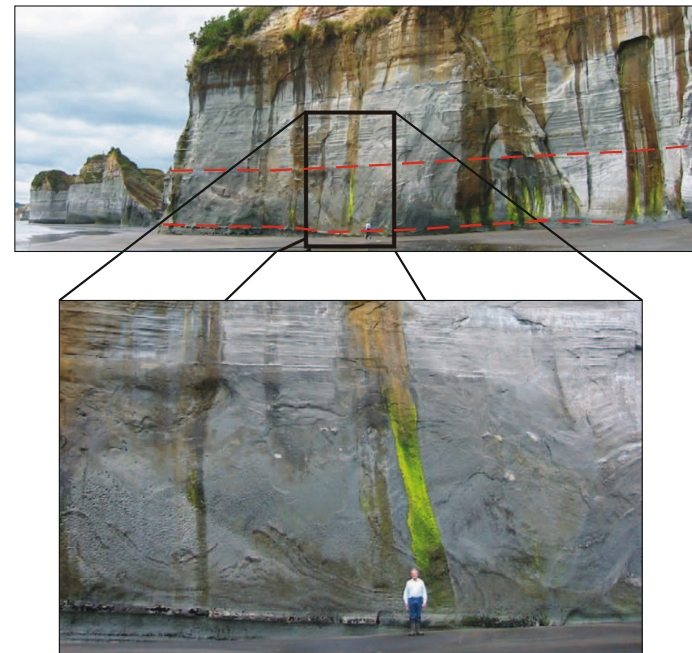
Figure 4.2. MTD section exposed underneath bedded siltstones. The MTD has sharp, planar upper and lower contacts, and comprisesdeformed siltstone beds with some sandstone blocks.

Figure 4.3. Close up showing intense deformation which could possibly have low seal risk. However, the presence of sandstone blocks might prove risky. Man for scale.

Planner upper surfaces

Figure 4.4. Again we see intensely deformed MTD unit with relicts of folded structures preserved. The MTD is bounded by a planner upper. Man for scale.
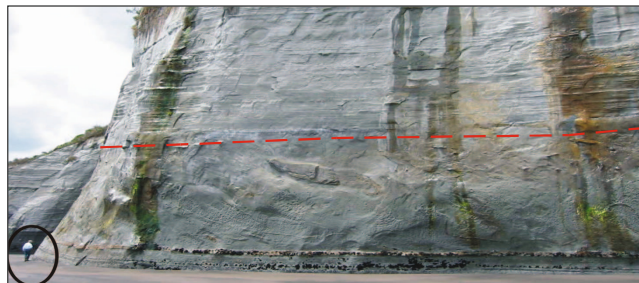
Figure 4.5. The figure provides a closer view of the head-and region just left of Fig. 4.2. Notice the planner upper surface.
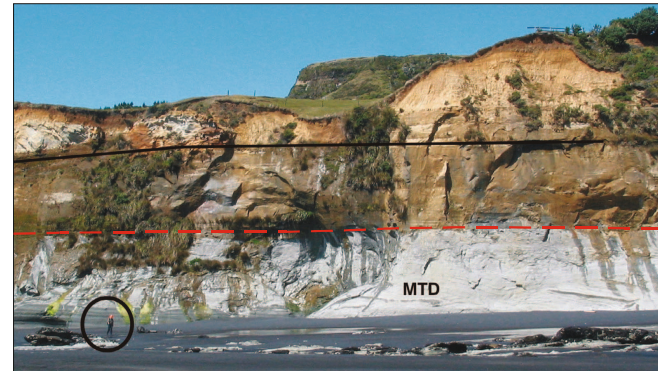
Figure 4.6. MTD is composed of gray deformed siltstones and is overlain by thick bedded channelized sandstones (golden brown). MTD is intensely deformed and would make a low risk seal.The black line in both photos marks a wave-cut unconformity (120 ka interglacial) overlain by Quaternary deposits.

Figure 4.7. Intensely deformed MTD. Notice how the upper and lower contacts appear relatively planar, with only minor relief. The black line in both photos marks a wave-cut unconformity (120 ka interglacial) overlain by Quaternary deposits.

The upper contact is clearlyexposed and visible in all figures. It relatively planar over the length of the outcrop. The black line in all figures marks a wave-cut un-conformity (120 ka interglacial) overlain by Quaternary deposits.
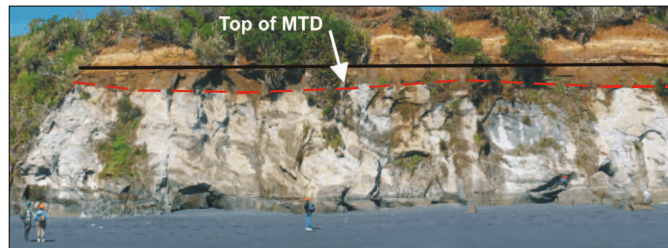
Figure 4.8. Here we see relatively preserved structures within the highly deformed MTD.

Figure 4.9. Again we see the planar nature of the upper contact of the MTD.
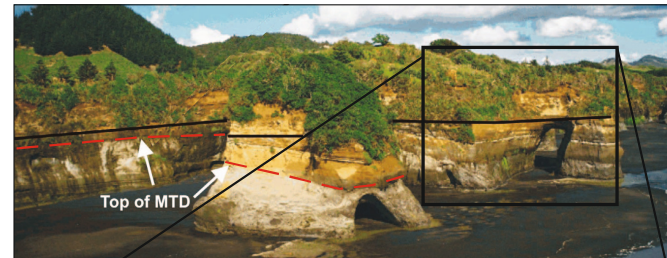
Figure 4.9. Planar upper surface.
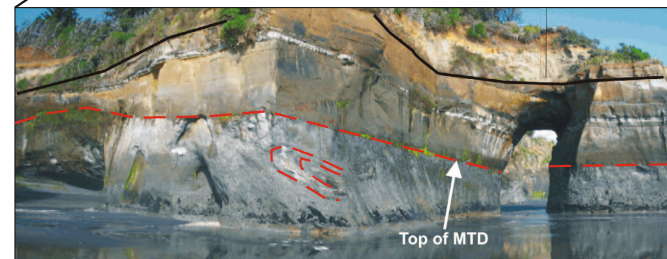
Figure 4.10. Close-up of previous figure shows some preserved structure within the MTD.

Internal detachment within MTDs

Figure 4.11. Deformed medium- to thick-bedded sandstones (greenish brown–orange brown) and siltstones (gray). Notice the isolated sandstone block and the internal detachment (black arrow).

Figure 4.12. Below the internal detachment surface, the sandstone and siltstone beds have retained some coherency whereas beds above it are more highly contorted and more tightly folded.

Figure 4.13. Deformed medium- to thick-bedded sandstones (greenish brown–orange brown) and siltstones (gray).

Figure 4.15. Here we see another example of internal detachment.
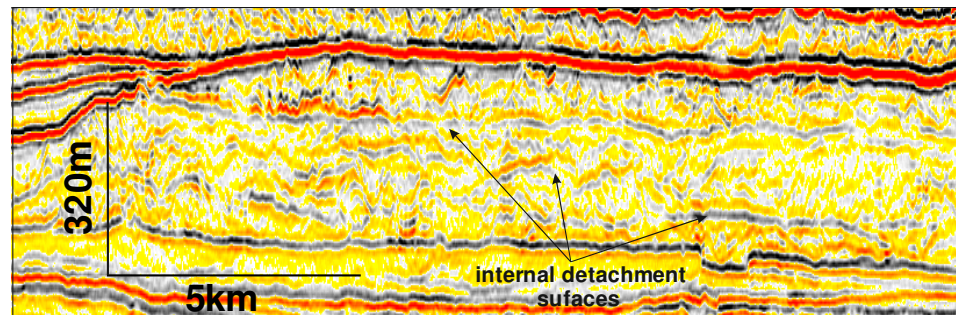
Figure 4.16. Seismic profile showing multiple internal detachment within a single MTD.

Basal shear surface
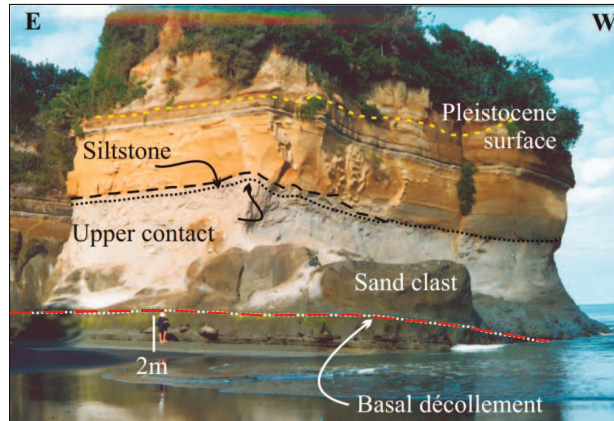
Figure 4.17. Here we see a sea stack showing the upper part of the MTD, consisting of rafted blocks of sandstone (dark) overlying siltstones a concordant basal suface.

Figure 4.18. a) Here we see Small-scale folds within the MTD interval. Note the concordant basal surface. b) Close-up show a sand-filled dikes at the upper contact.

Figure 4.19. Concordant basal surface with small-scale folds
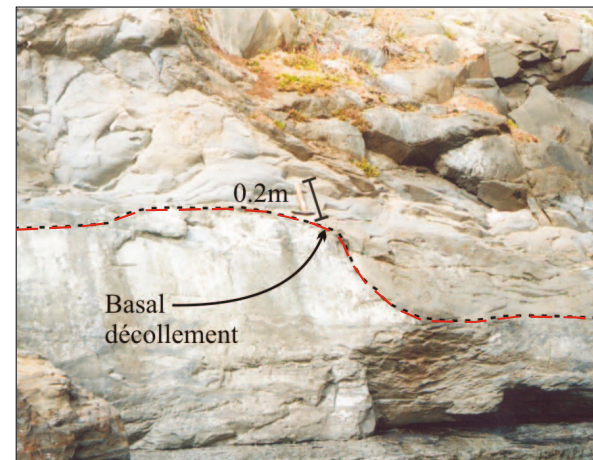
Figure 4.20. Closer views of the MTD, showing the basal décollement that is sharp and planar at outcrop scale, but also has some local relief.

Structurally complicated MTDs

Figure 4.21.

Figure 4.22.

Figure 4.21. Deformed thin-bedded sandstones (mid-gray) and siltstones (pale gray). The black line marks a wave-cut unconformity (120 ka interglacial) overlain by Quaternary deposits.

Figure 4.22. Close-up view of Figure 4.21 showing multiple slide events exposed in the sea stack. The MTD will constitute a poor seal.
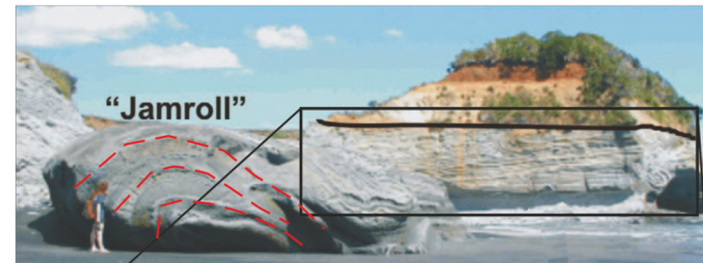
Figure 4.23.

Figure 4.24.

Figure 4.23. The MTDs observed are structurally very complicated, and are characterised by open folds as well as recumbent folds with sub-horizontal axial planes. Here we can tensional cracks in siltstone beds in the core of the "jamroll" fold. Note person for scale.

Figure 4.24. Close-up view of Fig. 4.23 shows a sub-horizontal recumbent fold verging toward the east (inland), and a locally deformed underlying strata which appear to be deformed by the overriding slump. These MTDs will constitute a poor seal because of the low N/G.

Large Scale folding

Figure 4.25. Seismic-scale folding in observed in outcrop. The fold is cut by a wave-cut unconformity (120 ka inter-glacial) and overlain by Quaternary deposits. Person (circled) for scale in Fig. 4.26. MTD comprise of siltstone and mudstone. The low N/G in this MTD will render it a poor seal.

Figure 4.26. Here is a view of the previous image from the left under a different light.

Figure 4.27. Another large-scale folding.

Figure 4.24. Just to remind ourselves that we can also observe a time slice view of large scale folds in outcrops (shore platform). Note people (circled) for scale.

Figure 4.25. Here we see different scale of folding in this Coastal cliffs view (the island or sea stack).

Figure 4.26. A large recumbent fold is evident at bottom left. A marked planar surface separates deformed strata (below) from undeformed strata (above).Note person for scale.

Figure 4.27. Close- up of figure 4.26.
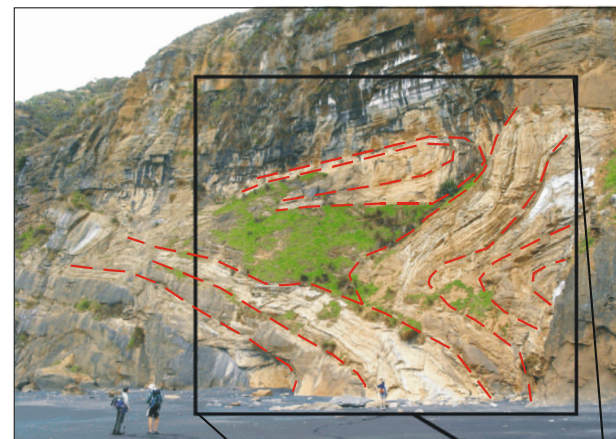
Figure 4.28. Different view of the large recumbent fold shown in Fig. 4.27.

Figure 4.29. Similar feature in fig. 4.29 can be seen on seismic. Here is a seismic profile from onshore Taranaki Peninsula. The vertical scale is in mili-seconds (ms) TWTT (25 ms increments) the horizontal width of view is 1870 m.
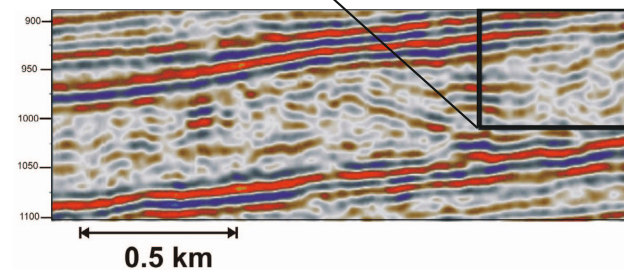
Figure 4.28.

Figure 4.29.

Figure 4.30. Notice the large scale isoclinal open fold

Figure 4.31. An example of seismic scale recumbent fold.
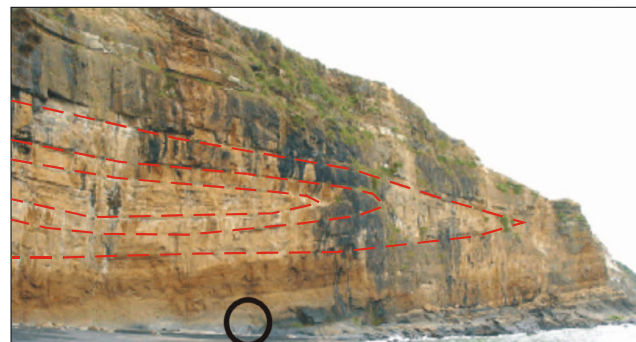
Figure 4.32. Another example of seismic scale mud-rich recumbent fold.
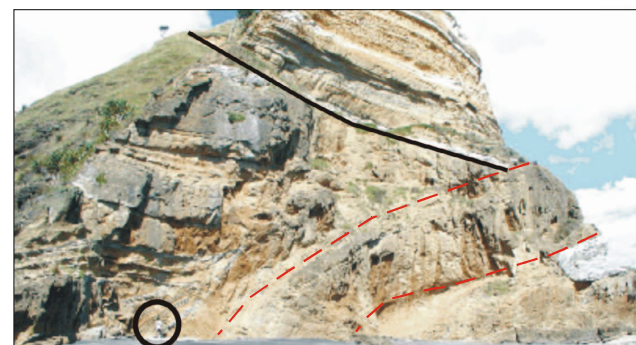
Figure 4.33. The large recumbent fold is inferred to be the same feature, viewed in Fig. 4.36 but from a different locality along strike of its axis, about 500 m apart. The MTD appear sand-rich and interpreted to have incorporated a channel levee system. Note person for scale photo.

Figure 4.34. Complex broad scale folding in MTD. Would this MTD constitute an excellent seal?Note person for scale

Figure 4.36. Here we see broadscale folding in MTD close to the water-fall. Note person for scale.

Figure 4.35. Large scale recumbent folding in MTD.Note person for scale.

Figure 4.37. Here we see an MTD consisting of subtle open folds within upper-most slope siltstones below a slope-filled channel (exposed farther to the right out of picture). The low N/G of the MTD suggest a low risk seal. Upper interval (brown) is Quaternary deposits.Note person for scale (Browne et al., 2006).

Bed Scale Deformation

Figure 4.39.The slumped bed (labelled i) comprises a 2 m-thick interval, strati-graphically bounded by thick-bedded basin-floor fan sandstones. Note persons for scale (Browne et al., 2006).

Figure 4.40. Details of the slumped bed (shown in Fig. 4.40 above) showing fluidized load structures and water escape features. It overlies another more sand-rich MTC bed (ii) at the base of the outcrop. Scale bar in center of photo near (ii) is 1 m long (Browne et al., 2006).

Figure 4.38. Thick-bedded sandstone beds that have been sheared (first two photos), tightly folded, and in part overturned (where marked by "a" in each photo). Note person for scale in each photo. Possibly similar features on seismic are shown.

Summary

1) MTDs in the north Taranaki outcrop section range widely in scale from seismic (> 10 m), through sub-seismic (up to 10 m) to bed scale (few meters). They also vary in depositional setting (mid fan to slope), degree of deformation, and types of beds involved.

2) Structures observed are mainly open to isoclinally folds with upright to recumbent axial planes, and commonly sheared by low-angle thrust faults and internal slump detachment surfaces or glide planes.

3) The main lithology in the MTDs issiltstone, with minor intercalated mudstone and sandstone.

4) The upper surfaces of thenorth Taranaki outcrop are planar and sheared. The same observation is true for the basal surfaces where exposed. However most of the basal detachment of thenorth Taranaki outcrop are buried.

References

Browne G.H., Strachan L. J., King P. R., Arnot M. J., 2006. Mass Transport Complexes from a Late Miocene Deep-Water Succession, Taranaki Basin, New Zealand: Scales, Styles, and Significance in Relation to Tectonic, Eustatic, andAutocyclic Drivers.Extended abstract prepared for AAPG Annual Convention, Houston, Texas, April 9-12.

King P. R., Ilg B. R., Arnot M., Browne G. H., Strachan L. J., Crundwell M., Helle k. 2011. Outcrop and Seismic Examples of Mass Transport deposits from Late Miocene Deepwater Succession, Taranaki Basin New Zealand. Mass-Transport Deposits in Deepwater Settings SEPM (Society for Sedimentary Geology) Special Publication No. 96, p. 311–348.

King P. R., Browne G. H., Arnot M., Slatt, R.M., Helle, K., Stromsoyen I., 2007b, An overview of the Miocene Mount Messenger Urenui Formations, New Zealand: a 2-D, oblique-dip outcrop transect through an entire third-order, progradational, deep-water clastic succession, in Nilsen, T.H., Shew, R.D., Steffens, G.S.,and Studlick, J.R.J., eds., Atlas of Deep-Water Outcrops: American Association of Petroleum Geologists, Studies in Geology 56, Ch.60, p. 238–240.

Chapter 5: Mass-transport deposits in the Semantan Formation, central Peninsular Malaysia
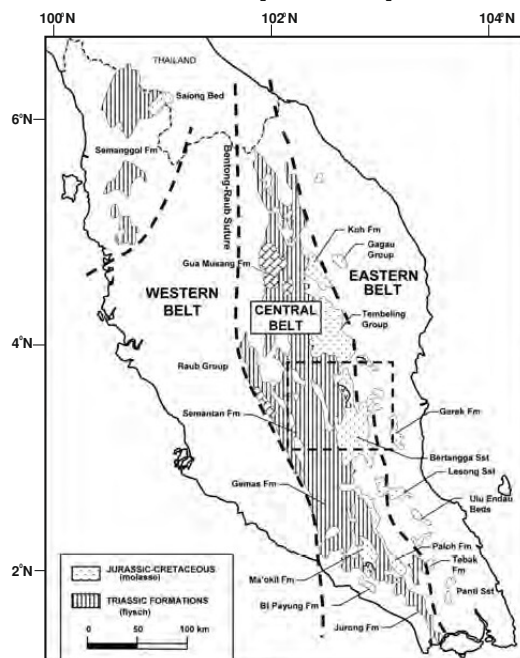

Figure 5.1. Simplified geological map of Peninsular Malaysia showing the pre- and post-indosinian formations (from Madon, 2010).

Geological Setting:

Peninsular Malaysia is divided into three north-south aligned structural domains: the West, Central and Eastern belts (Lee, 2009; Fig. 5.1).

The Central Belt region of Peninsular Malaysia, covering mainly central Pahang and Johor, is dominated by middle-upper Triassic flysch-like rocks, which are thought to represent a fore-arc "accretionary" complex (e.g. Hutchison, 1989). It represents the relict of, the Paleo- Tethys Ocean, a deep marine basin that once separated West and East Malaya.

Its western margin is marked by the Bentong-Raub Suture, comprising ophiolites and olistostromes, while the nature of its eastern margin remains inconclusive. Shale and tuffaceous siltstone sequences make up the bulk of the Semantan (Jaafar, 1976), are highly fossiliferous locally, but are mostly barren.

The depositional environment and origin of the Semantan Formation is still being debated. The apparent lack of imbrication and thrusting was quoted by Metcalfe & Chakraborty (1994) as evidence against the Semantan being an accretionary wedge or prism. The regional geology however, indicates that the Semantan basin was the foreland basin associated with the subduction and collision at the western margin of Eastmal.
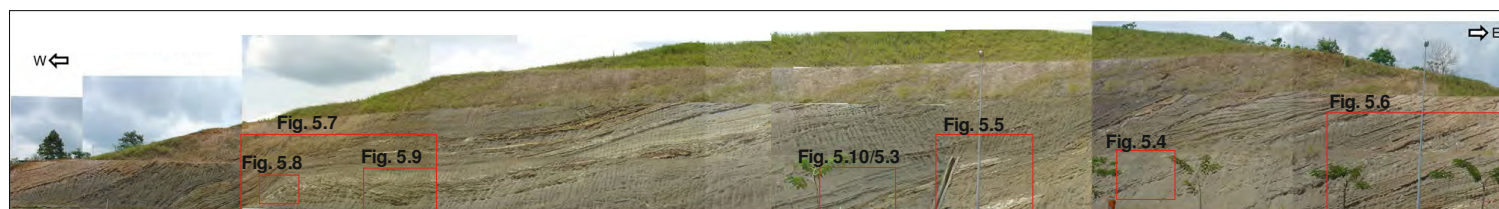

Figure 5.2. North face of the the Chenor outcrop, showing numerous sedimentary and deformational features. Towards the east, we see chaotic mud rich debrites with floating sandstone blocks alternating with zones of regularly bedded turbidites, with common occurrence od cross-cutting inclined surfaces. Towards the west, we see a distinctive sharp fold verging towards the west. In addition, there is a a zone of broken formation within the core of the fold. Way-up is to the west/left.

Isolated blocks

Figure 5.3. MTD with characteristic floating shale clast in sandy matrix. Hammer for scale.

Figure 5.4. MTD is characterised by sandstone blocks in argillaceous matrix. These sandstone blocks would probably not compromise the seal integrity because they isolated.
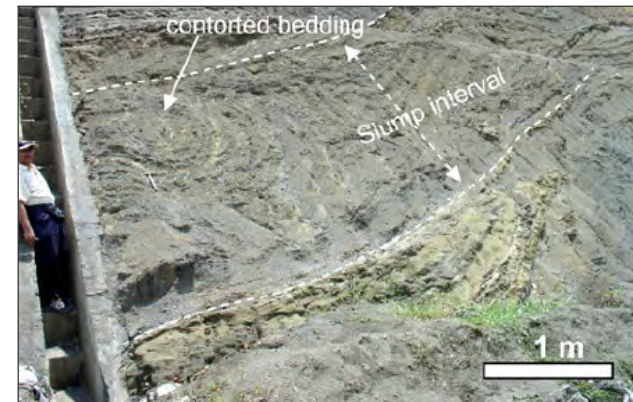
Slump beds

Figure 5.5. MTD showing chaotic bedding and convoluted layering as the result of syn-sedimentay deformation.

Figure 5.6. MTD showing chaotic and discontinuous bedding.

Folds and thrusts

Figure 5.7. Seismic scale asymmetric fold verging towards the east. Would the broken beds compromise seal integrity?
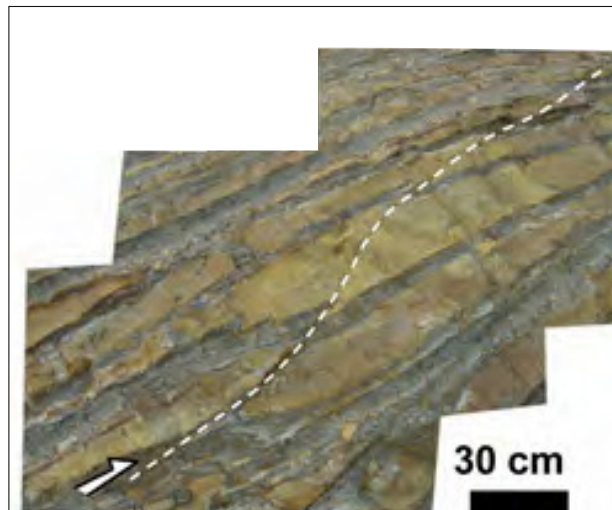
Figure 5.8. Here we see a minor thrust fault in sand-shale interbeds. Towards the western edge of the fold shown in Fig. 5. 7,

Broken beds

Figure 5.9. Here we see a different facies "broken beds" zone which consist of heterolithic sand-shale facies that have been fragmented by numerous small scale faults.

Figure 5.10.Thin beds of debrite intercalated with argilaceous zones
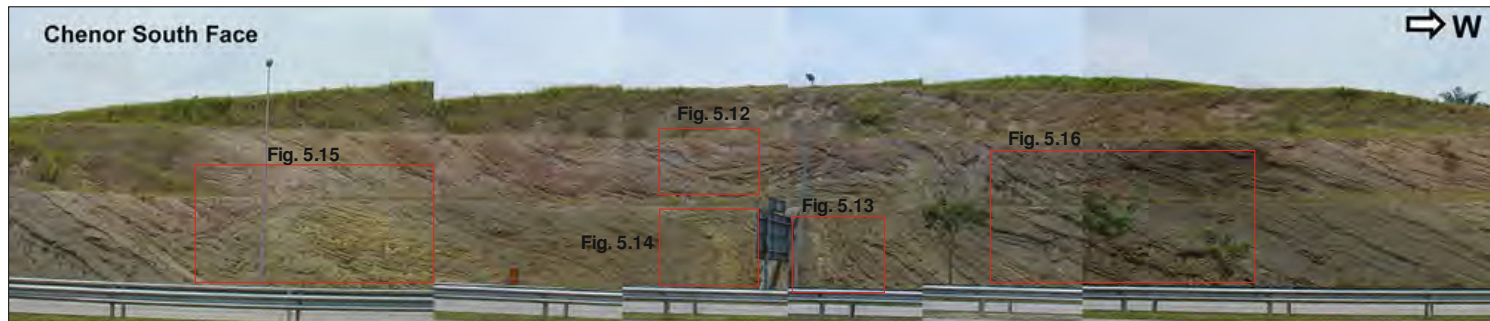
Figure 5.11. South face of the Chenor junction outcrop, showing a moderately dipping succession of debrites and turbidites, with common intercalations of MTD. Way-up is to the west/right.

Folds and thrusts
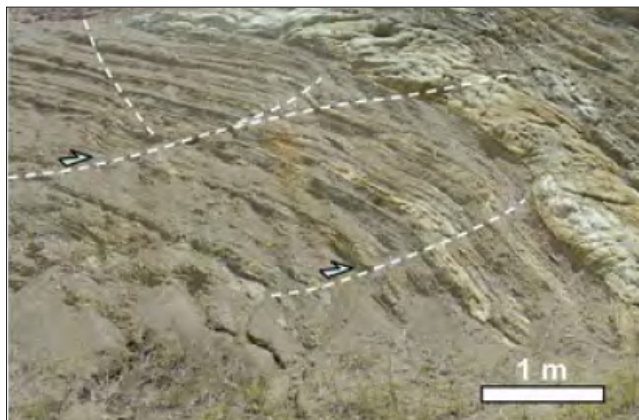
Figure 5.12. Small scale thrust and reverse faults in mud rich interval with thin beds of sandstone.

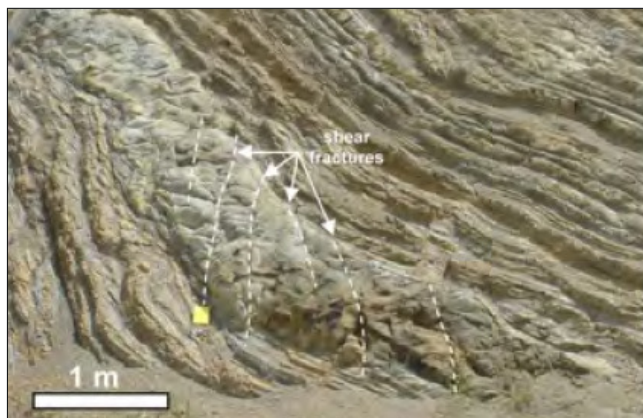**Figure 5.13.** Here we see tight folds with thrust surfaces.

Isolated blocks

Figure 5.14. Numerous shear fracture developed in sandstone block as a result of extension.

Figure 5.15. Large sandstone blocks enclosed in argillaceous matrix. Block has a different facies from surrounding road and appears to have been sourced from a different parent material.
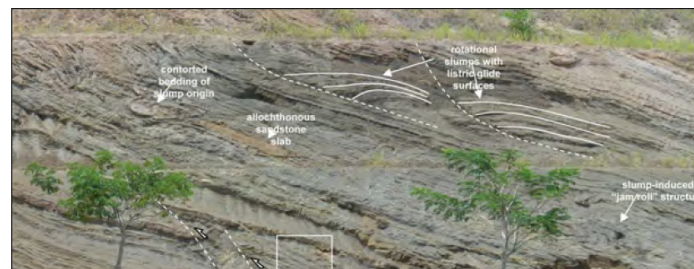
Figure 5.16. Here we see the rotational glide planes of the individual MTDs. Note the contorted bedding in the muddy intervals and minor faults.

Summary

1) The MTD in the Semantan Formation, exposed at the Chenor Junction (South- and north-facing cuts on either sides of the highway) reveal large gravity-slide blocks, slumps, debris flow deposits, and associated syn-sedimentary thrust faults and associated soft-sediment folds and glide surfaces.

2) In the lower part of the succession, sandstone-mudstone blocks (that are highly deformed internally by numerous meso-scale normal faults) are encased in a plastically deformed silty matrix.

References

Hutchison, C.S., 1989, Geological Evolution of South-east Asia. Oxford monographs on Geology and Geophysics no. 13, Clarendon Press, Oxford.

Jaafar Ahmad, 1976. The Geology and Mineral Resources of Karak and Temerluh Area, Pahang. Geological Survey of Malaysia Memoir 15: 127p.

Lee, C.P., 2009. Palaeozoic stratigraphy. In: Hutchison, C.S. & Tan, D.N.K., eds., Geology of Peninsular Malaysia. University Malaya and Geological Society of Malaysia, Kuala Lumpur, p. 55-86.

Mazlan Madon, 2010. Submarine mass-transport deposits in the Semantan Formation (Middle-Upper Triassic), central Peninsular Malaysia Bulletin of the Geological Society of Malaysia 56, 15 – 26.

Metcalfe, I. & Chakraborty, K.R., 1994. A stratigraphic log of Semantan Formation along part of the Mentakab-Temerloh Bypass, Pahang. Geological Society of Malaysia Bull., 35, 37-46.

Chapter 6: Mass Transport Deposit of the Dead Sea Basin
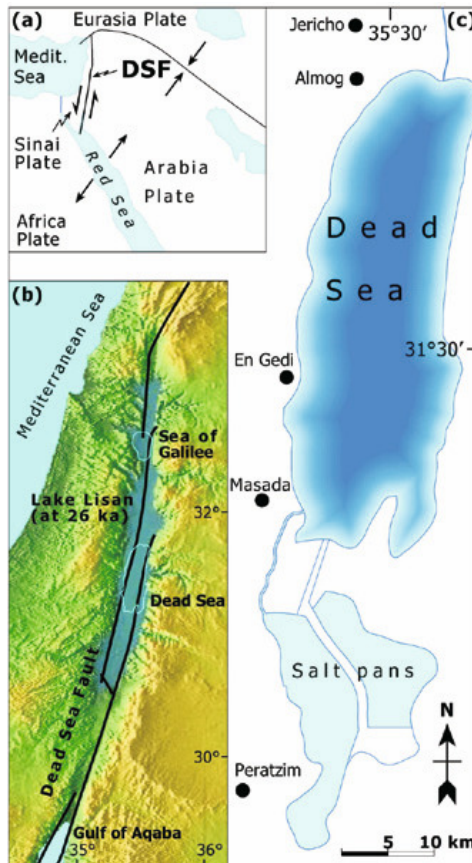

Figure 6.1.a) General tectonic map showing the location of the present Dead Sea. b) General map showing the maximum extent of the Lake Lisan along the Dead Sea fault at 26 ka. Map of the Dead Sea showing the localities where the outcrops are exposed (Alsop and Marco, 2012).

Geological Setting:

The Dead Sea Basin is a pronounced but relatively simple basin, where subtle slopes controlling gravity-driven slump complexes are exceptionally well preserved. Consequently it is an ideal place to study sediment deformation associated with slope failure.

The Basin is a pull-apart structure on the Dead Sea transform, which is marked by two parallel fault strands (Garfunkel and Ben-Avraham,1996) that generate numerous earthquakes with which to trigger slope failure and slumping (Migowski et al., 2004) The transform is considered to have been active since the Miocene, including during deposition of the Lisan Formation in the Late Pleistocene (70–15 ka) (e.g., Bartov et al., 1980; Garfunkel, 1981).
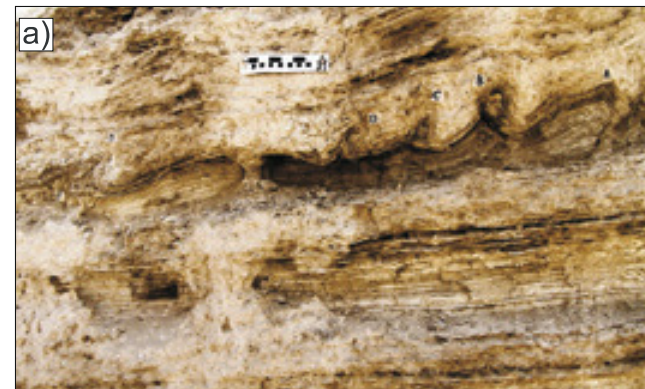

Figure 6.2. Upright slump fold showing angular hinge.

Slumping within the Lisan Formation is thought to have been triggered by seismic activity along the Dead Sea transform, with the very subtle depositional dips of <1° noted above controlling the direction of radial slumping toward the Dead Sea Basin (Alsop and Marco, 2012b). Slumped units are exceptionally well preserved, are typically less tha 1.5 m thick, and are capped by undeformed sediment of the overlying Lisan Formation (Alsop and Marco, 2011).
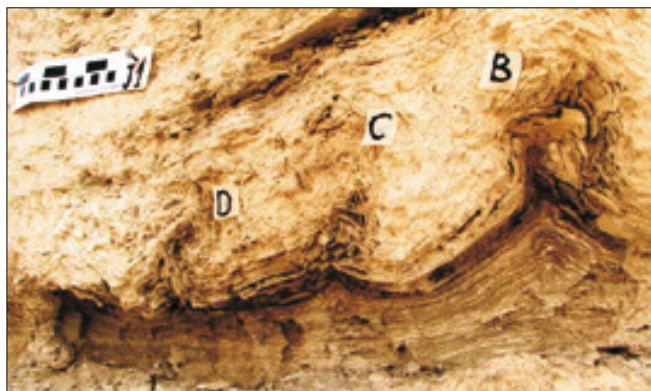
Small scale folds and thrust structures

Figure 6.3. Close-up of Fig.6.2 showing the upright slump fold in detail showing evidence if brittle deformation in the hinge.

Figure 6.5. Here we see upright to recumbent folds which tighten as they become overturned.

Figure 6.4. Slump sequence containing folds and thrust, which are overlain by undeformed horizontal beds. Notice the highly irregular upper surface.

Figure 6.6. Here we see recumbent slump folds with rounded hinges that display distinct asymmetry with thinning of fold limbs relative to the hinge.

Figure 6.7. Here is another example of a recumbent slump fold with rounded hinge.

Figure 6.9. Here is another example of a recumbent slump fold with faulted hinge.
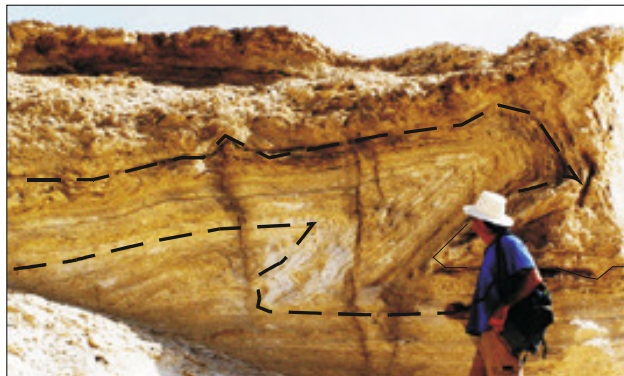

Figure 6.8. An example of a sub-recumbent slump fold (c. 2 m amplitude and 2 m wavelength) marked by well defined asymmetry and vergence.

Figure 6.10. Here we see a Large-scale thrusts associated with displacement up to c. 5 m which dies out upwards into the c. 5 m fold.

Mud-rich detachment

Figure 6.11. The <1.5m thick slump is consistently positioned above, a detachment on to, 5-10 cm thick mud-rich horizons that acted as weak decollement.

Figure 6.12. Here we see pronounced asymmetry to folds with vergence directed consistently towards the NNE. Notice how the mud infill the core of the folds.

Figure 6.13. As noted above, we see another example of pronounced asymmetry to folds as a result of simple shear modification of upright symmetrical folds.

Figure 6.14. Here we see a the weak mud-rich layer immediately above the detachment flows to fill the hinges of the fold and accommodate the parallel fold style in the overlying layers that are completely decoupled from the undeformed substrate

Figure 6.15. Representative photographs of folds from coherent portions of the slump at Peratzim. Note that bedding can be traced continuously around folds in coherent slumps,
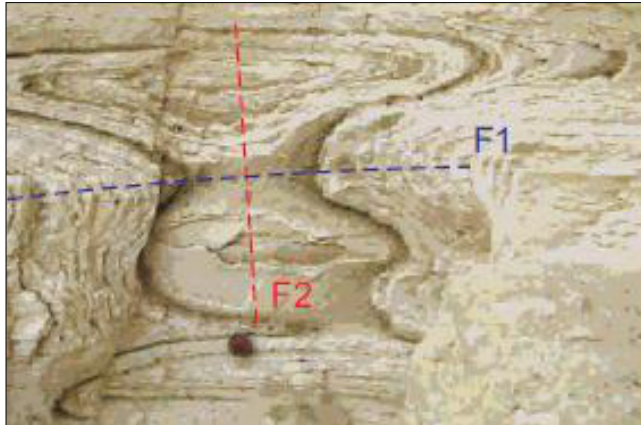
Refolded folds

Figure 6.17. Here we see original (F1) and superposed (F2) hinges and axial planes are both normal to one another resulting in classic dome and basin or egg box interference pattern.
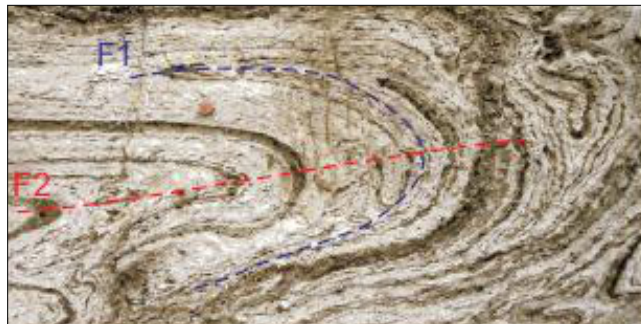

Figure 6.18. Here we see original and superposed hinges are coaxial and axial surfaces are at high angles to one another which results in classic hook or fish-hook interference pattern.
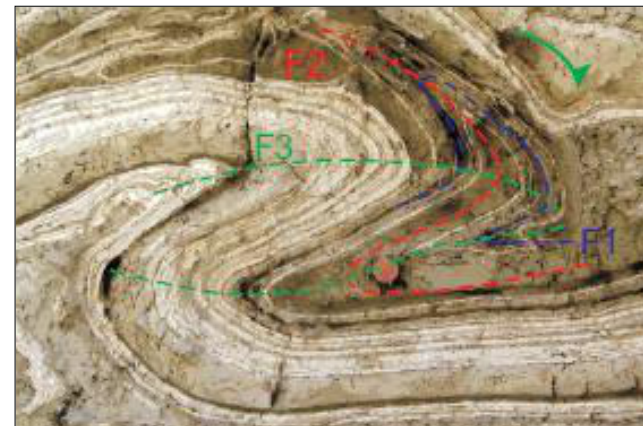

Figure 6.19. Here we see original and superposed hinges are normal to one another and axial surfaces are also at high angles resulting in a classic variety of angel wings, mushroom or boomerang interference pattern.

Figure 6.20. In some instances, up to 3 phases of folding are identified, such that F1-F2 interference patterns are themselves being re-folded by yet later (F3) folds generating complex refolded hook patterns
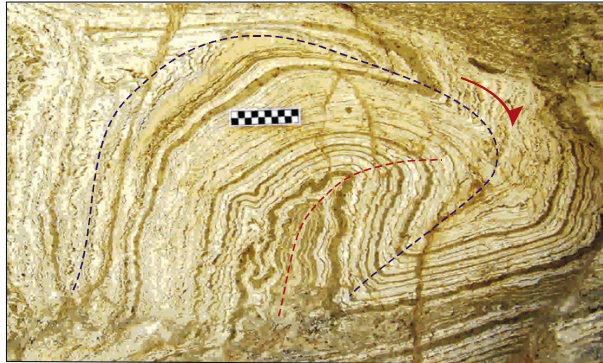
Spiral folds

Figure 6.21. Another example of Spiral fold that display curved axial surfaces (highlighted by blue and red dashed lines) that are wrapping around one another in sections parallel to transport.

5cm

Figure 6.22. Examples of sheath folds marked by elliptical eye-fold closures in sections normal to transport.
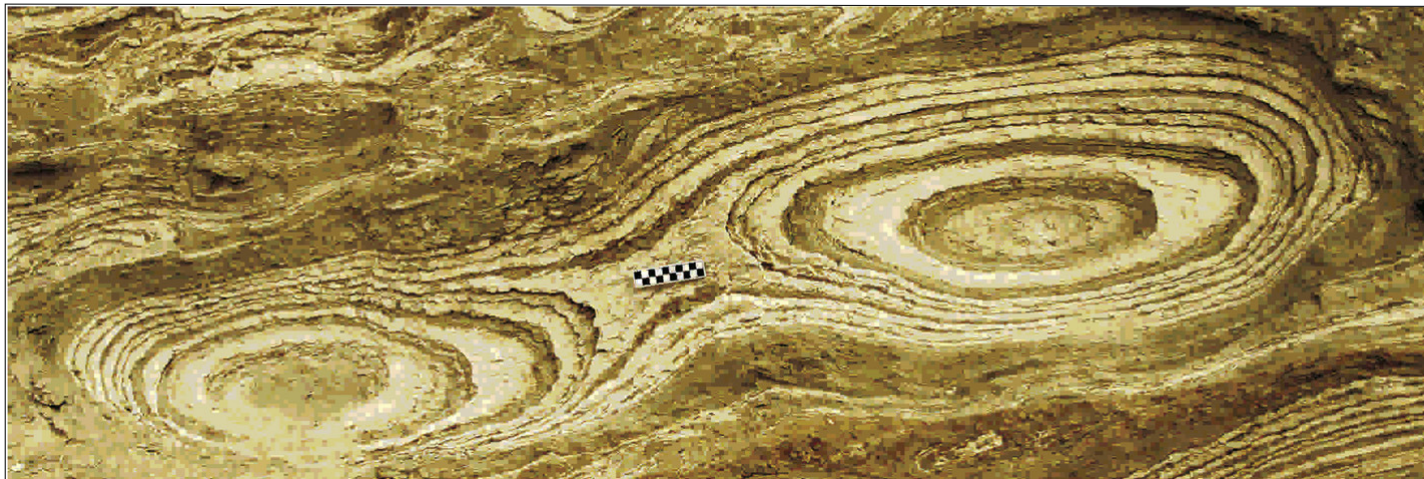

Figure 6.23. An example of Sheath folds that form multiple en-echelon closures that collectively form spectacle-shaped eye-fold closures

Summary

1) The MTD within the Lisan Fm is characterised by small scale folding and thrusting in distinct layers that are capped by overlying undeformed horizontal beds.

2) Different refold types can be observed within an individual slump sheet and thus implies that they were created during a single progressive deformation, rather than multiple phases of punctuated deformation.

3) The recognition that many slumps detach in, or just above, clastic and mud-rich horizons implies that fluids trapped within these units play a significant role in the slumping process.

References

Alsop, G.I., Marco, S. 2011. Soft-sediment deformation within seismogenic slumps of the Dead Sea Basin. Journal of Structural Geology 33, 433-457.

Alsop, G.I., Marco, S. 2012. A large-scale radial pattern of seismogenic slumping towards the Dead Sea Basin, Journal of the Geological Society v.169; p99-110.

Alsop, G.I., Marco, S. 2012b. Tsunami and seiche-triggered deformation within offshore sediments. Sedimentary Geology 261, 90-107.

Alsop, G.I, Marco, S., 2013.Seismogenic slump folds formed by gravity-driven tectonics down a negligible subaqueous slope, Tectonophysics doi: 10.1016/j.tecto.2013.04.004.

Bartov, Y., Steinitz, G., Eyal, M. & Eyal, Y. 1980. Sinistral movement along the Gulf of Aqaba—its age and relation to the opening of the Red Sea. Nature, 285, 220–221.

Garfunkel, Z. 1981. Internal structure of the Dead Sea leaky transform (rift) in relation to plate kinematics. Tectonophysics, 80, 81–108.

Garfunkel, Z. and Ben-Avraham, Z., 1996. The structure of the Dead Sea basin. Tectonophysics 266 (1-4), pp 155 – 176.

Migowski, C., Agnon, A., Bookman, R., Negendank, J.F.W., Stein, M., 2004, Recurrence pattern of Holocene earthquakes along the Dead Sea transform revealed by varve-counting and radiocarbon dating of lacustrine sediments: Earth and Planetary Science Letters, v. 222, p. 301-314.

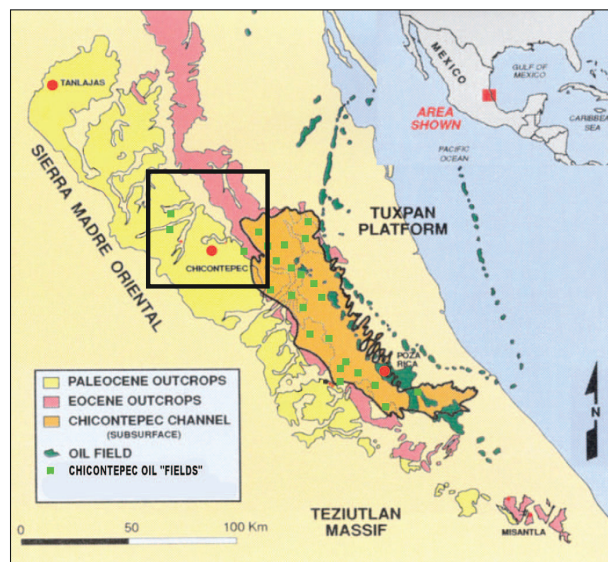# Chapter 7: Mass Transport Deposit in the Chicontepec Formation, Eastern Mexico.

Figure 7.1. The map shows the location of the study area (black box) in the northern part of the Chicontepec Outcrop belt, Eastern Mexico (from Cossey, 2011).

The basin is bounded to the north by the Tamaulipas Arch and the Sierra de San Carlos, on the west by the Sierra Madre Oriental, on the southeast by the Golden Lane platform (Tuxpan platform), and on the south by the Jalapa High and the Teziutlan Massif (Fig. 7.1).

Between the end of the Cretaceous and Eocene, the area was affected by active uplift and thrusting from the west, in the Sierra Madre Oriental, associated with the Laramide Orogeny. Thrusting in the Sierra Madre Oriental is interpreted to have occurred between the late Maastrichtian and the late Paleocene (Suter, 1984). Some overturned folds and reverse faults occur within the westernmost outcrops of the Chicontepec Formation, indicating that deformation continued after the Paleocene. By late Eocene time, uplift and erosion had proceeded to the extent that clasts of the Chicontepec sandstones were apparently eroded and deposited into the "molasse" deposits of the Tantoyuca Formation (Benavides, 1956), which are thought to mark the end of major orogenic activity to the west (Najera, 1952).

Geological Setting:

The Chicontepec Formation is exposed along the western margin of the Tampico Embayment, also known as the Tampico-Misantla Basin in the states of Veracruz, Hidalgo, and San Luis Potosi (Fig. 7.1). This area existed as a depositional basin throughout the Cretaceous, Paleocene, and Eocene (Enos, 1983) and was the site of deep-marine sedimentation during at least the latter part of this time period

Folds and thrusts

Figure 7.2. Coherent slump above basal glide plane (dashed). Movement of slump was from right to left (in a southeastward direction).
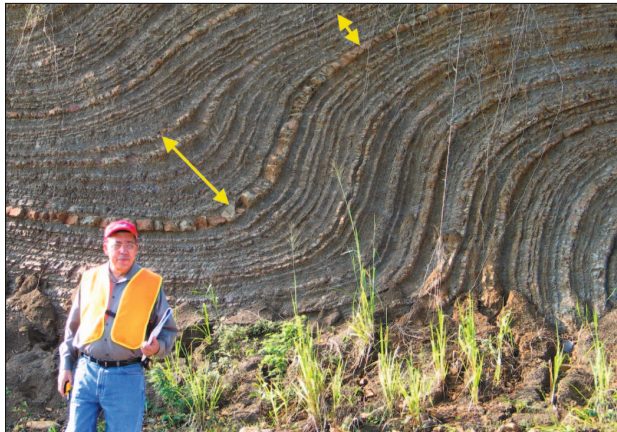

Figure 7.3. Close-up of figure 7.2. showing section thickening in synclinal axis and thinning in the anticlinal axis (arrows).
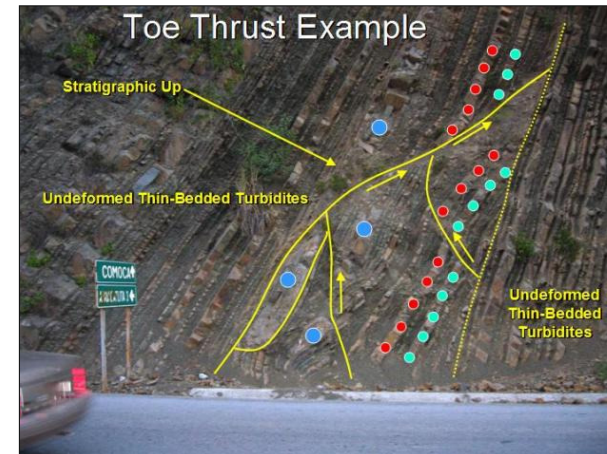

Figure 7.4. A preserved toe thrust immediately west. Beds stratigraphically above and below the toe thrust are undeformed (apart from structural deformation). Correlation across the syn-depositional faults is shown by colored dots.

Figure 7.5. MTD showing Syn-depositional thrust.
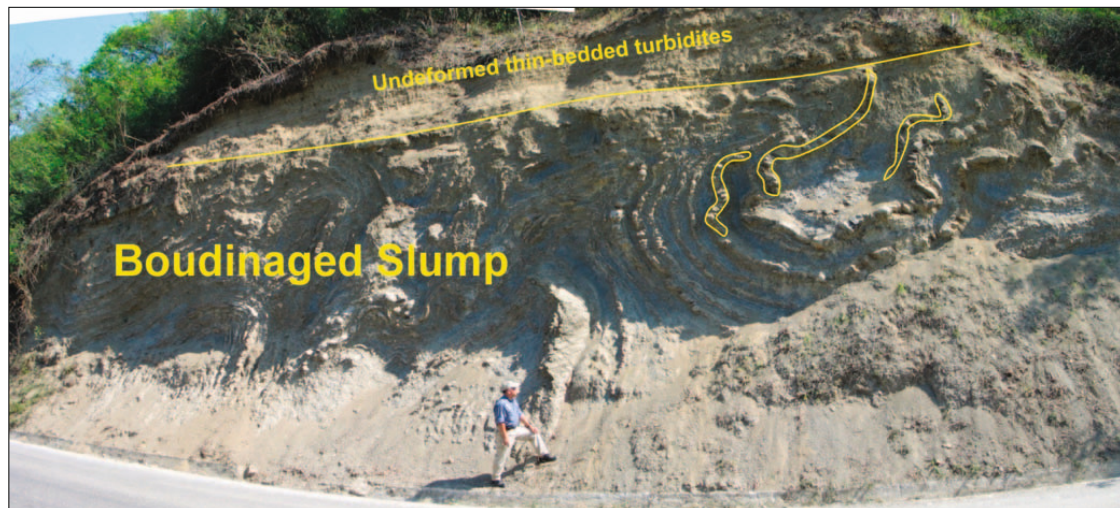
Boudinaged Slump

Figure 7.5. Boudinaged slump with overlying undeformed thin bedded turbidites between Atlapexco and Huejutla. Note the pinching and swelling of the sandstones in the right hand part of the slump (outlined in yellow). The high N/G would make this TD a poor seal.

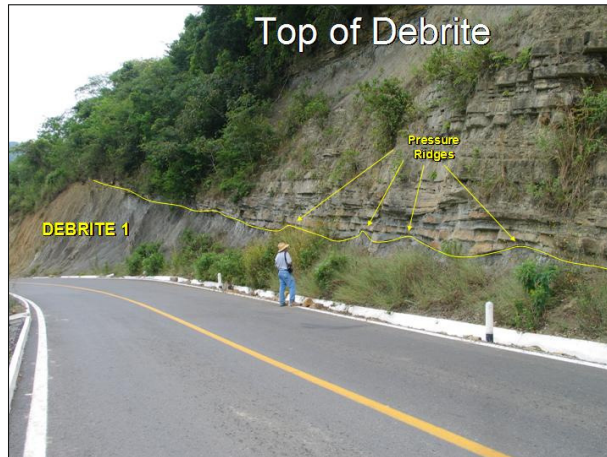
Figure 7.6. Another view of the Boudinaged slump

Upper surfaces

Figure 7.7. MTD is characterised by ridges and swales topography (interpreted as pressure ridges).

Figure 7.8. Close-up of Fig. 7.7 showing the pressure ridges in detail.

Figure 7.9. A large "boulder" floating at the top of Debrite 1
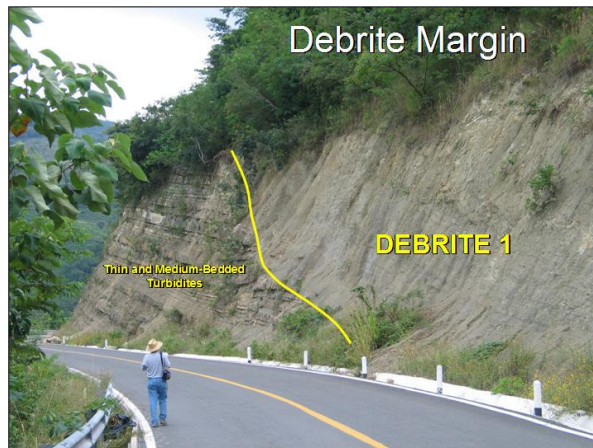
Lateral margins

Figure 7.10. Lateral margin of debrite 1.

Figure 7.11. Lateral margin of Debrite 1, showing two small margin faults and the apparently erosional base
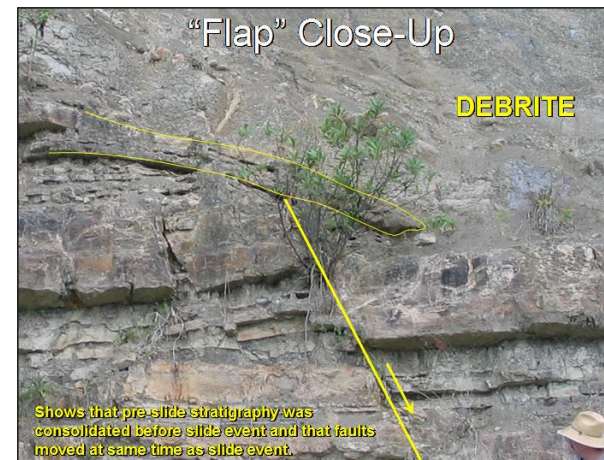

Figure 7.12. Here we see a thin sandstone bed draped over debrite margin fault. Can the thin sandstone bed act as a carrier bed?

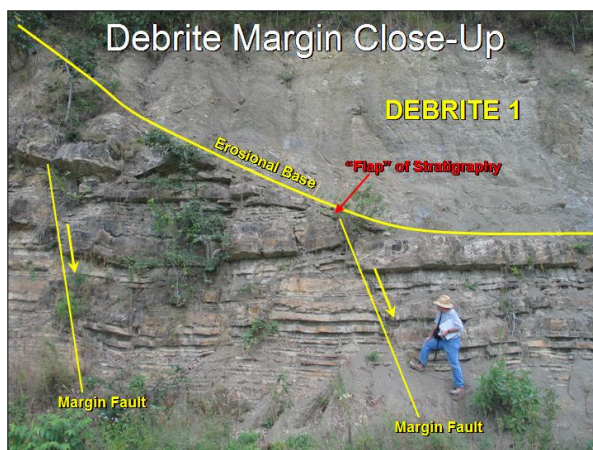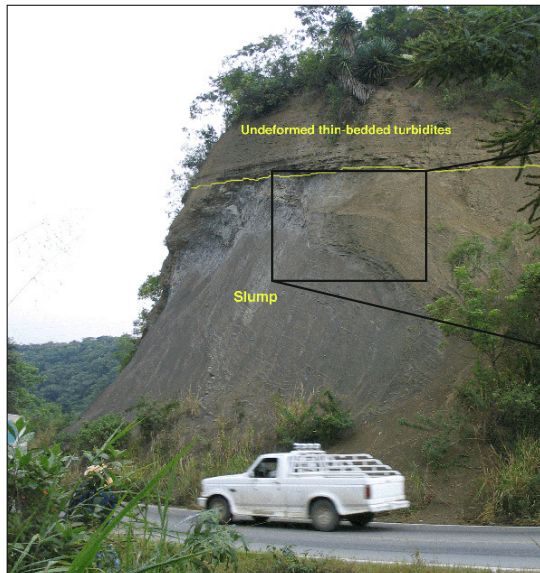**Figure 7.13.** Massive sand dominated slump. Cliff height is c. 20 m.
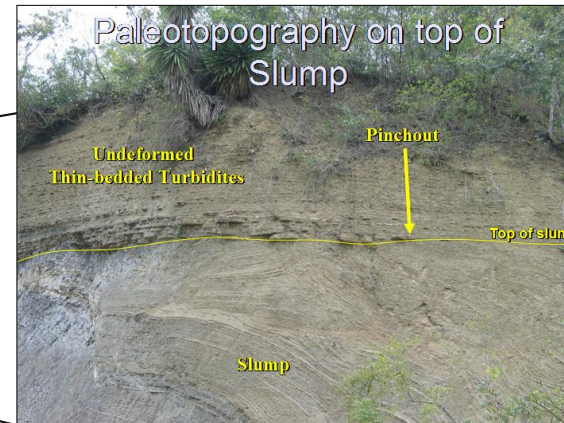

Figure 7.14. Pinchout of a single medium bedded sandstone on top of slumped unit
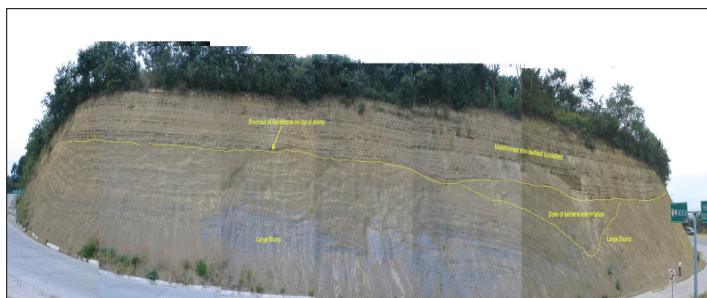
Figure 7.15. Photo showing faulted slumps, a younger chaotically slumped unit and undeformed turbidites overlying the slumped unit exposed near Atlapexco.

Figure 7.16. Close-up of figure 7.15 showing the faulted MTD in detail. Would these faults compromise seal integrity?

Figure 7.17. Here we see a chaotic MTD on the road between Atlapexco and Calnali. Note extremely flat base of slump with no evidence of erosion and the calcite-filled fracture (red arrow), which terminates at the base of the MTD

Figure 7.19. Cross beds within debrite.

Figure 7.18. Less chaotic MTD. Also notice the pinch-out of two medium bedded sandstone beds on top of slumped unit

Figure 7.20. Thin scale slump unit.

Summary

1) The MTD within the Chicontepec Formation is characterised large variety of slump types.
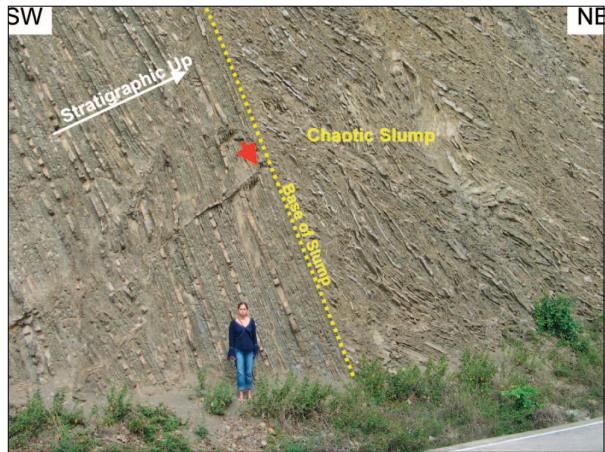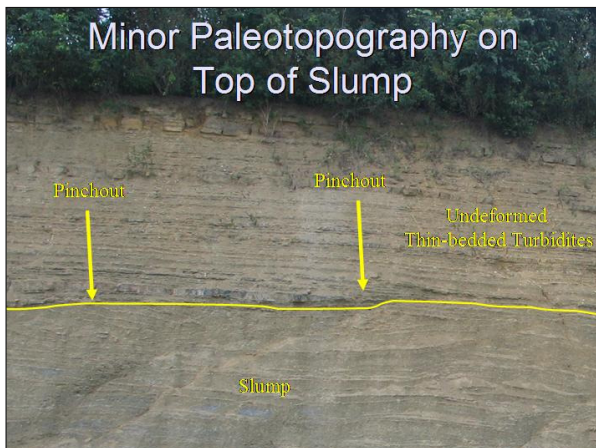
2) Most of the slumped units show very flat tops, indicative of bypass erosion after the slump event. In all slump types, the base will be much more difficult to identify than the top.

3) At their margins, the debrites preserve evidence of erosion or failure of at least partly consolidated turbidites, indicating very large-scale failure events creating low areas on the slope which were then subsequent focal points for large debris flows.

References

Benavides, L., 1956, Notas sobre la geologia petrolera de Mexico: Symposium on Accumulations of Oil and Gas, 20th International Geological Congress, v. 3, p. 351–562.

Cossey Stephen P.J., 2011, Mass transport deposits in the Upper Paleocene Chicontepec Formation, Mexico, in: Shipp C. R., Weimer P., Posamentier H. W., (eds)Mass-Transport Deposits in Deepwater Settings. Society for Sedimentary Geology (SEPM) Special Publication No. 96, p. 269–277.

Enos, P., 1983, Late Mesozoic paleogeography of Mexico, in Reynolds, M.W., and Dolly, E.D., eds., Mesozoic Paleogeography of the West-Central United States: SEPM, Rocky Mountain Section, Rocky Mountain Paleogeography, v. 2, p. 133–157.

Najera Chiapa, H., 1952, Estudio de las formaciones del Eoceno en la region de Poza Rica: Asociacion Mexicana de Geologos Petroleros, Boletin, v. 4, nos. 3-4, p. 71–115.

Suter, M., 1984, Cordilleran deformation along the eastern edge of the Valles–San Luis Potosi carbonate platform, Sierra Madre Oriental Fold-Thrust Belt, East–Central Mexico: Geological Society of America, Bulletin, v. 95, p. 1387–1397.

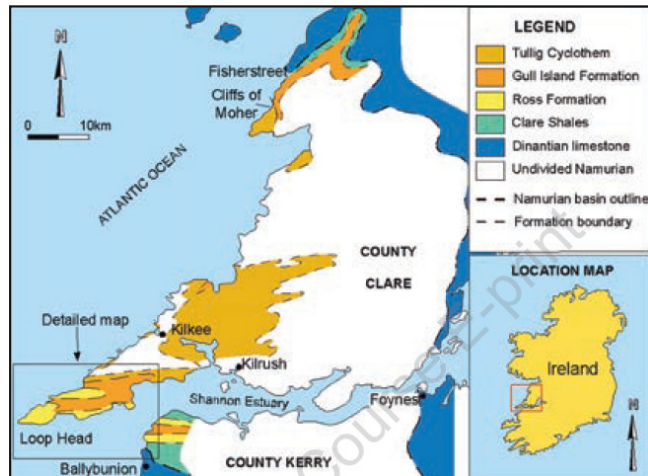# Chapter 8: Mass Transport Deposit of the Gull Island Formation, Ireland.

Figure 8.1. Location map of Ireland, with the rectangle showing the enlarged area of county clare. Colors marks the different Carboniferous formations (from Lien et al., 2007).
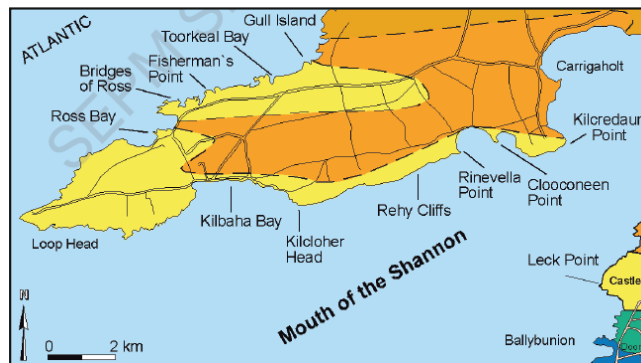

Figure 8.2. Detailed map of Loop Head Peninsula.

Geological Setting:

Upper Carboniferous (Namurian) outcrops in western Ireland lie in a N-S-trending zone divided by the Shannon Estuary (Fig. 1). A recent study (Martinsen 1987) showed that all the Namurian rocks in western Ireland appear to have been deposited within the same basin, and a regionally more valid name, the Western Irish Namurian Basin, was suggested. The basin was initiated during the Dinantian by NNW-SSE extension, probably associated with a minor right-lateral strike-slip component (Martinsen 1987).

Figure 8.3. Mud-rich MTD(Ross Slide) overlain by undeformed thin bedded sandstone sheets (from Lien et al., 2007).

Sedimentation in the early Namurian was dominated by basinal mudstones and shales(Clare Shales) which pass gradually upwards into the Ross Formation which, in the central parts of the basin, is represented by thick sandy turbidites with no apparent systematic vertical sequences. On the basin margins, this formation is only represented by thin shales. Conformably above and separated from the Ross Formation by the Reticuloceraspaucicrenulatum marine band lies the Gull Island Formation. In the lower part, this comprises extensively deformed slope deposits dominated by mud slumps and turbidites, while the upper part contains mud slumps and undeformed mudstone.

Mud dominated MTDs
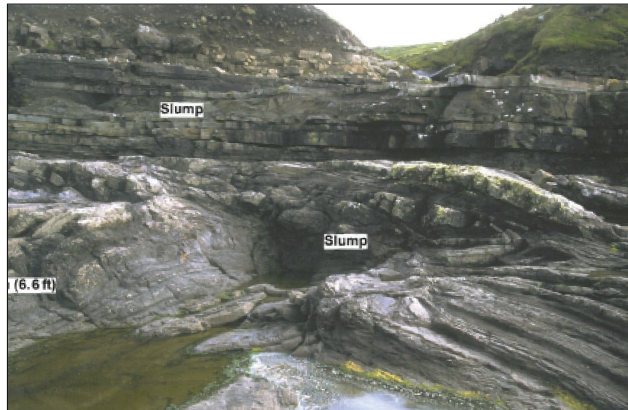
Figure 8.4. Sandstone sheets separated by mud dominated slump units at Fishers street, County Clare (from Martinsen and Lien 2007).
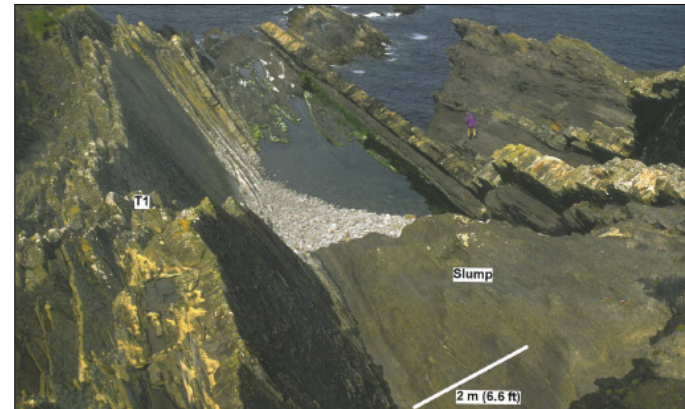
Figure 8.6. MTD interbedded with thin beded sandstone units exposed at the Gull Island, County Clare. Note person for scale(from Martinsen and Lien 2007).

Figure 8.5. Again here we see mud dominated slump units and sandstone sheets occuring together exposed at souhern Gull Island(from Martinsen and Lien 2007).

Figure 8.7. Another example of mud-rich MTD exposed at Ballybunion, County Kerry, in the basin axis (from Martinsen and Lien 2007).

MTD Scars

Figure 8.8. Here we see two upper-slope slump scars and fill of mass-transport deposits from the Upper Carboniferous Gull Island Formation. Their lower boundaries are marked with dashed lines, and their upper boundaries by stippled lines. Note floating rafts of sandstone in the mass-transport deposit. Cliff is approximately 50 m high (Posamentier and Martinsen 2011).

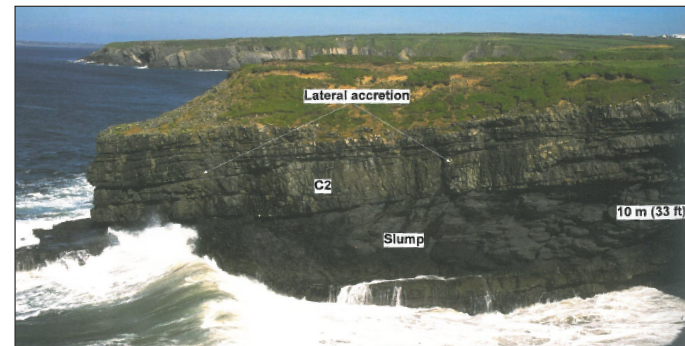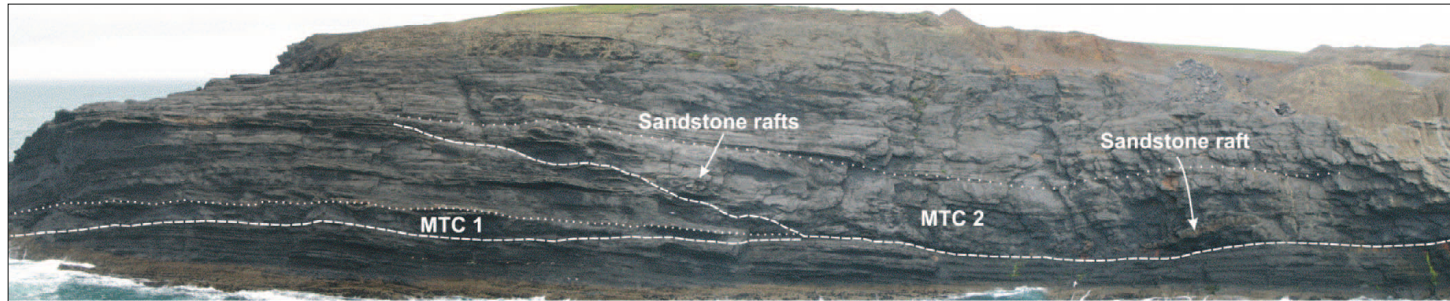Scars dominate many upper-slope areas of modern slopes and are also commonly seen in seismic sections. These features can usually be differentiated from channels cut by turbidity currents by their lower aspect ratios (lower depth/width ratios) and by their fill, which usually is composed of MTDs or undeformed mudstones, if the mass-transport deposit is transported out of its scar.

The extensive soft-sediment deformation present within the Gull Island Formation was probably induced by a combination of differential subsidence in the basin causing delta-slope oversteepening, high sediment accumulation rates leading to under consolidation and local rapid loading by deposition from turbidity currents.

Figure 8.10. Photograph of part of a slumped channel margin in an upper-slope setting, Upper Carboniferous Gull Island Formation. Note growth-faulted (indicated by dash line) nature of deformation with increase of turbidite - bed thickness across faults, suggesting that these faults were active during deposition (Posamentier and Martinsen 2011).

Pressure Ridges
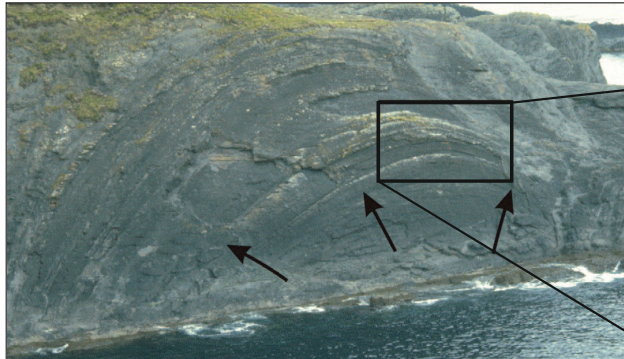
Figure 8.11. Planview expression of pressure ridges at the downslope end of minor slide. Beds dip steeply towards viewer, and the movement direction was probably towards top left of the picture as indicated by the arrows. Height of the cliff is approximately 25 mPosamentier and Martinsen 2011).
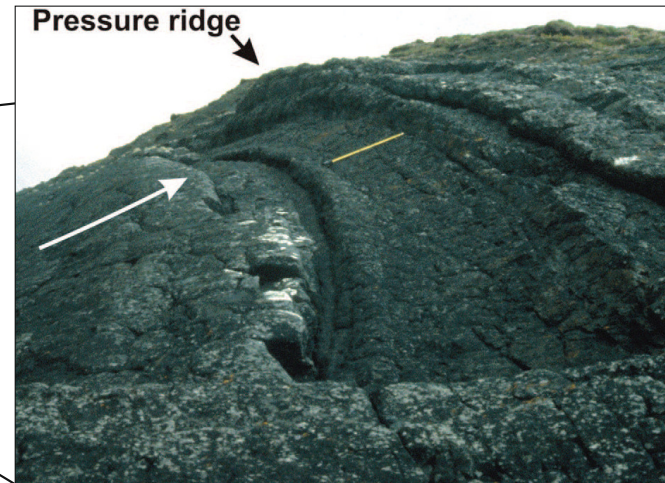
Pressure ridge

Figure 8.12. Close-up of pressure ridges in fig. 8.11 viewed obliquely up-section from right to left. Ridges are clearly expressed, and the depression immediately left of measuring tape in Part B is the surface expression of a thrust plane, separating the ridge on the left from the ridge on the right. Direction of thrusting was to the right as indicated by the arrow. Measuring tape is 1 m long.

Strain overprinting in MTDs
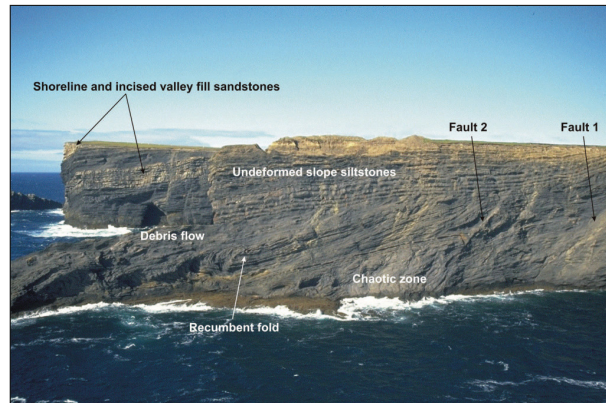
Figure 8.13. Here we see a complex upper-slope MTD in which two extensional faults overprint already existing recumbent fold stucture. The cliff is approximately 50 m high(from Posamentier and Martinsen 2011).

Figure 8.14. A classic example of a thrust fault overprinting a recumbent fold indicating that the mass-transport deposit stopped at its downslope margin first and that subsequent structures developed in an overstep fashion rather than in a piggy-back fashion(from Posamentier and Martinsen 2011)

Rugose Upper Surface of MTDs

Figure 8.15. Here we see the rugose top of an MTD. Note change in deformational style from near to far outcrop (lower left to upper right) of the mass-transport deposit where it appears as a debris-flow deposit (debrite) with extensive internal deformation in the near view and a slide in the back view with only little internal deformation.Person for scale in foreground (from Posamentier and Martinsen 2011).

Summary

1) Most of the MTDs observed in the Gull Island Formation, Ireland are mud dominated.

2) MTDs fill scars that dominate many upper-slope areas of modern slopes and are also commonly seen in seismic sections.

3) Evidence of strain overprinting is observed.

4) MTDs experience a rapid change of deformational style which is reflected in outcrops. Furthermore, it shows that MTDs are part of a continuum of deposits formed by changing processes, depending on internal strain and local factors.

References

Lien T., Martinsen O. J., Walker R., 2007, An Overview of the Ross Formation, Shannon Nasin, Western Ireland, in Nilsen, T.H., Shew, R.D., Steffens, G.S., and Studlick, J.R.J. eds., Atlas of Deep-Water Outcrops: American Association of Petroleum Geologists, Studies in Geology 56, Ch. 49, p. 192–195.

Martinsen, O.J., 1987, Sedimentology and Syndepositional Deformation of the Gull Island Formation (Namurian R1), Western Irish Namurian Basin, Ireland—With Notes on the Basin Evolution [unpublished Cand. Scient. thesis], Geological Institute, Dep. A, University of Bergen, Bergen, Norway, 327 p.

Martinsen O. J., Lien T., 2007, Contrasting styles of slope deposition in the Gull Island Formation, Ireland, in Nilsen, T.H., Shew, R.D., Steffens, G.S., and Studlick, J.R.J. eds., Atlas of Deep-Water Outcrops: American Association of Petroleum Geologists, Studies in Geology 56, Ch. 53, p. 210–214.

Posamentier H. W., Martinsen O. J., 2011, The Character and Genesis of Submarine Mass Transport Deposits: Insights from Outcrop and 3D Seismic Data, in: Shipp C. R., Weimer P., Posamentier H. W., (eds) Mass-Transport Deposits in Deepwater Settings. Society for Sedimentary Geology (SEPM) Special Publication No. 96, p. 7–38.

Chapter 9: Miscellaneous Mass Transport Deposit Outcrops

Is there evidence for liquefaction in outcrops?

Figure 9.1. Large slump resulting in almost complete disruption of bedding, Carboniferous Bude Sandstones at Efford, southwest England (from Posamentier and Walker 2006).

Figure 9.3. Here we see an MTD involving stratified blocks in the Upper Cretaceous Great Valley Sequence, Lake Berryessa, California. The two heavy black lines show bedding (top to the left). The matrix is a silty mudstone with a large variety of pebbles and cobbles. The stratified blocks consist of layers of sandstone and mudstone. Slumped bed is about 7 m thick (from Posamentier and Martinsen 2011).

Figure 9.2. Floating clasts in a thin debrite, Eocene slope strata of Sant Llorenc del Munt, northeastern Spain. Note the highly incisive base of the bed (arrowed), a feature also seen at much larger scales on continental margins (from Posamentier and Martinsen 2011).

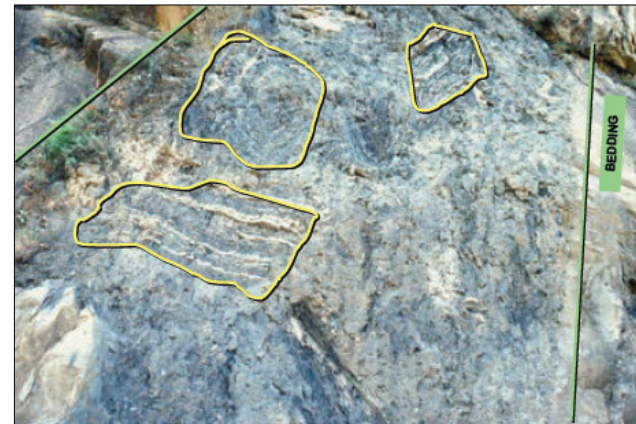# Strain overprinting

Figure 9.3. Small scale examples of folds and faults in a slump from West Wales (ordovician).

Figure 9.4. Here we see another small scale examples of recumbent fold and faults in a slump from West Wales (ordovician).

Seismic scale fold

Figure 9.5. Here we see huge (seismic scale) complex MTD from Antarctica. Note the thrust out recumbent fold (black arrow).

Figure 9.6. Here is another seismic scale upright fold. Cliff height is c. 50 m.

Figure 9.7. Isoclinal recumbent folding in the complex middle Miocene Gordo megabed mass-transport deposit in the Tabernas Basin, southern Spain. Note the tripartite structure with a lower slumped unit, truncated by a middle graded sandstone (turbidite or debrite) and a mudcap. General transport direction was from left to right. Note people in foreground for scale. This is an example of the linked nature of several processes within mass-transport deposits (from Posamentier and Martinsen 2011).

Sand dominated MTDs
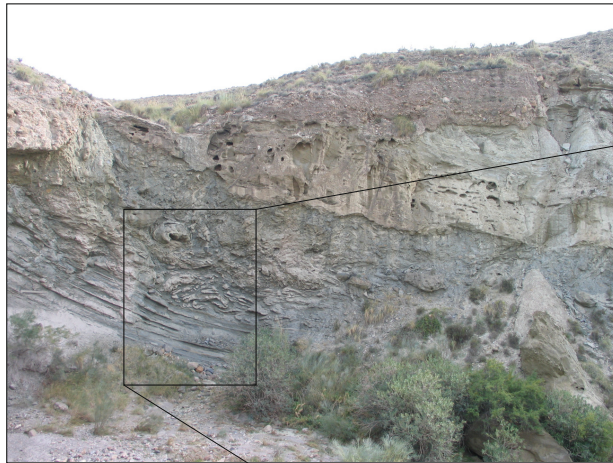
Figure 9.8. Gordon megabed.
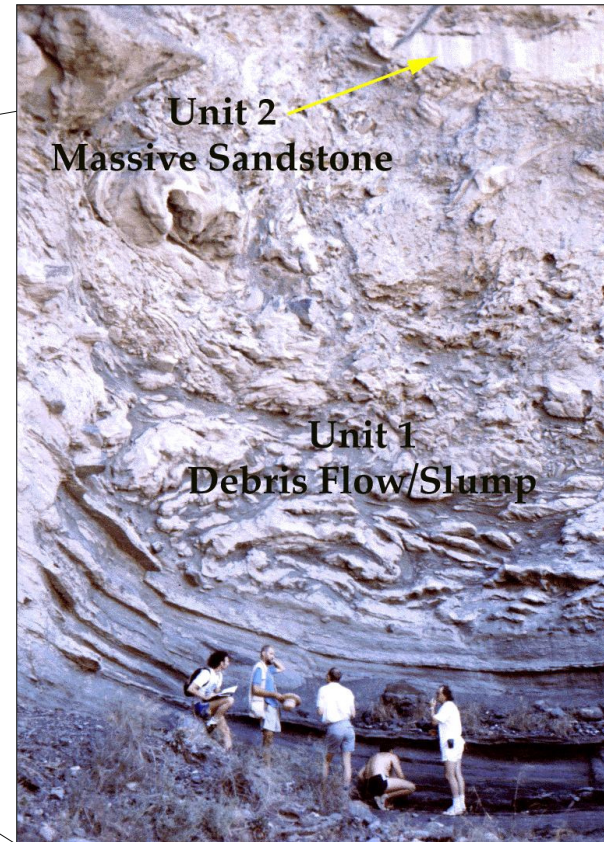
Figure 9.9. Here we see evidence of sand dominated MTD in the Gordon megabed. Such high N/G MTD would constitute a poor seal (from Cossey, 2006).

MTD Scars
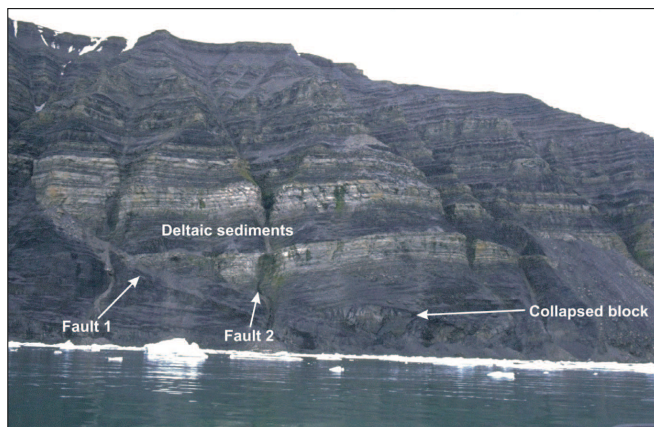
Figure 9.10. A growth-fault complex in shelf-edge mega-slide head zone with two closely spaced faults (arrowed) in Triassic deltaic strata, Edgeøya, Svalbard. This slide cuts approximately 150 m of section, and the cliff is approximately 400 m high Note also the collapsed block at the base of the cliff above the upper fault (from Edwards,1976).

Figure 9.11. Channelised sandstones onlap (orange arrows) the underlying MTD exposed at Labuan Island, East Malaysia, northwest Borneo . MTD consist of folded and sheared claystone/sandstone. Deformed internal bedding in MTD is shown by green dotted lines; faults are shown by red dotted lines. Note people for scale. Stratigraphic top is to the left (from Posamentier and Martinsen 2011).

Summary

1) The block in matrix texture observed in outcrop could possibly suggest evidence for liquefaction in MTDs.

2) Faults cross-cutting folds suggest the common overprinting of contractional structures by extentional structures in MTDs.

3) Although MTDs are often thought to be mud dominated, we see evidence in outcrops that they can also be sand dominated.

References

Cossey Stephen P. J., 2006, Photos from our fieldwork. http://www.cosseygeo.com/images/gallery/folder/Tabernas

Cossey Stephen P. J., 2011, Mass transport deposits in the Upper Paleocene Chicontepec Formation, Mexico, in: Shipp C. R., Weimer P., Posamentier H. W., (eds)Mass-Transport Deposits in Deepwater Settings. Society for Sedimentary Geology (SEPM) Special Publication No. 96, p. 269–277.

Edwards, M., 1976, Growth faults in upper Triassic deltaic sediments, Svalbard: American Association of Petroleum Geologists, Bulletin, v.60, p. 341–355.

Posamentier H. W., Walker R. G. 2006 Deep-Water Turbidites and Submarine Fans , in: Posamentier H. W., Walker R. G. (eds) Facies Models Revisited, SEPM Special Publication No. 84, 2006 p. 397–520.

Posamentier H. W., Martinsen O. J., 2011, The Character and Genesis of Submarine Mass Transport Deposits: Insights from Outcrop and 3D Seismic Data, in: Shipp C. R., Weimer P., Posamentier H. W., (eds)Mass-Transport Deposits in Deepwater Settings. Societyfor Sedimentary Geology (SEPM) Special Publication No. 96, p. 7–38.

Chapter 10: Lessons learned from Mass Transport Deposit Outcrops

The preceding chapters in this atlas have presented detailed analysis of the architecture of mass transport deposit outcrops from a diverse range of geological settings. Unlike seismic-scale studies of MTDs, where interpretation of seismic facies can be sometimes ambiguous due to seismic resolution, this outcrop atlas has shown that the internal architecture of MTDs generally exhibit substantial lateral and vertical variations both in composition and structure. It is also important to note here that many of the structures are below seismic resolution.

Several common observations from the outcrops atlas are summarised below:
1) Contractional domain structures e.g thrusts, recumbent folds, upright folds appear to be the most common deformational structures observed (Fig. 10.1). There are evidences of the preservation of stratigraphic beds within these structures and this is seen in almost all the field examples. The whole thickness of the mass-transport deposit appears quite well organized with beds exhibiting a higher degree of stratigraphic continuity.

Figure 10. 2. Large-scale thrusts associated with displacement up to c. 5 m which dies out upwards into the c. 5 m fold(From Alsop and Marco 2012).

Conversely, these structures can be intensely deformed such that different polyphase fold types can be observed within an individual slump sheet and thus implies that they formed during a single progressive deformation, rather than via multiple phases of punctuated deformation.

2) Strain overprinting is common within mass-transport deposits and it may be complex and heterogeneous and can occur at any scale in contractional zones (Figs.10.3 and 10.4).
In the Antarctica example (Fig. 10.3), the mass transport deposit is dominated by compression, with semi-brittle strains superimposed on earlier more penetrative ductile strains indicating a complex strain history during transport. It is quite rare, however, to find extensional structures being overprinted by contractional structures.
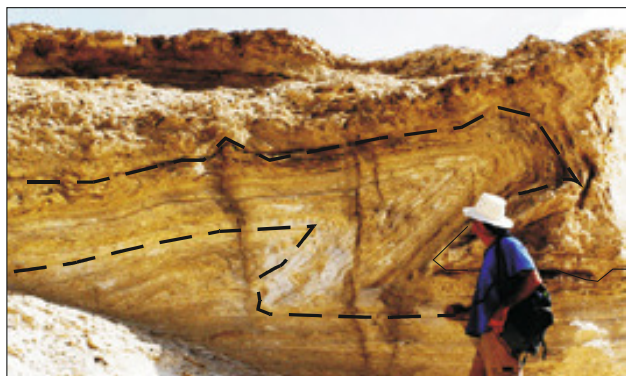

Figure 10. 1. A) An example of a sub-recumbent slump fold (c. 2 m amplitude and 2 m wavelength) marked by well-defined asymmetry and vergence (From Alsop and Marco 2012).

Figure10. 3. Seismic scale complex MTD from Antarctica showing the nose of a recumbent fold being cut-out by a thrust.
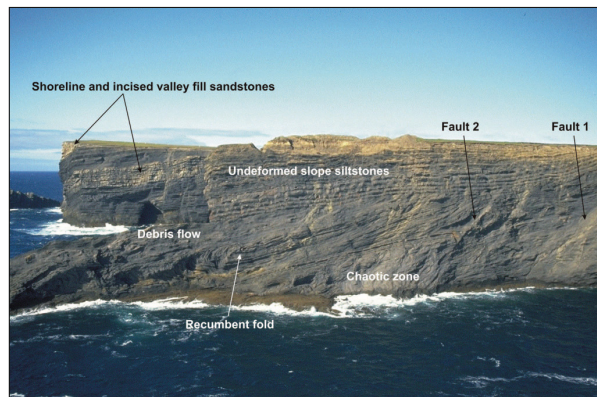
Figure10. 4. Complex upper-slope MTD in which two extensional faults overprint already existing recumbent fold structure (from Posamentier and Martinsen 2011).

3) Extensional domain structures such as growth faults are potentially both source and staging areas for major MTDs such as the example shown in Figure 10.5. Although, there are very few good examples of the extensional and/or translational domain. However, it is possible that these domains may evolve in time and space.
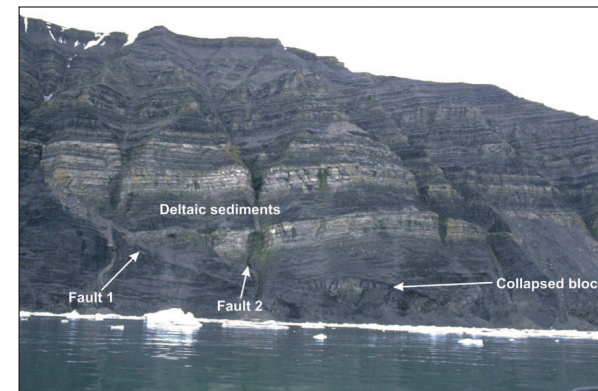
Figure 10. 5. A growth-fault complex in shelf-edge mega-slide head zone with two closely spaced faults (arrowed) in Triassic deltaic strata, Edgeøya, Svalbard. This slide cuts approximately 150 m of section, and the cliff is approximately 400 m high. Note also the collapsed block at the base of the cliff above the upper fault (from Edwards 1976).

4) Where basal basal detachments are present, they are usually sharp with more or less translational upper surfaces. It was also observed that many slumps detach in, or just above, clastic and mud-rich horizons. Stratigraphic jumps of the basal shear surfaces are also evident in some examples.


Figure 10.6. An example of a concordant basal surface, that detaches on a mud-rich horizon. Cliff height is 10 m.

5) There is also the widespread occurrence of fine-grained unsorted matrix and remnant stratified blocks in many outcrop examples. These two lithological associations emerge therefore as a common and fundamental internal component which could possibly suggest that at least some MTDs experience liquefaction during the general disaggregation process that transforms the original sediment into failed mass (Fig. 5.7).

Figure 10.7. Large slump resulting in almost complete disruption of bedding, Carboniferous Bude Sandstones at Efford, southwest England (from Posamentier and Walker 2006).

6) Mass-transport complexes are usually made up of zones of incoherent slump deposits intercalated with well-bedded turbidite/debrite facies. The association of incoherent mass-flow units with the more well-stratified deposits reflects the close spatial and temporal relationship between submarine mass-transport events and turbidity flows i.e. there is a spectrum of gravity flow deposits in any single MTD.

Figure10. 8. Intercalation of incoherent and well bedded turbidite facies that have been folded and over-turned from New, Zealand. Cliff height is c. 50 m.

Some of these features observed at outcrop scale are also seen at seismic scale, suggesting scale independence of genetic processes. In the following section, we introduce the three main MTD seismic facies types proposed in the Caprocks meeting presentation (see Durham, July 2013), providing unequivocal outcrop examples (Fig. 10.9). We try to place outcrop examples into this facies classification, recognising the inherent difficulty of scaling up from outcrop to seismic scales. Although details of folding and faulting are limited by seismic resolution, our direct observations of slump folds and their associated regional patterns allow greater controls and confidence to be placed on such seismically imaged systems.

1) Layered seismic facies

The layered unit are the least well observed unit in this atlas and it is a stratified less deformed unit which commonly exist as thin packages (< 100 m). In most cases the layered unit is crosscut by faults.

2) Blocky seismic facies

The blocky facies is defined here as a discrete components (meter- to hundreds of meter-sized possibly up to km-scale), with some degree of internal coherence and primary features and thus can be separated from the background lithologies (i.e.matrix).

3) Amorphous seismic facies

The amorphous unit (otherwise known as matrix) is defined by relatively fine-grained unsorted lithology of a mass transport deposit, which envelopes, injects and in most cases, sustains discrete slide elements ranging from km-scale slabs to mm-scale particles.

		Seismic Facies	Interpretation	Outcrop example
Layered	Translational		Stratified less deformed unit which commonly exist as thin packages (< 100 m). In most cases the layered unit is crosscut by faults.	
Blocky	Extentional		Discrete components (meter- to hundreds of meter-sized possibly up to km-scale), with some degree of internal coherence and primary features and thus can be separated from the background lithologies (i.e.matrix)	
	Contractional			
	Hybrid(Over-print)			
Amorphous	Incomplete		Relatively fine-grained unsorted lithology of a mass transport deposit, which envelopes, injects and in most cases, sustains discrete slide elements ranging from km-scale slabs to mm-scale particles.	
	Complete			

Figure 10.9. Systematic comparison of the internal architecture of MTDs from outcrops

Implications of outcrop examples for understanding seal quality of MTDs

The relative degree of risk associated with MTD seals of the three main seismic classes of MTDs are discussed in this section considering a variety of geological circumstances (e.g range of layer geometries and connectivity in low N/G versus high N/G systems) as observed from outcrop. However, we first considered, two important factors from a seal quality perspective.

Firstly, the seal quality critically depends on N/G of the MTD. This is determined by the provenance or staging area of the mass-transport deposits. For example, a sand-rich MTD like the example from the Gordo Megabed Spain (Fig. 10. 11) would prove to be high risk seal compared to the mud-rich MTD of the Ross slide (Fig. 10. 10) whose thorough disaggregation renders any limited sand layers completely unconnected and hence would constitute a high quality seal. Slope derived MTDs will likely be mud rich because the slopes are commonly the site of predominantly mud deposition while shelf-edge derived MTDs or those involving basin floor sediments may be sand rich (Luente and Pini, 2003; Dykstra et al. 2011; Posamentier and Martisen 2011).
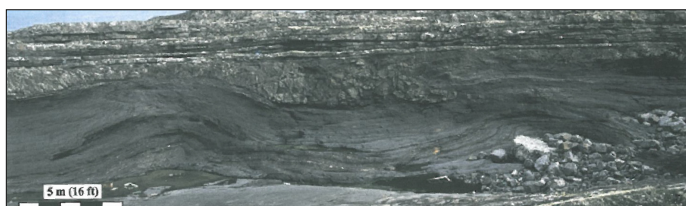

Figure 10.10. Mud-rich MTD from the Ross Slide, SE Ireland would constitute an excellent seal (from Lien et al., 2007).

Unit 2
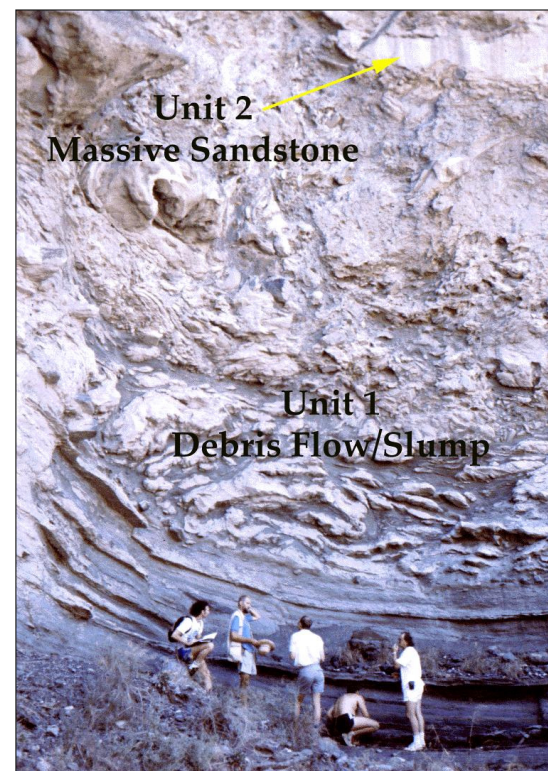Massive Sandstone

Unit 1
Debris Flow/Slump

Figure 10.11. Sand-rich MTD from the Gordo Megabed, SE Spain would constitute a poor seal (from Cossey, 2006).

Secondly, the incorporation of strata below the main detachment during MTD translation may be important in determining the seal characteristics of the MTD. Figure10. 12, illustrates a MTD incorporating a mangled channel levee which will eventually alter the initial composition of the MTD by incorporated substantial amounts of sand thus rendering the MTD high risk.
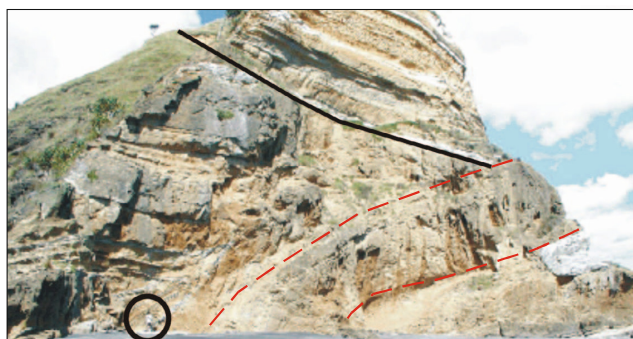

Figure 10.12. MTD incorporating a highly deformed channel/levee.

The layered facies does not represent high risk due to the semi-continuous and continuous beds within the MTD and the consequent lack of cross-stratal flow routes will engender this with good sealing potential (Fig. 10.9). However the presence of through-going faults transecting this unit might prove render the unit as high risk as evidenced in figure10.13. The seemingly tight fault zones are infilled with mineralised veins. In addition the sand-rich layered unit will represent high risk seal since leakage can occur via the pore network over geologic time.

Figure 10.13. Through going fault in a layered unit filled with mineralised vein This provides evidence that these seemingly tight faults can be migration paths through an otherwise flat sealing unit.

The seal risk associated with the extensional blocky facies would depend on the preservation of the original stratigraphy of a remnant block, height of block and the presence of internal or fault bounded fault as opposed to the variability in net-to-gross values (Fig. 10.9). However, the extensional blocky units will become high seal risk with an increased net-to-gross because possible migration pathway might occur via permeable beds without any faulting.

In reality, most of the normal faults that define the extensional blocky class will not represent a threat to the integrity of the seal because any significant vertical stress would generally keep the low angle fault surfaces tightly closed to fluid flow with a commensurately low static vertical permeability. Therefore, only dilation under high pore fluid pressure (probably from the underlying reservoir) would open them up and increase permeability along the fault zone, and this would be a mechanical seal failure involving reactivation.

The seal risk associated with the folded structures comprising the contractional blocky unit probably mainly depends on the extent and character of numerous sub seismic faults and fractures on the crest of folds which could possibly act to connect permeable sandy carrier beds of the fold limbs. However this leakage mechanism requires that the sub-seismic faults do not form clay smear or cataclastic seals against the leaky strata (Ingram & Urai, 1999). Evidence for leakage through crestal faults is visible in outcrops example (Fig. 10.14) and it is thought that the carbonate concretions aligned parallel to the axis of a recumbent fold indicated persistent migration of formation fluids (Sporli & Rowland, 2007).

Figure 10.14. Can folds be leaky? Here we see a another 3D exposure of recumbent fold with consistent bed thickness. However, through the hinge of the fold there is no ductile deformation rather we see carbonate concretions aligned parallel to the fold axis on the left side of the fold possibly indicating persistent leakage of formation fluids (from Sporli and Rowland, 2007).

The seal risk associated with the thrusted structures in the contractional blocky facies will be the headwall dipping thrust faults that might act as migration conduit for hydrocarbon. Just like in the extensional blocky facies, these thrust faults are expected to be closed because confining stress but would probably dilate under high pore fluid pressure, thus acting as a conduit for leakage. In addition, thrusted units sometimes comprise a succession of thrusted, deep-water turbidite deposits that have largely remained intact extending from the basal surface to the upper surface of MTDs (Fig. 10.15). From a seal perspective, such mass-transport deposits, characterized strong stratigraphic continuity form base to top, would constitute relatively poor seals as leakage can occur via permeable beds.
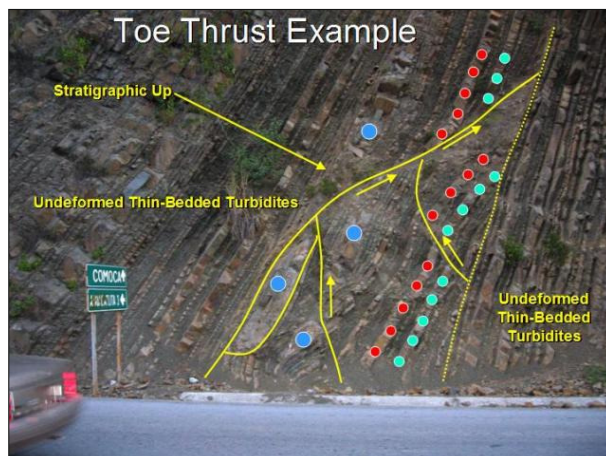
Figure. 10.15. Stratigraphic continuity preserved in a toe thrust comprising of deep-water turbidite deposits. These beds might extend from the base to the top of the MTD and as such constitute poor seal (from Cossey, 2011).

The seal risks associated with the amorphous unit mainly depend on N/G and connectivity of the highly mobilised sediments (e.g isolated blocks).

In cases where the amorphous unit is mud-rich (Figs. 10.7 and 10.10), high capillary entry pressure layers overly the sealing surfaces, thus the fluid transmissibility of the contacts will be very low and stratigraphically assisted trapping of hydrocarbons is possible. Many muddy debrites are described from ODP boreholes penetrating this seismic facies class (see CAPROCKS MTD Database). These often have a higher density than the neighbouring units of undeformed clay, implying loss of water during mobilisation and consequent strengthening of the remoulded clay fabrics.

However with an increased N/G the amorphous unit will represent high risk (e.g Fig. 10.8A) since it is more likely that any sandy units will be connected with relatively high permeabilities of the matrix components.

Furthermore, the seal risk associated with the incomplete amorphous unit may be fluid migration pathways provided by connections between sandy units via the thinly bedded sand and silts or faults existing in isolated blocks within the unit.

Based on outcrop observation of MTDs a seal risk diagram for the proposed MTD classes has been created(Fig. 10.16). Given a low N/G system, the blocky unit will constitute the highest seal risk. However, as N/G increases, all three classes of MTD will constitute high risk seals.
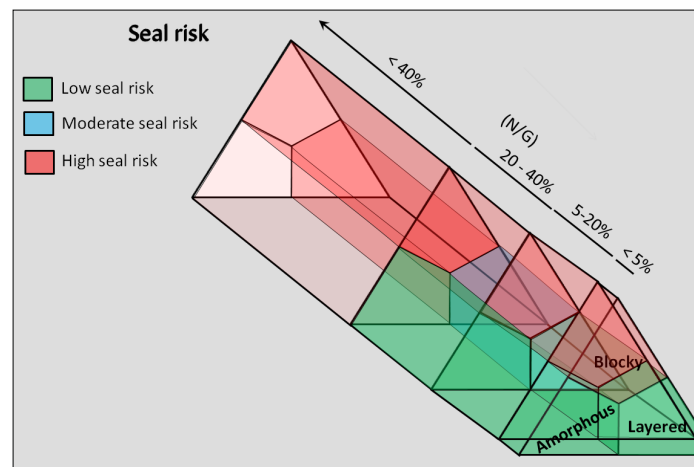

Figure. 10.16. A ternary seal risk diagram for MTDs.

Conclusion

1. Features that physically compromise sealing lithologies within MTDs, i.e., faults and sand beds are first order risks and should be incorporated into any risk assessment.

2. Detailed outcrop study of MTDs coupled with accurate subsurface mapping is the approach that will result in the most accurate risk characterization. This requires both detailed mapping and prediction of the stratigraphic and structural geometry of MTDs.

References

Alsop, G.I., Marco, S. 2012. A large-scale radial pattern of seismogenic slumping towards the Dead Sea Basin, Journal of the Geological Society v.169; p99-110.

Cossey Stephen P. J., 2006, Photos from our fieldwork. http://www.cosseygeo.com/images/gallery/folder/Tabernas

Cossey Stephen P. J., 2011, Mass transport deposits in the Upper Paleocene Chicontepec Formation, Mexico, in: Shipp C. R., Weimer P., Posamentier H. W., (eds)Mass-Transport Deposits in Deepwater Settings. Society for Sedimentary Geology (SEPM) Special Publication No. 96, p. 269–277.

Edwards, M., 1976, Growth faults in upper Triassic deltaic sediments, Svalbard: American Association of Petroleum Geologists, Bulletin, v.60, p. 341–355.

Dykstra M., Garyfalou K., Kertznus V., Kneller B., Milana J. P., Molinaro M., Szuman M., Thompson P., 2011, Mass transport Deposits: Combining Outcrops and Seismic Forward Modelling to understand Lithofacies Distributions, Deformation and their Seismic Stratigraphic Expression, in: Shipp C. R., Weimer P., Posamentier H. W., (eds)Mass-Transport Deposits in Deepwater Settings. Society for Sedimentary Geology (SEPM) Special Publication No. 96, p. 293–310.

Ingram, G.M. and Urai J.L. 1999. Top-seal leakage through faults and fractures; the role of mudrock properties, in: Aplin A. C., Fleet A., J., & Macquaker J. H. S., (eds) Muds and Mudstones: Physical and Fluid flow Properties. Geological Society Special Publications, v. 158, p. 125-135.

Lien T., Martinsen O. J., Walker R., 2007, An Overview of the Ross Formation, Shannon Nasin, Western Ireland, in Nilsen, T.H., Shew, R.D., Steffens, G.S., and Studlick, J.R.J. eds., Atlas of Deep-Water Outcrops: American Association of Petroleum Geologists, Studies in Geology 56, Ch. 49, p. 192–195.

Lucente, C.C., Pini, G.A., 2003. Anatomy and emplacement mechanism of a large submarine slide within the Miocene foredeep in the Northern Apennines, Italy: A field perspective. American Journal of Science 303, 565–602.

Posamentier H. W., Walker R. G. 2006 Deep-Water Turbidites and Submarine Fans , in: Posamentier H. W., Walker R. G. (eds) Facies Models Revisted, SEPM Special Publication No. 84, 2006 p. 397–520.

Posamentier H. W., Martinsen O. J., 2011, The Character and Genesis of Submarine Mass Transport Deposits: Insights from Outcrop and 3D Seismic Data, in: Shipp C. R., Weimer P., Posamentier H. W., (eds)Mass-Transport Deposits in Deepwater Settings. Society for Sedimentary Geology (SEPM) Special Publication No. 96, p. 7–38.

Sporli K. B., Rowland J. V. (2007). Superposed deformation in turbidites and syn-sedimentary slides of the tectonicallyactive Miocene Waitemata Basin, northern New Zealand. Basin Research 19, 199–216.